Springer Series in Materials Science 229

Michael J. Serpe
Youngjong Kang
Qiang Matthew Zhang *Editors*

Photonic Materials for Sensing, Biosensing and Display Devices

Springer

Springer Series in Materials Science

Volume 229

The Springer Series in Materials Science covers the complete spectrum of materials physics, including fundamental principles, physical properties, materials theory and design. Recognizing the increasing importance of materials science in future device technologies, the book titles in this series reflect the state-of-the-art in understanding and controlling the structure and properties of all important classes of materials.

More information about this series at http://www.springer.com/series/856

Michael J. Serpe · Youngjong Kang
Qiang Matthew Zhang
Editors

Photonic Materials for Sensing, Biosensing and Display Devices

Springer

Editors
Michael J. Serpe
Department of Chemistry
University of Alberta
Edmonton, AB
Canada

Qiang Matthew Zhang
Department of Chemistry
University of Alberta
Edmonton, AB
Canada

Youngjong Kang
Hanyang University
Seoul
Korea, Republic of (South Korea)

ISSN 0933-033X ISSN 2196-2812 (electronic)
Springer Series in Materials Science
ISBN 978-3-319-24988-9 ISBN 978-3-319-24990-2 (eBook)
DOI 10.1007/978-3-319-24990-2

Library of Congress Control Number: 2015955887

Springer Cham Heidelberg New York Dordrecht London

Printed on acid-free paper

Springer International Publishing AG Switzerland is part of Springer Science+Business Media (www.springer.com)

Preface

For many hundreds of years, photonic materials have captured the attention of researchers, philosophers, and the general public alike. Initially, this was due to the bright and vivid colors that the materials exhibit. For example, the beautiful colors of butterfly wings, many beetles, and the opal gemstone are a result of the way light interacts with the material's structure—all of these examples can be considered photonic materials. Furthermore, many nanoparticles (such as Au and Ag) can absorb specific wavelengths of light as a result of surface plasmon resonance—this phenomenon is responsible for the color of many old pieces of stained glass and many other works of art. Nowadays, the focus of photonic materials has shifted from their beauty to their application.

Important applications of photonic materials include sensing, biosensing, and display devices—these topics are all detailed in this volume. There are a number of examples that clearly illustrate how the structure of a material can interact with light to yield color (and other unique optical properties). One very well-known class of such materials are called colloidal crystalline arrays made by packing colloidal particles in an ordered fashion (typically hexagonal close packed) into a volume. The ordered arrangement of the colloidal particles interacts with light to reflect specific light wavelengths, oftentimes yielding color. Many have embedded these ordered particle arrays into responsive polymer matrices, which can change the lattice spacing of the colloidal crystalline array, to yield a change in the material color (and optical properties). These materials have been exploited to sense species of interest in their environment and for display devices. Layered and other structured materials have also been developed to yield materials with bright colors and unique optical properties. For example, layering responsive polymers one on top of another, or embedding a responsive polymer layer between two thin reflective layers, can also yield properties akin to colloidal crystalline arrays. Diffraction gratings can also be made into holographic materials, and exploited for sensing applications. Other well-known plasmonic effects have been used extensively for sensing applications, e.g., the surface plasmon resonance effect that is found with certain metals and metal-based nanoparticles (e.g., Au and Ag). This plasmonic

effect leads to solution color, which can be manipulated by changing the distance between the particles. Systems have been constructed that exploit this distance-dependent solution color for sensing and biosensing. Relatedly, microcavities and fiber optics can be combined with the plasmonic effects found in metal films and particles, to yield sensors with very high sensitivity and low detection limits. Leaders in these respective areas have submitted to this volume, which is meant to showcase the breadth of the field and the promise it holds.

Editing this book required extensive work by our respective groups to aid in the organization and review of the chapters. We owe a great deal of gratitude to Dr. Claus Ascheron for allowing us the opportunity to edit this volume, and for his assistance along the way. We also thank Ms. Adelheid Duhm for her assistance with completing this volume.

Canada — Michael J. Serpe
Korea, Republic of (South Korea) — Youngjong Kang
Canada — Qiang Matthew Zhang

Contents

Contributors

Eliathamby Ambikairajah School of Electrical Engineering and Telecommunications, UNSW, Kensington, Australia

Hussein Awala LCS, 7CRISMAT, University of Caen, Caen Cedex, France

Chinna Bathula Department of Chemistry, Research Institute for Natural Sciences, Hanyang University, Seoul, South Korea; Institute of Nano Science and Technology, Hanyang University, Seoul, South Korea

Kishore Bhowmik School of Electrical Engineering and Telecommunications, UNSW, Kensington, Australia

Haider Butt School of Mechanical Engineering, University of Birmingham, Birmingham, UK

Dervil Cody Centre for Industrial and Engineering Optics, School of Physics, College of Sciences and Health, Dublin Institute of Technology, Dublin 8, Ireland

Jiaqi Duan Department of Chemistry, University of Alberta, Edmonton, AB, Canada

A. François Institute for Photonics and Advanced Sensing, ARC Centre of Excellence for Nanoscale BioPhotonics, School of Physical Sciences, The University of Adelaide, Adelaide, SA, Australia

Jianping Ge School of Chemistry and Molecular Engineering, Shanghai Key Laboratory of Green Chemistry and Chemical Processes, East China Normal University, Shanghai, People's Republic of China

Siyuan Guo Department of Chemistry, University of Alberta, Edmonton, AB, Canada

Jinho Hyon Department of Chemistry, Research Institute for Natural Sciences, Hanyang University, Seoul, South Korea; Institute of Nano Science and Technology, Hanyang University, Seoul, South Korea

Chao Jing Key Laboratory for Advanced Materials, East China University of Science and Technology, Shanghai, People's Republic of China

Youngjong Kang Department of Chemistry, Research Institute for Natural Sciences, Hanyang University, Seoul, South Korea; Institute of Nano Science and Technology, Hanyang University, Seoul, South Korea

Shin-Hyun Kim Department of Chemical and Biomolecular Engineering, KAIST, Daejeon, Korea

Mark A. Lifson Department of Biomedical Engineering, University of Rochester, Rochester, NY, USA; Department of Dermatology, University of Rochester, Rochester, NY, USA

Wendong Liu State Key Laboratory of Supramolecular Structure and Materials, International Joint Research Laboratory of Nano-Micro Architecture Chemistry, College of Chemistry, Jilin University, Changchun, People's Republic of China

Xueyao Liu State Key Laboratory of Supramolecular Structure and Materials, International Joint Research Laboratory of Nano-Micro Architecture Chemistry, College of Chemistry, Jilin University, Changchun, People's Republic of China

Yi-Tao Long Key Laboratory for Advanced Materials, East China University of Science and Technology, Shanghai, People's Republic of China

Suzanne Martin Centre for Industrial and Engineering Optics, School of Physics, College of Sciences and Health, Dublin Institute of Technology, Dublin 8, Ireland

Juan Leonardo Martinez-Hurtado Department of Chemical Engineering and Biotechnology, University of Cambridge, Cambridge, UK

A. Meldrum Department of Physics, University of Alberta, Edmonton, AB, Canada

Emilia Mihaylova Centre for Industrial and Engineering Optics, School of Physics, College of Sciences and Health, Dublin Institute of Technology, Dublin 8, Ireland; Department of Mathematics, Informatics and Physics, Agricultural University, Plovdiv, Bulgaria

Tatsiana Mikulchyk Centre for Industrial and Engineering Optics, School of Physics, College of Sciences and Health, Dublin Institute of Technology, Dublin 8, Ireland

Benjamin L. Miller Department of Biomedical Engineering, University of Rochester, Rochester, NY, USA; Department of Dermatology, University of Rochester, Rochester, NY, USA

Svetlana Mintova LCS, 7CRISMAT, University of Caen, Caen Cedex, France

Izabela Naydenova Centre for Industrial and Engineering Optics, School of Physics, College of Sciences and Health, Dublin Institute of Technology, Dublin 8, Ireland

Gang-Ding Peng School of Electrical Engineering and Telecommunications, UNSW, Kensington, Australia

Ginu Rajan School of Electrical, Computer and Telecommunications Engineering, University of Wollongong, Wollongong, Australia; School of Electrical Engineering and Telecommunications, UNSW, Kensington, Australia

Chunhee Seo Department of Chemistry, Research Institute for Natural Sciences, Hanyang University, Seoul, South Korea; Institute of Nano Science and Technology, Hanyang University, Seoul, South Korea

Michael J. Serpe Department of Chemistry, University of Alberta, Edmonton, AB, Canada

Yukikazu Takeoka Department of Molecular Design and Engineering, Nagoya University, Nagoya, Japan

Bai Yang State Key Laboratory of Supramolecular Structure and Materials, International Joint Research Laboratory of Nano-Micro Architecture Chemistry, College of Chemistry, Jilin University, Changchun, People's Republic of China

Siyun Ye School of Chemistry and Molecular Engineering, Shanghai Key Laboratory of Green Chemistry and Chemical Processes, East China Normal University, Shanghai, People's Republic of China

Ali Kemal Yetisen Harvard Medical School and Wellman Center for Photomedicine, Massachusetts General Hospital, Boston, MA, USA

Gi-Ra Yi Department of Chemical Engineering, SKKU, Suwon, Korea

Seok Hyun Yun Harvard Medical School and Wellman Center for Photomedicine, Massachusetts General Hospital, Boston, MA, USA

Monika Zawadzka Centre for Industrial and Engineering Optics, School of Physics, College of Sciences and Health, Dublin Institute of Technology, Dublin 8, Ireland

Qiang Matthew Zhang Department of Chemistry, University of Alberta, Edmonton, AB, Canada

Y. Zhi State Key Laboratory for Mesoscopic Physics and School of Physics, Peking University, Beijing, People's Republic of China

Chapter 1
Ordered Responsive Materials for Sensing Applications

Qiang Matthew Zhang, Siyuan Guo, Jiaqi Duan and Michael J. Serpe

Abstract Detection of small molecules, macromolecules, and biomolecules is of utmost importance for protecting human health and ensuring our well-being. Therefore, a tremendous amount of research goes into the development of novel sensing motifs with increased sensitivity and selectivity to analytes, with very short analysis times, and ease of usability. Of these technologies, 1D, 2D and 3D ordered materials receive a lot of attention due to low cost and visual color change in presence of analytes. These materials were composed of a close packed array of particles or nanocavities, which are capable of interacting with wavelengths of light in the visible region. These interactions lead to constructive and destructive interference of the light in the assembly, resulting in specific wavelengths of light being reflected. Analytes cause shrinking or swelling of these materials and a concomitant change in the critical dimensions of the materials optical components, yielding color changes. This is very convenient, as the naked eye can be used as the "detector". In this review, we cover many examples of 1D, 2D and 3D ordered materials for sensing applications, ending with examples of other significant sensing technologies.

1.1 Introduction

The beautiful and vivid colors of many objects found in nature (e.g., beetles, butterflies, and the opal gemstone) have fascinated many for ages. Unlike many other colored materials found in nature, which exhibit color due to the absorbance of light by small molecule chromophores, the examples above exhibit color as a result of light interacting with components of the material's structure and resulting constructive and destructive interference. For example, opal gemstones are composed of an ordered

Q. M. Zhang · S. Guo · J. Duan · M. J. Serpe (✉)
Department of Chemistry, University of Alberta, Edmonton, AB T6G 2G2, Canada
e-mail: michael.serpe@ualberta.ca

M. J. Serpe et al. (eds.), *Photonic Materials for Sensing, Biosensing and Display Devices*, Springer Series in Materials Science 229,
DOI 10.1007/978-3-319-24990-2_1

close packed array of particles (typically silica), which are capable of interacting with visible wavelengths of light (via reflection/refraction/diffraction), leading to constructive/destructive interference, and their brilliant visual colors [1]. More generally, when light impinges on a material with refractive index periodicity, it is reflected/refracted/diffracted from each of the structure's interfaces. This light, under suitable conditions, interferes constructively/destructively and reflects/transmits certain wavelengths of light according to the well-known Bragg equation, modified for photonic crystals, as given [2–5]:

$$m\lambda = 2nd \sin\theta \tag{1.1}$$

where m is the diffraction order, λ is the wavelength of the reflected light, n is the mean refractive index of the periodic structure, d is the lattice period of the crystalline direction of propagation of light, and θ is the angle between the incident light and diffraction crystal planes.

Structured photonic materials can be classified as one-dimensional (1D), two-dimensional (2D), or three-dimensional (3D), depending on if the periodicity of their structure is in 1D, 2D, or 3D, respectively. Structured photonic materials play an important role in telecommunications [6], information processing and storage [7], solar cells [8], and other important applications [9]. Furthermore, chemical and biological sensors with visual color readouts can be developed by combining photonic materials with stimuli-responsive materials that change conformation in response to external stimuli such as pH [10, 11], ionic strength [12], solvent [13], vapors [14], temperature [15], and light [16]. In this review, we highlight the most relevant examples of structured photonic materials (photonic crystals) and devices for sensing applications. The general approach is based on the ability of species of interest (analyte) to induce changes in the spacing and/or refractive index of the structural elements of the devices [17, 18]. These changes together lead to observable optical property changes, i.e., color changes. Compared with complicated analytical instruments that can be used for sensing, structured photonic materials exhibit many advantages as sensors including: their low cost, ease of signal readout (a visual color change), and simple operation.

1.2 One-Dimensional Ordered Materials

In recent years, due to the development of simple bottom-up techniques, various functional one-dimensional ordered materials (1DOMs) were fabricated [19]. 1DOMs are typically layered structures, the layers being composed of materials with different refractive indices. One of the most common examples of 1DOMs is a Bragg stack typically used for light filtering applications. 1DOMs can also be fabricated from materials that are sensitive to their environment, i.e., they change dimensions as a function of the environmental conditions. These materials exhibit the very interesting and useful ability to change color; the color can be indicative of

their surroundings. Recently, a variety of materials have been used to prepare functional and responsive 1DOMs such as inorganic materials [20], organic/inorganic hybrid materials [21], and polymer or organic materials [22].

In one example, SiO_2/TiO_2 1DOMs were prepared by alternatively exposing a surface (glass or silicon) to solutions of $Si(OEt)_4$ and $TiCl_4$ via dip-coating, followed by curing/solidification of the layers via controlled thermal treatments to form SiO_2/TiO_2 layers [20]. As can be seen in Fig. 1.1, alternate deposition of two types of mesoporous layers (presenting different framework composition and/or porosity) gives rise to the desired one-dimensional periodicity in the z-dimension. The sequence of deposition and treatments is essential to obtain ordered 1DOMs with substantial porosity. After thermal treatment, the pore structures are interconnected with neighboring pores, resulting in the accessibility and transport of host molecules. The authors then used the devices for sensing applications, using them to detect dihexadecyl phosphate (DHDP), which selectively binds to the

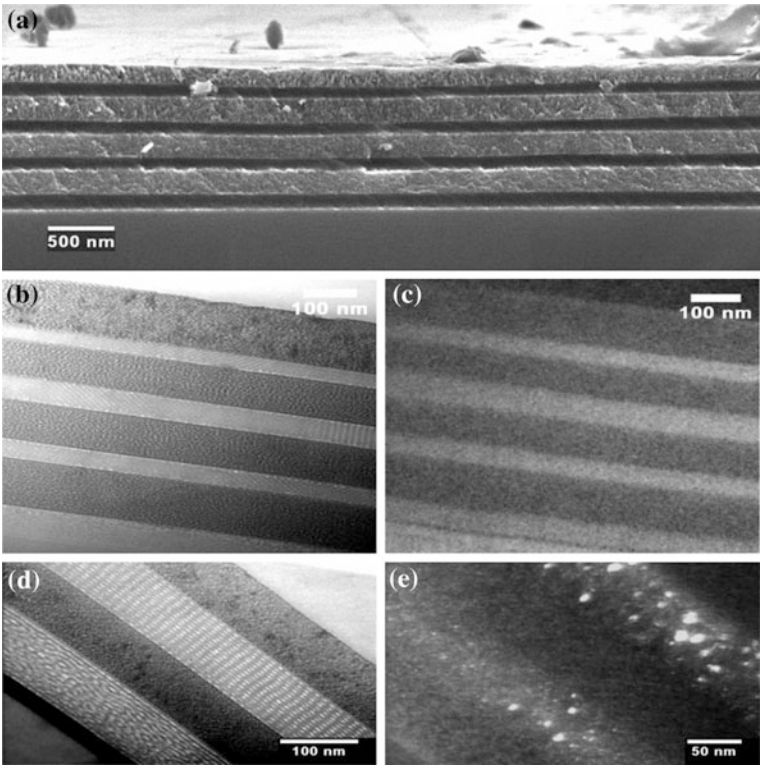

Fig. 1.1 Electron microscopy images of mesoporous Bragg multilayers. **a** FESEM, **b** TEM, and **c** energy-filtered mapping analysis of an 8-layered Bragg reflector, 4 × (SF–TF); *dark grey* Ti, *light grey* Si. **d** TEM of a 2 × (SF–TB) multilayer (see the experimental section for terminology), showing two ordered mesophases with different pore size. **e** Dark-field image of sample presented in (**d**); crystalline anatase domains are observed as *bright spots*. Reproduced with permission [20]

titania sites. Once DHDP enters the ordered mesopores of the material, it increases the refractive index of the titania layer. That leads to a dramatic change in the device's optical properties, as shown in Fig. 1.2.

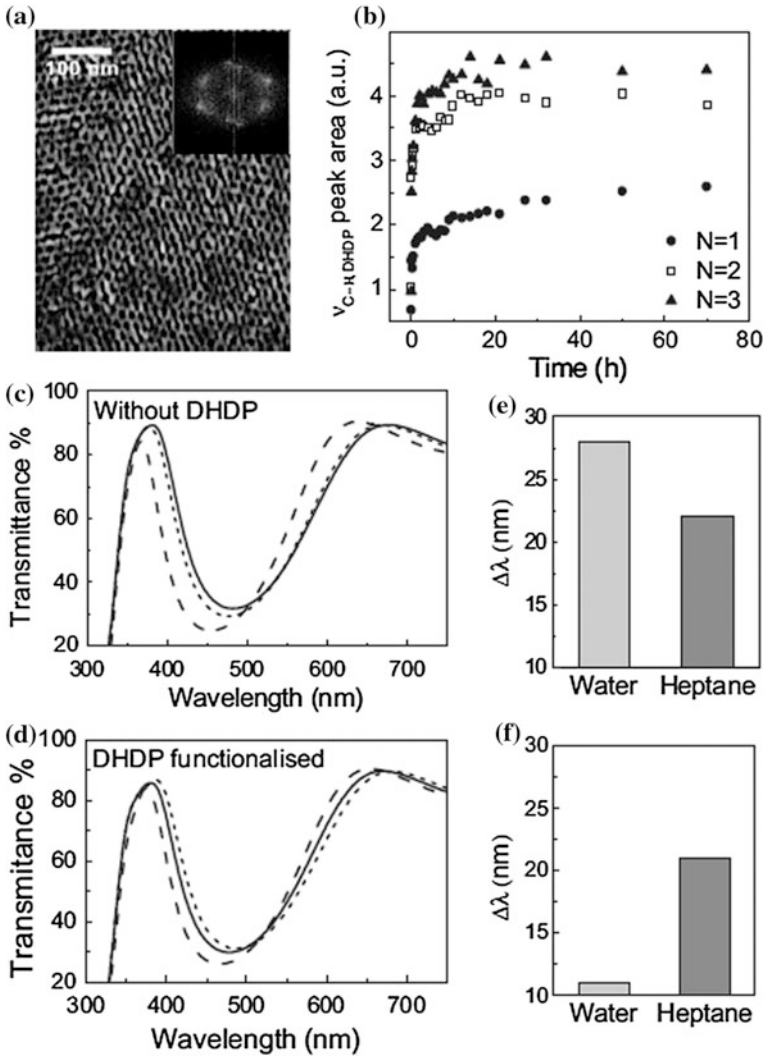

Fig. 1.2 Analysis of accessibility and the effect of functionalization on the optical response. **a** FESEM top view of the most external layer of a 4 × (SF–TF) multilayer showing the presence of ordered open pores on its surface. The *inset* corresponds to the Fourier transform of the image. **b** Kinetics of DHDP molecule uptake for multilayers of the same composition possessing a different number of layers. **c** Transmission spectra of 3 × (SF–TB) pristine stack (*dashed line*); same multilayer after immersion in water (*solid line*), and heptane (*dotted line*). **d** Same optical measurements for a DHDP-functionalized mesoporous 3 × (SF–TB) stack. **e**, **f** Bar graph showing the different Bragg diffraction shifts obtained for the pristine and DHDP-functionalized mesoporous multilayers shown in (**c**, **d**). Reproduced with permission [20]

In another example, an organic/inorganic hybrid 1DOM was prepared by alternate deposition of titania sol and poly(2-hydroxyethylmethacrylate-co-glycidyl methacrylate) (PHEMA-co-PGMA) films via spin coating (Fig. 1.3) [23]. Their optical properties were tuned by changing the number, and thickness, of the layers. By changing the spacing and/or the refractive index of the layers, the devices can interact with the entire visible spectral range. Due to the interaction of PHEMA-co-PGMA with water vapor, the 1DOMs can be used as a sensor for environmental humidity, changing color over the full spectral range as humidity is varied (Fig. 1.4). Specifically, at high humidity the color of the 1DOM was red, which changes to blue at low humidity. It was shown that this behavior could be repeated more than 100 times (Fig. 1.4).

Polymeric 1DOMs can also be fabricated using polyelectrolyte multilayers with alternating porosities, i.e., porous and less porous materials [24]. Layers were prepared via assembly of poly(acrylic acid) (PAA), poly(allylamine hydrochloride) (PAH), and poly(sodium 4-styrenesulfonate) (SPS) in specific combinations, which exhibit reflectivity bands in the visible region of the spectrum. This system was used to detect various solvent vapors, and the data is shown in Fig. 1.5. The change in the device's optical properties upon exposure to the various vapors is a result of selective solvation of the layers, leading to swelling/deswelling of the assembly, and the concomitant optical response (both a wavelength shift and a change in transmitted light intensity). As can be seen in Fig. 1.5, exposing the devices to saturated vapors of either water, ethanol, acetone, or toluene, yields a decrease in the reflectivity of the devices, and a shift of the transmitted peak to longer wavelengths.

Another class of 1DOMs was prepared via self-assembly of block copolymers into lamellar stacks, which consist of alternating layers of nonswellable glassy layers and swellable gel layers. The swelling of gel layers by some solvents can cause an increase in the distance between the glassy layers, and a change of the layer's

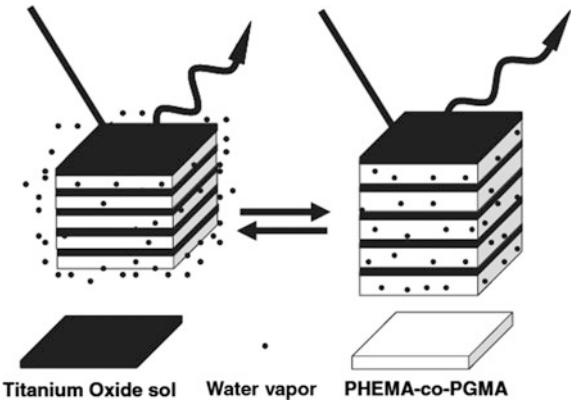

Fig. 1.3 Schematic of organic/inorganic hybrid 1DOMs generated by alternated spin-coating of titania sol and PHEMA-co-PGMA. Reproduced with permission [23]

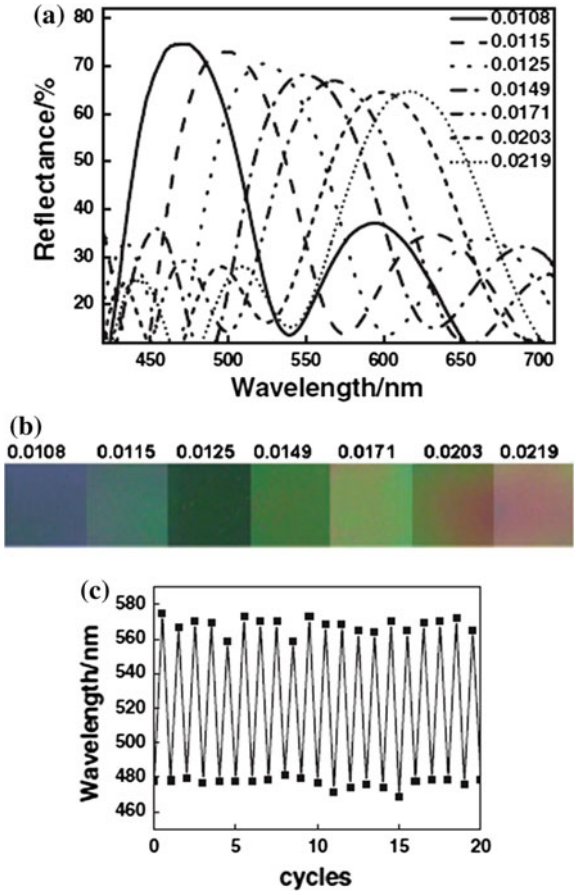

Fig. 1.4 **a** Sensitivity of the 1DOMs towards water vapor; **b** color variation of the 1DOMs with water-vapor concentration; **c** swelling–deswelling cycles of the 1DOMs with water-vapor concentration at 0.0177. The total number of layers is ten. Reproduced with permission [23]

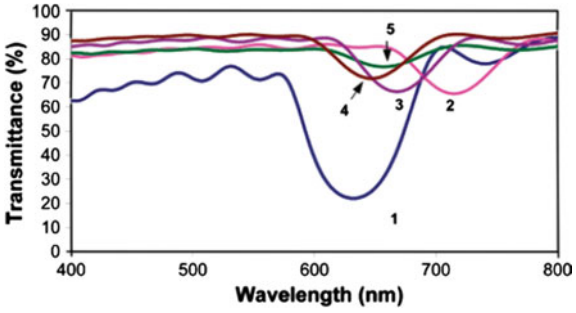

Fig. 1.5 Transmittance spectra of a treated $[(PAH/PAA)_8–(PAH/SPS)_{50}]_9$ film in air (*1*) and after exposure to water (*2*), ethanol (*3*), acetone (*4*), and toluene (*5*) vapors. Reproduced with permission [24]

refractive index, which results in strong reflectivity change and a shift of the stop-band position to longer wavelengths (Fig. 1.6) [22]. The block copolymer can be quaternized using iodomethane, which was used as a colorimetric humidity sensor.

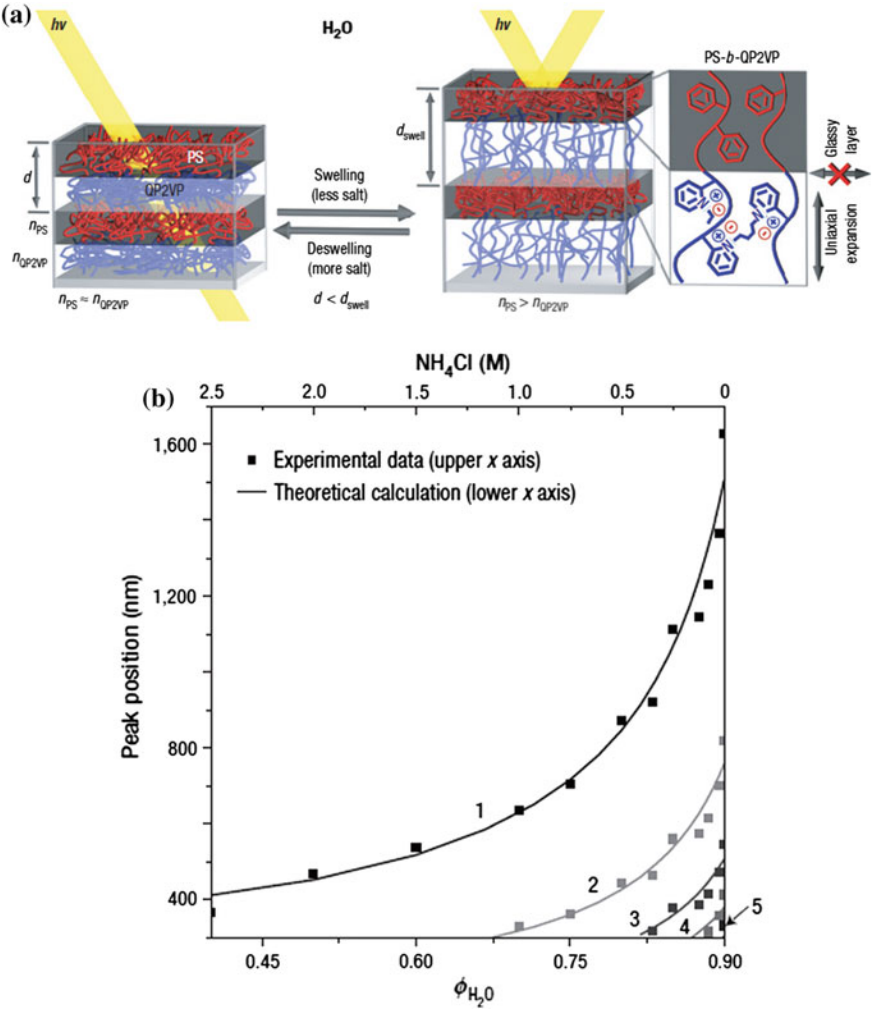

Fig. 1.6 **a** Schematic diagram of the structure of photonic gel film and the tuning mechanism. The photonic gel film was prepared by self-assembly of a diblock copolymer (PS-b-QP2VP). Swelling/deswelling of the QP2VP gel layers (*blue*) by aqueous solvents modulates both the domain spacing and the refractive-index contrast, and accordingly shifts the wavelengths of light reflected by the stop band. The hydrophobic and glassy polystyrene layers (*red*) limit expansion of the gel layers to the direction normal to the layers. **b** The change of stop-band position by approximately 575 % from 364 to 1627 nm as a function of the NH_4Cl concentration (*symbols*), or versus ϕ_{H_2O} (*solid line*) for each band. Reproduced with permission [22] (Color figure online)

Its sensitivity and dynamic range can be modulated by varying the pyridinium's counter ion or by varying the molecular weight of the block copolymers [25].

The Serpe group recently showed that layered poly(N-isopropylacrylamide) (pNIPAm) microgel-based materials could be used to sense pH, glucose, proteins and DNA [26–33]. These devices were constructed by "painting" responsive microgels onto an Au coated glass substrate [27]. Following further treatment, another Au layer was deposited onto the microgel layer. As can be seen in Fig. 1.7, [29] this yields a mirror-dielectric-mirror structure akin to a classic Fabry–Perot etalon. When the device is immersed in water, the microgels swell and separate the Au layers from one another. Light impinging on the structure can enter the microgel-based cavity and resonate between the two Au layers, which results in specific wavelengths of light being reflected/transmitted according to the following equation:

$$m\lambda = 2nd\cos\theta \tag{1.2}$$

where λ is the wavelength maximum of the peak(s), m is the peak order, n is the refractive index of the dielectric, d is the spacing between the mirrors, and θ is the angle of incidence [26]. A reflectance spectrum from a representative etalon can be seen in Fig. 1.7.

Many functional groups, such as carboxylic acid, amine, and boronic acid groups, were incorporated into the microgels. In one example, carboxylic acid groups were deprotonated at high pH, which led to microgel swelling due to Coulombic repulsion in the microgel network, as well as osmotic swelling [29]. The swelling of the microgels increased the distance between the mirrors, which leads to a change of the visible color of the devices, and a red shift in the position of the peaks in the device reflectance spectrum. The optical properties of spatially isolated regions of a single etalon can be changed independently in response to pH, as can be seen in Fig. 1.8 [29].

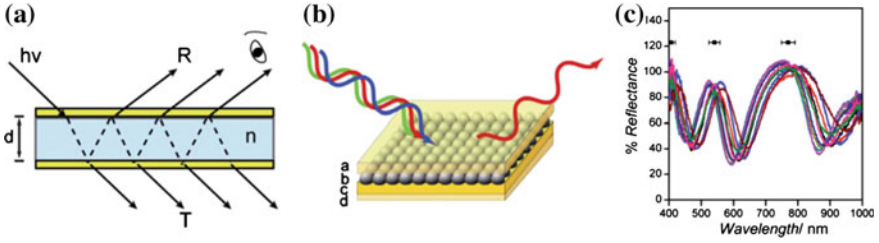

Fig. 1.7 **a** Schematic of a traditional Fabry-Perot etalon (d, distance between two mirrors; n, refractive index of the dielectric). **b** Schematic structure and proposed mechanism for our poly (N-isopropylacrylamide) microgel based etalons fabricated by sandwiching (**b**) a microgel layer between (**a**, **c**) two reflective Cr/Au surfaces, all on **d** a cover glass. **c** Reflectance spectra for an etalon immersed in pH 3.0 solution at 25 °C at 10 randomly chosen regions. The data points above each peak are the average peak positions and associated standard deviations for the respective peaks in the 10 individual spectra. Reproduced with permission [29]

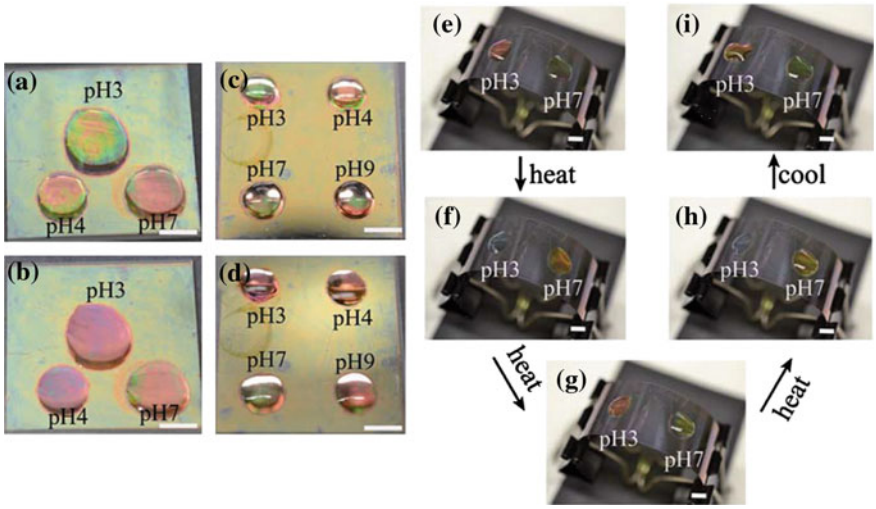

Fig. 1.8 Photographs of an etalon with solutions of various pH spotted on a single surface (**a**, **c**, **e**, **i**) 25 °C and (**b**, **d**, **f**, **g**, **h**) 37 °C. **f** 3 min after heating; **g** 5 min after heating; **h** 6 min after heating. In each panel, the scale bar is 5 mm. Reproduced with permission [29]

The devices were also used to sense glucose [34]. To accomplish this, microgels modified with 3-aminophenylboronic acid (APBA) were synthesized. In a basic buffer the boronic acid moieties on the APBA (pK_a = 8.2) were hydroxylated such that the boron possesses a negative charge (Fig. 1.9). The binding of glucose is favored for boronic acids in the charged state. As glucose binds, more boronic acid groups must convert to the charged state in order to maintain the equilibrium. In the presence of glucose, the bound state is preferred promoting more hydroxylation of the boron atoms into a charged form, leading to an increase in the Coulombic repulsion inside the microgel, which results in a swelling response. In the etalons this will be observed as a red shift, according to (1.1).

The Serpe group has also shown that etalons could be used for biosensing application [35]. In an early study, they showed that biotinylated polycationic polymer can penetrate through the Au overlayer of an etalon resulting in the collapse of a negatively charged microgel layer (due to electrostatics-mediated crosslinking), and a blue shift of the reflectance peaks. The extent of the peak shift depended on the amount of biotinylated polycation added to the etalon; high polycation concentration yielded a large shift, and vice versa. This phenomenon was exploited to sense the concentration of streptavidin in solution at μM concentrations, as detailed in Fig. 1.10. To accomplish this, the polycation, poly(allylaminehydrochloride) (PAH) was modified with biotin. Excess amounts of PAH–biotin were exposed to various amounts of streptavidin leaving behind specific amounts of unbound PAH–biotin—the amount of PAH–biotin unbound is inversely related to the streptavidin concentration. Biotin modified magnetic particles were added to the solution, which bound to the PAH–biotin-streptavidin complex, and an

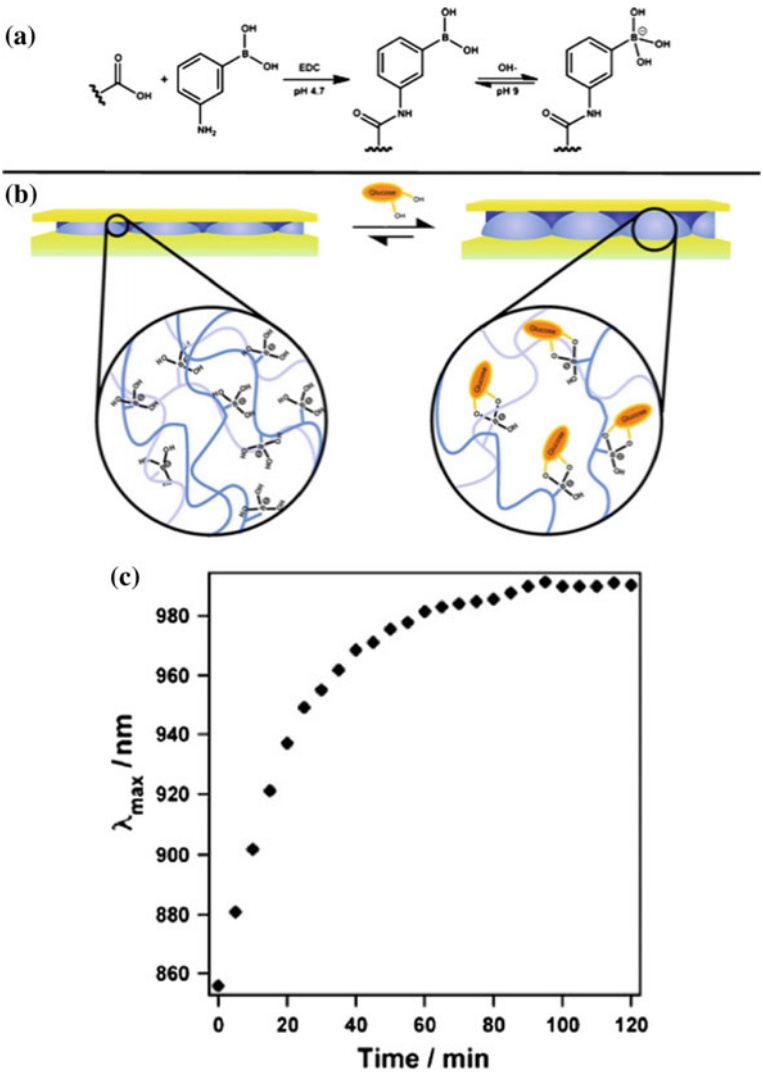

Fig. 1.9 Reaction scheme for **a** the functionalization of the acrylic acid moieties on the microgel with 3-aminophenylboronic acid (APBA) followed by the activation of the boronic acid with base, **b** a cartoon depiction of the glucose responsivity of an APBA functionalized microgel etalon at pH 9, **c** the peak position for the most red-shifted peak is plotted as a function of time after glucose introduction. Total spectral shift is 134 nm. Reproduced with permission [34]

external magnet was used to remove the magnetic particles bound with PAH–biotin-streptavidin from the solution. The solution containing the excess, unbound PAH–biotin was subsequently added to the pNIPAm-co-AAc etalon stabilized in pH 7.2 solution. The PAH–biotin was able to penetrate the etalon and crosslink the

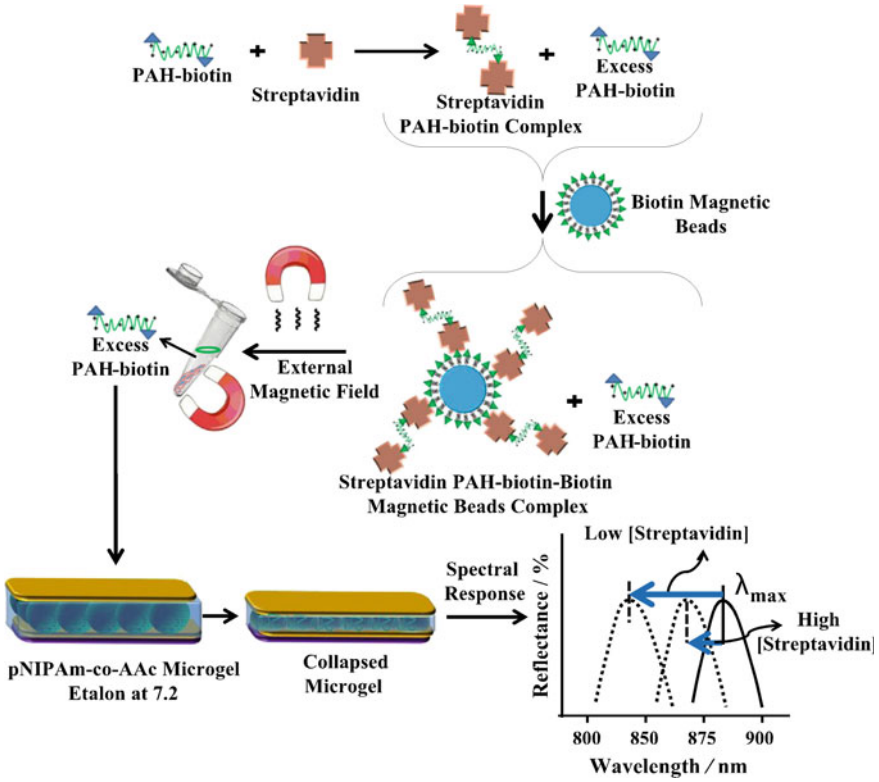

Fig. 1.10 Streptavidin (the analyte) is added to an excess amount of biotin-modified poly (allylamine hydrochloride) (PAH). The streptavidin–biotin–PAH complex is then removed from solution using biotin modified magnetic particles, leaving behind free, unbound PAH. The unbound PAH is subsequently added to a pNIPAm-co-AAc microgel-based etalon immersed in aqueous solution at a pH that renders both the microgel layer and the PAH charged. As a result, the etalo's spectral peaks shift in proportion to the amount of PAH–biotin that was added. This, in turn can be related back to the original amount of streptavidin added to the PAH–biotin. Reproduced with permission [35]

microgels, causing them to collapse resulting in a blue shift of the etalon's spectral peaks (Fig. 1.10). As can be seen, in this concentration range, the extent of the blue shift depends linearly on the amount of PAH–biotin added to the etalon, which can be easily related to the amount of streptavidin in initially added to the PAH–biotin. Etalons of this type are very interesting because unlike most biosensors, a large signal is obtained for low analyte concentration, as can be seen in Fig. 1.11 [35].

The Serpe group has also shown that etalons can be used to detect μM concentrations of target DNA in solutions [32]. This is a direct result of the polyanionic nature of DNA, and it's penetration into the microgel layer of etalons composed of positively charged microgels. Specifically, when the DNA interacts with the positively charged microgels, electrostatic crosslinking results, causing the microgel

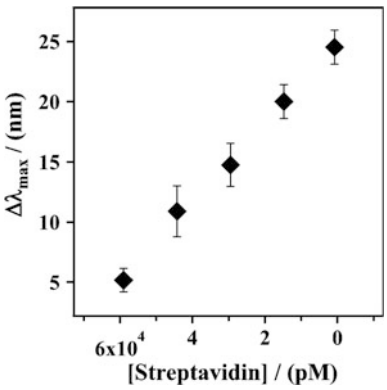

Fig. 1.11 Cumulative shift of the etalon's reflectance peak upon addition of the indicated amounts of streptavidin to PAH–biotin 100:1. The pNIPAm-co-AAc microgel-based etalon was soaked in pH 7.2 throughout the experiment, while the temperature was maintained at 25 °C. Each data point represents the average of at least three independent measurements, and the error bars are the standard deviation for those values. Reproduced with permission [35]

layer to collapse, leading to a shift in the position of the reflectance peaks to lower wavelength. The extent of shift can be related to the concentration of target DNA present in the sample solution, as shown in Fig. 1.12.

Recently, the Serpe group prepared etalons from lipase loaded microgels (also containing pyridine) that were capable of sensing triglyceride concentration [36]. The lipase inside of the microgels can degrade triglyceride into glycerinum and fatty acid, which could attach to the microgels by acid-base reaction with pyridine

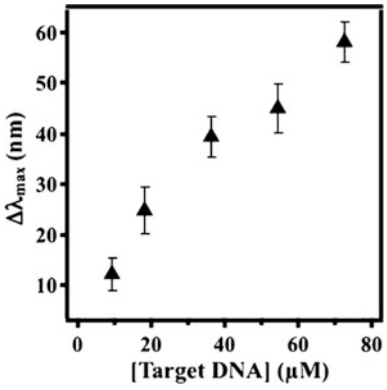

Fig. 1.12 Shift of a reflectance peak for a pNIPAm-co-APMAH etalon upon addition of separated TDNA solution of different concentrations. The pNIPAm-co-APMAH microgel-based etalon was soaked in pH 7.2 solution throughout the experiment, while the temperature was maintained at 25 °C. Each point in the plot represents the average of at least three independent measurements, and the error bars are standard deviation for those values. A new device was used for each experiment. Reproduced with permission [32]

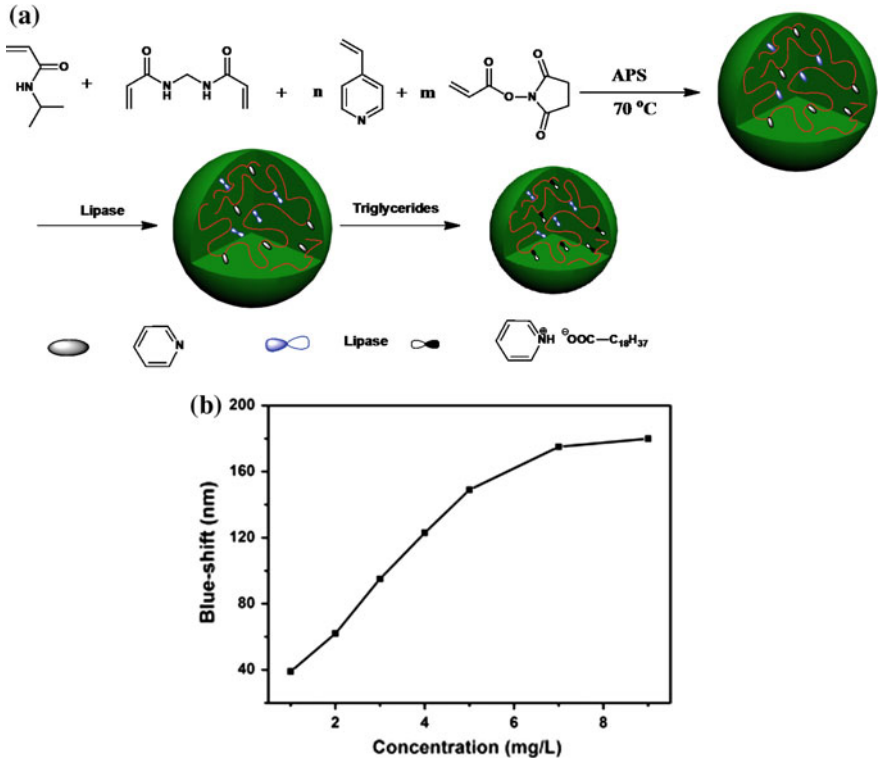

Fig. 1.13 **a** Microgel synthesis scheme; **b** blue-shift as function of triglyceride concentration. Reproduced with permission [36]

(Fig. 1.13). The introduction of fatty acid into microgels increased hydrophobicity of microgels, resulting in their collapse and a concomitant blue-shift in peaks of the reflectance spectrum. As can be seen in Fig. 1.13, the extent of the blue-shift depended on triglyceride concentration [36].

1.3 Two-Dimensional Ordered Materials

Two-dimensional ordered materials (2DOMs) possess structural periodicity in two spatial directions [37]. Generally, they are prepared using top-down methods such as photolithography, etching techniques and chemical methods [1]. Here, we mainly focus on 2DOMs prepared by chemical methods. 2DOMs diffract light at wavelengths that depend on their 2D array element spacing. These 2DOMs have been developed for the visual determination of pH, ionic strength, charged surfactants, and proteins in aqueous media [37].

Carbohydrate-functionalized 2DOMs were fabricated by attaching polystyrene (PS) particles onto a hydrogel surface (Fig. 1.14) [38]. Lectin–carbohydrate interactions create hydrogel crosslinks that collapse the hydrogel, which decreases the 2D particle spacing. This mannose containing 2D photonic crystal sensor detects Concanavalin A (Con A) through shifts in the 2D diffraction wavelength. Con A concentrations can be determined by measuring the diffracted wavelength or visually determined from the change in the observed visual color. Figure 1.15 shows the dependence of the diffraction wavelength maximum of the 2DOMs sensor as a function of the Con A concentration. In the absence of Con A, the 2D array diffraction maximum occurs at 600 nm. The diffraction wavelength blue shifts with increasing Con A concentrations; at 2 mg/mL, the diffraction blue shifts to 554 nm. The inset photograph in Fig. 1.15 clearly shows the visual color changes as a function of Con A concentration. Thus, Con A concentrations can be roughly determined by visually observing color changes of the sensor. The 2D photonic crystal sensors are completely reversible and can monitor Con A solution concentration changes. The detection limit for Con A was determined to be 0.02 mg/mL (0.7 μM).

A stimuli-responsive 2DOM made of a polyelectrolyte gel with an monolayer inverse opal structure was developed [39]. To prepare these 2DOMs, a monolayer of a PS colloids was first assembled into an ordered array on a glass or silicon substrate, onto which a solution of quaternized poly-(2-vinyl pyridine) (qP2VP) was spin-coated. The PS monolayer was then selectively removed by dissolution in toluene. Finally, a mechanically stable inverse opal 2DOMs was obtained after thermal crosslinking at 120 °C. Figure 1.16 shows the SEM images of a 2DOM prepared by using a monolayer of close packed PS spheres with 470 nm diameter. From the SEM images, it can be seen that a thin layer covers the void spaces, and

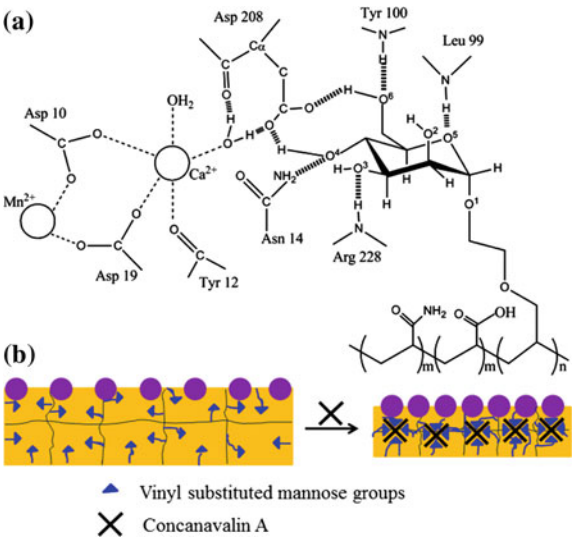

Fig. 1.14 Mechanism of **a** Con A attachment to mannose attached to hydrogel. **b** Shrinkage and particle spacing decrease in Man-1 hydrogel sensor that results from Con A binding. Reproduced with permission [38]

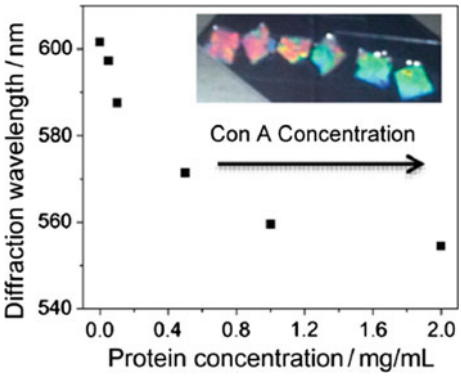

Fig. 1.15 Dependence of normalized diffraction spectra of the 2DOMs mannose hydrogel sensors upon Con A concentration in 0.1 M NaCl aqueous solutions that contain 1 mm Ca^{2+} and 0.5 mm Mn^{2+}. Reproduced with permission [38]

replicates the hexagonal packing of the opal monolayer that was initially present. The critical dimension of the resulting 2DOMs depends on the diameter of the template PS spheres. The evidence of the top layer and the height of the voids can be obtained from the cross-section SEM image in Fig. 1.16b.

P2VP is a weak polycation, and the pyridine group can be protonated at acidic pH, resulting in fast and substantial swelling. Transmission spectra of a 2DOMs exhibit 6, 15, 29 and 26 nm red-shifts in response to pH 5, 4, 3 and 2, respectively, as shown in Fig. 1.17a. Therefore, the variation of pH conditions can be readily read out from the wavelength shift of the 2DOMs. More importantly, the varying hues from purple, blue, green to yellow upon different pH conditions (pH 5–2) were observed (Fig. 1.17b). Therefore, this material can be used as a pH sensor.

An ion sensor has been prepared by using a similar 2DOM structure. In this case, PS particles self-assembled into 2D ordered structure in hydrogel thin films, which was functionalized using 4-acryloylamidobenzo-18-crown-6 (4AB18C6). 4AB18C6 is a molecular recognition agent, which responds specifically to Pb^{2+}

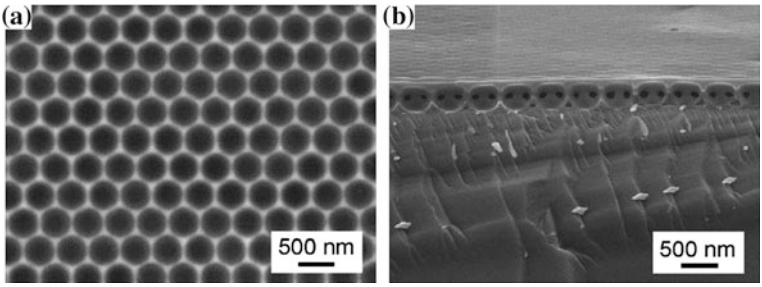

Fig. 1.16 SEM images of the 2DOMs based on a monolayer inverse opal of polyelectrolyte gel on a silicon wafer: **a** top-view and **b** side-view. Reproduced with permission [39]

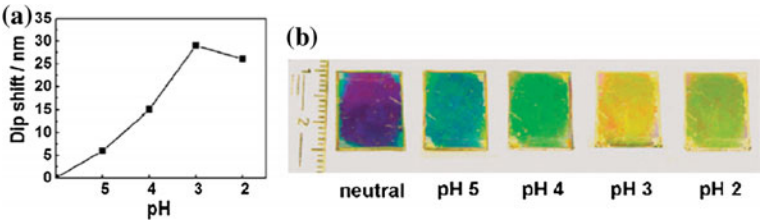

Fig. 1.17 Transmission dip shift (**a**) and interference colors (**b**) of 2DOMs in response to different pH conditions. Reproduced with permission from [39]

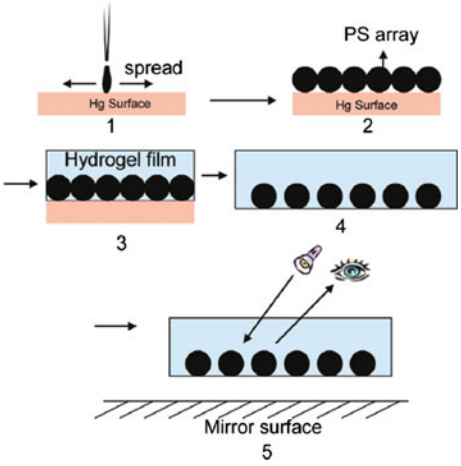

Fig. 1.18 Fabrication of a 2-dimensional (2-D) photonic crystal for sensing applications. *1*, *2* PS particles self-assembled into a 2-D close-packed array. *3* A hydrogel film is polymerized around the 2-D array. *4* The swollen hydrogel with the embedded 2-D array is peeled from the glass substrate. *5* Diffraction from the 2-D array/hydrogel sandwich is monitored visually. Reproduced with permission from [40]

(Fig. 1.18) [40]. When exposed to Pb^{2+} solution, 4AB18C6 selectively incorporated with Pb^{2+}, which increased the charge density in the polymer network. This resulted in hydrogel swelling and correspondingly increased the distance between PS particles, which led to a color change of the thin film.

1.4 Three-Dimensional Ordered Materials

Three-dimensional ordered materials (3DOMs) have structures ordered periodically in three spatial directions [41, 42]. The most common example of a 3DOM is the opal gemstone, which consists of a close-packed ordered array of silica colloids—this is also known as a colloidal crystalline array (CCA) [43, 44]. Inspired by

nature, color tunable 3DOMs have been fabricated in the lab by entrapping CCAs in stimuli responsive hydrogels [45–47]. The CCA exhibits visual color, similar to an opal gemstone, but interestingly allows the color to be tuned by the swelling and deswelling of the hydrogel in response to external stimuli [48–50].

A CCA/hydrogel-based system was developed by Asher's group, which could be used for noninvasive glucose sensing in tear fluid. The sensor was designed and used in contact lenses or in ocular inserts under the lower eyelid. It exhibits different colors when exposed to different glucose concentrations. The concept is that users could monitor glucose concentration by viewing the color of the sensor [51–53]. In another example, Asher's group fixed highly charged monodisperse PS colloids into a hydrogel network. Boronic acid derivatives were incorporated into the hydrogel backbone, rendering them glucose responsive [52]. Glucose can interact with the boronic acid derivative to form glucose boronate crosslinks, therefore higher glucose concentration results in higher crosslink density and the hydrogel shrinks leading to a blue shift of reflectance spectra.

Another CCA/hydrogel-based glucose sensor was prepared by incorporation of a periodic array of PS spheres with different geometries into a polyacrylamide hydrogel [55]. The enzyme glucose oxidase was also incorporated into this system, which allowed the material to sense glucose (Fig. 1.19) [54]. These materials exhibited Bragg diffraction in the visible wavelengths [54]. Glucose solutions caused the hydrogel to swell, resulting in a red shift of the diffracted light. The hydrogel swelling is a result of the formation of reduced glucose oxidase after reaction with glucose, which is anionic at neutral pH. This charged state causes the hydrogel to swell. The reduced glucose oxidase is reoxidized by O_2; all these reactions are detailed in reactions (1.3) and (1.4).

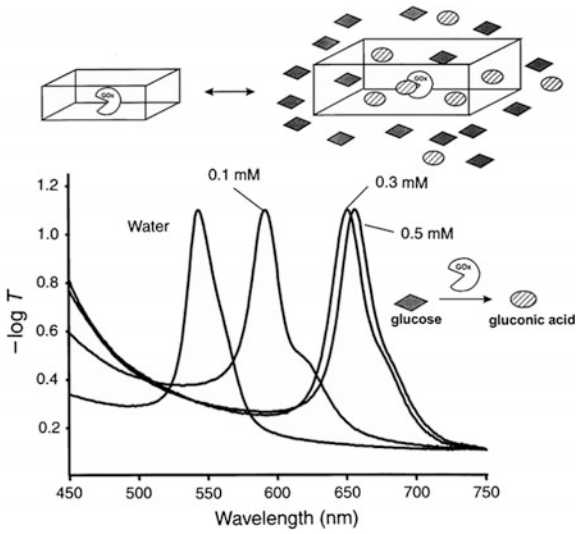

Fig. 1.19 Visible extinction spectra showing how diffraction depends on glucose concentration for a 125-mm-thick CCA glucose sensor. Reproduced with permission [54]

$$\mathrm{GOx(ox)} + \mathrm{glucose} \rightarrow \mathrm{GOx^-(red)} + \mathrm{gluconic\ acid} + \mathrm{H^+} \tag{1.3}$$

$$\mathrm{H^+} + \mathrm{GOx(red)} + \mathrm{O_2} \rightarrow \mathrm{H_2O_2} + \mathrm{GOx(ox)} \tag{1.4}$$

No response was observed using similar concentrations of sucrose or mannose, because of the enzyme selectivity.

CCA/hydrogels were also used to monitor hydrogel volume-phase transitions using Bragg diffraction in response to pH changes [56]. In this case, hydrogels were composed of poly(acrylic acid) (PAAc), which has a pK_a of $\sim$4.7. Therefore, the PAAc groups will be protonated/deprotonated in response to pH and will induce volume-transitions; these solvation state changes causes the lattice spacing of the colloidal crystal to change, which can be detected as optical property (color) changes. From this, a detailed hydrogel volume-phase transition model has been built, which accurately models swelling with no adjustable parameters.

Poly(hydroxyethyl methacrylate) hydrogel-based CCAs were also prepared and used as a pH sensor [57]. To accomplish this, the surfaces of monodisperse silica particles were coated with a thin layer of PS-co-SPS (sulfonated PS). Surface charge groups were introduced into the system due to the negative SPS block. The resulting highly charged monodisperse silica particles were self-assembled into a CCA in deionized water. Polymerization of hydroxyethyl methacrylate (HEMA) occurred around the CCA to form a pHEMA-CCA. The silica particles were etched away using hydrofluoric acid to produce a three-dimensional periodic array of voids in the HEMA-CCA, i.e., an inverse opal. The authors also fabricated a CCA by utilizing a second polymerization to incorporate carboxyl groups into the HEMA-CCA. This system can be used to model the pH dependence of diffraction of the HEMA-CCA using Flory theory, which predicts polymer conformation in solutions, and can be used to determine polymer network elasticity [19]. These sensors exhibited reversible pH response in different ionic strength solutions.

An unusual feature of the pH response above is the hysteresis in response to titration. The kinetics of equilibration are very slow due to the ultralow diffusion constant of protons in the carboxylated CCA as predicted earlier by the Tanaka group [58]. In spite of its simplicity, the long response time of the hydrogel photonic crystal materials has limited their utility. This results from the slow diffusion of analytes in the hydrogel, which act to change their optical properties. New procedures to fabricate CCA hydrogels were developed to reduce the response time. The Lee Group demonstrated a mechanically robust CCA hydrogel that exhibited fast response kinetics. This was done by fabricating the materials using templated photo-polymerization of hydrogel monomers within the interstitial space of a self-assembled colloidal crystal, as shown in Fig. 1.20 [59].

By a rigorous optimization of photopolymerization conditions, the pH sensors show a response time of less than 10 s in response to solution pH changes. Lee's inverse opal hydrogels primarily consists of void spaces interconnected by holes (Fig. 1.20), once the voids are connected, the diffusion of proton can take place

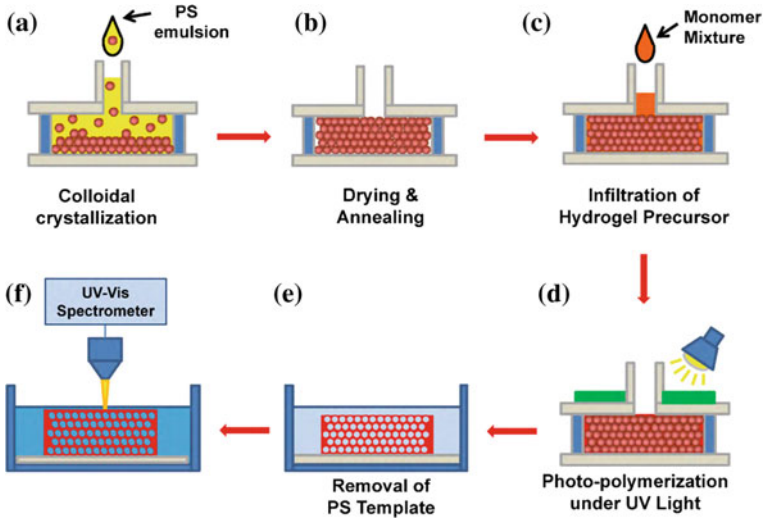

Fig. 1.20 Schematic illustration of fabrication procedures. Reproduced with permission [59]

both through the void space and the hydrogel network [59]. Most ionic species are expected to diffuse rapidly through the voids, and then into the hydrogel, resulting in an aqueous diffusion limited response time. Repeated pH changes revealed that the sensor has a long lifetime (>6 months) without change of the response time or reproducibility in pH-induced color change. Mangeney's group also fabricated a novel CCA for sensing solution pH, with enhanced pH response by incorporating a planar defect inside the CCA hydrogel, as shown in Fig. 1.21a [60]. Figure 1.21b shows the SEM images of the colloidal-crystal template with an embedded planar defect layer and the resultant photonic polymer hydrogel films.

In a more biologically relevant application, a creatinine (a molecular marker of renal dysfunction) sensor has been fabricated by immobilizing creatinine deiminase (CD) into polyacrylamide hydrogel. The hydrogel was functionalized with two recognition molecules, CD enzyme and a 2-nitrophenol (2NPh), and swells as a result of two sequential reactions: hydrolysis of creatinine by the enzyme CD, which releases OH, and increases the pH within the gel—this leads to a concomitant deprotonation of 2NPh. The overall effect is an increased hydrophilicity (and charge) of the hydrogel, causing the hydrogel to swell (Fig. 1.22) yielding a red shift in diffraction [61]. In another example, by covalently linking the amine groups of cholesterol oxidase (ChOx) to an epoxide-functionalized CCA (from acrylamide and glycidyl methacrylate), a photonic crystal-based sensor capable of detecting cholesterol with concentrations up to 5 mm could be fabricated [62].

In recent years, 3DOMs have been used to sense specific analytes. Generally speaking, to achieve molecular recognition, recognition motifs will be incorporated into the photonic crystal system and the recognition process will change the photonic crystal ordered structure/spacing, leading to a color change. One way this can

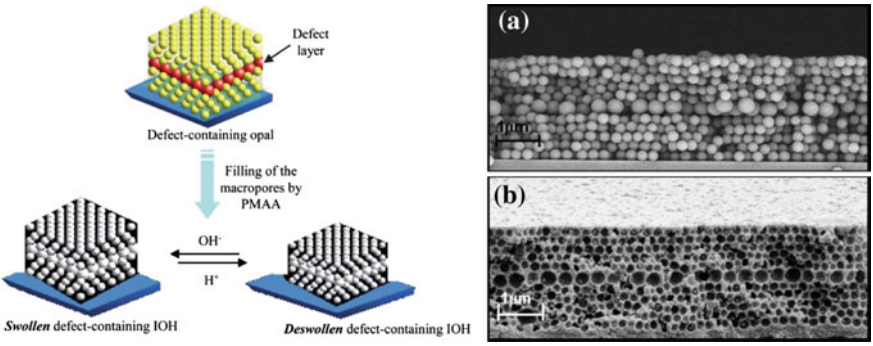

Fig. 1.21 **a** Schematic illustration of the defect-containing opal and inverse opal hydrogel (IOH) films. **b** SEM images of (**a**) the colloidal-crystal template with embedded planar defect layer of larger particles and (**b**) the resulting inverse opal hydrogel film with a defect layer of larger macropores. The resulting materials consists of a three-dimensional, highly-ordered, and interconnected macroporous array of poly(methacrylic acid), which is sensitive to pH. Reproduced with permission [60]

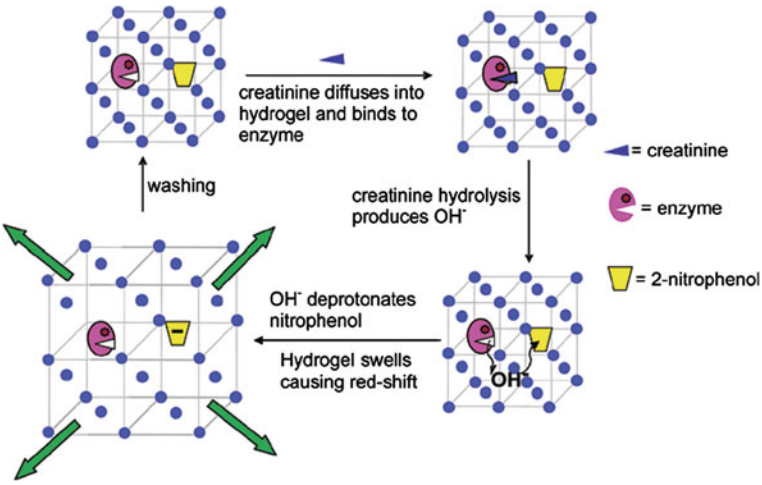

Fig. 1.22 Schematic depiction of the creatinine sensor concept. Creatinine deiminase causes the production of hydroxide ions. In a second step, 2-nitrophenol is deprotonated. The increased solubility of the phenolate ion and its negative charge causes the swelling in the polymer. Reproduced with permission [61]

be achieved is via molecular imprinting. Molecular imprinting is a technique used to create nanocavities inside a polymer network that are capable of binding specific molecules. This is achieved by incorporating the molecules of interest into the gels, followed by their extraction. The resulting cavities left in the gel are now chemically and conformationally templated to rebind the imprinted molecule. These nanocavities work as artificial antibodies which can recognize target molecule

through the specific shape and binding site between them and target molecules [63]. Combination of molecular imprinting and photonic crystal technology to prepare a photonic crystal based sensor can yield label-free colorimetric detectors [64–67].

Bisphenol A (BPA) is a common monomer for synthesis of plastics and epoxy resins. However, recent studies have found out BPA is an emerging contaminant which can disrupt the endocrine system and potentially cause cancer [68]. By molecular imprinting, numerous nanocavities were created in polymethyl methacrylate (PMMA) spheres, which can specifically target BPA (Fig. 1.23) [26]. The monodisperse PMMA spheres can be made into a 3DOMs that has been used as optical sensor. Once the sensor was exposed to BPA solution, binding occurred due to the hydrogen bonding and spatial effects, changing the diffraction peak intensity [65].

In another example, this method was used to detect atrazine that is a widely used in pesticide. This pesticide has recently shown up as a contaminant in drinking water and consumption of this pesticide above the maximum contaminant level (MCLs) has been associated with adverse human health effects. Li's group develop atrazine-imprinted photonic polymers (MIPP) (Fig. 1.24) [66]. First, silica colloids were deposited onto a glass substrate and formed a 3D ordered array as a template. Pre-gel solution containing template molecule (atrazine) was filled into the void space of the 3D ordered array. After polymerization, silica and the atrazine molecular templates were removed from the hydrogel film, forming highly ordered porous arrays with specific nanocavities capable of recognizing atrazine through noncovalent interaction. When exposed to different concentration of atrazine, the device's color visually changed.

The MacLachlan group recently prepared photonic materials from nanocrystalline cellulose films, and used supramolecular templating to yield a sensor [69–

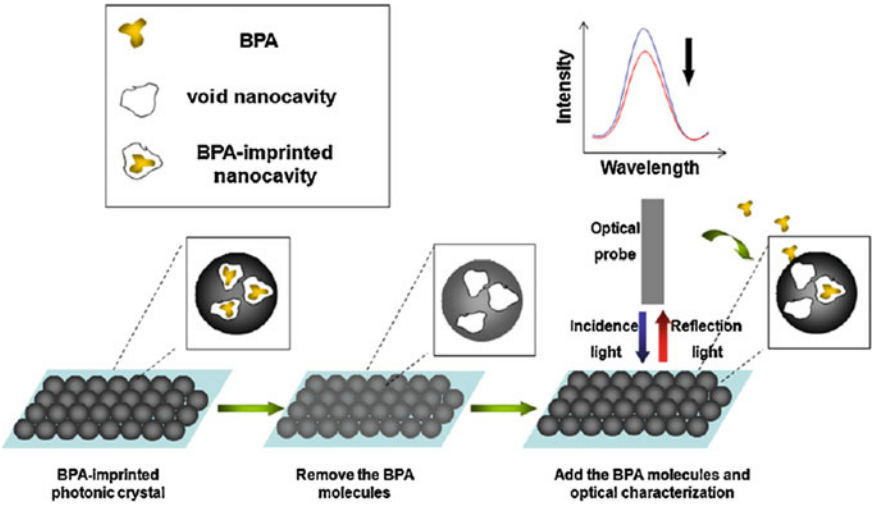

Fig. 1.23 Experimental procedures for the reflectometric detection of BPA using an imprinted nanocavity opal photonic crystal sensor. Reproduced with permission [65]

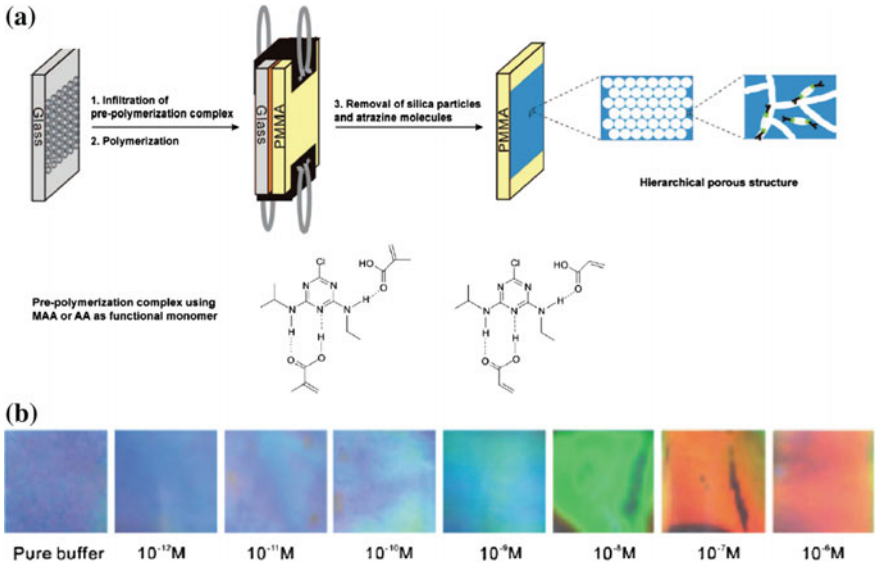

Fig. 1.24 **a** Schematic illustration of the procedure used for the preparation of the molecularly imprinted photonic polymer (MIPP). **b** Color change induced by exposure to atrazine at different concentrations. Reproduced with permission [66]

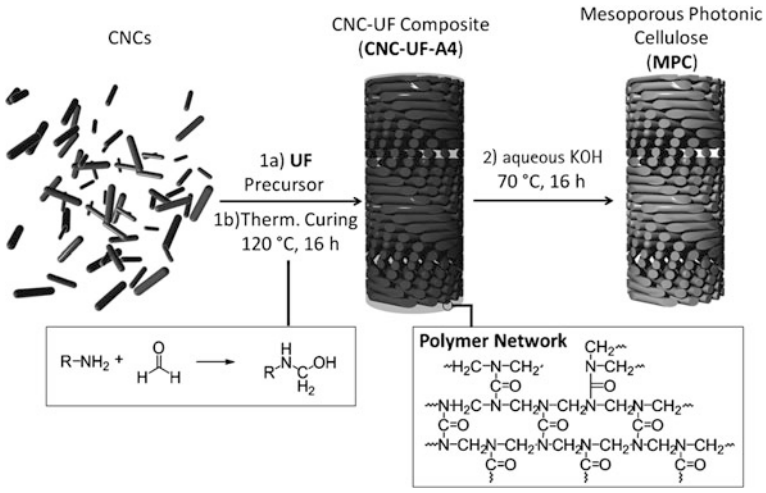

Fig. 1.25 Synthetic route to generate mesoporous photonic cellulose (MPC). An aqueous suspension of CNCs is combined with a UF precursor. Following evaporation-induced self-assembly, a CNC-UF composite with chiral nematic order is obtained. Thermal curing of the composite is followed by treatment with aqueous KOH to yield MPC. Reproduced with permission [71]

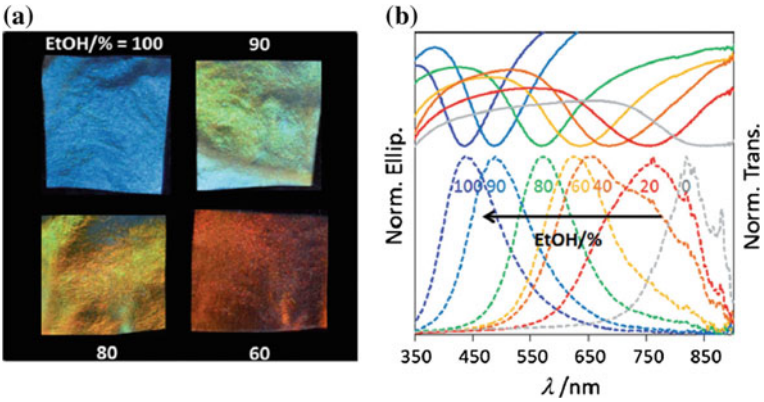

Fig. 1.26 Sensing performance of the functional MPC films. **a** Photographs and **b** UV/Vis (*solid lines*) and CD spectra (*dashed lines*) of MPC soaked in EtOH/H_2O at different ratios as indicated. Reproduced with permission [71]

71]. A schematic depiction of the device preparation is shown in Fig. 1.25. Briefly, chiral nematic cellulose films were synthesized by the self-assembly of cellulose nanocrystals (CNCs) in the presence of a resin precursor. The mixture was dried overnight under ambient conditions, followed by heat curing at 120 °C to complete the polymerization. Subsequently, CNCs were removed from resin, generating a periodic mesoscopic structure with a photonic band gap. The periodicity can be tuned by changing the reaction conditions, and therefore the optical property and potential application of these materials can be controlled. These films showed a rapid red shift of their reflection peak when immersed in polar solvents (Fig. 1.26). Also, film colors depend on solvent polarity and composition, which can be observed by the naked eye (Fig. 1.26b). The vibrant visible colors could be tuned from 430 nm in pure ethanol to 840 nm in pure water (Fig. 1.26).

1.5 Other Noteworthy Photonic Materials for Sensing

Trinitrotoluene (TNT) is one of the most widely used and well-known explosives that can be used as a weapon and is a threat to our security. Another potential threat to human security is the use of biological warfare and nerve gases. Over the years, researchers worldwide have been developing sensors for weapons of mass destruction, but most of them are limited by sensitivity, selectivity and/or reliability [72]. Conjugated polymer-based molecular wires has been used for sensing these dangerous chemicals [73]. Molecular wires are molecular-scale objects, which conduct electrical current. The use of molecular wires significantly enhances the chemosensory response. A number of advanced sensing technologies have been developed based on this approach. Nomadics Inc. who markets Fido produces devices capable

of detecting very low levels of explosives, which is based on the chemoresistivity of molecular wires [74–77].

Porous silicon has also attracted significant attention for sensor applications. Tokranova et al. reported [78] a porous silicon microcavity (PSi MC) infiltrated with poly(2-methoxy-5-(2-ethylhexyloxy)-p-phenylenevinylene) (MEH-PPV) (M_W = 139,000) for TNT sensing. The unique architecture of the polymer/PS nanohybrid makes it very attractive for sensing of nitroaromatic compounds especially with low vapor pressure (e.g., TNT) because of the combination of high sensitivity (due to extra thin polymer film inside the PSi) with an intense optical signal (as a result of sufficient polymer mass adsorbed by the PSi). The PSi MC/MEH-PPV composite exhibited excellent sensitivity of TNT vapors significantly exceeding that of the conventional thin films of MEH-PPV deposited on flat Si. The spectral shift of the MC resonance peak upon TNT vapor exposure offers an additional advantage. Sensor specificity could be substantially improved by discriminating nitroaromatic explosives with low vapor pressure (spectral shift $\sim$1 nm) from explosive interferants with medium and high vapor pressures (spectral shift $\sim$several nanometers, e.g., dinitrotoluene, nitrotoluene). These PSi MC/polymer nanocomposites were used as a novel system for various applications in sensing and trace detection of toxic gases.

Interestingly, single crystal porous silicon (PSi) was also used for sensing applications. Because the optical signature of these photonic crystals is sensitive to the average refractive index of the structure, materials are able to absorb (and desorb) to the pore walls (and from the pore walls), which is the basis for biosensing. While the adsorption of materials to the pore walls causes a red-shift (if it has a higher refractive index than the material it replaces), the desorption of materials from the pore walls results in a blue shift (thus the average refractive index decreases). PSi photonic crystals can be made into very sensitive and selective label-free optical sensors by modifying the pore walls with the appropriate surface chemistry [79]. Interest in the use of PSi photonic crystals for biosensing arises from the fact that their optical signatures can be tuned by means of changing the porosity and periodicity of the multilayer photonic crystals, over the whole visible and infrared regions of the electromagnetic spectrum [80]. PSi biosensors have focused on affinity sensing motif for the detection of DNA [81, 82], proteins [83, 84] and microorganisms [85].

In a similar approach, a flexible photonic crystal cavity system was developed, which was consisted of a regular array of silicon nanowires embedded in a polydimethylsiloxane (PDMS) matrix that enables wide-range tuning of its resonance frequency (Fig. 1.27) [86]. This mechanical stretchable assembly exhibits a cavity resonance in the telecommunication band that can be reversibly tuned over 60 nm. Specifically, the optical response of the cavities towards various solvents, such as ethanol, isopropanol (IPA), and tert-butanol (TBA), was investigated. The swelling ratios were found to be 4, 9, and 21 %, respectively as shown in Fig. 1.28 at room temperature.

In another example, a sensor was fabricated by incorporation of a chemo-responsive hydrogel into a PSi transducer (Fig. 1.29) [87]. When exposed to the model analyte, which was the reducing agent tris(2-carboxyethyl) phosphine

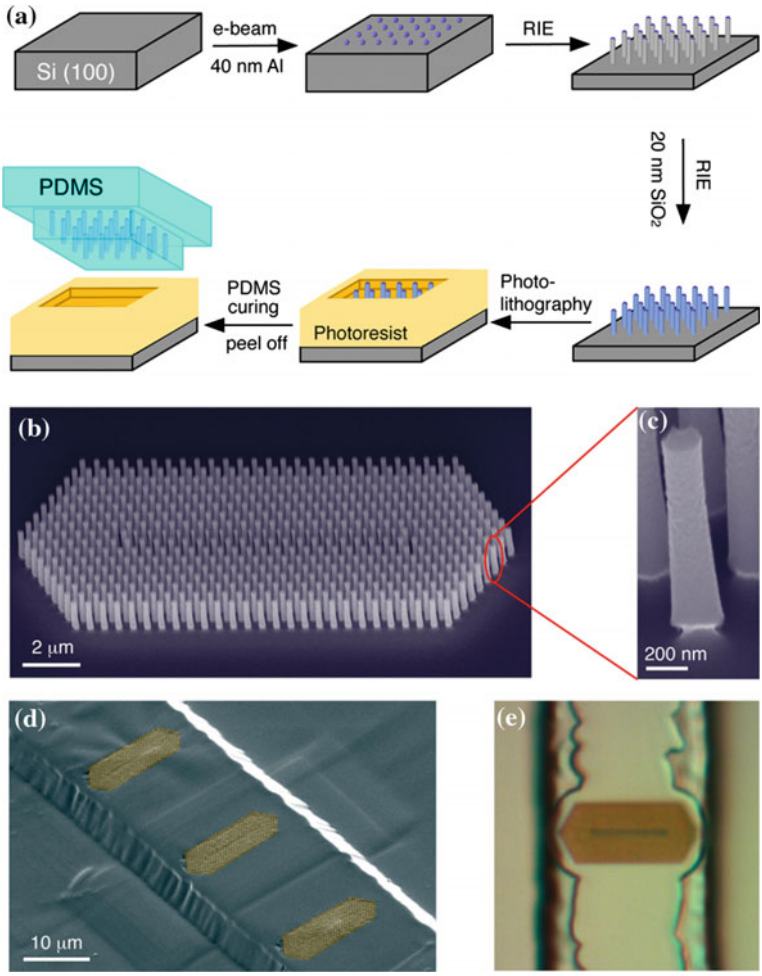

Fig. 1.27 Flexible PC cavities. **a** Schematic for flexible PC cavity fabrication: the PC patterns on a Si (1, 0, 0) wafer were made by electron-beam lithography; 40 nm Al was deposited as an etch mask; Si was etched to form Si nanowires; 20 nm of SiO_2 was deposited by atomic layer deposition; SiO_2 was selectively etched on the substrate; the nanowire bases were thinned by etching; a window by photolithography; pour and cure PDMS; and then finally peel off the PDMS. **b** Scanning electron microscope (SEM) image of the PC tilted at 45°. Design dimensions: regular nanowire diameter is 200 nm; defect nanowire diameter is 140 nm; nanowire length is 1.2 μm. The hexagonal lattice spacing is 500 nm. **c** Zoom-in view of an undercut NW at the PC edge, also tilted at 45°. **d** SEM image of the PDMS mesa structure containing several PC cavities. **e** Optical image of the top-down view of a PC embedded in PDMS. The *dark line* in the middle of the PC is the line defect. Reproduced with permission [86]

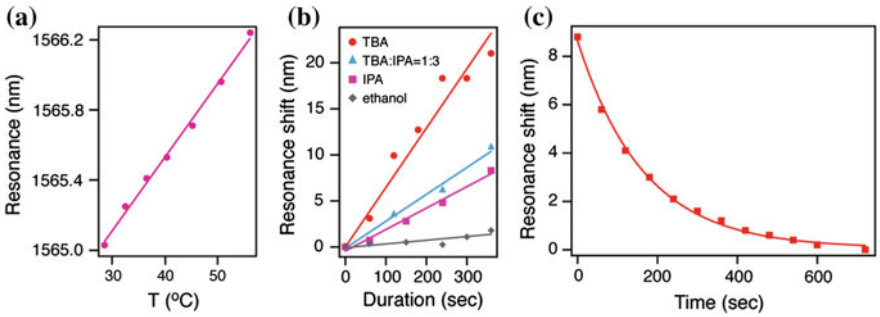

Fig. 1.28 Resonance shift as a function of temperature and solvent swelling. **a** Resonance peak red-shifted as temperature increased. **b** Resonance shift as a function of time that PDMS stayed in a solvent bath. **c** As TBA evaporated over time, the resonance moved back to the original position (without solvent swelling) with exponential time dependence. Reproduced with permission [86]

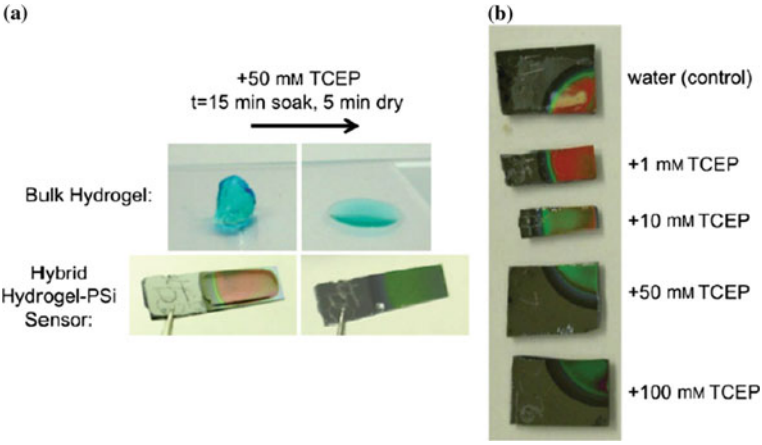

Fig. 1.29 Visual color readout of hybrid hydrogel–PSi sensor upon exposed to different concentration of TCEP. Reproduced with permission [87]

(TCEP), the disulfide bond used as cross-linker cleaves and thus the color of the sensor changes.

For biological sensing, it is desired that the sensing material be free from legitimate concerns of toxicity; these concerns have limited the use of CdSe quantum dots especially for in vivo imaging and sensing applications. For these reasons, there has been a quest to develop non-Cd-based quantum dots. Silicon nanocrystals (ncSi) have been identified as one of the best candidates; although they exhibit lower quantum efficiencies [88]. The Ozin group focused on the possibility of synthesizing colloidally-stable monodispersed ncSi for in vitro fluorescence labeling of human breast tumor cells [88, 89].

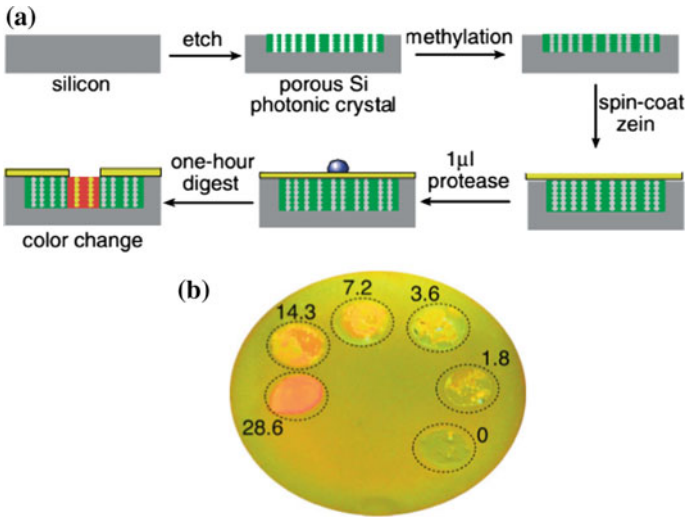

Fig. 1.30 **a** Enzymatic assay using a protein-coated porous Si photonic crystal; **b** Dilution series for active protease pepsin, showing the effect of pepsin concentration on the observed color change in the porous Si photonic crystal. Reproduced with permission [91]

Traditional staining technology to differentiate Gram (+) from Gram (−) bacteria is cumbersome. Miller's group proposed a simple way to realize reliable Gram (−) bacteria identification [90]. The authors designed and synthesized an organic receptor, tetratryptophanter-cyclo pentane, designated TWTCP, which specifically binds to Gram (−) bacteria and functionalized porous silicon surface with this receptor. Only exposed to Gram (−) bacteria, the device exhibited red-shift. Sailor's group developed a porous Si photonic crystal probe to colorimetric monitor protease activity (Fig. 1.30) [91]. This method is high sensitive even the picomoles in a 1 μL can cause make probe's color visually changed. The introduction of protease will cause the total refractive index of the porous film increase, generating red shift.

Related to Si, TiO_2 has been used as sensing material for biomolecules. This is primarily due to its large internal surface area, good biocompatibility and broad application [92, 93]. Proteins can be directly immobilized on the pore surfaces of TiO_2 substrates by physical adsorption. The change of the diffraction peak shifts can be monitored to obtain information about the binding of analytes [92]. Photonic crystal biosensors (based on TiO_2) for measuring HIV viral load have recently been developed [93].

1.6 Summary

This chapter has reviewed only a portion of the available examples of photonic materials for sensing applications. The systems that were described primarily exhibited their unique optical properties due to refractive index periodicity (in 1D, 2D, or 3D), although, the final section of the chapter detailed alternative systems that can be used for sensing—primarily using porous Si. Many of the devices were fabricated using self-assembly processes, and relied on visual color changes for the readout. These facts made the devices not only easy and cost effective to fabricate, but allow them to be used without complex analytical instrumentation to get a result. The examples illustrated the exciting applications of such materials, and clearly demonstrated how the devices can be used to positively impact human health. While much progress has been made, many challenges still exist that prevent the use of these materials in everyday applications. For example, regarding sensing, polymers with enhanced sensitivities to specific species need to be developed and investigated. Furthermore, response times need to be enhanced and the ability of the devices to sense analytes in complex media (saliva, blood, urine) demonstrated. Regardless of the challenges, continuous development of such devices and related technologies makes us optimistic about the future positive impacts these materials can have on human life.

Acknowledgements MJS acknowledges funding from the University of Alberta (the Department of Chemistry and the Faculty of Science), the Natural Sciences and Engineering Research Council of Canada (NSERC), the Canada Foundation for Innovation (CFI), the Alberta Advanced Education and Technology Small Equipment Grants Program (AET/SEGP), Grand Challenges Canada and IC-IMPACTS. QMZ acknowledges financial support through an Alberta Innovates Technology Futures (AITF) Postdoctoral Fellowship.

References

1. J. Ge, Y. Yin, Angew. Chem. Int. Ed. **50**, 1492–1522 (2011)
2. P. Yeh, *Optical Waves in Layered Media* (Wiley, New York, 1988)
3. L. Hu, M.J. Serpe, Chem. Commun. **49**, 2649–2651 (2013)
4. F.H. Schacher, P.A. Rupar, I. Manners, Angew. Chem. Int. Ed. **51**, 7898–7921 (2012)
5. X. Ye, L. Qi, Nano Today **6**, 608–631 (2011)
6. S. Itabashi, H. Nishi, T. Tsuchizawa, T. Watanabe, H. Shinojima, R. Kou, K. Yamada, IEICE Trans. Electron. **E95C**, 199–205 (2012)
7. A. Chen, *Introduction to Polymer Photonics for Information Technology* (Crc Press-Taylor & Francis Group, Boca Raton, 2008)
8. C.X. Guo, G.H. Guai, C.M. Li, Adv. Energy Mater. **1**, 448–452 (2011)
9. S.Q. Feng, T. Lei, H. Chen, H. Cai, X.S. Luo, A.W. Poon, Laser Photonics Rev. **6**, 145–177 (2012)
10. A. Moutsiopoulou, A.K. Andreopoulou, G. Lainioti, G. Bokias, G. Voyiatzis, J.K. Kallitsis, Sens. Actuators B Chem. **211**, 235–244 (2015)
11. H.B.D. Thai, J.K. Yu, Y.-J. Park, D.-R. Ahn, Analyst **140**, 2804–2809 (2015)

12. S. Sun, X.-Y. Hu, D. Chen, J. Shi, Y. Dong, C. Lin, Y. Pan, L. Wang, Polym. Chem. Uk **4**, 2224–2229 (2013)
13. Z. Zhang, D.S. Kim, C.-Y. Lin, H. Zhang, A.D. Lammer, V.M. Lynch, I. Popov, O.S. Miljanic, E.V. Anslyn, J.L. Sessler, J. Am. Chem. Soc. **137**, 7769–7774 (2015)
14. A. Afzal, N. Iqbal, A. Mujahid, R. Schirhagl, Anal. Chim. Acta **787**, 36–49 (2013)
15. Y.-J. Jin, B.S.-I. Kim, W.-E. Lee, C.-L. Lee, H. Kim, K.-H. Song, S.-Y. Jang, G. Kwak, Npg Asia Mat. **6** (2014)
16. Q.M. Zhang, X. Li, M.R. Islam, M. Wei, M.J. Serpe, J. Mater. Chem. C **2**, 6961–6965 (2014)
17. H. Wang, K.-Q. Zhang, Sensors **13**, 4192–4213 (2013)
18. C. Fenzl, S. Wilhelm, T. Hirsch, O.S. Wolfbeis, ACS Appl. Mater. Interfaces **5**, 173–178 (2012)
19. L.D. Bonifacio, B.V. Lotsch, D.P. Puzzo, F. Scotognella, G.A. Ozin, Adv. Mater. **21**, 1641–1646 (2009)
20. M.C. Fuertes, F.J. López-Alcaraz, M.C. Marchi, H.E. Troiani, V. Luca, H. Míguez, G.D.A. Soler-Illia, Adv. Funct. Mater. **17**, 1247–1254 (2007)
21. C. Kang, E. Kim, H. Baek, K. Hwang, D. Kwak, Y. Kang, E.L. Thomas, J. Am. Chem. Soc. **131**, 7538–7539 (2009)
22. Y. Kang, J.J. Walish, T. Gorishnyy, E.L. Thomas, Nat. Mater. **6**, 957–960 (2007)
23. Z. Wang, J. Zhang, J. Xie, C. Li, Y. Li, S. Liang, Z. Tian, T. Wang, H. Zhang, H. Li, Adv. Funct. Mater. **20**, 3784–3790 (2010)
24. L. Zhai, A.J. Nolte, R.E. Cohen, M.F. Rubner, Macromolecules **37**, 6113–6123 (2004)
25. Y. Kang, Macromol. Res. **20**, 1223–1225 (2012)
26. C.D. Sorrell, M.J. Serpe, Adv. Mater. **23**, 4088–4092 (2011)
27. C.D. Sorrell, M.C. Carter, M.J. Serpe, Adv. Funct. Mater. **21**, 425–433 (2011)
28. M.R. Islam, M.J. Serpe, Chem. Commun. **49**, 2646–2648 (2013)
29. L. Hu, M.J. Serpe, J. Mater. Chem. **22**, 8199–8202 (2012)
30. M.R. Islam, M.J. Serpe, Macromolecules **46**, 1599–1606 (2013)
31. M.R. Islam, M.J. Serpe, Anal. Bioanal. Chem. 1–7 (2014)
32. M.R. Islam, M.J. Serpe, Anal. Chim. Acta **843**, 83–88 (2014)
33. Q.M. Zhang, W. Xu, M.J. Serpe, Angew. Chem. Int. Ed. **53**, 4827–4831 (2014)
34. C.D. Sorrell, M.J. Serpe, Anal. Bioanal. Chem. **402**, 2385–2393 (2012)
35. M.R. Islam, M.J. Serpe, Biosens. Bioelectron. **49**, 133–138 (2013)
36. Q.M. Zhang, D. Berg, S.M. Mugo, M.J. Serpe, Chem. Commun. **51**, 9726–9728 (2015)
37. J.T. Zhang, L. Wang, D.N. Lamont, S.S. Velankar, S.A. Asher, Angew. Chem. Int. Ed. **51**, 6117–6120 (2012)
38. J.-T. Zhang, Z. Cai, D.H. Kwak, X. Liu, S.A. Asher, Anal. Chem. **86**, 9036–9041 (2014)
39. C. Li, B.V. Lotsch, Chem. Commun. **48**, 6169–6171 (2012)
40. J.-T. Zhang, L. Wang, J. Luo, A. Tikhonov, N. Kornienko, S.A. Asher, J. Am. Chem. Soc. **133**, 9152–9155 (2011)
41. Y. Cheng, Z. Yang, J. Liao, J. Qiu, Z. Song, Y. Yang, J. Rare Earths **33**, 599–603 (2015)
42. H. Wakayama, H. Yonekura, Y. Kawai, Acs Macro Lett. **2**, 284–287 (2013)
43. J. Jirasek, M. Vavro, J. Jiranek, Chem. Listy **103**, 647–651 (2009)
44. J.B. Lambert, G.O. Poinar, Acc. Chem. Res. **35**, 628–636 (2002)
45. J. Liao, Z. Yang, J. Sun, S. Lai, B. Shao, J. Li, J. Qiu, Z. Song, Y. Yang, Sci. Reports **5** (2015)
46. K.T. Hufziger, S.V. Bykov, S.A. Asher, Appl. Spectrosc. **68**, 1219–1223 (2014)
47. D. Yang, S. Ye, J. Ge, Adv. Funct. Mater. **24**, 3197–3205 (2014)
48. J.H. Holtz, S.A. Asher, Nature **389**, 829–832 (1997)
49. J.M. Weissman, H.B. Sunkara, A.S. Tse, S.A. Asher, Science **274**, 959–963 (1996)
50. D. Kang, J.E. Maclennan, N.A. Clark, A.A. Zakhidov, R.H. Baughman, Phys. Rev. Lett. **86**, 4052–4055 (2001)
51. V.L. Alexeev, S. Das, D.N. Finegold, S.A. Asher, Clin. Chem. **50**, 2353–2360 (2004)
52. M. Ben-Moshe, V.L. Alexeev, S.A. Asher, Anal. Chem. **78**, 5149–5157 (2006)
53. V.L. Alexeev, A.C. Sharma, A.V. Goponenko, S. Das, I.K. Lednev, C.S. Wilcox, D.N. Finegold, S.A. Asher, Anal. Chem. **75**, 2316–2323 (2003)

54. J.H. Holtz, S.A. Asher, Nature **389**, 829–832 (1997)
55. S.A. Asher, J. Holtz, L. Liu, Z. Wu, J. Am. Chem. Soc. **116**, 4997–4998 (1994)
56. K. Lee, S.A. Asher, J. Am. Chem. Soc. **122**, 9534–9537 (2000)
57. X. Xu, A.V. Goponenko, S.A. Asher, J. Am. Chem. Soc. **130**, 3113–3119 (2008)
58. S. Mafé, J.A. Manzanares, A.E. English, T. Tanaka, Phys. Rev. Lett. **79**, 3086–3089 (1997)
59. J. Shin, P.V. Braun, W. Lee, Sens. Actuators B: Chem. **150**, 183–190 (2010)
60. N. Griffete, H. Frederich, A. Maître, M.M. Chehimi, S. Ravaine, C. Mangeney, J. Mater. Chem. **21**, 13052–13055 (2011)
61. A.C. Sharma, T. Jana, R. Kesavamoorthy, L. Shi, M.A. Virji, D.N. Finegold, S.A. Asher, J. Am. Chem. Soc. **126**, 2971–2977 (2004)
62. M.K. Maurer, S.E. Gould, P.J. Scott, Sens. Actuators B **134**, 736–742 (2008)
63. K. Mosbach, O. Ramström, Nat. Biotechnol. **14**, 163–170 (1996)
64. Z. Wu, X. Hu, C.-A. Tao, Y. Li, J. Liu, C. Yang, D. Shen, G. Li, J. Mater. Chem. **18**, 5452–5458 (2008)
65. C. Guo, C. Zhou, N. Sai, B. Ning, M. Liu, H. Chen, Z. Gao, Sens. Actuators B: Chem. **166**, 17–23 (2012)
66. Z. Wu, C.A. Tao, C. Lin, D. Shen, G. Li, Chem. A Eur. J. **14**, 11358–11368 (2008)
67. Y.-X. Zhang, P.-Y. Zhao, L.-P. Yu, Sens. Actuators B: Chem. **181**, 850–857 (2013)
68. C.A. Staples, P.B. Dome, G.M. Klecka, S.T. Oblock, L.R. Harris, Chemosphere **36**, 2149–2173 (1998)
69. M.K. Khan, M. Giese, M. Yu, J.A. Kelly, W.Y. Hamad, M.J. MacLachlan, Angew. Chem. Int. Ed. **52**, 8921–8924 (2013)
70. K.E. Shopsowitz, J.A. Kelly, W.Y. Hamad, M.J. MacLachlan, Adv. Funct. Mater. **24**, 327–338 (2014)
71. M. Giese, L.K. Blusch, M.K. Khan, W.Y. Hamad, M.J. MacLachlan, Angew. Chem. Int. Ed. **53**, 8880–8884 (2014)
72. H. Xu, P. Wu, C. Zhu, A. Elbaz, Z.Z. Gu, J Mater Chem C **1**, 6087–6098 (2013)
73. C.J. Cumming, C. Aker, M. Fisher, M. Fok, M.J. La Grone, D. Reust, M.G. Rockley, T.M. Swager, E. Towers, V. Williams, IEEE Trans. Geosci. Remote Sens. **39**, 1119–1128 (2001)
74. M.J. Marsella, P.J. Carroll, T.M. Swager, J. Am. Chem. Soc. **116**, 9347–9348 (1994)
75. M.J. Marsella, P.J. Carroll, T.M. Swager, J. Am. Chem. Soc. **117**, 9832–9841 (1995)
76. T.M. Swager, M.J. Marsella, Adv. Mater. **6**, 595–597 (1994)
77. Q. Zhou, T.M. Swager, J. Am. Chem. Soc. **117**, 12593–12602 (1995)
78. N.A. Tokranova, S.W. Novak, J. Castracane, I.A. Levitsky, J. Phys. Chem. C **117**, 22667–22676 (2013)
79. K.A. Kilian, T. Bocking, J.J. Gooding, Chem. Commun. 630–640 (2009)
80. B. Guan, A. Magenau, K.A. Kilian, S. Ciampi, K. Gaus, P.J. Reece, J.J. Gooding, Faraday Discuss. **149**, 301 (2011)
81. S. Chan, P.M. Fauchet, Y. Li, L.J. Rothberg, B.L. Miller, Phys. Stat. Sol. A. **182**, 541–546 (2000)
82. V.S. Lin, Science **278**, 840–843 (1997)
83. H. Ouyang, L.A. DeLouise, B.L. Miller, P.M. Fauchet, Anal. Chem. **79**, 1502–1506 (2007)
84. K.-P.S. Dancil, D.P. Greiner, M.J. Sailor, J. Am. Chem. Soc. **121**, 7925–7930 (1999)
85. S. Chan, S.R. Horner, P.M. Fauchet, B.L. Miller, J. Am. Chem. Soc. **123**, 11797–11798 (2001)
86. C.L. Yu, H. Kim, N. de Leon, I.W. Frank, J.T. Robinson, M. McCutcheon, M. Liu, M.D. Lukin, M. Loncar, H. Park, Nano Lett. **13**, 248–252 (2013)
87. L.M. Bonanno, L.A. DeLouise, Adv. Funct. Mater. **20**, 573–578 (2010)
88. E.J. Henderson, A.J. Shuhendler, P. Prasad, V. Baumann, F. Maier-Flaig, D.O. Faulkner, U. Lemmer, X.Y. Wu, G.A. Ozin, Small **7**, 2507–2516 (2011)
89. M.L. Mastronardi, E.J. Henderson, D.P. Puzzo, G.A. Ozin, Adv. Mater. **24**, 5890–5898 (2012)
90. S. Chan, S.R. Horner, P.M. Fauchet, B.L. Miller, J. Am. Chem. Soc. **123**, 11797–11798 (2001)

91. M.M. Orosco, C. Pacholski, G.M. Miskelly, M.J. Sailor, Adv. Mater. **18**, 1393–1396 (2006)
92. J. Li, X. Zhao, H. Wei, Z.Z. Gu, Z. Lu, Anal. Chim. Acta **625**, 63–69 (2008)
93. H. Shafiee, E.A. Lidstone, M. Jahangir, F. Inci, E. Hanhauser, T.J. Henrich, D.R. Kuritzkes, B.T. Cunningham, U. Demirci, Sci. Reports **4**, 4116 (2014)

Chapter 2
Stimulus-Responsive Colored Materials for Sensing and Display Devices

Yukikazu Takeoka

Abstract In this chapter, two types of angle-independent colored systems are described that are achieved without using dyes and pigments: one is a colloidal amorphous array composed of fine colloidal particles, and the other is a phase-separated colored material based on the Christiansen effect. Stimuli-responsive systems using these materials are also introduced.

2.1 Introduction

Since the conceptual development of the photonic crystal, which is a periodically structured material with differing refractive indices [1], the fabrication of this material has been attempted by top-down approaches, such as photolithography, and by bottom-up approaches, such as the self-assembly of building blocks from colloidal parts [2]. In photonic crystals, the refractive index varies in a periodic manner on a length scale that is comparable to the wavelength of light, which causes multiple Bragg reflections. This effect prevents the propagation of light in a range of frequencies known as the photonic band gap (PBG). This property enables one to freely manipulate electromagnetic waves and to produce effects that are impossible to achieve with conventional optical approaches.

Numerous studies have been performed on colloidal crystals, which are considered to be a leading candidate for photonic crystals because they can be prepared by relatively simple and inexpensive procedures [3]. In theory, colloidal crystals lack a complete PBG, in which electromagnetic propagation is completely prohibited throughout a specified frequency band. However, inverse opals, which exhibit the inverse structure of colloidal crystals, can have a complete PBG if the refractive index contrast exceeds 2.85 [4]. The creation of photonic crystals with inverse opal structures and reliable optical properties requires the exact placement

Y. Takeoka (✉)
Department of Molecular Design and Engineering, Nagoya University, Furo-cho, Chikusa-ku, Nagoya 464-8603, Japan
e-mail: ytakeoka@apchem.nagoya-u.ac.jp

M. J. Serpe et al. (eds.), *Photonic Materials for Sensing, Biosensing and Display Devices*, Springer Series in Materials Science 229,
DOI 10.1007/978-3-319-24990-2_2

of well-defined point and line defects in colloidal crystals as a template; however, attaining a controlled nanostructure of colloidal crystals using self-assembly techniques is difficult in practice. Thus, studies of colloidal crystals for colored material applications that do not require exact nanostructures became very popular in the 2000s [5]. This color property is referred to as structural color and is caused by the interaction of light with microstructures at the scale of visible wavelengths [6].

An extensive variety of colloidal crystals and inverse opals, which display structural color that is reversibly tunable by external stimuli, have been reported over the last decade [7–10]. For future applications in optical devices, such as sensor systems and displays, tunability of these optical materials should be realized. Various approaches exist for tuning the structural color, including the infiltration of stimulus-responsive liquid crystals or dyes, which can transform the refractive indices, into a periodical open structure and mechanical control of the periodicity of polymer-based flexible nanostructured materials. In most cases in which external control of the refractive indices is employed, the change in structural color is not notable. For tuning the structural color, periodicity control using soft materials such as gels is a more powerful method. Our group has analyzed several types of stimulus-responsive structural colored colloidal crystal gels and inverse opal gels for (bio)chemical sensors and displays [9, 11, 12].

Over the past five years, our interest in colored systems has focused on colloidal amorphous arrays that display angle-independent structural colors [13]. Colloidal amorphous arrays composed of colloidal particles became a hot topic several years ago in the field of physics. The possibility of obtaining a PBG for a colloidal amorphous array prepared using colloidal particles with high refractive indexes, such as TiO_2, was reported in 1987 [14]. Recently, lasing was experimentally realized using a colloidal amorphous array [15]. However, when we use an actual colloidal amorphous array composed of easily available silica (SiO_2) colloidal particles or polymer colloidal particles, the array is less attractive to the eye compared with colloidal crystals due to its whitish appearance. The whitish appearance indicates that the colloidal amorphous array refracts visible light over an extensive wavelength range. However, colloidal amorphous arrays have been recently demonstrated to display satisfactory color saturation by the addition of black components [16, 17].

We also developed new colored materials without the use of pigments, dyes or nanostructures on the scale of visible wavelengths. Our research on the development of artificial angle-independent colored materials with phase-separated structures resulted in the development of a new type of angle-independent colored material based on the Christiansen effect [18, 19]. The Christiansen effect is a reduced scattering of multi-phase microstructure at wavelengths where their refractive indices match. Because chromogenic development using the Christiansen effect does not require precise structural control, we can easily obtain angle-independent colored materials simply by selecting a combination of materials that produce appropriate dispersions. Living organisms that employ the Christiansen effect have not been discovered; thus, these colored materials are

synthetic materials that were developed following principles that are not based on biological systems.

In this review, I describe our previous studies of stimulus-responsive colored systems generated without pigments and dyes with the aim of discussing materials useful for sensing and display devices.

2.2 Stimulus-Responsive Structurally Colored Materials Using Colloidal Crystals

Materials that exhibit PBG or pseudo-PBG (p-PBG) properties, in which the propagation of electromagnetic waves is inhibited in the visible light range, significantly reflect visible light in a particular region and display a structural color. Structural color delivers superior performance in terms of material durability because structurally colored materials do not experience light energy absorption issues or color fade-out, unlike materials containing pigment. One of the easiest methods for creating inexpensive and structurally colored materials is through the self-assembly of submicron colloidal particles to prepare a close-packing colloidal crystal (referred to as a "colloidal crystal" in this paper) [20], which can have a p-PBG in the visible region. Colloidal crystals composed of submicron colloidal SiO_2 particles occur in nature. These naturally occurring colloidal silica crystals are referred to as opals [9, 21]. These precious opals are composed of tiny spheres of SiO_2 and are formed over an extended period of time, but they are not completely crystalline. However, a portion of the colloidal crystal structure of an opal (referred to as the "opal structure" in this paper) exhibits vivid colors due to the presence of a p-PBG in the visible region. Iridescence from the opal structure is produced by the angle-dependent color from Bragg diffraction. The opal structure can be used as a template to prepare porous structures (referred to as the "inverse opal structure" in this paper), which has a beneficial effect not only on the optical properties but also on the substance permeation properties of other chemicals. However, the majority of opals and inverse opals have specific optical properties that cannot be altered after the nanostructures have been produced. If the periodicities or refractive indices of the components of these optical materials can be varied by external stimuli, such as electric and magnetic fields, "tunable structural colored materials" can be obtained. The use of "soft materials", such as surfactant solutions, liquid crystals, and gels, as the components of these optical materials enables the energy levels in the p-PBG to be altered by modifying the periodicity or the refractive indices. These tunable optical materials display exceptionally bright and brilliant structural colors that are produced by coherent Bragg optical diffraction and can be tuned across the entire visible region in response to external stimuli.

We have investigated inverse opal gels that exhibit volume changes in response to environmental changes; these gels were prepared using a colloidal crystal as a template [12, 22–34] (Fig. 2.1). Colloidal crystals prepared with SiO_2 particles

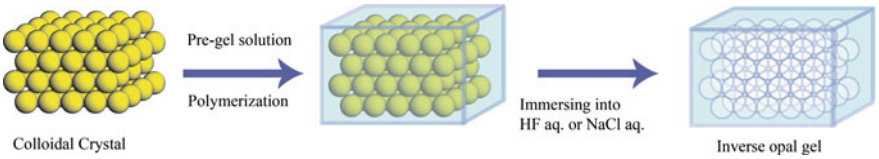

Fig. 2.1 Schematic procedure of the preparation of an inverse opal gel using a colloidal crystal of the closest-packed silica particles as a template

were applied to fabricate structurally colored inverse opal gels. To fabricate the inverse opal gels, the colloidal crystals were infiltrated with a pre-gel solution, followed by polymerization. Next, the samples were immersed in appropriate aqueous solutions to etch out the SiO_2. The resultant porous, structurally colored inverse opal gels were carefully washed with distilled water.

The displayed color can vary with a change in the volume of the inverse opal gel depending on the environment (Fig. 2.2). If the inverse opal gel maintains the fine structure of the precursor colloidal crystal and the volume change is isotropic, the peak wavelength (λ_{max}) observed in the reflection spectrum of the inverse opal gel can be estimated by the following equation:

$$\lambda_{max} = 1.633(d/m)(D/D_0)(n_a^2 - \sin^2\theta)^{1/2} \tag{2.1}$$

where d is the diameter of the colloidal particle; m is the order of the Bragg reflection, which is typically 2.1; D/D_0 (D and D_0 are the characteristic sizes of the gel in the equilibrium state for a given condition and for the preparation state, respectively) is defined as the degree of equilibrium swelling of the gel; n_a is the average refractive index of the inverse opal gel; and θ is the angle measured from the normal to the plane of the gel. According to this equation, the environmental dependence of D/D_0 and n_a should be experimentally determined to estimate the observed value of λ_{max} for the inverse opal gel because d and θ can be arbitrarily

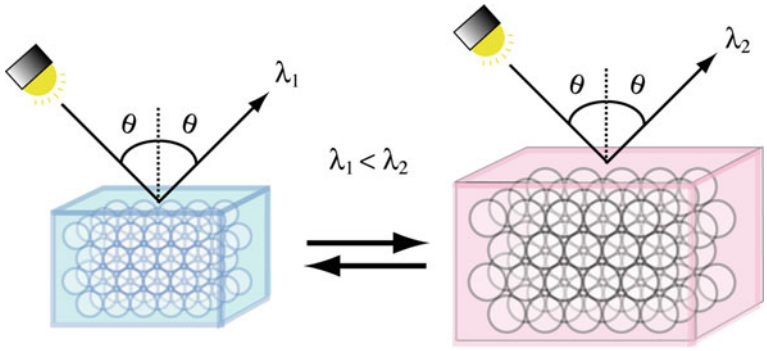

Fig. 2.2 A schematic of the optical behavior of an inverse opal gel under white light while subjected to isotropic volume changes

selected. The swelling ratio can be experimentally estimated by monitoring the diameter of a cylindrical gel prepared in a glass capillary using the same recipe employed to fabricate the inverse opal gel. The variation in the refractive indices of the bulk gel and the solvent for various conditions were measured by a refractometer. Although the rate of change in n_a for the inverse opal gel obtained using the described recipe was only a few percent when the conditions were changed, the swelling ratio more than doubled. Thus, the effect of the swelling ratio is dominant over that of λ_{max} for the inverse opal gel [27].

By changing the number of target molecules, applying light, tuning the pH applied to the stimulus-sensitive inverse opal gels, and varying the degree of

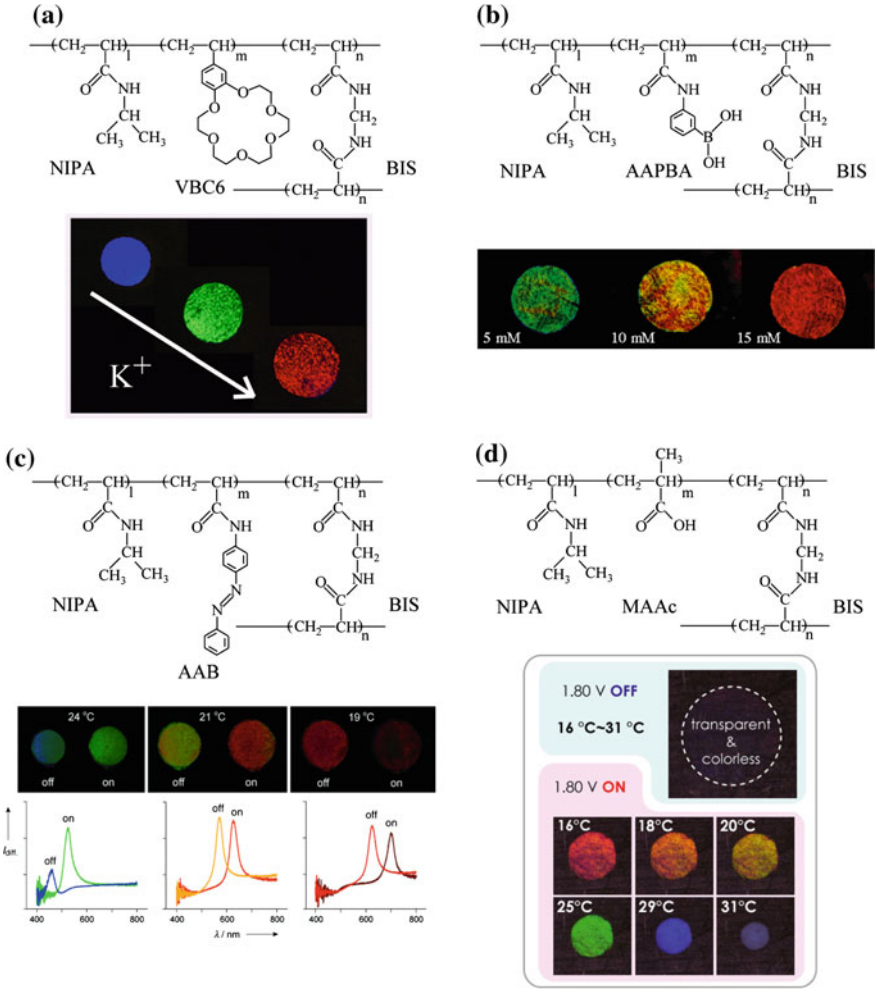

Fig. 2.3 Various applications of stimulus-responsive inverse opal gels in sensors and displays: **a** ion response, **b** glucose response, **c** light response, and **d** electric field response

swelling of the gels, the spacing between the submicron pores can be altered. Consequently, the obtained environmentally sensitive inverse opal gels exhibit a rapid change in both structural color and volume, making them useful for sensors [24, 25] and displays [28, 30, 34] (Fig. 2.3). These stimulus-responsive, structurally colored materials may find applications in visual systems, such as the paper-like color displays that have attracted attention over the years. Recently, some groups have independently developed electrically tunable soft photonic crystals using colloidal crystals, which may be applicable for flexible electronic paper and multi-color display technologies [30, 34–36]. These newly created tunable soft photonic crystals exhibit hue changes over the entire visible region; these changes are voltage-tunable without the need for other complicated systems in contrast to existing displays.

2.3 Stimulus-Responsive Structurally Colored Materials Using Colloidal Amorphous Arrays with Short-Range Order

Although structural coloration can be caused by ordered structures, recent studies of artificial structurally colored materials have primarily focused on the fabrication of particular periodical microstructures, such as multilayer films [37] and photonic crystals. This trend is partly attributed to the relative ease of understanding these structures and the simple principle of Bragg diffraction, which generates structural color from periodic dielectric structures. However, to design a reflective full-color paper-like display with a wide viewing angle, the angle dependence of the structural color based on Bragg diffraction becomes a major issue.

Recently, we demonstrated that amorphous arrays with a short-range order prepared from submicron spherical colloidal particles are capable of displaying angle-independent structural color and can be applied to non-fading color materials and full-color paper-like displays [38] (Fig. 2.4).

Colloidal amorphous arrays composed of hard colloidal particles are generally difficult to fabricate because submicrometer-sized hard particles have a strong tendency to crystallize [39]. By mixing two different types of submicrometer-sized hard particles, such as SiO_2 and polymeric colloidal particles, we can easily prepare colloidal amorphous arrays with a short-range order but without a long-range order or periodicity (Fig. 2.5a) [40]. The discrete ring observed in the two-dimensional Fourier transform (Fig. 2.5b) of a scanning electron microscopic (SEM) image indicates that the microstructure of an aggregate composed of SiO_2 particles is isotropic with a short-range order. The size variation of the hard colloidal particles causes them to be arranged in a disordered state. The short-range order in the colloidal amorphous arrays causes them to coherently scatter light; thus, the arrays exhibit structural color. By simply varying the ratio of the two different-sized particles during mixing, the hue of the angle-independent structural color can be controlled due to the

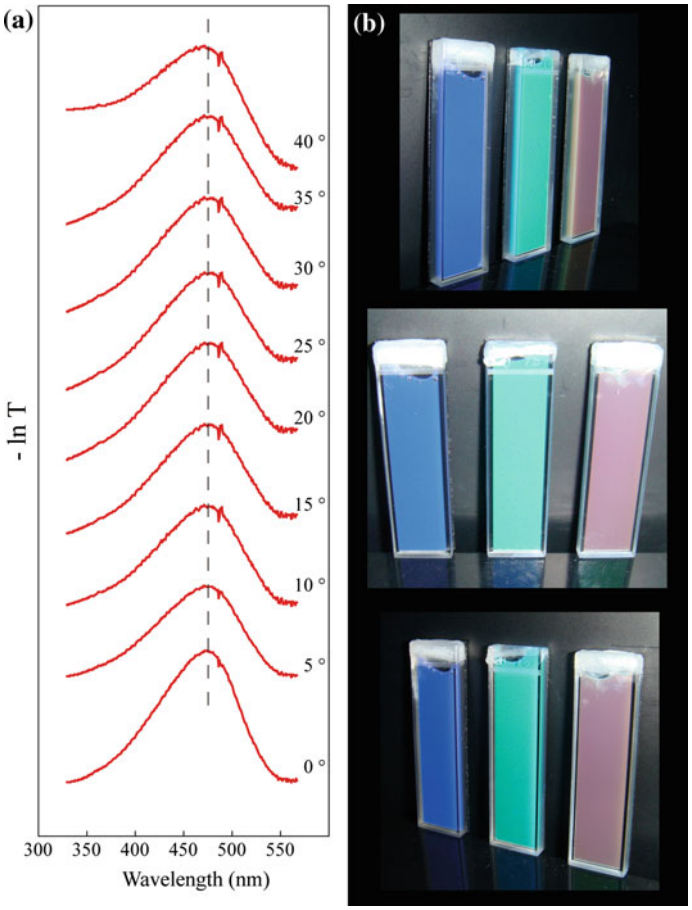

Fig. 2.4 **a** Transmission spectra of a gel particle suspension containing 5.0 wt% polymer content measured at various angles at 25 °C. The peak position λ_{max} observed at 470 nm remains unchanged from 0 to 40°. **b** Images of gel particle suspensions with 2.5, 4.2, and 5.6 wt% polymer concentrations. The structural colors observed for the samples do not change when observed from different viewing angles

change in the short-range order distance. However, the colors emitted from these colloidal amorphous arrays are very pale because the incoherent light scattering across the entire visible region is very strong in cases of a high refractive index contrast (i.e., the difference in the refractive index of the particle relative to the gap portion), such as air-filled SiO_2 colloidal arrays. In addition, the thickness of membranal colloidal amorphous arrays critically affects their color; their appearance becomes whitish as its thickness increases [16]. Even colloidal amorphous arrays composed of monodisperse fine colloidal particles, prepared by the spray method or another appropriate method, have faint whitish structural colors (Fig. 2.6) [17].

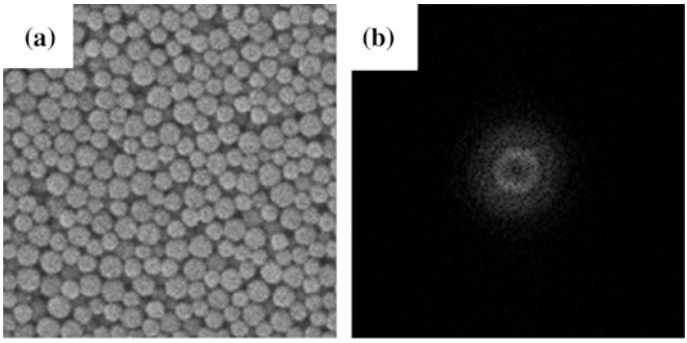

Fig. 2.5 **a** SEM and **b** 2D FT images of an amorphous array composed of 310- and 220-nm SiO_2 particles. The scale bar is 1 μm

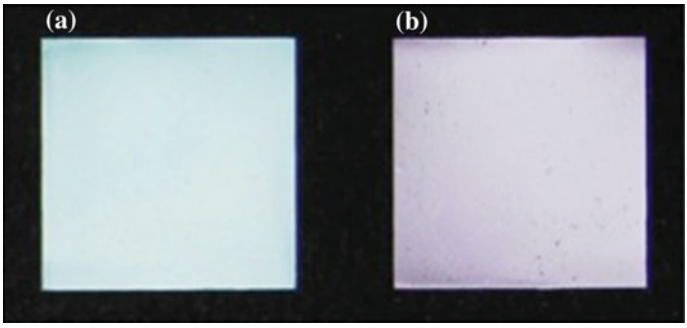

Fig. 2.6 Optical photographs of membranes composed of **a** 280-nm SiO_2 particles and **b** 360-nm SiO_2 particles

To determine the cause of incoherent light scattering across the entire visible region in colloidal amorphous arrays, the polarization spectra of membranal colloidal amorphous arrays were measured [17]. The spectra were obtained using the methods illustrated in Fig. 2.7. White light passes through a linear polarizer before it reaches the colloidal amorphous array. The polarization is parallel to the scattering plane formed by the incident beam and the detector. The incident angle between the surface normal and the planar surface of the membrane is 0°. The detector used to collect the scattered light was fixed at 10° from the surface normal. An additional linear polarizer was placed in front of the detector to change the polarization direction to be parallel (p-polarization) or perpendicular (s-polarization) to the scattering plane. The acquired polarization spectra of membranes composed of 360 nm SiO_2 colloidal particles are shown in Fig. 2.8. A peak at approximately 680 nm appeared in the spectrum of the co-polarized light (p-polarization) scattered from the membrane. The scattering spectrum of s-polarized light passing through the membrane shows nearly uniform scattering,

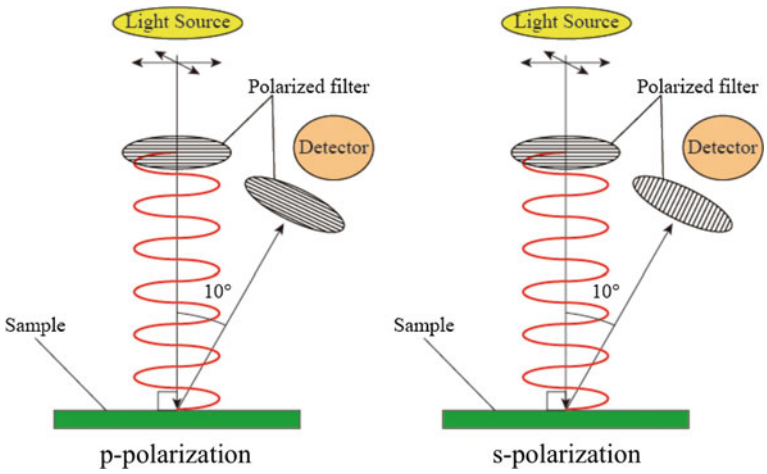

Fig. 2.7 Schematic of the instrument setup used to obtain the p-polarization and s-polarization spectra

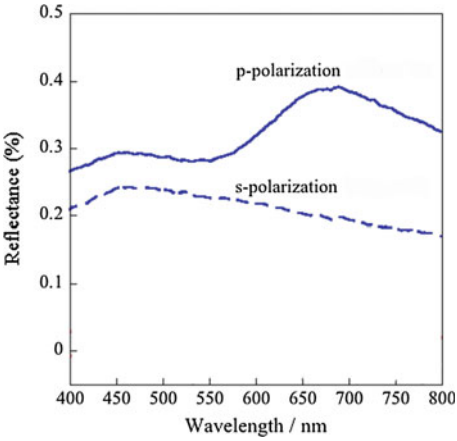

Fig. 2.8 The p-polarization and s-polarization scattering spectra of a colloidal amorphous array composed of 360-nm SiO_2 particles

with no distinct peak across the entire visible region. Conversely, in the scattering spectrum of p-polarized light, we observed that the light scattered from the membrane did not depolarize. From these results, we conclude that a single scattering process produced the peak observed in the spectrum of the colloidal amorphous array. However, in the case of the s-polarization scattering spectrum, we observed that the depolarized light passing through the membrane scattered as a result of a high-order scattering process. We hypothesized that light that scattered multiple times in the colloidal amorphous array significantly contributes to the nearly uniform scattering observed for the s-polarized light passing through the membrane.

To reduce the contribution of multiple scattered light rays to the total scattering spectrum and to enhance the structural color of the colloidal amorphous array, a black component that uniformly absorbs light across the entire visible region can be incorporated into the array. Carbon black (CB) is one of the most common and environmentally preferable black components; it reflects very little light in the visible region of the spectrum. Therefore, we prepared membranal colloidal amorphous arrays using suspensions of SiO_2 colloidal particles mixed with various small amounts of CB with an average particle size of 28 nm [17, 41, 42]. Figure 2.9a shows the membranes obtained by changing the amount of added CB. The color saturation observed on membranes composed of 360 nm SiO_2 colloidal particles increased with an increase in the amount of CB added to the suspension. The peak intensities of the reflection spectra were only slightly diminished, whereas the scattered intensities due to incoherent scattering across the entire visible region were significantly reduced (Fig. 2.9b). The color of the membrane can be controlled by the diameter of the SiO_2 colloidal particles (Fig. 2.9c). Because of the amorphous structure of the membrane, the colors are not dependent on the observation angle during illumination.

Consequently, we obtained vivid, angle-independent, structurally colored colloidal amorphous arrays by mixing black components with white colloidal particles. Theoretical interpretations regarding the existence of a photonic band gap, which causes structural color in amorphous array systems, have also been provided by some groups [43, 44].

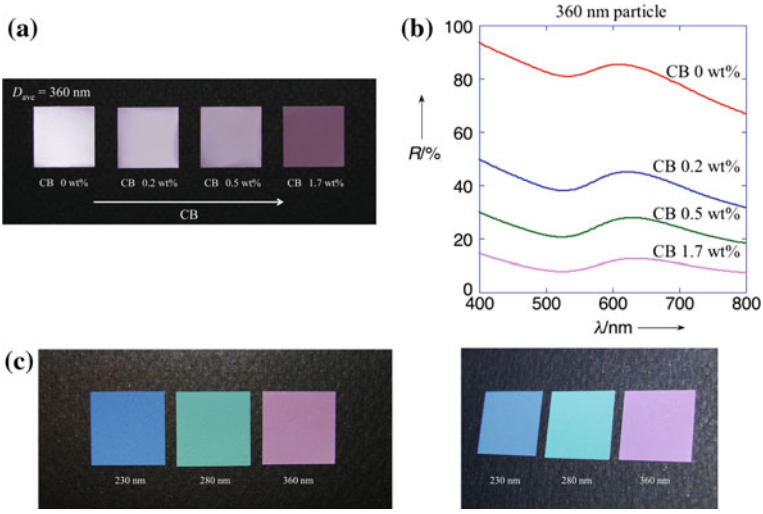

Fig. 2.9 **a** Optical photograph showing the color variation in colloidal amorphous arrays composed of 360-nm SiO_2 particles with various quantities of CB, **b** reflection spectra of the colloidal amorphous arrays shown in Fig. 2.9a, which were obtained using an integrating sphere measurement, and **c** optical photographs of colloidal amorphous arrays composed of 230, 280, and 360-nm SiO_2 particles with 1.7 wt% CB

Black melanin granules exist in structurally colored blue bird feathers, with a nanostructure exhibiting short-range order. However, the melanin granules are located beneath the nanostructure of the blue bird feathers [45], whereas the carbon black in our system is distributed throughout the colloidal amorphous array. Thus, the melanin granules in the bird feathers function to prevent light scattering from beneath the nanostructure; however, the carbon black reduces the total scattering within the colloidal amorphous arrays. In the near future, our research group will report on a biomimetic system that displays vivid and angle-independent structural color.

The practical fabrication of amorphous arrays from colloidal particle suspensions remains a complicated task and one of the most important challenges in large-scale production. Biological systems may guide us in the attainment of angle-independent structurally colored materials based on a simpler method. Analogous structures and the principle of structural coloration have also been linked to some living matter. For example, the amorphous packing of submicron spheres or tortuous channels composed of β-keratin and air nanostructures detected in the feather barbs of birds produce vivid structural color without angular dependence. The structural color of the feather barbs may be produced by wavelength-selective scattering of light from nanostructures with a short-range order, which must arise from the same principle as the previously described artificial systems. According to [46], the nanostructures in the feather barbs are self-assembled by the phase separation of β-keratin from a cellular cytoplasm, which drives phase separation within a cell; the arrest of the phase separation is facilitated by the entanglement or cross-linking of β-keratin filaments. As the molecular weight of the β-keratin filaments increases, the entropic incentive for mixing decreases and the phase boundary shifts to higher temperatures, which results in phase separation. If nucleation and growth occur, the system forms a submicron sphere-type nanostructure. When the phase separation is preceded by spinodal decomposition, a tortuous channel-type nanostructure can spontaneously evolve. This assumption stimulated our interest in the fabrication of phase-separated structures based on self-assembly approaches for artificial structurally colored materials. Therefore, we are now investigating a facile biomimetic preparation of self-assembled nanostructured and structurally colored materials with short-range order at scales comparable to the wavelength of visible light.

2.4 Angle-Independent Colored Materials Using the Christiansen Effect

In a different manner, we can obtain colored materials without angle-dependence by using self-assembled polymer microstructures instead of pigments and dyes [18, 19]. The microstructure is self-assembled by the phase separation of polymers. The self-assembled fabricated porous polymers reveal unexpected tunable color in response to solvent composition and temperature, although the average domain size in the porous polymers is approximately 10 μm, which is significantly larger than

the wavelength of visible light (Fig. 2.10). Here, I explain our new discovery regarding the facile preparation of this angle-independent colored material and its reversible tuning coloration, which is dependent on the solvent composition and the environmental temperature. The size of a scattering substance is parameterized by the ratio of its characteristic length r and the wavelength of light λ as $\alpha = 2\pi r/\lambda$. If the value of α becomes significantly larger than 1, the geometrical optic approximation can be applied to evaluate the interaction between the light and the scattering substance. Consequently, we must be able to treat these porous polymers as a diffuse reflective material.

Figure 2.11a displays the transmission spectra of the porous polymer in toluene/acetone solvents at 20 °C. The polymer is swollen with the solvent, whereas the pores are filled with the solvent. A broad peak is observed at approximately 766 nm for the porous polymer in pure toluene. However, the color of the porous polymer in pure toluene is brilliant blue (Fig. 2.11b). From the transmission spectra, we can assume that the blue color must be primarily caused by the diffuse reflection of short-wavelength visible light. The position of the peak λ_{max} moves to a shorter wavelength, and the peak sharpens with increasing acetone in the mixed solvent. The color of the porous polymer also changes depending on the composition of the mixed solvent; the color must be generated by the diffuse reflection of visible light at wavelengths that are both shorter and longer than the peak wavelength. Note that light within a certain wavelength range, corresponding to the sharp peak in the transmission spectra, can pass through this porous polymer depending on the solvent composition. This optical property is distinct from the optical properties of colloidal amorphous arrays prepared from submicron spherical particles and the nanostructures of feather barbs. A downward peak, which can be attributed to a p-PBG, can be observed in the transmission spectra of the colloidal amorphous arrays. Transmission spectra measured at different angles for the porous polymer in

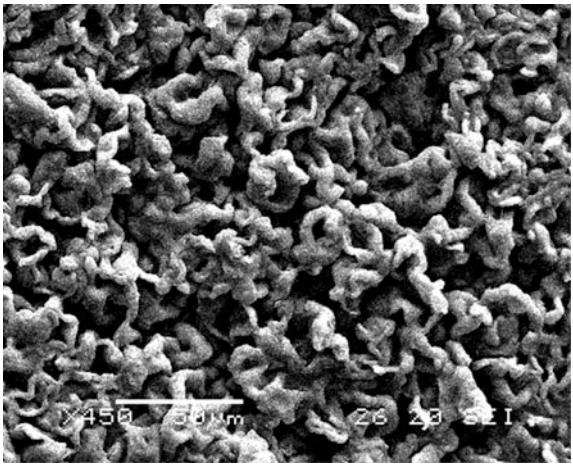

Fig. 2.10 SEM image of a self-assembled fabricated porous polymer

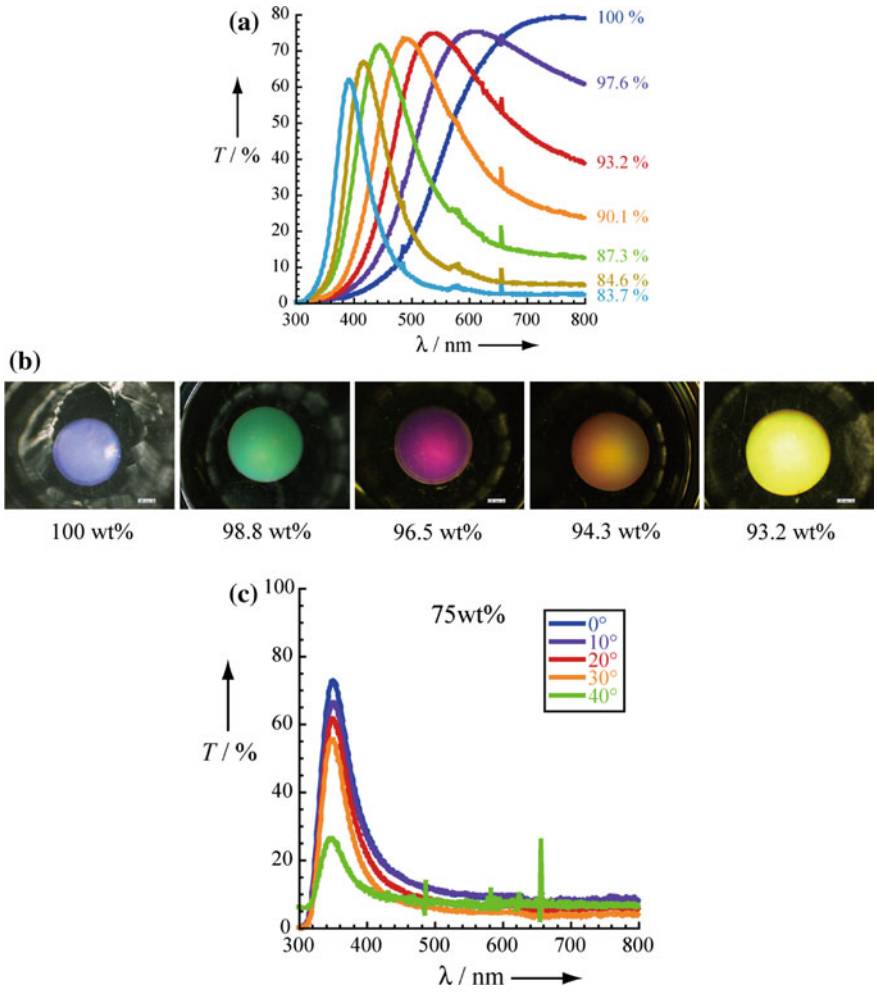

Fig. 2.11 **a** Solvent composition dependence of the transmission spectra and **b** optical photographs of the porous polymer at 20 °C. The scale bar in (**b**) is 1 mm. **c** Transmission spectra of the porous polymer in 75 wt% toluene measured at various angles at 20 °C

various solvent compositions are shown in Fig. 2.11c. The peaks occurred at specific wavelengths depending on the solvent composition and were angle-independent for angles from 0° to 40°.

Temperature-dependent transmission spectra of the porous polymer in pure toluene were also observed because the refractive index of the solvent is influenced by temperature variations. As shown in Fig. 2.12a, the peak position of the spectra is shifted to a shorter wavelength, and the peak becomes sharper with an increase in temperature. The refractive index of toluene and the peak position also decrease with increasing temperature (Fig. 2.12b). The swelling degrees of the porous

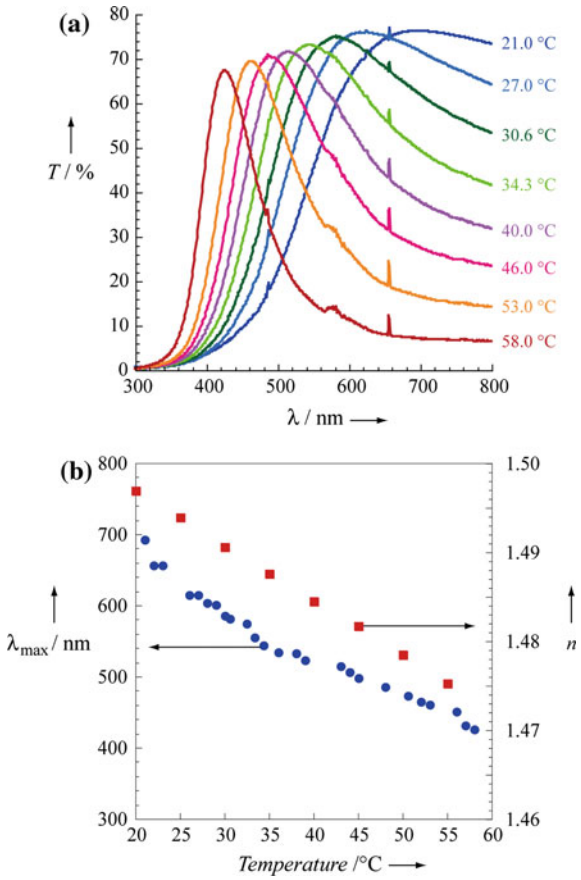

Fig. 2.12 **a** Temperature dependence of the transmission spectra of the porous polymer in pure toluene. **b** Plots showing λ_{max} for the transmission spectra of the porous polymer in pure toluene and the refractive index n of toluene at 589 (D) nm versus temperature

polymers remain unchanged with variations in solvent composition and temperature, which indicates that the variation in the size of the microstructure does not contribute to the change in color.

If the refractive indices of the swollen polymer portion and the solvent are equal, light at a certain wavelength near the intersection can pass through the porous polymer while light of other wavelengths can be diffusely reflected. As a result, we should see upward peaks in the transmission spectra of the porous polymer. To test this hypothesis, the dispersion curve of a 10 wt% linear polymer solution, identified based on the swollen polymer portion of the porous polymer, and that of toluene were estimated for different temperatures, and the intersection between the two curves as a function of temperature was identified. Cauchy's approximate equation was used to estimate the appropriate dispersion curves for each condition, based on the five experimentally measured plots of refractive indices (Fig. 2.13a). The estimated intersections between the curves for the 10 wt% polymer solution and toluene, which are dependent on temperature, were compared with the peak

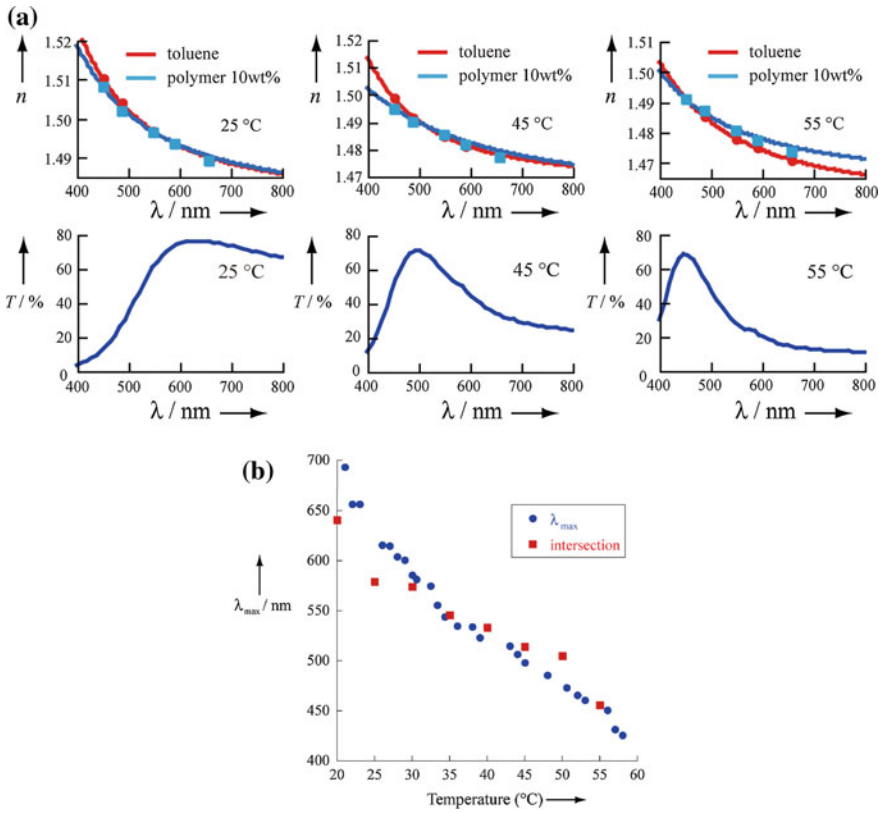

Fig. 2.13 **a** Dispersion curves of pure toluene compared to 10 wt% linear polymer in a toluene solution at various temperatures. The intersection of these curves varied with temperature. The transmission spectra were obtained from the porous polymer in toluene at different temperatures. **b** λ_{max} for the transmission spectra of 10 wt% linear polymer in a toluene solution at different temperatures compared with the temperature-dependent intersections obtained by Cauchy's approximate equation

wavelength of the spectra (Fig. 2.13b) for various temperatures. The intersections provided a reasonable estimate of the trend of the peak position of the transmission spectra with increasing temperature. This finding supports our hypothesis that the tunable coloration of the porous polymer is caused by the coincidence of the dispersion curve of the swollen-polymer portion and that of the solvent portion at a single wavelength, which is dependent on the solvent composition and temperature. According to Fig. 2.13a, the sharpness of the peak must be attributed to the intersection of two dispersion curves with a large angle. As a result, the porous polymer exhibits brilliant colors. These results indicate that the colors are caused by the Christiansen effect.

In contrast to previously studied structurally colored materials, this system can easily be applied to produce a large-sized display because of its facile one-pot

preparation method and its mechanism of coloration. Because this porous polymer displays color with a low angle dependence and can act as a multi-color polymer-dispersed liquid crystal when using liquid crystals as solvents [19], we believe that this system may also be suitable for energy-saving multi-color displays.

2.5 Conclusions

In this chapter, I described different types of stimulus-responsive colored materials generated without pigments or dyes. Because these stimulus-responsive colored materials exhibit unique properties, they are promising candidates for future sensing and display devices.

References

1. E. Yablonovitch, Inhibited spontaneous emission in solid-state physics and electronics. Phys. Rev. Lett. **58**, 2059–2062 (1987). doi:10.1103/Physrevlett.58.2059
2. C. Lopez, Materials aspects of photonic crystals. Adv. Mater. **15**, 1679–1704 (2003). doi:10.1002/Adma.200300386
3. H. Miguez et al., Control of the photonic crystal properties of fcc-packed submicrometer SiO_2 spheres by sintering. Adv. Mater. **10**, 480–483 (1998). doi:10.1002/(Sici)1521-4095(199804)10:6<480:Aid-Adma480>3.0.Co;2-Y
4. H.S. Sozuer, J.W. Haus, R. Inguva, Photonic bands—convergence problems with the plane-wave method. Phys. Rev. B **45**, 13962–13972 (1992). doi:10.1103/Physrevb.45.13962
5. Z.Z. Gu et al., Angew. Chem. Int. Edit. **42**, 894 (2003). doi:10.1002/Anie.200390235
6. S. Kinoshita, S. Yoshioka, Structural colors in nature: the role of regularity and irregularity in the structure. Chem. Phys. Chem. **6**, 1442–1459 (2005). doi:10.1002/Cphc.200500007
7. M. Harun-Ur-Rashid, T. Seki, Y. Takeoka, Gels for tunable soft photonic crystals. Chem. Rec. **9**, 87–105 (2009). doi:10.1002/Tcr.20169
8. J.P. Ge, Y.D. Yin, Responsive photonic crystals. Angew. Chem. Int. Edit. **50**, 1492–1522 (2011). doi:10.1002/Anie.200907091
9. Y. Takeoka, Stimuli-responsive opals: colloidal crystals and s for use in functional structurally colored materials. J. Mater. Chem. C **1**, 6059–6074 (2013). doi:10.1039/C3tc30885e
10. H. Fudouzi, Tunable in organisms and photonic materials for design of bioinspired materials. Sci. Technol. Adv. Mater. **12**, 064704 (2011). doi:10.1088/1468-6996/12/6/064704
11. Y. Hayata, S. Nagano, Y. Takeoka, T. Seki, Photoinduced volume transition in liquid crystalline polymer gels swollen by a nematic solvent. ACS Macro Lett. **1**, 1357–1361 (2012). doi:10.1021/Mz300447j
12. H. Murayama et al., Chromic slide-ring gel based on reflection from photonic bandgap. Macromolecules **41**, 1808–1814 (2008). doi:10.1021/Ma0715627
13. Y. Takeoka, Structural coloured amorphous arrays. J. Mater. Chem. **22**, 23299–23309 (2012). doi:10.1039/C2jm33643j
14. S. John, Strong localization of photons in certain disordered dielectric superlattices. Phys. Rev. Lett. **58**, 2486–2489 (1987). doi:10.1103/Physrevlett.58.2486
15. J.F. Galisteo-Lopez et al., Self-assembled photonic structures. Adv. Mater. **23**, 30–69 (2011). doi:10.1002/Adma.201000356

16. J.D. Forster et al., Biomimetic isotropic nanostructures formation. Adv. Mater. **22**, 2939–2944 (2010). doi:10.1002/Adma.200903693
17. Y. Takeoka et al., Production of colored pigments with amorphous arrays of black and white colloidal particles. Angew. Chem. Int. Edit. **52**, 7261–7265 (2013). doi:10.1002/Anie.201301321
18. N. Kumano, T. Seki, M. Ishii, H. Nakamura, Y. Takeoka, Tunable from a phase-separated porous gel. Angew. Chem. Int. Edit. **50**, 4012–4015 (2011). doi:10.1002/Anie.201008182
19. N. Kumano et al., Multicolor polymer-dispersed liquid crystals. Adv. Mater. **23**, 884–888 (2011). doi:10.1002/Adma.201003660
20. R. Mayoral et al., 3D long-range ordering in an SiO_2 submicrometer-sphere sintered superstructure. Adv. Mater. **9**, 257–260 (1997). doi:10.1002/Adma.19970090318
21. F. Marlow, P. Sharifi, R. Brinkmann, C. Mendive, Opals: status and prospects. Angew. Chem. Int. Edit. **48**, 6212–6233 (2009). doi:10.1002/Anie.200900210 (2009)
22. Y. Takeoka, M. Watanabe, Polymer gels that memorize structures of mesoscopically sized templates. Dynamic and optical nature of periodic ordered mesoporous chemical gels. Langmuir **18**, 5977–5980 (2002). doi:10.1021/La020133t
23. Y. Takeoka, M. Watanabe, Template synthesis and optical properties of chameleonic poly (N-isopropylacrylamide) gels using closest-packed self-assembled colloidal silica crystals. Adv. Mater. **15**, 199–201 (2003). doi:10.1002/Adma.200390044
24. D. Nakayama, Y. Takeoka, M. Watanabe, K. Kataoka, Simple and precise preparation of a porous gel for a colorimetric glucose sensor by a templating technique. Angew. Chem. Int. Edit. **42**, 4197–4200 (2003). doi:10.1002/Anie.200351746
25. H. Saito, Y. Takeoka, M. Watanabe, Simple and precision design of porous gel as a visible indicator for ionic species and concentration. Chem. Commun. 2126–2127 (2003). doi:10.1039/B304306a
26. Y. Takeoka, M. Watanabe, R. Yoshida, Self-sustaining peristaltic motion on the surface of a porous gel. J. Am. Chem. Soc. **125**, 13320–13321 (2003). doi:10.1021/Ja036904c
27. Y. Takeoka, T. Seki, Visualizing conformations of subchains by creating optical wavelength-sized periodically ordered structure in hydrogel. Langmuir **22**, 10223–10232 (2006). doi:10.1021/La061945i
28. K. Matsubara, M. Watanabe, Y. Takeoka, A thermally adjustable multicolor photochromic hydrogel. Angew. Chem. Int. Edit. **46**, 1688–1692 (2007). doi:10.1002/Anie.200603554
29. Y. Takeoka, T. Seki, Biform structural colored hydrogel for observation of subchain conformations. Macromolecules **40**, 5513–5518 (2007). doi:10.1021/Ma0701078
30. K. Ueno, K. Matsubara, M. Watanabe, Y. Takeoka, An electro- and thermochromic hydrogel as a full-color indicator. Adv. Mater. **19**, 2807 (2007). doi:10.1002/Adma.200700159
31. S. Shinohara, T. Seki, T. Sakai, R. Yoshida, Y. Takeoka, Photoregulated wormlike motion of a gel. Angew. Chem. Int. Edit. **47**, 9039–9043 (2008). doi:10.1002/Anie.200803046
32. S. Shinohara, T. Seki, T. Sakai, R. Yoshida, Y. Takeoka, Chemical and optical control of peristaltic actuator based on self-oscillating porous gel. Chem. Commun. 4735–4737 (2008). doi:10.1039/B808427k
33. M. Honda, T. Seki, Y. Takeoka, Dual tuning of the photonic band-gap structure in soft photonic crystals. Adv. Mater. **21**, 1801–1804 (2009). doi:10.1002/Adma.200801258
34. K. Ueno, J. Sakamoto, Y. Takeoka, M. Watanabe, Electrochromism based on structural colour changes in a polyelectrolyte gel. J. Mater. Chem. **19**, 4778–4783 (2009). doi:10.1039/B900261h
35. A.C. Arsenault, D.P. Puzzo, I. Manners, G.A. Ozin, Photonic-crystal full-colour displays. Nat. Photonics **1**, 468–472 (2007). doi:10.1038/Nphoton.2007.140
36. G.R. Yi, J.H. Moon, S.M. Yang, Macrocrystalline colloidal assemblies in an electric field. Adv. Mater. **13**, 1185–1188 (2001). doi:10.1002/1521-4095(200108)13:15<1185:Aid-Adma1185>3.0.Co;2-I
37. Y. Kang, J.J. Walish, T. Gorishnyy, E.L. Thomas, Broad-wavelength-range chemically tunable block-copolymer photonic gels. Nat. Mater. **6**, 957–960 (2007). doi:10.1038/Nmat2032

38. Y. Takeoka, M. Honda, T. Seki, M. Ishii, H. Nakamura, Liquid membrane without angle dependence. ACS Appl. Mater. Inter. **1**, 982–986 (2009). doi:10.1021/Am900074v
39. J. Mattsson et al., Soft colloids make strong glasses. Nature **462**, 83–86 (2009). doi:10.1038/Nature08457
40. M. Harun-Ur-Rashid et al., Chem. Phys. Chem. **11**, 579–583 (2010). doi:10.1002/Cphc.200900869
41. Takeoka, Y. et al., Structurally coloured secondary particles composed of black and white colloidal particles. Sci. Rep.-UK **3**, 2371 (2013). doi:10.1038/Srep02371
42. S. Yoshioka, Y. Takeoka, Production of colourful pigments consisting of amorphous arrays of silica particles. Chem. Phys. Chem. **15**, 2209–2215 (2014). doi:10.1002/cphc.201402095
43. S.F. Liew et al., Short-range order and near-field effects on optical scattering and structural coloration. Opt. Express **19**, 8208–8217 (2011)
44. S.F. Liew et al., Photonic band gaps in three-dimensional network structures with short-range order. Phys. Rev. A **84**, 063818 (2011). doi:10.1103/Physreva.84.063818
45. M.D. Shawkey, G.E. Hill, Significance of a basal melanin layer to production of non-iridescent structural plumage color: evidence from an amelanotic Steller's jay (Cyanocitta stelleri). J. Exp. Biol. **209**, 1245–1250 (2006). doi:10.1242/Jeb.02115
46. R.O. Prum, E.R. Dufresne, T. Quinn, K. Waters, Development of colour-producing beta-keratin nanostructures in avian feather barbs. J. R. Soc. Interface **6**, S253–S265 (2009). doi:10.1098/Rsif.2008.0466.Focus

Chapter 3
Colloidal Photonic Crystals for Sensor Applications

Shin-Hyun Kim and Gi-Ra Yi

Abstract Colloidal crystals can be formed by self-assembly in which structural reflective color can be highly sensitive to interparticle distance or reflective index mismatch between particle and matrix. Therefore, if either matrix or particles are made out of stimuli-responsive materials, various environmental parameters can be sensed such as pH, temperature, pressure, mechanical deformation and so on. Also, by introducing chemical probes, various biomolecules (DNA) or toxic chemicals including gas and volatiles can be detected, which would be further extended to biomedical sensor platform. Compared with other sensor device, colloidal crystals are mechanically and chemical stable and their color change is reversible and could be operated without external (electrical or photon) energy. In this chapter, basic design principle of colloidal photonic crystals and sensors are described and representative examples of sensors are provided for various stimulus.

Monodisperse colloidal particles can spontaneously organize into highly ordered arrays, known as colloidal crystals, when they are concentrated or possess repulsive interparticle potentials. The colloidal crystals provide periodic modulation of refractive index, which gives rise to selective diffraction of light through constructive interference. In particular, when the size of colloids is comparable to half the wavelength of visible light, the crystals exhibit iridescent reflection colors. The resonance wavelength is determined by periodicity and refractive index of the lattice structure. Therefore, if the periodicity or refractive index are changed under specific conditions, the wavelength or equivalently reflection color is also altered. This enables us to make colloidal crystal-based sensors. The wavelength shift or color change is quantitatively analyzable with reflectance or transmittance spectra. The design principles of the sensors rely on stimuli-responsive change of periodicity or refractive index. Several distinct structures of colloidal crystals and their

S.-H. Kim (✉)
Department of Chemical and Biomolecular Engineering, KAIST, Daejeon, Korea
e-mail: kim.sh@kaist.ac.kr

G.-R. Yi (✉)
Department of Chemical Engineering, SKKU, Suwon, Korea
e-mail: yigira@skku.edu

M. J. Serpe et al. (eds.), *Photonic Materials for Sensing, Biosensing and Display Devices*, Springer Series in Materials Science 229,
DOI 10.1007/978-3-319-24990-2_3

derivatives have been prepared with various sets of stimuli-responsive materials to provide such sensors and provided new opportunity in various sensing applications.

This chapter covers basic design principle of colloidal photonic crystals and sensors. In subsequent four sections, we discuss (1) the basic mechanisms of colloidal crystallization, (2) optical and mechanical properties of colloidal crystals and their derivatives, (3) stimuli-responsive materials, and (4) three distinct formats of colloidal structures. In fifth section, we classify sensors with respect of stimulus and provide a short review of representative examples of sensors for each stimulus.

3.1 Self-assembled Colloidal Crystals

3.1.1 Close-Packed Colloidal Crystals

Colloidal particles dispersed in a liquid medium at low concentration have no restriction to diffuse and therefore show Brownian random motion. When the concentration of the colloids slowly increases, interparticle distance becomes shorter and the motion is limited by neighbors at certain concentration. Obviously, attractive particles will be aggregated even at relatively low concentration, commonly into disordered structure. By contrast, repulsive particles could form ordered structure. 'Hard spheres', which do not have any interaction potential but divergently repel only when they contact each other, will keep moving randomly when their volume fraction is relatively low. However, at high volume fraction ($\sim$49.4 %), they begin to form regular array [1]. The fraction of ordered region over whole volume of dispersion increases until the colloids are further concentrated to volume fraction of 54.5 %. For higher volume fraction than 54.5 %, they can get closer without aggregation maintaining the dispersion fully crystallized. At volume fraction of 74 %, colloids are closely packed forming face-centered cubic (FCC) structure, in which they are not able to be further compressed.

The mechanism of the hard-sphere packing is related with entropy [2]. The spheres are moving randomly until 49.4 % of volume fraction. Such Brownian random motion is not favored any more above 49.4 % of volume fraction. In other words, the random motion is strongly restricted by neighbor particles at that volume fraction. If the spheres are ordered, each sphere has larger room to move, which provides many more configurational states which colloids can take in comparison with random arrangement, thereby yielding higher entropy. Therefore, ordered array of hard spheres is thermodynamically more favored than random disordered structure. In most experiments, hard spheres form a mixture of FCC and hexagonal close packed (HCP) structures because they are structurally similar and have the same maximum volume fraction of 74 %. Both FCC and HCP are stacking structure of hexagonal array, but the hexagonal arrays at three different positions are sequentially stacked in FCC, whereas the array at two different positions are

repeatedly stacked in HCP. Although FCC is known more favored than HCP, entropy discrepancy is very small, leading to coexistence of both structures [3].

To form FCC or opal structure on flat substrate, dip-coating method has been extensively used [4–6]. Hydrophilic substrate is dipped into the aqueous colloidal suspension and then slowly pulled out or kept until water is evaporated out completely. Water evaporates faster on the meniscus than other surface region, which induce the particles to move toward meniscus from bulk. Therefore, particles are concentrated near the meniscus and finally crystallized on the substrate. Because those colloids are repulsive due to electrostatic interaction, crystallization might occur at lower volume fraction than 49.4 %. However, evaporation of water compresses the non-close-packed FCC structure and finally close-packed FCC structure remains on the substrate after complete drying. This concentration-induced formation of close-packed FCC structure is denoted with top arrow in Fig. 3.1a and resulting structure is shown in Fig. 3.1b.

Fast evaporation of water during the dip coating process can kinetically arrest random arrangement of colloids, leaving less ordered structure with volume fraction lower than 0.74. Large size of colloids and large density contrast between colloids and dispersion medium causes fast sedimentation, leading to thickness variation of deposited structure. Therefore, to prepare highly ordered array with uniform thickness, colloids need to be slowly concentrated from homogeneous suspension.

For two-dimensional colloidal monolayers, dielectrophoretic (DEP) force on relatively large particles (>1μm) can be applied to colloidal suspension in which coplanar colloidal crystals could be formed quickly within tens of seconds [7].

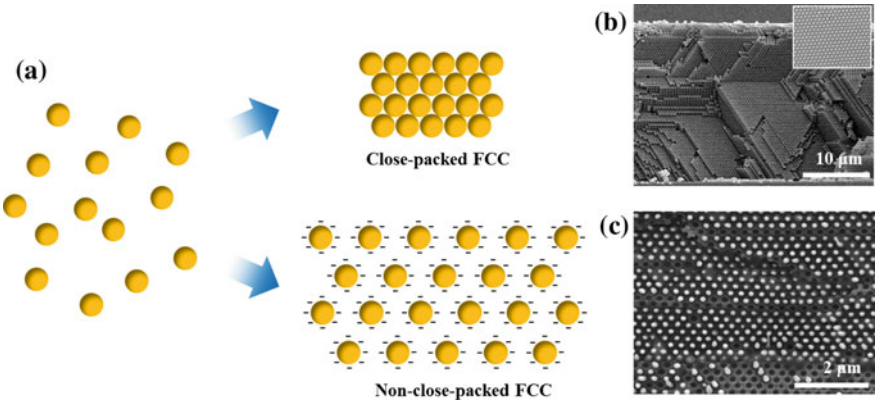

Fig. 3.1 **a** Concentration-induced crystallization into close-packed face-centered cubic (FCC) lattice (*top*) and interparticle repulsion-induced crystallization into non-close-packed FCC lattice (*bottom*). **b** Scanning electron microscope (SEM) images showing cross-section (*main panel*) and top view (*Inset*) of close-packed FCC structures formed on the surface of glass substrate. **c** SEM image of cross-section of non-close-packed FCC where colloids are immobilized in a dried hydrogel matrix. Reproduced from [11] with permission

In similar manner, Trau et al. demonstrated that patterned monolayed or multilayered colloidal crystals could be formed under AC or DC electric field, respectively, in which electric field was applied in perpendicular direction of colloidal crystals [8].

3.1.2 Non-close-Packed Colloidal Crystals

In case of repulsive colloids, they also form crystals not by maximizing entropy but minimizing total interaction energy; colloids which interact with their neighbors even when they are separated are referred to as soft spheres and here we restrict our attention to repulsive potential because attractive potential usually leads to random aggregates. When the interparticle potential is repulsive in long range, soft spheres are crystallized at very low volume fraction. In aqueous suspensions, electrostatic repulsion between surface charges on the particles usually overwhelms van der Waals attraction in absence of ionic impurities, thereby providing dispersion stability and sometimes leading to spontaneous crystallization of particles without concentration as denoted with bottom arrow in Fig. 3.1a. In non-polar media, polymer brushes which have high affinity to the media can be grafted on the surface of colloids to render them repulsive. When two colloids approach each other, the brushes are overlapped, which increases osmotic pressure in their gap, thereby leading to inward flow and separation between two; this is called steric effect. When particles are dispersed in solvents which can form a dense solvation layer on the surface through forming hydrogen bonds, strong disjoining pressure can separate particles and leads to repulsion. Such various origins of repulsive potential can be used to crystallize colloids at relatively low concentration.

For a wide range of particle volume fraction and repulsive potential, non-close-packed FCC crystal is formed to minimize repulsive energy. Body-centered cubic (BCC) is favored only for a small window at low volume fraction and very long-range repulsive potential [9, 10]. The crystalline structures formed in a liquid state are fragile against impurity and shear flow. One way to stabilize the structures is immobilization of colloids by polymers. To achieve this, non-ionic monomers are dissolved in dispersion media of crystalline colloidal array (CCA), which are then polymerized to immobilize colloids as shown in Fig. 3.1c; such a polymerized CCA is referred to as PCCA [11]. The colloidal crystals embedded in the polymer matrix can maintain their regular array against impurity and mechanical stress. Moreover, the polymer matrix can be designed to be stimuli-responsive as we will study in Sects. 3.4 and 3.5, thereby serving as useful materials for sensors.

3.2 Properties of Colloidal Crystals and Their Derivatives

3.2.1 Optical Property

The periodic modulation of refractive index in colloidal crystals gives rise to photonic bandgap property. At the bandgap, photon density of states becomes very low within the materials, thereby resulting in selective reflection of light at the bandgap [12]. This usually develops iridescent colors. The bandgap position and band width can be precisely calculated by solving Maxwell equation for periodic colloidal structures. MIT photonic-bands (MPB) software which was developed by Joannopoulos and Johnson groups in MIT is available for construction of photonic band structures [13]. Alternatively, we can simply estimate the bandgap position using Bragg's law and the band width with refractive index contrast. When a light is scattered by regular lattice of colloids, scattered waves constructively interfere if they are in phase. Therefore, when the path difference between two waves is equal to an integer multiple of the wavelength, amplitude of the scattered waves increases. This Bragg's condition is able to predict bandgap position of colloidal crystals. In a colloidal crystal, there are several different crystal planes which can provide constructive interference of light by scattering. When the plane spacing is denoted by d_{hkl}, the Bragg's condition provides wavelength of light for constructive interference as shown in Fig. 3.2a:

$$\mathrm{n}\lambda = 2d_{hkl}\sqrt{n_{eff}^2 - \sin\theta}, \tag{3.1}$$

where n is diffraction order, n_{eff} is effective refractive index of colloidal structure and θ is angle of incident light measured from plane normal. To determine d_{hkl} for (h k l) plane, we can use

$$d_{hkl} = \frac{a}{\sqrt{h^2 + k^2 + l^2}}, \tag{3.2}$$

where a is lattice constant of crystal unit cell. The value of n_{eff} can be estimated by averaging refractive indices of colloidal particles and matrix, n_{p} and n_{m}. Among several different averaging methods, the Maxwell–Garnett average is widely used for this purpose:

$$n_{eff}^2 = n_p^2\phi_p + n_m^2\phi_m, \tag{3.3}$$

where ϕ_{p} and ϕ_{m} are volume fractions of colloidal particles and matrix, respectively; $\phi_{\mathrm{m}} = 1 - \phi_{\mathrm{p}}$ when only two materials comprise the structure. Above equations can be used for any crystal structures including FCC and BCC and any combinations of refractive indices of particles and matrix.

Colloidal crystals usually have close-packed or non-close-packed FCC lattice although many of them is mixed with HCP; BCC only appears for highly repulsive

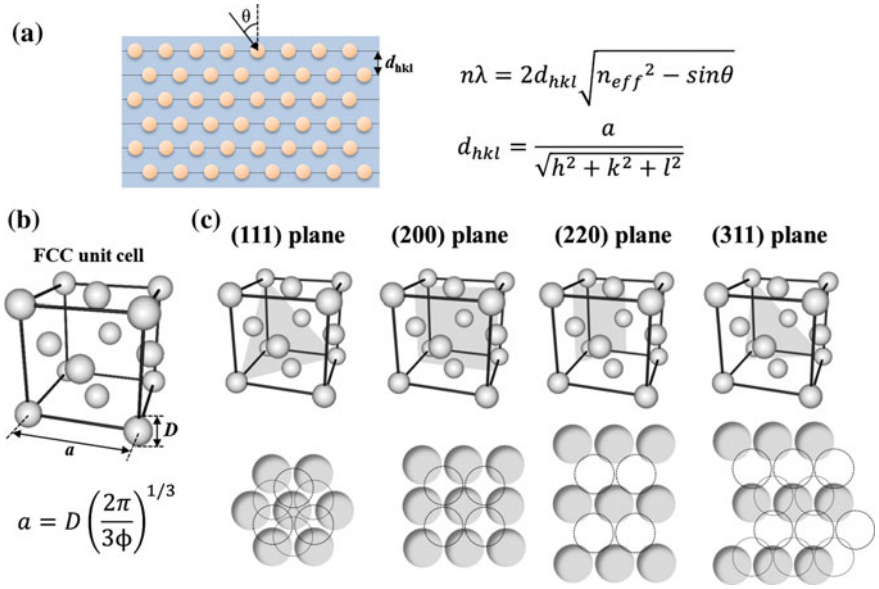

Fig. 3.2 **a** Diffraction from a regular lattice with interplane spacing of d_{hkl} and incident angle of θ. The diffraction wavelength, λ, is influenced by d_{hkl}, θ, and effective refractive index, n_{eff}, where d_{hkl} is determined by lattice constant, a, and Miller indices of plane. **b** Unit cell of FCC structures composed of spheres with diameter, D, where a is determined by D and volume fraction of spheres, ϕ. **c** Four representative crystal planes of FCC structure responsible for diffraction, where *shaded region* in *top row* indicates the corresponding plane in unit cell and *filled circles* in *bottom row* shows arrangement of spheres in the plane

colloids at low volume fraction. A unit cell of FCC contains half spheres on six planes of cubic and one-eighth spheres at eight corners, thereby involving 4 full spheres. Therefore, lattice constant, a, can be written with volume fraction of particles with diameter, D:

$$a = \mathrm{D}\left(\frac{2\pi}{3\phi_p}\right)^{1/3}. \tag{3.4}$$

This equation provides value of a for FCC with any volume fraction smaller than 0.74, which can be used in (3.2). For close-packed FCC with $\phi_p = 0.74$, the equation returns $a = 1.414D$; close-packed FCC structure is called opal structure because natural opals have close-packed FCC structure composed of silica particles.

For a FCC lattice, reflection presents only for h, k, l which are all odd or all even; for a BCC lattice, reflection is effective when sum of h, k, and l is even. Therefore, representative crystal plane groups, responsible for reflection, are {111}, {200}, {220}, and {311} as shown in Fig. 3.2b. The (111) plane is composed of hexagonal array of particles. Along the [111] direction, the hexagonal arrays are stacked,

where three neighboring layers are placed in all different lateral positions and the set of three layers is repeated. In most experiments, the (111) planes are formed along surface of confining geometry by heterogeneous nucleation. Therefore, surface of crystal structure is usually composed of (111) plane. Therefore, stack of (111) planes provides dominant photonic effect among stacks of all planes and has been used for most sensor applications. The (200) plane is composed of square array and the (220) plane is composed of rectangular array. The (311) plane is also composed of rectangular array, but their stacking structures are more complicate than (220) plane.

The width of bandgap, $\Delta\lambda$, normalized with bandgap wavelength is roughly proportional to refractive index contrast between particles and matrix normalized with effective refractive index [14]:

$$\frac{\Delta\lambda}{\lambda} \sim \frac{|n_p - n_m|}{n_{eff}}. \tag{3.5}$$

Therefore, higher contrast in refractive index provides wider band. This proportionality is generally correct for any regular colloidal structures and crystal planes, although the proportional constant might depend on several different parameters such as crystal structures, crystal planes, and volume fraction of particles.

3.2.2 Mechanical Property

Colloidal crystal films with close-packed FCC structure or opaline thin films are often prepared by dip-coating method as we studied in the first section, in which particles are stacked and physically bonded due to intermolecular attractive force or van der Waals force. Therefore, the structures are fragile. The opaline thin films subjected to bending are usually cracked as illustrated in Fig. 3.3a. To improve mechanical stability, the opals are thermally annealed to make necks between neighboring particles, while maintaining voids in interstices; each particle in FCC lattice has 12 nearest neighbors. However, particles typically used for colloidal crystals, including polystyrene, poly(methyl methacrylate), and silica particles, are not elastic or flexible, providing a limited mechanical stability against bending and stretching even after the neck formation. One way to achieve higher mechanical stability and flexibility is to make inverse opals which is phase-inverted structure from opal. Interstices between colloids in opal is fully filled with second material, from which colloids are selectively removed, thereby leaving behind regular air cavities with FCC lattice in solid matrix. The interstitial space is not isolated but continuous, which yields monolithic structure at which spherical cavities are completely isolated or connected with small windows. Therefore, mechanical stability can be highly enhanced from opal structure. In particular, the mechanical property is dominantly determined by matrix materials which can be selected

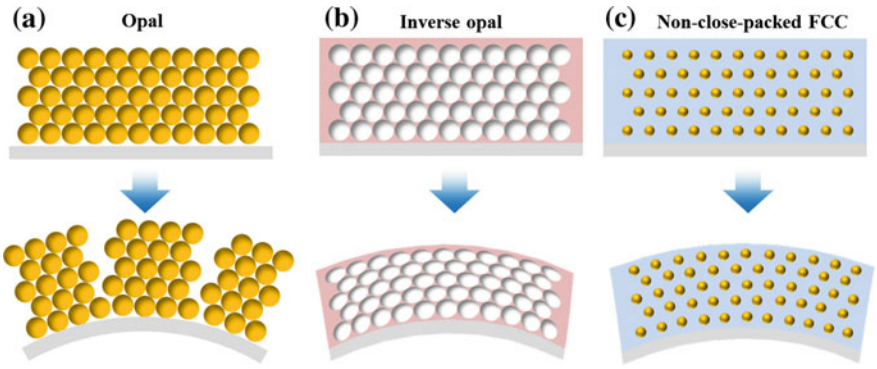

Fig. 3.3 Mechanical response of three distinct structures under bending: **a** Opal, close-packed FCC structure of spherical particles, shows crack formation, **b** inverse opal, phase-inverted structure from opal, shows deformation of both matrix and air cavities, and **c** non-close-packed FCC structure embedded in *solid matrix* shows deformation of matrix with negligible deformation of colloids

among various rubbery materials. Therefore, they could be flexible and stretchable structure as illustrated in Fig. 3.3b; for the flexible structures, the matrix becomes deformed during stretching or bending, providing mechanochromic property. Moreover, stimuli-responsive hydrogels can be used to make colorimetric sensors as we will further study in following sections. The inverse opal is beneficial not just for mechanical stability but also for photonic properties; the inverse opal possesses narrow but full bandgap when refractive index of matrix is larger than 2.8, indicating the light at the bandgap is not allowed to propagate through all the directions of the materials [15]. This is very important property for wave guiding and creation of photonic circuits. In addition, large void fraction is also beneficial in sensor application; inverse opals provide larger change of effective refractive index when their pores are filled with liquid in comparison with opals.

Non-close-packed colloidal crystals are fragile against impurities and shear stress. However, their stability can be dramatically enhanced by permanently immobilizing the colloids in solid matrix. For this, monomers can be dissolved in the dispersion media or liquid monomers themselves can be used as the media. When non-close-packed FCC structure, or CCA, is formed in such media by repulsive interparticle potential, the media can be polymerized resulting in PCCA. Such composite structures are more stable than inverse opal due to higher volume fraction of the matrix and absence of air cavities, if the matrix is made of same materials. When PCCA made of a flexible matrix is subjected to stretching or bending, colloids usually maintain their spherical shape with negligible deformation as illustrated in Fig. 3.3c. However, sets of colloidal and matrix materials to make PCCAs are restricted in comparison with that of inverse opals. Therefore, PCCAs have limited property and functionality. Nevertheless, PCCAs have been used for various chemical and biological sensors due to relatively simple fabrication scheme and high compatibility to hydrogels which are predominantly used for sensors.

3.3 Stimuli-Responsive Materials

3.3.1 Responsive Colloids

For sensing application of colloidal crystals, periodicity or refractive index should be changed under specific environments or target conditions, which leads to shift of resonance wavelength or equivalently change of reflection color as we can notice from (3.1). In general, change of refractive index is small or negligible for most target conditions, except replacement of whole surrounding medium, thereby yielding insignificant color change; this is still detectable with a spectrometer. By contrast, periodicity can be highly modulated by swelling and deswelling of materials or deformation of structures under specific conditions, providing discernable change of color by naked eye or large shift of reflectance peak in spectrum. Such stimuli-induced changes of periodicity can be achieved by employing either responsive colloids or matrix.

Colloidal materials typically used for crystallization, such as polystyrene, poly (methyl methacrylate), and silica exhibit negligible swelling or deformation under various physical and chemical conditions near room temperature, thereby being inappropriate for sensing applications. By contrast, colloidal particles can be synthesized with special materials to render them stimuli-responsive. Therefore, the colloidal crystals composed of such responsive particles can provide stimuli-induced changes of periodicity and therefore shift of bandgap position as shown in Fig. 3.4a and c. For example, particles can be made of poly (N-isopropylacrylamide) (PNIPAM) which is thermoresponsive hydrogel materials with the lower critical solution temperature (LCST) around 32 °C [16]; the particles can be sometimes designed to have core-shell structure of which shell is made of such hydrogels [17]. Because PNIPAM nanogels are swollen at temperature lower than LCST and deswollen at temperature higher than LCST, the colloidal crystals composed of such nanogels exhibit temperature-dependent color change, thereby serving as colorimetric thermometer. Another example is particles made of copolymers of methylmethacrylate (MMA), N-isopropylacrylamide (NIPAM), and 3-acrylamidophenylboronic acid (AAPBA) [18]. The particles are swollen by glucose in water around pH 8 because glucose molecules are bound to AAPBA. Therefore, colloidal crystals composed of the particles exhibit red shift of reflection spectrum when they are immersed in aqueous solution of glucose, where the shift is roughly proportional to concentration of glucose, thereby being useful as glucose sensors. However, available materials for synthesis of monodisperse particles in size range of 100–500 nm are restricted and close-packed colloidal crystals are susceptible to mechanical stress, only providing limited applications.

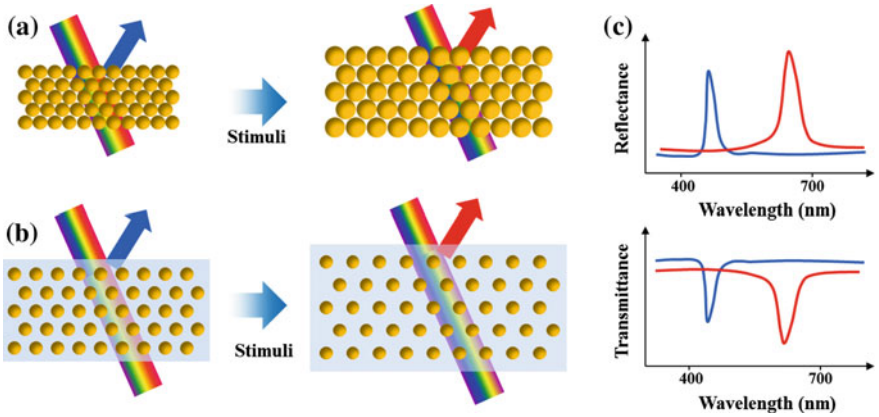

Fig. 3.4 **a**, **b** Color change by volume transition of (**a**) responsive colloids and (**b**) responsive matrix. **c** Spectral shift expected from volume change in reflectance (*top*) and transmittance (*bottom*)

3.3.2 Responsive Matrix

Inverse opals and PCCAs have high mechanical stability due to monolithic matrix. In addition, they can provide larger change in periodicity than opals. Moreover, a variety of responsive materials can be used to compose the matrix. Therefore, most sensors have been designed to have structural forms of inverse opals or PCCAs rather than opals. PCCAs can be readily prepared by one-step polymerization of monomers typically dissolved in aqueous suspension of repulsive colloids in absence of ionic impurity. Stimuli-responsive hydrogels have been widely used for matrix materials of PCCAs to implement colorimetric sensors, as illustrated in Fig. 3.4b and c. Inverse opals require typically three sequential steps of dip coating, material infiltration, and particle removal. In spite of complicate steps for fabrication, inverse opals also have been intensively studied for sensor applications due to relatively low restriction for material selection. Various types of hydrogels and elastomers have been used as matrix materials for sensing. Details will be covered in Sect. 3.5.

3.4 Formats of Photonic Structures

3.4.1 Planar Films

The most common format of colloidal crystals and their derivatives is a planar film type as shown in Fig. 3.5a. This is because the films are useful for many applications and compatible with typical fabrication processes such as dip coating [4–6],

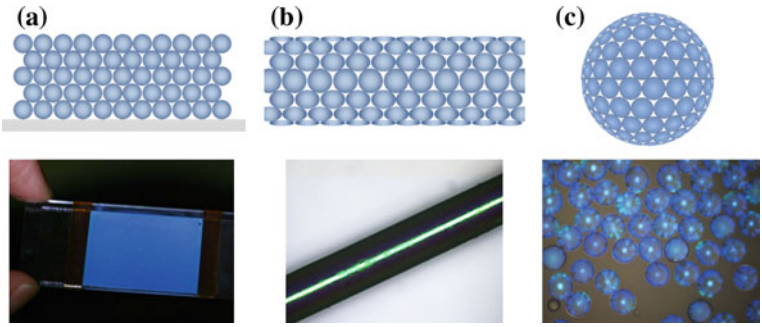

Fig. 3.5 Sets of schematic and image for three different formats of colloidal crystals: **a** a planar film, **b** a cylindrical fiber and **c** spherical beads

spin coating [19, 20], and infiltration [21]. During the crystal formation in planar geometry, (111) plane of FCC structure is always formed along the planar surface, which is stacked along the thickness. This leads to a consistent optical property along the whole area and therefore spectral shift or color change are readily detectable from any position. Moreover, FCC lattice is compatible with a planar geometry, which enables us to minimize defects, thereby providing high optical performance. Nevertheless, film format is not preferred in some applications and other formats of cylindrical fibers and spherical granules have been also developed.

3.4.2 Cylindrical Fibers

Colloidal crystals can be designed in a form of cylinders using templates of cylindrical capillaries or rods as shown in Fig. 3.5b. When particles are concentrated in capillary by preferential drying at one end or centrifugal force, they are assembled into close-packed FCC structure with cylindrical shape [22]. When a photo-curable suspension of repulsive particles is infiltrated into cylinders, non-close-packed FCC structure can be also prepared after photo-polymerization. In addition, immiscible fluid with low affinity to capillary wall can be further injected into suspension-filled capillary to drain the suspension out from the central portion of capillary and make hollow photonic fibers [23]. On the other hand, cylindrical rods can be used as deposition template [24, 25]. Dip coating with rods makes cylindrical shell of close-packed FCC crystals. Alternatively, the particles can be electrophoretically deposited on the surface of cylinders under electric field to provide the photonic shell [26].

On the cylindrical surface, (111) plane is curved along azimuthal direction. For a single layer, the hexagonal array of colloids can be deposited without defects on cylindrical surface. However, defects in multilayer are inevitable. Nevertheless, cylindrical geometry is beneficial for specific applications. For example, flexible

fibers are potentially used for fabrics, which are then integrated with wearable devices or clothes for sensing strain or detecting specific molecules involved in sweat. In addition, core-shell fibers whose shell is composed of colloidal photonic crystals can be directly used for waveguides and further modified to be used as sensors.

3.4.3 Spherical Granules

Planar or cylindrical geometries have restricted mobility. Colloidal crystals with granular format are able to be dispersed in liquid or gas media as shown in Fig. 3.5c. Therefore, they can be rapidly mixed with surrounding media and provide fast binding kinetics. In addition, small granules can be injected into target samples or even living organisms with a needle, providing new opportunity for in situ or in vivo sensor applications. To make spherical photonic granules, emulsion drops have been used as templates for colloidal assemblies. Emulsion drops confining monodisperse colloids yield close-packed colloidal crystals with spherical geometry through evaporation-induced concentration [27–34]. When the emulsion drops contain nanoparticles or polymers, composite structures can be prepared by drying, which are then transformed into spherical inverse opals through selective removal of colloids. Alternatively, the matrix materials can be infiltrated into the interstices between colloids after colloidal-crystal balls are prepared to make spherical inverse opals. When the emulsion drops are composed of a photo-curable suspension of CCA, the drops are simply transformed into spherical PCCAs through photopolymerization [21, 35]. Double-emulsion drops, or drops-in-drop, can be also used as template. Colloidal particles can be laden in either core or shell drops. When the particles are included in the core, they can be crystallized either by interparticle repulsion or osmotic-pressure-induced concentration, which are then encapsulated by solidification of shell [36–39]. Crystalline colloidal array formed in the shell are stabilized by forming PCCA in the shell, providing hollow spherical photonic shells. A few examples of sensors with spherical granule format will be reviewed in the following section.

3.5 Sensor Applications

3.5.1 Refractive Index Sensors

Resonance wavelength of colloidal crystals and their derivatives is refractive index-dependent, as denoted in (3.1) and (3.3). Therefore, refractive index of fluid can be indirectly measured from shift of reflectance peak as illustrated in Fig. 3.6a. The most primitive form of the index sensor is opals. When unknown liquid is

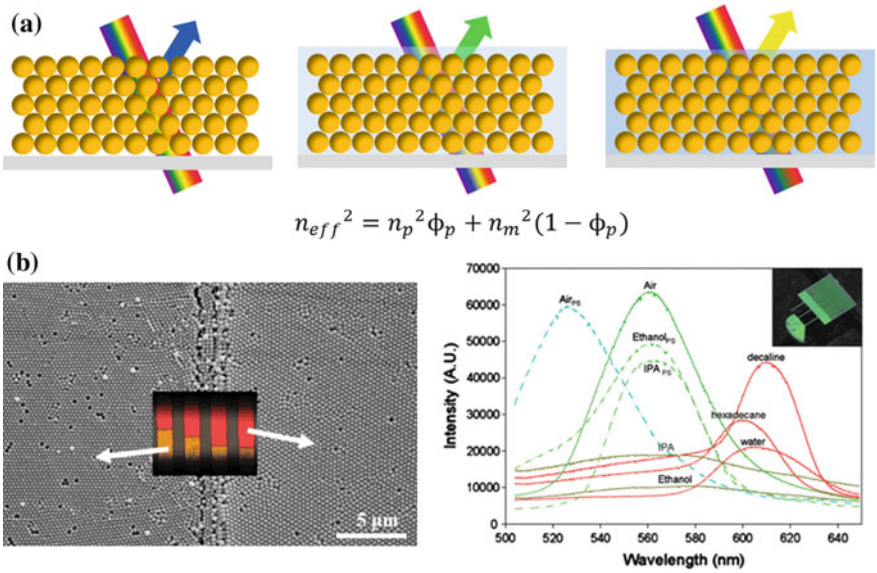

Fig. 3.6 **a** Influence of refractive index of filling fluids on reflection color of colloidal crystals. Effective refractive index can be closely estimated from the Maxwell–Garnett average of the refractive indices of particles and matrix. **b** SEM image showing boundary between two distinct colloidal crystals formed in rectangular microchannels, one of which is composed of polystyrene (PS) particles and the other is composed of silica particles, respectively (*left panel*). Reflectance spectra of colloidal crystals filled with various fluids, as indicated, where *solid* and *dotted lines* are obtained from silica and PS, respectively. Reproduced from [40] with permission

dropped on the surface of opals, it will infiltrate the interstices of colloids, leading to red shift of colors; at the same time, the color becomes timid due to decrease of index contrast. Resonance wavelength is proportional to effective refractive index for normal incident light. Therefore, when opal structure made of silica with void fraction of 0.26 becomes wetted with water (n = 1.333), reflectance peak position red shifts as much as 5 % of initial position; if opal with stop band at 550.0 nm in air is used, peak is expected at 579.8 nm for water infiltration. If the water is replaced with ethanol (n = 1.36), the peak position will be located at 582.5 nm. Therefore, peak shift per refractive index unit (RIU) for green opal is only 90.3 nm/RIU. Furthermore, the peak diminishes as refractive index of liquid approaches to that of colloids. The index-matching problem can be partially overcome by employing hybrid colloidal crystals of which one part is made of silica particles (n ∼ 1.45) and the other part is made of polystyrene particles (n ∼ 1. 59) as shown in Fig. 3.6b [40]. The hybrid opals can provide enhanced precision of measurement by using reflectance peaks from both parts. Another way to improve the precision is to use opal of which surface is decorated with gold nanoparticles [41]. Such a structure shows both photonic bandgap and localized surface plasmon resonance (LSPR). Therefore, refractive index change in surrounding liquid can be

detected by monitoring both shifts of stop band and LSPR wavelength. However, both approaches still have low value of wavelength shift per RIU.

Inverse opal provides improved sensitivity in comparison with opals due to their high void fraction of 0.74 [42, 43]. Higher fraction of void yields larger change of effective refractive index. Inverse opal made of silica with stop band at 550 nm in air is expected to have stop band at 661.6 nm in water and 671.1 nm in ethanol. Therefore, the inverse opal with green color has value of wavelength shift per RIU as 336.4 nm/RIU which is approximately 3.7 times larger than that of opal with same stop band position in air.

To precisely measure refractive index of fluids, opals or inverse opals should maintain their periodicities during the liquid infiltration. If the liquid swells the structures, both of refractive index and periodicity are simultaneously changed, leading to ambiguous additional red shift of stop band [44]. Therefore, materials should be carefully selected for colloids and matrix of opals and inverse opals, respectively; in general, inorganic materials are preferred due to their low degree of swelling for most solvents.

3.5.2 Strain Sensors

Mechanical deformation of colloidal crystals leads to change of periodicity and therefore shift of reflectance peak position. Using such a mechanochromic property, degree of deformation or stain can be measured from color changes. For example, CCA immobilized with hydrogel shows blue shift of their reflection color when it is vertically compressed and recovers original color when it is free from compression [45]. Such reversible change of color is only achieved when the film of hydrogel is elastically compressed. In addition, degree of compression determines magnitude of color shift. Therefore, hydrogels should be highly swollen by liquid to achieve reversible and discernable color change under mechanical compression. This also indicates that a liquid environment is prerequisite for measurement of degree of compression. Hydrogels are prone to be torn under small extensional strain, being inappropriate for strain sensors. Instead of hydrogel-based PCCAs, poly (dimethylsiloxane) (PDMS) elastomer has been widely used as matrix materials for opals and inverse opals. For example, interstices of opal composed of polystyrene particles are filled with PDMS, which is then swollen with silicone oil. During the swelling, close-packed particles are separated to form non-close-packed structure, which provides larger change of periodicity when the film is stretched and therefore wider range of wavelength shift; otherwise, the shift is limited because polystyrene particles are inelastic and even small strain requires rearrangement of the particles. The oil-swollen composite structures are highly elastic, thereby exhibiting reversible change of reflection color for repeated cycles of stretching and releasing. In addition, the blue shift of wavelength is proportional to strain up to 20 %, serving as colorimetric strain sensors [46]. Another structural platform for strain sensing is inverse opal. Although the swelling of opal-embedded elastomer film can separate

particles, high rigidity of particles restricts sensitivity. Voids in inverse opals do not have any elastic resistance, thereby providing low threshold of deformation and high sensitivity of strain measurement [47]. Moreover, such a film of inverse opal can provide spatial distribution of compressive strain through simple color imaging when the film is compressed with stamps of complex height profile such as fingerprint.

Although oil-swollen elastomeric composites and inverse opals are useful for strain sensing, fabrication of them in a wide area is challenging and time-consuming. By contrast, to use of specially synthesized core-shell particles enables to simply create elastomeric non-close-packed FCC structures in a dimension as large as tens of centimeters [48]. The core-shell particles are composed of crosslinked polystyrene core and uncrosslinked polyethylacrylate (PEA) shell; thin interlayer made of PMMA is used to graft the PEA on the polystyrene core. The core-shell particles are mixed with benzophenone at 120 °C, which are then compressed between two parallel plates at 130 °C at which the non-crosslinked soft shell is molten, whereas crosslinked hard core remains spherical. During the hot compression, molten shell forms a continuous phase and radially flows, whereas the intact polystyrene cores dispersed in the molten shell phase are crystallized under influence of shear flow. Upon ultraviolet (UV) illumination, radicals are generated from benzophenone, which crosslink the PEA, forming an elastic film at which non-close-packed FCC crystal is embedded. The film exhibits reversible change of colors for mechanical strain.

The elastic colloidal crystals can be prepared in a form of cylinders to provide mechanochromic fibers [26]. For this, carbon nanotubes are coated on the surface of PDMS fiber and negatively charged polystyrene particles are deposited over the layer of carbon nanotube under electric field. This electrophoretic deposition yields a cylindrical shell of close-packed FCC crystal, of which interstices are then infiltrated with PDMS. Therefore, a core-shell elastic fiber showing reflection color is prepared. When the fiber is stretched, rigid polystyrene particles are rearranged to accommodate the strain as illustrated in Fig. 3.7a; the hexagonal array of particles on the surface, which is (111) plane of FCC structure, is transformed into square array. This entails decrease of inter-plane distance, thereby leading to blue shift of reflection colors as shown in Fig. 3.7b. Although close-packed structure is limited in sensitivity, the fiber format is appealing for advanced applications of strain sensing such as sensors integrated in wearable devices.

3.5.3 Temperature Sensors

Colloidal photonic crystals can be designed to be temperature responsive by employing either colloids or matrix made of polymers with LCST or the upper critical solution temperature (UCST). The polymers with LCST are soluble in low temperature and insoluble in high temperature; polymers with UCST exhibit opposite behavior. Therefore, hydrogels made of such polymer show volume phase

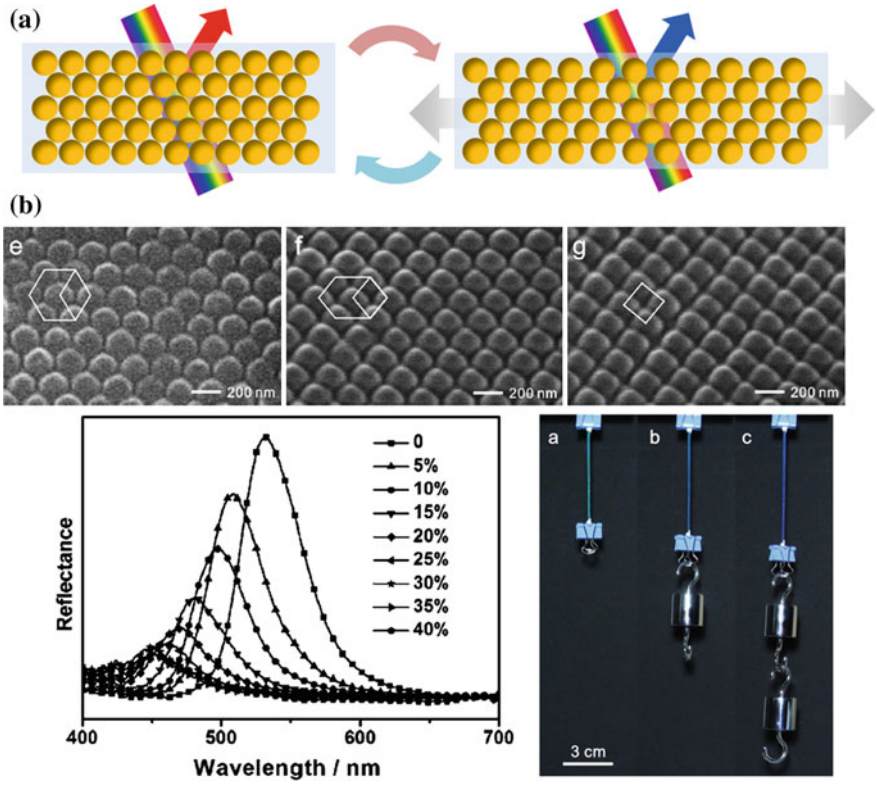

Fig. 3.7 **a** Influence of stretching of opals embedded in elastomer on reflection color. **b** A series of SEM images showing structural transition of colloidal arrays formed on the surface of cylindrical fiber during stretching (*top*). Spectral transition of the colloidal crystals for given strains (*bottom left*) and image showing strain-dependent colors of the fiber (*bottom right*). Reproduced from [26] with permission

transition; hydrogels are highly swollen by water at low temperature, whereas being shrunken at high temperature due to collapse of gel network. One of polymers with LCST most frequently used is PNIPAM which has LCST around 32 °C. When matrix of PCCA is made of PNIPAM, periodicity of non-close-packed FCC and therefore stop band position is determined by temperature as illustrated in Fig. 3.8a [49]. As temperature increases from 10 to 25 °C, stop band wavelength of the PCCA gradually decreases. When the temperature is further increased to about 35 °C, the wavelength steeply decreases and, then slowly decreases again above 35 °C; the steep change of the wavelength is caused of steep volume change which is characteristics of most polymers with LCST or UCST. This temperature-dependent change of bandgap wavelength is reversible. Therefore, temperature in a range of 10–40 °C can be measured by observing reflection color or more precisely by monitoring shift of reflectance peak. Alternatively, PNIPAM can be used for matrix materials for inverse opals. The inverse opals have interconnected macropores,

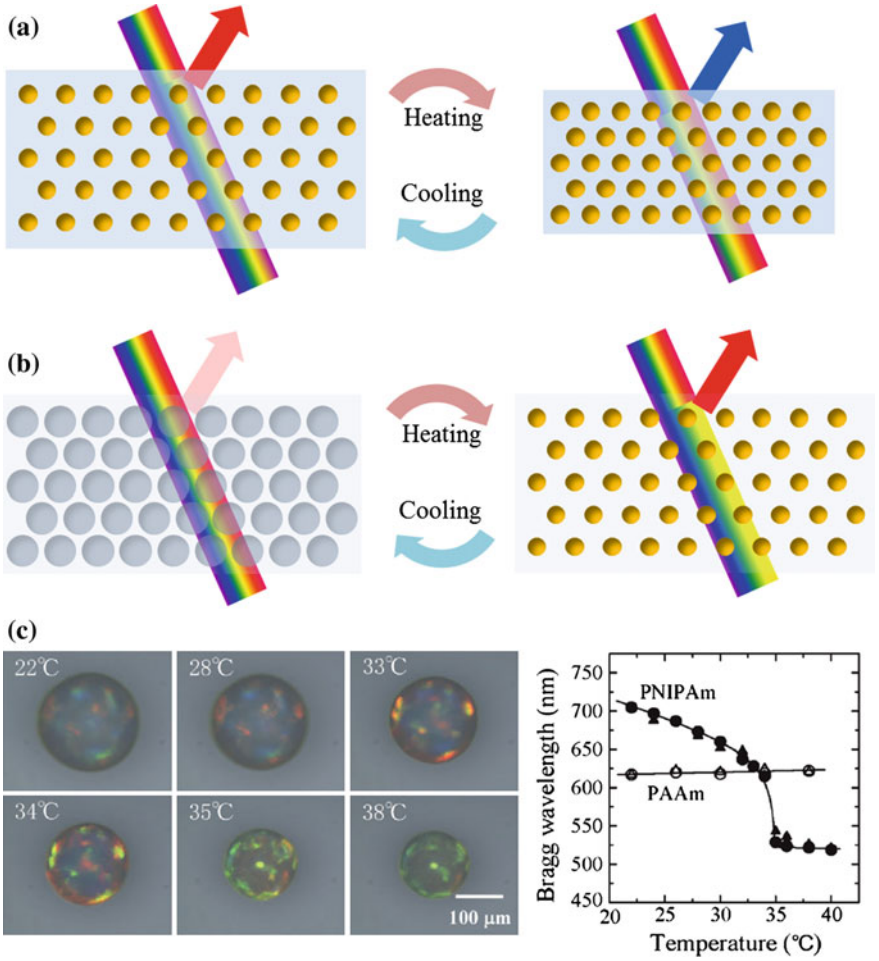

Fig. 3.8 **a**, **b** Two different mechanisms of temperature sensing using colloidal crystals: **a** thermoresponsive matrix is used to develop temperature-dependent color and **b** thermoresponsive nanogels are used to make temperature-dependent reflection intensity. **c** A series of optical microscope images of spherical microgel containing crystalline colloidal array taken at denoted temperatures (*left*) and temperature-dependence of reflectance peak wavelength for microgels made of poly(N-isopropylacrylamide) (PNIPAM) and polyacrylamide (PAAM), respectively (*right*). Reproduced from [53] with permission

which facilitates diffusion of water molecules, thereby providing faster response than PCCAs [50]; diffusion path through hydrogel is comparable to void size in inverse opal, whereas that is a film thickness in PCCAs. In addition, the voids are able to be highly shrunken, which leads to large volume change and therefore large shift of stop band wavelength; particles in PCCA are incompressible, which restricts magnitude of wavelength shift, in particular for high particle fraction in the gel.

Monodisperse PNIPAM particles can be synthesized and used to make colloidal crystals. However, conventional form of close-packed-structure composed of PNIPAM particles is prone to be disassembled during volume transition. Therefore, crystal structure should be stabilized. When the PNIPAM particles form non-close-packed FCC structure in water though electrostatic repulsion, the structure can be stabilized by forming a loose-knit hydrogel in the medium. Such a PCCA maintains periodicity during volume transition of colloids, thereby leading to negligible shift of stop band position. Instead, swelling of particles at low temperature reduces index contrast between particles and hydrogel matrix, making weak reflection, whereas shrinkage of particles at high temperature increases the contrast, thereby developing strong reflection colors, as illustrated in Fig. 3.8b. Therefore, temperature can be measured not from reflectance peak position but from intensity of the peak. In this mechanism, the response becomes very fast because diffusion path of water molecules is only radius of particles and no flux between the hydrogel film and surrounding; the response time scale is only order of 100 ns [51]. Alternative way to stabilize colloidal crystals composed of PNIPAM particles is to form chemical bonds between the particles. For this, the particles are further modified with polymerizable vinyl groups, which are then assembled into close-packed colloidal crystals. The vinyl groups form chemical linkages between two contacting particles upon UV irradiation, locking the crystal structure. Such a film maintains their overall order, while allowing the change of periodicity during volume transition of particles, thereby providing high stability and thermochromic property [52].

With assistance of microfluidics, uniform thermochromic microgels can be also prepared. The microgels are dispersed and distributed in a medium, which are able to report temperature profile in the medium. In addition, response time can be reduced from bulk film if dimension of microgel is comparable to or smaller than thickness of the film. When aqueous solution of PNIPAM precursors containing highly charged polystyrene particles is emulsified into drops in continuous oil phase, the particles form spherical CCA in each drop. The structure can be stabilized by photopolymerization of precursors, which is then transferred from oil to water. The resulting microgels show reflection color due to array of colloids. The color blue shifts when temperature increases in the same manner to thermochromic PCCA films, as shown in Fig. 3.8c [53]. The magnitude of wavelength shift can be further improved by employing oil-in-water-in-oil double-emulsion drops as template, at which middle water layer contains the same composition of materials [54].

3.5.4 Ionic Strength and pH Sensors

To measure ionic strength and pH of aqueous solution, colloidal structures similar to that used for temperature sensing, such as PCCAs and inverse opals, have been employed by replacing thermoresponsive hydrogels with ionic hydrogels. PCCAs whose matrix is made of ionic hydrogels exhibit pH-dependent colors. When the

PCCA film made of polyacrylamide (PAAM) is subjected to pH 9.6, the gel is hydrolyzed and fully ionized. Therefore, counter ions are immobilized in the gel, which increases osmotic pressure, thereby causing inward flux of water. This leads to swelling of the gel and therefore increase of crystal periodicity. As pH value decreases, so does the osmotic pressure difference between the gel and surrounding, leading to reduction of periodicity and blue shift of reflection color, as shown in Fig. 3.9a [55]. For further increase of pH above 9.6, the color does not remain, but blue shift. This is because ionic strength is larger in higher pH. Although ions are permeable through gel, concentration of ions in the gel is lower than that of surrounding due to gel volume. Therefore, osmotic pressure induces outward flux of water, leading to shrinkage of the gel. This causes reflection color of PCCAs blue shifts at higher pH than 9.6. Therefore, pH can be measured from reflection color or spectrum for known value of ionic strength. In addition, ionic strength solely

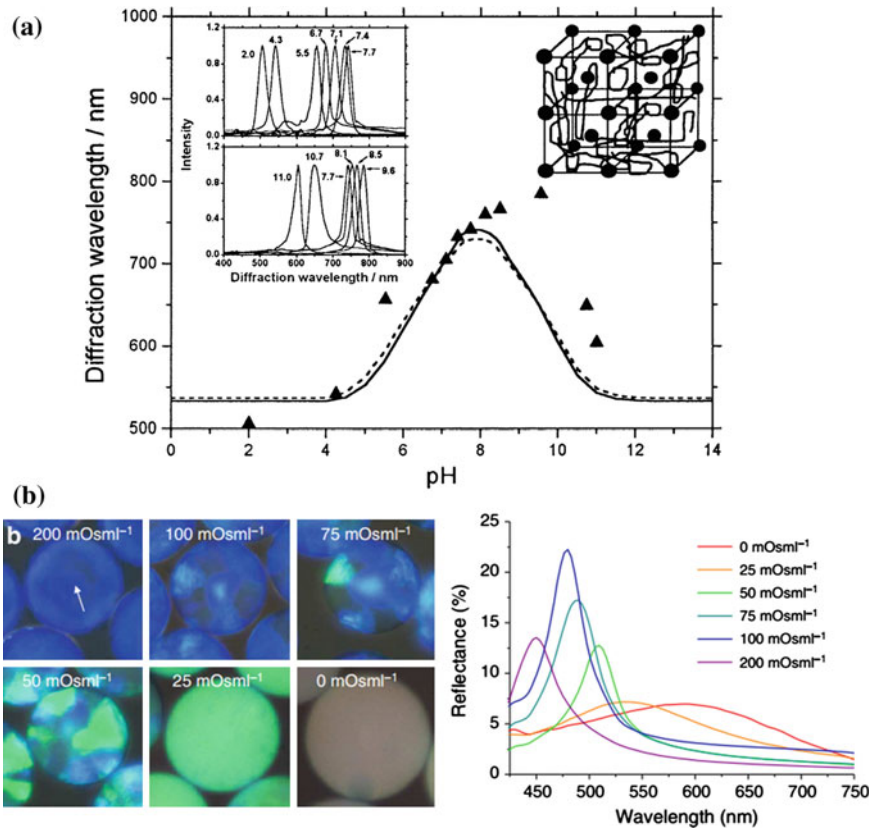

Fig. 3.9 **a** pH-dependence of stop band wavelength for PCCA whose matrix is made of polyacrylamide (PAAM). Reproduced from [55] with permission **b** Osmolarity-dependence of reflection colors for microcapsules composed of colloidal crystal-laden core and semipermeable rubbery membrane. Reproduced from [58] with permission

determines the degree of swelling at constant value of pH and therefore, the strength can be measured in the same manner [56].

Inverse opals can be made to be pH-responsive by using copolymer of 2-hydroxylethyl methacrylate (HEMA) and acrylic acid (AA) as matrix materials [57]. In the similar manner to PCCA made of polyacrylamide, reflection color of the inverse opal is blue shifted as value of pH is decreased from 7 to 2. Use of copolymer enables the control of pH-sensitivity. For example, the gel containing 5 % AA shows large shift of stop band wavelength, whereas the gel containing 2.5 % AA shows relatively small shift for the same pH change. The inverse opal made of the copolymers also has ionic strength dependence.

Osmotic pressure in aqueous solution can be also measured using different format of colloidal crystals. Non-close packed colloidal crystals encapsulated with semipermeable rubbery membrane exhibit osmotic pressure-dependent reflection colors [58]. The microcapsules become inflated when they are subjected to hypotonic condition at which osmotic pressure of surrounding fluid is lower than that of capsule core. The degree of inflation is determined by balance between the osmotic pressure and membrane elasticity. Therefore, concentration of particles within the microcapsules depends on osmotic pressure of surrounding fluid. Because the particle concentration determines periodicity of colloidal structure, osmotic pressure of the surrounding can be measured from reflection color of microcapsules, as shown in Fig. 3.9b.

3.5.5 Detection of Specific Ions and Small Molecules

Colloidal crystals can be used for the detection of specific ions or molecules if receptors are incorporated in hydrogel matrix, while avoiding fluorescent labeling of the analytes. For example, hydrogel matrix of PCCAs can be chemically modified to have crown ether groups which selectively form complexes with specific cation such as Pb^{2+}. Therefore, when the modified PCCA is immersed in aqueous solution of the cation, the crown ether molecules in the gel capture the cation, which leads to concentration of counter-ions around them through electrostatic attraction. Therefore, osmotic pressure in the gel increases, which yields swelling of the gel and therefore red shift of reflection color, in the same manner to pH sensors. The formation of complex between crown ether and cation is ion-selective. Therefore, this method enables the detection of specific ions such as Pb^{2+} from red shift of reflection color; limit of detection is as low as 50 ppb [59].

In a similar manner, glucose concentration can be measured by attaching glucose oxidase in PCCA which is an enzyme that catalyzes oxidation of glucose to gluconic acid in oxygen environment [59]; avidinated glucose oxidase can be attached to biotinylated PCCA. When the enzyme-immobilized PCCA is immersed in glucose solution, glucose is oxidized and flavin on the enzyme is reduced at the same time, being anionic. This yields higher osmotic pressure, leading to swelling of PCCA and red shift of reflection color. Although oxygen concentration and ionic

strength also influence the color, concentration of glucose can be measured from the color shift in a controlled environment. Moreover, such an enzymatic reaction is highly specific, excluding other sugar molecules such as sucrose or mannose in the measurement. However, enzymes are susceptible to denaturation which restricts long-term use.

Alternative method to measure glucose concentration is to use inverse opals made of hydrogel modified with synthetic chemical receptor [60]. Phenylboronic acid (PBA) compounds are partially dissociated to form negative charge in weakly basic condition, making equilibrium with undissociated neutral ones. When the hydrogel modified with PBA derivative is immersed in a basic glucose solution, the dissociated PBA form charged complexes with glucose, leading to shift of equilibrium in a direction to be more dissociated, as shown in Fig. 3.10a. Therefore, the inverse opal becomes swollen due to osmotic pressure in glucose environment, which leads to red shift of stop band position. On the other hand, the chemical receptor of PBA can be copolymerized with NIPAM and MMA to form colloidal particles through soap-free emulsion polymerization. The opal film composed of the particles is simply prepared by dip-coating, which can serve as a glucose sensor in the same mechanism to inverse opals [18]. The receptor can be used in a combination of volume resetting agent in PCCAs to provide linear and fast response to glucose concentration, as shown in Fig. 3.10b [61]. Polyacrylamide which comprises matrix of PCCA can be modified to have PBA groups on their backbone. Although this PCCA can response to glucose in the same manner to previous examples, it is further subjected to treatment with poly(vinyl alcohol) (PVA) to achieve better sensor performance. PVA molecules bind and crosslink PBA groups, reducing volume of PCCA; therefore, PVA is here referred to as the volume resetting agent. When the PBA-PVA-modified PCCA is immersed in glucose solution, PBA-PVA complexes are partially dissociated and PBA-glucose complexes are formed; glucose concentration determines amount of the complex dissociated. Therefore, shrunk PCCA by PVA is suddenly swollen in glucose environment, which provide red shift of reflection color. Moreover, time scale of the swelling is only a few minutes and a linear relation between glucose concentration and the wavelength shift is observed, enabling fast and precise measurement of glucose concentration.

The sensing scheme can be further used for other molecules by replacing receptors. For example, hydrogel matrix of PCCA can be modified with enzyme, acethylcholinesterase (AChE) to detect organophosphorus compound such as parathion [62]; parathion is extremely toxic pesticides, which inhibits nervous system function. The enzyme, AChE, irreversibly binds the parathion, making anionic phosphonyl compound. Therefore, PCCA modified with AChE becomes swollen in the aqueous solution of parathion, exhibiting red shift of reflection colors. The magnitude of the red shift is as large as approximately 35 nm even for very low concentration of 42 fM. Therefore, the PCCA platform provides ultrahigh sensitivity of the parathion detection.

It is not necessary to directly modify matrix of hydrogel for molecular detection. Instead, PCCA film can be located in vicinity of modified hydrogel which does not

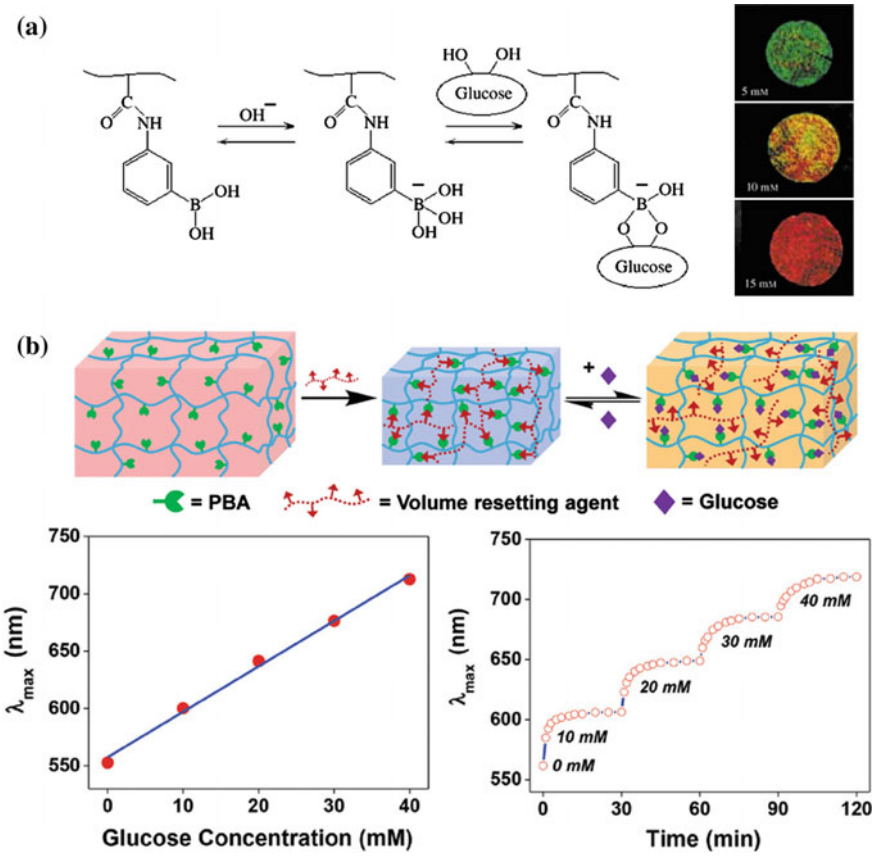

Fig. 3.10 **a** Colorimetric glucose sensor composed of hydrogel inverse opals modified with phenylboronic acid (PBA) compounds. The dissociated PBA and glucose form a charged complex, which leads to swelling of inverse opals and red shift of reflection color. Reproduced from [60] with permission. **b** Glucose sensor composed of PCCA whose matrix is modified with PBA and volume resetting agent. In glucose environment, the complex of PBA and the agent is partially dissociated, allowing swelling of PCCA. The red shift of reflectance peak is linearly proportional to glucose concentration and the shift is done in a few minutes. Reproduced from [61] with permission

contain any colloidal array. The modified hydrogel provides specific chemical reaction under certain condition, of which product changes the environment condition, influencing the swelling behavior of PCCA film. For example, AChE-modified hydrogel film is placed between glass slide and pH-responsive PCCA film to detect acetylcholines [63]. The analyte is permeable through PCCA layer and becomes acetic acid and choline through enzymatic reaction in the underlying hydrogel layer. Therefore, pH in surrounding decreases, leading to shrinkage of PCCA film and blue shift of reflection color. This scheme does not

involve direct modification of hydrogel matrix of photonic structure and therefore provides a facile method to create colloidal crystal-based sensors, although sets of materials for specific target molecules are restricted.

3.5.6 *Detection of Large Biomolecules*

The PCCA platform of which matrix is modified with peptide substrate can provides a tool for evaluating enzyme activity. The specific peptide sequence is selectively recognized and phosphorylated by kinases, which leads to change of electrostatic environment in PCCA. Therefore, kinases activity can be monitored by shift of reflectance peak from the peptide-modified PCCA. For example, PCCA modified with LRRASLG shows red shift of reflection color in the aqueous suspension of enzyme, protein kinase A (PKA), due to increase of negative charge in the hydrogel by phosphorylation of the peptide [64]. The response time scale is a few hours due to instability and low diffusivity of enzymes.

Deoxyribonucleic acid (DNA) molecules with specific sequence can be detected using different mechanism of deswelling. The inverse opal whose hydrogel matrix is modified with specific sequence of DNA molecules shows blue shift of reflectance spectrum only when the DNA in the gel is hybridized with target DNA [65]. This is because counter-ions in the hydrogels are taken during the hybridization and newly formed double-stranded DNA is shorter and more stiff than single-stranded one, as illustrated in Fig. 3.11b. Therefore, hybridization leads to shrinkage of inverse opals and therefore blue shift of spectrum. The magnitude of shrinkage and therefore that of blue shift is not as large as these of most photonic gel sensors with a response mechanism of osmotic pressure-driven volume change; the magnitude of peak shift is approximately 20 nm or less than that.

There are no many reports about swelling-based approach for detection of large biomolecules such as proteins and antibodies. This is because their selective bindings usually do not alter electrostatic environments and therefore, volume remains almost unchanged. Instead, the binding events can causes small increase of refractive index, thereby resulting in small but measurable magnitude of red shift. For example, hydrogel matrix of spherical inverse opals can be modified with antibody probe, such as anti-human CA19-9 [66]. The spherical photonic microgels exhibit red shift of reflectance peak when they are dispersed in aqueous solution of antigen, such as human CA19-9, which can selectively bind with the antibody. The magnitude of the shift is as small as a few nanometers. However, such small change can be detected with spectrometers, although difficult to detect with bare eye. One the other hand, large protein molecules can also be detected with molecule-imprinted photonic structures [67, 68]. When hydrogel inverse opals are prepared by using templates of protein molecules-adsorbed opals, they have macropores from opals and nanocavities from the protein molecules. Such inverse opals are able to selectively accommodate the protein molecules in the nanocavities when the shape of protein is matched with that of nanocavity, as illustrated in

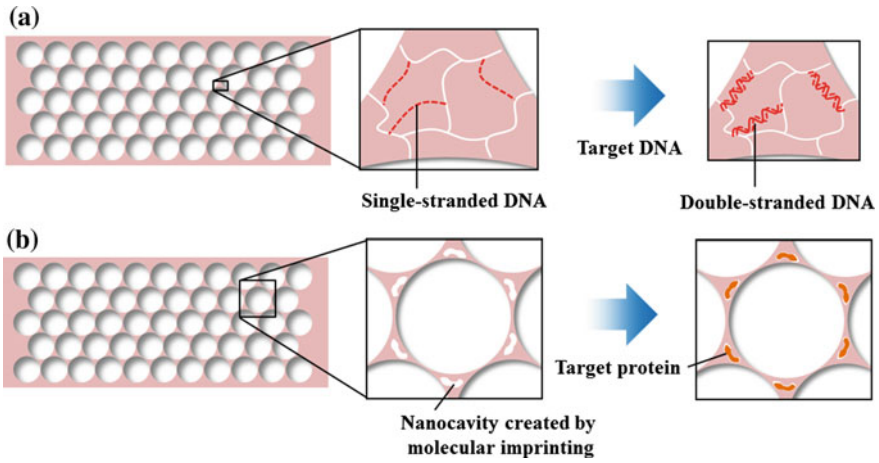

Fig. 3.11 **a** Inverse opal-based DNA sensors. Hybridization of DNA in hydrogel matrix with target DNA leads to shrinkage of the hydrogel, resulting in blue shift of reflectance peak. **b** Inverse opal-based protein sensors. Inverse opal is designed to have nanocavities through molecular imprinting technique. The cavities selectively accommodate the protein, used for the cavity formation, leading to increase of effective refractive index and therefore red shift of reflectance peak

Fig. 3.11b. Therefore, the inverse opals exhibit meaningful red shift of reflectance peak only for the protein molecules, used for cavity formation, in solution. The magnitude of shift is as small as a few or maximum 20 nm due to negligible swelling of matrix [69, 70].

3.6 Summary and Outlook

Close-packed or non-closed packed colloidal crystals can be formed by self-assembly in various forms. They can show structural reflective color which is highly sensitive to interparticle distance or reflective index mismatch between particle and matrix. Therefore, by using stimuli-responsive materials as either matrix or particles, various environmental parameters can be sensed such as pH, temperature, pressure, mechanical deformation and so on. Also, by introducing chemical probes, various biomolecules (DNA) or toxic chemicals including gas and volatiles [71–73] can be detected, which would be further extended to biomedical sensor platform. Compared with other sensor device, colloidal crystals are mechanically and chemical stable and their color change is reversible and could be operated without external (electrical or photon) energy. In some application, the difference of color after detection could be monitored by our naked eye. However, it is still challenging to develop efficient method for amplifying detection signal in colloidal crystals particularly for biomedical applications which requires extremely

high sensitivity [74]. In case of environmental sensor application, reproducibility or reliability is now major challenging issue for commercialization. One of the possible approaches to address those problem may be combining other new technologies such as quantum dots, graphene, plasmonic materials [75–78], which are implemented on colloidal photonic crystals but not explored extensively for sensor applications.

References

1. P.N. Pusey, W. van Megen, Phase behaviour of concentrated suspensions of nearly hard colloidal spheres. Nature **320**, 340–342 (1986)
2. W.G. Hoover, F.H. Ree, Melting transition and communal entropy for hard spheres. J. Chem. Phys. **49**, 3609–3617 (1968)
3. S.-C. Mau, D.A. Huse, Stacking entropy of hard-sphere crystals. Phys. Rev. E **59**, 4396–4401 (1999)
4. P. Jiang, J.F. Bertone, K.S. Hwang, V.L. Colvin, Single-crystal colloidal multilayers of controlled thickness. Chem. Mater. **11**, 2132–2140 (1999)
5. S. Wong, V. Kitaev, G.A. Ozin, Colloidal crystal films: advances in universality and perfection. J. Am. Chem. Soc. **125**, 15589–15598 (2003)
6. Z. Zhou, X.S. Zhao, Flow-controlled vertical deposition method for the fabrication of photonic crystals. Langmuir **20**, 1524–1526 (2004)
7. S.O. Lumsdon, E.W. Kaler, O.D. Velev, Two-dimensional crystallization of microspheres by a coplanar AC electric field. Langmuir **20**, 2108–2116 (2004)
8. M. Trau, S.A. Saville, I.A. Aksay, Field-induced layering of colloidal crystals. Nature **272**, 706–709 (1996)
9. Y. Monovoukas, A.P. Gast, The experimental phase diagram of charged colloidal suspensions. J. Colloid Interface Sci. **128**, 533–548 (1989)
10. A. Yethiraj, A. van Blaaderen, A colloidal model system with an interaction tubable from hard sphere to soft and dipolar. Nature **421**, 513–517 (2003)
11. M. Michelle, W. Muscatello, L.E. Stunja, P. Thareja, L. Wang, J.J. Bohn, S.S. Velankar, S.A. Asher, Dependence of photonic crystal nanocomposite elasticity on crystalline colloidal array particle size. Macromolecules **42**, 4403–4406 (2009)
12. J.D. Joannopoulos, S.G. Johnson, J.N. Winn, R.D. Meade, *Photonic Crystals: Molding the Flow of Light* (Princeton University Press, New Jersey, 2008)
13. http://ab-initio.mit.edu/wiki/index.php/MIT_Photonic_Bands
14. M.N. Shkunov, Z. Valy Vardeny, M.C. DeLong, R.C. Polson, A.A. Zakhidov, R.H. Baughman, Tunable, gap-state lasing in switchable directions for opal photonic crystals. Adv. Funct. Mater. **12**, 21–26 (2002)
15. K. Busch, S. John, Photonic band gap formation in certain self-organizing systems. Phys. Rev. E **58**, 3896–3908 (1998)
16. H. Senff, W. Richtering, Temperature sensitive microgel suspensions: colloidal phase behavior and rheology of soft spheres. J. Chem. Phys. **111**, 1705–1711 (1999)
17. N. Dingenouts, Ch. Norhausen, M. Ballauff, Observation of the volume transition in thermosensitive core-shell latex particles by small-angle X-ray scattering. Macromolecules **31**, 8912–8917 (1998)
18. X. Hong, Y. Peng, J. Bai, B. Ning, Y. Liu, Z. Zhou, Z. Gao, A novel opal closest-packing photonic crystal for naked-eye glucose detection. Small **10**, 1308–1313 (2014)
19. A. Mihi, M. Ocaña, H. Míguez, Oriented colloidal-crystal thin films by spin-coating microspheres dispersed in volatile media. Adv. Mater. **18**, 2244–2249 (2006)

20. P. Jiang, M.J. McFarland, Large-scale fabrication of wafer-size colloidal crystals, macroporous polymers and nanocomposites by spin-coating. J. Am. Chem. Soc. **126**, 13778–13786 (2004)
21. S.-H. Kim, S.-J. Jeon, G.-R. Yi, C.-J. Heo, J.H. Choi, S.-M. Yang, Optofluidic assembly of colloidal photonic crystals with controlled sizes, shapes and structures. Adv. Mater. **20**, 1649–1655 (2008)
22. J.H. Moon, S. Kim, G.-R. Yi, Y.-H. Lee, S.-M. Yang, Fabrication of ordered macroporous cylinders by colloidal templating in microcapillaries. Langmuir **20**, 2033–2035 (2004)
23. S.-H. Kim, H. Hwang, S.-M. Yang, Fabrication of robust optical fibers by controlling film drainage of colloids in capillaries. Angew. Chem. Int. Ed. **51**, 3601–3605 (2012)
24. J.H. Moon, G.-R. Yi, S.-M. Yang, Fabrication of hollow colloidal crystal cylinders and their inverted polymeric replicas. J. Colloid Interface Sci. **287**, 173–177 (2005)
25. J. Li, P.R. Herman, C.E. Valdivia, V. Kitaev, G.A. Ozin, Colloidal photonic crystal cladded optical fibers: towards a new type of photonic band gap fiber. Opt. Express **13**, 6454–6459 (2005)
26. X. Sun, J. Zhang, L. Xin, X. Fang, H. Peng, Mechanochromic photonic-crystal fibers based on continuous sheets of aligned carbon nanotubes. Angew. Chem. Int. Ed. **54**, 3630–3634 (2015)
27. O.D. Velev, A.M. Lenhoff, E.W. Kaler, A class of microstructured particles through colloidal crystallization. Science **287**, 2240–2243 (2001)
28. Y. Gi-Ra, M. Jun Hyuk, Y. Seung-Man, Ordered macroporous particles by colloidal templating. Chem. Mater. **13**, 2613–2618 (2001)
29. G.-R. Yi, V.N. Manoharan, S. Klein, K.R. Brzezinska, D.J. Pine, F.F. Lange, S.-M. Yang, Monodisperse micrometer-scale spherical assemblies of polymer particles. Adv. Mater. **14**, 1137–1140 (2002)
30. G.-R. Yi, S.-J. Jeon, T. Thorsen, V.N. Manoharan, D.J. Pine, S.R. Quake, S.-M. Yang, Generation of uniform photonic balls by template-assisted colloidal crystallization. Synth. Met. **139**, 803–806 (2003)
31. J.H. Moon, Y. Gi-Ra, S.-M. Yang, D.J. Pine, S.B. Park, Electrospray-assisted fabrication of uniform photonic balls. Adv. Mater. **16**, 605–609 (2004)
32. S.H. Kim, S.Y. Lee, G.-R. Yi, D.J. Pine, Y. Seung-Man, Microwave-assisted self-organization of colloidal particles in confining aqueous droplets. J. Am. Chem. Soc. **128**, 10897–10904 (2006)
33. X. Zhao, Y. Cao, F. Ito, H.-H. Chen, K. Nagai, Y.-H. Zhao, Z.-Z. Gu, Colloidal crystal beads as supports for biomolecular screening. Angew. Chem. Int. Ed. **45**, 6835–6838 (2006)
34. Y. Zhao, X. Zhao, C. Sun, J. Li, R. Zhu, Z. Gu, Encoded silica colloidal crystal beads as supports for potential multiplex immunoassay. Anal. Chem. **80**, 1598–1605 (2008)
35. S.-H. Kim, J. Seog-Jin, W.C. Jeong, H.S. Park, S.-M. Yang, Optofluidic synthesis of electroresponsive photonic janus balls with isotropic structural colors. Adv. Mater. **20**, 4129–4134 (2008)
36. S.-H. Kim, S.-J. Jeon, S.-M. Yang, Optofluidic encapsulation of crystalline colloidal arrays into spherical membrane. J. Am. Chem. Soc. **130**, 6040–6046 (2008)
37. K. Shirk, C. Steiner, J.W. Kim, M. Marquez, C.J. Martinez, Assembly of colloidal silica crystals inside double emulsion drops. Langmuir **29**, 11849–11857 (2013)
38. T.M. Choi, J.-G. Park, Y.-S. Kim, V.N. Manoharan, S.-H. Kim, Osmotic-pressure-mediated control of structural colors of photonic capsules. Chem. Mater. **27**, 1014–1020 (2015)
39. S.J. Yeo, F. Tu, S.-H. Kim, G.-R. Yi, P.J. Yoo, D. Lee, Angle- and strain-independent coloured freestanding films incorporating non-spherical colloidal photonic crystals. Soft Matter **11**, 1582–1588 (2015)
40. S.-K. Lee, G.-R. Yi, S.-M. Yang, High-speed fabrication of patterned colloidal photonic structures in centrifugal microfluidic chips. Lab. Chip **6**, 1171–1177 (2006)
41. Z.-Z. Gu, R. Horie, S. Kubo, Y. Yamada, A. Fujishima, O. Sato, Fabrication of a metal-coated three-dimensionally ordered macroporous film and its application as a refractive index sensor. Angew. Chem. **114**, 1201–1204 (2002)

42. S. Kim, A.N. Mitropoulos, J.D. Spitzberg, H. Tao, D.L. Kaplan, F.G. Omenetto, Silk inverse opals. Nat. Photonics **6**, 818–823 (2012)
43. H. Li, L. Chang, J. Wang, L. Yang, Y. Song, A colorful oil-sensitive carbon inverse opal. J. Mater. Chem. **18**, 5098–5103 (2008)
44. HSoo Lee, J.H. Kim, J.-S. Lee, J.Y. Sim, J.Y. Seo, Y.-K. Oh, S.-M. Yang, S.-H. Kim, Magnetoresponsive discoidal photonic crystals towards active color pigments. Adv. Mater. **26**, 5801–5807 (2014)
45. S.A. Asher, J. Holtz, L. Liu, Z. Wu, Self-assembly motif for creating submicron periodic materials, polymerized crystalline colloidal arrays. J. Am. Chem. Soc. **116**, 4997–4998 (1994)
46. H. Fudouzi, T. Sawada, Photonic rubber sheets with tunable color by elastic deformation. Langmuir **22**, 1365–1368 (2006)
47. A.C. Arsenault, T.J. Clark, G.V. Feymann, L. Cademartiri, R. Sapienza, J. Bertolotti, E. Vekris, S. Wong, V. Kitaev, I. Manners, R.Z. Wang, S. John, D. Wiersma, G.A. Ozin, From colour fingerprinting to the control of photoluminescence in elastic photonic crystals. Nat. Mater. **5**, 179–184 (2006)
48. B. Viel, T. Ruhl, G.P. Hellmann, Reversible deformation of opal elastomers. Chem. Mater. **19**, 5673–5679 (2007)
49. J.M. Weissman, H.B. Sunkara, A.S. Tse, Sanford A. Asher, Thermally switchable periodicities and diffraction from mesoscopically ordered materials. Science **274**, 959–960 (1996)
50. Y. Takeoka, M. Watanabe, Template synthesis and optical properties of chameleonic poly (N-isopropylacrylamide) gels using closest-packed self-assembled colloidal silica crystals. Adv. Mater. **15**, 199–201 (2003)
51. C.E. Reese, A.V. Mikhonin, M. Kamenjicki, A. Tikhonov, S.A. Asher, Nanogel nanosecond photonic crystal optical switching. J. Am. Chem. Soc. **126**, 1493–1496 (2004)
52. M. Chen, L. Zhou, Y. Guan, Y. Zhang, Polymerized microgel colloidal crystals: photonic hydrogels with tunable band gaps and fast response rates. Angewandte Chemie Int. Edn. **52**, 9961–9965 (2013)
53. T. Kanai, D. Lee, H.C. Shum, D.A. Weitz, Fabrication of tunable spherical colloidal crystals immobilized in soft hydrogels. Small **6**, 807–810 (2010)
54. T. Kanai, D. Lee, H.C. Shum, R.K. Shah, D.A. Weitz, Gel-immobilized colloidal crystal shell with enhanced thermal sensitivity at photonic wavelengths. Adv. Mater. **22**, 4998–5002 (2010)
55. K. Lee, S.A. Asher, Photonic crystal chemical sensors pH and ionic strength. J. Am. Chem. Soc. **122**, 9534–9537 (2000)
56. C. Fenzl, S. Wilhelm, T. Hirsch, O.S. Wolfbeis, Optical sensing of the ionic strength using photonic crystals in a hydrogel matrix. ACS Appl. Mater. Interfaces **5**, 173–178 (2013)
57. Y.-J. Lee, P.V. Braun, Tunable inverse opal hydrogel pH sensors. Adv. Mater. **15**, 563–566 (2003)
58. S.-H. Kim, J.-G. Park, T.M. Choi, V.N. Manoharan, D.A. Weitz, Osmotic-pressure-controlled concentration of colloidal particles in thin-shelled capsules. Nat. Commun. **5**, 3068 (2014)
59. J.H. Holtz, S.A. Asher, Polymerized colloidal crystal hydrogel films as intelligent chemical sensing materials. Nature **389**, 829–832 (1997)
60. D. Nakayama, Y. Takeoka, M. Watanabe, K. Kataoka, Simple and precise preparation of a porous gel for a colorimetric glucose sensor by a templating technique. Angew. Chem. Int. Ed. **42**, 4197–4200 (2003)
61. C. Zhang, G.G. Cano, P.V. Braun, Linear and fast hydrogel glucose sensor materials enabled by volume resetting agents. Adv. Mater. **26**, 5678–5683 (2014)
62. J.P. Walker, S.A. Asher, Acetylcholinesterase-based organophosphate nerve agent sensing photonic crystal. Anal. Chem. **77**, 1596–1600 (2005)
63. C. Fenzl, C. Genslein, A. Zopfl, A.J. Baeumner, T. Hirsch, A photonic crystal based sensing scheme for acetylcholine and acetylcholinesterase inhibitors. J. Mater. Chem. B **3**, 2089–2095 (2015)
64. K.I. MacConaghy, C.I. Geary, J.L. Kaar, M.P. Stoykovich, Photonic crystal kinase biosensor. J. Am. Chem. Soc. **136**, 6896–6899 (2014)

65. Y. Zhao, X. Zhao, B. Tang, W. Xu, J. Li, J. Hu, Z. Gu, Quantum-dot-tagged bioresponsive hydrogel suspension array for multiplex label-free DNA detection. Adv. Funct. Mater. **20**, 976–982 (2010)
66. Y. Zhao, X. Hu, J. Jing, M. Xu, W. Zhao, L. Sun, C. Zhu, H. Xu, Z. Gu, Encoded porous beads for label-free multiplex detection of tumor markers. Adv. Mater. **21**, 569–572 (2009)
67. K. Haupt, K. Mosbach, Molecularly imprinted polymers and their use in biomimetic sensors. Chem. Rev. **100**, 2495–2504 (2000)
68. B. Sellergren, Imprinted polymers with memory for small molecules, proteins, or crystals. Angewandte Chemie Int. Ed. **39**, 1031–1037 (2000)
69. X. Hu, G. Li, J. Huang, Z. Di, Y. Qiu, Construction of self-reporting specific chemical sensors with high sensitivity. Adv. Mater. **19**, 4327–4332 (2007)
70. Y.-J. Zhao, X.-W. Z, Hu J, J. Li, W.-Y. Xu, Z.-Z. Gu, Multiplex label-free detection of biomolecules with an imprinted suspension array. Angew. Chem. Int. Ed. **48**, 7350–7352 (2009)
71. L.D. Bonifacio, D.P. Puzzo, S. Breslav, B.M. Willey, A. McGeer, G.A. Ozin, Towards the photonic nose: a novel platform for molecule and bacteria identification. Adv. Mater. **22**, 1351–1354 (2010)
72. L.D. Bonifacio, G.A. Ozin, A.C. Arsenault, Photonic nose-sensor platform for water and food quality control. Small **7**, 3153–3157 (2011)
73. H. Xu, P. Wu, C. Zhu, A. Elbaz, Z.-Z. Gu, Photonic crystal for gas sensing. J. Mater. Chem. C **1**, 6087–6098 (2013)
74. Y. Nazirizadeh, T. Karrock, M. Gerken, Visual device for pressure measurement using photonic crystal slabs. Opt. Lett. **37**, 3081–3083 (2012)
75. Z.-H. Chen, Y. Wang, Y. Yang, Q. Na, Y. Wang, Z. Yu, Enhanced normal-direction excitation and emission of dual-emitting quantum dots on a cascaded photonic crystal surface. Nanoscale **6**, 14708–14715 (2014)
76. R.E. Galian, M. Laferrière, J.C. Scaiano, Doping of photonic crystal fibers with fluorescent probes: possible functional materials for optrode sensors. J. Mater. Chem. **16**, 1697–1701 (2006)
77. J.N. Dash, R. Jha, Graphene-based birefringent photonic crystal fiber sensor using surface plasmon resonance. IEEE Photonics Technol. Lett. **26**, 1092–1095 (2014)
78. K.V. Sreekanth, S. Zeng, K.-T. Yong, T. Yu, Sensitivity enhanced biosensor using graphene-based one-dimensional photonic crystal. Sens. Actuators B **182**, 424–428 (2013)

Chapter 4
Responsive Photonic Gels Based on Block Copolymers

Youngjong Kang, Jinho Hyon, Chunhee Seo and Chinna Bathula

Abstract Self-assembly of block copolymers has been widely employed in the fabrication of various 1D, 2D and 3D photonic crystals by utilizing the abundant morphologies of block copolymers. When one or both domains of block copolymers were swollen with a significant amount of diluents, they form photonic gels. Comparing with conventional dry polymer or inorganic photonic crystals, photonic gels are very flexible and responsive to the various external stimuli. Especially, polyelectrolyte block copolymer 1D photonic gels swollen with solvents exhibited extremely large tunability of optical properties by chemical, mechanical, thermal, and electrical stimuli. These unique features have been proved to be useful for applications in sensors and displays. In this chapter, we will review the recent works on block copolymer photonic gels. The scope of this review will cover (1) theoretical background of photonic stopbands, (2) fabrication and characterization of photonic gels by self-assembly, and (3) various applications of photonic gels in sensors and displays.

4.1 Introduction

Photonic crystals are periodic dielectric structures where the dielectric constant profile changes periodically along one or more principal axes on the order of an optical wavelength. Multiple Bragg reflections at the dielectric interfaces generate forbidden energy gaps called "photonic bandgaps (PBGs)", in which the propagation of light with a specific wavelength is prohibited. Incident light with certain frequencies is thereby rejected from photonic crystals. Due to their unique properties to interact and control light propagation, photonic crystals have received a great deal of

Y. Kang (✉) · J. Hyon · C. Seo · C. Bathula
Department of Chemistry, Research Institute for Natural Sciences, Hanyang University, 222 Wangsimni-Ro, Seongdong-Gu, Seoul 133-791, South Korea
e-mail: youngjkang@hanyang.ac.kr

Y. Kang · J. Hyon · C. Seo · C. Bathula
Institute of Nano Science and Technology, Hanyang University, 222 Wangsimni-Ro, Seongdong-Gu, Seoul 133-791, South Korea

M. J. Serpe et al. (eds.), *Photonic Materials for Sensing, Biosensing and Display Devices*, Springer Series in Materials Science 229,
DOI 10.1007/978-3-319-24990-2_4

attention for their applications in lasers, photovoltaic devices, low-loss Bragg mirrors, reflective coating materials, waveguides, displays and sensors [1–27].

When the periodicity is matched with the wavelengths in visible region, distinct interference colors are reflected from the photonic crystals. These colorful photonic crystals are often observed in nature such as opals, morpho butterfly, cephalopod, and more [28, 29]. Furthermore, many of living creatures bearing photonic crystals show the capability of tuning PBGs in response to the surrounding environment. For example, cephalopods display incredible color changes of their skin for camouflage and visual communication utilizing tunable photonic crystals known as iridophores. The color changes are mainly because of the modulation of the spacing between high refractive index platelets in the iridophores [30].

Inspired by nature, many of artificial photonic crystals have recently been developed as a new class of chromotropic materials. Photonic crystals can be artificially fabricated at various length scales and dimensions. The fabrication methods include conventional lithography techniques such as photolithography, glancing-angle deposition, layer-by-layer stacking, electrochemical etching and holographic lithography. Although these "top-down" approaches are well developed for fabricating precisely controlled photonic crystals, "bottom-up" methods now provide simpler and cheaper routes for creating photonic crystals in large area. The primary bottom-up approaches are based on self-assembly of nanoscopic building block materials.

Among a number of material choices, polymers have been extensively used for tunable photonic crystals due to their unique properties. The control of the refractive index contrast and periodicity between dielectric materials plays a crucial role for modulating the PBGs. Polymers provides large selection of the refraction index (n). As shown in Table 4.1, the refractive index of common polymers varies from 1.3 to 1.7. The refractive index of polymer can be further regulated by mixing with other polymers, solvents, small organic molecules or inorganic nanoparticles.

Utilizing this feature, various photonic crystals with high refractive index contrast can be easily prepared by choosing appropriate polymer pairs. Additionally, polymers exhibit large volume changes when they are subjected to not only mechanical force but also chemical or electric stimuli. Such volume change becomes more apparent when polymers are partially swollen with diluents. For example, polymer gels, which are physically- or chemically-crosslinked polymer networks swollen with significant amount of diluents such as solvents, low-molecular weight polymers, ionic liquids or plasticizers, exhibit the large volume changes in response to the various chemical, biological, physical, and electromagnetic stimuli. When polymer gels are coupled with photonic crystal structures, photonic crystals display large shift of PBGs in response to the various external stimuli. These tunable photonic crystals based on polymer gels, which we will name "photonic gels" in this review, have been widely employed for displays as well as colorimetric sensors including solvents, vapors, temperature, ions, pH, biomolecules and mechanical force.

In this review, we will discuss photonic gels based on the self-assembly of block copolymers and the recent development related to the synthesis, characterizations and applications.

Table 4.1 Refractive index of polymers

Polymer	Refractive index
Poly(hexafluoropropylene oxide)	1.30
Alginic acid, sodium salt	1.33
Poly(tetrafluoroethylene)	1.35
Poly(trifluorovinyl acetate)	1.38
Poly(dimethyl siloxane)	1.40
Poly(vinylidene fluoride)	1.42
Poly(isobutyl methacrylate)	1.45
Poly(ethylene oxide)	1.45
Poly(vinyl ethyl ether)	1.45
Poly(t-butyl methacrylate)	1.46
Poly(vinyl acetate)	1.47
Poly(ethyl acrylate)	1.47
Ethyl cellulose	1.48
Poly(methyl acrylate)	1.48
Poly(methyl methacrylate)	1.49
Poly(vinyl alcohol)	1.5
Poly(1,2-butadiene)	1.5
Poly(isobutylene)	1.51
Poly(N-butyl methacrylamide)	1.51
Poly(acrylonitrile)	1.52
Poly(acrylic acid)	1.53
Poly(N-vinyl pyrrolidone)	1.53
Poly(vinyl chloride)	1.54
Cellulose	1.54
Nylon 6,6	1.57
Polystyrene	1.59
Poly(2-vinyl pyridine)	1.59
Poly(vinylidene chloride)	1.6
Poly(2,6-dichlorostyrene)	1.62
Poly(2-vinylthiophene)	1.64
Poly(styrene sulfide)	1.66
Poly(N-vinyl carbazole)	1.68
Poly(pentabromophenyl methacrylate)	1.71

4.2 Fundamentals of Photonic Crystals

According to the dimension of spatial periodicity, photonic crystal can be classified as one-dimensional (1D), two-dimensional (2D) and three-dimensional (3D) (Fig. 4.1). Light reflection from a multilayered dielectric mirror (1D photonic crystal) was first explained by Lord Rayleigh in 1887, but the comprehensive

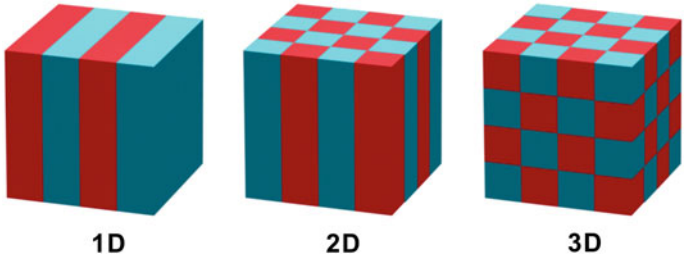

Fig. 4.1 Schematic illustration of 1D, 2D, and 3D photonic crystals

theoretical concept of photonic crystals was established one hundred year later by Yablonovitch and John in 1987 [4, 31].

The photonic bands occur by multiple constructive and destructive interference reflection at the interfaces. While determining the detailed band structure of a photonic crystal involves principles of solid-state physics and electromagnetism, the position of PBGs in 1D photonic crystals can be easily calculated utilizing Bragg's law. For the simplest 1D photonic crystal (Bragg mirror) where a pair of layers of thickness d_1 and d_2 with refractive indices n_1 and n_2 stacks periodically ($n_1 < n_2$), the central wavelength of stopband (λ_0) is determined by optical thickness of each dielectric layer (nd) and the glancing angle between the incident light and reflection plane (θ) (4.1). The optical thickness of a dielectric layer is given by the product of the refractive index (n) and the physical thickness (d).

$$\lambda_0 = 2(n_1 d_1 + n_2 d_2) \times \sin\theta \tag{4.1}$$

At the fixed glancing angle (for example $\theta = 90°$), the positon of stopband is only determined by the optical thickness. For the typical polymers with refractive indices $n_1 = 1.4$ and $n_2 = 1.6$, the thickness of polymer layer should be in the range of $d = 65$–100 nm to exhibit primary stopband in visible regime. The stopband can be tune by changing either (or both) the refractive index or the thickness of layers. From (4.1), the stopband is also dependent on the view or incident angle of light. The stopband shifts to the shorter wavelength, as the incident angle of light is lowered from the normal direction. In this case, the bandwidth ($\Delta\lambda$) of the stopband is dependent on the refractive index contrast of layers (4.2). The (4.2) shows that the stopband becomes broader as increasing the refractive index contrast between the layers.

$$\Delta\lambda = \frac{4\lambda_0}{\pi}\sin^{-1}\left(\frac{n_2 - n_1}{n_2 + n_1}\right) \tag{4.2}$$

The reflectivity of the Bragg mirror (R) depends also on the refractive index contrast and the number of bilayers (N) (4.3):

$$R = \left[\frac{n_0 - n_s(n_1/n_2)^{2N}}{n_0 + n_s(n_1/n_2)^{2N}}\right]^2 \tag{4.3}$$

where n_0 and n_s are the refractive indices of the surrounding medium and the substrate, respectively [32]. For a typical condition with n_0 = 1.0 (air), n_s = 1.5 (crown glass), n_1 = 1.4, and n_2 = 1.6, the reflectivity can easily reach to almost 100 % by increasing the number of bilayers over 20.

As seen from above equations, the photonic stopband properties of 1D photonic crystals are highly dependent on the layer thickness and the refractive index. Hence their optical properties can be tuned by modulating the layer thickness and the refractive index. In this sense, polymer gels provide large tunability of the photonic stopband due to their large volume and index change by swelling.

4.3 Preparation of Photonic Gels

4.3.1 Self-assembly of Block Copolymers

Block copolymers are composed of two or more chemically distinct homopolymer chains covalently connected each other. Due to the positive mixing enthalpy of chains, block copolymers undergo phase separation and form well defined microstructures including lamellae, cylinders, spheres, and gyroids. These diverse microstructures of block copolymers have been employed for creating photonic crystals: 1D photonic crystals from lamellae, 2D photonic crystals from hexagonally packed cylinders, and 3D photonic crystals from double gyroid structures. To exhibit photonic bands in visible regime, the domain size of each polymer block should be approximately 100 nm. Typical polymers with molecular weight $\sim 10^4$ g/mol give domain size of 10–20 nm. The domain size of block copolymers varies with molecular weight, and well-known scaling laws describes that the domain size increases with molecular weight of polymers by factor of $M^{2/3}$ [33]. To increase the domain spacing over 100 nm, very high molecular weight block copolymers ($>10^6$ g/mol) are demanded.

The pioneer work on block copolymer photonic crystals was first reported by Thomas group using symmetric poly(styrene-*b*-isoprene) (PS-*b*-PI) diblock copolymers with molecular weights of $\sim 10^5$ g/mol [34–37]. Due to the symmetric structure of copolymer, PS-*b*-PI diblock copolymers formed the lamellar microstructure which corresponds to 1D photonic crystals. The domain spacing formed by the original molecular weights of diblock copolymers was not sufficient to exhibit the photonic band gap in visible region. The copolymers were, hence, blended with low-molecular-weight PS and PI homopolymers to increase the

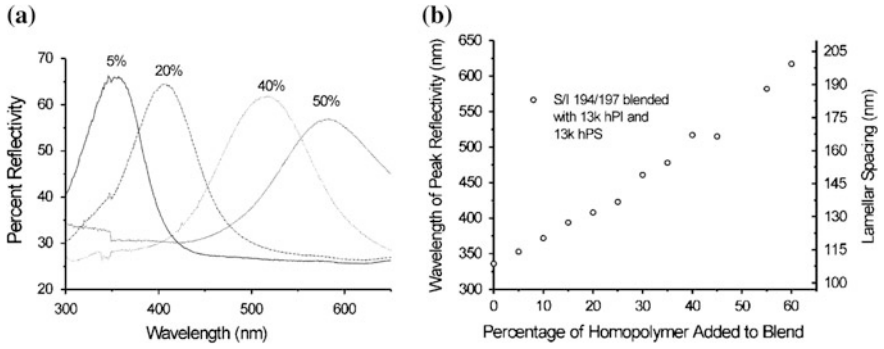

Fig. 4.2 **a** Reflectivity of samples containing 5, 20, 40 and 50 % total added homopolymer. The progression to longer wavelengths and broader peaks with increasing homopolymer content is evident. **b** Wavelength of peak reflectivity versus homopolymer weight fraction. Reproduced from [36] with permission

domain spacing sufficiently. When the PS-*b*-PI copolymers were systematically blended with homopolymers by 5–50 %, the photonic bandgaps were tuned from $\lambda_0 = 350$ to 600 nm (Fig. 4.2).

In terms of controlling domain size, this ternary blending approach provides a way to tune the photonic bandgap across the entire visible wavelength range. The wavelength of peak reflectance of particular diblock copolymers varies in an approximately linear manner by adjusting the amount of homopolymer.

Recently, Grubbs and coworkers demonstrated stopband tunable photonic crystals based on binary blending block copolymers [38–40]. Two block copolymers having molecular weights of 1.51×10^6 g/mol (BCP-1) and 4.17×10^6 g/mol (BCP-2) were prepared by ring opening polymerization of two macro-monomers, *exo*-norbornene-functionalized hexyl isocyanate ($M_w = 6.77 \times 10^3$ g/mol) and 4-phenyl butyl isocyanate ($M_w = 5.99 \times 10^3$ g/mol). The solvent casted films of BCP-1 and BCP-2 exhibited a photonic stopband at $\lambda = 360$ and 785 nm respectively. As BCP-2 was added to BCP-1, the photonic stopband gradually shifted from 360 to 785 nm depending on the blending ratio. In this case, the photonic stopband is almost proportional to the weight fraction of BCP-2 (Fig. 4.3).

The hexagonally packed cylinders and double gyroids prepared by self-assembly of block copolymers can be used for producing 2D and 3D photonic crystals, respectively. Hexagonally packed cylinders are produced with 21–30 % minority block composition in diblock copolymers. Similar to 1D block copolymer photonic crystals, very high-molecular-weight polymers are required to get large domain spacing enough to exhibit the photonic bands at visible wavelength regime. For example, 2D block copolymer photonic crystals have been prepared by roll casting of PS-*b*-PI (3.2×10^5 g/mol for PS, 6.8×10^5 g/mol for PI) block copolymer [41]. During roll casting, solvent slowly evaporates and the self-assembly process takes place in an evaporating solution. Due to the high molecular weight ($\sim 10^6$ g/mol), the periodicity of cylinder was relatively large ($d \approx 120$ nm), and accordingly the sample exhibit a reflection peak centered at 415 nm.

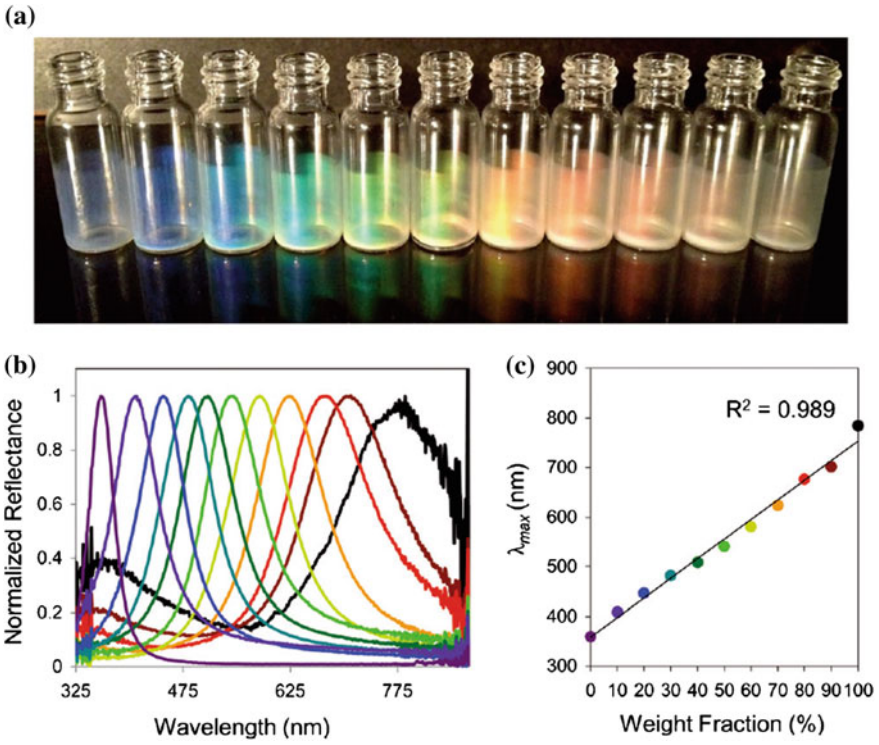

Fig. 4.3 **a** Photograph of brush block copolymer blends reflecting light across the visible spectrum. Plots of **b** reflectance against wavelength and **c** maximum peak wavelength of reflectance against weight fraction of blend (% BCP-2) of the different brush block copolymer blends. Reproduced from [38] with permission

The double gyroid microdomain structure occurs in the relatively narrow composition regime between the lamellar and cylindrical phase of block copolymers. The first 3D block copolymer photonic crystals were based on the double gyroid structure made of PS-*b*-PI with total molecular weight of 7.5×10^5 g/mol (3.0×10^5 g/mol for PS, 4.5×10^5 g/mol for PI) (Fig. 4.3) [42]. The domain size of the gyroids was sufficiently large to interact with visible light. In this case, the reflective index contrast can be enhanced by removing PI domains using UV/O_3 treatment (Fig. 4.4).

The preceding examples show that block copolymers with the extremely high molecular weight (>10^6 g/mol) are demanded to produce 1D, 2D or 3D photonic crystals exhibiting colors in visible region. Fabrication of photonic crystals using such high molecular weight of polymers is, however, often hampered by difficulties in polymer synthesis. Typically, severely controlled anionic polymerization technique is demanded for synthesizing high-molecular-weight block copolymers with well-controlled geometry and polydispersity. Furthermore, the microphase separation process is retarded by very slow chain diffusion of high-molecular-weight

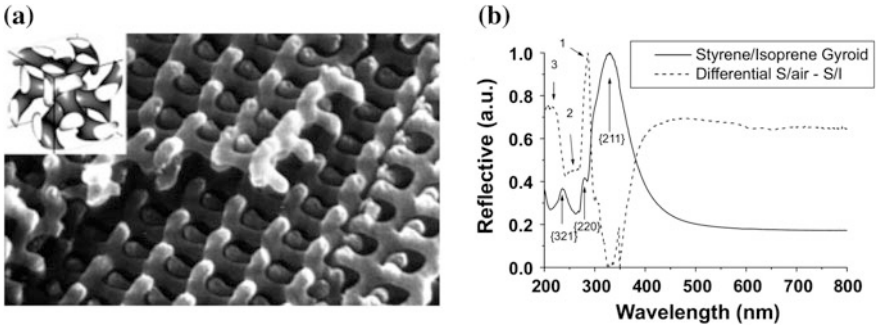

Fig. 4.4 **a** SEM image of the PS-*b*-PI double gyroid structure after removing PI domain by treating with UV/O_3. **b** The reflectivity plots of the unetched and etched PS-*b*-PI double gyroid films. Reproduced from [42] with permission

polymers. These problems can be alleviated by swelling either one or both of polymer domains with substantial amount of diluents during or after the microphase separation of low-molecular-weight block copolymers.

4.3.2 *Block Copolymer Photonic Gels by Swelling with Diluents*

Swelling with diluents provides simple and versatile route for modifying physical and optical properties of polymer photonic crystals. In this case, two key parameters determining the photonic bands, the domain spacing and the refractive index contrast can be easily modulated by changing the extent of swelling without synthesizing other new polymers. Furthermore, swelling increase responsivity of block copolymer photonic crystals to the external mechanical or chemical stimuli. Various materials have been used as swelling diluents of block copolymer photonic crystals. Examples include small molecule solvents, homopolymers, organic and inorganic colloidal particles. Depending on the chemical affinity of the polymer to the diluents, the extent of swelling can span from 10 % to over 1000 %. Considering such high swelling ratio, photonic gels exhibiting the photonic band gaps in visible region are easily achievable using moderately low molecular weight of block copolymers ($M_n > 10^4$ g/mol). Either one or both of domains can be swollen with diluents depending on the compatibility of diluents with domains. For example, PS-*b*-PI block copolymer (8.4×10^5 g/mol, PS/PI = 57/43) swollen with extensive amount of cumene, a good solvent for both PS and PI block, exhibited strong photonic stop bands at visible wavelength regime [43]. In this case, the thermal responsivity of the photonic gel was increased to a larger extent. The photonic stop band was observed at 510 nm when the photonic gel film was subjected to 30 °C. As increasing the temperature to 140 °C, the photonic stop band gradually decreased to 450 nm. Similarly, PS-*b*-PI block copolymer photonic gel films

swollen with solvents exhibited apparent shifts of photonic stop bands during the solvent drying process [44]. Non-volatile solvents or organic plasticizer can also be used to swell the polymer domains. A common plasticizer, dioctyl phthalate (DOP) was used to swell PS-*b*-PI block copolymers [45]. Both the PS and PI domains swell since DOP is a non-selective solvent for both polymers.

The prior examples showed that the both PS and PI domains were fully swollen with non-selective solvents. When only one domain is selectively swollen by diluents, photonic gels form *meso*-gels. Since one domain is not swollen by diluents, the photonic *meso*-gels have characteristics of both gels and dry polymers. One main advantage of selective swelling is that the physical integrity of photonic gels is not deteriorated by swelling because the swollen polymer chains are grafted on the surface of the unswollen hard domain. To prepare photonic *meso*-gels, diluents should be selectively sequestered in one domain. As shown in the previous section, an early demonstration of this selective swelling was the incorporation of low-molecular-weight homopolymers into diblock copolymers [34–37, 41, 42]. The interaction between homopolymers and block copolymers selectively localized homopolymer chains at a certain domain, and increased the domain size.

Similarly, nanoparticles modified with homopolymers were also utilized as selective diluents to modify dielectric properties of block copolymer photonic crystals [46–48]. For example, gold nanoparticles functionalized with polystyrene were blended into a symmetric polystyrene-*b*-polyethylene/propylene (PS-*b*-PEP) (M_n = 8.0 × 10^5 g/mol, PS/PEP = 50/50) which formed the lamellar structure [46, 47]. Due to PS modification, gold nanoparticles were selectively segregated to the PS domains (Fig. 4.5). While the domain size was not much changed, the photonic stopband shifted to a slightly longer wavelength due to an enhancement in the refractive index of the PS domains and the refractive index contrast. Some other specific interactions such as hydrogen bonding and ionic interactions can be utilized

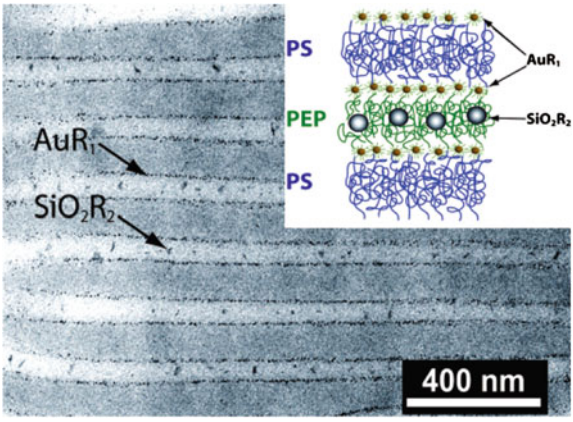

Fig. 4.5 Ternary blend of PS-b-PEP/Au nanoparticles/SiO_2 nanoparticles. Gold nanoparticles appear as *dark spots* along the IMDS; SiO_2 nanoparticles reside in the center of the PEP domain. Reproduced from [46] with permission

for selective sequestering. Osuji and coworkers utilized hydrogen bonding interaction to selectively sequester varying amount of imidazole terminated liquid crystal mesogens within PMMA domains in poly[styrene-*b*-(methacrylic acid)] (PS-*b*-PMMA) [49]. Due to strong hydrogen bonding between imidazole and acid group, liquid crystal molecules were selectively located at PMMA domains. These results in increase of the size of PMMA domain, and accordingly the photonic stopband shifted to the longer wavelength.

Various photonic *meso*-gels can be easily prepared by using selective solvents. Unlike homopolymers and nanoparticles, photonic *meso*-gels can be directly prepared simply by immersing the samples into a certain selective solvent. In this case, the photonic stopbands can be reversibly and dynamically tuned by varying the solvent quality. Kang et al. first report polystyrene-b-[quaternized-poly(2-vinylpyridine)] block copolymer (PS-*b*-QP2VP) photonic *meso*-gels where the QP2VP domains are selectively swollen by aqueous solvent [50]. To prepare PS-*b*-QP2VP photonic *meso*-gels, the lamellar films were first made from symmetric PS-*b*-P2VP block copolymers with moderately low molecular weight, and then the pyridine groups of P2VP chains were quaternized with short alkyl groups (Fig. 4.6). The PS-*b*-QP2VP photonic *meso*-gels were originally transparent because of the small domain spacing (<100 nm) and the almost same refractive indexes of PS and QP2VP domains ($n \approx 1.6$). However

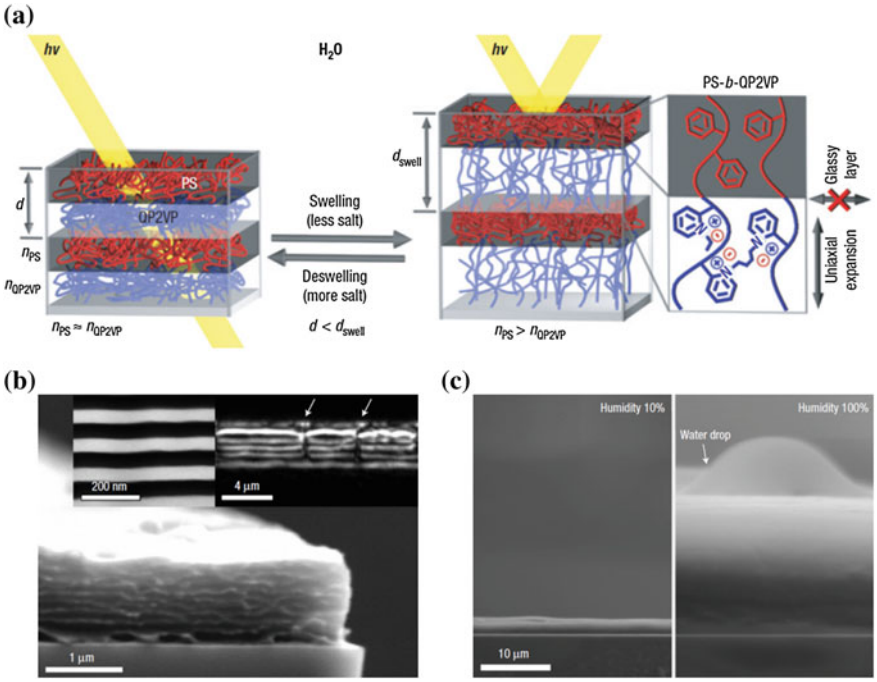

Fig. 4.6 **a** Schematic diagram of the structure of photonic gel film and the tuning mechanism. **b** SEM micrograph of a dry PS-b-QP2VP lamellar photonic film deposited on a silicon wafer. **c** ESEM micrographs of a film at different humidity levels. Reproduced from [50] with permission

they showed strong reflection colors in water by swelling of QP2VP domains. In this case, PS-*b*-QP2VP photonic *meso*-gels showed the largest shift of photonic stopband by swelling ($\Delta\lambda$ = 1600 nm). The large shift of photonic stopbands was mainly by the large swelling ratio ($\sim$1100 %). The swelling ratio was much higher than other system using organic solvents, polymers, and plasticizers, because the quaternized pyridine groups in QP2VP domains are positively charged. QP2VP chains can be highly stretched by ionic repulsion due to the ionic repulsion between quaternized pyridine groups. It is notable that the films were stable at such high swelling ratio, which was mainly because the glassy PS domains maintained the structure.

4.4 Stimuli Responsive Photonic Gels

Gels swollen with a significant amount of diluents show the large volume changes in response to the various chemical, physical and electrical stimuli. The volume changes of gels can be utilized to modulate the photonic stopbands when the gels are incorporated in photonic crystals. These responsive photonic gels have been widely investigated as a component of sensors and displays. For those applications, reversible changes of photonic properties with variation of the external stimuli are demanded. Comparing with 2D or 3D structures, 1D photonic crystals are more favorable for making reversible responsive photonic crystals because of the easiness of fabrication and uniaxial dimension changes which minimize the structural deformation by swelling/deswelling process. A good responsive photonic crystal is usually characterized by a high response rate, reversible tuning, and a large tuning range of photonic stopbands.

4.4.1 Chemochromic Photonic Gels

Chemochromism in photonic gels is based on the changes of refractive index contrast or/and optical path length of each layer by various chemical stimuli including solvents, humidity, ions, pH and etc. Most of chemochromic photonic gels have been based on the 1D photonic structures because of their structural simplicity and stability comparing with 2D or 3D photonic crystals. The diblock copolymer lamellae swollen by solvents have been employed for fabricating 1D photonic gels. When one or both domains are swollen with solvents, polymer layers exhibited characteristic volume changes of gel with variation of a swelling solvent amount. In this case, since the volume changes of gel layers in photonic gels are directly associated with the photonic stopbands, the photonic gels have been utilized for studying fundamental physics of polymer gels as well as sensor applications. One simplest chemochromic photonic gel system is consisting of PS-*b*-PI block copolymer photonic gels swollen with toluene (Fig. 4.7) [44]. Since toluene is a good solvent for both PS and PI domains, fully swollen photonic gels were

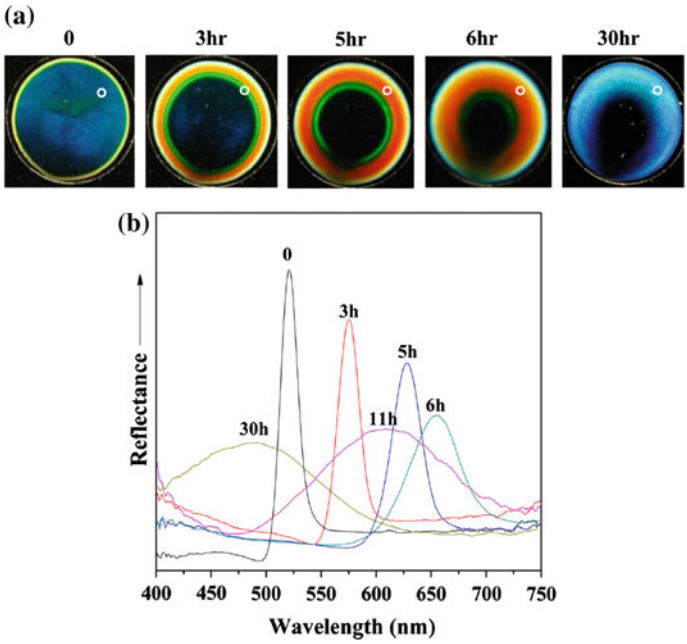

Fig. 4.7 **a** Time-dependent color change for the PS/PI-505/520 photonic gel films during solvent evaporation. **b** Corresponding time dependent reflectivity spectra taken at the *white circle* position in the PS/PI-505/520 photonic gel. Reproduced from [44] with permission

formed. As gradually drying toluene, the photonic gels exhibited serial changes of reflection colors. Interestingly, the photonic gels initially showed a red-shift of photonic stopband, and then a blue-shift at the end of toluene drying. This phenomenon was attributed to the competition of thermodynamic and kinetic assembly of block copolymer chains in solution.

It is known that some polyelectrolyte gels show the first-order volume transitions with the changes of external stimuli [51–62]. The polyelectrolytes were after incorporating into photonic gels, the abrupt volume phase transition can be exploited for increasing sensitivity of photonic gels against solvent changes. Kang et al. demonstrated that photonic gels prepared using PS-*b*-QP2VP showed very high sensitivity to the changes of solvent and humidity [63–65]. It was shown that photonic stopbands in PS-*b*-QP2VP photonic gels abruptly increased at certain range of dielectric value (ε = 10–30). Taking advantage of this, alcohol sensors based on PS-*b*-QP2VP photonic gels were demonstrated (Fig. 4.8) [63]. Strikingly, PS-*b*-QP2VP photonic gels exhibited all different colors when they were swollen with different conformational isomers of propanol and butanol. For example, the photonic stopbands of four different isomers of butanol were observed at λ_{peak} = 651 nm (*n*-butanol), 601 nm (*iso*-butanol), 372 nm (*sec*-butanol) and transparent (*tert*-butanol) respectively. Due to large shift of the photonic stopbands, each of isomers can be detected with bare eyes.

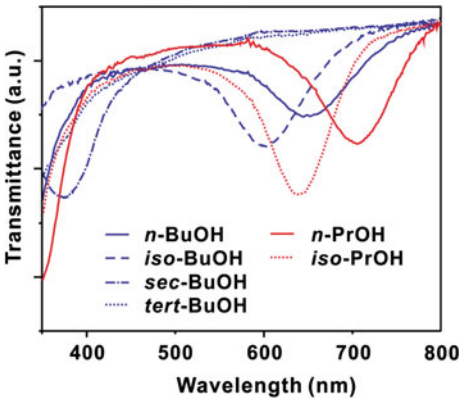

Fig. 4.8 The photonic stopband changes of PS-*b*-QP2VP block copolymer photonic gel films swollen with isomeric alcohols; *n*-propanol and *iso*-propanol, *n*-butanol, *iso*-butanol, *sec*-butanol and *tert*-butanol. Reproduced from [63] with permission

Since the position of photonic stopbands directly represents the extent of swelling in the gel layers, the photonic gels can be utilized for investigating the volume phase transition of gels. Typically, the volume phase transitions occur at very narrow range of conditions. In the case of PS-*b*-QP2VP photonic gels, the volume phase transitions can be tuned by changing both the extent of quaternization of pyridine groups in P2VP chains and their counter anions. Jang and coworkers investigated the behaviors of volume phase transition of QP2VP gels using PS-*b*-QP2VP photonic gels [64]. The thickness of QP2VP gel layers can be directly monitored by photonic stopbands. The swelling behavior of QP2VP gel layers varied depending on the extent of quaternization. The thickness of QP2VP gel layers linearly increased with increasing solvent quality when the pyridine groups were slightly quaternized, but they showed apparent first order transitions when the pyridine groups were sufficiently quaternized. At moderate quaternization conditions, QP2VP gel layers showed unusual dual first order transitions with increasing solvent quality; an expansion transition was followed by a collapse transition. Such dual transitions were disappeared when pyridine groups were fully quaternized. In PS-*b*-QP2VP photonic gels, hydrogen bonding played an important role for inducing the first-order volume phase transitions [57, 64, 66, 67].

The swelling behaviors of polyelectrolyte gels also can be controlled by modulating ionic strength or species of counter ions [51, 54]. For example, the volume transition behaviors of QP2VP gel layers in fully quaternized PS-*b*-QP2VP photonic gels have been modulated by exchanging the counter anions of pyridinium groups in QP2VP layers (Fig. 4.9) [64]. Depending on the ion-pairing affinity between pyridinium groups and counter anions, QP2VP layers in PS-*b*-QP2VP photonic gels showed different swelling behaviors. In this case, the hydrophobicity of polyelectrolytes follows the Hofmeister series [68], and increases depending on the counter anions in the order of $F^- < Cl^- < Br^- < I^-$. Hence the hydrophobic

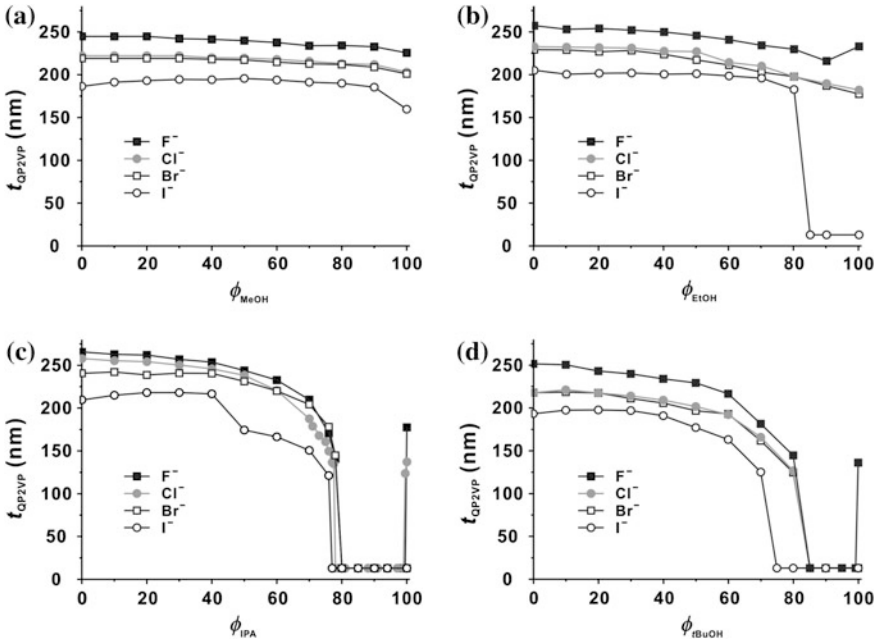

Fig. 4.9 The effects of gegenions and solvents on the phase transition behaviors of the photonic *meso*-gels. Reproduced from [64] with permission

interaction between chains become more important in the PS-*b*-QP2VP photonic gels modified with iodide or bromide ions than the one modified with chloride or fluoride ions. Hydrophobicity control of PS-*b*-QP2VP photonic gels by anion exchange is useful for controlling the sensitivity of photonic gels to the change of humidity [65]. For example, PS-*b*-QP2VP photonic gels modified with acetate showed photonic stopband shifts in a wide range of humidity (from 20 to 100 %) while the photonic gels modified with chloride responded only at high humidity (>70 %).

PS-*b*-QP2VP photonic gels also sensitively response to the change of ionic strength [50, 69]. The photonic stopbands shift to the shorter wavelength as increasing ionic strength. In this case, the tunability of the photonic stopband against ionic strength was highly dependent on the molecular weight of PS-*b*-QP2VP. The PS-*b*-QP2VP photonic gels prepared with higher molecular weight ($M_n \times 10^3$ = 190/190) response more sensitively to the salt concentration than low molecular weight one ($M_n \times 10^3$ = 57/57). Furthermore, PS-*b*-QP2VP photonic gels were also dependent on the size of cations. The photonic stopband increased in the order of $K^+ < Na^+ < Ca^{2+} < Cu^{2+}$, which is consistent with the order of ionic radii of cations: K^+ (1.38 Å), Na^+ (1.02 Å), Ca^{2+} (1.00 Å) and Cu^{2+} (0.73 Å). This cation size dependent optical property of photonic gels also can be explained with Hofmeister series [68]. It is known that larger cations induce more efficiently ordering of water molecules which increase the surface tension of water. Salts with

these properties are called kosmotropes; they are effective at aggregating polyelectrolyte gels [70, 71]. These ion dependent optical properties of polyelectrolyte photonic gels can be utilized for detecting ions by colors (Fig. 4.10) [72].

Ion pairing between pyridinium and anions in PS-*b*-QP2VP photonic gels can be further utilized for fabricating photonic memories (Fig. 4.11) [73, 74]. It was known that some polyelectrolyte gels showed hysteric volume change during cyclic swelling/deswelling process, but it was not well utilized because of insufficient controllability [75–78]. Kim and coworkers demonstrated tunable hysteresis of photonic stopband in the PS-*b*-P2VP photonic gels. The photonic hysteresis in the photonic gels were induced by disproportional volume changes during cyclic shifts of pH [73]. PS-*b*-P2VP photonic gels exhibited different photonic stop bands at the same pH depending on the direction of pH change. It was found that the strength of

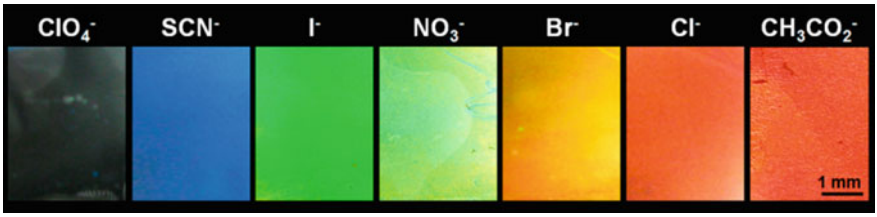

Fig. 4.10 Color change of the PS-b-QP2VP photonic gel films with direct exchange of counter anions. Reproduced from [72] with permission

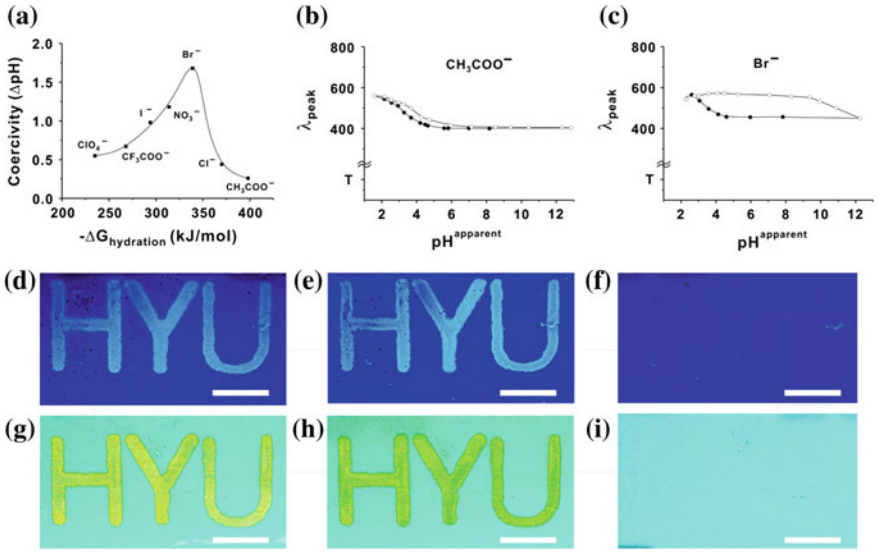

Fig. 4.11 **a** Variation of pH coercivity with the hydration free energy of anions. Hysteresis loops of photonic gel films obtained in **b** CH_3COOH and **c** HBr ethanoic solution. **d–i** Photographs of photonic memory films in 0.03 M NaBr ethanoic solution. Reproduced from [73] with permission

hysteresis which can be characterized by pH coercivity was highly dependent on the ion pairing affinity between pyridinium and its counter anion. When pyridinium ions have strong ion pairing affinity with anions, the photonic gels showed strong hysteresis in photonic stopband against the cyclic pH changes, and vice versa. In this case, pyridinium ions have the stronger ion pairing affinity as their hydration Gibbs free energy is more similar to that of anions. Since bromide has very similar hydration Gibbs free energy with pyridinium, the photonic gels modified with bromide showed very large hysteresis while the one modified with acetate which has quite different hydration Gibbs free energy exhibited weak hysteresis. Utilizing the tunable hysteresis by exchanging ions, photonic memory films which can write and erase with acids and bases were demonstrated.

When photonic gels were modified with specified molecules interacting with a certain chemical or biomolecule, photonic gels can be used as chemo- or bio-sensor [79, 80]. Omar and coworkers demonstrated fructose sensors based on PS-*b*-QP2VP photonic gels functionalized with 2-(bromomethyl)phenylboronic acid. The boronic acid moiety in QP2VP gel layers are reversibly binding with fructose, which imparts the change of photonic stopband in the photonic gels. When the boronic acid moiety bound with fructose molecules, photonic stopbands shifted to the longer wavelength due to the increased volume by fructose.

4.4.2 Mechano-, Thermochromic Photonic Gels

Besides chemical stimuli, photonic gels are also highly sensitive to the physical stimuli such as mechanical force and temperature. Due to the elasticity of gels, photonic gels show relatively large shift of photonic stopband upon applying strain (Fig. 4.12) [81, 82].

The block copolymer photonic gels are responsive to various mechanical deformations, including uniaxial tension, peel and shear. Chan and coworkers investigated the change of photonic stopband of PS-*b*-P2VP block copolymer photonic gels by applying uniaxial compression force [82]. It was observed that the photonic stopband shifted to the shorter wavelength as increasing stress. The extent of wavelength change with compression depends on the relative mechanical stiffness of the domains. Since the modulus of the glassy PS and the highly swollen P2VP domains are significantly different ($E_{PS}/E_{sP2VP} \sim 10^9/10^5$ N/m^2 = 10^4), the PS domains are remained to be undeformed throughout the compression. The stiffness of P2VP domains can be easily modulated by changing the swelling ratio of P2VP layers, and accordingly the mechanical sensitivity and sensing resolution of photonic gels can be adjusted.

Thermal heating affect both two key parameters determining the optical properties of photonic crystals, the refractive index and domain spacing [43, 49, 83]. Yoon and coworkers demonstrated that thermochromics photonic gels based on PS-*b*-PI block copolymers [43]. PS-*b*-PI block copolymer photonic gels swollen with cumene exhibited negative thermochromic response, the photonic stopband shifted to the

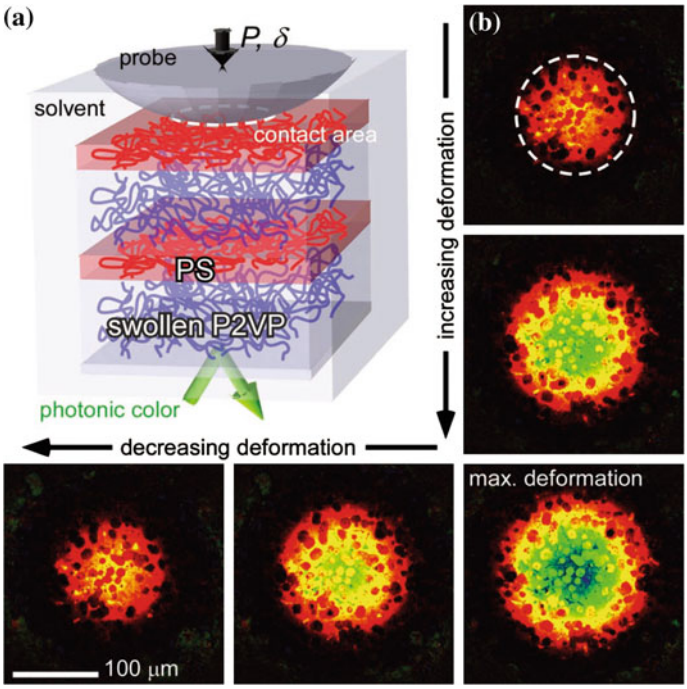

Fig. 4.12 **a** Mechanochromism of a PS-*b*-P2VP block copolymer photonic gel deformed with an indenter. **b** Color changes of the gel as a function of deformation. Reproduced from [82] with permission

shorter wavelength as increasing temperature. It was found that both the refractive index and the domain spacing contributed to the negative thermochromic response. The refractive indices of both PS and PI decrease with temperature ($dn/dT = \sim -1.42 \times 10^{-4}\ K^{-1}$), [84] and both domain spacings also decrease with temperature ($L \sim T^{-1/3}$) [85]. Because of these negative responses of refractive index and domain spacing with temperature, the photonic stopband of PS-*b*-PI block copolymer photonic gels shifted to the shorter wavelength as increasing temperature. Temperature induced change in the pKa of pyridine was utilized to make thermochromics photonic behavior in PS-*b*-P2VP block copolymer photonic gels [83]. The PS-*b*-P2VP block copolymer photonic gels swollen with acidic aqueous solution exhibited negative thermochromic response. This was attributed to the change of pKa of pyridine groups in P2VP chains. As increasing the temperature, the fraction of protonated pyridine groups decreased because of increased pKa of pyridine at the elevated temperature. PS-*b*-PMMA block copolymer photonic gels swollen with liquid crystal mesogens showed positive thermochromic behavior [49]. This thermochromic response of PS-*b*-PAA block copolymer photonic gels was mainly by the change of the order parameter of liquid crystal domains by heating into the isotropic state, which increased the PAA domain size and shifted the photonic stopband to the longer wavelength.

4.4.3 *Electrochromic Photonic Gels*

It is well known that polyelectrolyte gels are responsive to electric fields [54, 86]. This property of gels has been utilized for electrochromic photonic gels [30, 74, 87, 88]. Walish and coworkers employed the electrochemically induced pH gradient to control the photonic stopband in PS-*b*-P2VP block copolymer photonic gels [30]. A swelling solvent, trifluoroethanol generated H^+ by electrolysis at the anode, and which protonated the pyridine groups in P2VP chains. As increasing the fraction of the protonated pyridine, PS-*b*-P2VP photonic gels showed a red-shift of photonic stopband.

Electrochemically controlled pH gradient can be further utilized for nonvolatile photonic pixels. Kang et al. demonstrated that photonic gels with strong pH hysteresis can be utilized for nonvolatile photonic pixels using PS-*b*-P2VP block copolymer photonic gels (Fig. 4.13) [74]. It was found that PS-*b*-P2VP photonic gels showed anion-dependent relaxation of photonic stopband after application of a short pulse bias voltage. Similar to the pH hysteresis of photonic gels shown in the previous section, the order of relaxation time corresponds to the order of the hysteresis strength of the photonic gels dependent on anions [73]. It was demonstrated that the optical volatility of photonic pixels was tuned by controlling the hysteresis strength and the position of pH_c, which were both highly dependent on the species of anions pairing with pyridinium groups. Some different types of electrochromic photonic gels were also reported [21, 87]. For example, Lee and coworkers demonstrated that highly concentrated colloidal nanoparticle solutions exhibited unique angle independent photonic colors, and which can be tuned either by changing the solution concentration, or by electrophoretic control [87].

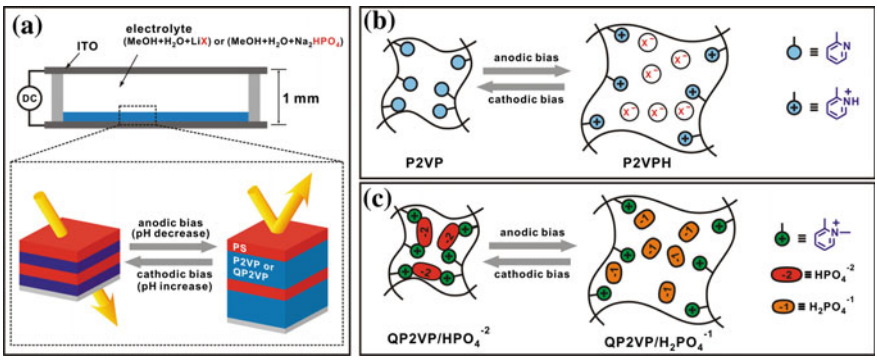

Fig. 4.13 Schematic structure of photonic pixel and proposed mechanisms for gel swelling and deswelling by an electrically induced pH gradient. Reproduced from [74] with permission

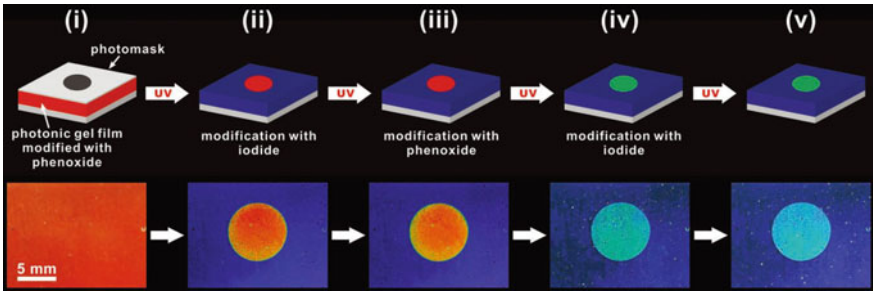

Fig. 4.14 Fixation and reactivation of photonic patterns by ion-exchange. Reproduced from [89] with permission

4.4.4 Photochromic Photonic Gels

Polymers are decomposed or crosslinked by light. When they are swollen with solvents, polymer gels show large volume changes by photoreactions. Kang et al. demonstrated photoresponsive PS-*b*-QP2VP block copolymer photonic gel films exhibiting strong reflective multicolors in the visible regime in response to near-UV radiation (Fig. 4.14) [89]. Since they were highly swollen with solvents, the photonic gels exhibited very large shifts of photonic stopband against the weak exposure energy of UV. In this case, the photosensitivity of photonic gels can be tuned by varying counter-anions. For example, large halide ions including iodide and bromide retard photocrosslinking, while phenoxide and carboxylate facilitate photocrosslinking. Utilizing the anion-dependent photosensitivity, photonic gels where the photonic patterns can be imprinted, fixated, and reactivated by UV were demonstrated by ion-exchange.

4.5 Summary and Outlook

Various photonic gels can be formed by self-assembly of block copolymers. The phase separation of block copolymers forms various morphologies including lamellae, cylinders, and gyroids, and which have been employed for 1D, 2D, and 3D photonic crystals. When one or both domains of block copolymers were swollen with a significant amount of diluents, photonic gels become flexible and responsive to the external stimuli. Especially, polyelectrolyte block copolymer 1D photonic gels swollen with solvents exhibited extremely large tunability of optical properties by chemical, mechanical, thermal, and electrical stimuli. Compared with other 3D photonic crystals, 1D block copolymer photonic gels are mechanically and chemically stable with a large reversibility because of uniaxial expansion/compression. The ionic interactions in polyelectrolytes can give unique optical properties of photonic gels which may not be possible from other neutral photonic gels. Especially, photonic

properties of PS-*b*-QP2VP photonic gels can be easily modified simply by exchanging counter anions of pyridinium moieties. Taking advantage of many features including easy fabrication, low molecular weight requirement, large sensitivity, and easy photonic stopband tunability by ion exchange, block copolymer photonic gels have been demonstrated as a good component of sensors and displays. In sensor applications, however, it is still challenging to developing efficient methods for detecting specific targets with high selectivity and sensitivity. In display applications, angle dependent hue of block copolymer photonic gels should be addressed as well as their stability to chemical and electrical environment.

References

1. J.B. Pendry, A. MacKinnon, Phys. Rev. Lett. **69**, 2772 (1992)
2. H. Míguez, F. Meseguer, C. Lopez et al., Adv. Mater. **10**, 480 (1998)
3. V. Astratov, Y.A. Vlasov, O. Karimov et al., Phys. Lett. A **222**, 349 (1996)
4. E. Yablonovitch, T.J. Gmitter, Phys. Rev. Lett. **63**, 1950 (1989)
5. E. Yablonovitch, T.J. Gmitter, K.M. Leung, Phys. Rev. Lett. **67**, 2295 (1991)
6. E. Yablonovitch, J. Opt. Soc. Am. B: Opt. Phys. **10**, 283 (1993)
7. J.D. Joannopoulos, R.D. Meade, J.N. Winn, *Photonic Crystals: Molding the flow of light* (Princeton University Press, Princeton, 1995)
8. J.D. Joannopoulos, P.R. Villeneuve, S. Fan, Nature (London) **386**, 143 (1997)
9. S. Rowson, A. Chelnokov, C. Cuisin, J.M. Lourtioz, IEE Proc. Optoelectron. **145**, 403 (1998)
10. L. Alexeev Vladimir, C. Sharma Anjal, V. Goponenko Alexander et al., Anal. Chem. **75**, 2316 (2003)
11. J.H. Holtz, J.S.W. Holtz, C.H. Munro, S.A. Asher, Anal. Chem. **70**, 780 (1998)
12. A. Asher Sanford, L. Alexeev Vladimir, V. Goponenko Alexander et al., J. Am. Chem. Soc. **125**, 3322 (2003)
13. K. Lee, S.A. Asher, J. Am. Chem. Soc. **122**, 9534 (2000)
14. L. Alexeev Vladimir, S. Das, N. Finegold David, A. Asher Sanford, Clin. Chem. **50**, 2353 (2004)
15. M.M.W. Muscatello, S.A. Asher, Adv. Funct. Mater. **18**, 1186 (2008)
16. J.H. Holtz, S.A. Asher, Nature (London) **389**, 829 (1997)
17. X. Xu, A.V. Goponenko, S.A. Asher, J. Am. Chem. Soc. **130**, 3113 (2008)
18. X.L. Xu, G. Friedman, K.D. Humfeld, S.A. Majetich, S.A. Asher, Adv. Mater. **13**, 1681 (2001)
19. J.M. Weissman, H.B. Sunkara, A.S. Tse, S.A. Asher, Science (Washington, DC, U.S.) **274**, 959 (1996)
20. C.R. Johnson, M. Ludwig, S.A. Asher, J. Am. Chem. Soc. **108**, 905 (1986)
21. A.C. Arsenault, T.J. Clark, G. von Freymann et al., Nat. Mater. **5**, 179 (2006)
22. A. Blanco, E. Chomski, S. Grabtchak et al., Nature (London) **405**, 437 (2000)
23. S.Y. Choi, M. Mamak, G. von Freymann, N. Chopra, G.A. Ozin, Nano Lett. **6**, 2456 (2006)
24. F. Fleischhaker, A.C. Arsenault, V. Kitaev et al., J. Am. Chem. Soc. **127**, 9318 (2005)
25. A. Arsenault, D. Puzzo, I. Manners, G. Ozin, Nat. Photonics **1**, 468 (2007)
26. B.V. Lotsch, C.B. Knobbe, G.A. Ozin, Small **5**(13), 1498–1503 (2009)
27. A. Ledermann, L. Cademartiri, M. Hermatschweiler et al., Nat. Mater. **5**, 942 (2006)
28. P. Vukusic, J. Sambles, Nature (London, U.K.) **424**, 852 (2003)
29. R.M. Kramer, W.J. Crookes-Goodson, R.R. Naik, Nat. Mater. **6**, 533 (2007)
30. J.J. Walish, Y. Kang, R.A. Mickiewicz, E.L. Thomas, Adv. Mater. **21**, 3078 (2009)
31. S. John, Phys. Rev. Lett. **58**, 2486 (1987)

32. L.D. Bonifacio, B.V. Lotsch, D.P. Puzzo, F. Scotognella, G.A. Ozin, Adv. Mater. **21**, 1641 (2009)
33. T. Hashimoto, M. Fujimura, H. Kawai, Macromolecules **13**, 1660 (1980)
34. Y. Fink, A.M. Urbas, M.G. Bawendi, J.D. Joannopoulos, E.L. Thomas, J. Lightwave Technol. **17**, 1963 (1999)
35. A. Urbas, Y. Fink, E.L. Thomas, Macromolecules **32**, 4748 (1999)
36. A. Urbas, R. Sharp, Y. Fink, E.L. Thomas, M. Xenidou, L.J. Fetters, Adv. Mater. (Weinheim, Germany) **12**, 812 (2000)
37. A.C. Edrington, A.M. Urbas, P. DeRege et al., Adv. Mater. (Weinheim, Germany) **13**, 421 (2001)
38. G.M. Miyake, V.A. Piunova, R.A. Weitekamp, R.H. Grubbs, Angew. Chem. Int. Ed. **51**, 11246 (2012)
39. B.R. Sveinbjörnsson, R.A. Weitekamp, G.M. Miyake, Y. Xia, H.A. Atwater, R.H. Grubbs, Proc. Natl. Acad. Sci. **109**, 14332 (2012)
40. G.M. Miyake, R.A. Weitekamp, V.A. Piunova, R.H. Grubbs, J. Am. Chem. Soc. **134**, 14249 (2012)
41. T. Deng, C. Chen, C. Honeker, E.L. Thomas, Polymer **44**, 6549 (2003)
42. A.M. Urbas, M. Maldovan, P. DeRege, E.L. Thomas, Adv. Mater. (Weinheim, Germany) **14**, 1850 (2002)
43. J. Yoon, W. Lee, E.L. Thomas, Macromolecules **41**, 4582 (2008)
44. Y.-W. Chiang, C.-Y. Chou, C.-S. Wu, E.-L. Lin, J. Yoon, E.L. Thomas, Macromolecules **48**, 4004–4011 (2015)
45. A.M. Urbas, *Department of Materials Science and Engineering* (Massachusetts Institute of Technology, Massachusetts, 2003)
46. M.R. Bockstaller, Y. Lapetnikov, S. Margel, E.L. Thomas, J. Am. Chem. Soc. **125**, 5276 (2003)
47. M. Bockstaller, R. Kolb, E.L. Thomas, Adv. Mater. (Weinheim, Germany) **13**, 1783 (2001)
48. R.B. Thompson, V.V. Ginzburg, M.W. Matsen, A.C. Balazs, Macromolecules **35**, 1060 (2002)
49. C. Osuji, C.-Y. Chao, I. Bita, C.K. Ober, E.L. Thomas, Adv. Funct. Mater. **12**, 753 (2002)
50. Y. Kang, J.J. Walish, T. Gorishnyy, E.L. Thomas, Nat. Mater. **6**, 957 (2007)
51. T. Tanaka, D. Fillmore, S.-T. Sun, I. Nishio, G. Swislow, A. Shah, Phys. Rev. Lett. **45**, 1636 (1980)
52. S. Stephenson, R. Offeman, G. Robertson, W. Orts, Chem. Eng. Sci. **62**, 3019 (2007)
53. T. Tanaka, Phys. Rev. Lett. **40**, 820 (1978)
54. T. Tanaka, Sci. Am. **244**, 124 (1981)
55. T. Tanaka, D.J. Fillmore, J. Chem. Phys. **70**, 1214 (1979)
56. Y. Li, T. Tanaka, Annu. Rev. Mater. Sci. **22**, 243 (1992)
57. M. Shibayama, T. Tanaka, *Responsive Gels: Volume Transitions I* (Springer, New York, 1993)
58. F. Ilmain, T. Tanaka, E. Kokufuta, Nature (London, U.K.) **349**, 400 (1991)
59. S. Hirotsu, Y. Hirokawa, T. Tanaka, J. Chem. Phys. **87**, 1392 (1987)
60. L. Brannon-Peppas, N.A. Peppas, Chem. Eng. Sci. **46**, 715 (1991)
61. A.E. English, S. Mafe, J.A. Manzanares, X. Yu, A.Y. Grosberg, T. Tanaka, J. Chem. Phys. **104**, 8713 (1996)
62. A.R. Khare, N.A. Peppas, Biomaterials **16**, 559 (1995)
63. Y. Kang, Bull. Korean Chem. Soc. **33**, 2847 (2012)
64. Y. Jang, J. Chung, S. Lee, H. Lim, H. Baek, Y. Kang, Polym. Bull. **70**, 593 (2013)
65. Y. Kang, Macromol. Res. **20**, 1223 (2012)
66. E. Kokufuta, H. Suzuki, R. Yoshida, K. Yamada, M. Hirata, F. Kaneko, Langmuir **14**, 788 (1998)
67. H. Xia, J. Zhao, C. Meng et al., Soft Matter **7**, 4156 (2011)
68. F. Hofmeister, Archiv fur Experimentelle Pathologie und Pharmakologie **24**, 247 (1888)
69. Y. Kang, Bull. Korean Chem. Soc. **29**, 2329 (2008)

70. M.G. Cacace, E.M. Landau, J.J. Ramsden, Q. Rev. Biophys. **30**, 241 (1997)
71. K.D. Collins, P Natl. Acad. Sci. USA **92**, 5553 (1995)
72. H.S. Lim, J.-H. Lee, J.J. Walish, E.L. Thomas, ACS Nano **6**, 8933 (2012)
73. E. Kim, C. Kang, H. Baek et al., Adv. Funct. Mater. **20**, 1728 (2010)
74. K. Hwang, D. Kwak, C. Kang, D. Kim, Y. Ahn, Y. Kang, Angew. Chem. Int. Ed. **50**, 6311 (2011)
75. Y.-J. Lee, P.V. Braun, Adv. Mater. **15**, 563 (2003)
76. J.-H. Jang, C.Y. Koh, K. Bertoldi, M.C. Boyce, E.L. Thomas, Nano Lett. **9**, 2113 (2009)
77. M.M.W. Muscatello, S.A. Asher, Adv. Funct. Mater. **18**, 1186 (2008)
78. X. Xu, A.V. Goponenko, S.A. Asher, J. Am. Chem. Soc. **130**, 3113 (2008)
79. E. Lee, J. Kim, J. Myung, Y. Kang, Macromol. Res.: **1** (2012)
80. O.B. Ayyub, M.B. Ibrahim, R.M. Briber, P. Kofinas, Biosens. Bioelectron. **46**, 124 (2013)
81. E.P. Chan, J.J. Walish, A.M. Urbas, E.L. Thomas, Adv. Mater. **25**, 3934 (2013)
82. E.P. Chan, J.J. Walish, E.L. Thomas, C.M. Stafford, Adv. Mater. **23**, 4702 (2011)
83. J.J. Walish, Y. Fan, A. Centrone, E.L. Thomas, Macromol. Rapid Commun. **33**, 1504 (2012)
84. J. Brandrup, E.H. Immergut, E.A. Grulke, A. Abe, D.R. Bloch, *Polymer Handbook* (Wiley, New York, 1999)
85. T. Hashimoto, M. Shibayama, H. Kawai, Macromolecules **16**, 1093 (1983)
86. T. Tanaka, I. Nishio, S.T. Sun, S. Ueno-Nishio, Science **218**, 467 (1982)
87. I. Lee, D. Kim, J. Kal et al., Adv. Mater. **22**, 4973 (2010)
88. Y. Lu, H. Xia, G. Zhang, C. Wu, J. Mater. Chem. **19**, 5952 (2009)
89. Y. Ahn, E. Kim, J. Hyon, C. Kang, Y. Kang, Adv. Mater. **24**: OP127 (2012)

Chapter 5
Photonic Crystals Fabricated via Facile Methods and Their Applications

Wendong Liu, Xueyao Liu and Bai Yang

Abstract Many important breakthroughs are a result of a deep understanding of the properties of materials. In these years, photonic crystal structure has been proposed to have a lot of potential for novel optical devices, sensors [1–10] and play a key role in the next generation of information technology.

5.1 Introduction

Many important breakthroughs are a result of a deep understanding of the properties of materials. In these years, photonic crystal structure has been proposed to have a lot of potential for novel optical devices, sensors [1–10] and play a key role in the next generation of information technology [11–19]. The photonic crystal structure can finely control the optical properties of materials and respond to light waves over a desired range of frequencies by perfectly reflecting, or allowing them to propagate only in certain directions, or confining them within a specified volume, which is caused by the one dimensional (1D), two dimensional (2D), and three dimensional (3D) photonic crystal (Fig. 5.1d) [20–22]. Crystals in which the atoms or molecules are replaced by macroscopic media with differing dielectric constants, and the periodic potential is replaced by a periodic dielectric give rise to selective transmission or reflection of particular light wavelengths. In the last few decades, researchers have paid great attention on studying the structural colors existing in nature. The color of many organisms are beautiful, such as the paradise whiptail, *Pentapodus paradiseus*; insect compound eye; *Pachyrhynchus weevil* (Fig. 5.1a–c) and so on [23–27]. By studying the micro- or nano-structure of these organisms, researchers found that these structure colors are caused by the interaction of light

W. Liu · X. Liu · B. Yang (✉)
State Key Laboratory of Supramolecular Structure and Materials, International Joint Research Laboratory of Nano-Micro Architecture Chemistry, College of Chemistry, Jilin University, Changchun 130012, People's Republic of China
e-mail: byangchem@jlu.edu.cn

M. J. Serpe et al. (eds.), *Photonic Materials for Sensing, Biosensing and Display Devices*, Springer Series in Materials Science 229,
DOI 10.1007/978-3-319-24990-2_5

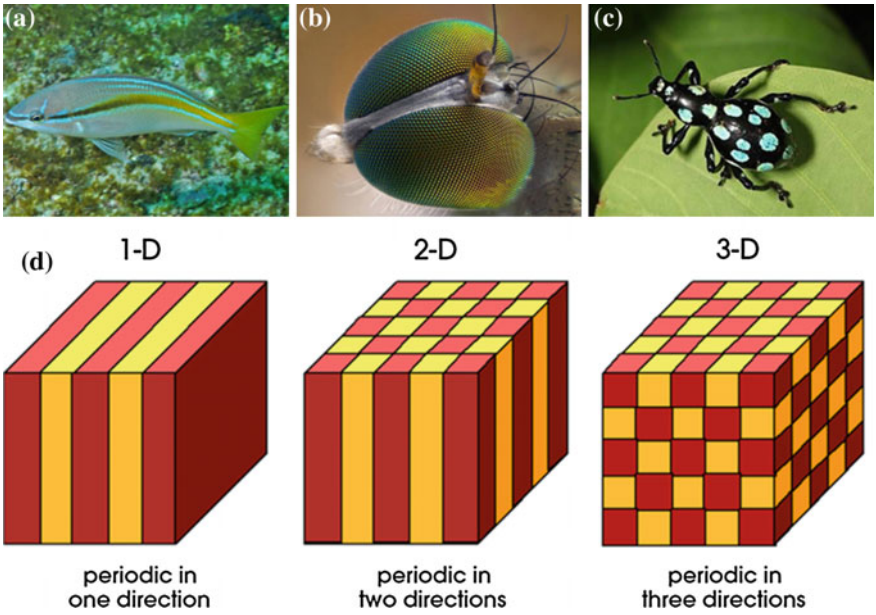

Fig. 5.1 Simple examples of structural color in nature: **a** the paradise whiptail, *Pentapodus paradiseus*, **b** insect compound eye, **c** *Pachyrhynchus weevil*; and schematic of one-, two-, and three-dimensional photonic crystals, **d** the different colors represent materials with different dielectric constants. The defining feature of a photonic crystal is the periodicity of dielectric material along one or more axes [22]

with dielectric structures on one, two, and three dimensions. These dimensions are on the order of visible-light wavelengths, the same as the 1D, 2D, and 3D photonic crystal effect (Fig. 5.1d), leading to the generation of structural color. Thus, photonic crystals of nature provide a wider design idea for photonic crystal fabricating. Recently, many micro- and nano-fabrication methods have been developed to prepare photonic crystals such as holographic laser lithography, phase-mask holography, direct ink writing, and direct laser writing. Amount of 1D, 2D and 3D photonic crystals have been achieved as described in other reviews [22, 28].

With the interiorizing of sustainable development, it has become people's growing energy consumption pursuit to use a simple process and in an energy efficiency producing method to replace the time-consuming mode of production. At the same time, along with people's living standard and the improvement of their health consciousness, it's becoming a necessity to simply detect the matters produced during the production, which may be harmful to their health. And it is still a challenge to fabricate photonic crystals which can be used for sensing in a facile method in the field of photonic crystals preparation. Recently, some researchers have made effort in this aspect and obtained encouraging results.

Herein, we will present a review focus on the fabrication of photonic crystals from 1D to 3D via facile methods and applications in the fields of sensing and

display. This chapter is structured as follows. This section serves as an introduction to the basics and aims. Section 5.2 is devoted to fabrication techniques, reviewing some simple methods for the preparation of 1D–3D photonic crystals which mainly based on colloidal chemistry. Section 5.3 is focused on reviewing some applications of the prepared photonic crystals in the fields of display and sensing. In the final, we will give a summary and perspective of the developing direction of the field of photonic crystals, including fabrication techniques developing and broadening of the application fields in near future.

5.2 Photonic Crystals Simply Fabricated

5.2.1 *One-Dimensional Photonic Crystals (1DPC) Prepared by Spin-Coating*

Unlike three-dimensional photonic crystals or two-dimensional hexagonal close-packed monolayers, 1DPC cannot be obtained by self-assembly. Instead, spin-coating, dip coating and layer-by-layer deposition [22] are the most common measures to prepare it: a periodic multilayers with copies of bilayers of two different materials. Owing to its periodic modulation of the refractive index of high (n_H) and low (n_L) refractive indices, it can exhibit changeable optical properties [29–35]. The 1DPC Bragg peak position and its stop-band width can be calculated with the help of following equations [36, 37]:

$$\mathbf{m}\lambda_{\mathbf{Bragg}} = 2\sqrt{n_{eff}^2 - \sin^2\theta}$$

$$\mathbf{n}_{\mathbf{eff}}^2 = \mathbf{n}_1^2\mathbf{f}_1 + \mathbf{n}_2^2\mathbf{f}_2$$

$$\mathbf{w} = \frac{4}{\mathbf{\Pi}}\lambda_{\mathbf{Bragg}}\left|\frac{\mathbf{n}_2 - \mathbf{n}_1}{\mathbf{n}_2 + \mathbf{n}_1}\right|$$

where m is the diffraction order, D is the period, λ_{Bragg} is the position of Bragg peak, θ is the incident angle, n_{eff} is the effective refractive index, W is the stop bandwidth, and n_1, f_1, n_2 and f_2 are the refractive indexes and volume fractions of the two different layers. Then 1DPCs with different optical properties can be achieved via regulating the period, the layer number, the refractive index, and the incident angle of light. Based on that, the relative applications such as display devices, sensors, and responsive hydrogels can be obtained by simply modulating the parameters mentioned above.

In this section, we emphasize on the 1DPCs fabricated by the simplest spin coating method and applications on account of its bilayer category: both organic layer pack, both inorganic layer pack and hybrid type (organic/inorganic pack).

5.2.1.1 Alternate Organic Layer Packs

The optical property of organic materials is relatively easy to modulate compared with inorganic material. The organic layer's internal bonding or conformation transmission can be controlled by external conditions, such as, temperature, pH, stress, and light. Consequently, the 1DPC's optical properties can be tuned. Thomas et al. obtained photonic crystals spanning the visible spectrum, which can be easily fabricated from a ternary blend of a diblock copolymer and two homopolymers [38]. Bunning and his coworkers incorporated azobenzene liquid crystal into the periodically distributed polymer's porous layer [39]. Due to the liquid crystal responses to the UV light, experiencing a nematic-isotropic transition, the index contrast between the layers of the structure will reduce, changing the diffraction efficiency. The reverse conversion can be induced by the visible light. By applying the electric field, the Bragg grating can be switched "off". Gong et al. fabricated a 1DPC hydrogel which can be responsive to temperature, pH and stress simultaneously, based on the hydrogen bonding situation (association or disassociation) between the poly(acrylamide) (PAAm) and poly(acrylic acid) (PAAc) in the soft layer [40]. The tough layer poly(dodecylglyceryl itaconate) (PDGI) confers the material robust mechanical strength. Recently, Liu et al. used flexible polyethylene terephthalate (PET) as substrate, two layers of PET embed helical structure liquid crystal imprinted polymer in the middle. Stretching can convert the reflection color [41]. This technique can potentially be applied as flexible displays. By spin-coating poly(methyl methacrylate) (PMMA) and poly(*N*-isopropyl acrylamide)-co-(glycidyl methacrylate) (PNIPAM-co-PGMA) in turn, combined with photolithography method as shown in Fig. 5.2, Yang et al. obtained the photonic paper [42]. Prewritten by UV light crosslinking, the paper can be read with water as ink. The paper's color can be conveniently modulated by cross-linking degree and the temperature of "ink" water.

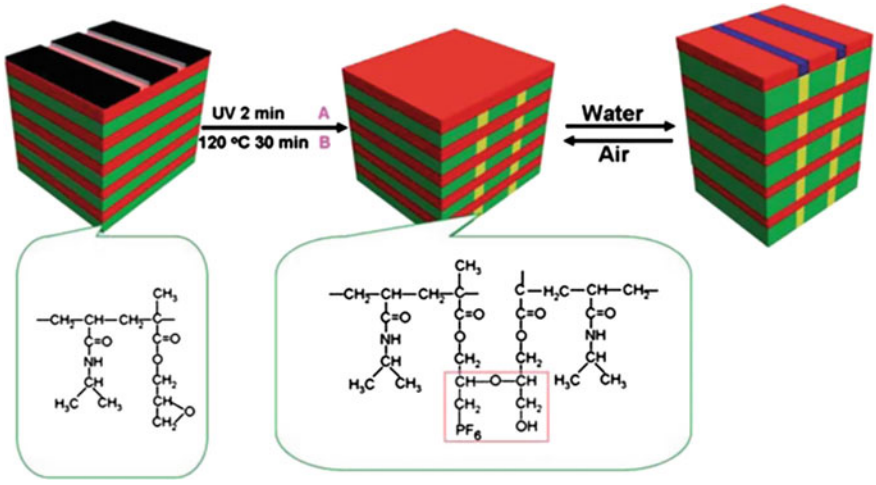

Fig. 5.2 Fabrication process of the photonic paper [42]

5.2.1.2 Periodical Inorganic Layer Packs

Relying on the porous structure and the stable existence of inorganic material, thickness and refractive index of the layer can be operated in order to change its color. Many research works have been reported which successfully fabricated inorganic-layer packed 1DPCs [43–46]. Ozin et al. tailored the 1DPC's layer property in order to considering the specific functionality and sensitivity [43]. As shown in Fig. 5.3, the optical property of the typical SiO_2–TiO_2 1DPC can be easily regulated via changing the physical thickness and refractive index of the inorganic layer.

Derived from the sol-gel and silicon-based Bragg stacks prototype, metal oxide nanoparticle-based Bragg stacks, clay Bragg stacks and zeolite Bragg stacks are also elaborated based on the goal of introduction of dynamically and statically tunable structural color. Earlier, Ozin et al. did some research on clay-based 1DPC, aiming at fabricating an optical sensor [44]. Due to the intercalation and ion exchange, the layer thickness will change, resulting in color change; Míguez et al. used sol-gel method and coating technique to prepare thin, porous TiO_2 defect layer doped dense SiO_2–TiO_2 multilayers [45]. The defect layer confers the structure definite dip in the reflectance spectrum, which ensures great sensitivity when the pore absorbs or condenses vapor. In addition, they also did some thorough research exploring the effect of spin coating protocol during the process of fabricating a nanoparticle-based 1DPC structure [47]. Wei and his coworkers deposited layered double hydroxides (LDH), layered anionic clays generally expressed by the formula

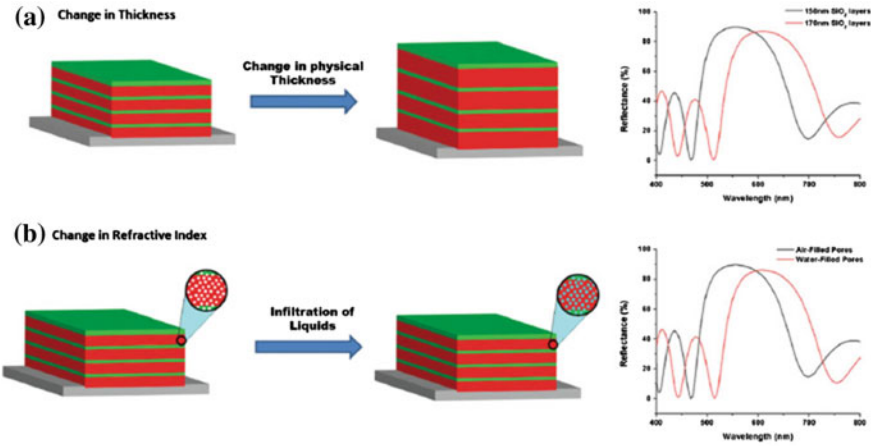

Fig. 5.3 Scheme shows different facets of optical tuning of Bragg stacks. **a** Effect of physical thickness tuning for a four-bilayered SiO_2/TiO_2 Bragg stack (40 % porosity). The thickness of the TiO_2 is kept at 50 nm and SiO_2 is varied from 150 to 170 nm in the simulations. **b** Four-bilayer Bragg stack made up of 150 nm SiO_2 and 50 nm TiO_2 layers. The composition of each layer is varied from 60 % material 40 % air to 60 % material 40 % water, simulating the effect of water infiltration in the pores [43]

$[M^{2+}_{1-x}M^{3+}_{x}(OH)_2](A^{n-})_{x/n}\cdot mH_2O$, where M^{2+} and M^{3+} are metal cations and A^{n-} is a charge-compensating anion, which can experience a reversible structural change between the mixed metal oxide and the LDH phase upon calcination and rehydration, and TiO_2 alternately to fabricate a reversibly responsive 1DPC, by altering the layer thickness, it can exhibit whole visible light range color [48]. As the structure undergoes a reversible phase transformation during the calcination-rehydration cycle, it can tune the layer double hydroxide refractive index. Subsequently, the stop band can reversibly shift. Inorganic matrix based 1DPC can also be coupled to the working electrode of solar cell to make an increase in both the photocurrent and the cell photovoltage, resulting from the enlarged pore size and the structural modulation [49].

5.2.1.3 Organic-Inorganic Hybrid Packs

Though inorganic material are stable and porous, its layer thickness is quite difficult to modulate. On the other hand, the refractive index difference of organic components is small, which need to prepare many layers to achieve an obvious stop band, and it is inconvenient to prepare while the responsiveness is also greatly affected. Then researchers turned their interests to the organic-inorganic hybrid type 1DPC. Many research works have been reported about the 1DPC composed of organic-inorganic hybrid packs. Recently, Ge and coworkers made a progress on the basis of their prework [50, 51]. They improved the titania/graphene oxide (TiO_2/GO) pH responsiveness by embedding the poly (ethylene glycol) (PEG) cross-linked poly [(methyl vinyl ether)-co-maleic acid] (PMVE-co-MA) hydrogel into the 1DPC. The hydrogel tends to be more sensitive to the environment, compared with TiO_2 and GO, whose layer thickness are rather hard to modulate. Therefore the hydrogel incorporation leads to a faster and increased response. Inspired by the surface structure of jewel beetle elytra, Yabu et al. prepared Os and poly(1,2-butadiene) (PB) periodically, the film prepared exhibit visible color and the color can be tuned by immersing in organic solvent [52]. Ge et al. used porous polyaniline (PANI) as the low refractive index layer. The refractive index can be altered during the vapor adsorption resulting from the conducting polymer's doping-dedoping process. Subsequently, there will be a color response of the 1DPC, a visible read-out [53]. Yang et al. reported much work focusing on hybrid type 1DPC's fabrication and their related application these years [54–58]. They fabricated the 1DPC by alternately spin-coating titania and PHEMA-co-PGMA [poly(2-hydroxyethyl methacrylate-co-glycidyl methacrylate)], [54] which can exhibit color from blue to red, covering the whole visible light spectrum. The 1DPC achieved can be color tunable by modulating the period, incidence angle and layer thickness. Since the polymer is hydrophilic, it shows water-vapor response sensitively with distinct color change spanning the whole visible scope as shown in Fig. 5.4.

The spin-coating method is simple and cost-efficient, which confers its great potential for humid sensor. Instead of alternately spin-coating or depositing organic

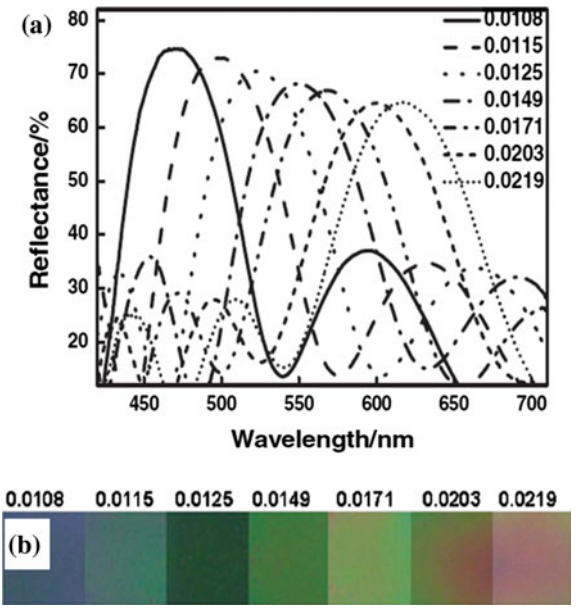

Fig. 5.4 **a** Sensitivity of the 1DPCs towards water vapor; **b** color variation of the 1DPCs with water-vapor concentration [54]

and inorganic material, Ozin's [59] group took advantage of the inorganic 1DPC, infiltrating it with organic material, and they found 1DPC's great application in lasing. Owing to the mesoporous structure of SiO_2/TiO_2 1DPC, it can be infiltrated functional emitting polymers (PPV), whose optical properties can be operated facilely.

On the whole, 1DPC can be facilely fabricated through simply alternately spin-coating. Organic component can be utilized to tune the optical property. Inorganic component, owing for its porous and stable structure and relatively high refractive index, can be used to stabilize the structure and reduce the total layer number required to fabricate a high-performance 1DPC.

5.2.2 *Two-Dimensional Photonic Crystals (2DPC) Evolved by Colloidal Chemistry*

2DPC are didn't appear as early as the one-dimensional and three-dimensional photonic crystals. It is because that two-dimensional structures are greatly limited by the factor of light confinement, which requires the structures be either large enough compared to the incident beam spot-size [60], or the beam confined in the third dimension with the assistant of traditional heterostructure slab waveguide [61]. Though it is difficult to realize two-dimensional photonic crystals, great effort has also been made to fabricate two-dimensional photonic crystals and investigate their

properties. It is due to their easily controlled fabrication process, potential applications for future planar photonic integrated devices and lab on chips for chemical and biological sensing.

During the last decades, many micro- and nano-fabrication techniques have been proposed to fabricate two-dimensional photonic crystals. Among those techniques, imprinting lithography and electron-beam lithography are the most widely used methods. Because the ordering and the sizes of the structures can be finely controlled which ensures the reproducibility of the fabrication process [62–65]. Awschalom and coworkers prepared silicon carbide photonic crystal cavities with integrated color centers via the electron-beam lithography method. The high quality factor (Q) to mode volume ratios of the achieved photonic crystal cavities in 3C SiC films is similar to those achieved in diamond [66]. Osada and cooperators prepared a tunable photonic crystal with gold nanopatterns on hydrogels by electron-beam lithography. The fabricated photonic crystal produces brilliant iridescent colors and the spectra were modulated by varying the salt concentration [67]. Allsopp and coworkers fabricated taper arrays of core-shell and quantum disc InGaN/GaN nanorod with the GaN epitaxial from the nickel nano-dots patterns prepared by the nano-imprinting lithography method. The tapered nanorods with a positive sidewall angle display more conventional Bragg diffractive behavior. And the prepared structure resulted in significant increase in light extraction efficiency when it was combined with light emitting diodes (LEDs) [68]. Although these techniques are widely accepted, but are not as commonly used as imagined since they require complicated apparatus, the fabrication processes are time-consuming, and expensive. Under this background, the techniques evolved by colloidal chemistry which can be divided into two groups: colloidal lithography and colloidal self assembly have become the alternatives. They possess the following advantages compared with the other methods mentioned above: the colloidal crystals used as masks and assembly units during the etching and assembly processes can easily obtained, the diameter and composition can be finely regulated. Thus the structure parameters, such as period, can be finely regulated via modulating the diameter of the colloidal particles, and nanostructures with specific symmetry can be fabricated as well [69–74]. Therefore colloidal lithography and colloidal self assembly are considered as comprehensive, low-consumption, and high throughput method for the fabrication of two dimensional photonic crystals. In the following, we will give a brief reviewing of the two dimensional photonic crystals fabricated via colloidal lithography and colloidal self assembly during recent years.

5.2.2.1 Colloidal Lithography

Colloidal lithography is a powerful chemical patterning method with the advantages of low cost, high throughput, and ease of adoption on various planar and curved surfaces. Different with traditional mask-assisted lithography methods, in which the preparation of the mask usually remains a challenge to scaling down the feature size

and diversifying the feature shape, colloidal lithography employ a facile method for mask-assembly of monodispersed microspheres on target substrate. The feature size can be finely controlled via regulating the diameter of the microspheres, while the shape can be easily modulated by the crystalline structure of the colloidal mask, the time of anisotropic etching of the mask and the incidence angle of the vapor beam [75]. Thus, this method has been introduced to the process of fabricating two-dimensional photonic crystals.

López and coworkers fabricated two-dimensional photonic crystal via etching the close-packed polystyrene microspheres into none-close-packed one using gold film as substrate (Fig. 5.5a) [76]. The optical response of this structure is tuned by homogeneously reducing each sphere, meanwhile keeping the lattice parameter constant. Thus it forms an effective refractive index of the dielectric region over the gold film, and the spheres' volume fraction is reduced as changing the filling fraction of the hexagonal lattice. It is demonstrated that a small reduction of the filling fraction of the lattice produces large spectral blue-shifts (Fig. 5.5b), as well as the variations on the spatial distribution of total field intensity. Soon later, Jeon and cooperators reported a 2DPC band-edge laser that was fabricated in an InGaAsP multiple-quantum-well structure by colloidal lithography. They use a self-assembled nanosphere monolayer with a hexagonal lattice as mask to fabricate a 2DPC composed of circular air holes. A clear laser emission at around 1550 nm

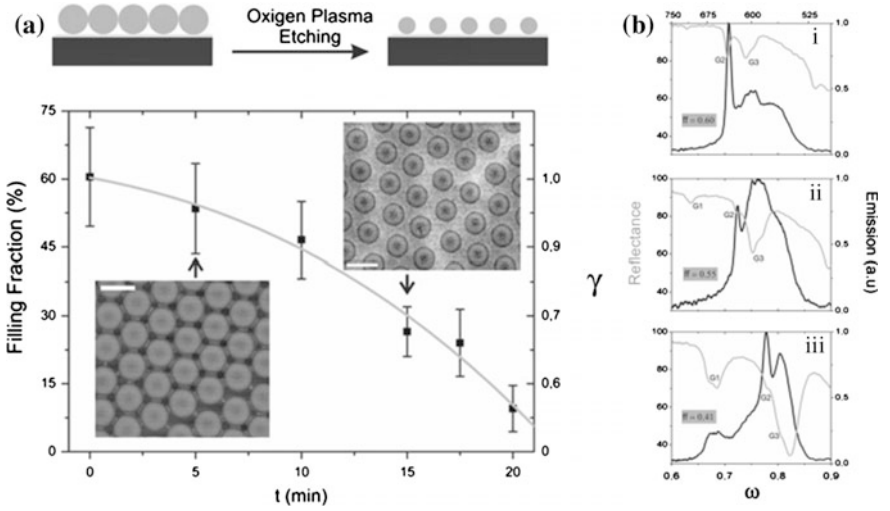

Fig. 5.5 **a** Plasma-etching reduction of initial diameter (Φ_0) = 1 μm PS spheres over a 20 min period. *Insets* show SEM images for the same sample at two different etching times: 5 (*bottom*) and 15 (*top*) min. *Scale bars* correspond to 1 μm in both images. γ stands for the ratio between the final diameter (Φ_f) and the original Φ_0 one. The *grey line* fits to a third degree polynomial. **b** Normal incidence reflectance (*grey*) and emission (*black*) spectra for ϕ = 520 nm dye-doped spheres at three different filling fractions corresponding to γ = 1 (a), γ = 0.97 (b), and γ = 0.88 (c) [76]

was observed under a pulsed optical pumping. From the calculated band structure and polarization dependence measurement, the lasing is confirmed to occur at the M1-point band-edge mode [77].

Besides the works mentioned above, Yang's group also did some meaningful works to fabricate 2DPC based on colloidal lithography, which promoted the utilization of the colloidal lithography method in preparing 2DPC. With the help of colloidal lithography, a two-dimensional bioinspired silica nanocone array was achieved [78]. Firstly, close packed polystyrene microspheres monolayer was assembled on silica substrate. Then the reactive ion etching process was carried out to etch off the PS and the substrate. During this process, with the diameter of the PS decreasing, the exposed substrate was etched at the same time. Due to the etching rate of silica is slower than PS, the silica nanocone arrays were obtained when the PS was etched off clearly (Fig. 5.6a, b). This bioinspired two-dimensional PC dramatically suppresses reflection over a large range of wavelengths and a large field of view and performs highly antireflective property. By using a similar method, silicon nanopost photonic crystal was achieved (Fig. 5.6c, d), and the optical property of this structure can be regulated. The colors can be tuned from green to red via grafting a layer of PHEMA with different thickness. Besides, due to

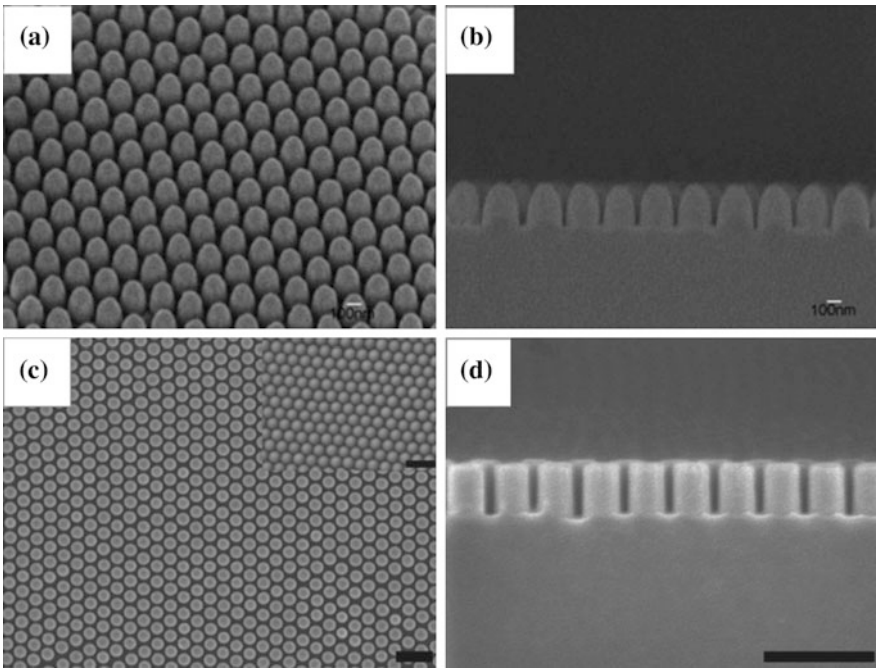

Fig. 5.6 Tilt view SEM image (**a**), cross-sectional view SEM image (**b**) of the nanocone arrays [78]; and the top-view (**c**) and cross-sectional (**d**) SEM images of the silicon nanopost arrays prepared by colloidal lithography. *Inset* of (**c**) shows SEM images of the 2D PS colloidal crystals used as masks in the colloidal lithography process. *Scale bars* in (**c**) and (**d**) are 500 nm [79]

the hydrophilic properties of the PHEMA and the durable nature of the composite nanopost arrays, such arrays can be used as highly stable and reproducible sensors to rapidly detect water vapor [79].

When combined the colloidal lithography with vapor deposition, two-dimensional metal structures with the dielectric constants periodically changed can be fabricated. In this respect, Yang group prepared elliptical hemisphere arrays [80], silver nanohole arrays (Fig. 5.7a–c) [81], nanovolcano arrays (Fig. 5.7d) [82], hollow nanocone arrays [83], asymmetric half-cone/nanohole arrays [84], with modulating the feature structure parameter of the two-dimensional structures, such as period, height, thickness of the metal film, distance between adjacent structures, and so on. The optical properties of this feature structures can be well regulated with the structural color changed from red to green as shown in Fig. 5.7 which can be used as full color display.

As an advanced technique, by using colloidal lithography one can prepare large area two dimensional structure with the dielectric region changed periodically with low cost and without the auxiliary of expensive equipments. At the same time, the colloidal crystals can be easily prepared; the feature size of the structures can be simply regulated by changing the colloidal particle diameter, which can be as small as tens of nanometers. The feature size can also be modulated by adjusting the experimental parameters such as the pre-annealing of the colloidal crystals or slope vapor deposition to change the structure's feature size. The same as other techniques, colloidal lithography has its own drawbacks. The mask used in this technique is colloidal spheres which limited the pattern's symmetry, and the defects can't be avoided during the assembling process of the microspheres. In general, colloidal lithography provides a new method to fabricate two-dimensional photonic crystals and injects a new vitality for the development of the techniques.

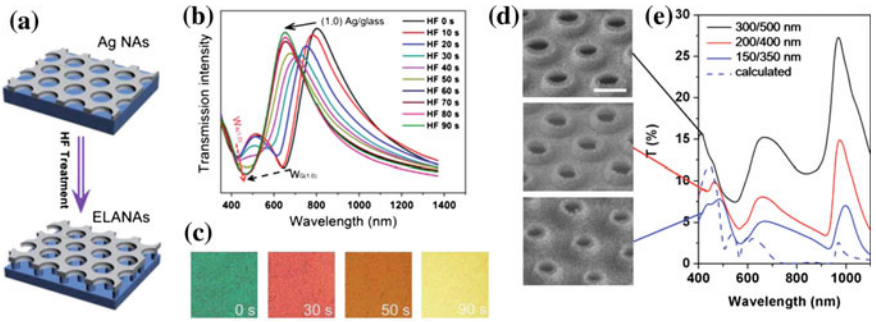

Fig. 5.7 **a** A schematic illustration of the etching process from Ag NAs on the glass substrate to ELANAs. **b** Transmission spectrum evolution for Ag NAs upon different etching durations in dilute HF solution. **c** Apparent color changing at various etching durations [81]. And **d** SEM images and **e** transmission spectra of the Ag nanovolcano arrays with heights of 200 nm and different hole diameters of 300/500, 200/400 and 150/350 nm. The *dotted line* is the calculated spectrum of the one with hole diameters of 150/350 nm. The SEM image is taken from the 45° tilting views. The *scale bar* corresponds to 500 nm and applies to all the SEM images [82]

5.2.2.2 Colloidal Self Assembly

2DPC comprised of ordering arrangements of monodispersed colloidal particles have been studied extensively over the past decade. Because their have potential applications as sensing, optical, and photonic bandgap materials as well as templates for fabrication of highly ordered macroporous materials and biopatterns [85]. Recently, colloidal self assembly has attracted renewed interest because they provide a simple, fast and cheap approach to create 2DPC as the colloid affords period, spatial variations in dielectric properties on the submicrometer length scale. Bragg diffraction of light within these colloidal crystals gives rise to a stop-band, in which the propagation of light within a narrow range of wavelengths in specific directions is prohibited. And the period and the dielectric constant can be easily modulated via regulating the diameter and composition of the colloidal microspheres used as assembly units.

Park and coworkers prepared binary colloidal crystals with two-dimensional superlattices. They achieved this structure by the confined convective assembly of colloidal spheres with different diameters, and they could finely modulate the structure by regulating the size ratio and concentrations of the large and small spheres (Fig. 5.8) [86].

Combined with deformable soft lithography, Yang group developed a simple and versatile lift-up and transfer-printing method. Using this method, they could manipulate the lattice structure and the lattice spacing of two-dimensional non-close packed (ncp) colloidal crystal arrays in a controlled fashion. In brief, PDMS

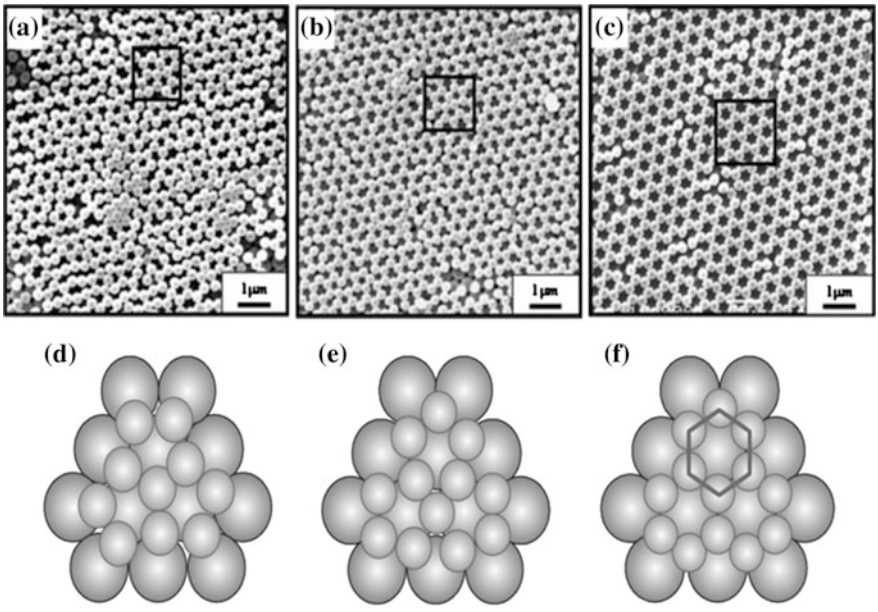

Fig. 5.8 SEM surface images of small PS colloidal particles deposited on the template (**a**–**c**), and schematic illustrations of the crystal lattices (**d**–**f**). The small particles are 300 nm (**a**, **d**), 280 nm (**b**, **e**), and 260 nm (**c**, **f**) [86]

elastomer stamp was wetted by ethanol and then applied to lift up 2D self-assembled close-packed colloidal crystal arrays. After the evaporation of the ethanol, the sample was heated at 100 °C for 3 h, then the stamp was carefully peeled away, and a single layer of 2D colloidal crystals was transferred onto the surface of PDMS. After that, the PDMS stamp containing the silica microspheres was swollen with toluene solution, or stretched along one direction, and the deformed PDMS stamp was brought into contact with the PVA-coated substrate under a pressure about 0.2×10^5 Pa. After that, the system was heated at 100 °C for 1.5 h. After peeling away the PDMS stamp carefully, 2D ncp silicon microsphere arrays were achieved on the PVA-surface. After sintering at 400 °C for 2 h, the PVA film disappeared and the silicon microspheres with adjusted lattice structures fell on the substrate. Taking advantage of this method, the lattice feature could be changed step by step. Combining circular lift-up process and modified soft lithography technique, two-dimensional none close packed colloidal crystal with Bravais lattice structures and controllable lattice features could be obtained as well as new types of patterned colloidal crystals (Fig. 5.9) [85, 87, 88].

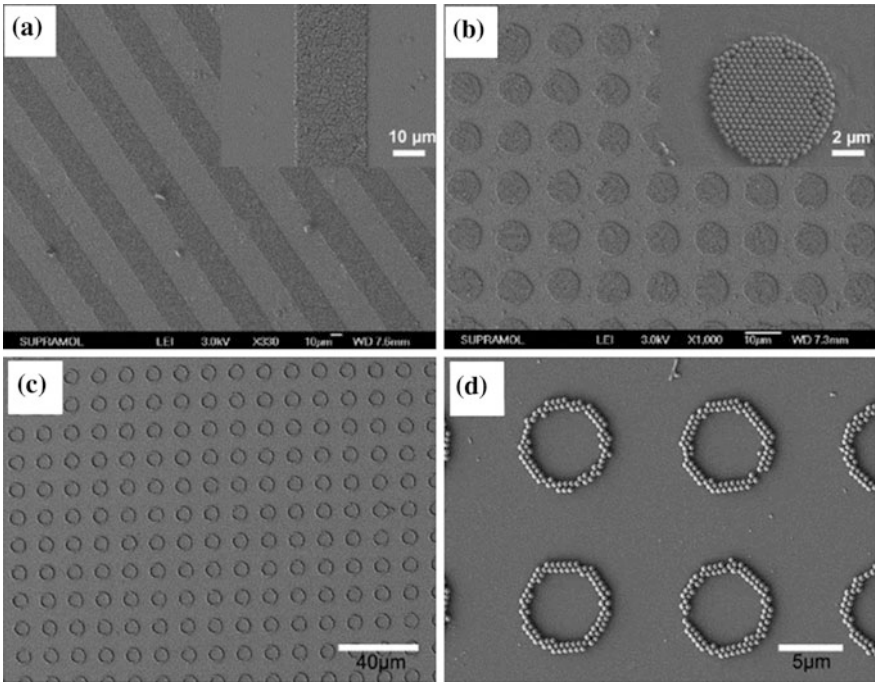

Fig. 5.9 Top-view and inset magnified top-view SEM images of patterned 2D ordered arrays of colloidal crystals. **a** The width of the stripe is 20 μm, the distance between the stripes is 20 μm, the PSS sphere (diameter is 410 nm); **b** The diameter of the circle is 10 μm, the distance of the circle to the center of the circle is 14 μm, the PSS sphere (diameter is 410 nm) [87]; and **c** 2D microsphere hexagon array in large area; **d** High resolution image of hexagon array with double-microsphere width [85]

Besides the works mentioned above, many works have been done to fabricate two-dimensional photonic crystals via the colloidal self assembly in these years [89–91]. Gu and coworkers reported novel 2DPC with the desired feature of either anisotropic angle independence or full angle independence by using colloidal crystal fibers and colloidal crystal beads as their elements [92]. The photonic crystal films composed of colloidal crystal fibers could show anisotropic angle independence. Because the colloidal crystal fibers can show identical reflective color around the center axis, and angle dependent colors along the axis while the photonic crystals derived from the replication of colloidal crystal beads arrays could display identical structural colors. When viewed at different angles, the color caused by colloidal crystal beads can show identical photonic responses independent of the rotation of the axes. And they demonstrated that the prepared photonic crystal film materials can be used as photonic papers with vivid colors, wide viewing angles, rewritable surfaces, and flexibility (Fig. 5.10).

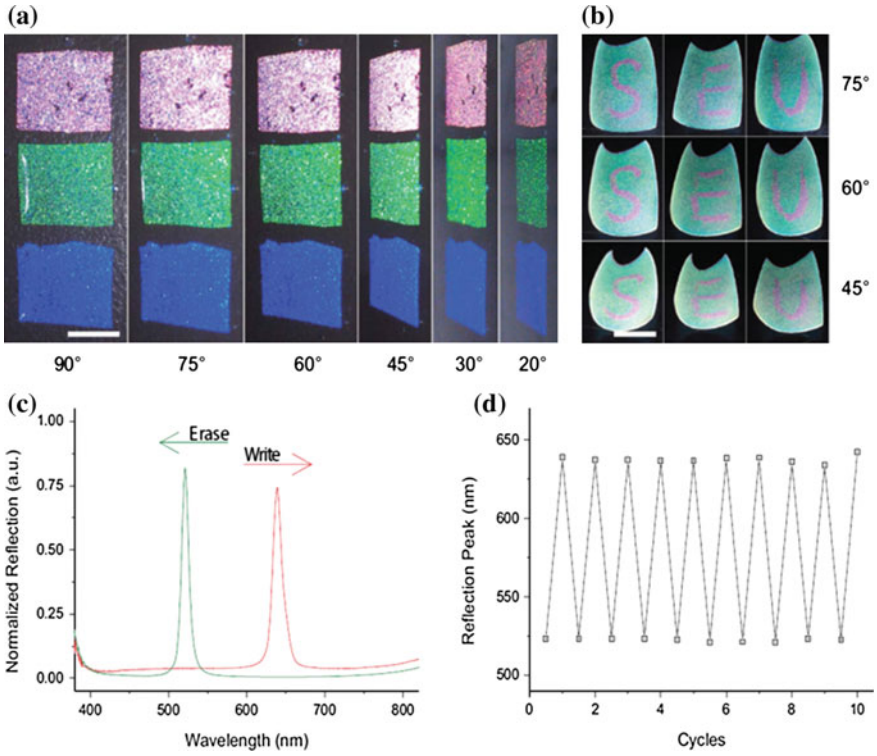

Fig. 5.10 Writing and erasing test of the photonic papers: **a** photographs of three photonic papers viewed at different angles; **b** a *green* photonic paper with *ink marks* of "*S*", "*E*", and "*U*"; **c** reflection spectra of the original photonic paper and the ink mark; **d** the reflection peaks over several write–erase cycles [92]

Reinhard and cooperators demonstrated the template-guided self-assembly strategies for photonic crystal fabrication. And they prepared hybrid arrays that contain TiO_2 nanoparticles and clusters of electromagnetically strongly coupled Au nanoparticles at pre-defined lattice sites. These hetero-nanoparticles arrays sustain simultaneous electromagnetic interactions on multiple length scales [93]. The few nanometer gap separations within the Au nanoparticle clusters give rise to strong direct near-field coupling, whereas the TiO_2 nanoparticles and nanoparticle clusters with separations of a few hundreds of nanometers are diffractively coupled. In addition, Chen and coworkers used well-defined dendrimers to construct zero dimension and two dimension reactors, which facilitate the fabrication of photonic crystals with high-uptake nanocrystals. Meanwhile, the resulting nanocrystal-latex hybrids can directly self-assemble into large-scale ordered colloidal arrays, providing high-quality photonic crystals with uniform fluorescence [94].

In general, colloidal self assembly provides a facile method to fabricate two-dimensional photonic crystals, as the optical properties can be finely controlled by regulating the assembly process. In the future, this technique will still be one of the main techniques to fabricate 2DPC, and it should be extended to prepare multiplexed two-dimensional crystals with the composition and size diversified, less defects and finely regulated feature lattices.

5.2.3 Three-Dimensional Photonic Crystals (3DPC) Fabricated via the Assembly of Colloidal Crystal and Other Facile Methods

Three-dimensional photonic crystal (3DPC) exhibits band-gap as 2DPC and 1DPC, but it possesses many more advantages since it is periodic in three dimensions: the three-dimensional periodic change of the refractive index combining with the crystalline order confers the 3DPC common applications such as optical sensors and waveguides; large surface area of 3DPC produce huge interfaces to be utilized in catalyzing or filtrating contrast with bulk materials of the same volume; ingenious 3D architectures with lattice constants in nature, compared with the simpler 1D or 2D structures, can span the whole visible region, a complete band-gap can only be accessed by 3DPC; 3DPC is able to control light in three dimensions simultaneously. To date, 3DPCs which possess opaline-like or woodpile-like structure occupied the most part of the 3DPC field. The opaline-like structures are always prepared by assembly and post modification of three dimensional colloidal. Because this method can take the advantage of the assembly of colloidal crystal method which is cost-efficiency, and the feature structure can be finely modulated via changing colloids with different diameters and the assembly conditions. But for the woodpile-like structures, they are always fabricated by direct writing techniques. Which ensured the processing speed and the ordering of the three dimensional structure. Thus, in this part, some examples of 3DPC which were

successfully prepared via assembly of colloidal crystal and other facile methods will be presented mainly from three categories: woodpile stacked 3DPC and opal 3DPC, inverse woodpile stacked 3DPC and inverse opal 3DPC, and the other structures of 3DPC like spiral type and diamond lattice type.

5.2.3.1 3DPCs Possess Opal or Woodpile-like Structures

Woodpile Type 3DPCs

Previously, Noda et al. fabricated full 3D photonic band gap crystals with woodpile structure at near infrared wavelength. They also stacked gallium arsenide striped layers to form a woodpile three-dimensional photonic crystal [13, 95]. The active layer Indium-gallium arsenide-phosphide quantum-well layer was integrated in the middle of the 3DPC. They systematically explored the artificial point-defect cavities' effects on 3DPC photonic emission. Erigin et al. achieved a three-dimensional invisibility-cloaking structure at optical wavelength based on a woodpile photonic crystal [96]. Since the beginning of 21st century, reports about woodpile type 3DPC advanced rapidly. Varied shapes of woodpile photonic crystal have been fabricated through different kinds of methods: Si hollow woodpile 3DPC through direct-write assembly [97], 3D metallic photonic crystals fabricated via soft lithography and electrodespositon [98], direct ink writing finely featured shapes [99]. Recently, Wegener and his coworkers reported the titania woodpile photonic crystals with complete photonic band gaps in the visible for the first time. Using double ZnO/TiO_2 inversion, they transferred the original polymer template to a titania structure. Characterized by angle- and polarization resolved spectroscopy, they confirmed the complete band gap's existence [100]. Noda published their work on nature materials in 2009 about the direct creation of woodpile 3DPC by top-down method. They overcame the difficulty of achievement of large-area-3DPC without unintentional defects through a double-angled deep-etching method [101]. Subramania et al. fabricated a logpile photonic crystal and proved that the practical operational frequency range of a silicon based 3DPC can be extended nearly into the visible above the absorption edge of silicon [102]. Farsari achieved the woodpile structure as shown in Fig. 5.11 used sol-gel chemistry, direct laser writing, and electroless plating metallization to build a polymer network and metalize it selectively, which is at the near IR to optical region. And it is the first report of a visible-range bandgap 3D metallic structure [103].

Using a single prism holographic lithography technique, Park et al. achieved high-quality woodpile structure with photonic band gaps in the visible wavelength range. Varying the crosslinking degree in the negative photoresist can obtain multicolor. Owing for the large surface area and the periodic interconnected pores, it also exhibits outstanding fluorescence enhancement [104]. Lately, Watkins and coworkers fabricated patterned Nanoparticle (NP)/Nanoimprint lithography (NIL) resist composites by solvent-assisted UV-NIL using an all-solution-processable strategy [105].

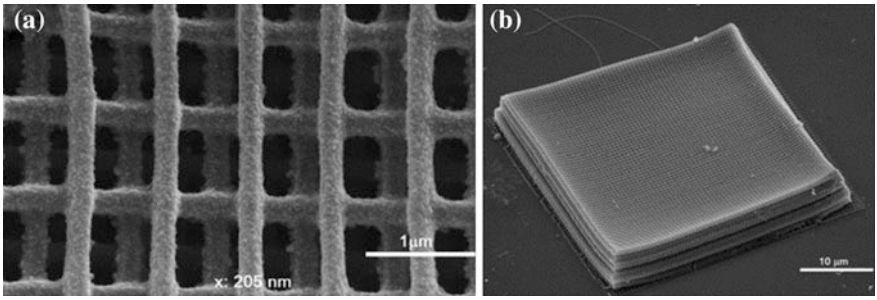

Fig. 5.11 **a** Metalized woodpile structure at 900 nm periodicity. The value at the *bottom left corner* depicts the average thickness of the rods. **b** Perspecitive view of a 600 nm periodicity and 3-unit-cell (12-layer) thickness woodpile structure [103]

Opal Type 3DPC

To date, there has been numerous works reported regarding with regard to opal-based 3DPC [106–115]. Researchers have attempted to fabricate 3DPC in the visible region, incorporate point or planar defects into the self-assembled 3DPC, build metallodielectric photonic crystals, and visualize the stacking faults in the 3DPC. In the recent five years, the 3DPC has tended to be visualized and tunable on one hand. On the other hand, using facile and advanced technology has become the mainstream. Kim et al. prepared colloidal photonic crystals with high optical transparency and rigidity using photocurable colloidal suspensions. The narrow peaks provide high selectivity in optical identification, which is considered to be of great potential for security application [116]. Han et al. enhanced tuning stability of the colloidal photonic crystal composed of long-range ordered crystalline colloidal arrays through modifying the indium tin oxide (ITO) electrode with ion exchange resins. They achieved more than 800 cycles of very reliable, wide-range photonic color switching for the first time [117]. Comparatively, the previous work reported can reach a repeatable stop-band tuning for less times: Ozin et al. utilized EAP-infiltrated photonic crystal oxidation/reduction reaction to achieve 100 times' stop-band switching ranging around 100 nm [118], Kang et al. made it 30 times of switching with stop-band tuning of 75 nm [119], and Li et al. reported for 10 times tuning cycles [120]. Attributed to the ion-exchange layer coating, minimizing the diffusion of the ions which limits the material's repeatability significantly for thinner electrical double layer caused by the ionic impurities in dispersion medium, the tuning repeatability of photonic crystal system in Han's work was highly improved compared with previous work mentioned above. Lin et al. used centrifugation to induce the self-assembly of polystyrene-co-poly(*N*,*N*-dimethyl acrylamide) (PS-co-PDMAA) microsphere to prepare opal structure as shown in Fig. 5.12. The inner region is hydrophobic and hard, which is rich in PS and the

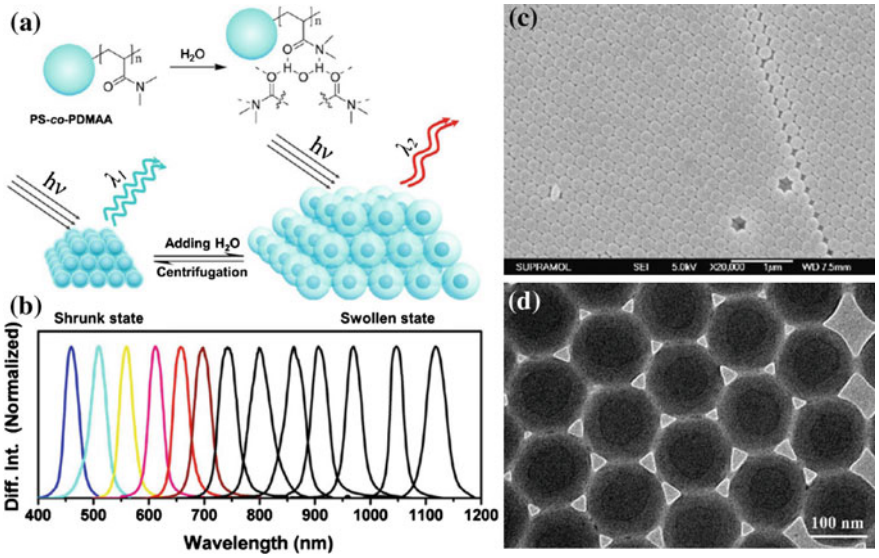

Fig. 5.12 **a** Schematic drawing of the formation of hydrogen bonds between water and the amide side groups of the DMAA repeat units of the surface PDMAA of PS-co-PDMAA microspheres. **b** The water-induced red shift of the diffraction of the centrifugation induced PCCs is related to the swelling behavior of the PS-co-PDMAA PCCs, which exhibit narrow diffraction bandwidth. And the SEM (**c**) and TEM (**d**) images of the PS-*co*-PDMAA microspheres [121]

outer region is hydrophilic and soft, which is rich in PDMAA. The resulting opal hydrogel is water-responsive, which can be read by the color change [121].

Furthermore, due to the interaction between SCN^- and DMAA, blocking the hydrogen bonds between DMAA and water molecules, the hydrogel can be sensitive to SCN^-. Clays patterned colloidal photonic crystal by ultrasonication to remove certain parts of the colloidal photonic crystal from the substrate. The pattern can act as a template to grow the second layer of colloidal photonic crystal, resulting in a dual-patterned hydrogel with both hydrophilic and hydrophobic domains, which can be applied in sensing further [122]. Do et al. used simple method, self-assembly of PS at the interface and layer-by-layer scooping transfer, to fabricate multilayered photonic crystal of wafer scale [123]. Zhao et al. fabricated fiber Bragg grating with stress-responsive colloidal crystals which shows dynamically altering multiple wavelengths for incorporation of multiple colloidal crystal segments, and the relative application can be photonic circuits, laser cavities and biosensors [124]. Yan et al. used facile approach of solvent vapor annealing to build the 3DPC heterostructure. Tuning the density and surface tension of liquid, the immersed multilayer's liquid level can be finely controlled. Annealing the solvent cause the lattice constant contrast between the two parts increase, resulting in a heterostructure 3DPC [125].

5.2.3.2 3D Photonic Crystals Perform Inverse Opal or Inverse Woodpile Structures

Inverse Opal 3DPC

Attributed to the long-range ordering of the submicrometer or nanometer air voids, inverse opal structured 3DPC is considered to be applied in electro- and nonlinear optics, optical and magnetic information processing and storage, catalyst and sensors. In the past 10 years, much work reported about inverse opal 3DPC [126–137]. Omenetto reported 3DPC composed of entirely nature material, silk fibroin. By pouring the silk solution onto the PMMA opal and subsequent acetone dispose, they removed the PMMA successfully and got a silk inverse opal (SIO) [138]. Afterwards, they attempted many application areas of the SIO obtained. Firstly, they used it within the tissue to provide a non-endogenous spectral signature, which was successfully achieved, evidenced by the transmission spectrum. Then they applied it in glucose colorimetric sensing. At last they tried to use gold nanoparticle doped SIO to enhance the adsorption. Considering the spectral emissivity of 3D metallic photonic crystals, which is of great use for solar thermophotovoltaics. Braun et al. took opal structure as template and conformal deposited Tungsten using atomic layer deposition (ALD). Template was at last removed by HF. The obtained structure exhibit high temperature stability up to more than 1400 °C modulate thermal emission of otherwise photons lost at increased temperature. They also presented great potential of hafnium diboride (HfB2) for solar thermophotovoltaic (sTPV) application [139]. Zhang et al. fabricated inverse opals by simple methods, combining self-assembly of colloidal crystals and sol-gel method. The achieved structure morphology is shown in Fig. 5.13.

The rutile titania was obtained at a rather mild condition, a calcination temperature of 500 °C. They thoroughly investigated various characteristics between the anatase and rutile type, including pore size, backbone filling fraction, reflection peaks and so on. The highly ordered three dimensional macroporous structures may have application in catalysis and humidity sensing [140]. Aizenberg et al. proved that colloidal self-assembly can be systematically studied and manipulated with rationally designed micrometer-scale topographical substrates to form the expected structure [141]. Retsch et al. fabricated hierarchially structured inverse opals by two step colloidal templating. Sequentially infiltrating and pyrolysing confer the material double periodic pore lattice of SiO_2, Al_2O_3 and TiO_2 [142]. Bartl et al. studied the beetle's 3D photonic structure and found interesting microstructure, including quasi-periodic lattice, opal-like colloidal crystal with non-close-packed lattice and diamond-based architectures. They therefore tended to use these biological structures as templates to fabricate inorganic-matrix (silica) inverse opal photonic crystals of high photo-, heat- and structural stability [143]. Li et al. used conventional colloidal crystal assembly method to form the opal structure and infiltrated it with polysilazane, which show reheology property, resulting in the crack's self-healing trait [144]. Inversed opal 3DPC based on colloidal crystals can also be used in probing photonic effect on photocatalytic degradation of dyes [145].

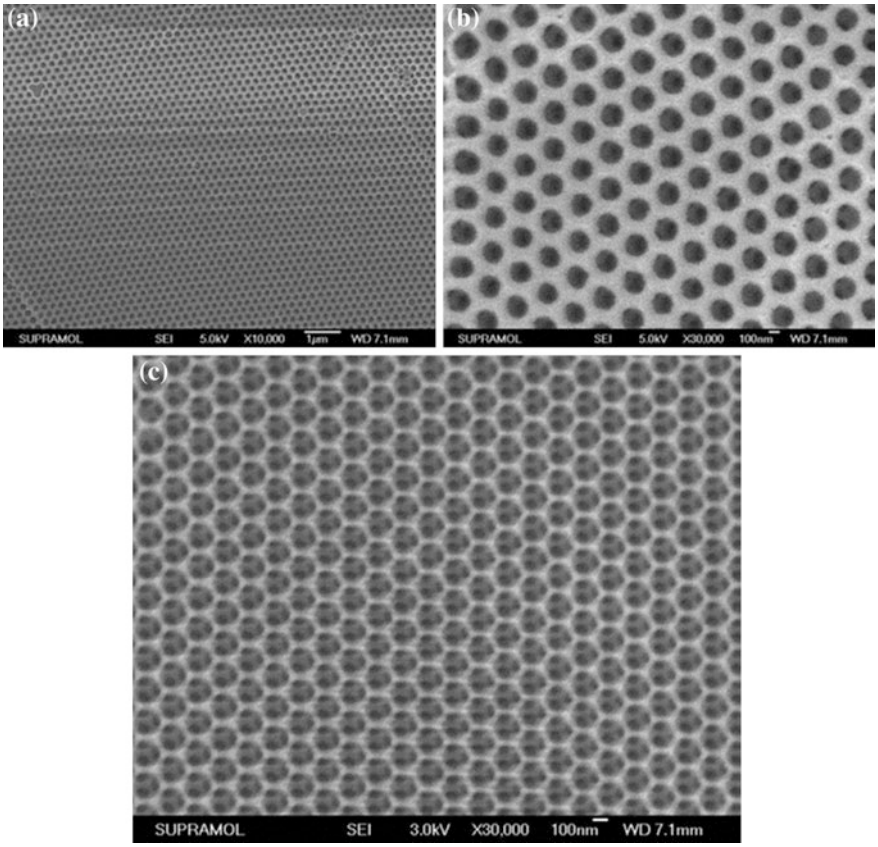

Fig. 5.13 SEM images of inverse rutile TiO_2 opals using **a** P(St-MMA-AA) spheres, **b** PMMA spheres, **c** PS spheres as templates [140]

Inverse Woodpile 3DPC

Inverse woodpile 3DPC has seldom been reported so far. In 2007, Hermatschweiler firstly reported silicon inverse woodpile photonic crystals. Their approach was based on direct laser writing of polymeric templates and a silicon single-inversion procedure. The photonic Bragg grating was predicted to be shifted to telecommunication wavelengths for the progress in direct laser writing [146]. Yang used single prism holographic lithography and electrodeposition to construct 3D inverse woodpile structure of high refractive index, which exhibits a complete PBG in the visible range. The relative application therefore can be solid state lighting and solar energy conversion [147]. By means of complementary metal oxide-semiconductor (CMOS)-compatible methods, Broek achieved 3DPC with a cubic diamond-like symmetry. Worth mentioned, the approach utilized to obtain inverse woodpile

3DPC are tedious and expensive, which may considered to be the main factor that limit its development [148].

In general, with the rapid progress of technology, we witnessed different complex and ingenious design of 3DPC achieved in the recent 5 years. Besides the 3DPC fabricated by colloidal crystal self-assembly, including opal/woodpile and inverse-opal/woodpile type, there are several other different structures of 3DPC achieved by other advanced technologies. Categorized by the shape obtained, we summarize the 3DPC in those works into the following main types: 3DPC derived from 2DPC arrays [149], partially oxidized macroporous silicon membranes with large pore aspect ratio [150], 3D anisotropic mesoscale architectures [151], highly ordered porous 3DPC achieved by holographic lithography [152–155], biomimicking structure containing hierarchical structure or using biomaterials as templates [156–162], gyroid structure using biotemplate, or artificial direct laser writing [163–165], non-sphere building block fabricated 3DPC [166]; chiral 3DPC or bi-chiral 3DPC [167–169] square spiral 3DPC by glancing angle deposition [170]; chirped 3DPC [171] and 3D metamateials [172]. Though those amazing structures are of great importance for the improvement of science and technology, the time and cost to accomplish are not of the counterpart. Facile approaches still needed to achieve different kinds of 3DPC in order to put in the practical application conveniently.

5.3 Applications of Photonic Crystals

5.3.1 Photonic Crystals Used in the Field of Display

The photonic band gap in a material arises from periodic modulations in the refractive index of the material over a length scale that is half the wavelength of the light. Photons having energy within the band gap range cannot pass through the photonic crystals and are reflected. Near the stop band of a PC, light propagates at a reduced group velocity owing to resonant Bragg scattering, which can enhance optical gain leading to stimulated emission [173]. Thus, the use of photonic crystal structure in optoelectronic devices draws much attention, since it provides a novel method of controlling optical modes to improve the light extraction by efficiently coupling guided modes out of devices. Besides, photonic crystals having a band gap in the visible range exhibit sparking interference colors that are useful in colorimetric sensors, full-color displays. So in this part, we will give a review focus on the applications of the photonic crystals in the field of display.

5.3.1.1 Photonic Crystals Integrated in LED to Enhance Light Extraction

In the field of light-emitting diodes (LED), it maintains the objective to enhance light extraction and regulate the directionality of light extraction. Thus utilizing

photonic crystal to modulate the light is considered to be the promising method for LEDs based on coupling theory. It believes that the guided modes within LEDs can be radiated to the air with new wave vectors. The additional lattice vector is provided by the periodically structured surface, which is called diffracted modes [174]. The enhanced light extraction efficiency can be attained via the diffracted modes leaking to the air with specific angles. And photonic crystals have been widely introduced into the LED system in these years. Since it can regulate the parameters which are correlated to maximize extraction efficiency, and then the guided modes in all directions are coupled to the air, which results in the enhancement of light extraction [175–179].

Scarpa and coworkers fabricated a miniaturized photonic sensing platform. It reduced the dimensions of the device and simultaneously the required alignment effort and device complexity. The platform is achieved via integrating 1D photonic crystals with organic light-emitting diodes as shown in Fig. 5.14 [180]. Through converting the color shift of a stimuli-responsive 1D PC into a current signal, the relation between photocurrent and stop-band shift for low concentrations was determined to be 7.4 nA nm^{-1}. It translated into a sensitivity of as small as 27 pm without signal processing at an integration time of 100 ms, and the capabilities of this integrated system performed a response down to 10 ppm ethanol at room temperature.

Yang and cooperators integrated biomimetic antireflective surfaces into OLED devices to increase the light extraction [181]. As shown in Fig. 5.15, silica nanocone arrays were fabricated on the opposite side of the indium-tin-oxide coated fused silica substrate via directly etching the silica. Owing to their broadband and

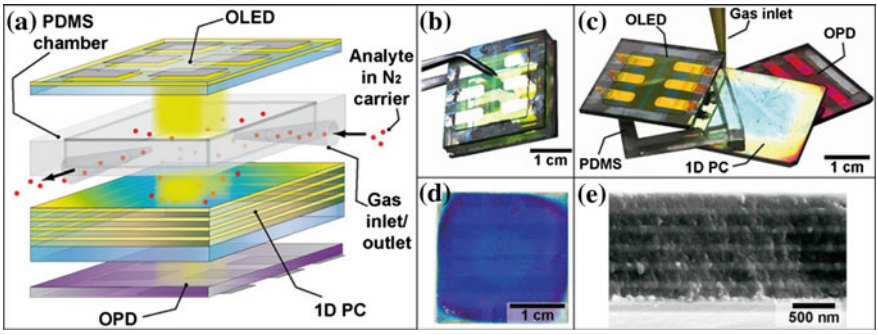

Fig. 5.14 **a** The scheme of the proposed electrophotonic sensor: An OLED emits through the PDMS chamber, which is continuously purged with the analyte of interest mixed with a gas carrier, and through the responsive 1D PC, which is being infiltrated through the top layer with the analyte at various relative pressures. The modulated intensity of light is detected by an OPD, which translates the decrease/increase of the light intensity into a current change. **b** Photograph of the integrated sensing platform shown in Scheme a. **c** Photograph of the individual components of the sensor shown in Scheme 1a. **d** Photograph of the 1D PC deposited on the ITO-coated glass. **e** Cross-sectional SEM image of the 1D PC, composed of 6 nanoparticle-based SiO_2 (*dark layers*)/ TiO_2 (*bright layers*) bilayers [180]

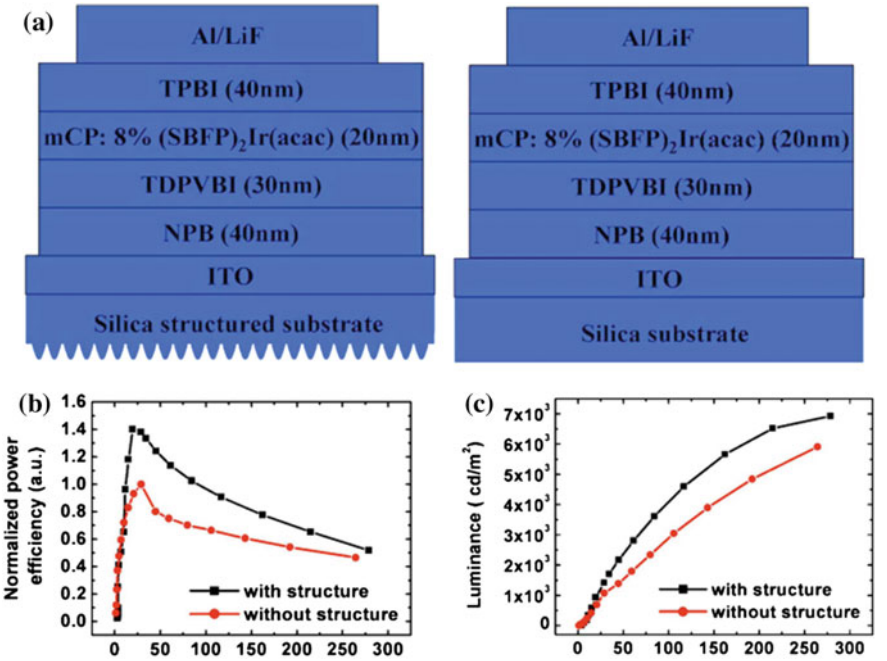

Fig. 5.15 **a** The white OLEDs structures with *left* and without *right* antireflective surfaces; normalized power efficiency (**b**) and output light intensity (**c**) of white OLEDs as a function of current density (Color figure online) [181]

large view of antireflective properties, the antireflective surfaces can dramatically suppress the reflection loss, and increase the transmission of light over a large range of wavelength and a large field of view. The luminance efficiency in the normal direction for the white OLED is increased by about 1.4 times. The enhancement can be very large for the viewing angle above 40°. He and coworkers presented an effective light extraction scheme for GaN-based multi-quantum-well (MQW) light emitting diodes with periodic SiO_2 nano-honeycomb arrays. The SiO_2 nano-honeycomb arrays were fabricated by the combination of natural lithography and reactive ion etching. The nano-honeycombs significantly boost light output by providing additional light extraction channels. These channels not only guiding the internal modes into the air, but also alleviating the sever droop effect at high input power. At the driving current of 400 mA, light output power through the nano-honeycombs is 77.8 % higher than that of the bare device. In addition, the output power is particularly enhanced at the diffraction angle around 651, which is attributed to the intensive first order diffraction on the honeycombs [176]. Besides these works, Park and coworkers successfully fabricated 2D TiO_2 inverse opal with a closed top-surface structure that has a thin flat layer on top. This enhancement is mainly due to diffraction of wave-guided light by the 2D TiO_2 inverse opal acting

as 2D photonic crystals. The light extraction of the polymer LED was enhanced by 92 % without change in the electrical properties after inserting the 2D TiO_2 inverse opal. And this polymer LED possess closed top-surface structure between the glass and the anode electrode compared with conventional devices [182].

5.3.1.2 Two-Dimensional Structures for Antireflective Surfaces (ARS)

Ordered two dimensional micro- or nano-structures widely existing in biological systems since these structures possess anti-reflective property and increase light transmission in dark environment which improves sensitivity of light vision which can help organisms in nature prevent the attack from their natural enemy. These inspired scientists to mimic them for optical applications, which simultaneously suppressing surface reflection and increasing transmission of light is crucial to the performance of an optical system, especially when there are several optical components involved. Based on this practical application prospect, many two dimension microstructures have been fabricated to be used in optical applications via series techniques [183–188].

Yang and coworkers prepared some two dimensional structures on the substrate for the application of antireflection with the help of colloidal lithography. Using polystyrene microspheres as masks on both sides of silica substrate, silica nanocone arrays were achieved via etching off the polystyrene and the exposed substrate at the same time. This double side microstructured surface performs antireflective property. Because this structure dramatically suppress reflection over a large range of wavelengths, and a large field of view and the transmission substantially increases from 330 to 800 nm [78]. After this work, they fabricated bioinspired silicon hollow-tip arrays for high performance broadband anti-reflective. During the fabrication process, introduced metal catalytic wet etching silicon method followed by a short time reactive ion etching process [189]. During this process, silicon hollow-tip arrays with the aspect ratio above 12 can be easily obtained. This specific structure performed antireflective property, since the tip arrays introduce the gradient refractive index, and the pores in the tip arrays can dramatically reduce the effective refractive index of them which results in the suppress of the Fresnel reflection (Fig. 5.16a, b).

Besides the works mentioned above, they also reported the surfaces with high performance near-infrared (NIR) antireflective and improved transmittance which were fabricated via colloidal lithography as well [190]. By tuning the reactive ion etching conditions, silica structures with different morphologies, such as post-like profile, truncated cone-shaped profile, paraboloid-like profile and pillar arrays with a cone top profile can be obtained, and the optical properties of the antireflective surfaces can be controlled via the morphologies changing (Fig. 5.16c–h). The double-sided ARS surfaces with paraboloid-like profile exhibits a reflectance below 2.5 % over the spectral range 800–2500 nm, while the planar silica substrate is above 8 %. These surfaces dramatically suppress the reflection over a large range of wavelength. At the same time, the transmittance substantially increases from 800 to

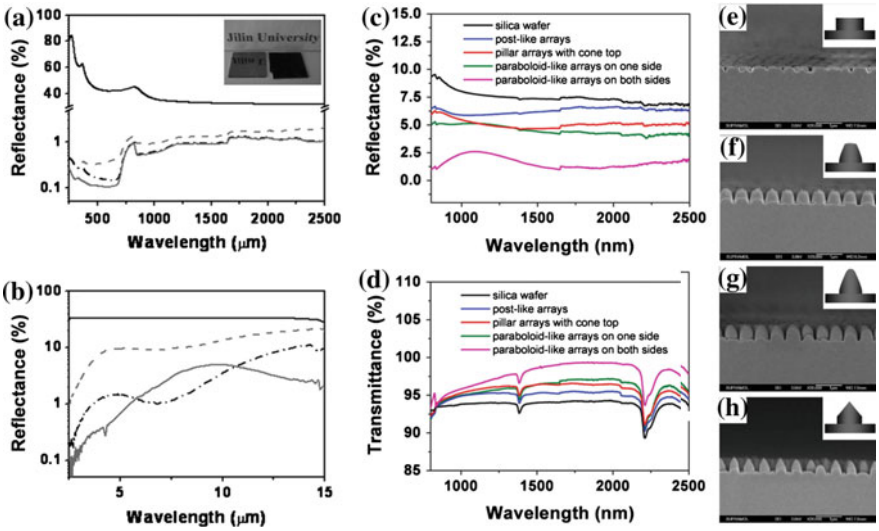

Fig. 5.16 **a–b** High performance broadband anti-reflective properties of silicon hollow-tip arrays. **c–d** High performance antireflective properties of the silica ARS arrays. **e–h** Morphology of silica ARS arrays by etching 4 min (**e**), 11 min (**f**), 23 min (**g**), and 40 min (**h**). All the *scale bars* are 1 μm. The *insets* are the schematic illustrations of different ARS [78, 190]

2500 nm. Because of the time efficient and reproducible fabricating process, these antireflective surfaces are promising for many applications, such as NIR high-power lasers, optical lenses, NIR spectrum, NIR shielding field, and night vision system.

5.3.1.3 Photonic Crystals Used for Fluorescence Enhancement

Besides the applications as mentioned above, photonic crystals are also used for fluorescence enhancement, the photonic crystal provides an efficient optical resonator [191–194]. Furthermore, PC supports leaky eigenmodes to which higher diffracted orders can couple through phase matching. These leaky eigenmodes are highly localized within and in direct proximity to the PC surface. Thus a large energy density is obtained which in the form of enhanced electromagnetic fields throughout the structure. So an enhanced fluorescence excitation is obtained when the fluorophore is close to the device surface, which is caused by an enhanced electric field at the locations of the leaky eigenmodes. Based on this theory, photonic crystals become a candidate for the enhancement of fluorescence. Cunningham and coworkers prepared photonic crystal by nanoreplica molding technique and used it for fluorescence enhancement. In their experiment, they demonstrated fluorescence enhancement from the fluorescent dye Cyanine-5 (Cy5). The signal-to-noise ratio for fluorescent spots on the photonic crystal is increased by at least 5-fold compared with the glass substrate. It allows a TNF-α

concentration of 1.6 pg/mL to be distinguished from noise on a photonic crystal surface [195]. After this work reported, photonic crystals evolved by colloidal chemistry were paid more attention by researchers and efforts were tried to use them in this field. Song and cooperators prepared 3-D pc on glass substrate and then cover it with a film consists of 1,2-bis(2′-methyl-5′-phenyl-3′-thienyl) perfluorocyclopentene (BP-BTE) (The BP-BTE is introduced as a photochromic switch since it possesses excellent fatigue resistance, thermally irreversible properties, rapid response time, and reactivity in solid state. The coumarin, as an available fluorescent dye, is selected for the detection of fluorescent signal.) to form an optical storage system which performs an amplification of fluorescent contrast (Fig. 5.17a) [196]. With the help of PC, the fluorescence signal is enhanced about 40 folds while the amplification of ON/OFF ratio can reach sevenfold. In addition, the fluorescence on PC integrated surface performs higher brightness and contrast than that on glass (Fig. 5.17b–e). Thus, it provides an alternative system with better sensitivity and resolution in the bistable photo-switching and proposes a simple method to design and develop high-performance optical memory devices. Recently, Marabelli and coworkers demonstrated photoluminescence excitation enhancement in an all-polymer flexible one dimensional photonic crystal structure capped with a fluorescent organic ultrathin film. When optical matching conditions between the excitation beam and the Bloch Surface Wave mode supported by the photonic structure are achieved, a ten times enhancement of the photoluminescence is observed [197]. Cunningham and cooperators incorporated photonic crystal surface into traditional microscope slide to develop a photonic crystal enhanced fluorescence microscopy. It performs as a surface-specific fluorescence imaging technique to study the adhesion of live cells by visualizing variations in cell–substrate gap distance [198]. And this technique allows for the visualization of the profiles of cell nucleus surface and the cell plasma membrane surface in three dimensions in the context of cell adhesion. It provides a novel approach for the investigation of some specific attributes in cellular processes without the need of coupling prisms, spatial pinhole, or special microscope objectives.

5.3.1.4 Full Color Display and Photonic Paper Based on Photonic Crystals

Photonic crystals, possessing nanoscale periodic structures that cause Bragg diffraction to light within specific wavelength and produce charming colors, have attracted many researchers' interests to make this specific structure be used in the field of full color display and photonic paper. However, most of these works are based on three dimensional photonic crystals which possess opal or inverse opal structures. These three dimensional phtotonic crystals are mostly obtained from the self-assembly of colloidal crystals. Thus it is greatly limited by the disadvantage of the fabrication method since it is difficult to prepare homogenous 3D colloidal photonic crystals in large areas [199–202]. Fortunately, during last five years, much more methods have been proposed to fabricate kinds of photonic crystals from one

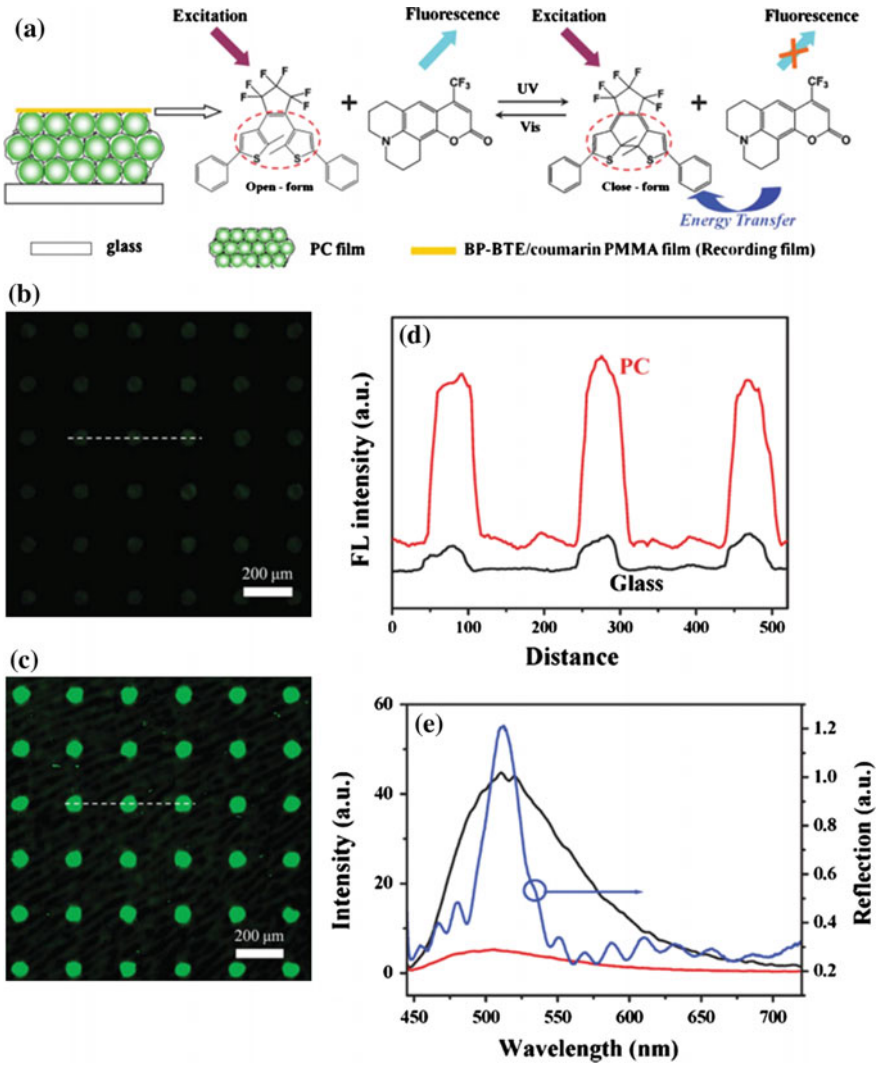

Fig. 5.17 **a** Schematic of the BP-BTE/coumarin-loaded PMMA film on the PC surface. **b**–**c** Fluorescence images generated from irradiation (5 min) at 365 nm of the BP-BTE/coumarin-loaded PMMA film on the glass and matched PC through a *dot-patterned* contact mask. The *light regions* indicate luminescence and the *dark regions* are weakly luminescent. **d** Fluorescence intensity associated line profiles from the glass and PC surfaces. **e** Fluorescence emission spectra of the BP-BTE/coumarin-loaded PMMA film on the glass surface before (*black line*) and after (*red line*) irradiation with UV light and UV–Vis reflection spectra of the matched PC [196]

dimensional to three dimensional, thus 1D and 2D photonic crystal have been successfully introduced into this field, and it also got a great development for the 3D one to be used for full color displays.

Yang and coworkers prepared polymer 1D photonic crystals with finely regulated optical properties. The photonic crystal is achieved via alternating thin films of PMMA and PNIPAM-co-PGMA, after they obtained this 1D photonic crystal. And they processed it as photonic paper by combining with top-down assisted photolithography. The photonic paper was prewritten via ultraviolet light cross-linking by using a photo mask on the top of the multilayered photonic crystal and read with water as ink. The writing and erasing process can be easily reversed through repeatedly exposing of the material to water and air. The color of letters written on the paper can be regulated via modulating the cross-linking density and ink temperature (Fig. 5.18a). Moreover, multicolors can be integrated onto the photonic paper simultaneously by making the degree of cross-linking of different regions of the photonic paper different (Fig. 5.18b) [42].

Besides the work mentioned above, many groups have prepared 1D photonic crystals which can be used for full color display. Such as, Ha and coworkers reported an inorganic glass film with engineered multiple photonic bandgaps through a sol–gel processing approach. Their sol–gel film consists of TiO_2, SiO_2, and mixed SiO_2–TiO_2 films which possess controllable spectral characteristics in the overall visible region. By using this sol–gel film as a resonator, a red–green–blue pixelated liquid-crystal laser was also demonstrated, at the same time, spatially controllable red, green, and blue lasing emissions were acquired in a single lasing device with pixelated cavity and active medium by single-wavelength optical pumping [203]. Recently, Chen et al. prepared mechanochromic elastic photonic hydrogels. They introduced a method which combined a magnetically controlled self-assembly of monodisperse magnetic colloid nanocrystal clusters of carbon-encapsulated Fe_3O_4 and in situ polymerization of acrylamide (AM)- or *N*-vinylcaprolactam (VCL)-based monomers. The film performs different color with the wavelength range of the visible spectrum from 460 to 630 nm through regulating the magnetic strength and

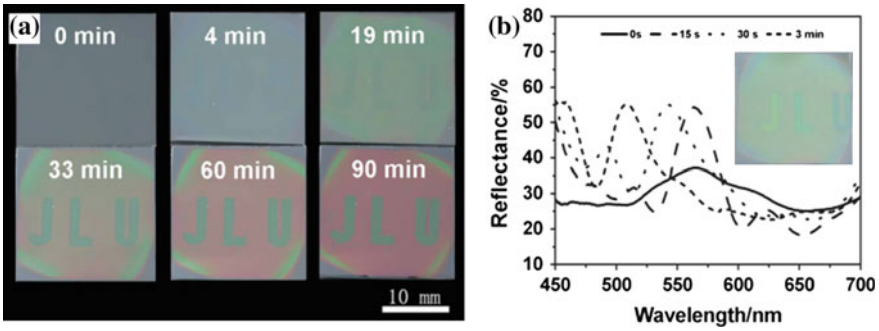

Fig. 5.18 **a** Time evolution of the photonic paper with water as ink. The size of the photograph is about 2 by 2 cm. **b** Reflective spectra and corresponding photograph of the photonic paper with different cross-linking density. The *solid line* corresponds to the substrate, the *dashed line*, *dotted line*, and *short dashed line* correspond to the letters *J*, *L*, and *U* respectively. The letters *J*, *L*, and *U* are lit by UV for 15 s, 30 s, and 3 min, respectively, while the other parts are not lit by UV. The size of the photograph is about 2 by 2 cm [42]

the size of the monodisperse magnetic colloid nanocrystal clusters. This photonic film presents great sensitivity and reversibility towards optical touch sensing, color-based switching, and a mechanically flexible display [204]. Gong et al. reported a mechano-actuated ultrafast full-colour switching bio-inspired 1D photonic hydrogel. The hydrogel consists of thousands of rigid lamellar bilayer domains uniaxially aligned in a quasi-elastic h-PAAm hydrogel matrix. The photonic hydrogel possesses excellent mechanical stability. The colour can be reversibly switched at high frequency more than 10,000 times without degradation with the reflection spectra shifted from red to blue via increase strain. And this photonic hydrogel can be used in optical devices for full-colour display [205].

With the development of the techniques used to fabricate 2D microstructures, 2D photonic crystals can also be used for full color display through modulating the feature parameters of each kind of ordering 2D microstructures. In 2010, Yang et al. prepared two dimensional full color nanostructured surfaces. In their experiment, close packed polystyrene microsphere monolayer was firstly assembled on the surface of flat substrates, and then none close packed microsphere arrays were achieved via the etching process of reactive ion etching. Then a layer of gold was sputtered on the surface of the close packed and none close packed polystyrene microsphere arrays. During this process, the color of the gold modified surfaces can be changed from red to blue via regulating the etching time of the reactive ion etching process and the thickness of the gold film (Fig. 5.19a, b) [206]. And the

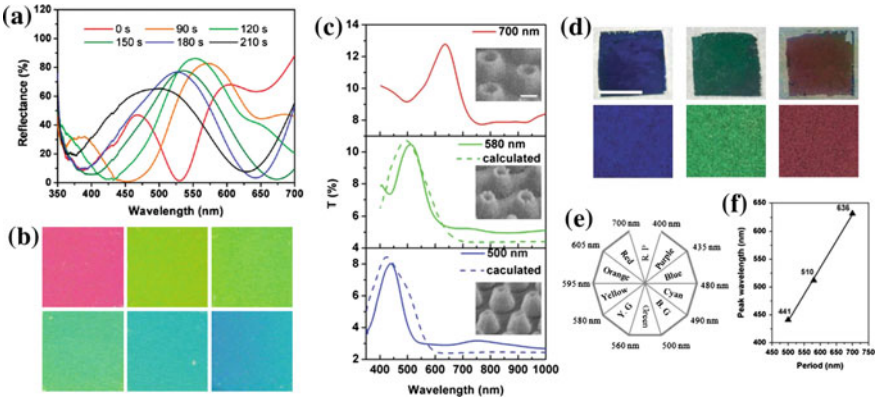

Fig. 5.19 **a** Optical properties of two dimensional structures with RIE time from 0 to 210 s. **b** Photographs of two dimensional structures; the sizes of PNSs are 20 mm × 20 mm [206] **c** SEM images and transmission spectra of Ag nanovolcano arrays with periods of 700, 580 and 500 nm. The hole diameters of the ones with 500 and 580 nm period are ~80/380 and ~120/420 nm, respectively. The *dotted lines* are the corresponding calculated spectra. The SEM images are taken from the 45° tilting views. The *scale bar* corresponds to 200 nm and applies to all the SEM images. **d** The macro-microscopic optical images of the ~1.5 cm × 1.5 cm Ag nanovolcano array. The RGB colors are generated by Ag nanovolcano arrays with periods of 700, 580, and 500 nm, respectively. The *scale bar* corresponds to 1 cm. **e** Schematic *color ring* relating the peak wavelength to color. **f** Linear fit of the peak wavelength with the period. The R^2 is 0.99794. The *numbers* indicate the peak wavelengths [82]

color of the nanostructured surfaces did not change with the viewing angle up to 45° while the optical properties could be tuned almost over the visible light region. Recently, Zhang et al. fabricated silver nanohole arrays with volcano-shaped holes, this two dimensional structure performs structural colors with excellent purity without using index-matching layers. Through regulating the lattice constant via changing the diameter of the microspheres, which were used as masks during the etching process, three primary red–green–blue (RGB) monochromatic colors were obtained. In addition, the colors of the ordered two dimensional nanoarrays could be tuned easily and inexpensively across the whole visible range, while retaining a single sharp transmission peak, showing an efficient responsive color display (Fig. 5.19c–f) [82].

Besides the 1D and 2D photonic crystals were greatly introduced into full color display, 3D photonic crystals also got a great development in the application of this field. Ozin et al. prepared photonic-crystal full-colour displays which was the first example of a dynamic electrical tunability, a working display device architecture [118]. In their experiment, 3D photonic crystal was prepared on the surface of indium tin oxide coated glass plates via convective self-assembly, and then infiltrated the voids between the silica spheres with a low molecular-weight PFS which possess pendant unsaturated C=C bonds, to which was added a small amount of a multifunctional thiol and radical photoinitiator. Then ultraviolet irradiation was used to generate chemical crosslinks between the polymer chains through a well-known thiol-ene reaction, leading to an infinite metallopolymer network matrix. After this matrix achieved, it was incorporated into a sealed thin-layer electrochemical cell for electrical actuation (Fig. 5.20a). When an oxidative potential is applied to the device, the reflected optical diffraction peak was red-shifted (Fig. 5.20b–e), and with incrementally varying the applied voltage, the Bragg peak can continuous shift. Through depositing the photonic crystal film onto arrays of 0.3-mm-wide ITO strips on glass, they demonstrated the potential of electroactive photonic crystals in full-colour displays. Compared with other display technologies, these photonic crystals can reflect colours having a wavelength that is voltage tunable throughout the visible range. And the photonic crystals without the need for expensive colour filters or sub-pixellation of red–green–blue elements, thereby wasting much less of the accessible light output.

Recently, Kim et al. expanded the application of inverse opaline structures towards reflection-mode displays, while the inverse opal micropatterns can be multicolored via the combination of convective self-assembly of colloidal microspheres and photolithography techniques [207]. In their experiment, colloidal crystals were embedded into photoresist, which performs patterns prepared via traditional photolithography. After the removal of the colloidal microspheres from the polymerized photoresist, then inverse opal micropatterns formed and successfully increased the refractive index contrast. As a result, inverse opal micropatterns having three distinctive R, G, and B colors were achieved on these surfaces via

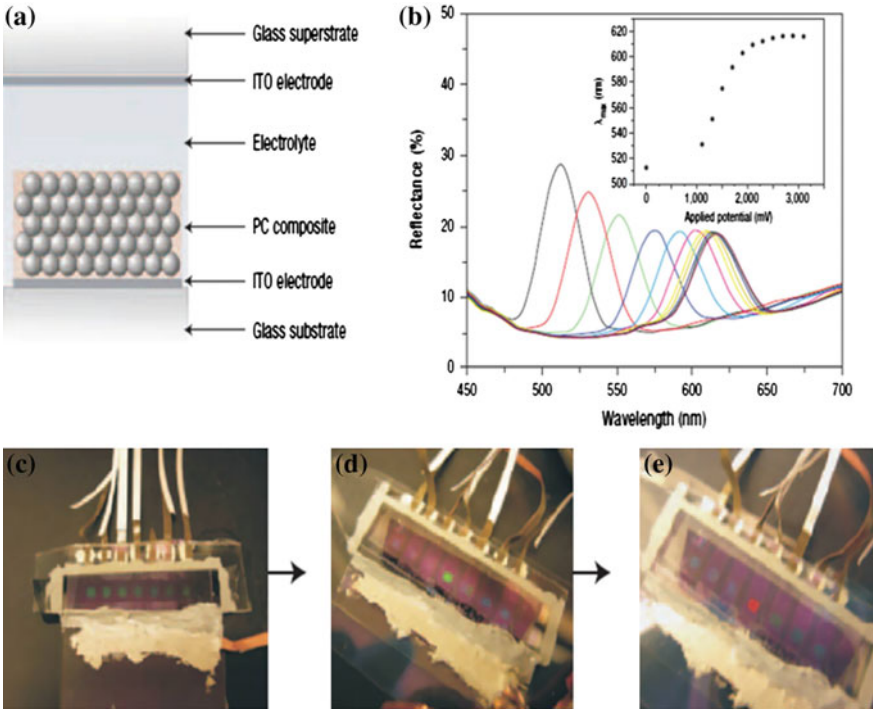

Fig. 5.20 Constructing a PC electrochemical cell. **a** Schematic of the two-electrode electrochemical cell with relevant components. The P-Ink film is approximately 3–5 mm in thickness, and the cell gap can range from tens to hundreds of micrometres. **b** Reflection spectra taken at increasing applied voltages. The *inset* shows the dependence of the peak position on the applied voltage, clearly showing a continuum of accessible colours. **c** Image of an assembled multipixel electrochemical cell with attached electrode leads. **d**, **e** The same cell after oxidizing the middle pixel with 1.5 V (**d**) and 2.0 V (**e**). The reflected colours are due to Bragg diffraction from the composite PC [118]

tuning the diameter of the colloidal microspheres used as templates. When the crystal deposition and photolithography step were multiplied, multi-colored patterns with finely regulated shape, size, and color were achieved (Fig. 5.21), and these multi-colored inverse opal micropatterns possess the potential to be applied in color display devices operated in the reflection mode.

In general, photonic crystals have great potential and superiority to be applied in various display devices, since it possesses significant advantages, including ease fabrication, low cost, controllable structures, and optical properties. We have the reason to believe that it will play a wichtige role in human production and life activities in the future with the development of materials and the photonic crystal fabrication techniques.

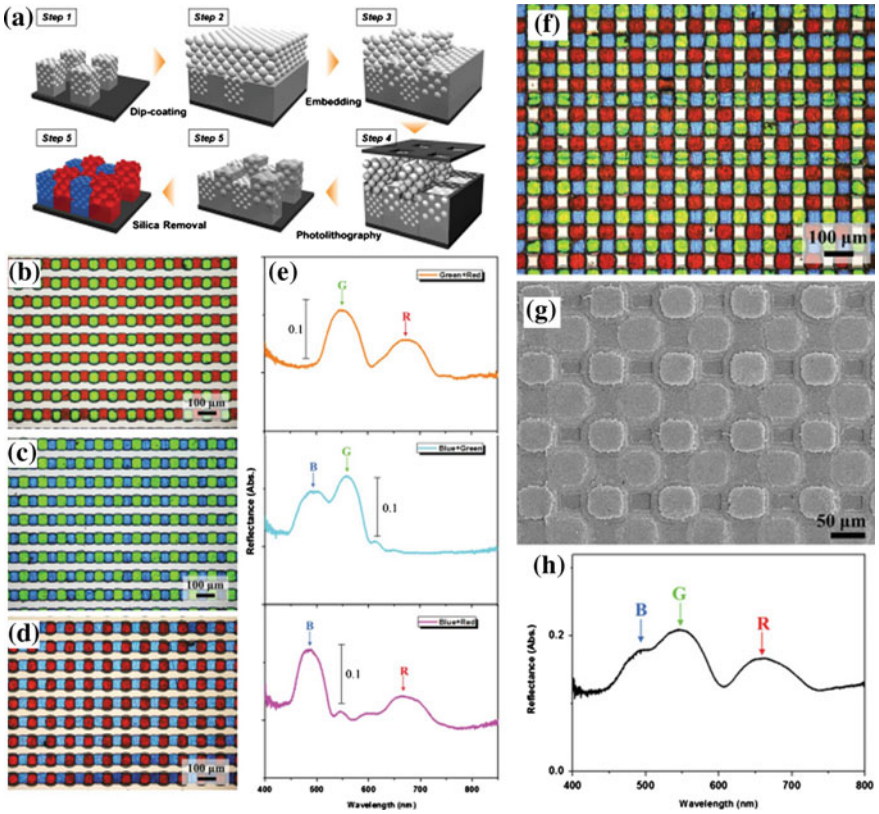

Fig. 5.21 **a** Schematic diagram illustrating the preparation of a pixelated inverse opal prepared to reflect two distinct colors. **b–d** OM images of dual-color pixelated inverse opals: **b** *red* and *green*, **c** *green* and *blue*, and **d** *blue* and *red*. **e** Reflectance spectra of the pixelated inverse opals shown in (**b–d**), where each spectrum displayed two distinct peaks, as indicated by the *arrows*. **f** OM image of the pixelated inverse opal prepared to have three distinct squares reflecting *red*, *green*, or *blue* colors. **g** SEM image of the pixelated inverse opal. A *white rectangle* denotes a single pixel unit. **h** Reflectance spectrum of the pixelated inverse opal, showing the presence of three distinct peaks, as indicated by the *arrows* [207]

5.3.2 *Photonic Crystals Used for Sensing*

Photonic crystals, from one dimensional to three dimensional, can be viewed as periodically distributed materials with different dielectric constants. When the photonic crystal is imposed to stimuli, like magnetic field, chemical substance, biological sample, thermo-change and so on, the period of the sphere or the layer will be altered, which resulting in a colorimetric change or a reflectance spectrum peak shift. This facile sensing approach aroused researchers' great attention. This part we'll give a brief introduction of the reports of photonic crystals employed as sensors, separated into physical sensors, chemical sensors, and biosensors herein.

5.3.2.1 Physical Sensors

Temperature Measuring

In recent five years, plenty of thermo-sensors based on photonic crystal (PC), such as infrared imaging sensor [208], fiber-tip temperature sensor [209], photonic multilayer sensor [210], and so on are reported continually. Hayward et al. fabricated one dimensional photonic crystal (1DPC) by alternatively spin-coating high refractive index layer poly(para-methyl styrene) (PpMS) and low refractive index layer poly(N-isopropylacrylamide) (PNIPAM) (as shown in Fig. 5.22), which roles as the thermo-responsive component with acrylic acid mixed to enhance the swelling effect [210].

The Bragg stack stays in a swelled state in the ambient-temperature water, while the PNIPAM layer de-swell upon heating, resulting in a blue-shift of the reflectance spectrum and visible color change. The approach is facile and scalable, indicating great prospect in the future.

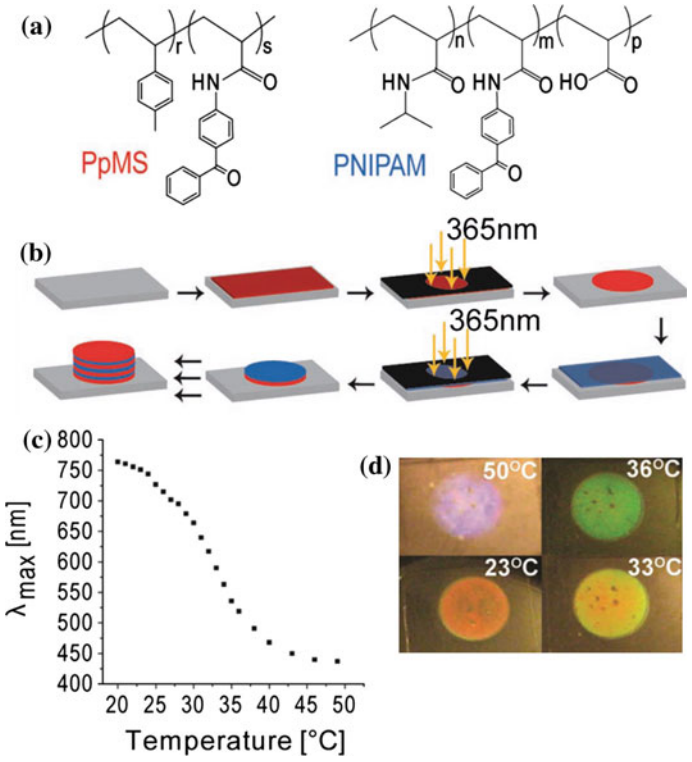

Fig. 5.22 **a** Chemical structures of the photo-crosslinkable random copolymers, **b** a schematic of sensor fabrication, whereby polymers are sequentially spin-coated, crosslinked and developed to create a multilayer 1D photonic stack, **c** peak reflectance wavelength and **d** photographs of sensors swelled in water show clear colorimetric changes with temperature [210]

Mechanical Sensor

Mechanochromic materials have promising prospects in sensing and monitoring. Chan and his coworkers systematically summerized different kinds of mechanochromic photonic gels' application as sensors and their mechanism thoroughly [211]. Recently, Chen et al. reported a facile approach to fabricate highly sensitive and reversible elastic photonic crystals, which possess touch-induced chromatic behavior even under forces less than 0.5 N or pressure down to 1 kPa. The fabrication procedure is shown within Fig. 5.23. The magnetic colloidal nanocrystal clusters were employed as building blocks, which can self-assemble orderly under magnetic field, and the pre-added monomers can in situ polymerize to form a hydrogel matrix. Under compression the cross-section of the hydrogel streches perpendicularly, resulting in an increase of the intercluster spacing and a redshift in optical diffraction, a changed color. In addition, the 1D photonic chains will confined in a certain area of the hydrogel upon compression, increasing the reflection intensity (Fig. 5.23) [204].

Other kinds of physical sensors are also reported including photoacoustic sensor [212], magnetic field sensor [213], and refractive index sensor [214] as well. As we mainly focus on the photonic sensors fabricated by chemical methods, we only reference these works here without unnecessary verbosity.

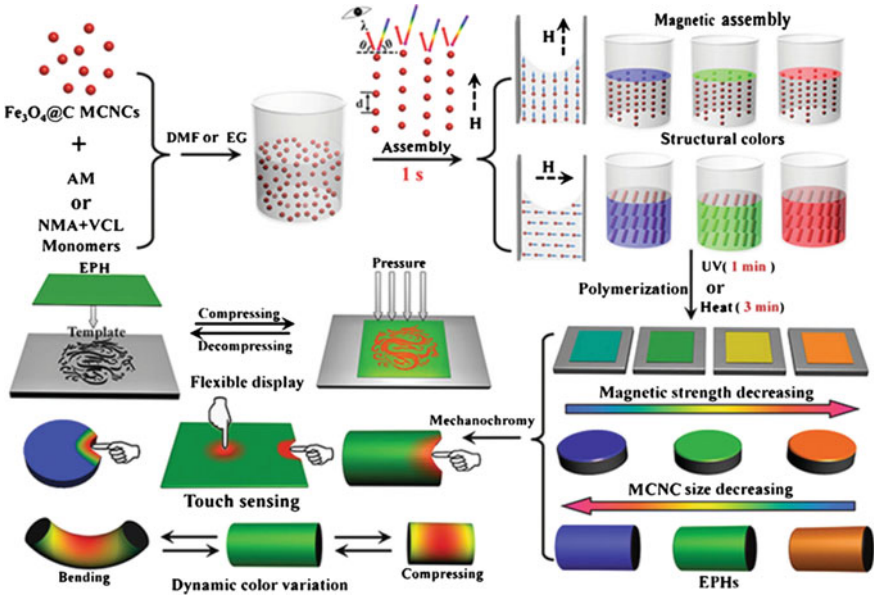

Fig. 5.23 Fabrication and mechanochromic applications of EPHs. Magnetic assembly of magnetic colloid nanocrystal clusters dispersing in monomer solutions followed by UV- and heat-initiated radical polymerization to afford different shapes (films, slices, and cylinders) of multicolor EPHs within minutes. Mechanochromic behavior of the obtained EPHs makes them useful for mechanical flexible display, touch color changing and reversible color switching [204]

5.3.2.2 Chemical Sensor

pH Responsive

Lotsch et al. fabricated 2D inverse opal monolayers with P2VP polyelectrolyte gel matrix through spin-coating. P2VP swells under acidic conditions for the protonation of the pyridine group, giving rise to the PC pH sensing. The sensor responsed fast and visible [215]. Zhang and coworkers smartly used biotemplate, combining with surface bonding and polymerization, to prepare a pH-responsive hierachical PC [162]. Recently, Pace and coworkers coated porous silicon photonic films with pH-responsive polymer poly(2-diethylaminoethyl acrylate), which can prevent the water permeating into the porous matrix at neutral pH. The polymer becomes hydrophilic when it comes to acidic, opening up the pores and gradually allow water's permeation, resulting in a shift of the reflector's resonance and an optical signal accordingly [216]. Asher and his coworkers fabricated photonic crystal hydrogels of poly(vinyl alcohol) (PVA), which own the diffraction and swelling properties of polymerized crystalline colloidal arrays (PCCA). The structure achieved can sense pH and Pb^{2+}. What differentiate this work with previous ones is its ability to reversibly dehydrated and rehydrated [217]. Afterwards, Zhu et al. prepared a gelated colloidal crystalline array likewise and functionalized it with chitosan to make it pH-responsive [218]. Based on the pH sensitive polymer poly(N,N′-dimethylaminoethyl methacrylate) (PDMAEMA), Yang et al. employed it as the organic layer of the organic/inorganic hybrid one dimensional photonic crystal (1DPC). The 1DPC exhibit changeable vivid color upon altered pH. Owing for its capability to detect pH visibly, they applied it to dynamically detect the glucose oxidation reaction, whose pH can gradually decrease during the catalysis. The sensing effect is as shown in Fig. 5.24.

The fabricating approach is of low-cost and facile. The optical read-out is convenient and offers great potential for practical application [58].

Vapor Sensing

For PC-based vapor detection or gas sensing, we mainly divide the sensor into three types on account of the gas it senses: vapor pressure (existence detection) sensor, acidic/alkali vapor sensor and multiplex vapor sensor. For the first kind, Miguez and his coworkers reported a nanoparticle-based 1DPC for the change of the ambient vapor pressure [219]. Li et al. took advantage of the photonic crystal nanobeam cavities with high-quality factors and chemically functionalized them by specific polymer, which can interact with the gas, to fabricate an ultrasensitive gas sensor [220]. Hu et al. reported a full-color CO_2 sensor formed by inverse opal photonic hydrogel. When CO_2 reacts with the amino group within the hydrogel, it'll become ionic, which is more hydrophilic than the original non-ionic one, leading to a rise of Donnan potential and the swelling of the hydrogel [221]. As for the second type, Sailor constructed a pH-responsive sensor for NH_3 (g) by infusing an indicator

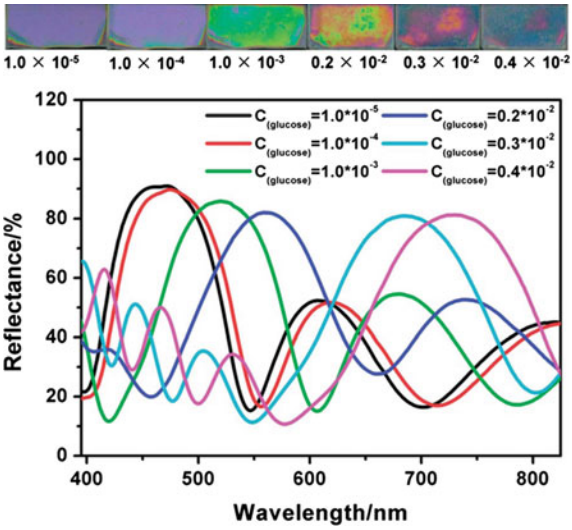

Fig. 5.24 *Top* Images of a five-bilayer hybrid BS soaked in glucose solutions with different GOx concentrations. *Bottom* Experimental optical spectra showing the different peak positions corresponding with the images [58]

dye into a porous photonic crystal [222]. Zhang et al. employed polyaniline (PANI)-infiltrated inverse opal PC as an acidic/alkali vapor sensor due to the PANI's state of doped/dedoped transformation and the effective refractive index change [223]. Similarly, Ge and coworkers reported 1DPC acidic/alkali vapor sensor by alternating TiO_2 and PANI [53]. For multiplex gas sensing, Sailor et al. utilized multilayered stacks of porous Si 1DPC to sense volatile organic compounds [224]. Potyrailo et al. took advantage of the Morpho butterfly wing's hierarchical structure to fabricate a vapor sensor [225]. Gu et al. obtained mesoporous PC vapor sensing chip by incorporating fluorescent dyes into mesoporous colloidal crystals, which can detect both the category and concentration of the vapor. They used the integraged sensor array fluorescence to distinguish the vapor species and the wavelength shift of an unmodified mesoporous colloidal PC to tell the concentration once the species are confirmed as shown in Fig. 5.25. The porous structure confers large surface area, offers the gas analyte great access to the fluorescence indicator, ensuring high sensitivity [226].

Ion Detector

Photonic crystal based ion sensing is of great importance for application in human health and environmental pollution. Many works have been reported these days on photonic-nose Pb^{2+} sensing [227], Hg^{2+} sensing [228, 229], Fe^{3+} and Hg^{2+} sensing [230], ionic strength sensing [231], and even simultaneous anions, cations and zwitterions sensing [232]. Yang and his coworkers reported a facile method to sense SCN^- by naked eye via the organic/inorganic hybrid 1DPC hydrogel, alternating poly dimethylaminoethyl methacrylateco-ethylene glycol dimethacrylate (PDMAEMA-co-PEGDMA) and titania sol by spin-coating. Depending on the

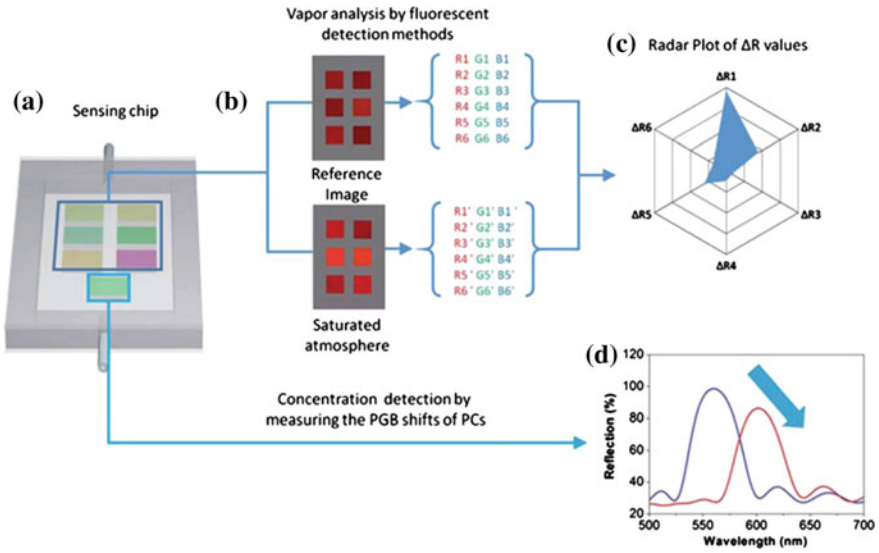

Fig. 5.25 Schematic illustration of **a** the sensing chip and **b–d** the basic steps of the fluorescence and reflection detection [226]

surface charge density, viscosity coefficients, and entropy of hydration, which can affect the dominating force, the osmotic pressure, the photonic hydrogels contract more in SCN^- than in other anion solutions. Therefore the hydrogel achieved has high selectivity. The selectivity test is shown in Fig. 5.26. The detection limit is pretty low as well, reaching 10^{-6} mol l^{-1} (Fig. 5.26) [55].

With the aim of expanding the sensing behavior to multiplex sensing, Li et al. achieved high-performance multi-ion recognition by multi-stopband PC microchip. The microchip was fabricated combining photolithography and colloidal crystal self-assembly. The patterned hydrophilic-hydrophobic substrate confers different channels, which can provide different stopbands of photonic crystals to

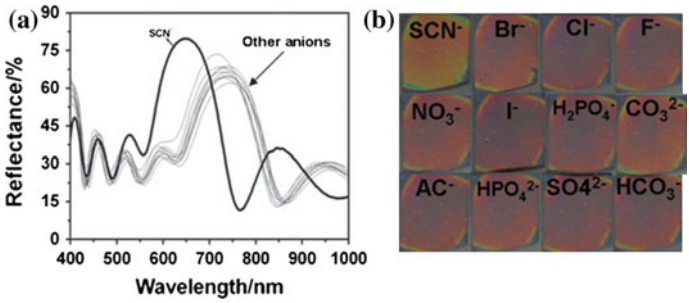

Fig. 5.26 Reflective spectra **a** and photographs **b** of the photonic hydrogel in different anion solutions. The size of the photographs is about 20 mm by 20 mm [55]

self-assembly separately. The 8-HQ (8-hydroxy-quinoline), a metal coordination compound with tunable fluorescence by the metal ions, was used to functionalize the self-assembled photonic crystal. As a result, the microchip can selectively enhance the sensing fluorescence in different channels, and perform a high-efficient multi-analyte discriminant testing [233].

Humidity Sensor

Most works about humidity sensor focus on the colorimetric humidity sensor fabrication. Hawkeye using glancing angle deposition to fabricate the colorimetric humidity sensor [234]. Song et al. used 3DPC as template to make a humidity sensitive hydrogel [235]. Liu et al. used silk-fibroin to make inverse opal structure of different colors and applied it in humidity sensing [236]. Yang et al. prepared core/shell polymer-grafted silicon nanopost arrays through atom-transfer radical polymerization (ATRP) combined with colloidal lithography. The fabrication process is as shown in Fig. 5.27.

The silicon post template can be achieved through colloidal lithography, and the functional polymer poly(2-hydroxyethyl methacrylate) (PHEMA) are covalently grafted from the template by surface initialized ATRP. The composite nanopost arrays display tunable color by modulating the layer thickness. Due to the hydrophily of the polymer poly(2-hydroxyethyl methacrylate), it can absorb water molecule and swell, resulting in a change of the effective refractive index and a red-shift of the reflectance peak. Various colors can be achieved from green to red when the thickness changes. The structure was demonstrated to be employed as a stable and reproducible sensor in sensing humidity [79]. They also fabricated full-color visible humidity sensor based on 1DPC [54].

Organic Solvents Analyzing

Organic solvent sensors based on photonic crystals can be divided into the following three kinds generally: 1DPC based colorimetric sensor caused by the

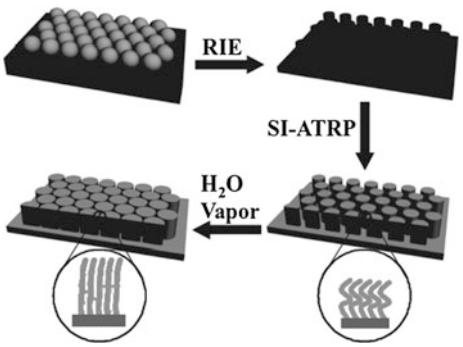

Fig. 5.27 The procedure used to fabricate composite nanopost arrays, and the resulting water-vapor sensing processes [79]

swelling behavior of the polymer when immersed in the organic solvents [57], PC based color-tunable sensor attributed to the polarity difference of solvents induced polymer swelling [237], and mesoporous Bragg stack sensor owing for the refractive index change when absorbing solvents in the pores [236]. By alternating polymer and titania nanoparticles with high refractive index contrast to construct the 1DPC, Yang and his coworkers can obtain obvious bandgap within several layers. The color can be easily seen with naked eye when the photonic bandgap fall into the visible region. Owing for the interaction between the polymer and the organic solvents, the bandgap will shift, leading to a change of the color of the chip, as shown in Fig. 5.28.

The sensor achieved owns high sensitivity and response speed. It can sense both pure and mixture of organic solvents [56].

Specific Chemical Substance Analysis

Besides the analytes mentioned above, we can also see reports about the detection of some specific chemical substance, including TNT [238], oil [239], organophosphorus [240], and so on. Yu et al. took advantage of the stepwise red-shift of the diffraction wavelength during the interaction between ceprofloxacin and tryptophan, which is bridged by the Zn(II) within the ceprofloxacin, to make the tryptophan contained responsive photonic crystal be able to detect the ceprofloxacin [241]. Zhang et al. combined inverse opal PC with specific reaction among cyanide and trifluoroacetyl (TFA) to fabricate a label-free cyanide sensor. The fabrication procedure and mechanism interpretation is as shown in Fig. 5.29.

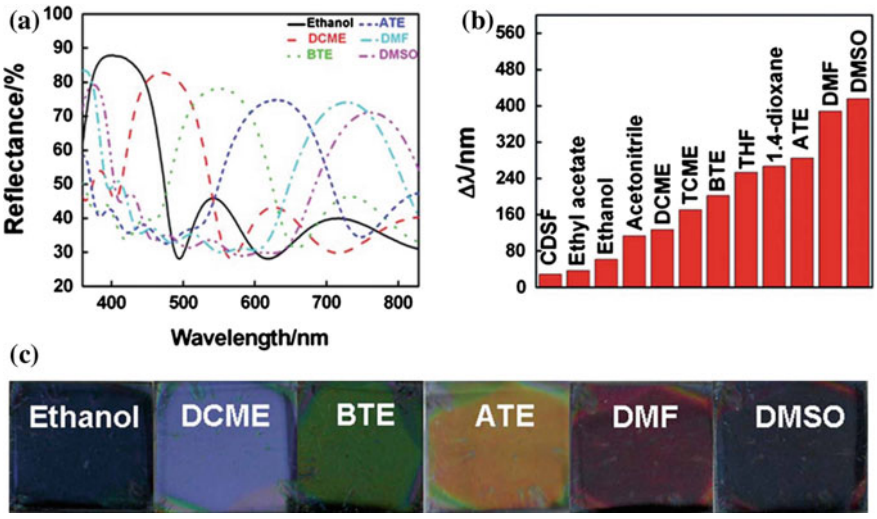

Fig. 5.28 **a** Reflective spectra of a 1DPC in different solvents. **b** Shift of the photonic stop band of a 1DPC in different solvents. **c** Photographs of 1DPC in different solvents [56]

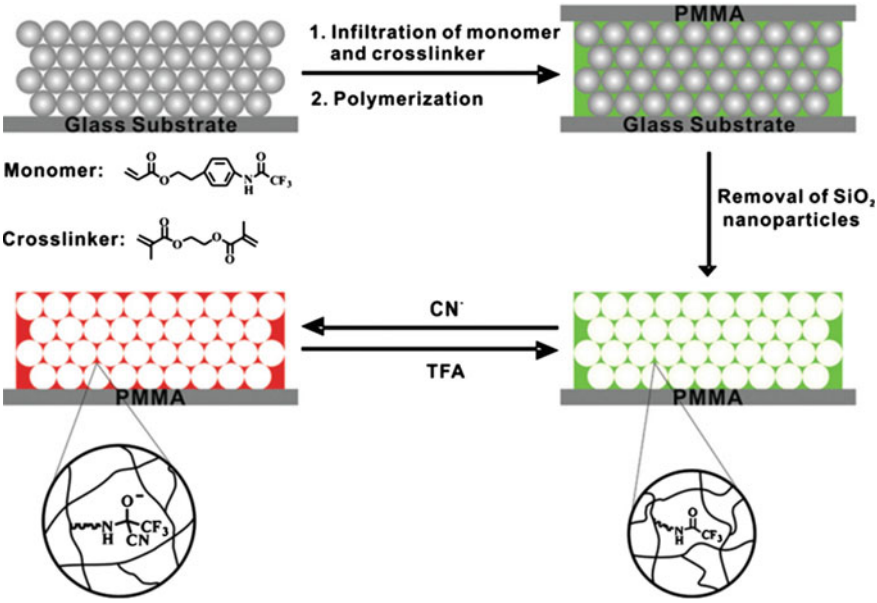

Fig. 5.29 Schematic illustration of the fabrication of reactive photonic film for label-free and selective sensing of cyanide through the specific reaction between cyanide and trifluoroacetyl group [216]

When exposed to cyanide, it'll turn from a neutral (hydrophobic) state to a charged (hydrophilic) state, resulting in osmotic pressure and swelling. Upon exposure to TFA solution, the chemically absorbed cyanide can be completely removed, and the sensing process can be reversible in that case. The sensor is label-free and convenient, and even visible when the concentration is high enough [216].

5.3.2.3 Biological Sensors

DNA Sensing

Zentel et al. integrated DNA into the 3DPC, fabricating a biologically active defect structure. The DNA's denaturation and hybridization state can be read from the optical response [242]. Song and coworkers also researched on detection of DNA hybridization. They labeled ssDNAs with donar and acceptor, using fluorescence resonance energy transfer (FRET) effect to produce a fluorescence signal, amplified by PC [243]. Li et al. achieved DNA detection by sputtering the inverse opal 3DPC with gold nanoparticles, which can enhance the light-harvesting and light-matter interaction through localized surface plasmon resonance (LSPR). The fabrication method is as shown in Fig. 5.30.

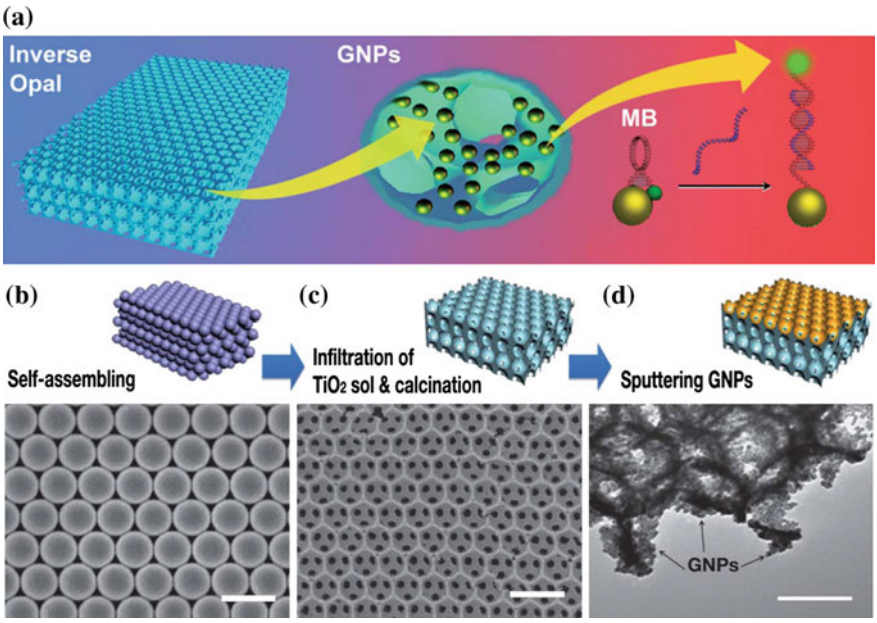

Fig. 5.30 **a** Schematic illustration of the Au–IO used for label-free DNA detection. The detection system is composed of a TiO_2 inverse opal, GNPs and labeled molecular beacons (MBs). The inverse opal and the GNPs serve as a hierarchical optical antenna for energy enrichment. The MB with the hairpin structure can respond to the complementary target DNA and the fluorescent signal can be enhanced by the intense excitation field. **b**, **c**, and **d** The fabrication of Au–IO. **b** The opal template is fabricated from assembling monodisperse polymer microspheres (*SEM scale bar* 500 nm). **c** The TiO_2 precursor sol infiltrates into the opal template and is calcinated to form the TiO_2 inverse opal (*SEM scale bar* 500 nm). **d** The GNPs are sputtered on the surface of the inverse opal framework, forming the hierarchical optical antenna Au–IO (*TEM scale bar* 200 nm). The diameters of GNPs were measured as ca. 7.6 ± 2.1 nm [244]

When PC band edge overlaps the LSPR absoption and excitation wavelength, the fluorescence will be enhanced then [244].

Protein Detecting

As for this part, we'll divide the sensor mainly into three parts based on the analyte it senses: enzyme sensor, biomarker sensor and other protein sensor. Firstly, for the enzyme sensor, we can see works upon 1DPC [245], 3DPC [246, 247] based enzyme activity sensor. Kaar polymerized opal structure into a hydrogel matrix to functionalize it with kinase recognition sequence. The environmental electrostatics change will make the ionic hydrogel swell due to the osmotic pressure, resulting in

a red-shift of the peak wavelength [247]. Secondly, as for the biomarker sensor, there are plenty of works reported in recent years, including the combination of enzyme linked immunosorbent assay (ELISA) and photonic crystal surface [248, 249], quantum-dot-tagged photonic crystal beads self-assembly [250], photonic crystals coupling laser scanning platform [251], and nanoparticle-assembled photonic crystal [252]. Photonic crystals can be facilely obtained and exhibit excellent property in enhancing the fluorescent signal, thus most of these works chose photonic crystals as ideal assistant for biomarker detection. Last, for the other protein sensor, Hergenrother et al. used PC as substrate to explore the protein-protein interaction by the peak wavelength value shift [253]. 2DPC based hydrogel's analyte-responsive shrinkage [254] or swelling [255] will lead to a shift of the diffraction wavelength, a optical read-out then. We can also see antigen sensors based on antigen-antibody interaction [256]. Zhang et al. fabricated plasmonic biosensor with structure of 2D Ag nanowell plasmonic crystal, as shown in Fig. 5.31.

Being attributed to the well operated nanowell size, there'll be a coupling of surface plasmon polaritons and Raleigh anomanlies, resulting in a sharp reflectance dip. They also explored to tune the lineshape by depth and sensitivity by the lattice constant. The structure achieved was then attempted to act like a quantitative biosensor by antigen-antibody couple incorporation. The sensor test outcome was satisfying, indicating its great potential for biosensing application [257].

Toxin, Bacteria, and Viral Analyzing

For toxin detection, researchers took advantage of the photonic crystal's ability to enhance the fluorescence for a guided mode resonance [258], and to act as a spectrum-encoding carrier [259]. As for bacteria detection, Segal et al. prepared self-report porous Si photonic crystal that can not only capture the bacteria, but monitor the concentration, growth and physiological state of bacteria cells [260]. With regard to viral sensor, Demirci et al. used PC to trap and quantify HIV-1 to attain a label-free optical sensor. The general mechanism and fabrication process is as shown in Fig. 5.32.

The PC itself reflects a narrow wavelength band under the light source. When absorbing biotargets by antigen-antibody interaction, there'll be a shift of the peak wavelength value, which is proportional to the biotargets binded to the surface of sensor. Thus the sensor can both identify and quantify the biotarget [261].

All in all, we conclude that sensors based on photonic crystals can be attained cost-efficiently and optically readable. PC based biosensors will show promising prospects for point-of-care owing for their visibly color change and facile fabrication methods. However, the selectivity and sensitivity improvement still need to be paid great attention for practical application.

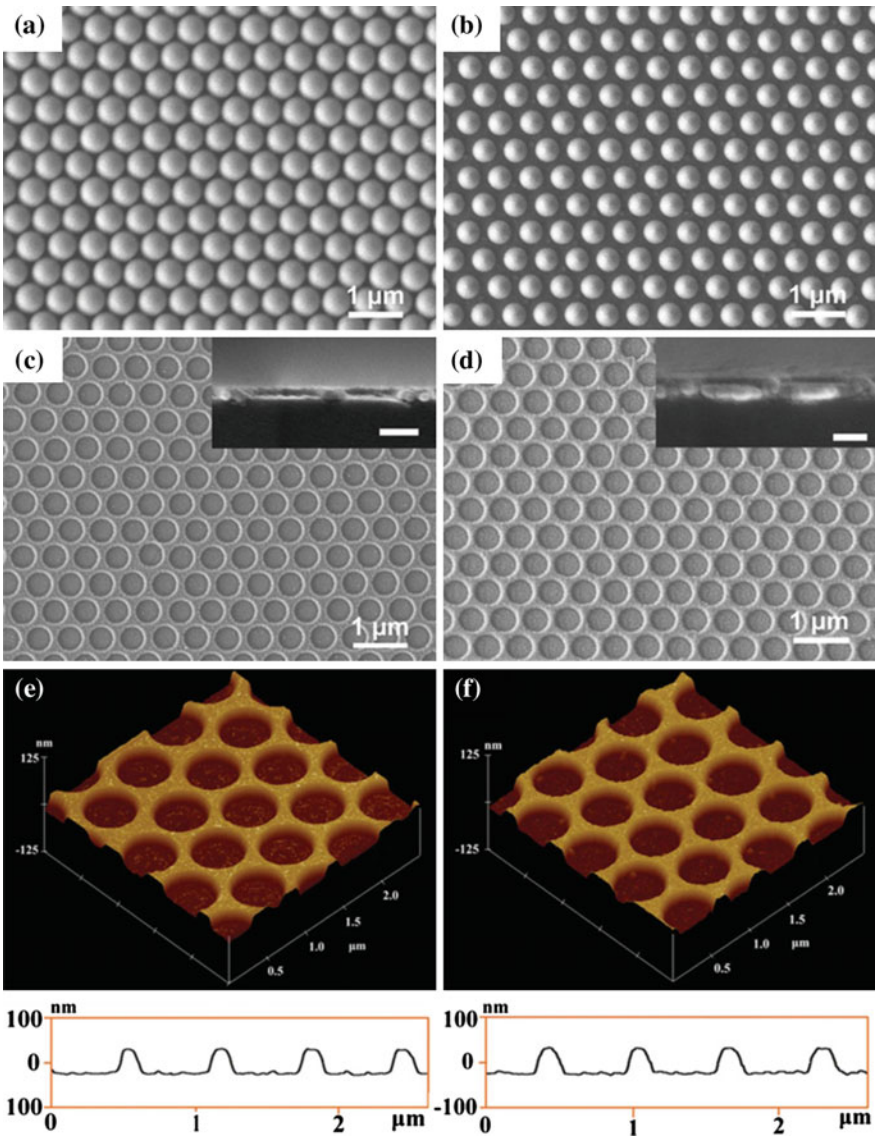

Fig. 5.31 Typical SEM images of: **a** close-packed PS colloidal spheres with diameter of 580 nm, **b** PS spheres after being etched for 7 min in O_2 plasma, **c** original Ag nanohole array, and **d** Ag nanowell crystal. The *insets* in **c** and **d** are their corresponding cross-sectional SEM images and the *scale bars* both represent 200 nm. AFM images of: **e** original Ag nanohole array and **f** Ag nanowell crystal, accompanied by corresponding *scan lines*. The depths of them are both around 60 nm [257]

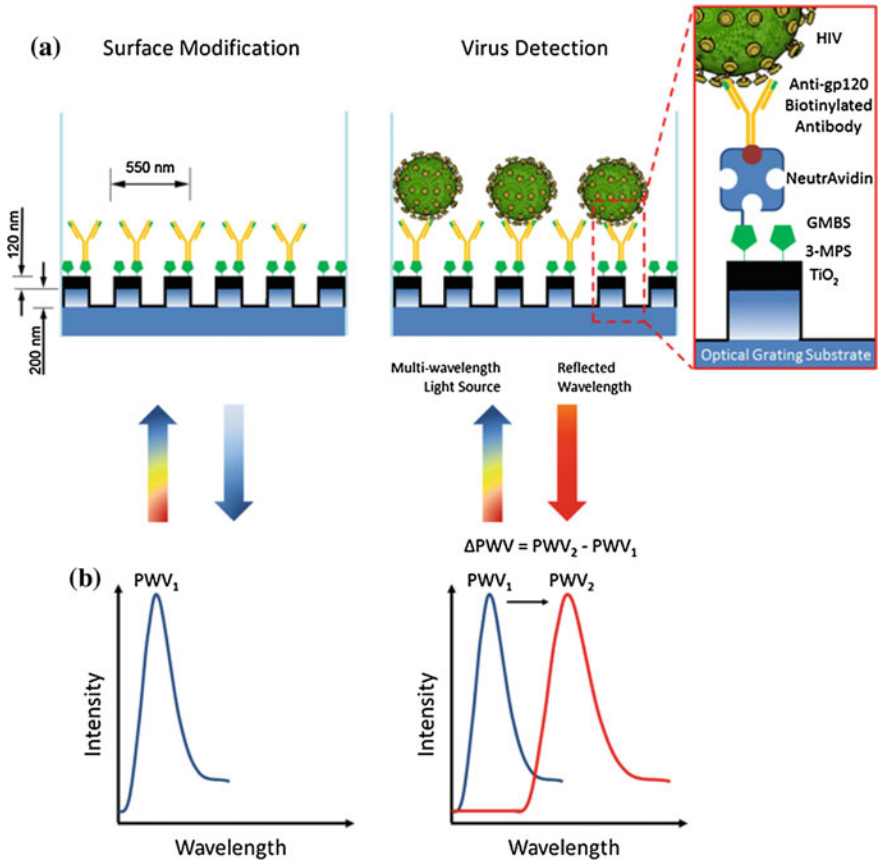

Fig. 5.32 Schematic of Photonic Crystal (PC)-based intact virus detection platform. **a** The bottom surface of PC biosensor microplate wells is comprised of a nanostructured subwavelength grating that is coated with TiO_2. **b** Binding events within the close vicinity of the sensing area change the bulk index of refraction, thus, the peak wavelength value (PWV) of the reflected light is altered. The shift in the peak wavelength (DPWV) is directly proportional to the binding of molecules and/or bioagents (e.g., cells and viruses) onto the biosensing surface [261]

5.4 Summary and Perspectives

Photonic crystal has exhibited great potential application in many fields, since its feature structure and optical properties can be finely controlled via modulating the conditions during the fabrication process. In this chapter, we reviewed the relatively facile methods (mainly including spin-coating and colloidal chemistry derived techniques) used for fabricating photonic crystals from one dimensional to three dimensional, and applications of photonic crystals in the field of display and sensing. With the help of the operability, controllability, and cost-efficiency of spin-coating and colloidal chemistry, series of one dimensional photonic crystals

composed of organic, inorganic, and organic/inorganic hybrid materials, two dimensional and three dimensional photonic crystal structures prepared by colloidal chemistry derived techniques have been achieved. And these photonic crystals can be used for investigating the feasibility to apply these structures in display and sensing. Though series of fabrication techniques have been developed and relative application values have been proved by experiments, there still remain some challenges and problems which run through the aspects of materials and preparation technologies. These problems urgently need to be addressed in the next ten to twenty years. For the fabrication of one dimensional photonic crystal via spin coating, it needs to realize the integration of multi-component and multi-layer and overcome the incompatibility issues between the adjacent layers, while expanding the combination of inorganic and organic materials. For the preparation of two dimensional and three dimensional photonic crystals via the colloidal assembly method, it needs to solve three main issues. First, preparing 2D and 3D photonic crystals with no defects in a large area and suitable for commercial use via more ease and controllable method; Second, anisotropic colloidal photonic crystal which possess advanced optical properties should be fabricated by preparing monodispersed and functionalized non-spherical nanospheres with high quality synthetic methods; Third, specific stimuli-responsive photonic crystals should be obtained by the assembling method to expanding the application field of photonic crystal. For the aspect of fabricating two dimensional even three dimensional photonic crystals with the microfabrication techniques derived from colloidal chemistry, it need to take the advantage of the adjustable features of the two or three dimensional assemblies. At the same time, the combination with other processing methods to prepare bran-new and integrated two and three dimensional structures, and achieve ideally designed defects in the assembled photonic crystal under special request. Besides, it need to reduce the processing cost through technology improvement to enhance the processing speed, to improve the production yield, and to accelerate their business applications. In addition, the practical applications of the photonic crystals prepared via the simply spin-coating, assembly, and mircofabricaiton techniques derived from colloidal chemistry will be further promoted. And some valuable devices such as thresholdless laser, mirror and bending optical path without loss, optical microchamber with high quality factor, nonlinear switch and amplifier with low driving energy, superprim with small volume and high wavelength resolution, photonic crystal fiber with the function of dispersion compensation, photonic crystal ‘diodes’ and ‘transistors’, photonic crystal logical circuit, and photonic crystal driven computer will be manufactured and industrialized. At the same time, the role of photonic crystals in sensing area will be increased by refining the specificity and sensitivity to specific stimuli, and then different optical, electrical, and magnetic signals and various chemical/biological substances will be rapidly detected.

References

1. Y.J. Zhao, X.W. Zhao, Z.Z. Gu, Photonic crystals in bioassays. Adv. Funct. Mater. **20**, 2970–2988 (2010)
2. H.K. Hunt, A.M. Armani, Label-free biological and chemical sensors. Nanoscale **2**, 1544–1559 (2010)
3. J.T. Heeres, P.J. Hergenrother, High-throughput screening for modulators of protein–protein interactions: use of photonic crystal biosensors and complementary technologies. Chem. Soc. Rev. **40**, 4398–4410 (2011)
4. H. Xu, P. Wu, C. Zhu, A. Elbaz, Z.Z. Gu, Photonic crystal for gas sensing. J. Mater. Chem. C **1**, 6087–6098 (2013)
5. H. Wang, K.Q. Zhang, Photonic crystal structures with tunable structure color as colorimetric sensors. Sensors **13**, 4192–4213 (2013)
6. C. Pacholski, Photonic crystal sensors based on porous silicon. Sensors **13**, 4694–4713 (2013)
7. C. Fenzl, T. Hirsch, O.S. Wolfbeis, photonic crystals for chemical sensing and biosensing. Angew. Chem. Int. Ed. **53**, 3318–3335 (2014)
8. F.A. Harraz, Porous silicon chemical sensors and biosensors: a review. Sens. Actuators B **202**, 897–912 (2014)
9. S.A. Kolpakov, N.T. Gordon, C.B. Mou, K.M. Zhou, Toward a new generation of photonic humidity sensors. Sensors **14**, 3986–4013 (2014)
10. M.R. Islam, A. Ahiabu, X. Li, M.J. Serpe, Poly(*N*-isopropylacrylamide) microgel-based optical devices for sensing and biosensing. Sensors **14**, 8984–8995 (2014)
11. A.C. Edrington, A.M. Urbas, P.D. Rege, C.X. Chen, T.M. Swager, N. Hadjichristidis, M. Xenidou, L.J. Fetters, J.D. Joannopoulos, Y. Fink, E.L. Thomas, Polymer-based photonic crystals. Adv. Mater. **13**, 421–425 (2001)
12. L. Thylén, M. Qiu, S. Anand, Photonic crystals—a step towards integrated circuits for photonics. ChemPhysChem **5**, 1268–1283 (2004)
13. S. Ogawa, M. Imada, S. Yoshimoto, M. Okano, S. Noda, Control of light emission by 3D photonic crystals. Science **305**, 227–229 (2004)
14. M. Fujita, S. Takahashi, Y. Tanaka, T. Asano, S. Noda, Simultaneous inhibition and redistribution of spontaneous light emission in photonic crystals. Science **308**, 1296–1298 (2005)
15. C.N. LaFratta, J.T. Fourkas, T. Baldacchini, R.A. Farrer, Multiphoton fabrication. Angew. Chem. Int. Ed. **46**, 6238–6258 (2007)
16. S. Kinoshita, S. Yoshioka, J. Miyazaki, Physics of structural colors. Rep. Prog. Phys. **71**, 076401 (2008)
17. A.R. Parker, Natural photonics for industrial inspiration. Phil. Trans. R. Soc. A **367**, 1759–1782 (2009)
18. C. Wiesmann, K. Bergenek, N. Linder, U.T. Schwarz, Photonic crystal LEDs–designing light extraction. Laser Photon. Rev. **3**, 262–286 (2009)
19. E. Kuramochi, K. Nozaki, A. Shinya, K. Takeda, T. Sato, S. Matsuo, H. Taniyama, H. Sumikura, M. Notomi, Large-scale integration of wavelength-addressable all-optical memories on a photonic crystal chip. Nat. Photon. **8**, 474–481 (2014)
20. C. López, Materials aspects of photonic crystals. Adv. Mater. **15**, 1679–1704 (2003)
21. J.D. Joannopoulos, S.G. Johnson, J.N. Winn, R.D. Meade, *Photonic crystals: molding the flow of light*, 2nd edn. (Princeton University Press, Princeton, New Jersey, USA, 2008)
22. G.V. Freymann, V. Kitaev, B.V. Lotschzc, G.A. Ozin, Bottom-up assembly of photonic crystals. Chem. Soc. Rev. **42**, 2528–2554 (2013)
23. A.R. Parker, A vision for natural photonics. Phil. Trans. R. Soc. Lond. A **362**, 2709–2720 (2004)
24. S. Kinoshita, S. Yoshioka, Structural colors in nature: the role of regularity and irregularity in the structure. ChemPhysChem **6**, 1442–1459 (2005)

25. K. Busch, G.V. Freymann, S. Linden, S.F. Mingaleev, L. Tkeshelashvili, M. Wegener, Periodic nanostructures for photonics. Phys. Rep. **444**, 101–202 (2007)
26. J.Y. Sun, B. Bhushan, J. Tong, Structural coloration in nature. RSC Adv. **3**, 14862–14889 (2013)
27. J.H. Lee, C.Y. Koh, J.P. Singer, S.J. Jeon, M. Maldovan, O. Stein, E.L. Thomas, 25th anniversary article: ordered polymer structures for the engineering of photons and phonons. Adv. Mater. **26**, 532–569 (2014)
28. G.V. Freymann, A. Ledermann, M. Thiel, I. Staude, S. Essig, K. Busch, M. Wegener, Three-dimensional nanostructures for photonics. Adv. Funct. Mater. **20**, 1038–1052 (2010)
29. M.S. Yoon, K.H. Ahn, R.W. Cheung, H. Sohn, J.R. Link, F. Cunin, M.J. Sailor, Covalent crosslinking of 1-D photonic crystals of microporous Si by hydrosilylation and ring-opening metathesis polymerization. Chem. Commun. **6**, 680–681 (2003)
30. J.H. Holtz, S.A. Asher, Polymerized colloidal crystal hydrogel films as intelligent chemical sensing materials. Nature **389**, 829–832 (1997)
31. S. Kubo, Z. Gu, K. Takahashi, A. Fujishima, H. Segawa, O. Sato, Tunable photonic band gap crystals based on a liquid crystal-infiltrated inverse opal structure. J. Am. Chem. Soc. **126**, 8314–8319 (2004)
32. B.V. Lotsch, G.A. Ozin, Photonic clays: a new family of functional 1d photonic crystals. ACS Nano **2**, 2065–2074 (2008)
33. F.M. Hinterholzinger, A. Ranft, J.M. Feckl, B. Rühle, T. Bein, B.V. Lotsch, One-dimensional metal–organic framework photonic crystals used as platforms for vapor sorption. J. Mater. Chem. **22**, 10356–10362 (2012)
34. O. Sánchez-Sobrado, G. Lozano, M.E. Calvo, A. Sánchez-Lglesias, L.M. Liz-Marzán, H. Míguez, Interplay of resonant cavity modes with localized surface plasmons: optical absorption properties of Bragg stacks integrating gold nanoparticles. Adv. Mater. **23**, 2108–2112 (2011)
35. J. Ge, Y. Yin, Responsive photonic crystals. Angew. Chem. Int. Ed. **50**, 1492–1522 (2011)
36. V. Morandi, F. Marabelli, V. Amendola, M. Meneghetti, D. Comoretto, Colloidal photonic crystals doped with gold nanoparticles: spectroscopy and optical switching properties. Adv. Funct. Mater. **17**, 2779–2786 (2007)
37. B. Li, J. Zhou, L.Q. Li, Q. Li, S. Han, Z.B. Hao, One-dimensional photonic bandgap structure in abalone shell. Chin. Sci. Bull. **50**, 1529–1531 (2005)
38. A. Urbas, R. Sharp, Y. Fink, E.L. Thomas, M. Xenidou, L.J. Fetters, Tunable block copolymer/homopolymer photonic crystals. Adv. Mater. **12**, 812–814 (2000)
39. A. Urbas, J. Klosterman, V. Tondiglia, L. Natarajan, R. Sutherland, O. Tsutsumi, T. Ikeda, T. Bunning, Optically switchable Bragg reflectors. Adv. Mater. **16**, 1453–1456 (2004)
40. Y.F. Yue, M.A. Haque, T. Kurokawa, T. Nakajima, J.P. Gong, Lamellar hydrogels with high toughness and ternary tunable photonic stop-band. Adv. Mater. **25**, 3106–3110 (2013)
41. C.C. Chien, J.H. Liu, Optical behaviors of flexible photonic films via the developed multiple UV-exposed fabrications. Macromol. Rapid Commun. **35**, 1185–1190 (2014)
42. Z.H. Wang, J.H. Zhang, J. Xie, Z.Y. Wang, Y.S. Yin, J.X. Li, Y.F. Li, S. Liang, L. Zhang, L.Y. Cui, H. Zhang, B. Yang, Polymer Bragg stack as color tunable photonic paper. J. Mater. Chem. **22**, 7887–7893 (2012)
43. L.D. Bonifacio, B.V. Lotsch, D.P. Puzzo, F. Scotognella, G.A. Ozin, Stacking the nanochemistry deck: structural and compositional diversity in one-dimensional photonic crystals. Adv. Mater. **21**, 1641–1646 (2009)
44. B.V. Lotsch, G.A. Ozin, Clay Bragg stack optical sensors. Adv. Mater. **20**, 4079–4084 (2008)
45. N. Hidalgo, M.E. Calvo, M.G. Bellino, G.J.A.A. Soler-Illia, H. Míguez, Porous supramolecularly templated optical resonators built in 1D photonic crystals. Adv. Funct. Mater. **21**, 2534–2540 (2011)
46. S. Colodrero, M. Ocaña, H. Míguez, Nanoparticle-based one-dimensional photonic crystals. Langmuir **24**, 4430–4434 (2008)

47. M.E. Calvo, O. Sánchez-Sobrado, S. Colodrero, H. Míguez, Control over the structural and optical features of nanoparticle-based one-dimensional photonic crystals. Langmuir **25**, 2443–2448 (2009)
48. J.B. Han, Y.B. Dou, M. Wei, D.G. Evans, X. Duan, Tunable/switchable one-dimensional photonic crystals based on a multilayer architecture of layered double hydroxides and titanium dioxide. RSC Adv. **2**, 10488–10491 (2012)
49. S. Colodrero, A. Forneli, C. López-López, L. Pellejà, H. Míguez, E. Palomares, Efficient transparent thin dye solar cells based on highly porous 1D photonic crystals. Adv. Funct. Mater. **22**, 1303–1310 (2012)
50. C. Yao, J.Y. Ren, C.H. Liu, T. Yin, Y.X. Zhu, L.Q. Ge, Hydrogel improved the response in the titania/graphene oxide one-dimensional photonic crystals. ACS Appl. Mater. Interfaces **6**, 16727–16733 (2014)
51. C. Yao, J. Zhao, H.Q. Ge, J.Y. Ren, T. Yin, Y.X. Zhu, L.Q. Ge, Fabrication of dual sensitive titania (TiO_2)/graphene oxide (GO)one-dimensional photonic crystals (1DPCs). Colloids Surf. A: Physicochem. Eng. Aspects **452**, 89–94 (2014)
52. H. Yabu, T. Nakanishi, Y. Hiraia, M. Shimomuraacd, Black thin layers generate strong structural colors: a biomimetic approach for creating one-dimensional (1D) photonic crystals. J. Mater. Chem. **21**, 15154–15156 (2011)
53. C.H. Liu, C. Yao, Y.X. Zhu, J.Y. Ren, K. Lan, H. Peng, L.Q. Ge, Patterned one-dimensional photonic crystals with acidic/alkali vapor responsivity. RSC Adv. **4**, 27281–27285 (2014)
54. Z.H. Wang, J.H. Zhang, J. Xie, C. Li, Y.F. Li, S. Liang, Z.C. Tian, T.Q. Wang, H. Zhang, H. B. Li, W.Q. Xu, B. Yang, Bioinspired water-vapor-responsive organic/inorganic hybrid one-dimensional photonic crystals with tunable full-color stop band. Adv. Funct. Mater. **20**, 3784–3790 (2010)
55. Z.H. Wang, J.H. Zhang, Z.C. Tian, Z.Y. Wang, Y.F. Li, S. Liang, L.Y. Cui, L. Zhang, H. Zhang, B. Yang, Organic–inorganic hybrid photonic hydrogels as a colorful platform for visual detection of SCN^-. Chem. Commun. **46**, 8636–8638 (2010)
56. Z.H. Wang, J.H. Zhang, J.X. Li, J. Xie, Y.F. Li, S. Liang, Z.C. Tian, C. Li, Z.Y. Wang, T.Q. Wang, H. Zhang, B. Yang, Colorful detection of organic solvents based on responsive organic/inorganic hybrid one-dimensional photonic crystals. J. Mater. Chem. **21**, 1264–1270 (2011)
57. Z.H. Wang, J.H. Zhang, J. Xie, Y.S. Yin, Z.Y. Wang, H.Z. Shen, Y.F. Li, J.X. Li, S. Liang, L.Y. Cui, L. Zhang, H. Zhang, B. Yang, Patterning organic/inorganic hybrid Bragg stacks by integrating one-dimensional photonic crystals and macrocavities through photolithography: toward tunable colorful patterns as highly selective sensors. ACS Appl. Mater. Interfaces **4**, 1397–1403 (2012)
58. Z.Y. Wang, J.H. Zhang, Z.H. Wang, H.Z. Shen, J. Xie, Y.F. Li, L. Lin, B. Yang, Biochemical-to-optical signal transduction by pH sensitive organic–inorganic hybrid Bragg stacks with a full color display. J. Mater. Chem. C **1**, 977–983 (2013)
59. D.P. Puzzo, F. Scotognella, M. Zavelani-Rossi, M. Sebastian, A.J. Lough, I. Manners, G. Lanzani, R. Tubino, G.A. Ozin, Distributed feedback lasing from a composite poly (phenylene vinylene)-nanoparticle one-dimensional photonic crystal. Nano Lett. **9**, 4273–4278 (2009)
60. U. Grüning, V. Lehmann, C.M. Engelhardt, Two-dimensional infrared photonic band gap structure based on porous silicon. Appl. Phys. Lett. **66**, 3254–3256 (1995)
61. T.F. Krauss, R.M. De La Rue, S. Brand, Two-dimensional photonic-bandgap structures operating at near-infrared wavelengths. Nature **383**, 699–702 (1996)
62. J.Y. Park, J.H. Park, E. Kim, C.W. Ahn, H.I. Jang, J.A. Rogers, S. Jeon, Conformable solid-index phase masks composed of high-aspect-ratio micropillar arrays and their application to 3D nanopatterning. Adv. Mater. **23**, 860–864 (2011)
63. V. Stelmakh, V. Rinnerbauer, R.D. Geil, P.R. Aimone, J.J. Senkevich, J.D. Joannopoulos, M. Soljačić, I. Celanovic, High-temperature tantalum tungsten alloy photonic crystals: stability, optical properties, and fabrication. Appl. Phys. Lett. **103**, 123903 (2013)

64. I. Roland, Y. Zeng, Z. Han, X. Checoury, C. Blin, M.E. Kurdi, A. Ghrib, S. Sauvage, B. Gayral, C. Brimont, T. Guillet, F. Semond, P. Boucaud, Near-infrared gallium nitride two-dimensional photonic crystal platform on silicon. Appl. Phys. Lett. **105**, 011104 (2014)
65. M.N. Hossain, J. Justice, P. Lovera, B. McCarthy, A. O'Riordan, B. Corbett, High aspect ratio nano-fabrication of photonic crystal structures on glass wafers using chrome as hard mask. Nanotechnology **25**, 355301 (2014)
66. G. Calusine, A. Politi, D.D. Awschalom, Silicon carbide photonic crystal cavities with integrated color centers. Appl. Phys. Lett. **105**, 011123 (2014)
67. N. Shimamoto, Y. Tanaka, H. Mitomo, R. Kawamura, K. Ijiro, K. Sasaki, Y. Osada, Nanopattern fabrication of gold on hydrogels and application to tunable photonic crystal. Adv. Mater. **24**, 5243–5248 (2012)
68. C.J. Lewins, E.D. Le Boulbar, S.M. Lis, P.R. Edwards, R.W. Martin, P.A. Shields, D.W.E. Allsopp, Strong photonic crystal behavior in regular arrays of core-shell and quantum disc InGaN/GaN nanorod light-emitting diodes. J. Appl. Phys. **116**, 044305 (2014)
69. J.H. Zhang, Y.F. Li, X.M. Zhang, B. Yang, Colloidal self-assembly meets nanofabrication: from two-dimensional colloidal crystals to nanostructure arrays. Adv. Mater. **22**, 4249–4269 (2010)
70. Y.F. Li, J.H. Zhang, B. Yang, Antireflective surfaces based on biomimetic nanopillared arrays. Nano Today **5**, 117–127 (2010)
71. Y.F. Li, J.H. Zhang, W.D. Liu, D.W. Li, L.P. Fang, H.C. Sun, B. Yang, Hierarchical polymer brush nanoarrays: a versatile way to prepare multiscale patterns of proteins. ACS Appl. Mater. Interfaces **5**, 2126–2132 (2013)
72. W.D. Liu, Y.F. Li, B. Yang, Fabrication and applications of the protein patterns. Sci. China Chem. **56**, 1087–1100 (2013)
73. W.D. Liu, Y.F. Li, T.Q. Wang, D.W. Li, L.P. Fang, S.J. Zhu, H.Z. Shen, J.H. Zhang, H.C. Sun, B. Yang, Elliptical polymer brush ring array mediated protein patterning and cell adhesion on patterned protein surfaces. ACS Appl. Mater. Interfaces **5**, 12587–12593 (2013)
74. W.D. Liu, X.Y. Liu, J.Z. Fangteng, S.L. Wang, L.P. Fang, H.Z. Shen, S.Y. Xiang, H.C. Sun, B. Yang, Bioinspired polyethylene terephthalate nanocone arrays with underwater superoleophobicity and anti-bioadhesion properties. Nanoscale **6**, 13845–13853 (2014)
75. G. Zhang, D.Y. Wang, Colloidal lithography-the art of nanochemical patterning. Chem. Asian J. **4**, 236–245 (2009)
76. M. López-García, J.F. Galisteo-López, Á. Blanco, C. López, A. García-Martín, High degree of optical tunability of self-assembled photonic-plasmonic crystals by filling fraction modification. Adv. Funct. Mater. **20**, 4338–4343 (2010)
77. S. Ahn, H. Kim, H. Jeon, J.R. Oh, Y.R. Do, H.J. Kim, Two-dimensional hexagonal lattice photonic crystal band-edge laser patterned by nanosphere lithography. Appl. Phys. Express **5**, 042102 (2012)
78. Y.F. Li, J.H. Zhang, S.J. Zhu, H.P. Dong, F. Jia, Z.H. Wang, Z.Q. Sun, L. Zhang, Y. Li, H. B. Li, W.Q. Xu, B. Yang, Biomimetic surfaces for high-performance optics. Adv. Mater. **21**, 4731–4734 (2009)
79. Y.F. Li, J.H. Zhang, L.P. Fang, T.Q. Wang, S.J. Zhu, Y. Li, Z.H. Wang, L. Zhang, L.Y. Cui, B. Yang, Fabrication of silicon/polymer composite nanopost arrays and their sensing applications. Small **7**, 2769–2774 (2011)
80. T.Q. Wang, X. Li, J.H. Zhang, Z.Y. Ren, X.M. Zhang, X. Zhang, D.F. Zhu, Z.H. Wang, F. Han, X.Z. Wang, B. Yang, Morphology-controlled two-dimensional elliptical hemisphere arrays fabricated by a colloidal crystal based micromolding method. J. Mater. Chem. **20**, 152–158 (2010)
81. X.M. Zhang, S.S. Ye, X. Zhang, Z.B. Li, S. Wu, J.H. Zhang, T.Q. Wang, B. Yang, Panchromatic plasmonic color patterns: from embedded Ag nanohole arrays to elevated Ag nanohole arrays. J. Mater. Chem. C **1**, 933–940 (2013)
82. B. Ai, Y. Yu, H. Möhwald, G. Zhang, Responsive monochromatic color display based on nanovolcano arrays. Adv. Optical Mater. **1**, 724–731 (2013)

83. B. Ai, Y. Yu, H. Möhwald, L.M. Wang, G. Zhang, Resonant optical transmission through topologically continuous films. ACS Nano **8**, 1566–1575 (2014)
84. B. Ai, L.M. Wang, H. Möhwald, Y. Yu, G. Zhang, Asymmetric half-cone/nanohole array films with structural and directional reshaping of extraordinary optical transmission. Nanoscale **6**, 8997–9005 (2014)
85. X. Li, T.Q. Wang, J.H. Zhang, X. Yan, X.M. Zhang, D.F. Zhu, W. Li, X. Zhang, B. Yang, Modulating two-dimensional non-close-packed colloidal crystal arrays by deformable soft lithography. Langmuir **26**, 2930–2936 (2010)
86. M.H. Kim, S.H. Im, O.O. Park, Fabrication and structural analysis of binary colloidal crystals with two-dimensional superlattices. Adv. Mater. **17**, 2501–2505 (2005)
87. X. Zhang, J.H. Zhang, D.F. Zhu, X. Li, X.M. Zhang, T.Q. Wang, B. Yang, A universal approach to fabricate ordered colloidal crystals arrays based on electrostatic self-assembly. Langmuir **26**, 17936–17942 (2010)
88. Z.Q. Sun, Y.F. Li, Y.F. Wang, X. Chen, J.H. Zhang, K. Zhang, Z.F. Wang, C.X. Bao, J.B. Zeng, B. Zhao, B. Yang, Three-dimensional colloidal crystal-assisted lithography for two-dimensional patterned arrays. Langmuir **23**, 10725–10731 (2007)
89. J.T. Zhang, L.L. Wang, J. Luo, A. Tikhonov, N. Kornienko, S.A. Asher, 2-D array photonic crystal sensing motif. J. Am. Chem. Soc. **133**, 9152–9155 (2011)
90. Y. Huang, J.M. Zhou, B. Su, L. Shi, J.X. Wang, S.R. Chen, L.B. Wang, J. Zi, Y.L. Song, L. Jiang, Colloidal photonic crystals with narrow stopbands assembled from low-adhesive superhydrophobic substrates. J. Am. Chem. Soc. **134**, 17053–17058 (2012)
91. J.T. Zhang, X. Chao, S.A. Asher, Asymmetric free-standing 2-D photonic crystal films and their janus particles. J. Mater. Chem. C **1**, 6099–6102 (2013)
92. H.C. Gu, Y.J. Zhao, Y. Cheng, Z.Y. Xie, F. Rong, J.Q. Li, B.Q. Wang, D.G. Fu, Z.Z. Gu, Tailoring colloidal photonic crystals with wide viewing angles. Small **9**, 2266–2271 (2013)
93. Y. Hong, Y. Qiu, T.H. Chen, B.M. Reinhard, Rational assembly of optoplasmonic hetero-nanoparticle arrays with tunable photonic–plasmonic resonances. Adv. Funct. Mater. **24**, 739–746 (2014)
94. J. Zhang, L.T. Ling, C.F. Wang, S. Chen, L. Chen, D.Y. Son, Versatile dendrimer-derived nanocrystal microreactors towards fluorescence colloidal photonic crystals. J. Mater. Chem. C **2**, 3610–3616 (2014)
95. S. Noda, K. Tomoda, N. Yamamoto, A. Chutinan, Full three-dimensional photonic bandgap crystals at near-infrared wavelengths. Science **289**, 604–606 (2000)
96. T. Ergin, N. Stenger, P. Brenner, J.B. Pendry, M. Wegener, Three-dimensional invisibility cloak at optical wavelengths. Science **328**, 337–339 (2010)
97. G.M. Gratson, F. García-Santamaría, V. Lousse, M.J. Xu, S.H. Fan, J.A. Lewis, P.V. Braun, Dilithioplumbole: a lead-bearing aromatic cyclopentadienyl analog. Adv. Mater. **18**, 461–465 (2006)
98. J.H. Lee, Y.S. Kim, K. Constant, K.M. Ho, Woodpile metallic photonic crystals fabricated by using soft lithography for tailored thermal emission. Adv. Mater. **19**, 791–794 (2007)
99. J.A. Lewis, Direct ink writing of 3D functional materials. Adv. Funct. Mater. **16**, 2193–2204 (2006)
100. A. Frölich, J. Fischer, T. Zebrowski, K. Busch, M. Wegener, Titania woodpiles with complete three-dimensional photonic bandgaps in the visible. Adv. Mater. **25**, 3588–3592 (2013)
101. S. Takahashi, K. Suzuki, M. Okano, M. Imada, T. Nakamori, Y. Ota, K. Ishizaki, S. Noda, Direct creation of three-dimensional photonic crystals by a top-down approach. Nat. Mater. **8**, 721–725 (2009)
102. G. Subramania, Y.L. Lee, A.J. Fischer, Silicon-based near-visible logpile photonic crystal. Adv. Mater. **22**, 4180–4185 (2010)
103. N. Vasilantonakis, K. Terzaki, I. Sakellari, V. Purlys, D. Gray, C.M. Soukoulis, M. Vamvakaki, M. Kafesaki, M. Farsari, Three-dimensional metallic photonic crystals with optical bandgaps. Adv. Mater. **24**, 1101–1105 (2012)

104. S.G. Park, S.M. Yang, Multicolor patterning using holographic woodpile photonic crystals at visible wavelengths. Nanoscale **5**, 4110–4113 (2013)
105. M.R. Beaulieu, N.R. Hendricks, J.J. Watkins, Large-area printing of optical gratings and 3D photonic crystals using solution-processable nanoparticle/polymer composites. ACS Photonics **1**, 799–805 (2014)
106. S.H. Park, B. Gates, Y.N. Xia, A three-dimensional photonic crystal operating in the visible region. Adv. Mater. **11**, 462–466 (1999)
107. Q.F. Yan, A. Chen, S.J. Chua, X.S. Zhao, Incorporation of point defects into self-assembled three-dimensional colloidal crystals. Adv. Mater. **17**, 2849–2853 (2005)
108. U. Jeong, Y.N. Xia, Photonic crystals with thermally switchable stop bands fabricated from Se@Ag_2Se spherical colloids. Angew. Chem. Int. Ed. **44**, 3099–3103 (2005)
109. J. Scrimgeour, D.N. Sharp, C.F. Blanford, O.M. Roche, R.G. Denning, A.J. Turberfield, Three-dimensional optical lithography for photonic microstructures. Adv. Mater. **18**, 1557–1560 (2006)
110. Y.L. Wang, M. Ibisate, Z.Y. Li, Y.N. Xia, Metallodielectric photonic crystals assembled from monodisperse spherical colloids of bismuth and lead. Adv. Mater. **1**(8), 471–476 (2006)
111. R. Pozas, A. Mihi, M. Ocaña, H. Míguez, Building nanocrystalline planar defects within self-assembled photonic crystals by spin-coating. Adv. Mater. **1**(8), 1183–1187 (2006)
112. J.H. Ye, R. Zentel, S. Arpiainen, J. Ahopelto, F. Jonsson, S.G. Romanov, C.M. Sotomayor Torres, Integration of self-assembled three-dimensional photonic crystals onto structured silicon wafers. Langmuir **22**, 7378–7383 (2006)
113. E. Vekris, V. Kitaev, D.D. Perovic, J.S. Aitchison, G.A. Ozin, Visualization of stacking faults and their formation in colloidal photonic crystal films. Adv. Mater. **20**, 1110–1116 (2008)
114. Z.Y. Zhiyu Ren, X.M. Xuemin Zhang, J.H. Junhu Zhang, Li X. Xiao, X.Q. Xiaqian Pan, Fei X. Xu, Z.C. Zhanchen Cui, B. Yang, Assembly of non-close-packed 3D colloidal crystals from 2D ones in a polymer matrix via in situ layer-by-layer photopolymerization. J. Mater. Chem. **18**, 3536–3538 (2008)
115. W. Sun, F. Jia, Z.Q. Sun, J.H. Zhang, Y. Li, X. Zhang, B. Yang, Manipulation of cracks in three-dimensional colloidal crystal films via recognition of surface energy patterns: an approach to regulating crack patterns and shaping microcrystals. Langmuir **27**, 8018–8026 (2011)
116. H.S. Lee, T.S. Shim, H. Hwang, S.M. Yang, S.H. Kim, Colloidal photonic crystals toward structural color palettes for security materials. Chem. Mater. **25**, 2684–2690 (2013)
117. M.Y. Han, C.J. Heo, H. Shim, C.G. Shin, S.J. Lim, J.W. Kim, Y.W. Jin, S. Lee, Structural color manipulation using tunable photonic crystals with enhanced switching reliability. Adv. Optical Mater. **2**, 535–541 (2014)
118. A.C. Arsenault, D.P. Puzzo, I. Manners, G.A. Ozin, Photonic-crystal full-colour displays. Nat. Photonics **1**, 468–472 (2007)
119. K. Hwang, D. Kwak, C. Kang, D. Kim, Y. Ahn, Y. Kang, Electrically tunable hysteretic photonic gels for nonvolatile display pixels. Angew. Chem. Int. Ed. **50**, 6311–6314 (2011)
120. J. Huang, C.A. Tao, Q. An, W.X. Zhang, Y.G. Wu, X.S. Li, D.Z. Shen, G.T. Li, 3D-ordered macroporous poly(ionic liquid) films as multifunctional materials. Chem. Commun. **46**, 967–969 (2010)
121. C. Ma, Y.N. Jiang, X.D. Yang, C.X. Wang, H. Li, F.X. Dong, B. Yang, K. Yu, Q. Lin, Centrifugation-induced water-tunable photonic colloidal crystals with narrow diffraction bandwidth and highly sensitive detection of SCN^-. ACS Appl. Mater. Interfaces **5**, 1990–1996 (2013)
122. T. Ding, L. Luo, H. Wang, L. Chen, K. Liang, K. Clays, K. Song, G.Q. Yang, C.H. Tung, Patterning and pixelation of colloidal photonic crystals for addressable integrated photonics. J. Mater. Chem. **21**, 11330–11334 (2011)
123. J.R. Oh, J.H. Moon, S. Yoon, C.R. Park, Y.R. Do, Fabrication of wafer-scale polystyrene photonic crystal multilayers via the layer-by-layer scooping transfer technique. J. Mater. Chem. **21**, 14167–14172 (2011)

124. H.B. Ding, Y. Cheng, H.C. Gu, Y.J. Zhao, B.P. Wang, Z.Z. Gu, Tunable fiber Bragg grating based on responsive photonic crystals. Nanoscale **5**, 11572–11576 (2013)
125. X.M. Liu, D.B. Zhao, C. Geng, L.J. Zhang, T.Y. Tan, M.Z. Hu, Q.F. Yan, Fabrication of colloidal photonic crystal heterostructures free of interface imperfection based on solvent vapor annealing. J. Colloid Interface Sci. **434**, 98–103 (2014)
126. F. Zeng, C.Y. Sun Wang, B.Y. Ren, X.X. Liu, Z. Tong, Fabrication of inverse opal via ordered highly charged colloidal spheres. Langmuir **18**, 9116–9120 (2002)
127. M. Deutsch, Y.A. Vlasov, D.J. Norris, Conjugated-polymer photonic crystals. Adv. Mater. **12**, 1176–1180 (2000)
128. H. Míguez, F. Meseguer, C. López, F. López-Tejeira, J. Sμnchez-Dehesa, Synthesis and photonic band gap characterization of polymer inverse opals. Adv. Mater. **13**, 393–396 (2001)
129. J.S. King, D.P. Gaillot, E. Graugnard, C.J. Summers, Conformally back-filled, non-close-packed inverse-opal photonic crystals. Adv. Mater. **1**(8), 1063–1067 (2006)
130. E. Vekris, G.A. Ozin, V. Kitaev, Curling colloidal photonic crystals. Adv. Mater. **1**(8), 2481–2485 (2006)
131. T. Ruhl, P. Spahn, C. Hermann, C. Jamois, O. Hess, Double-inverse-opal photonic crystals: the route to photonic band gap switching. Adv. Funct. Mater. **16**, 885–890 (2006)
132. S.K. Lee, G.R. Yi, J.H. Moon, S.M. Yang, D.J. Pine, Pixellated photonic crystal films by selective photopolymerization. Adv. Mater. **1**(8), 2111–2116 (2006)
133. E. Graugnard, J.S. King, D.P. Gaillot, C.J. Summers, Sacrificial-layer atomic layer deposition for fabrication of non-close-packed inverse-opal photonic crystals. Adv. Funct. Mater. **16**, 1187–1196 (2006)
134. Z.M. Chen, T. Gang, Y.F. Wang, X. Chen, C. Guan, J.H. Zhang, Z.Q. Sun, K. Zhang, B. Zhao, B. Yang, A simple method of preparing Ag nanoparticles coated silica colloidal crystals and polymer-Ag nanoparticles composite macroporous films. Colloids and Surfaces A: Physicochem. Eng. Aspects **277**, 37–43 (2006)
135. J.C. Hong, J.H. Park, C. Chun, D.Y. Kim, Photoinduced tuning of optical stop bands in azopolymer based inverse opal photonic crystals. Adv. Funct. Mater. **17**, 2462–2469 (2007)
136. Z.Y. Xie, L.G. Sun, G.Z. Han, Z.Z. Gu, Optical switching of a birefringent photonic crystal. Adv. Mater. **20**, 3601–3604 (2008)
137. H. Migurz, S.M. Yang, N. Tetreault, G.A. Ozin, Oriented free-standing three-dimensional silicon inverted colloidal photonic crystal microribers. Adv. Mater. **14**, 1805–1808 (2002)
138. S. Kim, A.N. Mitropoulos, J.D. Spitzberg, H. Tao, D.L. Kaplan, F.G. Omenetto, Silk inverse opals. Nat. Photonics **6**, 817–822 (2012)
139. A. Kevin, Arpin K.A., D. Mark, M.D. Losego, N. Andrew, A.N. Cloud, H.L. Hailong Ning, J. Justin Mallek, P. Nicholas, N.P. Sergeant, L.X. Linxiao Zhu, Z.F. Zongfu Yu, B. Berc¸ Kalanyan, G.N. Parsons, G.S. Girolami, J.R. Abelson, S.H. Fan, P.V. Braun. Three-dimensional self-assembled photonic crystals with high temperature stability for thermal emission modification. Nat. Commun. **4** (2013), in press. doi:10.1038/ncomms3630
140. F. Jia, W. Sun, J.H. Zhang, Y.F. Li, B. Yang, A facile approach to fabricate three-dimensional ordered macroporous rutile titania at low calcination temperature. J. Mater. Chem. **22**, 2435–2441 (2012)
141. L. Mishchenko, B. Hatton, M. Kolle, J. Aizenberg, Patterning hierarchy in direct and inverse opal crystals. Small **8**, 1904–1911 (2012)
142. M. Retsch, U. Jonas, Hierarchically structured, double-periodic inverse composite opals. Adv. Funct. Mater. **23**, 5381–5389 (2013)
143. J.W. Galusha, L.R. Richey, M.R. Jorgensen, J.S. Gardner, M.H. Bartl, Study of natural photonic crystals in beetle scales and their conversion into inorganic structures via a sol–gel bio-templating route. J. Mater. Chem. **20**, 1277–1284 (2010)
144. Z.B. Zhang, W.Z. Shen, C.Q. Ye, Y.M. Luo, S.H. Li, M.Z. Li, C.H. Xu, Y.L. Song, Large-area, crack-free polysilazane-based photonic crystals. J. Mater. Chem. **22**, 5300–5303 (2012)

145. S.G. Meng, D.Z. Li, P. Wang, X.Z. Zheng, J.X. Wang, J. Chen, J.L. Fang, X.Z. Fu, Probing photonic effect on photocatalytic degradation of dyes based on 3D inverse opal ZnO photonic crystal. RSC Adv. **3**, 17021–17028 (2013)
146. M. Hermatschweiler, A. Ledermann, G.A. Ozin, M. Wegener, G.V. Freymann, Fabrication of silicon inverse woodpile photonic crystals. Adv. Funct. Mater. **17**, 2273–2277 (2007)
147. S.G. Park, M. Miyake, S.M. Yang, P.V. Braun, Cu_2O inverse woodpile photonic crystals by prism holographic lithography and electrodeposition. Adv. Mater. **23**, 2749–2752 (2011)
148. J.M. Van den Broek, L.A. Woldering, R.W. Tjerkstra, F.B. Segerink, I.D. Setija, W.L. Vos, Inverse-woodpile photonic band gap crystals with a cubic diamond-like structure made from single-crystalline silicon. Adv. Funct. Mater. **22**, 25–31 (2012)
149. A. Vlad, A. Frölich, T. Zebrowski, C.A. Dutu, K. Busch, S. Melinte, M. Wegener, I. Huynen, Direct transcription of two-dimensional colloidal crystal arrays into three-dimensional photonic crystals. Adv. Funct. Mater. **23**, 1164–1171 (2013)
150. M.H. Klühr, A. Sauermann, C.A. Elsner, K.H. Thein, S.K. Dertinger, Partially oxidized macroporous silicon: a three-dimensional photonic matrix for microarray applications. Adv. Mater. **1**(8), 3135–3139 (2006)
151. M. Fu, K. Chaudhary, J.G. Lange, H.S. Kim, J.J. Juarez, J.A. Lewis, P.V. Braun, Anisotropic colloidal templating of 3D ceramic, semiconducting, metallic, and polymeric architectures. Adv. Mater. **26**, 1740–1745 (2014)
152. M. Campbell, D.N. Sharp, M.T. Harrison, R.G. Denning, A.J. Turberfield, Fabrication of photonic crystals for the visible spectrum by holographic lithography. Nature **404**, 53–56 (2000)
153. J.H. Kang, J.H. Moon, S.K. Lee, S.G. Park, S.G. Jang, S. Yang, S.M. Yang, Thermo responsive hydrogel photonic crystals by three-dimensional holographic lithography. Adv. Mater. **20**, 3061–3065 (2008)
154. M. Miyake, Y.C. Chen, P.V. Braun, P. Wiltzius, Fabrication of three-dimensional photonic crystals using multibeam interference lithography and electrodeposition. Adv. Mater. **21**, 3012–3015 (2009)
155. J. Li, G.Q. Liang, X.L. Zhu, S. Yang, Exploiting nanoroughness on holographically patterned three-dimensional photonic crystals. Adv. Funct. Mater. **22**, 2980–2986 (2012)
156. M. Kolle, P.M. Salgard-Cunha, M.R.J. Scherer, F.M. Huang, P. Vukusic, S. Mahajan, J. J. Baumberg, U. Steiner, Mimicking the colourful wing scale structure of the Papilio blumei butterfly. Nat. Nanotechnol. **5**, 511–515 (2010)
157. X. Wu, A. Erbe, D. Raabe, H.O. Fabritius, Extreme optical properties tuned through phase substitution in a structurally optimized biological photonic polycrystal. Adv. Funct. Mater. **23**, 3615–3620 (2013)
158. S.M. Zhu, D. Zhang, Z.X. Chen, J.J. Gu, W.F. Li, H.B. Jiang, G. Zhou, A simple and effective approach towards biomimetic replication of photonic structures from butterfly wings. Nanotechnology **20**, 315303 (2009)
159. M.R. Weatherspoon, Y. Cai, M. Crne, M. Srinivasarao, K.H. Sandhage, 3D rutile titania-based structures with morpho butterfly wing scale morphologies. Angew. Chem. In. Ed. **47**, 7921–7923 (2008)
160. Y.W. Tan, J.J. Gu, X.N. Zang, W. Xu, K.C. Shi, L.H. Xu, D. Zhang, Versatile fabrication of intact three-dimensional metallic butterfly wing scales with hierarchical sub-micrometer structures. Angew. Chem. Int. Ed. **50**, 8307–8311 (2011)
161. Y. Chen, J.J. Gu, D. Zhang, S.M. Zhu, H.L. Su, X.B. Hu, C.L. Feng, W. Zhang, Q.L. Liu, A. R. Parker, Tunable three-dimensional ZrO_2 photonic crystals replicated from single butterfly wing scales. J. Mater. Chem. **21**, 15237–15243 (2011)
162. Q.Q. Yang, S.M. Zhu, W.H. Peng, C. Yin, W.L. Wang, J.J. Gu, W. Zhang, J. Ma, T. Deng, C.L. Feng, D. Zhang, Bioinspired fabrication of hierarchically structured, ph-tunable photonic crystals with unique transition. ACS Nano **7**, 4911–4918 (2013)
163. C. Mille, E.C. Tyrode, R.W. Corkery, 3D titania photonic crystals replicated from gyroid structures in butterfly wing scales: approaching full band gaps at visible wavelengths. RSC Adv. **3**, 3109–3117 (2013)

164. M.D. Turner, M. Saba, Q.M. Zhang, B.P. Cumming, G.E. Schröder-Turk, M. Gu, Miniature chiral beamsplitter based on gyroid photonic crystals. Nat. Photonics **7**, 801–805 (2013)
165. C. Mille, E.C. Tyrode, R.W. Corkery, Inorganic chiral 3-D photonic crystals with bicontinuous gyroid structure replicated from butterfly wing scales. Chem. Commun. **47**, 9873–9875 (2011)
166. Y. Lu, Y.D. Yin, Y.N. Xia, Three-dimensional photonic crystals with non-spherical colloids as building blocks. Adv. Mater. **13**, 415–420 (2001)
167. K.K. Seet, V. Mizeikis, S. Matsuo, S. Juodkazis, H. Misawa, Three-dimensional spiral-architecture photonic crystals obtained by direct laser writing. Adv. Mater. **17**, 541–545 (2005)
168. M. Thiel, M. Decker, M. Deubel, M. Wegener, S. Linden, G.V. Freymann, Polarization stop bands in chiral polymeric three-dimensional photonic crystals. Adv. Mater. **1**(9), 207–210 (2007)
169. M. Thiel, M.S. Rill, G.V. Freymann, M. Wegener, Three-dimensional bi-chiral photonic crystals. Adv. Mater. **21**, 4680–4682 (2009)
170. R. Scott, S.R. Kennedy, M.J. Brett, Fabrication of tetragonal square spiral photonic crystals. Nano Lett. **2**, 59–62 (2002)
171. S.H. Kim, W.C. Jeong, H. Hwang, S.M. Yang, Robust chirped photonic crystals created by controlled colloidal diffusion. Angew. Chem. Int. Ed. **50**, 11649–11653 (2011)
172. N. Liu, H.C. Guo, L.W. Fu, S. Kaiser, H. Schweizer, H. Giessen, Three-dimensional photonic metamaterials at optical frequencies. Nat. Mater. **7**, 31–37 (2008)
173. P.H. Fu, G.J. Lin, H.P. Wang, K.Y. Lai, J.H. He, Enhanced lightextractionoflight-emitting diodes via nano-honeycomb photonic crystals. Nano Energy **8**, 78–83 (2014)
174. A. David, H. Benisty, C. Weisbuch, Optimization of light-diffracting photonic-crystals for high extraction efficiency LEDs. J. Disp. Technol. **3**, 133–148 (2007)
175. S.H. Kim, K.D. Lee, J.Y. Kim, M.K. Kwon, S.J. Park, Fabrication of photonic crystal structures on light emitting diodes by nanoimprint lithography. Nanotechnology **18**, 055306 (2007)
176. F. Li, X. Li, J.H. Zhang, B. Yang, Enhanced light extraction from organic light-emitting devices by using microcontact printed silica colloidal crystals. Org. Electron. **8**, 635–639 (2007)
177. Y.H. Zhang, T.B. Wei, Z. Xiong, L. Shang, Y.D. Tian, Y. Zhao, P.Y. Zhou, J.X. Wang, J.M. Li, Enhanced optical power of GaN-based light-emitting diode with compound photonic crystals by multiple-exposure nanosphere-lens lithography. Appl. Phys. Lett. **105**, 013108 (2014)
178. Y.F. Cheung, K.H. Li, R.S.Y. Hui, H.W. Choi, Observation of enhanced visible and infrared emissions in photonic crystal thin-film light-emitting diodes. Appl. Phys. Lett. **105**, 071104 (2014)
179. K. Wu, T.B. Wei, D. Lan, H.Y. Zheng, J.X. Wang, Y. Luo, J.M. Li, Large-scale SiO_2 photonic crystal for high efficiency GaN LEDs by nanospherical-lens lithography. Chin. Phys. B **23**, 028504 (2014)
180. A.T. Exner, I. Pavlichenko, D. Baierl, M. Schmidt, G. Derondeau, B.V. Lotsch, P. Lugli, G. Scarpa, A step towards the electrophotonic nose: integrating 1D photonic crystals with organic light-emitting diodes and photodetectors. Laser Photonics Rev. **8**, 726–733 (2014)
181. Y.F. Li, F. Li, J.H. Zhang, C.L. Wang, S.J. Zhu, H.J. Yu, Z.H. Wang, B. Yang, Improved light extraction efficiency of white organic light-emitting devices by biomimetic antireflective surfaces. Appl. Phys. Lett. **96**, 153305 (2010)
182. J.H. Hyun, H.K. Lee, S.S. Oh, O. Hess, C.G. Choi, S.H. Im, O.O. Park, Two-dimensional TiO_2 inverse opal with a closed top surface structure for enhanced light extraction from polymer light-emitting diodes. Adv. Mater. **23**, 1846–1850 (2011)
183. P.B. Clapham, M.C. Hutley, Reduction of lens reflexion by the "Moth Eye" principle. Nature **244**, 281–282 (1973)
184. S.J. Wilson, M.C. Hutley, The optical properties of 'Moth Eye' antireflection surfaces. Opt. Acta **29**, 993–1009 (1982)

185. H. Kikuta, H. Toyota, W.J. Yu, Optical elements with subwavelength structured surfaces. Opt. Rev. **10**, 63–73 (2003)
186. Y.F. Huang, S. Chattopadhyay, Y.J. Jen, C.Y. Peng, T.A. Liu, Y.K. Hsu, C.L. Pan, H.C. Lo, C.H. Hsu, Y.H. Chang, C.S. Lee, K.H. Chen, L.C. Chen, Improved broadband and quasi-omnidirectional anti-reflection properties with biomimetic silicon nanostructures. Nat. Nanotechnol. **2**, 770–774 (2007)
187. W.L. Min, B. Jiang, P. Jiang, Bioinspired self-cleaning antireflection coatings. Adv. Mater. **20**, 3914–3918 (2008)
188. J.W. Ha, I.J. Park, S.B. Lee, Antireflection surfaces prepared from fluorinated latex particles. Macromolecules **41**, 8800–8806 (2008)
189. Y.F. Li, J.H. Zhang, S.J. Zhu, H.P. Dong, Z.H. Wang, Z.Q. Sun, J.R. Guo, B. Yang, Bioinspired silicon hollow-tip arrays for high performance broadband anti-reflective and water-repellent coatings. J. Mater. Chem. **19**, 1806–1810 (2009)
190. Y.F. Li, J.H. Zhang, S.J. Zhu, H.P. Dong, F. Jia, Z.H. Wang, Y. Tang, L. Zhang, S.Y. Zhang, B. Yang, Bioinspired silica surfaces with near-infrared improved transmittance and superhydrophobicity by colloidal lithography. Langmuir **26**, 9842–9847 (2010)
191. P.C. Mathias, N. Ganesh, L.L. Chan, B.T. Cunningham, Combined enhanced fluorescence and label-free biomolecular detection with a photonic crystal surface. Appl. Opt. **46**, 2351–2360 (2007)
192. N. Ganesh, W. Zhang, P.C. Mathias, E. Chow, J.A.N.T. Soares, V. Malyarchuk, A.D. Smith, B.T. Cunningham, Enhanced fluorescence emission from quantum dots on a photonic crystal surface. Nat. Nanotechnol. **2**, 515–520 (2007)
193. N. Ganesh, P.C. Mathias, W. Zhang, B.T. Cunningham, Distance dependence of fluorescence enhancement from photonic crystal surfaces. J. Appl. Phys. **103**, 083104 (2008)
194. P.C. Mathias, N. Ganesh, W. Zhang, B.T. Cunningham, Graded wavelength one-dimensional photonic crystal reveals spectral characteristics of enhanced fluorescence. J. Appl. Phys. **103**, 094320 (2008)
195. P.C. Mathias, N. Ganesh, B.T. Cunningham, Application of photonic crystal enhanced fluorescence to a cytokine immunoassay. Anal. Chem. **80**, 9013–9020 (2008)
196. H. Li, J.X. Wang, H. Lin, L. Xu, W. Xu, R.M. Wang, Y.L. Song, D.B. Zhu, Amplification of fluorescent contrast by photonic crystals in optical storage. Adv. Mater. **22**, 1237–1241 (2010)
197. L. Fornasari, F. Floris, M. Patrini, G. Canazza, G. Guizzetti, D. Comoretto, F. Marabelli, Fluorescence excitation enhancement by Bloch surface wave in all-polymer onedimensional photonic structure. Appl. Phys. Lett. **105**, 053303 (2014)
198. W.L. Chen, K.D. Long, H. Yu, Y.F. Tan, J.S. Choi, B.A. Harley, B.T. Cunningham, Enhanced live cell imaging via photonic crystal enhanced fluorescence microscopy. Analyst **139**, 5954–5963 (2014)
199. A.C. Arsenault, H. Míguez, V. Kitaev, G.A. Oizn, I. Manners, A polychromic, fast response metallopolymer gel photonic crystal with solvent and redox tunability: a step towards photonic ink (P-Ink). Adv. Mater. **15**, 503–507 (2003)
200. H. Fudouzi, Y.N. Xia, Photonic papers and inks: color writing with colorless materials. Adv. Mater. **15**, 892–896 (2003)
201. P. Jiang, D.W. Smith, J.M. Ballato, S.H. Foulger, Multicolor pattern generation in photonic bandgap composites. Adv. Mater. **17**, 179–184 (2005)
202. J.P. Ge, J. Goebl, L. He, Z.D. Lu, Y.D. Yin, Rewritable photonic paper with hygroscopic salt solution as ink. Adv. Mater. **21**, 4259–4264 (2009)
203. S.H. Lee, N.Y. Ha, Sol–gel substrates with engineered multiple photonic bandgaps for full-color photonic devices. Small **7**, 2704–2708 (2011)
204. X.Q. Wang, C.F. Wang, Z.F. Zhou, S. Chen, Robust mechanochromic elastic one-dimensional photonic hydrogels for touch sensing and flexible displays. Adv. Optical Mater. **2**, 652–662 (2014)

205. Y.F. Yue, T. Kurokawa, M.A. Haque, T. Nakajima, T. Nonoyama, X.F. Li, I. Kajiwara, J. P. Gong. Mechano-actuated ultrafast full-colour switching in layered photonic hydrogels. Nat. Commun. **5** (2014), in press. doi:10.1038/ncomms5659
206. Y.F. Li, J.H. Zhang, T.Q. Wang, S.J. Zhu, H.J. Yu, L.P. Fang, Z.H. Wang, L.Y. Cui, B. Yang, Full color plasmonic nanostructured surfaces and their sensor applications. J. Phys. Chem. C **114**, 19908–19912 (2010)
207. S.Y. Lee, S.H. Kim, H. Hwang, J.Y. Sim, S.M. Yang, Controlled pixelation of inverse opaline structures towards reflection-mode displays. Adv. Mater. **26**, 2391–2397 (2014)
208. A.T. Exner, I. Pavlichenko, B.V. Lotsch, G. Scarpa, P. Lugli, Low-cost thermo-optic imaging sensors: a detection principle based on tunable one-dimensional photonic crystals. ACS Appl. Mater. Interfaces **5**, 1575–1582 (2013)
209. B. Park, J. Provine, A. Gellineau, J. Landry, R.T. Howe, O. Solgaard, Double-layer silicon photonic crystal fiber-tip temperature sensors. IEEE Photonics Technol. Lett. **26**, 900–903 (2014)
210. M.C. Chiappelli, R.C. Hayward, Photonic multilayer sensors from photo-crosslinkable polymer films. Adv. Mater. **24**, 6100–6104 (2012)
211. E.P. Chan, J.J. Walish, A.M. Urbas, E.L. Thomas, Mechanochromic photonic gels. Adv. Mater. **25**, 3934–3947 (2013)
212. Y.F. Zhao, K.Y. Liu, J. McClelland, M. Lu, Enhanced photoacoustic detection using photonic crystal substrate. Appl. Phys. Lett. **104**, 161110 (2014)
213. S.J. Qiu, Q. Liu, F. Xu, Y.Q. Lu, Ampere force based photonic crystal fiber magnetic field sensor. Sens. Actuators, A **210**, 95–98 (2014)
214. X.L. Wang, Q.F. Tan, C.X. Yang, N.G. Lu, G.F. Jin, Photonic crystal refractive index sensing based on sandwich structure. Optik **123**, 2113–2115 (2012)
215. C. Li, B.V. Lotsch, Stimuli-responsive 2D polyelectrolyte photonic crystals for optically encoded pH sensing. Chem. Commun. **48**, 6169–6171 (2012)
216. X.S. Li, L.H. Peng, J.C. Cui, W.N. Li, C.X. Lin, D. Xu, T. Tian, G.X. Zhang, D.Q. Zhang, G.T. Li, Reactive photonic film for label-free and selective sensing of cyanide. Small **8**, 612–618 (2012)
217. M.M.W. Muscatello, S.A. Asher, Poly(vinyl alcohol) rehydratable photonic crystal sensor materials. Adv. Funct. Mater. **18**, 1186–1193 (2008)
218. C. Chen, Y.H. Zhu, H. Bao, X.L. Yang, C.H. Li, Physically controlled cross-linking in gelated crystalline colloidal array photonic crystals. ACS Appl. Mater. Interfaces **2**, 1499–1504 (2010)
219. S. Colodrero, M. Ocanňa, A.R. González-Elipe, H. Mıguez, Response of nanoparticle-based one-dimensional photonic crystals to ambient vapor pressure. Langmuir **24**, 9135–9139 (2008)
220. Y. Chen, W.S. Fegadolli, W.M. Jones, A. Scherer, M. Li, Ultrasensitive gas-phase chemical sensing based on functionalized photonic crystal nanobeam cavities. ACS Nano **8**, 522–527 (2014)
221. W. Hong, Y. Chen, X. Feng, Y. Yan, X.B. Hu, B.Y. Zhao, F. Zhang, D. Zhang, Z. Xu, Y. J. Lai, Full-color CO_2 gas sensing by an inverse opal photonic hydrogel. Chem. Commun. **49**, 8229–8231 (2013)
222. G.H. King, A. Gramada, J.R. Link, M.J. Sailor, Internally referenced ammonia sensor based on an electrochemically prepared porous SiO_2 photonic crystal. Adv. Mater. **19**, 4044–4048 (2007)
223. C.H. Liu, G.Z. Gao, Y.Q. Zhang, L.B. Wang, J.X. Wang, Y.L. Song, The naked-eye detection of NH_3–HCl by polyaniline-infiltrated TiO_2 inverse opal photonic crystals. Macromol. Rapid Commun. **33**, 380–385 (2012)
224. A.M. Ruminski, M.M. Moore, M.J. Sailor, Humidity-compensating sensor for volatile organic compounds using stacked porous silicon photonic crystals. Adv. Funct. Mater. **18**, 3418–3426 (2008)

225. R.A. Potyrailo, H. Ghiradella, A. Vertiatchikh, K. Dovidenko, J.R. Cournoyer, E. Olson, Morpho butterfly wing scales demonstrate highly selective vapour response. Nat. Photonics **1**, 123–128 (2007)
226. L. Bai, Z.Y. Xie, K.D. Cao, XuH ZhaoYJ, C. Zhu, Z.D. Mu, Q.F. Zhong, Z.Z. Gu, Hybrid mesoporous colloid photonic crystal array for high performance vapor sensing. Nanoscale **6**, 5680 (2014)
227. L.D. Bonifacio, G.A. Ozin, A.C. Arsenault, Photonic nose–sensor platform for water and food quality control. Small **7**, 3153–3157 (2011)
228. B.F. Ye, F. Rong, H.C. Gu, Z.Y. Xie, Y.N. Cheng, Y.J. Zhao, Z.Z. Gu, Bioinspired angle-independent photonic crystal colorimetric sensing. Chem. Commun. **49**, 5331–5333 (2013)
229. D. Arunbabu, A. Sannigrahi, T. Jana, Photonic crystal hydrogel material for the sensing of toxic mercury ions (Hg^{2+}) in water. Soft Matter **7**, 2592–2599 (2011)
230. Y.Q. Zhang, X.D. Li, L.J. Gao, J.H. Qiu, L.P. Heng, B.Z. Tang, L. Jiang, Silole-infiltrated photonic crystal films as effective fluorescence sensor for Fe^{3+} and Hg^{2+}. ChemPhysChem **15**, 507–513 (2014)
231. M.C. Fenzl, S. Wilhelm, T. Hirsch, O.S. Wolfbeis, Optical sensing of the ionic strength using photonic crystals in a hydrogel. ACS Appl. Mater. Interfaces **5**, 173–178 (2013)
232. W. Hong, X.B. Hu, B.Y. Zhao, F. Zhang, D. Zhang, Tunable photonic polyelectrolyte colorimetric sensing for anions, cations and zwitterions. Adv. Mater. **22**, 5043–5047 (2010)
233. Y. Huang, F. Li, M. Qin, L. Jiang, Y. Song, A multi-stopband photonic-crystal microchip for high-performance metal-ion recognition based on fluorescent detection. Angew. Chem. Int. Ed. **52**, 7296–7299 (2013)
234. M.M. Hawkeye, M.J. Brett, Optimized colorimetric photonic-crystal humidity sensor fabricated using glancing angle deposition. Adv. Funct. Mater. **21**, 3652–3658 (2011)
235. E.T. Tian, J.X. Wang, Y.M. Zheng, Y.L. Song, L. Jiang, D.B. Zhu, Colorful humidity sensitive photonic crystal hydrogel. J. Mater. Chem. **18**, 1116–1122 (2008)
236. Y.Y. Diao, X.Y. Liu, G.W. Toh, L. Shi, J. Zi, Multiple structural coloring of silk-fibroin photonic crystals and humidity-responsive color sensing. Adv. Funct. Mater. **23**, 5373–5380 (2013)
237. C. Fenzl, T. Hirsch, O.S. Wolfbeis, Photonic crystal based sensor for organic solvents and for solvent-water mixtures. Sensors **12**, 16954–16963 (2012)
238. H. Li, J.X. Wang, Z.L. Pan, L.Y. Cui, L. Xu, R.M. Wang, Y.L. Song, L. Jiang, Amplifying fluorescence sensing based on inverse opal photonic crystal toward trace TNT detection. J. Mater. Chem. **21**, 1730–1735 (2011)
239. H.L. Li, J.X. Wang, L.M. Yang, Y.L. Song, Superoleophilic and superhydrophobic inverse opals for oil sensors. Adv. Funct. Mater. **18**, 3258–3264 (2008)
240. F. Liu, S.Y. Huang, F. Xue, Y.F. Wang, Z.H. Meng, M. Xue, Detection of organophosphorus compounds using a molecularly imprinted photonic crystal. Biosens. Bioelectron. **32**, 273–277 (2012)
241. Zhang R. Rong, Wang Y. Yong, L.P. Li-Ping Yu, Specific and ultrasensitive ciprofloxacin detection by responsive photonic crystal sensor. J. Hazard. Mater. **280**, 46–54 (2014)
242. F. Fleischhaker, A.C. Arsenault, F.C. Peiris, V. Kitaev, I. Manners, R. Zentel, G.A. Ozin, DNA Designer defects in photonic crystals: optically monitored biochemistry. Adv. Mater. **18**, 2387–2391 (2006)
243. M.Z. Li, F. He, Q. Liao, J. Liu, L. Xu, L. Jiang, Y.L. Song, S. Wang, D.B. Zhu, Ultrasensitive DNA detection using photonic crystals. Angew. Chem. Int. Ed. **47**, 7258–7262 (2008)
244. W.Z. Shen, M.Z. Li, B.L. Wang, J. Liu, Z.Y. Li, L. Jiang, Y.L. Song, Hierarchical optical antenna: gold nanoparticle-modified photonic crystal for highly-sensitive label-free DNA detection. J. Mater. Chem. **22**, 8127–8133 (2012)
245. M.M. Orosco, C. Pacholski, G.M. Miskelly, M.J. Sailor, Protein-coated porous-Silicon photonic crystals for amplified optical detection of protease activity. Adv. Mater. **18**, 1393–1396 (2006)

246. T. Tian, X.S. Li, J.C. Cui, J. Li, Y. Lan, C. Wang, M. Zhang, H. Wang, G.T. Li, Highly sensitive assay for acetylcholinesterase activity and inhibition based on a specifically reactive photonic nanostructure. ACS Appl. Mater. Interfaces **6**, 15456–15465 (2014)
247. K.I. MacConaghy, C.I. Geary, J.L. Kaar, M.P. Stoykovich, Photonic crystal kinase biosensor. J. Am. Chem. Soc. **136**, 6896–6899 (2014)
248. C.S. Huang, S. George, M. Lu, V. Chaudhery, R. Tan, R.C. Zangar, B.T. Cunningham, Application of photonic crystal enhanced fluorescence to cancer biomarker microarrays. Anal. Chem. **83**, 1425–1430 (2011)
249. C.S. Huang, V. Chaudhery, A. Pokhriyal, S. George, J. Polans, M. Lu, R. Tan, R.C. Zangar, B.T. Cunningham, Multiplexed cancer biomarker detection using quartz-based photonic crystal surfaces. Anal. Chem. **84**, 1126–1133 (2012)
250. J. Li, H. Wang, S.J. Dong, P.Z. Zhu, G.W. Diao, Z.J. Yang, Quantum-dot-tagged photonic crystal beads for multiplex detection of tumor markers. Chem. Commun. **50**, 14589–14592 (2014)
251. S. George, V. Chaudhery, M. Lu, M. Takagi, N. Amro, A. Pokhriyal, Y.F. Tan, P. Ferreirac, B.T. Cunningham, Sensitive detection of protein and miRNA cancer biomarkers using silicon-based photonic crystals and a resonance coupling laser scanning platform. Lab Chip **13**, 4053–4064 (2013)
252. J.H. Han, L. Sudheendra, H.J. Kim, S.J. Gee, B.D. Hammock, I.M. Kennedy, Ultrasensitive on-chip immunoassays with a nano particle-assembled photonic crystal. ACS Nano **6**, 8570–8582 (2012)
253. J.T. Heeres, S.H. Kim, B.J. Leslie, E.A. Lidstone, B.T. Cunningham, P.J. Hergenrother, Identifying modulators of protein-protein interactions using photonic crystal biosensors. J. Am. Chem. Soc. **131**, 18202–18203 (2009)
254. J.T. Zhang, Z.Y. Cai, D.H. Kwak, X.Y. Liu, S.A. Asher, Two-dimensional photonic crystal sensors for visual detection of lectin concanavalin A. Anal. Chem. **86**, 9036–9041 (2014)
255. Z.Y. Cai, J.T. Zhang, F. Xue, Z.M. Hong, D. Punihaole, S.A. Asher, 2D Photonic crystal protein hydrogel coulometer for sensing serum albumin ligand binding. Anal. Chem. **86**, 4840–4847 (2014)
256. X.M. Zhang, Z.B. Li, S.S. Ye, S. Wu, J.H. Zhang, L.Y. Cui, A.R. Li, T.Q. Wang, S.Z. Li, B. Yang, Elevated Ag nanohole arrays for high performance plasmonic sensors based on extraordinary optical transmission. J. Mater. Chem. **22**, 8903–8910 (2012)
257. S.S. Ye, X.M. Zhang, L.X. Chang, T.Q. Wang, Z.B. Li, J.H. Zhang, B. Yang, High-performance plasmonic sensors based on two-dimensional Ag nanowell crystals. Adv. Opt. Mater. **2**, 779–787 (2014)
258. J.H. Han, H.J. Kim, L. Sudheendra, S.J. Gee, B.D. Hammock, I.M. Kennedy, Photonic crystal lab-on-a-chip for detecting staphylococcal enterotoxin B at low attomolar concentration. Anal. Chem. **85**, 3104–3109 (2013)
259. G.Z. Deng, K. Xu, Y. Sun, Y. Chen, T.S. Zheng, J.L. Li, High sensitive immunoassay for multiplex mycotoxin detection with photonic crystal microsphere suspension array. Anal. Chem. **85**, 2833–2840 (2013)
260. N.M. Ivanir, Y. Mirsky, A. Nahor, E. Edrei, L.M. Bonanno-Young, N.B. Dov, A. Sa'arb, E. Segal, Trap and track: designing self-reporting porous Si photonic crystals for rapid bacteria detection. Analyst **139**, 3885–3894 (2014)
261. H. Shafiee, E.A. Lidstone, M. Jahangir, F. Inci, E. Hanhauser, T.J. Henrich, D.R. Kuritzkes, B.T. Cunningham, U. Demirci. Nanostructured optical photonic crystal biosensor for HIV viral load measurement. Sci. Reports. **4** (2014), in press. doi:10.1038/srep04116
262. S. Pace, R.B. Vasani, W. Zhao, S. Perrier, N.H. Voelcker, Photonic porous silicon as a pH sensor. Nanoscale Res. Lett. **9**, 420 (2014)
263. S.Y. Choi, M. Mamak, G.V. Freymann, N. Chopra, G.A. Ozin, Mesoporous Bragg stack color tunable sensors. Nano Lett. **6**, 2456–2461 (2006)

Chapter 6
Photonic Crystal Based Anti-Counterfeiting Materials

Siyun Ye and Jianping Ge

Abstract Photonic crystals based anti-counterfeiting materials have recently attracted great interests due to their unique optical properties and great market demand. As an essential step to prepare these antifraud materials, the creation of color contrast and thereby photonic crystal patterns based on ink-jet printing on flat substrate or localized tuning of premade photonic structures will be first introduced in this chapter. The antifraud labels could be photonic prints with angular dependent structural colors, since they are easy to be distinguished from most regular prints. They could also be invisible photonic prints under normal conditions, until special treatments such as water soakage, deformation and magnetic field are applied to reveal the hidden patterns. Finally, the photonic crystal multilayer has proved its potential in encryption applications, where the encrypted information of stacking sequence can be interpreted by the corresponding reflection spectra only.

6.1 Introduction

Photonic crystals are composed of periodic dielectric structures that affect the propagation of electromagnetic waves in the same way as the periodical potential in a semiconductor crystal affects the motion of electrons. The periodical modulation of the refractive index in a dielectric material creates a forbidden gap in the photonic band structures that excludes the existence of optical modes within a specific range of frequencies. Therefore, the photonic band gap (PBG) gives rise to some interesting optical phenomena such as inhibition of spontaneous emission, high-reflecting directional mirrors and low-loss wave guiding.

S. Ye · J. Ge (✉)
School of Chemistry and Molecular Engineering, Shanghai Key Laboratory of Green Chemistry and Chemical Processes, East China Normal University, Shanghai, People's Republic of China
e-mail: jpge@chem.ecnu.edu.cn

M. J. Serpe et al. (eds.), *Photonic Materials for Sensing, Biosensing and Display Devices*, Springer Series in Materials Science 229,
DOI 10.1007/978-3-319-24990-2_6

The synthesis of photonic crystals can be accomplished through "top-down" and "bottom-up" methods. The former strategy uses the well-developed microfabrication techniques, such as photo lithography [1, 2], holographic lithography [3, 4] and glancing-angle deposition to produce sophisticated and ordered microstructures from bulk materials. However, these fabrication methods of photonic crystals may not be suitable for large scale preparation due to their high cost and low efficiency in production. On the other hand, great enthusiasms have also been paid to the photonic crystals prepared by "bottom-up" strategies. Among all chemical and physical processes, people are especially interested in the self-assembly of uniform colloidal particles, as these building blocks can be flexibly arranged into 1D particle chains via templating [5], 2D hexagonal single layer at the liquid-air interface [6, 7] and 3D close pack colloidal crystals through evaporation induced self-assembly (EISA) [8–10].

One of the most important characteristics of photonic crystal is its iridescent structural color, which is caused by the reflection of visible light within the photonic band gap. In fact, 100 years before Eli Yablonovitch and Sajeev John formally proposed the term "photonic crystal" in 1987, the English physicist Lord Rayleigh had already discovered the structural color and strong reflection from the interaction of visible light with the periodical multi-layer dielectric stacks. (1) The structural color is intrinsically different from the emission colors from the bulbs, sun light or fluorescent materials. The structure color is visible only if the photonic crystals are exposed under incident light, and it is determined by the wavelength of specific back-scattering light whose propagation is forbidden in the photonic crystals. However, most emission colors are produced by the electron transition between energy levels. Therefore, the structural color has better visual effect under strong sunlight due to its antiglare properties, while the emission color is better to be used in a relatively dark environment. (2) The structural color of photonic crystal is similar to the color formed by dyes and pigments considering the principle of colors. Both of the photonic crystal and the pigments show the color from certain electromagnetic waves that can neither be absorbed nor be allowed to propagate through them. Even so, the structural colors have inherent advantages in durability, as it will not fade like the color of dyes and pigments due to the decomposition of chromophores.

In recent years, the study of photonic crystals has stepped into a new stage that people began to investigate responsive photonic crystals (RPC) [11], whose structure colors can be effectively tuned under external stimulus. According to Bragg Law, the reflection wavelength (λ) as well as the structural color is determined by the effective refractive index (n), the lattice constant (d) and the glancing angle (θ) between the incident light and diffraction crystal planes. Based on this relationship, the responsive photonic crystal can generally be obtained by combining the responsive contents with photonic structures, so that the structural color changes according to external conditions due to the change of n, d and θ. For example, the colloidal crystals embedded in an elastic polymer matrix change colors under deformation [12–15], because the lattice constant changes as the composite is stretched or squashed. The inverse opals with ordered macropores change color when they are soaked in solvents, because the effective refractive

index changes due to the infiltration of solvents [16, 17]. Through persistent efforts in the past 20 years, people have discovered various responsive photonic crystals including thermal [4], chemical [18], biological [19–21], mechanical, optical [22], electrical [23–26] and magnetic [27–29] RPCs, which have been widely used in photonic sensing [30–34], display unit [35, 36], photonic printing, security devices, thin film optics [37], photocatalysis [38–40] and solar energy conversions [41–43].

Among all these applications, photonic crystal composites with anti-counterfeiting functions have attracted more and more interests due to their unique optical properties. Today, there is an increasing demand for anti-counterfeiting materials around the world in almost every field from agriculture and industry products to medicine and daily supplies. The regular techniques of anti-counterfeiting labels for commercial products usually include laser holographic film, 1D or 2D barcode, and scratchable coatings covering the verification information. A special case for intense application of antifraud material is the banknotes, on which one can find even more advanced techniques, such as watermarks, invisible prints, concave-convex patterns, fluorescent ink and magnetic micro-printing security thread. With the development and spread of related science and technology, the preparation of aforementioned labels are gradually being mastered by illegal people, and new antifraud materials are urgently needed to confront the upcoming challenges. Due to the unique visual effects and the tunable structural colors responding to various external stimuli, the photonic crystals composites is believed to be a good supplement to traditional antifraud materials.

In this chapter, recent advances in the photonic crystal based anti-counterfeiting materials will be introduced and discussed. Although the working mechanism of these materials usually involves the basic theory of photonic band gap and responsive photonic crystal, they won't be discussed in detail here, as we believe the readers may find related discussions in other chapters. We shall first introduce the printing methods to create patterns based on photonic crystal composites, because it is the fundamental technology to prepare the labels. Then, we shall discuss some photonic prints with fixed PBG and angular dependent visual effect as well as several invisible photonic prints with changeable PBG, which can be shown by water soaking, deformation and magnetic field. Finally, we will introduce the photonic crystal codec techniques, which utilize the photonic crystal to carry information and use spectrometer to reveal the hidden information.

6.2 Photonic Printing Based on the Tuning of Photonic Structures

Photonic printing is the fundamental techniques for the fabrication of photonic crystal based anti-counterfeiting materials, because all the visual patterns are printed on the photonic crystal substrate through these techniques. In our daily life, there are various kinds of prints such as books, newspaper, posters, and so on. The texts and images can be recognized by the readers because a contrast exists between the ink marks and the blank paper. Similarly, photonic printing can be understood as a

process leading to a specific contrast of structural color based on the optical properties of photonic crystal based materials.

A most direct way to realize photonic printing is the controllable and instant assembly of photonic crystals at designed position on a substrate, so that a contrast between the structural color of photonic crystals and the intrinsic color of substrate will show a pre-designed pattern. In other word, it is prepared by the contrast between photonic crystal and non-photonic substrate. Based on this mechanism, ink-jet printing has been developed to fabricate patterned photonic crystals [44, 45]. By putting the particle suspensions into the cartridges of a common multi-cartridge ink-jet printer, patterns designed by computer can be printed on a substrate along with the self-assembly of colloidal particles. The key points of ink-jet printing are the well-ordered assembly of the photonic crystal and their spread condition on the substrates. In recent years, much effort has been paid to the improvement of resolution, including eliminating the coffee-ring effect and minimizing the feature size of printed dots or lines. Although this printing technique is very important, it won't be discussed in detail in this chapter as most of the reported anti-counterfeiting materials are not prepared by this method.

In addition to ink-jet printing technique, the photonic prints can also be prepared on a premade photonic paper through the change of photonic structures. In the past years, this method has attracted many interests because it offers a great diversity of printing modes by tuning the refractive index (n), lattice spacing (d), and crystal orientation (θ). Even slight differences in the refractive index, lattice spacing, and crystal orientation between neighboring regions will lead to difference in reflection signals, which can be utilized to accomplish the printing. Therefore, the contrast of structural color is created between two different photonic structures, which is intrinsically different from the direct-assembly printing techniques. Since there is no self-assembly in the printing process, the current printing method has potential advantages in fast and high resolution printing. These merits have been shown up when the printing is combined with photolithography techniques. In this section, typical printing methods based on the tuning of photonic structures will be introduced.

First of all, we shall introduce an erasable photonic print using a swellable PS-PDMS photonic crystal composite as paper and a nonpolar organic solvent as ink respectively [46]. The photonic paper was composed of well-ordered monodispersed PS beads whose voids are infiltrated with poly(dimethylsiloxane) (PDMS). Because the PDMS elastomer will expand when being swollen by organic solvents and shrink once the solvent evaporates, the photonic crystal lattice as well as the structural color of the paper will change accordingly. For instance, when the photonic paper composed of assembly of 202-nm PS particles in PDMS matrix is swollen by 2-propanol, its reflection wavelength turns from 545 to 604 nm and its color changes from green to red accordingly. After the evaporation of 2-propanol, the PDMS matrix gradually shrinks back to its original state, so that the reflection and structural color recovers as well. The swelling and evaporation induced color change is fully reversible for many times.

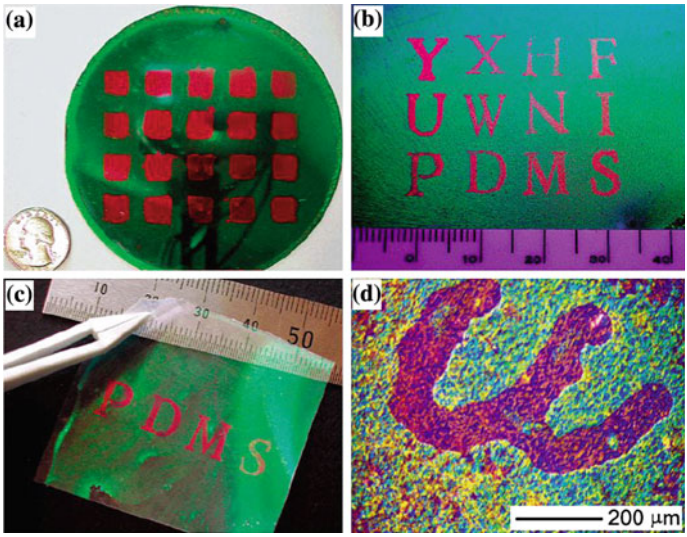

Fig. 6.1 Patterns printed on PS-PDMS photonic paper with silicone fluid DMS-T05 as ink [46]

Patterns and images will form if the aforementioned swelling process can be spatially limited within specific region on the photonic paper, which leads to a color contrast between swollen and nonswollen region. Generally, it can be realized with the help of stamp or protection masks. For example, a stamp of alphabetic letter is inked with the silicone fluid (ink) by Q-tip wiping and then brought into contact with the surface of a green photonic paper for a few seconds. The region in contact with the stamp turned to red locally as swollen by the silicone fluid, which formed a large color contrast with the nonswollen region and successfully transferred the pattern of the stamp to the surface of photonic paper. With a more subtle stamp, micropatterns with an edge resolution better than 50 μm can also be printed on the photonic paper (Fig. 6.1).

In this printing technology, the selection of ink is important as it controls the final color of the pattern printed on the paper. A variety of solvents such as silicone fluid, alcohol, hexane, or toluene can serve as ink because they are capable of swelling the PDMS matrix. However, their swelling abilities are different, so that different ink usually leads to different colors when they are applied to the same photonic paper. Taking silicone fluid as a typical example, when silicone fluids with different molecular weights are applied to photonic paper with original stop band of 555 nm, the reflection wavelength of the paper will change from 560 to 700 nm and its color change from green to red accordingly. Besides molecular weight, polarity of the solvent can also be used to select the ink. Comparing a range of different alcohols (polar solvents) and alkanes (nonpolar solvents), a conclusion was drawn that the shift caused by a polar solvent was less than 100 nm, while that caused by a nonpolar solvent was in the range of 200–300 nm. It is believed that the availability of diversified inks to tune the colors of photonic paper in the entire spectral range of

visible light should make this paper/ink system particularly useful for displaying letters and patterns with full colors.

In addition to the printed colors, the selection of ink also determines the duration time of the printed patterns. As mentioned above, the printed patterns will disappear along with the evaporation of infiltrated ink, so that the vapor pressures (or boiling points) of the ink is critical to the maintaining of photonic pattern. For example, as the molecular weight of silicone fluid was increased, the evaporation rate was reduced, and thus the duration time of the ink was monotonically increased. The duration time can be tuned from a few seconds to hundreds of hours by using silicone fluid of different molecular weight. It can be further extended to several months when using the mixture of silicone fluids and silicone oligomers as ink. If necessary, the photonic pattern can be permanently fixed by thermally grafting the ink molecules (silicone oligomer terminated in vinyl groups) to the PDMS photonic paper through additional curing process.

As a second example, we shall introduce a photonic printing process capable of generating permanent and multicolor patterns [47]. The photonic paper was prepared by a two-step polymerization process. Aqueous solution of monodisperse and crosslinked polystyrene (PS) particle is encapsulated in a methacrylate-functionalized polyethylene glycol matrix through photoinitiated and free-radical polymerization. The PS particles are electrostatically self-assembled in water and ordered structures are retained even after removing the water in hydrogel. The water-free film was then swollen in the mixture of 2-methoxyethly acrylate (MOEA), ethylene glycol dimethacrylate (crosslinker) and 2,2-diethoxyacetophenone (DEAP, the photoinitiator), which is converted to a water-free and robust photonic paper thorough another photo-polymerization process.

The as-made PS-PMOEA photonic paper can be used to prepare patterns through a photo-lithograph process. The paper is first soaked in a solution consisting of polymerizable monomer and photoinitiator, leading to the expansion of photonic crystal lattice and a red shift of reflection wavelength. The monomer-swollen paper is irradiated by UV light in the presence of a photo mask, so that the expanded photonic structures in the exposed region are permanently fixed. After UV irradiation, the paper is washed to remove the monomer, so that the photonic paper in the shielded regions recovers its original color. A large color contrast is formed between the exposed and shield region. In this way, the pattern of photo mask is successfully transferred to the photonic paper (Fig. 6.2).

Multicolor pattern can be realized with the framework of current printing technique. In a modified procedure, the initial water suspension used to make the composite film is mixed with a solution of poly(ethylene glycol) methacrylate (PEGMA), PEGDMA and DEAP, which is photo-polymerized with a photo-mask. The as-made photonic film is swollen again with the same solution and photo-polymerized with a different photo-mask. Different from the single color pattern prepared by typical printing procedures, this two-step polymerization will produce a multicolor pattern, which is certainly expected in the practical application.

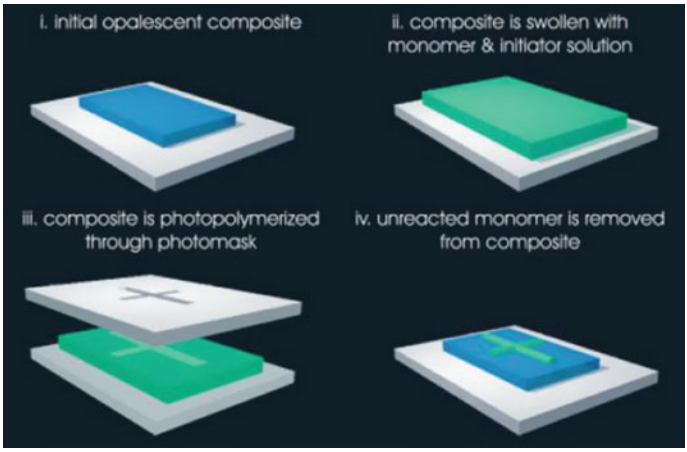

Fig. 6.2 Patterns printed on PS-PMOEA photonic paper through monomer swelling and lithographical photo-polymerization [47]

The examples introduced above usually involve the utilization of organic solvent or polymeric monomers, which might be not suitable for daily usage. In the 3rd demonstration of photonic printing, we shall introduce an erasable photonic pattern, which is prepared by using a $Fe_3O_4@SiO_2$ photonic composite as paper and a water-ethanol solution of hygroscopic salt as ink [48]. The photonic pattern is permanently recorded until they are erased by water rinsing, and the cleaned paper can be repeatedly used to print new patterns. The rewritability of the photonic paper and low toxicity of the salt ink, polymeric matrix and rinsing liquid make this paper/ink system environmentally friendly, inexpensive, and useful for general applications.

The working mechanism of this printing technique is also related to the swelling of polymeric photonic composite, lattice expansion and change of structural colors. The photonic paper is fabricated through the fast magnetically induced self-assembly of $Fe_3O_4@SiO_2$ colloids followed by an instant UV curing process to fix the photonic structures inside a poly(ethylene glycol) diacrylate (PEGDA) matrix. A water-ethanol solution of a chloride salt is found to be an ideal ink, because it can swell the polymer matrix but hardly evaporate at normal temperature and humidity due to the hygroscopic properties of these salts. The salt ink can be used as most traditional ink, and the photonic pattern can be easily prepared by handwriting or brushing. The ink mark on the photonic paper usually has a redshift reflection wavelength compared to the original photonic paper, which creates a color contrast and reveals the patterns (Fig. 6.3).

The hygroscopic salt solution ink is the key to create a retainable and durable color contrast. Similar to the printing based on PS-PDMS photonic paper and organic solvent ink, water or ethanol can also be directly used as inks to create

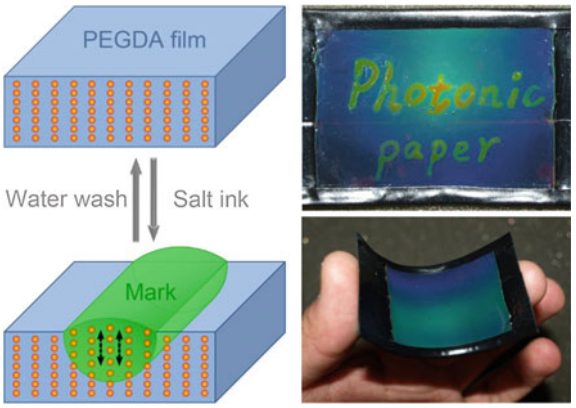

Fig. 6.3 Retainable and erasable patterns printed on Fe_3O_4@SiO_2-PEGDA photonic paper using aqueous and alcohol solution of hygroscopic salt as ink [48]

patterns on the Fe_3O_4@SiO_2-PEGDA photonic paper, which will soon disappear due to the evaporation of inks. However, by introducing LiCl into the mixture of water and ethanol, the durability of the photonic pattern can be greatly enhanced. In fact, there are many candidates that can also be selected as inks, including LiCl, $MgCl_2$, $CaCl_2$, $ZnCl_2$, and $AlCl_3$. The experimental results showed that the reflection red-shifts once the ink is spread on the paper, and then slowly blue-shifts due to the evaporation of ethanol and water in several hours or one day, depending on the concentration of salt in the ink. The presence of ethanol speeds up the swelling process and enhances the diffusion of saturated aqueous salt solution into the PEGDA polymer matrix. Because the hygroscopic salts absorb water in air, their solutions will hardly evaporate completely to precipitate solid powder, thus keeping the polymer matrix swollen for a much longer time. Unlike the application of low-volatility ink upon PS-PDMS paper, the final reflection wavelength of the salt ink marks does not decrease back to its original position, but reaches a balanced point in the following several days with a permanent color contrast (Fig. 6.4). When the photonic prints are kept in a temperature and humidity steady environment, the contrast could remain for months and it is believed to last even longer.

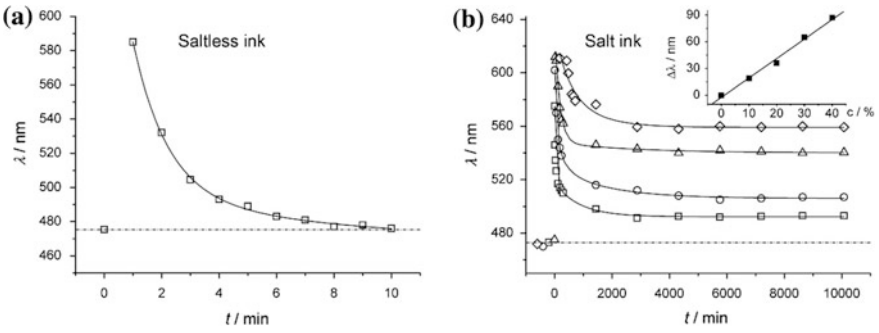

Fig. 6.4 Time evolution of reflection wavelength of photonic paper interact with **a** saltless water-ethanol ink and **b** LiCl ink with concentration ranging from 10 to 40 % [48]

Therefore, the current ink marks are always practically visible unless they are intentionally erased by water washing, which is a great improvement in durability over previous systems.

On the other hand, the durable ink marks can be erased by rinsing the paper in water and drying thereafter, so that the photonic paper can be repeatedly used. It is known that the color contrast is formed due to the retaining of small amount of salt solution in the photonic paper, which induces an expanded crystal lattice compared to the neighboring region. Therefore, when the paper is rinsed in distilled water and dried in air, the residual salts will be removed and the lattice constant will be restored, which naturally erase the photonic pattern and prepare the clean paper for the next round printing.

It should be supplied that the color contrast between the ink marks and original paper can be tuned by the amount of hygroscopic salts introduced into the polymer matrix. Generally, greater contrast will be achieved with a larger LiCl concentration in the ink. Here, the ink is usually named with the salt concentration, such as, 10 % LiCl ink is defined as a mixture of 10 % (volume ratio) LiCl saturated aqueous solution and 90 % ethanol, with a constant additive of hexadecyltrimethyl ammonium bromide (CTAB), which would improve the uniform wetting of the ink on the PEGDA surface during the writing process. By increasing the concentration of LiCl from 10 to 40 %, the balanced reflection contrast linearly increased from 19 to 86 nm. The current polymer matrix had a relatively high degree of cross-linking and the maximal swelling typically enabled a 100–150 nm shift in diffraction, which was enough to create high color contrast but still not yet wide enough to cover the whole visible spectrum. By using less crosslinked photonic paper, it should be possible in the future to accomplish the full color writing with a single-component ink.

6.3 Photonic Prints with Angular Dependent Structural Colors

6.3.1 Angular Dependent Effect in Photonic Crystal Patterns

Photonic crystals shows iridescent structural colors because electromagnetic waves with certain frequencies cannot propagate through the materials, which results in strong reflection of the corresponding visible light. Different from the common pigments and dyes, the photonic crystals have angular dependent colors, which changes with the alteration of incident light direction, crystal orientation or viewing angle. It can be explained by the Bragg's Law which describes the relationship between optical signals and structural factors. In (6.1), "m" is the order of reflection, "λ" is the wavelength of reflected light, "n" is the effective refractive index of the whole material, "d" is the spacing between the planes in lattice, and "θ" is the

glancing angle between the incident light and diffraction crystal planes. Although this equation is only applicable to the case where the incident angle equals to the reflected angle, it still shows that the reflection light will blue shift as the incident light being tilted from the normal direction of the photonic crystals. The angular dependent color is similar to the laser holographic film in visual effect, which renders the photonic crystal a potential material for antifraud applications.

$$m\lambda = 2nd \sin \theta \tag{6.1}$$

In fact, there has been demonstration which utilizes the angular dependent features of photonic printings to enhance the antifraud capabilities of banknotes. The photonic crystal alphabet "K" printed on banknotes is achieved based on photo-lithography, micro-printing and polymerization induced self-assembly of colloidal crystals [49]. First of all, a photo-curable photonic crystal ink composed of silica particle (33 vol%) and ETPTA monomers is prepared, which can be easily converted to a high quality photonic crystal in a very short time (1 s) under UV irradiation. The photonic ink is then infiltrated into a gap of 50 μm between a glass slide and an amorphous silicon photo-mask, which carries the patterns of arrays of small K windows. The photonic ink exposed to the UV irradiation is converted to polymerized photonic composites and the unpolymerized ink is washed by ethanol, leaving behind a same pattern as the one on photo-mask. Pure ETPTA monomer is added to fill in the gap between glass slide and silicon mask again, which turns the photonic prints into a free-standing and highly transparent film through a 2nd time UV curing process. Finally, the photonic crystal film is released from the silicon mask and transferred onto the banknote.

The as-made photonic prints on the banknote have brilliant structural colors, which does present angular dependent characteristics. Since the reflective index of ETPTA (n_{ETPTA} = 1.4689) is close to that of silica (n_{silica} = 1.45), the photonic prints exhibit strong and narrow reflection at the stop band position, which output bright and monochromic color. The color of PC film can be tuned by the average size and volume fraction of silica particles in the photonic ink, which make it possible to print colorful patterns. Generally, the larger particles and lower volume fraction of silica resulted in large lattice constant and reflection at longer wavelengths. It is known that any change of the incident angle, the viewing angle or the orientation of photonic crystal will lead to the change of structural color accordingly. As shown in Fig. 6.5, the reflection color gradually changes from green, sky blue, blue to purple as the angle of incident light increased from 10° to 55° through tilting the banknotes under illumination. When the incident light is fixed, the photonic print can be invisible from a specific angle and it also displays changeable colors with viewing angle tuned in a certain range. It should be mentioned that the photonic crystal film is transparent due to its thin thickness, and it is hard to be perceived when placed on the banknote. The alphabet "K" is composed of many small "K" under a magnifier, which is similar to the micro-printing techniques currently used for real banknotes.

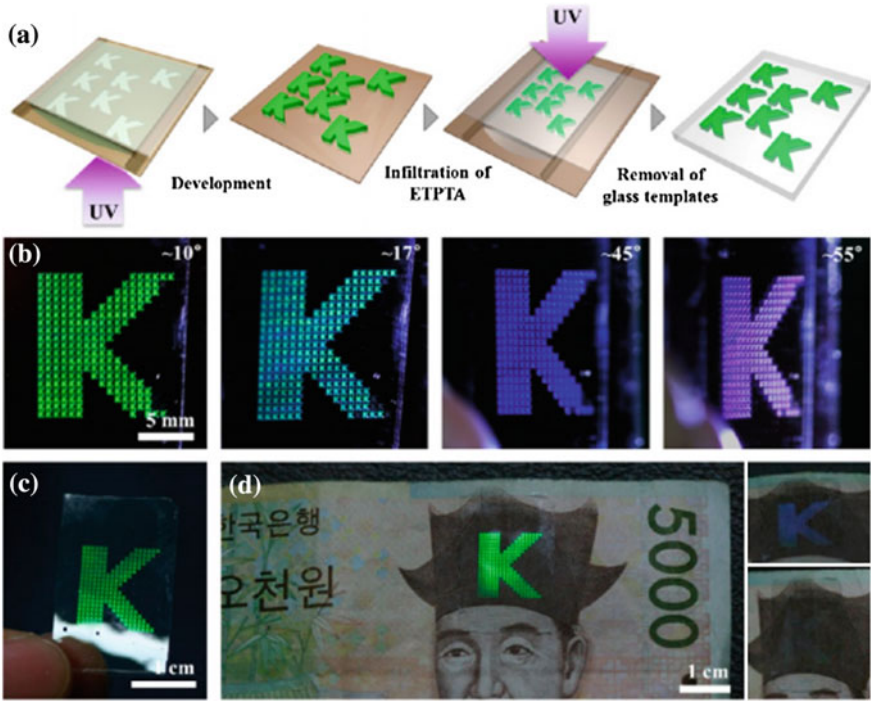

Fig. 6.5 Print alphabet K on the banknote through lithographical photo-polymerization. The photonic prints change color with the change of sample orientation and viewing angle [49]

Unlike traditional photonic crystal composite film, the current prints can display mixing colors through the stacking of multiple thin films. Generally, it is difficult to obtain clear mixing structural colors from multilayer photonic structures, because PC film thicker than several hundred micrometers has strong scattering effect and it presents opaque and pale white in some extent, while the thin film may not have adequate strong reflection signals due to the quality of colloidal assembly. However, multilayer films with no deterioration of the optical spectrum from each layer can indeed be realized due to the high reflectivity and high transparency of the as-made photonic crystal film. Through infiltration and subsequent photo-polymerization of the silica-ETPTA suspension on a preformed composite layer, bilayer film with a thickness of 50 μm in each layer is prepared. The stacking of blue (B) and green (G) PC film produces a bilayer film with cyan (C) colors. Similarly, yellow (Y) and magenta (M) films can be obtained by stacking the green (G)/red (R) film and red (R)/ blue (B) film, respectively. The reflectance spectra from all three bilayer films have two distinct reflection peaks without any reduction in the reflectivity or widening in peak width. Furthermore, triple-layer films composed of red, blue and green photonic crystal film can be prepared by similar method, except that a particle-free ETPTA layer is added between two PC layers to enhance their combination. The triple-layer film also has distinct reflection peaks and displays white color under an optical

microscope. Therefore, it is promising to provide a full optical palette of structural colors by controlling the relative reflectivity of each primary color, which is impossible to realize by traditional colloidal photonic crystals.

In some other cases, the angular dependent photonic prints may have other functions so that their structural colors will respond to multiple external stimuli [50]. As a typical example, we shall introduce a polymeric photonic crystal film, which not only has angular dependent visual effect, but also changes colors through deformation and temperature tuning. The photonic material is prepared from PS@PDEGMEMA-co-PEA particles, which possess soft and thermoresponsive shell and hard core. The core-shell particles are mixed with bifunctional monomer BDDA and photoinitiator by extrusion prior to the compression molding. During the melt-shear organization process, the hard PS core turned to be an almost perfectly ordered photonic structure while the soft PDEGMEMA-co-PEA shell converted to be a soft matrix. The subsequent crosslinking of the polymer matrix with BDDA under UV-irradiation eventually produced an elastic photonic film with certain mechanical stability. The as-made PC film shows typical structural color due to the arrangement of PS particles, and it has angular dependent characteristic either. At the same time, the film shows mechanical and thermal responsive behavior if it is swollen in water first to generate a photonic hydrogel film. The hydrogel shows a 25-nm blue shift in stop band as it is stretched for 10 %, and a 26-nm red shift as the temperature cools down from 20 to 0.5 °C.

The aforementioned photo polymerization process can be used to prepare photonic prints, because the crosslinking causes a blue shift in reflection and creates a contrast with the uncrosslinked section. Using typical photolithography procedures, the patterns on the photo mask can be easily transferred onto the PC film due to spatial crosslinking process. As shown in Fig. 6.6, the patterns composed of uncrosslinked polymer matrix is yellow while the crosslinked background

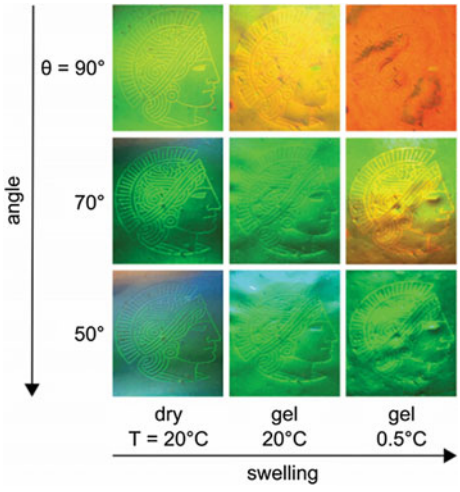

Fig. 6.6 The structural color of photonic hydrogel film depends on the incident and reflection angle, and the reflection blue-shift as the angle decreases. The swollen photonic hydrogel exhibits bright colors at 20 °C, and the reflection red-shifts as the film is cooled to 0.5 °C [50]

composed of crosslinked polymer is green when the angle of incident and reflected light to the prints are fixed at 90°. For the as-made dry photonic prints, the color of the pattern and background will change simultaneously with the view angles. More precisely, both the crosslinked and uncrosslinked section will blue shift as the angle tilted from 90° to 50°. Although the contrast in reflection wavelength between the crosslinked and uncrosslinked section is not very large, the photonic patterns are fully visible over a broad view angle.

It is interesting to find that the photonic print swollen by water has fast and reversible response to the temperature, and it maintains the angular dependent structural color either. (1) The photonic prints change from green to yellow after it is soaked in water at 20 °C. After being cooled down to about 0.5 °C, the photonic prints turn to red due to better swelling of polymer matrix in water at lower temperature. The color switching for the photonic prints between two temperatures is very fast and fully reversible. (2) Compared to the dry photonic prints, the patterns on wet prints become blurred probably because the contrast of reflection wavelength is decreased in the swelling state. The patterns on dry sample are visible because the reflection of crosslinked section blue shifts and forms a contrast with that of the uncrosslinked section. It is known that a slightly crosslinked polymer matrix has better swelling ability compared to the uncrosslinked one, which means the crosslinked section swells more and the reflection red shifts more accordingly. This compensates the blue shift of reflection in photo polymerization and decreases the contrast of photonic patters. (3) The wet photonic print keeps the angular dependent structural color, and the patterns are clear when observed at certain angles. These results suggest that the photonic prints have angular and temperature dependent structural colors and it can switch between the “clear” and “blurred” between dry and wet state. Such multi-function material will certainly find its application in anti-counterfeiting labels.

6.3.2 *Orientational Printing*

It is known that the photonic printing is usually realized by (1) the instant assembly of photonic structures on a flat non-photonic substrate or by (2) the formation of different photonic structures in the region of “pattern” and “background” respectively. As discussed in Sect. 6.3.1, one can print patterns and micropatterns made of SiO_2/ETPTA photonic composites on a transparent and colorless ETPTA substrate using the first printing method. Although the as-made photonic pattern has angular dependent structural color, it is usually monochromic everyplace in the pattern when the incident light and viewing angle is fixed. For daily life usage, people have already developed laser holographic anti-counterfeiting labels based on the interference of sunlight and surface micro structures, which present angular dependent and dynamically changeable colors or patterns. Therefore, is it possible to achieve a PC based anti-counterfeiting label which has more sophisticated and attractive visual effect?

In the past years, the photonic printing based on the change of photonic structures actually has attracted more interests because it offers a great diversity of printing modes by tuning the refractive index (n), lattice spacing (d), and crystal orientation (θ). Even slight differences in the refractive index, lattice spacing, and crystal orientation between neighboring regions will lead to the formation of color contrast, which can be utilized to accomplish the printing. Among these strategies, we are interested in the printing with manipulation of crystal orientations. However, compared to the printing based on tuning of "n" and "d", there are very few reports about the creation of θ-contrast pattern because of the difficulty in changing the crystal orientation in a preassembled photonic structure or controlling multiple orientations in neighboring regions during the self-assembly.

The recently reported magnetically responsible photonic crystal provides a good material system to realize photonic printing based on orientational tuning. Basically, the magnetic particles assembled into chain structures with periodical inter-particle distance, which strongly reflects the visible light due to its interaction with the periodical structures. The reflection wavelength as well as the structural color can be tuned by the magnetic field strength and the average particle size, because these parameters control the lattice constant of the photonic crystals. In addition, the optical signals can also be controlled by the orientation of magnetic field, because the chain structures are always kept along the external magnetic field. When the magnetic particles are assembled in monomer, the photonic structure can be fixed through photo-polymerization, so that the orientation of as-made photonic composites can be conveniently adjusted by tilting the magnet before polymerization.

A fundamental experiment is designed to check the reflection and transmittance of photonic structures with different orientations when the angles of incident, reflected and transmitted light are all fixed at 0°. As the particle chain tilted from 0° to 90°, the reflection peak blue shifts and gradually loses its intensity. At the same time, it is interesting to see that the transmittance over a broad range of wavelength increases accordingly, which is caused by the decrease of reflection signals although it seems more particles will block the transmitted light in that case. These two angle-dependent properties suggest that the θ-contrast can be realized by the variation of colors in reflection mode and the change in transparency in transmission mode.

Based on this magnetically tunable assembly system, one can develop a new photonic printing process which creates patterns via tuning the crystal orientations in the neighboring region on photonic paper [51]. Generally, the orientational photonic printing is accomplished by magnetic alignment, orientational tuning, and lithographical photopolymerization. For the printing of monochromic pattern, only one mask and two orientations are involved. Typically, the original disordered magnetic particles form chain structures along the direction of the external magnetic field. Once the particles have been assembled, the photonic structure exposed under a photo mask (green part) can be instantly fixed by UV polymerization. The unfixed magnetic particles reassemble into chains and change their orientation as the external field tilted to the opposite direction. Those photonic structures (blue part)

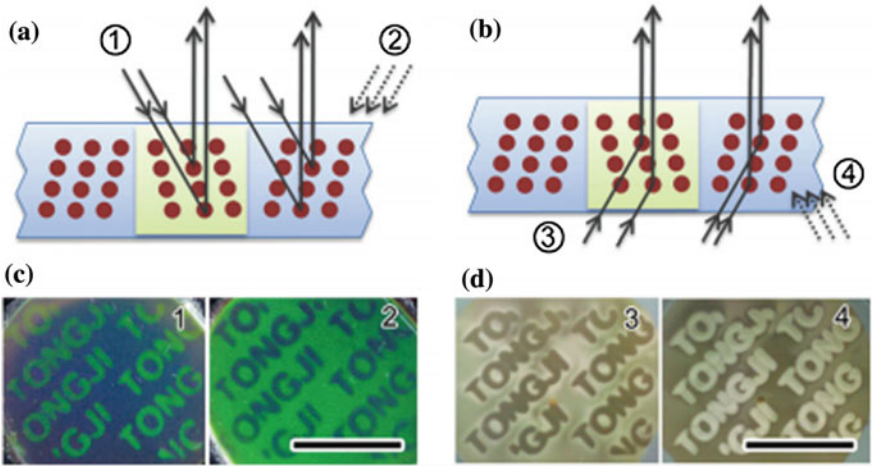

Fig. 6.7 **a**, **b** Schemes and **c**, **d** photos of photonic patterns with orientational contrast in **a**, **c** reflection and **b**, **d** transmission mode. The incident light is projected to the photonic prints parallel to orientation 1 and 2 [51]

are fixed in the second curing process after the mask is removed. Finally, a photonic crystal film with two crystal orientations are produced, forming θ-contrast patterns as expected.

Using the aforementioned printing strategy, an alphabetic logo composed of two kinds of photonic structures with mirror-symmetric orientations is fabricated. As shown in Fig. 6.7, the word and background sections are made of particle chains with tilting angles of +15° and −15°, respectively. When the incident light is close to the orientation of particle chains in the letters section (case 1), the letters and background region show reflection with longer and shorter wavelength, respectively. However, as the incident light is projected close to the orientation of particle chains in the background section (case 2), the letters and background region switch their structural colors. Similarly, the alphabetic logo has switchable transmitted signals when the angle of incident light changes. Either the letters or the background region becomes less transparent as the incident light is projected close to its orientation. Under the sunlight where the incident angle is fixed, the color or transparency switching can also be realized by rotating the samples horizontally for 180°.

The θ-contrast and color switching can be explained by theoretical calculations. A physical model was built to investigate the interference between incident light and colloidal particles, where light is projected at a specific angle and the reflections are collected along the normal direction of the film. The diffraction wavelength of photonic structures in the letters and background sections are described by (6.2) and (6.3), respectively, which suggests that λ in the letters section is larger than that of the background when θ is less than 0 and vice versa. The equations reveals that the blue shift of the reflection is actually caused by the separation of incident light from

the photonic chain structures. The calculation also predicts that when the incident light has a same separation angle with respect to particle chains in both the letters and background regions, the reflections will be the same and the θ contrast disappears. In fact, there is a specific angle of the light source (θ = 0) in which the words are blurred or invisible in observation.

$$\lambda_{\text{left}} = \text{nd}[\cos 15^\circ + \cos(\theta + 15^\circ)] \tag{6.2}$$

$$\lambda_{\text{right}} = \text{nd}[\cos 15^\circ + \cos(\theta - 15^\circ)] \tag{6.3}$$

Using various magnetic field distributions, the orientational printing is capable of creating more sophisticated patterns with multiple photonic orientations. Figure 6.8 shows a graphic logo in which the patterns are composed of photonic structures with a tilting angle of 90° and the backgrounds are made of particle chains with continuously tilted orientations, which are caused by the axially symmetric field distribution of a cylindrical magnet during the assembly process. The results reveal a convenient method for printing patterns with multiple orientations in one step because a distinctive field distribution can be designed in the manufacture of magnets or electromagnets. Generally, the logo shows a characteristic colorful halo in the region whose orientation is close to the incident light and pale brown in the rest. With the projected light surrounding the logo from angle 1 to 4, the colorful halo follows and moves around, showing a dynamic optical effect similar to that of laser holographic anti-counterfeiting labels. In the sunlight, this effect can be seen as the logo itself is slightly tilted by hand when the observation angle is fixed.

In summary, a new printing technique based on the orientational tuning of photonic structures has been developed to print angular dependent photonic crystal anti-fake labels. The whole printing process can be accomplished by repeating magnetic alignment, orientational tuning, and lithographical photopolymerization

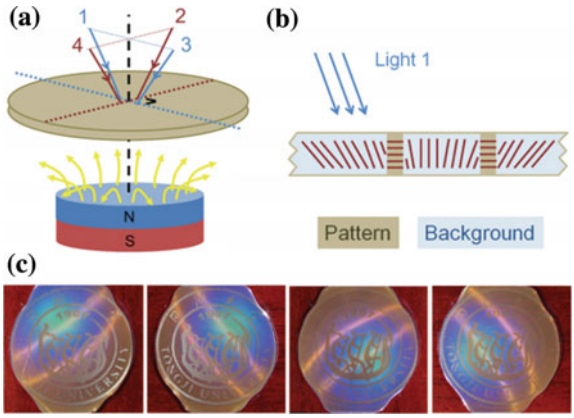

Fig. 6.8 **a** Fabrication of photonic logo with axially symmetric orientations above a cylindrical magnet. **b** Cross section of the logo and distribution of magnetic particle chains. **c** Photos of the logo when the incident light is projected from angle 1 to 4 in (**a**) [51]

using a single precursor containing magnetic particles and polymer. The as-printed labels composed of two kinds of photonic structures with mirror-symmetric orientations present a switchable color distribution when the angle of incident light changes. The labels printed with multiple axially symmetric orientations show colorful halo and dynamic optical effects when they are tilted under sunlight. These photonic prints with switchable distributions of color and transparency are hard to mimic by general prints, which are certainly very suitable for using as anti-fake label in daily life.

6.4 Invisible Photonic Prints

6.4.1 Invisible Photonic Prints Shown by Water

Invisible photonic prints have structural color based patterns that can't be seen under normal conditions but can be recognized by some specific methods when necessary. The invisible photonic print can be regarded as the combination of traditional photonic prints and responsive photonic materials, since it has recordable and self-maintaining patterns as prints and dynamically adjustable optical signals as responsive materials. Compared to the traditional photonic prints, which have a permanent contrast of reflection wavelength ($\Delta\lambda \neq 0$) between the patterns and background, the invisible version prefers a zero contrast ($\Delta\lambda_0 = 0$) at first and a large contrast ($\Delta\lambda_t \neq 0$) when the hidden information is revealed. Meanwhile, the invisible photonic prints are also different from most reported responsive photonic crystals, because the latter does not require retainable property and invisibility at the same time. In daily life, the invisible photonic prints are perfect for anti-counterfeiting labels, which are supposed to be quickly recognized by convenient and non-toxic means such as heating, deformation or soaking with water and drinks. In this section, an invisible photonic print shown by water will be introduced [52].

In order to realize the invisible prints shown by water, it is important to find out a qualified responsive photonic paper, based on which the printing strategy can be operated to meet the requirements of reflection wavelength in hiding and showing mode, respectively. Here, the qualified photonic paper is prepared by fixing the magnetic assembled $Fe_3O_4@SiO_2$ colloidal crystals in the mixture of three monomers (PEGDA, PEGMA, and TPM) through photo polymerization. Previous research work actually has demonstrated the synthesis of $Fe_3O_4@SiO_2$-PEGDA/PEGMA photonic composite through magnetic self-assembly and photo-polymerization. In the synthesis, the $Fe_3O_4@SiO_2$ particles are assembled into one-dimensional chain-like photonic structures in magnetic field due to the balance between magnetic attraction and electrostatic repulsion. Since the PEG acrylate matrix is highly hydrophilic, the photonic material responds to water quickly which can be a good candidate for photonic paper here. However, the pure PEG acrylate system seems to be short of enough flexibility in tuning the swelling speed and reflection shift, because it swells too fast in water without any control. For this reason, highly concentrated

3-trimethoxysilyl-propyl-methacrylate (TPM) is introduced to the PEG acrylate matrix to form a siloxane enriched ternary composite photonic structures, which renders the polymer matrix good tunability in tuning its swelling behavior through silane chemical reactions. It should be mentioned that the addition of TPM monomer will gradually destabilize the ordered structure in the magnetic assembly due to the replacement of ethylene glycol with TPM. The maximum volume fraction of TPM in acrylate monomer is 50 %, which creates adequate active sites for silane reactions without interfering with the magnetic assembly.

Based on this Fe_3O_4@SiO_2-PPT (PPT: PEGDA-PEGMA-TPM) photonic paper, two strategies are developed to control the swelling behavior and prepare the invisible photonic prints. One is the crosslinking method, which utilizes the crosslinking of silane in alkaline environment to inhibit the swelling of photonic paper, decrease its speed of diffraction redshift, and create a large contrast ($\Delta\lambda_t$) between the crosslinked and uncrosslinked region for prints soaked in water. The fast crosslinking process takes place mainly in the surface region of the photonic paper and no active components are introduced so that the change of refractive index and lattice constant is negligible, which causes the original contrast ($\Delta\lambda_0$) to be very close to zero. The other is the modification method, which utilizes silane coupling reaction to graft 3-aminopropyl-trimethoxysilane (APS) molecules to the polymer matrix. Similarly, the introduction of hydrophobic hydrocarbon chains slows down the polymer swelling and decreases the speed of reflection, which creates a large contrast ($\Delta\lambda_t$) between the modified and unmodified regions when soaked in water.

Using the crosslinking strategy, several photonic prints are prepared to demonstrate the showing and hiding effects as they are soaked and dried (Fig. 6.9). When the invisible prints are soaked in water for several minutes, the small difference in reflection wavelength (λ) between the pattern and the background is significantly amplified due to their different swelling speed, which leads to a visible image in the end. However, as the sample is dried in air, the photonic prints become invisible again as the difference in reflection wavelength decreases to zero. The showing and hiding of photonic patterns through soaking and drying are fully reversible and accessible in daily life.

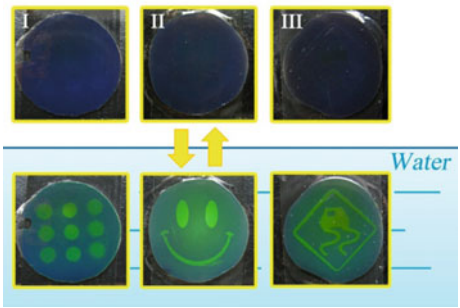

Fig. 6.9 Invisible photonic prints can be reversibly shown by water soakage and hidden by drying in air [52]

In the practical fabrication, the invisible photonic prints are prepared as follows. First, the graphics designed by computer and printed on a transparent slide are converted to a NOA61 (Norland Optical Adhesive) pattern on the surface of photonic paper through UV curing of NOA 61 liquid under photo mask. The intermediate prints are immersed into a NaOH solution or an APS solution, which crosslinks the polymer matrix by forming a –Si–O–Si– network or grafts hydrophobic hydrocarbon chains onto the polymer network in the unshielded region. Finally, the NOA61 shielding layer is removed by washing with acetone and the invisible photonic prints are produced after drying in vacuum. Here, NOA 61 has an appropriate adhesion to the photonic paper so that the shielding layer can effectively protect the Fe_3O_4@SiO_2-PPT film from crosslinking/modification and get itself easily removed with certain solvents.

The ratio of TPM in the blank photonic paper is crucial to optimize the performance of invisible prints. For uncrosslinked PEGDA/PEGMA based photonic paper, the swelling speed is slightly decreased with the increase of TPM ratio, because PEGMA is more favorable for swelling than TPM. For the crosslinked sample, the swelling speed seriously decreases with the increase of TPM ratio due to the higher level of crosslinking for the siloxane enriched matrix. Combining both influences of TPM ratio, one can find that the showing of invisible patterns is actually realized by the contrast of reflection wavelength caused by differential swelling of crosslinked and uncrosslinked photonic paper, and $\Delta\lambda_t$ increases from 32, 56 to 93 nm as the TPM ratio increases from 10, 20 to 40 % in the photonic paper. A similar conclusion about the influence of TPM ratio can be drawn in the printing using the modification strategy. Combining the current experimental results with those of the magnetic assembly one can find that the introduction of TPM is essential but the excessively addition of TPM will quench the structural color. An optimal ratio for PEGDA, PEGMA and TPM is finally determined to be 2:2:4.

The invisible photonic prints possess good reversibility and durability, because the showing and the hiding of patterns can be achieved for many cycles when the prints are soaked with water and dried in air. Time evolution of reflection wavelength for crosslinked (red curve) and uncrosslinked (black curve) photonic paper in

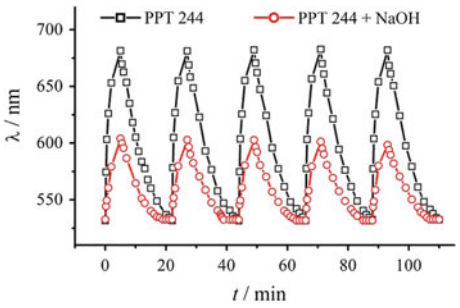

Fig. 6.10 Time evolution of reflection wavelength for crosslinked (*red*) and uncrosslinked (*black*) photonic paper in 5 continuous soaking-drying process [52] (Color figure online)

5 continuous soaking-drying processes is presented to demonstrate the reversibility (Fig. 6.10). The showing of the pattern usually takes 5–10 min as the increase of wavelength contrast ($\Delta\lambda_t$) begins to slow down thereafter, although the reflection of both photonic structures show a continuous red shift anyway. On the other hand, the hiding of the pattern usually takes 15 min at room temperature with moderate humidity.

In summary, a printing process based on the lithographic fabrication of shielding patterns and consequently crosslinking or hydrophobization of unshielded region on a pre-made photonic paper was developed to prepare the invisible photonic prints shown by water. The crosslinking or modification process will slightly change the refractive index or lattice constant so that the original contrast of diffraction wavelength is hard to distinguish. When the prints are dipped in water for several minutes, a large contrast of diffraction wavelength appears due to the different swelling speed and lattice expansion of the patterns and the background. The showing or hiding of the photonic prints can be circularly achieved many times by soaking or drying the sample. The showing process takes several minutes, and the only required substance is water, which is easy to obtain and friendly to the environment.

6.4.2 Invisible Photonic Prints Shown by Deformation

The most accessible method for the showing of invisible photonic prints is possibly the exertion of weak external force, which can be realized by hand in everywhere at any time. The photonic crystals may stretch, shrink, bend or twist as the external force is exerted in different ways. No matter what situation it is, the external force always causes a deformation so that the lattice constant and structural color of the photonic crystal changes accordingly. Using a photonic material responding to mechanic forces, one can design invisible photonic prints shown by deformation due to non-uniform mechanic responses between the neighboring photonic structures [53].

In order to fulfill the requirement of showing patterns by deformation, the original photonic paper must have good mechanochromic responses. Recently, a photonic crystal gel is fabricated by fixing the metastable SiO_2 colloidal crystals in the matrix of ethylene glycol (EG) and poly(ethylene glycol) methacrylate (PEGMA) through photo-polymerization [54]. It contains high volume fraction of nonvolatile organic solvent (EG), which greatly improves the gel's elasticity and thereby the sensitivity of structure color to the deformation. A total 150-nm reflection wavelength shift can be achieved by stretching and squeezing, which means the color change may cover the entire visible range. Meanwhile, the photonic

gel possesses a fast and reversible mechanochromic response with stable reflection intensities. All these properties make it an ideal photonic paper, on which invisible patterns can be printed.

Intrinsically, printing invisible photonic patterns can be regarded as the spatial arrangement of photonic structures, where the "pattern" and "background" section shall have close initial optical signals but non-uniform response to external stimuli. In this case, we need a pair of photonic structures, which will present different deformation and structural color by a same external force. Since the elasticity of the gel can usually be controlled by its chemical crosslinking level, the printing operation might be converted to a process of producing neighboring photonic gels with different crosslink level. As the original photonic paper has no chemical crosslinking at all, it is convenient to control its level by introducing crosslinker (PEGDA) to the whole paper followed by a selective UV curing treatment under photo mask, which produces invisible patterns on paper finally.

According to the above strategy, a simplest invisible pattern composed of two semicircles is printed on the photonic paper to verify the mechanism and performance of pattern showing and hiding. One semicircle is crosslinked by PEGDA and presents "hard" characteristic, while the other keeps uncrosslinked and retains the "soft" feature of original paper due to the shielding of photo-mask in UV curing. In the relaxed state, the semicircles are hidden due to the close reflection wavelength and similar structural color. However, when the sample is squeezed, the "soft" semicircle turns red due to the expansion of crystal lattice in vertical orientation, while the "hard" semicircle barely deforms and keeps on showing green, which forms a large contrast in color immediately. When it is horizontally stretched, the "soft" part turns blue due to the compression of crystal lattice and the "hard" one keeps unchanged, which eventually generates a visual contrast either.

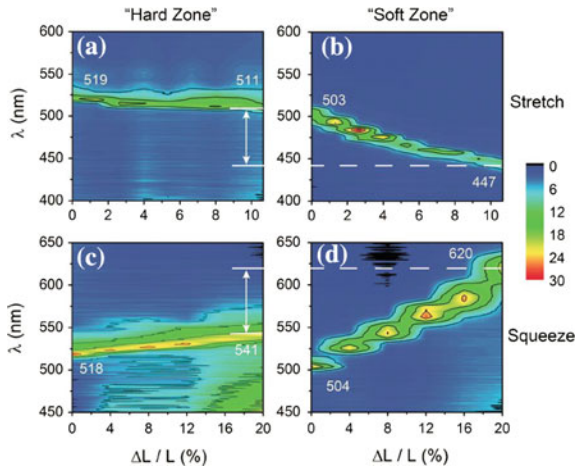

Fig. 6.11 Evolution of reflection signals for crosslinked (hard) and uncrosslinked (soft) photonic paper under stretching and squeezing [53]

The evolution of reflection spectra of two semicircles under deformation is recorded by a three-dimensional contour map with deformation ratio in x-axis, reflection wavelength in y-axis and reflection intensities in color (Fig. 6.11). Taking the stretching experiment as an example, the crosslinked (hard) semicircle has a λ of 519 nm in the relaxed state, while the uncrosslinked (soft) one has a λ of 503 nm. It shows that the crosslinking causes slight change to the reflection wavelength, so that the patterns are hard to be distinguished. However, as the whole photonic paper is stretched for 10.67 %, the reflection peak of crosslinked/uncrosslinked semicircle nonuniformly blue-shifts to 511/447 nm due to relatively small/large deformation ratio, which leads to a $\Delta\lambda_t$ of 64 nm and a large color contrast between them finally. For the case of squeezing, a reflection wavelength contrast of 14 nm is presented between two semicircles before deformation, and it amplifies to 79 nm after the sample is squeezed for 20 %, which leads to a similar hiding in release and showing under deformation.

The as-prepared photonic printing can reversibly show its patterns by deformation and hide them by releasing for many times. Two samples made from same SiO_2 particles are used to prove the reversibility in squeezing and stretching respectively, and the ratio of squeezing and stretching are set to be 16 and 6.67 %. For cycling squeezing-releasing experiment, the originally small reflection wavelength contrast in relaxation state between two semicircles always enlarges by squeezing and recovers immediately by relaxation. While the increasing of reflection intensities by squeezing and recovery by relaxation also present periodical changes during the test. For stretching experiments, similar reversibility can be concluded except for a relatively large fluctuation in the reflection intensity. In fact, invisible photonic prints encapsulated in polydimethylsiloxane (PDMS) rubber have been repeatedly squeezed and released for 100 times, and its showing-hiding function works well in all the cycles. Generally, this reversibility can be maintained unless the photonic gel breaks into pieces by over deformation or loses the mechanochromic effects due to EG evaporation.

Because the spatial control of crosslink level is realized by selective UV curing under photo mask, the current printing strategy can be seamlessly combined with well-developed photo lithography techniques, so that the sophisticated patterns designed in computer can be printed on the photonic gel to achieve corresponding products. Typically, the fabrication of invisible photonic prints includes the preparation of mechanochromic photonic paper and the printing of photonic patterns on it. The photonic gel was prepared by fixing the metastable SiO_2 colloidal crystalline array (CCA) in the matrix of EG and PEGMA through photo-polymerization, and it was swollen with the mixture of EG and PEGDA in volume ratio of 5:5. Then, the patterns designed in computer were printed on a transparent slide using commercial laser printer to generate a simplified photo-mask. When the swollen photonic paper covered with photo-mask was irradiated by UV light, the exposed gel would be chemically crosslinked while the shielded part would not, which produced invisible patterns on paper. Finally, the samples were sealed inside PDMS rubber before repeated usages.

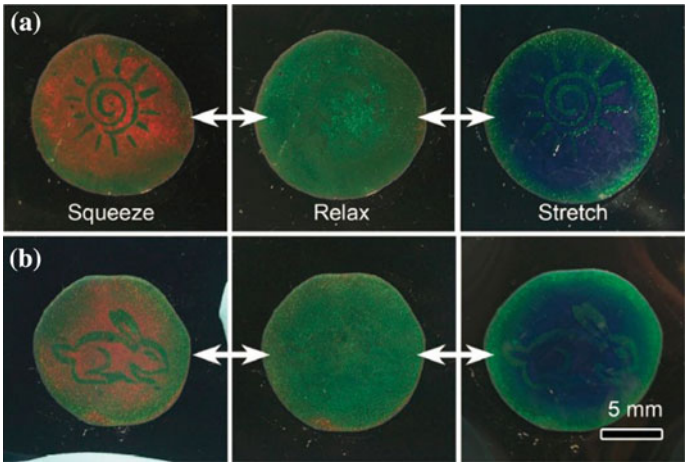

Fig. 6.12 Invisible **a** sunlight and **b** rabbit pattern hidden in relaxed state and shown by deformation [53]

As a demonstration, invisible photonic prints of "sunlight" and "rabbit" are printed (Fig. 6.12). These patterns are invisible under normal conditions. When the samples are squeezed, the background turns red and the patterns keep green, so that the hidden images are revealed. Showing by stretching is similar except that the color contrast is formed by the green pattern and blue background in that case. It should be noted that the latter visual effect is realized by pushing and slight bending the sample with its convex surface facing up, because such bending causes same change in crystal lattice as the horizontal stretching.

6.4.3 Invisible Photonic Prints Shown by Magnetic Interaction

The previous examples tell people that printing invisible photonic prints is actually the spatial arrangement of two kinds of photonic structures, which show the same optical signals in original state but nonuniformly change their photonic structures under external stimuli, so that the invisible patterns can be revealed by the contrast from different structural colors. Follow this principle, a magnetic interaction based invisible photonic prints might be developed if the non-uniform change of photonic structures between the patterns and background can be realized by the application of magnetic field. Similar to the water soakage and deformation under external forces, a weak magnetic field can be achieved in our daily life. In some occasions, the showing of patterns by a small magnet is even easier as no direct contact and no chemical substances are required, which has intrinsic advantages for antifraud related applications.

Recent study of responsive photonic crystal provides us a magnetically tunable photonic crystal (MPC) composed of superparamagnetic Fe_3O_4 colloidal nanocrystal clusters suspended in water. Through surface coating of silica or carbon layer, the Fe_3O_4@SiO_2 and Fe_3O_4@C nanoparticles can be further used to fabricate MPCs in many organic solvents, which greatly extends its application range. Basically, the magnetic particles dispersed in solution are in Brownian motion so that the dispersion shows the intrinsic brown color of iron oxide. When the solution is exposed in a magnetic field, the particles form one dimensional chain structures with periodical interparticle spacing in the order of hundreds of nanometers due to the balance of magnetic attraction and electrostatic or solvated repulsion, so that the solution strongly diffracts visible light and presents structural colors.

This liquid phase and magnetically tunable photonic crystal has several merits for being used to fabricate invisible photonic prints. For instance, one can adjust the reflection wavelength, namely the structural colors, by changing the strength of external magnetic field or using magnetic building blocks with different sizes. Owing to the high refractive index of iron oxide, strong reflection is realized at a low volume fraction of particles (ca. 0.06 %), which means the production cost of magnetic particles will be low if a large scale photonic prints are produced. A relatively weak magnetic field (ca. 100–400 Gauss) is sufficient to induce the magnetic assembly of superparamagnetic particles due to the high magnetic moment, so that the showing of invisible pattern can be realized by a small magnet. Most importantly, the optical response to the variation of magnetic field is fast and fully reversible, which means people can see the invisible patterns instantly once application of magnetic field. All these properties suggest it could be an ideal material for making magnetically responsive photonic paper.

In fabrication of invisible photonic prints, the solid state or soft matter photonic paper is highly expected due to the convenience in storage, transportation and

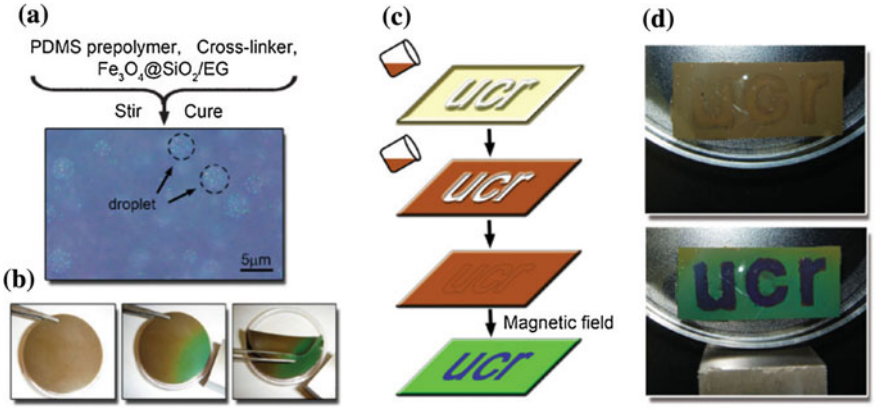

Fig. 6.13 **a** Droplet of EG solution of Fe_3O_4@SiO_2 particles embedded in PDMS prepolymer and **b** magnetically responsive silicone rubber prepared by curing the above precursor. **c** Fabrication of invisible photonic prints which **d** shows the letters in the magnetic field [55]

practical usage. However, the current MPC is composed of the solution of magnetic particles. A feasible solution to this problem is the encapsulation of the droplet of MPC inside an inert matrix, such as polydimethylsiloxane (PDMS), which produces a semi-solid photonic composite without losing the magnetic response (Fig. 6.13). Typically, the EG solution of $Fe_3O_4@SiO_2$ particles, the PDMS prepolymers and the curing agent are mixed together to form heterogeneous precursor, which is converted to a brown silicone rubber by being placed at room temperature for 24 h. The EG solution of magnetic particles disperses in the precursor in form of emulsion droplets due to the high viscosity of PDMS prepolymer as well as the match in density between glycol and PDMS, so that the as-prepared silicone rubber also contains numerous magnetically responsive liquid droplets. Similar to the solution of magnetic particles, the $Fe_3O_4@SiO_2$/EG-PDMS rubber shows the dark brown color of iron oxide in the absence of magnetic field. On the other side, it shows a brilliant structural color in magnetic field due to the assembly of $Fe_3O_4@SiO_2$ particles in EG droplets. Therefore, such composite material can be a qualified photonic paper for invisible prints shown by magnetic field, and the elastic characteristic of PDMS rubber will enhance the durability of paper in practical usage.

Based on the $Fe_3O_4@SiO_2$/EG-PDMS rubber, there are two strategies to realize invisible photonic prints shown by magnetic field. One strategy utilize two MPC composed of different-size magnetic particles to fabricate the patterns and background respectively, which shows different structural colors in magnetic field, leading to the showing of invisible prints [55]. As shown in Fig. 6.13, precursor 1 is poured into the mold and cured to form the background. Then, precursor 2 is added and cured to form the pattern section. In the absence of magnetic field, the sample is a dark brown silicone rubber showing no patterns, because both the pattern and background section show the intrinsic color of iron oxide no matter what size of magnetic particles it contains. However, the pattern and background section turns blue and green respectively in magnetic field, so that the striking color contrast reveals the invisible patterns. It should be noted that the reflection/structural color of MPC can be tuned by magnetic field, and it will reach a constant value when the magnetic field is increased to a critical strength, because the solvation layer of $Fe_3O_4@SiO_2$ particles will prevent them getting closer any more. Therefore, the stability of MPC under strong magnetic field is not a problem, and the showing of patterns is usually realized by applying a magnetic field stronger than both critical field strengths.

Another strategy utilizes the photolithography and UV irradiation to selectively evaporate EG content of the droplet and disable the capability of magnetic assembly in part of the photonic paper, so that a contrast between structural color of MPC and intrinsic color of iron oxide will be formed in magnetic field and the invisible prints will be revealed [56]. Typically, the precursor containing $Fe_3O_4@C$ particles, EG and PDMS are mixed and cured at 60 °C for 2 h to obtain a dark brown photonic paper. Covered by a photo-mask with patterns designed by computer, the photonic paper is exposed under UV irradiation to form the invisible pattern. UV irradiation will induce scissions of PDMS chain and lead to the rupture of PDMS networks on

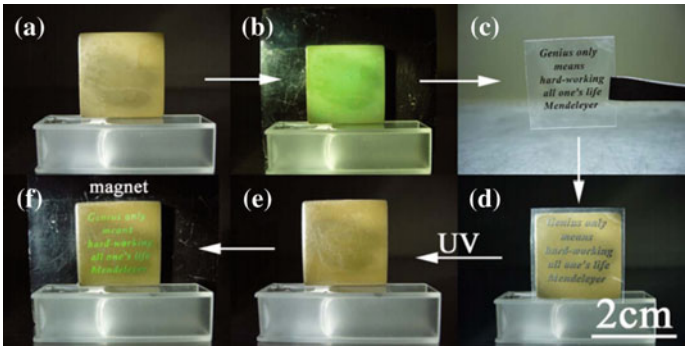

Fig. 6.14 Preparation of invisible photonic prints shown by magnetic field. The invisible information can be reversibly revealed and hidden by application and removal of a magnetic field [56]

the surface region, so that EG in the exposed region leaks during this process. As discussed above, the function and tuning of magnetic responsible photonic crystals is based on the well dispersion of super-paramagnetic Fe_3O_4@C particles in solvent. Therefore, the magnetically responsible characteristic in the exposed region of the paper will be disabled due to UV irradiation, but it can be maintained in the shielded region. In the absence of magnetic field, there is no visible pattern because both the dried particles and those dispersed in EG droplets show the intrinsic color of Fe_3O_4@C. Once the external magnetic field is applied, the shielded region displays brilliant structural color immediately as the particles assemble to form one-dimensional photonic structures while the exposed region remains brown, which brings a large contrast between them and reveals the invisible pattern (Fig. 6.14).

The invisible photonic prints shown under magnetic field have some common merits due to the instant and reversible response of MPC to the magnetic field, the showing or hiding of invisible pattern can be achieved as soon as the magnetic field is applied or removed, and it can be repeated for many times only if the silicone rubber retains its magnetic response. Unlike the regular colorful prints made by pigments, the structural color will not fade or degrade under harsh environment. But it should be noted that the gradual evaporation of EG from the silicone rubber is still a concern to the lifetime of the prints, and some technical improvements are required to prevent this process. Compared to other invisible photonic prints, the showing of patterns by magnetic field requires no deformation or infiltration of chemical substances, which brings much convenience to the users and prolongs the working life of the prints. Among the two strategies, the latter one is relatively easier to perform because the photo lithographic process can print sophisticated patterns onto the paper in high efficiency and low cost. In fact, such invisible patterns printed on a translucent and thin silicone rubber has been incorporated into banknotes to demonstrate its anti-counterfeiting functions, and it works fairly well with the application or removal of magnetic field [57].

6.5 Photonic Crystal Based Codec

Codec is a portmanteau of encode and decoder, which is usually considered as a device or computer program capable of encoding and decoding a digital data stream. It is most widely used in the video conferencing or streaming media application, where a codec encodes a data stream for transmission and storage or decodes it for playback and editing. Intrinsically speaking, the codec realizes the reversible conversion between "information" and "codes". If the involved "codes" can't be directly or easily understood by people, the codec naturally become an encryption device, which means the "information" can be embedded to the secure "codes" through encoding process and it can be translated from the "codes" through decoding process.

In this section, we shall introduce a photonic crystal multilayer based codec for encryption applications [58]. The stacking sequence of photonic crystal multilayers, as one kind of "information", is carried by the photonic film. While its reflection spectra can be considered as "codes", which can be used to reveal the information. Since the photonic crystal multilayers have similar appearance, the stacking sequence is well hidden and hard to be recognized by visual observation. However, through analysis of reflection intensity weight for each layer from the reflection spectra, one can translate the codes back to information and determine the stacking sequence.

Prior to the demonstration of photonic codec, the blocking effect of outer layer upon the reflection of inner layer shall be introduced first. For instance, a double layer PC film is prepared by sequential photo-polymerization of silica-ETPTA suspension, which is similar to the process introduced in Sect. 6.3.1. Its component, layer A and B, reflects visible light at 500 and 587 nm respectively. Layer A is fixed on a glass slide while layer B is stacked upon layer A one by one, and each layer is controlled to have an average thickness of 84 μm. Without layer B, the film only has reflection A with intensity around 30 %. However, as 6 layers of layer B stacked upon layer A, the intensity A decreases to 7 % and intensity B increases to 80 % gradually. The decreasing of reflection A suggests the outer PC films have blocking effect to the reflection signal from inner layers, because both the incident light illuminating the inner layer and the reflected light emitting from the inner layer are weakened due to the scattering of outer layers.

Based on the blocking effect, a codec system has been developed which utilize the reflection spectra ("codes") to identify the composition and stacking sequence of multilayer PC film ("information"). As shown in Fig. 6.15, three SiO_2-ETPTA precursors and triple layer structures are chosen for the demonstration. Since each layer can be prepared by any of the 3 precursor, there will be 27 combinations in total. Here, the stacking sequence is defined by three alphabets, such as ABC, which means in the corresponding film, A is the inner layer, B is in the middle and C is the outer layer. When the triple layer is composed of same precursor (A or B or C), the reflection spectra show a single peak, which is equivalent to that of single layer with triple thickness. When it is prepared by two components (A and B), the

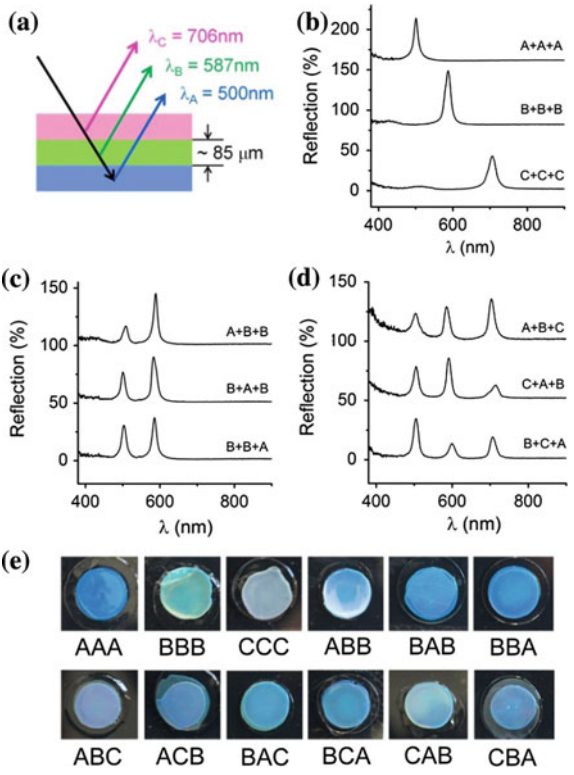

Fig. 6.15 **a** Scheme, **b**–**d** reflection spectra and **e** photos of triple layer photonic crystal film with different stacking sequence. A + B + C or ABC means A is the inner layer, B is the middle and C is the outer layer [32]

ratio of peak area (A:B) increases as the layer A moving outside. For multilayer consisted of three components (A, B and C), a qualitatively conclusion can be drawn that the outer layer has largest peak area, and the middle and inner layer has middle and smallest peak area respectively.

In addition to the qualitative analysis above, the reflection spectra can precisely tell the stacking sequence based on a quantitative analysis of reflection intensity weight for each layer. Since the light intensity is in proportion to the reflection peak area (S_A, S_B and S_C), one can estimate the weight of reflection intensity for each layer by calculating its percentage among the total area (S_A/S_T, S_B/S_T and S_C/S_T, $S_T = S_A + S_B + S_C$). The percentages around 20, 30 and 40 % indicate that this film is located in the bottom, middle and upper layer, respectively. Higher percentages may appear when some layers are using the same material. For a typical reflection spectra of PC multilayers, whose S_A/S_T, S_B/S_T and S_C/S_T are calculated to be 24.68, 30.33 and 44.98 %, the layer sequence can be determined as "ABC". These films are hard to distinguish by naked eye, but with the help of UV-VIS reflection spectrometer, one can easily determine their layer sequence by measuring their reflections.

References

1. H. Kim, J. Ge, J. Kim, S. Choi, H. Lee, H. Lee, W. Park, Y. Yin, S. Kwon, Nat. Photonics **3**, 534–540 (2009)
2. H. Hu, J. Tang, H. Zhong, Z. Xi, C. Chen, Q. Chen, Sci. Rep. **3**, 1484 (2013)
3. D.N. Sharp, M. Campbell, E.R. Dedman, M.T. Harrison, R.G. Denning, A.J. Turberfield, Opt. Quant. Electron. **34**, 3 (2002)
4. J.H. Kang, J.H. Moon, S.K. Lee, S.G. Park, S.G. Jang, S. Yang, S.M. Yang, Adv. Mater. **20**, 3061–3065 (2008)
5. S. Colodrero, M. Ocana, H. Miguez, Langmuir **24**, 4430–4434 (2008)
6. M. Szekeres, O. Kamalin, P.G. Grobet, R.A. Schoonheydt, K. Wostyn, K. Clays, A. Persoons, I. Dékány, Colloids Surf. A **227**, 77–83 (2003)
7. S. Fujii, M. Kappl, H.-J. Butt, T. Sugimoto, Y. Nakamura, Ange. Chem. Int. Edit. **51**, 9809–9813 (2012)
8. P. Jiang, J.F. Bertone, K.S. Hwang, V.L. Colvin, Chem. Mater. **11**, 2132–2140 (1999)
9. S. Wong, V. Kitaev, G.A. Ozin, J. Am. Chem. Soc. **125**, 15589–15598 (2003)
10. Y. Fu, Z. Jin, G. Liu, Y. Yin, Synth. Met. **159**, 1744–1750 (2009)
11. J.P. Ge, Y.D. Yin, Ange. Chem. Int. Edit. **50**, 1492–1522 (2011)
12. L.L. Duan, B. You, L.M. Wu, M. Chen, J. Colloid Interface Sci. **353**, 163–168 (2011)
13. H. Fudouzi, T. Sawada, Langmuir **22**, 1365–1368 (2006)
14. K. Sumioka, H. Kayashima, T. Tsutsui, Adv. Mater. **14**, 1284–1286 (2002)
15. X. Sun, J. Zhang, X. Lu, X. Fang, H. Peng, Ange. Chem. Int. Edit. **54**, 3630–3634 (2015)
16. W.H. Briscoe, R.G. Horn, Langmuir **18**, 3945–3956 (2002)
17. A.C. Arsenault, H. Miguez, V. Kitaev, G.A. Ozin, I. Manners, Adv. Mater. **15**, 503–507 (2003)
18. C.F. Blanford, R.C. Schroden, M. Al-Daous, A. Stein, Adv. Mater. **13**, 26–29 (2001)
19. J.T. Heeres, S.H. Kim, B.J. Leslie, E.A. Lidstone, B.T. Cunningham, P.J. Hergenrother, J. Am. Chem. Soc. **131**, 18202–18203 (2009)
20. Y.J. Zhao, X.W. Zhao, J. Hu, J. Li, W.Y. Xu, Z.Z. Gu, Ange. Chem. Int. Edit. **48**, 7350–7352 (2009)
21. J. Hu, X.-W. Zhao, Y.-J. Zhao, J. Li, W.-Y. Xu, Z.-Y. Wen, M. Xu, Z.-Z. Gu, J. Mater. Chem. **19**, 5730–5736 (2009)
22. Y. Iwayama, J. Yamanaka, Y. Takiguchi, M. Takasaka, K. Ito, T. Shinohara, T. Sawada, M. Yonese, Langmuir **19**, 977–980 (2003)
23. Y. Lu, H. Xia, G. Zhang, C. Wu, J. Mater. Chem. **19**, 5952–5955 (2009)
24. K. Ueno, J. Sakamoto, Y. Takeoka, M. Watanabe, J. Mater. Chem. **19**, 4778–4783 (2009)
25. I. Lee, D. Kim, J. Kal, H. Baek, D. Kwak, D. Go, E. Kim, C. Kang, J. Chung, Y. Jang, S. Ji, J. Joo, Y. Kang, Adv. Mater. **22**, 4973–4977 (2010)
26. Y. Luo, J. Zhang, A. Sun, C. Chu, S. Zhou, J. Guo, T. Chen, G. Xu, J. Mater. Chem. C **2**, 1990–1994 (2014)
27. H. Wang, Q.W. Chen, Y.F. Yu, K. Cheng, Y.B. Sun, J. Phys. Chem. C **115**, 11427–11434 (2011)
28. X.L. Xu, G. Friedman, K.D. Humfeld, S.A. Majetich, S.A. Asher, Chem. Mater. **14**, 1249–1256 (2002)
29. W. Luo, H. Ma, F. Mou, M. Zhu, J. Yan, J. Guan, Adv. Mater. **26**, 1058–1064 (2014)
30. S.-N. Yin, C.-F. Wang, S.-S. Liu, S. Chen, J. Mater. Chem. C **1**, 4685–4690 (2013)
31. B. Ye, H. Ding, Y. Cheng, H. Gu, Y. Zhao, Z. Xie, Z. Gu, Adv. Mater. **26**, 3270–3274 (2014)
32. C. Liu, G. Gao, Y. Zhang, L. Wang, J. Wang, Y. Song, Macromol. Rapid Commun. **33**, 380–385 (2012)
33. M. Chen, L. Zhou, Y. Guan, Y. Zhang, Ange. Chem. Int. Edit. **52**, 9961–9965 (2013)
34. Z. Xie, K. Cao, Y. Zhao, L. Bai, H. Gu, H. Xu, Z.-Z. Gu, Adv. Mater. **26**, 2413–2418 (2014)
35. S.Y. Lee, S.-H. Kim, H. Hwang, J.Y. Sim, S.-M. Yang, Adv. Mater. **26**, 2391–2397 (2014)
36. D. Ge, L. Yang, G. Wu, S. Yang, J. Mater. Chem. C **2**, 4395–4400 (2014)

37. V.L. Colvin, MRS Bull. **26**, 637–641 (2001)
38. Y. Lu, H.T. Yu, S. Chen, X. Quan, H.M. Zhao, Environ. Sci. Technol. **46**, 1724–1730 (2012)
39. G.Z. Liao, S. Chen, X. Quan, H. Chen, Y.B. Zhang, Environ. Sci. Technol. **44**, 3481–3485 (2010)
40. X.F. Li, X.Z. Zhen, S.G. Meng, J.J. Xian, Y. Shao, X.Z. Fu, D.Z. Li, Environ. Sci. Technol. **47**, 9911–9917 (2013)
41. X.Q. Chen, J.H. Ye, S.X. Ouyang, T. Kako, Z.S. Li, Z.G. Zou, ACS Nano **5**, 4310–4318 (2011)
42. S. Bayram, L. Halaoui, Part. Syst. Charact. **30**, 706–714 (2013)
43. Y. Park, J.W. Lee, S.-J. Ha, J.H. Moon, Nanoscale **6**, 3105–3109 (2014)
44. L. Cui, Y. Li, J. Wang, E. Tian, X. Zhang, Y. Zhang, Y. Song, L. Jiang, J. Mater. Chem. **19**, 5499–5502 (2009)
45. M. Kuang, J. Wang, B. Bao, F. Li, L. Wang, L. Jiang, Y. Song, Adv. Opt. Mater. **2**, 34–38 (2014)
46. H. Fudouzi, Y. Xia, Langmuir **19**, 9653–9660 (2003)
47. D.W. Smith, P. Jiang Jr., J.M. .Ballato, S.H. Foulger, Adv. Mater. 17, 179–184 (2005)
48. J. Ge, J. Goebl, L. He, Z. Lu, Y. Yin, Adv. Mater. **21**, 4259–4264 (2009)
49. H.S. Lee, T.S. Shim, H. Hwang, S.-M. Yang, S.-H. Kim, Chem. Mater. **25**, 2684–2690 (2013)
50. C.G. Schafer, C. Lederle, K. Zentel, B. Stuhn, M. Gallei, Macromol. Rapid Commun. **35**, 1852–1860 (2014)
51. R. Xuan, J. Ge, Langmuir **27**, 5694–5699 (2011)
52. R. Xuan, J. Ge, J. Mater. Chem. **22**, 367–372 (2012)
53. S. Ye, Q. Fu, J. Ge, Adv. Funct. Mater. **24**, 6430–6438 (2014)
54. D. Yang, S. Ye, J. Ge, Adv. Funct. Mater. **24**, 3197–3205 (2014)
55. J. Ge, Y. Yin, Adv. Mater. **20**, 3485–3491 (2008)
56. H. Hu, C. Chen, Q. Chen, J. Mater. Chem. C **1**, 6013 (2013)
57. H. Hu, H. Zhong, C. Chen, Q. Chen, J. Mater. Chem. C **2**, 3695 (2014)
58. D. Yang, Y. Qin, S. Ye, J. Ge, Adv. Funct. Mater. **24**, 817–825 (2014)

Chapter 7
Photonic Crystals as Robust Label-Free Biosensors

Mark A. Lifson and Benjamin L. Miller

Abstract This chapter focuses on a highly sensitive class of label-free optical sensor: photonic crystals (PhCs). One- and two-dimensional versions of these structures (1D-PhC, 2D-PhC) can be readily fabricated using standard techniques from the microelectronics industry. While many research groups have contributed to development of PhCs in the context of biosensing, the chapter primarily focuses on efforts from several groups at the University of Rochester. We discuss novel photonic crystal designs, methods to capture and quantify small molecules, proteins, and viruses with photonic crystals, and remarkable approaches to improving photonic crystals in terms of their ultimate limit of detection and sensitivity. Looking forward, we also discuss new ways to use photonic crystals to discriminate between specific and non-specific binding.

7.1 Introduction

Biosensor technology has evolved rapidly over the last five decades. One of the first biosensors was an electrochemical sensor that, in the presence of glucose, determined oxygen concentration using the enzyme glucose oxidase [1]. For the detection of large and complex molecules (such as bacteria, protein, and viruses), it was necessary to produce schemes for amplifying signals produced by target binding, due to the lack of sensitive biosensing transducers. One of the earliest methods used to amplify biological signals was the incorporation of radioactive nuclides, which were read out using a Geiger counter to determine concentrations [2–4]. As technology improved,

M. A. Lifson · B. L. Miller (✉)
Department of Biomedical Engineering, University of Rochester,
Rochester, NY 14642, USA
e-mail: Benjamin_miller@urmc.rochester.edu

M. A. Lifson · B. L. Miller
Department of Dermatology, University of Rochester, Rochester, NY 14642, USA

M. J. Serpe et al. (eds.), *Photonic Materials for Sensing, Biosensing and Display Devices*, Springer Series in Materials Science 229,
DOI 10.1007/978-3-319-24990-2_7

alternatives were developed such as enzyme-substrate amplification (horseradish peroxidase [5], alkaline phosphatase [6, 7]), and chemically linked fluorescent labels [8]. Though these methods remain popular and widely used, there has been a recognition in both the academic and commercial sectors that devices which can directly measure biological material are desirable both from the workflow improvements they can provide, but also because the use of labels and secondary reagents can hinder the versatility and accuracy of the assay [9, 10]. One class of "label-free" sensors centers on monitoring changes in the optical properties of substrates with bound material on their surfaces, including light polarization (ellipsometery), light intensity (thin film interferometers), or refractive index (surface plasmon resonance) [11–13]. Generally, these devices follow the same modular format in which receptor (probe) molecules are first immobilized onto a substrate, and then immersed in a solution to identify the presence of its partner ligand (analyte). More recently, advances in nanofabrication have enabled the development of substrates that guide and interact with light *inside* of their volume, such as waveguides, spectral gratings, optical reflectors, and optical absorbers [14, 15]. Due to their small size, these devices require very few receptor/ligand interactions to produce a signal due to the enhanced material interaction inside the substrate volume, resulting in increased device sensitivity [16]. Devices such as toroidal and ring resonators, optical cavities, interferometers, and waveguides have been used to sense biological materials including proteins, bacteria and viruses [17–19]. While still at a relatively early stage, both interferometric methods and ring resonators have been commercialized.

This chapter focuses primarily on one particularly attractive label-free sensor: the two-dimensional photonic crystal (2D-PhC). Due to its remarkable sensitivity, small footprint, and low cost, photonic crystals were initially investigated for telecommunications applications, but subsequently became of interest as transducers in a wide variety of label-free biosensing applications. The working principles of the 2D-PhC are based on the underlying structure of the substrate, which is engineered to contain a periodic variation in the dielectric constant in two spatial directions (e.g., a series of wells arranged in a hexagonal pattern on a substrate; a simpler photonic crystal design, which we also discuss, is called a 1-D PhC and only varies periodically in one dimension). Such devices exhibit a tunable photonic bandgap (PBG), which selectively allows (or blocks) a range of light wavelengths. Often, the periodic translational symmetry of the PhC is interrupted with a defect, creating a localized mode within the PBG [20]. For example, when a row of pillars or wells is removed from the lattice, light can be guided around tight corners (90°), which is an impossible task with fiber-based waveguides [21]. High Q-factor resonators (where "Q", the "quality factor" of the device, is defined by the ratio of the resonance frequency and its full width at half-maximum bandwidth) can be formed by introducing a defects into a 1- or 2D lattice to change the shape and confinement of the electric field. Since the electric field is strongly confined near the defects, changes in the local refractive index will result in a shift in the position of the localized mode. Using a tunable laser, it is possible to measure the optical changes occurring within a 2D-PhC by monitoring positions of this resonance. The initial

position of the peak is used as a baseline, and subsequent incubation with biological material will shift the position of the peak due to the refractive index changes occurring in the crystal (and particularly within and close to the defect) upon binding. The degree of peak shifting corresponds directly to the amount of material present. In this way, 2D-PhCs detect the presence of biological material by monitoring the shifts in absorption dips, and can quantify the concentration of chemical or biological targets in a sample [22].

While this chapter focuses primarily on the current state of the art in 2D-PhC based biosensing, it is useful to first discuss earlier efforts to develop sensors based on a simpler structure, the 1D PhC. Here, as in the remainder of the chapter, we will primarily focus on efforts by several groups at the University of Rochester, rather than being comprehensive. Many groups world wide have also made critical contributions to our understanding of the design principles and capabilities of PhC sensors.

7.2 1D-PhCs in Biosensing

Most of the early research into the use of 1-D PhCs as chemical and biosensors centered on a material called porous silicon. Originally discovered in the 1950s independently by Ulhir [23] and Turner [24], research into the uses of porous silicon accelerated when its room temperature photoluminescence was first observed by Canham and colleagues [25]. Porous silicon is produced when n- or p-type silicon is subjected to an electrochemical etch in hydrofluoric acid. By varying the etchant composition (HF alone, or HF plus a cosolvent) porous silicon may be produced with a wide range of pore sizes. These materials are generally described as members of one of three groups: nanoporous silicon (pore size <10 nm), mesoporous silicon (10–100 nm) or macroporous silicon (100 nm and higher). Porous silicon has an inherent optical response, either viewed in reflection or, for some types, as luminescence due to nanocrystalline silicon particles remaining within the pores. Of relevance to our discussion here, the density of pores produced during the etching process may be changed as a function of current density. Changes in the porosity of porous silicon produce differences in the refractive index of the material, which in turn are visible as differences in the optical properties (Fig. 7.1a). Since etching only occurs at an appreciable rate at the interface between the etchant solution and unmodified silicon, this means that the pore density (or, porosity) of the silicon, and hence the refractive index of the material, may be changed in a precise and programmable way. This allows for the production of complex structures including Bragg mirrors or microcavities, both examples of 1-D PhCs. An example of a porous silicon microcavity is shown in Fig. 7.1b. Early work on the use of porous silicon in optical sensing was conducted in parallel by the Rochester team and by the Sailor and Ghadiri groups [26, 27]; here, we will focus on applications using 1-D PhCs.

The first example of a 1-D porous silicon PhC microcavity biosensor involved a device derivatized with a 30 base-pair DNA probe specific for lambda

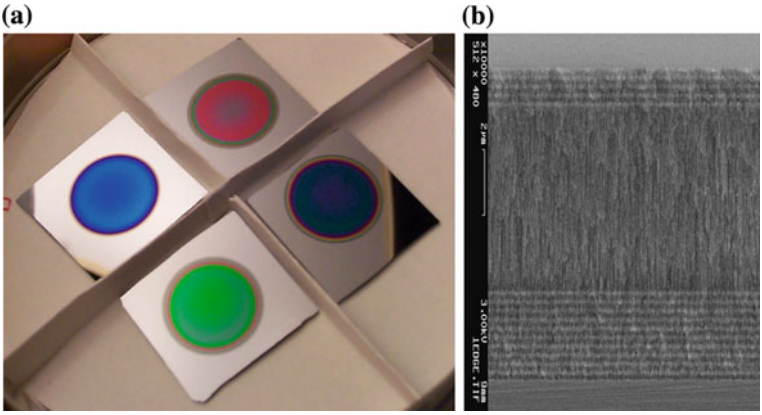

Fig. 7.1 **a** Porous silicon sensors. Each chip has a different pore density, producing readily observable differences in the reflectance spectrum. **b** Scanning electron micrograph of a microcavity resonator, or 1-D PhC, fabricated in porous silicon. Two multilayer mirrors flank an "active", or defect layer

bacteriophage. When treated with genomic DNA from lambda bacteriophage, the sensor yielded a strong red shift in its luminescence spectrum. In a control experiment, no red shift was observed for a sensor treated with synthetic, mismatched DNA [28]. While encouraging, questions remaining after this initial result included whether a porous silicon 1-D PhC sensor could be employed using other types of molecules as capture agents, and whether such a device could selectively detect a target in a complex biological sample. To address this question, a porous silicon microcavity sensor was functionalized with TWTCP (Fig. 7.2a), a designed, synthetic receptor for bacterial lipid A [29]. Since lipid A is a characteristic cell membrane constituent of Gram-(−) bacteria, it was anticipated that this sensor would constitute a silicon analog of the venerable Gram stain (in which a dye specifically adheres to lipoteichoic acid, a major constituent of Gram-(+) bacteria). Indeed, treatment of the sensor with lysate from *Escherichia coli*, a Gram-(−) bacterium, produced a readily discernible red shift (Fig. 7.2b) [30]. In contrast, exposure of the sensor to lysate from *Bacillus subtilis*, a common Gram-(+) soil bacterium, produced no change in the luminescence spectrum.

Macroporous 1D PhC structures are also suitable for biosensing, as detailed in a 2005 report of antibody-antigen detection [31]. While porosity of 1D PhCs may be tuned in order to favor infiltration of specific target analytes, an important feature of porous silicon is that its structure inherently prevents infiltration by large constituents of a sample. This is potentially useful in the context of diagnostics, as demonstrated most convincingly by an SEM image from the work of DeLouise and colleagues showing a red blood cell unable to penetrate a porous silicon matrix (Fig. 7.3). The DeLouise group has also provided a rare direct comparison between

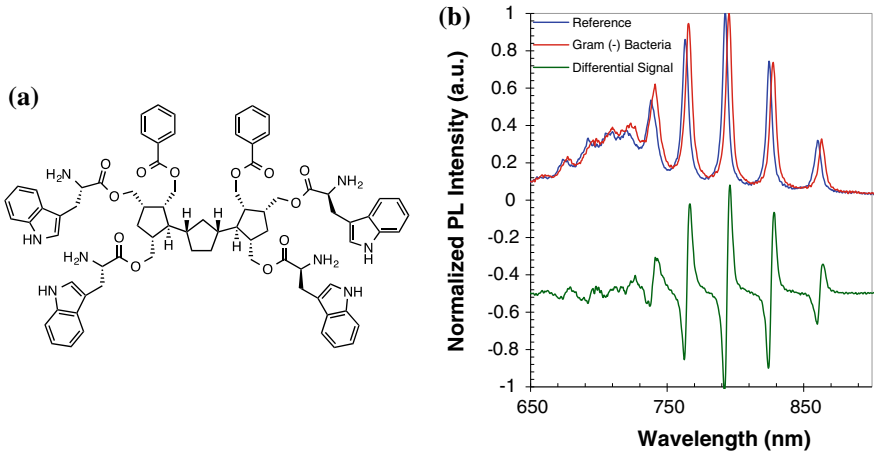

Fig. 7.2 **a** TWTCP, a synthetic receptor for bacterial lipid A. Treatment of a TWTCP-functionalized porous silicon 1D PhC with Gram-(−) bacterial lysate produces a red shift due to lipid A binding (**b**), while no signal is observed following exposure to a Gram-(+) bacterium

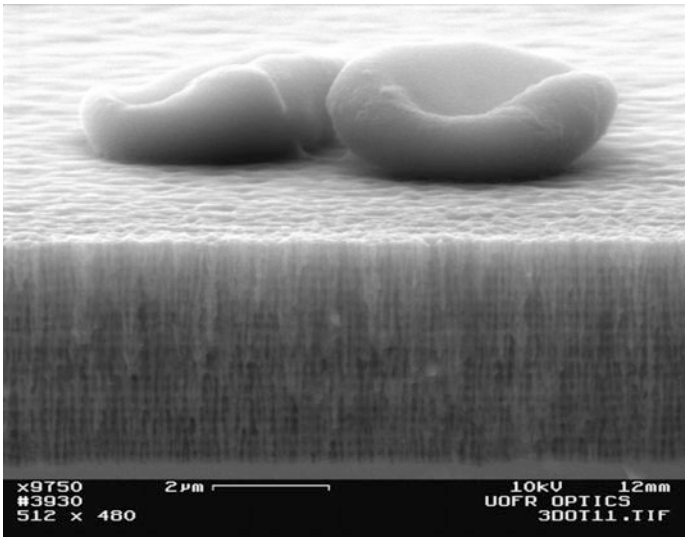

Fig. 7.3 SEM image highlighting the ability of porous silicon (here, a Bragg mirror of mesoporous silicon) to prevent infiltration of large sample constituents, such as a red blood cell (*courtesy* Dr. Lisa Bonanno and Prof. Lisa DeLouise)

the performance of a PhC sensor and a commercial diagnostic assay, in the context of developing an optical sensor for morphine. Here, a competitive assay for morphine and morphine derivatives was developed, and was found to provide results equivalent to those provided by the clinical assay [32].

While most experiments with porous silicon sensors have focused on materials embedded in a solid silicon wafer, it is possible for these devices to function following removal from the underlying substrate (which can be effected by a strong, electropolishing current at the end of the etch process). In a particularly notable example of this, the Rochester group reported in 2005 that a porous silicon sensor could be embedded in a hydrogel bandage material, and that its optical response was essentially unchanged after repeated cycles of hydration and drying over the course of a full year [33].

In addition to 1D PhCs fabricated in porous silicon, other materials systems have been the subject of considerable research and, in one case, even commercialization. The Cunningham group in particular has demonstrated a series of applications for 1D photonic crystal polymers; [34–36] these can be manufactured at large scale, and have been integrated with 96- and 384-well microtiter plates. A closely related technology has been commercialized by Corning, Inc. as the Epic® system. In a very different design, evanescently coupled 1-D PhCs have been fabricated by Erickson and colleagues. When coupled with optofluidic (i.e. optical forces combined with microfluidic forces) manipulation of analytes, these sensors have demonstrated very high sensitivity for targets [37].

7.3 Design, Development, and Optimization of 2D-PhCs

While our group and many others have (as discussed above) produced notable successes in the use of 1D PhCs for sensing, the potential for dramatically reducing the interaction volume, and in turn driving a dramatic increase in sensitivity, led to research on 2D PhCs. Several 2D-PhC designs have been examined in the context of biological and chemical sensing. In particular, our work has centered on the use of structures in which a single defect provides a readily observable resonance peak to detect the binding of target analyte, and as such will be the main focus of the remainder of this chapter [22, 38–40].

Our initial photonic crystal design included input and output waveguides terminating at the array, and a point defect (a hole with a larger diameter) in the center of the crystal (Fig. 7.4a). The optical spectrum for these devices have photonic bandgaps formed through the destructive interference of incident light, with the exception of a single wavelength which was transmitted through the crystal as a result of the perturbation in periodicity from a large point defect. A different design was also pursued, where a waveguide passing through a hexagonal array of air holes allowed many optical modes to be guided through the crystal within the photonic bandgap, with the exception of a single wavelength, which was absorbed as a result of the perturbation in periodicity from a smaller point defect (Fig. 7.4b).

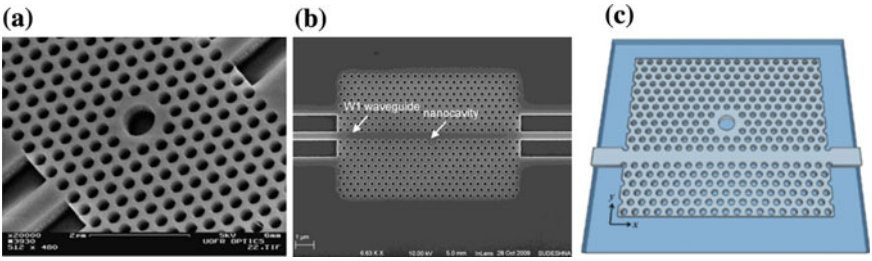

Fig. 7.4 SEM images of two dimensional photonic crystals with three different designs. **a** A large defect (600 nm) within a triangular lattice of smaller diameter (235 nm) air wells on a silicon-on-insulator wafer [39], **b** A small diameter defect (110 nm) within a triangular lattice of smaller diameter (235 nm) air wells and a removed row of wells (w1 waveguide) [38], and **c** A proposed design with a large diameter defect and a removed row of wells (w1 waveguide) [41]

This design allowed for multiplexing of many crystals along a single waveguide, since almost all optical modes, except those absorbed by the point defects, passed through the crystals. Our most recent design included a point detect that was larger than the surrounding lattice, and also included a w1 waveguide (i.e. a waveguide having the width of a single row) (Fig. 7.4c). Because the electric field is strongly localized to the defect region, having a well that was larger than the surrounding lattice could provide a means to selectively capture large biotargets such as viruses.

Typically, 2D-PhCs are fabricated using top-down approaches in a clean-room environment. The feature sizes of 2D-PhCs are accessible via widely used commercial photolithographic techniques. However, because research has focused on devices still in the prototyping stage, fabrication processes are typically performed using electron-beam lithography, since creating new masks with each design change is cost prohibitive when using photolithography. For all aforementioned designs, two different processes were used for 2D-PhC fabrication and were developed using a silicon-on-insulator wafer, which is comprised of a silicon layer (400 nm), buried oxide layer (1000 nm), and a silicon slab (>1 mm). The first process uses a negative electron-beam resist, polymethyl methacrylate (PMMA), to create features in SOI (Fig. 7.5top), while the second process uses a positive resist, hydrogen silsesquioxane (HSQ), (Fig. 7.5bottom).

Negative Resist:

1. Figure 7.5a, top: Oxide is first grown on an SOI wafer using a tube furnace, where ~100 nm of the underlying silicon layer is used to create ~150 nm of oxide. The process takes approximately 8 h.
2. Figure 7.5b, top: A negative resist is spun onto the wafer and cured for ~1 h.
3. Figure 7.5c, top: Locations to be removed (negative) are exposed to an electron beam to weaken the resist. This process takes on average 8 h, although the total time is dependent on the number of structures to be fabricated.
4. Figure 7.5d, top: The weakened resist is developed and washed away, leaving behind areas masked by unexposed resist.

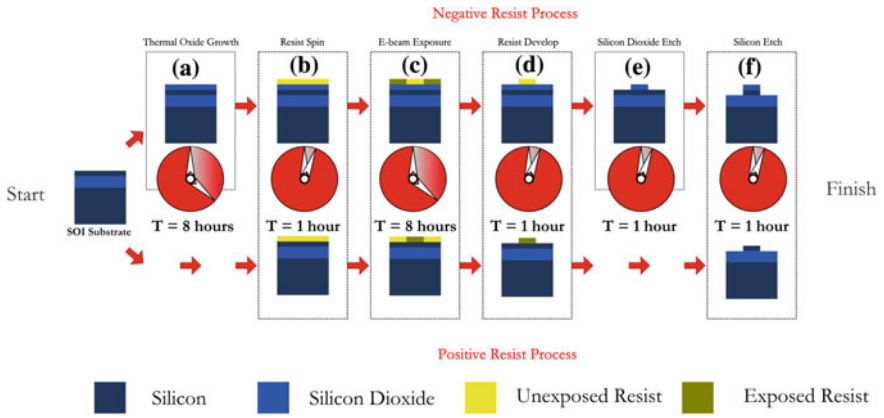

Fig. 7.5 Fabrication process for 2D-PhCs using a negative resist (*top*) or a positive resist (*bottom*). Steps include oxide growth (**a**), resist (**b**), electron-beaming (**c**), developing (**d**), silicon dioxide etching (**e**), and silicon etching (**f**)

5. Figure 7.5e, top: The resist is used as a soft mask for the underlying silicon oxide layer during a silicon dioxide-specific etch process.
6. Figure 7.5f, top: The leftover silicon oxide is then used as a hard mask for the underlying device layer (silicon), during a silicon-specific etch process.

Positive Resist:

1. Figure 7.5b, bottom: A positive resist is spun onto the wafer, no curing necessary.
2. Figure 7.5c, bottom: Locations to be masked (positive) are exposed to an electron beam to harden the resist. This process takes approximately 8 h, although the total time is dependent on the number of structures to be fabricated.
3. Figure 7.5d, top: The unhardened resist is developed and washed away, leaving behind areas masked by exposed resist.
4. Figure 7.5f, top: The resist is used as a soft mask for the underlying silicon layer during a silicon-specific etch process.

7.4 Biosensing with 2D-PhCs

While many different designs for 2D-PhCs have been proposed over the last decade, the Rochester group has been at the forefront of using them for the detection of biologically relevant targets. In the first report, a small defect design was used to measure transmission of light through the crystal after functionalization with capture molecules (Fig. 7.6a). The crystal was first modified with an amino silane followed by gluteraldehyde, allowing covalent capture of proteins and peptides via

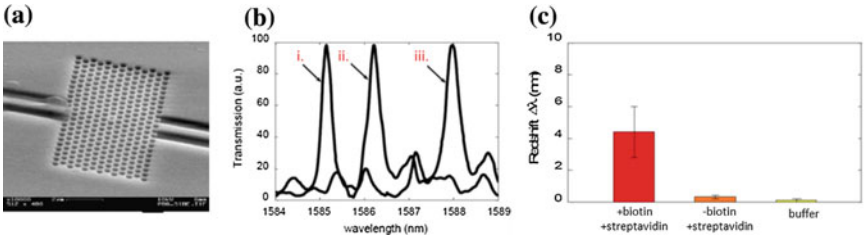

Fig. 7.6 Initial photonic crystal design (**a**), where spectrum measurements after silanization and oxidation (**b** i.), followed by gluteraldehyde (**b** ii.) and bovine serum albumin (**b** iii.) caused significant red-shifting of the maximum wavelength. Specificity and selectivity were determined using the same functionalization procedure for biotin binding streptavidin. Results demonstrated for the first time that 2D-PhCs could be used to detect biological molecules

reaction with surface lysines. After oxidation and silanization (Fig. 7.6b i.), gluteraldehyde treatment (Fig. 7.6b ii.), and bovine serum albumin deposition (Fig. 7.6b iii.) a spectrum was collected, and the red-shift of the defect resonance was observed. This non-specific, covalent capture of bovine serum albumin conclusively showed that proteins could be captured within the crystal surface and observed by measuring red-shifts. Specific detection was also measured using gluteraldehyde-immobilized biotin to capture streptavidin; significantly more streptavidin binding was observed relative to a chip lacking biotin Fig. 7.6c). Results with this design suggested that the limit of detection was approximately 2.5 fg, assuming a monolayer of material. This work set the stage for using 2D-PhCs to detect biological targets, and described a robust silane and gluteraldehyde surface chemistry for direct and covalent immobilization of proteins to the transducer surface, proving that the small sub-micron wells could be readily functionalized with biomolecules [22].

While this initial work studied the red-shift in response to non-specific binding, and high binding affinity pairs ($K_D \approx 10^{-15}$ mol/L), the response of the device for antibody/antigen interactions with more typical association thermodynamics was unknown. To answer this question, a different crystal design was used to measure lower affinity ($K_D \approx 10^{-9}$ mol/L) antibody/antigen interactions [42]. With this new design, crystals with slightly different defects were connected with a w1 waveguide to allow transmission of almost all wavelengths of light, except for those that were strongly absorbed independently by each crystal (Fig. 7.7a). Multiplexed devices were used to simultaneously measure multiple maximum wavelengths using a single waveguide and only one wavelength scan, providing redundant and statistically relevant data without having to run a separate control (Fig. 7.7b).

Since this design was robust and compact, large-scale protein binding studies could be performed. A dose-response experiment using multiplexed crystals functionalized with anti-human immunoglobulin gamma (IgG) specifically captured human IgG with a detection limit in the low nanomolar range (Fig. 7.7c) [38]. The calculated K_D for the h-IgG/IgG interaction based on these experiments was 7.2×10^{-7} mol/L, in agreement with values previously reported in the literature.

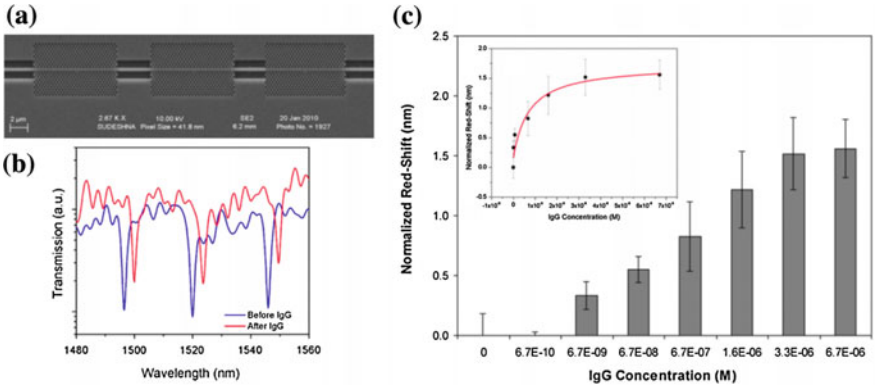

Fig. 7.7 Multiplexable, error-corrected 2D-PhC design (**a**). Multiple in-series crystals, with slightly different defect sizes, connected with waveguides could be used to track multiple red-shifts simultaneously on a single spectrum (**b**). Using this design, a dose-response for human immunoglobulin gamma (h-IgG) capture using anti-human IgG was experimentally determined (**c**). Error bars represent standard deviations from multiple measurements (n = 5)

These results indicated that the binding thermodynamics and biological interactions were well preserved and detectable with 2D-PhCs. Furthermore, this preliminary work suggested that 2D photonic crystals could be sufficient for real-time affinity analysis of biological molecules, if appropriate microfluidics were incorporated, since it was found to be sensitive to biomolecular capture in the relevant concentration ranges for these types of analyses.

Although label-free protein detection is important, there is a significant need to detect low levels of viruses that are known to be harmful to humans (e.g. human immunodeficiency virus, hepatitis B, human papillomavirus, etc.). Typical screening assays identify secondary reports to the virus (such as antibodies), which are detected many weeks after patients seroconvert from an acute infection. Therefore, it is important that viruses are measured directly and at the lowest possible concentration since a significant proportion of new infections, such as with HIV, are from individuals that have recently been infected [43]. While gold-standard nucleic acid-based tests can match the theoretical sensitivities of ultra-sensitive devices (detection can be performed down to single copies), the process is subject to large uncertainties and biases while also being labor intensive and time consuming to perform, since complex sample preparation steps are required [44–46]. Motivated by these reasons, researchers have attempted to use optical technologies for detection of whole viruses, since they strongly interact with light due to their large refractive index change per unit area [47, 48]. One attractive aspect of the 2D-PhC structures developed by the Rochester group is that the configuration of the substrate is particularly well suited for whole virus detection, since simulations show that the device is highly sensitive to materials which are size matched to the to the sensing regions, such as virus particle diameters (Fig. 7.8). Although the defect region is the most sensitive (largest light/matter interaction),

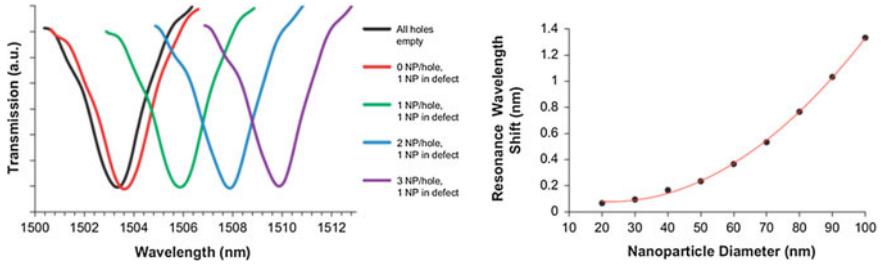

Fig. 7.8 Simulated transmission spectra of a 2D-PhC interacting with different numbers of nanoparticles inside the defect, neighboring wells, or combination (*left*). Simulated red-shift of a 2D-PhC design in response to differently sized nanoparticles infiltrating the defect (*right*). Results show that there is an observable red-shift for virus-sized objects

the surrounding wells can also interact with the electric field, albeit to lesser degrees, but still contribute a substantial amount of red-shift when material is bound to all of their interiors, such as capture of many virus-sized particles (Fig. 7.8a). Simulations also indicate that there is an observable red-shift when nanoparticles 20–100 nm in diameter are captured *only* at the defect, suggesting that 2D-PhCs are ideal for detecting virus-sized objects (Fig. 7.8b).

Almost all demonstrations of single particle sensitivities for 2D-PhCs use latex or polymeric spheres with refractive indices that are much higher than biological molecules (n = 1.45 vs. n = 1.35). It is well known that measured sensitivities are significantly higher when the refractive index contrast is large; therefore, it is important to use biological particles to demonstrate virus particle detection, which occurs with much less refractive index contrast. After showing that 2D-PhCs could be used to capture proteins and measure antibody/antigen interactions, the capability of the 2D-PhC devices to detect viruses was pursued. Using the same multiplexed transmission design previously described for h-IgG detection, detection experiments with ~55 nm diameter human papilloma virus-like particles (HP-VLP) were performed. HP-VLPs served as model viral pathogens, since they contained intact capsids but no replication machinery, and were therefore non-infectious and safe to handle. Motivated by the need to detect viruses at low concentrations from complex matrices (such as blood), detection experiments were conducted in 10 % bovine serum (Fig. 7.9a). It was found that the 2D PhC retained the ability to selectively and specifically detect HPV VLPs with no appreciable loss in signal (red-shift). Furthermore, mostly intact virus particles were captured, since using antibodies specific for intact capsids had significantly more red-shift compared to antibodies specific for the denatured form or with none at all (Fig. 7.9b). In addition to confirming that viruses could be captured selectively, the limit-of-detection was determined from an experimental dose-dependent response of HP-VLPs captured with multiple 2D-PhCs (Fig. 7.9c). Results demonstrated a detection limit in the low nanomolar range, similar to that observed with h-IgG,

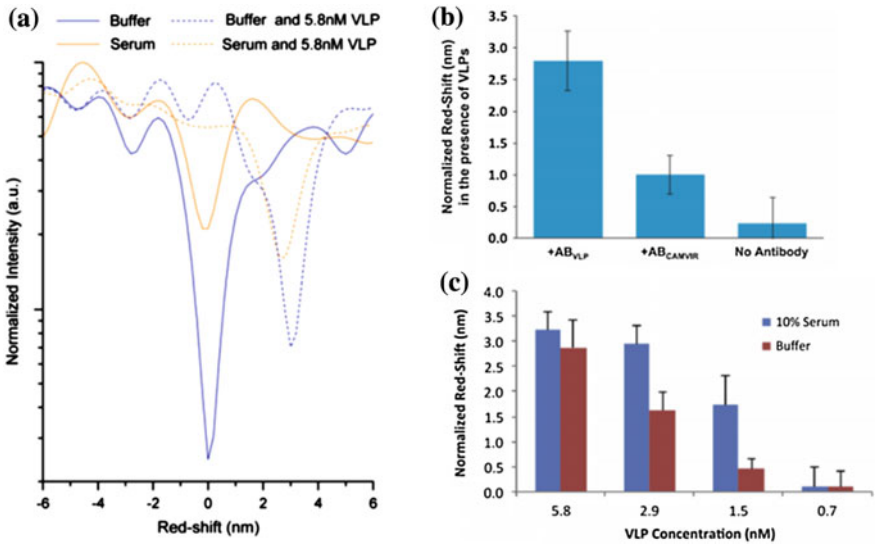

Fig. 7.9 Capture and quantitative detection of human papillomavirus-like particles (HP-VLP). Virus-like particles could be captured in buffer and 10 % serum with no noticeable difference in red-shift (**a**). Detection was sensitive for intact virus-like particles determined by using antibodies specific for the whole virus (**b**, $+AB_{VLP}$) compared to antibodies specific for denatured capsids (**b**, AB_{CAMVIR}) and absent any antibody (**c**, No Antibody)—error bars are standard deviations from average measurements (n=). Experimental dose-response of the 2D-PhC for different concentrations of HP-VLP in either 10 % serum or buffer (**c**)—error bars are the root-sum-squares of the standard deviation of red-shifts for the target and control chips

with a sensitivity of 0.5 nm/nM red-shift. These data provided the first demonstration that 2D-PhCs can serve as effective sensors for model viral pathogens, with high selectivity and low non-specific binding in serum [52].

7.5 Enhancing Sensitivity Through Directed Functionalization

Though detection was observed with 2D-PhCs, large amounts of target binding to areas outside the biosensor was expected to occur, since the functionalization procedure to capture biomolecules occurs not only at the crystal, but to the entire chip surface. It is well known that current methods of antibody immobilization, regardless of the type of label-free biosensor, can significantly deplete target (especially at low concentrations) and worsen the limit of detection [15, 19, 49]. While optical label-free biosensors have the capability to detect single particles (high sensitivity), in practice, this goal has been difficult to achieve. Capturing targets at low concentrations is fundamentally limited by the diffusion of molecules

and their binding to nanometer scale surfaces, which has been predicted to have picomolar detection limits within a reasonable time length for bioassays [50]. However, the reported detection limits for ultra-sensitive biosensors are significantly worse [14]. This is partly due to the placement of capture molecules over areas that are much larger than the sensor. In order to improve detection limits to match those of simulations, capture molecules need to be placed *only* on the active areas of nanoscale devices. However, this is nontrivial and an important issue that has not been specifically addressed in literature. Current immobilization strategies functionalize both sensing and non-sensing regions due to the inability to precisely place probes with nanometer precision in a reproducible and scalable way. As is often the case, large areas of surface are functionalized with probe molecules, and this in turn leads to target depletion and diminished limits of detection [49, 51, 52]. Since almost all optical label-free biosensors incorporate nanoscale features into their sensing modality, the topography of the design can potentially be exploited for selective functionalization of probe molecules. As discussed above, the Rochester group demonstrated that 2D-PhCs had nanomolar detection limits for proteins and viruses [38, 53]. Since the device was small (total area of 70 μm^2), it was hypothesized that the limit of detection could be improved if deposition of capture molecules was limited only to the photonic crystal. To test this hypothesis, a proof-of-concept experiment was performed, in which the ability of protein blocking nanoparticles (poly N-isopropylacrylamide, PNIPAM) to self-assemble around the distinct topography of a 2D PhC was exploited. Building on the previous work of Lyon, Serpe, and others that showed that PNIPAM nanoparticles readily self-assemble on surfaces [54, 55], we demonstrated that microgels self-assemble in a topographically selective manner—that is, they formed well packed patterns on planar surfaces, but did not enter into the well regions of the photonic crystal (Fig. 7.10).

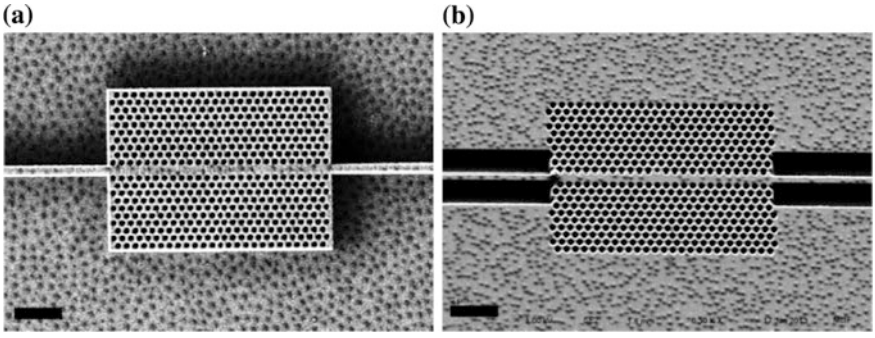

Fig. 7.10 Negative (**a**) and positive (**b**) 2D-PhC designs coated by dip-coating chips in a solution of protein blocking poly-N isopropylacrylamide micro-particles. Upon drying, particles spontaneously assembled into mosaic patterns in a topographically selective manner, avoiding the nanostructured regions of the photonic crystals

It was expected the large particle assemblies would block proteins from binding to the non-active surfaces and enhance the limit of detection by localizing capture molecules (antibody) to the photonic crystal but not the surrounding regions. Red-shifts of particle coated and control crystals were obtained for the IgG/h-IgG protein system. Red-shifts at 5.8 nM target were observed to be higher when antibody was localized to the photonic crystals compared to controls without nanoparticles (Fig. 7.11a). A dose-dependent response of IgG showed that immobilization of protein blocking nanoparticle onto the 2D-PhC surface caused the detection limit to improve by a factor of 100, closely matching the expected value from simulation (Fig. 7.11b, c) [56]. This method of blocking was simple, cost-effective, and could easily be modified to work for other types of label-free

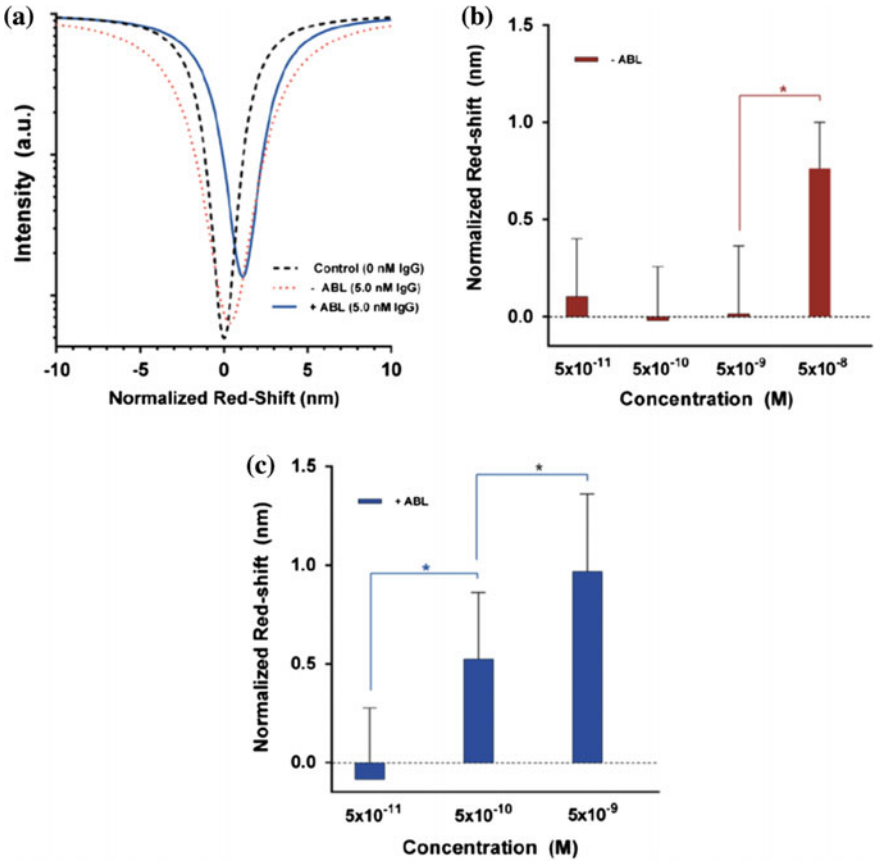

Fig. 7.11 2D-PhC capture of h-IgG with and without antibody localization (ABL) using protein blocking nanoparticles. At a high concentration, the red-shift was clearly observed (**a**). Without ABL, the highest observed concentration was 50 nM (**b**), while ABL the lower limit of detection was 0.5 nM (**c**). Error bars were calculated by taking the square root of the sum of the squares of the standard deviations between the experimental and control red-shifts

sensors. The key result of this work showed that simply adjusting the location of capture molecules to only the active regions of the device had large impacts on the lower limit of detection for 2D-PhCs.

One key problem with label-free sensing is the inability to discriminate between specific and non-specific binding of target molecules, which can severely restrict limits of detection and sensitivity. This is a particularly challenging problem with complex samples, such as serum, saliva, or other matrices that contain many molecules across a broad range of concentrations, all of which interfere with targeted detection. Recently, new crystal designs have been proposed which can monitor specific red-shifts resulting from target capture, while simultaneously and independently identifying non-specific binding. In most sensing experiments, a separate reference device (in this case a 2D-PhC) is treated in an identical manner to an experimental chip, except that the capture molecules are not immobilized. However, this method has several disadvantages. While the requirement that a portion of the total number of devices be dedicated as controls is most obvious, measurement of spectra either in parallel or in series means that performance deviations between devices as well as extrinsic factors, such as temperature or drift, are difficult to track. Sample composition can also change from experiment to experiment (especially with complex matrices), and so an on-chip and direct

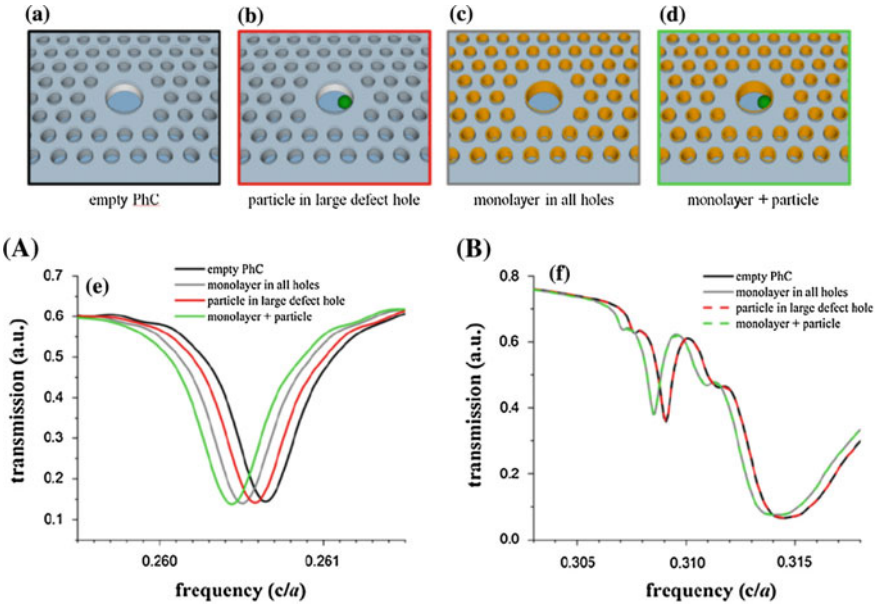

Fig. 7.12 Simulations of photonic crystals empty (*top*, **a**), containing a single large particle (*top*, **b**), coated with a monolayer of material (*top*, **c**), and with both particle and monolayer (*top*, **d**). Results show that the maximum absorption wavelength red-shifts when material is bound anywhere on the crystal (**A**), while the band-edge only shifts if material is present in the defect (**B**). Note, the x-axis is in units of frequency, and so a red-shift in wavelength is observed as a decrease in frequency

method is needed to monitor these types of changes on a sample-by-sample basis. A recent design from the Rochester group proposes a new way measure both specific and non-specific effects by monitoring the effects of band-edge shifting to determine if material is exclusively captured in the defect or by the surrounding neighboring wells (Fig. 7.12) [40]. The band-edge was found to be insensitive to monolayer thicknesses added to the 2D-PhC outer wells, but would shift if material were captured inside the defect. In this case, a large defect was fabricated so that selective capture of viruses and discrimination from particulates binding inside smaller, neighboring wells could be obtained.

7.6 Current Challenges and Future Outlook for 2D-PhCs

2D-PhCs serve as sensitive sensors for biodetection. In work conducted to date, experiments have demonstrated optical label-free detection of protein and viral targets in the presence of complex matrices. Additionally, unique designs may enable observation of changes at specific regions of the photonic crystals, enabling the discrimination between specific and non-specific binding based both on specific recognition and on the intrinsic geometry and optical properties of the crystal.

While these are encouraging results, the performance of 2D PhCs in "real world" applications remains far from the single-particle detection capability predicted by theory (and demonstrated for nonselective capture of latex particles in early experiments using highly specialized conditions). To close this gap, significant additional advances are required. First, as discussed in a seminal paper by Sheehan and Whitman [50], the sensitivity of nanoscale sensors is generally limited by the amount of material that can diffuse to the active area of the sensor within a "reasonable" time frame. Integration of the sensor with microfluidic channels can address the transport issue to an extent. However, further strategies will be needed to reach ultimate sensitivity. One promising approach is to utilize the optical trapping properties of the crystal to enhance binding; preliminary efforts along these lines have been published by our group and others [57–59]. Integration of sensors into full "lab on a chip" systems is also an important frontier: as stated at the outset, the dimensions and materials of 2D PhCs are compatible with standard photolithographic processes. Thus, when combined with an appropriate packaging strategy for on-chip light sources and detectors, reaching this goal should be feasible.

References

1. L. Clark, C. Lyons, Electrode systems for continuous monitoring in cardiovascular surgery. Ann. N. Y. Acad. Sci. **102**, 29–455 (1962)
2. A. McFarlane, Efficient trace-labelling of proteins with iodine. Nature **182**, 53 (1958)
3. R. Rice, G. Means, Radioactive labeling of proteins in vitro. J. Biol. Chem. **246**, 831–832 (1971)

4. A. Hershey, M. Chase, Independent functions of viral proteins and nucleic acid in growth of bacteriophage. J. Gen. Physiol. **36**, 39–56 (1952)
5. L.A. Sternberger, P.H. Hardy, J.J. Cuculis, H.G. Meyer, The unlabeled antibody enzyme method of immunohistochemistry: preparation and properties of soluble antigen-antibody complex (horseradish peroxidase-antihorseradish peroxidase) and its use in identification of spirochetes. J. Histochem. Cytochem. Cytochem. **18**, 315–333 (1970)
6. J.L. Cordell, B. Falini, W.N. Erber, A.K. Ghosh, Z. Abdulaziz, S. MacDonald, K.A. Pulford, H. Stein, D.Y. Mason, Immunoenzymatic labeling of monoclonal antibodies using immune complexes of alkaline phosphatase and monoclonal anti-alkaline phosphatase (APAAP complexes). J. Histochem. Cytochem. **32**, 219–229 (1984)
7. E. Engvall, P. Perlmann, Enzyme-linked immunosorbent assay, ELISA III. Quantitation of specific antibodies by enzyme-labeled anti-immunoglobulin in antigen-coated tubes. J. Immunol. **109**, 129–135 (1972)
8. T.H. The, T.E. Feltkamp, Conjugation of fluorescein isothiocyanate to antibodies. I. Experiments on the conditions of conjugation. Immunology **18**, 865–873 (1970)
9. D. Ivnitski, I. Abdel-Hamid, P. Atanasov, E. Wilkins, Biosensors for detection of pathogenic bacteria. Biosens. Bioelectron. **14**, 599–624 (1999)
10. K.K. Jain, Applications of nanobiotechnology in clinical diagnostics. Clin. Chem. **53**, 2002–2009 (2007)
11. J. Homola, S.S. Yee, G. Gauglitz, Surface plasmon resonance sensors: review. Sens. Actuators B Chem. **54**, 3–15 (1999)
12. J. Lu, C.M. Strohsahl, B.L. Miller, L.J. Rothberg, Reflective interferometric detection of label-free oligonucleotides. Anal. Chem. **76**, 4416–4420 (2004)
13. C.R. Mace, C.C. Striemer, B.L. Miller, Detection of human proteins using arrayed imaging reflectometry. Biosens. Bioelectron. **24**, 334–337 (2008)
14. X. Fan, I.M. White, S.I. Shopova, H. Zhu, J.D. Suter, Y. Sun, Sensitive optical biosensors for unlabeled targets: a review. Anal. Chim. Acta **620**, 8–26 (2008)
15. L.M. Bellan, D. Wu, R.S. Langer, Current trends in nanobiosensor technology. Wiley Interdiscip. Rev. Nanomed. Nanobiotechnol. **3**, 229–246 (2011)
16. L. Feuz, P. Jönsson, M.P. Jonsson, F. Höök, Improving the limit of detection of nanoscale sensors by directed binding to high-sensitivity areas. ACS Nano **4**, 2167–2177 (2010)
17. F. Patolsky, G. Zheng, O. Hayden, M. Lakadamyali, X. Zhuang, C.M. Lieber, Electrical detection of single viruses. Proc. Natl. Acad. Sci. USA **101**, 14017–14022 (2004)
18. H. Zhu, I.M. White, J.D. Suter, M. Zourob, X. Fan, Opto-fluidic micro-ring resonator for sensitive label-free viral detection. Analyst **133**, 356–360 (2008)
19. R.L. Caygill, G.E. Blair, Pa Millner, A review on viral biosensors to detect human pathogens. Anal. Chim. Acta **681**, 8–15 (2010)
20. S. Olivier, M. Rattier, H. Benisty, C. Weisbuch, C.J.M. Smith, R.M. De La Rue, T.F. Krauss, U. Oesterle, R. Houdré, Mini-stopbands of a one-dimensional system: the channel waveguide in a two-dimensional photonic crystal. Phys. Rev. B **63**, 113311 (2001)
21. J.D. Joannopoulos, Molding the flow of light. MIT Annual 32–43 (2001)
22. M.R. Lee, P.M. Fauchet, Two-dimensional silicon photonic crystal based biosensing platform for protein detection. Opt. Express **15**, 4530–4535 (2007)
23. A. Ulhir, Electrolytic shaping of germanium and silicon. Bell Syst. Tech. J. **35**, 333 (1956)
24. T.R. Turner, Electropolishing silicon in hydrofluoric acid solutions. J. Electrochem. Soc. **105**, 402–408 (1958)
25. L.T. Canham, Silicon quantum wire array fabrication by electrochemical and chemical dissolution of wafers. Appl. Phys. Lett. **57**, 1046–1048 (1990)
26. A. Janshoff, K.-P.S. Dancil, C. Steinem, D.P. Greiner, V.S.-Y. Lin, C. Gurtner, K. Motesharei, M.J. Sailor, M.R. Ghadiri, Macroporous p-type silicon Fabry-Perot layers. Fabrication, characterization, and applications in biosensing. J. Am. Chem. Soc. **120**, 12108–12116 (1998)
27. M.J. Sailor, Color me sensitive: amplification and discrimination in photonic silicon nanostructures. ACS Nano **1**, 248–251 (2007)

28. S. Chan, P.M. Fauchet, Y. Li, L.J. Rothberg, B.L. Miller, Porous silicon microcavities for biosensing applications. Phys. Status Solidi A **182**, 541–546 (2000)
29. R.D. Hubbard, S.R. Horner, B.L. Miller, Highly substituted *ter*-cyclopentanes as receptors for lipid A and simple carbohydrates in aqueous solution. J. Am. Chem. Soc. **123**, 5810–5811 (2001)
30. S. Chan, S.R. Horner, B.L. Miller, P.M. Fauchet, Identification of gram negative bacteria using nanoscale silicon microcavities. J. Am. Chem. Soc. **123**, 11797–11798 (2001)
31. H. Ouyang, M. Christophersen, R. Viard, B.L. Miller, P.M. Fauchet, Macroporous silicon microcavities for macromolecule detection. Adv. Func. Mat. **15**, 1851–1859 (2005)
32. L.M. Bonanno, T.C. Kwong, L.A. DeLouise, Label-free porous silicon immunosensor for broad detection of opiates in a blind clinical study and results comparison to commercial analytical chemistry techniques. Anal. Chem. **82**, 9711–9718 (2010)
33. L.A. DeLouise, P.M. Fauchet, B.L. Miller, A.P. Pentland, Hydrogel-supported optical microcavity sensors. Adv. Mater. **17**, 2199–2203 (2005)
34. C.-S. Huang, S. George, M. Lu, V. Chaudhery, R. Tan, R.C. Zangar, B.T. Cunningham, Application of photonic crystal enhanced fluorescence to cancer biomarker microarrays. Anal. Chem. **83**, 1425–1430 (2011)
35. B.T. Cunningham, Photnic crystal surfaces as a general purpose platform for label-free and fluorescent assays. J. Assoc. Lab. Automation **15**, 120–135 (2010)
36. L.L. Chan, M. Pineda, J.T. Heeres, P.J. Hergenrother, B.T. Cunningham, A general method for discovering inhibitors of protein-DNA interactions using photonic crystal biosensors. ACS Chem. Biol. **3**, 437–448 (2008)
37. S. Mandal, J.M. Goddard, D. Erickson, A multiplexed optofluidic biomolecular sensor for low mass detection. Lab Chip **9**, 2924–2932 (2009)
38. S. Pal, P.M. Fauchet, B.L. Miller, 1-D and 2-D photonic crystals as optical methods for amplifying biomolecular recognition. Anal. Chem. **84**, 8900–8908 (2012)
39. S. Pal, E. Guillermain, R. Sriram, B.L. Miller, P.M. Fauchet, Silicon photonic crystal nanocavity-coupled waveguides for error-corrected optical biosensing. Biosens. Bioelectron. **26**, 4024–4031 (2011)
40. M.R. Lee, P.M. Fauchet, Nanoscale microcavity sensor for single particle detection. Opt. Lett. **32**, 3284–3286 (2007)
41. J.E. Baker, B.L. Miller, Discrimination of specific and nonspecific binding in two-dimensional photonic crystals. Opt. Express **23**(6), 7101–7110 (2015)
42. S. Pal, E. Guillermain, R. Sriram, B.L. Miller, P.M. Fauchet, Microcavities in photonic crystal waveguides for biosensor applications. Proc. SPIE **7553**, 755304 (2011)
43. B.G. Brenner, M. Roger, J.P. Routy, D. Moisi, M. Ntemgwa, C. Matte, J.G. Baril, R. Thomas, D. Rouleau, J. Bruneau, R. Leblanc, M. Legault, C. Tremblay, H. Charest, M.A. Wainberg, Quebec primary HIV infection study group. High rates of forward transmission events after acute/early HIV-1 infection. J. Infect. Dis. **195**, 951–959 (2007)
44. M.C. Strain, S.M. Lada, T. Luong, S.E. Rought, S. Gianella, V.H. Terry, C.A. Spina, C.H. Woelk, D.D. Richman, Highly precise measurement of HIV DNA by droplet digital PCR. PLoS ONE **8**, e55943 (2013)
45. J. Zhang, J.P. Lang, F. Huber, A. Bietsch, W. Grange, U. Certa, R. Mckendry, H.-J. Güntherodt, M. Henger, Ch. Gerber, Rapid and label-free nanomechanical detection of biomarker transcripts in human RNA. Nat. Nanotechnol. **1**, 214–220 (2006)
46. R. Luo, M.J. Piovoso, R. Zurakowski, Modeling uncertainty in single-copy assays for HIV. J. Clin. Microbiol. **50**, 3381–3382 (2012)
47. H. Mukundan, A.S. Anderson, W.K. Grace, K.M. Grace, N. Hartman, J.S. Martinez, B.I. Swanson, Waveguide-based biosensors for pathogen detection. Sensors (Basel). **9**, 5783–5809 (2009)
48. H.K.P. Mulder, A. Ymeti, V. Subramaniam, J.S. Kanger, Size-selective detection in integrated optical interferometric biosensors. Opt. Express **20**, 20934–20950 (2012)
49. C.I.L. Justino, T.A. Rocha-Santos, A.C. Duarte, Review of analytical figures of merit of sensors and biosensors in clinical applications. Trends Anal. Chem. **29**, 1172–1183 (2010)

50. P.E. Sheehan, L.J. Whitman, Detection limits for nanoscale biosensors. Nano Lett. **5**, 803–807 (2005)
51. R.P. Ekins, Ligand assays: from electrophoresis to miniaturized microarrays. Clin. Chem. **44**, 2015–2030 (1998)
52. R.P. Ekins, F. Chu, Multianalyte microspot immunoassay–microanalytical "compact disk" of the future. Clin. Chem. **37**, 1955–1967 (1991)
53. S. Pal, A.R. Yadav, M.A. Lifson, J.E. Baker, P.M. Fauchet, B.L. Miller, Selective virus detection in complex sample matrices with photonic crystal optical cavities. Biosens. Bioelectron. **44**, 229–234 (2013)
54. M.J. Serpe, L.A. Lyon, Colloidal hydrogel microlenses. Adv. Mater. **16**, 184–187 (2004)
55. M.J. Serpe, C.D. Jones, L.A. Lyon, Layer-by-layer deposition of thermoresponsive microgel thin films. Langmuir **19**, 8759–8764 (2003)
56. M.A. Lifson, D.J. Basu Roy, B.L. Miller, Enhancing the detection limit of nanoscale biosensors via topographically selective functionalization. Anal. Chem. **86**, 1016–1022 (2014)
57. A.T. Heiniger, B.L. Miller, P.M. Fauchet, Proc. SPIE **7888**, 78880L (2011)
58. N. Descharmes, U.P. Dharanipathy, Z. Diao, M. Tonin, R. Houdré, Phys. Rev. Lett. **110**, 123601 (2013)
59. N. Descharmes, U.P. Dharanipathy, Z. Diao, M. Tonin, R. Houdré, Lab Chip **13**, 3268–3274 (2013)

Chapter 8
Sensing on Single Plasmonics

Chao Jing and Yi-Tao Long

Abstract Plasmonic nanoparticles (Au, Ag, Cu) have attracted increasing attentions due to their excellent optical, chemical and physical characters, especially localized surface plasmon resonance (LSPR) property. Plasmonic nanoparticles have been widely applied in the fields of catalysis, energy sources and various sensors. Notably, the development of optical techniques achieved the investigation of single plasmonic nanoparticles including dark-field microscopy, differential interference contrast (DIC) microscopy and surface plasmon resonance imaging, etc. The single-nanoparticle detection eliminates the average effect compared with bulk system and improves detection sensitivity dramatically, even to single molecule level. Thus, in this chapter, we focus on the determination on a single nanoparticle mainly based on plasmon resonance scattering spectroscopy under dark-field microscopy. The points of morphology and composition modulation, inter-particle coupling, plasmon resonance energy transfer and opto-electrochemical detection are highlighted.

8.1 Introduction

Localized surface plasmon resonance (LSPR) enables noble metal nanoparticles unique scattering and absorption spectroscopy [1–3]. After the incident light irradiating on nanoparticle whose size is far smaller than the light wavelength, the surface electrons are excited and collectively oscillated with the incident light. When the oscillation frequencies of the incident light and surface electrons come to resonance, LSPR occurs and gives rise to the strong extinction light and catalysis ability owing to the abundant active surface electrons [4, 5]. The scattering light of a single plasmonic nanoparticle was obtained since 2000, via dark-field microscopy

C. Jing · Y.-T. Long (✉)
Key Laboratory for Advanced Materials, East China University of Science and Technology, Shanghai 200237, People's Republic of China
e-mail: ytlong@ecust.edu.cn

M. J. Serpe et al. (eds.), *Photonic Materials for Sensing, Biosensing and Display Devices*, Springer Series in Materials Science 229,
DOI 10.1007/978-3-319-24990-2_8

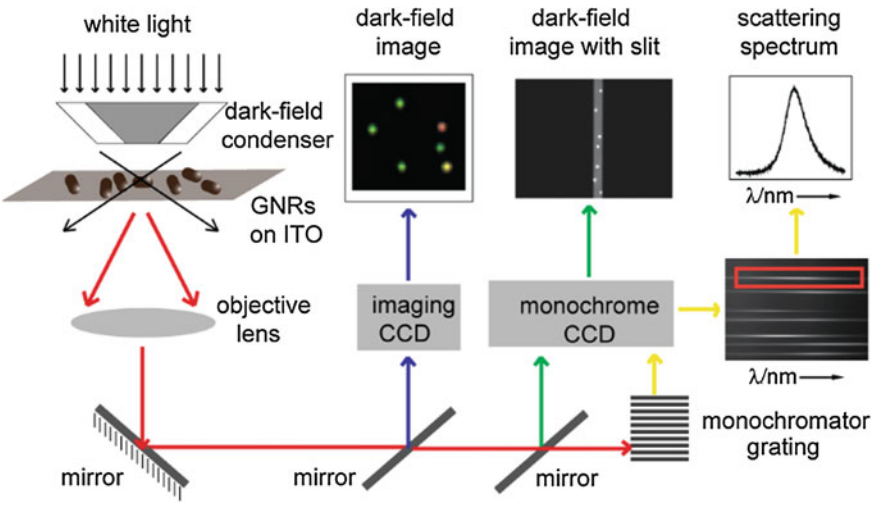

Fig. 8.1 Schematic of the experimental arrangement for dark-field microscopy studies of metal nanoparticles. Reproduced by permission from [10] of The Royal Society of Chemistry

[6, 7]. After that, scattering spectra of single nanoparticles have been exploited in ultra-sensitive sensors and cell imaging, etc. [8, 9].

Dark-field microscopy as a side illumination technique has extremely high contrast with distinguished signal to noise ratio. The setup of a dark-field microscopy is illustrated in Fig. 8.1 [10]. Dark-field condenser contains an opaque solid center that a ring-like pathway is formed for the incident light transferring. After the reflection of a prism, the ring-like beam of incident light is irradiated on the sample with an angle. With a transparent substrate, the incident light will keep transferring as the incoming direction and only the scattering light is collected by objective lens, resulting in a dark background. Due to the special functions of dark-field microscopy, the scattering spectra of a single plasmonic nanoparticle is obtained readily with equipment of spectrograph and light collection device.

8.2 Morphology and Composition Modulated Sensors

Size factor plays important roles in the optical properties and sensing abilities of nanoparticles [11, 12]. As single-nanoparticle detection has attracted more and more interest, analyzing the size of single nanoparticles readily and rapidly has become critical issues. Therefore, we proposed a novel method to measure the size of gold nanoparticles (GNPs) in situ and in real-time using the RGB (red, green, and blue) information from dark-field images [13]. After obtaining a dark-field image of single nanoparticles, as depicted in Fig. 8.2a, the RGB values of every pixel in one scattering color spot were calculated. Then RGB values were converted

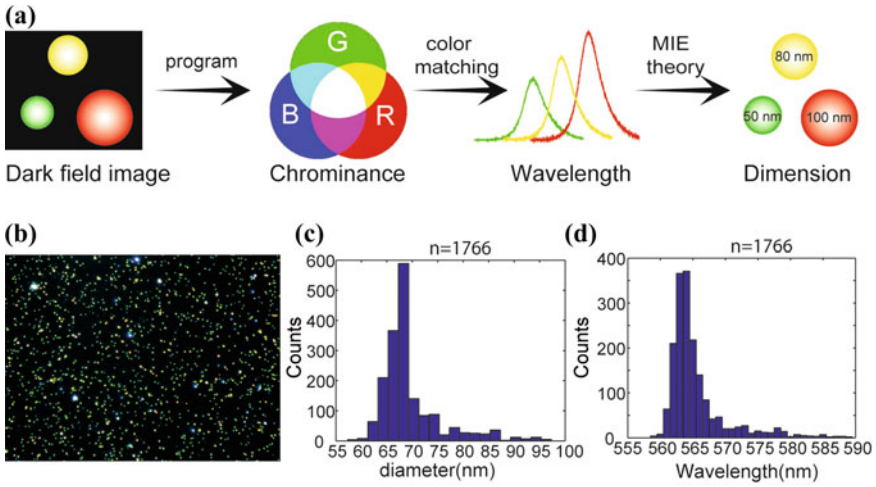

Fig. 8.2 **a** Calculation process of the RGB-based method. **b** Dark-field image and **c** calculated wavelength peaks and **d** diameter distribution of 1766 GNPs. Reprinted with permission from [13]. Copyright (2012) American Chemical Society

into spectral wavelength and intensity based on the chromaticity diagram. The calculated intensity of pixels with the same wavelength were added together and we considered the wavelength with the highest intensity as scattering spectral peak of nanoparticles. After that, the diameters of nanoparticles were calculated according to Mie theory correlating the relationship between size and scattering wavelength. Owing to the limitations of CCD sensitivity and color recognition, this method is only applicable to the calculation of gold nanospheres at the current stage. However, it opens a new way for the measurement of particle size which is more facile and economical than SEM and TEM characterization. Notably, by optimizing the calculation program, this approach enables measurements of thousands of nanoparticles within several minutes using a laptop computer. In Fig. 8.2c–d, the statistical wavelengths and diameters of 1766 particles in Fig. 8.2b were calculated in 1 min. Furthermore, observation of numerous individual nanoparticles not only eliminates the average effect of the bulk system, but also prevents random events in single nanoparticle detection.

In addition, gold nanoparticles have been widely applied in cell imaging as contrast agents for their excellent biocompatibility and stability. However, it is difficult to recognize the scattering spectra of single gold nanoparticles in living cells for the strong background such as scattering interference of organelles. Thus, we optimized the RGB-based method to obtain the scattering information of single gold nanoparticles in cells with high sensitivity and high throughput [14]. The flow diagram of data calculation process is depicted in Fig. 8.3a. The recorded dark-field image for living cell incubated with GNPs (Fig. 8.3b) is converted into gray scale image (Fig. 8.3c). Figure 8.3d is the binary image converted from the gray scale

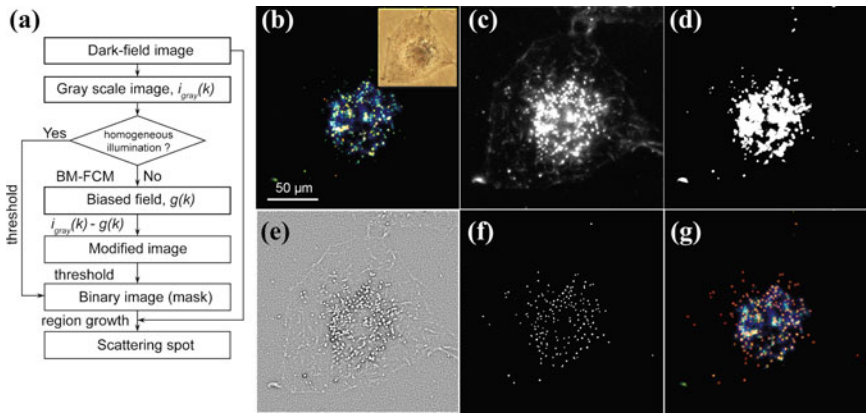

Fig. 8.3 **a** Flow diagram of the data process. **b** Dark-field image of HeLa cell incubated with GNPs and the corresponding bright-field image (*insertion*). **c** Gray scale image converted from the original image. **d** Binary image converted from the gray scale image through a threshold. **e** Modified image by substrate the biased illumination from the gray scale image. **f** Binary image converted from the modified image through a threshold. **g** Result of recognition, scattering spots of GNPs are framed by *red rectangle*. *Scale bars* in (**b**)–(**g**) are 50 μm. The thresholds are calculated by the Otsu method, respectively. Adapted with permission from [14]. Copyright (2015) Ivyspring International Publisher (Color figure online)

image through a threshold. In Fig. 8.3d, white pixels reflect to the recognized region of scattering light. It is obvious that the pixels belong to the scattering background of cells have been merged with the pixels of scattering spots for GNPs. GNPs in the binary image are difficult to be distinguished. This result is mainly due to the high intensity of biased field caused by the high background light and it is hard to find an appropriate threshold to segment the scattering area of nanoparticles. Thus, the bias-modified fuzzy C-means (BM-FCM) algorithm was introduced to the program to estimate the biased field in the image. Thus, a modified image was obtained by subtracting the biased field from the gray scale image to remove the strong scattering background in the cell as shown in Fig. 8.3e. Figure 8.3f is the binary image calculated from the modified image through a threshold. Then, the recognized pixels of GNPs were merged with the pixels of cell background through the region growth method. As shown in Fig. 8.3g, a total number of 264 GNPs were recognized and labeled in red rectangle. After this, the scattering spectra peak wavelength and intensity of every GNP were calculated using the above RGB-based method. This work provides a facile and rapid approach for the quantitative or semi-quantitative cell imaging detection.

The excellent catalytic activity of gold nanoparticles expands their applications in sensing fields [15–17]. Fan constructed a DNA sensor utilizing the glucose oxidase (GOx)-like activity of gold nanoparticles. Glucose was oxidized into gluconic acid and hydrogen peroxide by GNPs in the presence of oxygen [18]. After the addition of $HAuCl_4$, the catalytic product H_2O_2 reduced gold ions into gold

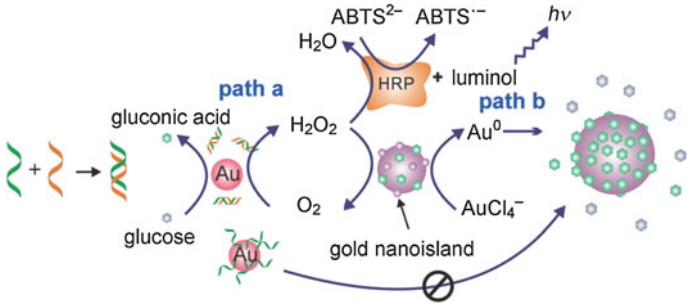

Fig. 8.4 Illustration of the GOx-like catalytic activity of AuNPs regulated by DNA hybridization, which can be either amplified by HRP-cascaded color or chemiluminescence variations (path **a**) or lead to nanoplasmonic changes owing to size enlargement (path **b**). *Orange strand* = target, *green strand* = adsorption probe. Reprinted with permission from [18]. Copyright 2011 WILEY-VCH Verlag GmbH & Co. KGaA, Weinheim (Color figure online)

atoms leading to the particle growth as illustrated in Fig. 8.4. It was proved that when GNP surface was covered with molecules such as soft single strand DNA (ssDNA), the enzyme-like catalytic ability was being confined. After the addition of complementary DNA, the hybridized double strand DNA (dsDNA) had rough structure and high surface charge. The interaction between GNP and dsDNA was very weak resulting in the dsDNA leaving and recovery of the surface activity. Thus, the GNP growth was modulated by the surface DNA structure offering a sensitive method to detect DNA according to the size dependent resonance scattering spectral shift of single GNP. This method achieved the recognition of 1-base mismatched DNA hybridization. Based on the GOx-like catalytic ability, an

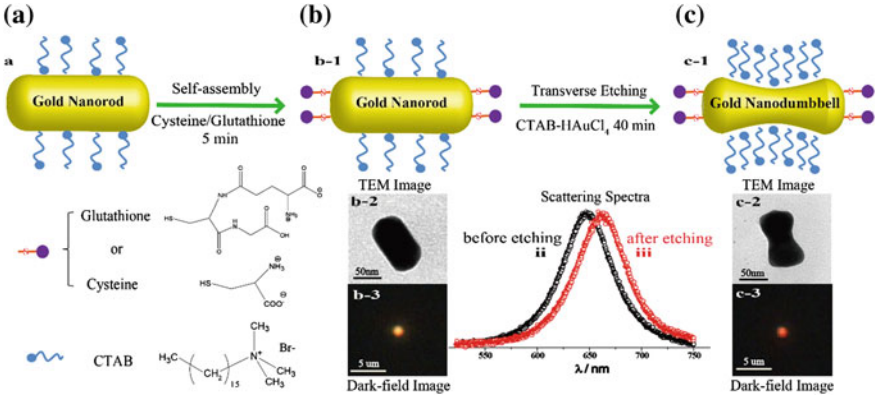

Fig. 8.5 Schematic illustration of transverse etching reaction on the single particle level. **a** Diagram of GNRs before reaction. **b–c** Diagram, TEM image, dark-field image and scattering spectra of GNRs in the solution of 0.1 mm cysteine before (**b**) and after (**c**) adding micellar solution of CTAB and $HAuCl_4$. Reproduced by permission from [24] of The Royal Society of Chemistry

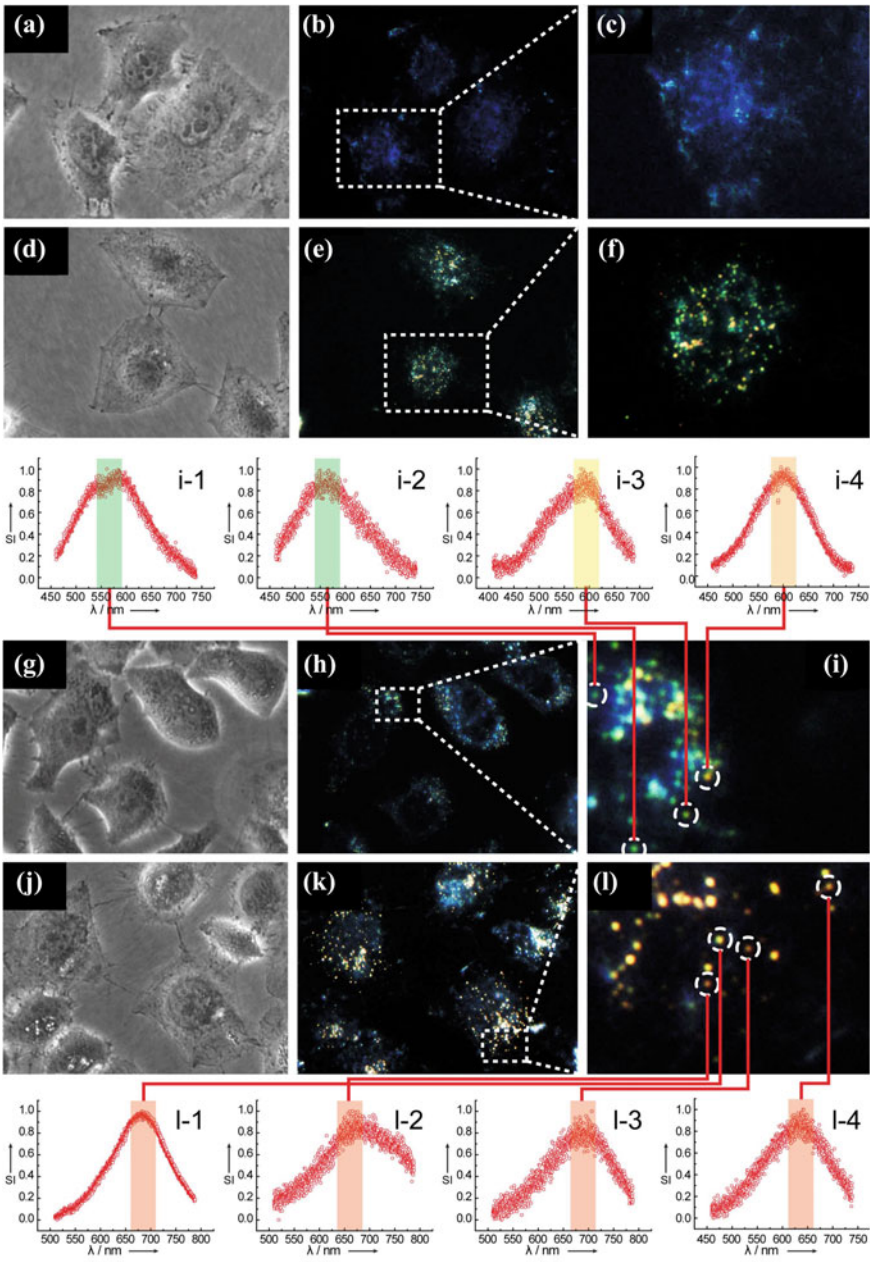
(a)
(b)
(c)
(d)
(e)
(f)
i-1
i-2
i-3
i-4
(g)
(h)
(i)
(j)
(k)
(l)
l-1
l-2
l-3
l-4
SI
λ / nm

◂**Fig. 8.6** **a** Bright-field images of HeLa cell. **b** DFM images of corresponding HeLa cell in (**a**). **c** The detail view of HeLa cell DFM images (**b**). **d** Bright-field images of HeLa cell after 24 h incubation with AuNPs. **e** DFM images of corresponding HeLa cell in (**d**). **f** The detail view of HeLa cell containing AuNPs DFM images (**e**). **g** Bright-field images of HeLa cell containing AuNPs with treatment by taxol (10 μm) and then incubation in TBS containing 50 μm $CuCl_2$ for 3 h. **h** DFM images of corresponding HeLa cell in (**g**). **i** The detailed view of HeLa cell DFM images (**h**), i-1 to i-4: Corresponding scattering spectra of different AuNPs in living HeLa cell. **j** Bright-field images of HeLa cell containing AuNPs without treatment by taxol and then incubation in TBS containing 50 μm $CuCl_2$ for 3 h. **k** DFM images of corresponding HeLa cell in (**j**). **l** The detailed view of HeLa cell DFM images (**k**), l-1 to l-4: Corresponding scattering spectra of different Au@Cu core–shell NPs in living HeLa cell (the *color bar* in the scattering spectra indicate the wavelength of the maximum scattering intensity, and reflect the resulting color). Reprinted with permission from [25]. Copyright 2011 WILEY-VCH Verlag GmbH & Co. KGaA, Weinheim

ultra-sensitive ATP sensor was also fabricated through modulation of GNP surface catalytic activity via ATP/aptamar interaction [19].

Except size factor, the shape of plasmonic nanoparticles also has crucial influence on the LSPR band. Particles with various shapes have been synthesized for different applications [20–22]. Exploring the particle producing process is important to the preparation method for nanomaterials [23]. Recently, we monitored the controllable morphological changing process of a single gold nanorod using dark-field microscopy and resonance scattering spectroscopy [24]. Gold nanoparticles were corroded under the condition of $HAuCl_4$ and cetyltrimethylammonium bromide (CTAB). To determine the dissolving mechanism, nanorods were modified with cysteine which selectively conjugated with the ends of nanoparticles. Figure 8.5 illustrates the modification process of nanoparticles. GNR was firstly capped with CTAB, and then assembled via cysteine through Au–S bonding on nanorods' ends. After the addition of $HAuCl_4$ and CTAB micellar solution, the nanorods showed distinct spectral red shift, as well as the color change in dark-field image as shown in Fig. 8.5c. In TEM images, the nanorod exhibited a dumbbell shape that the side parts of GNR were etched. This result was attributed to the change of GNR curvature that the gold [110] surface was changed into [111] surface under the CTAB micellar solution. CTAB (0.8–9.4 mM) as spherical micelle is more easily reacted with gold atoms and tends to react on low curvature structures. In addition, modified glutathione (GSH) also induced the transverse etching, yet mercaptoethylamine and 11-mercaptoundecanoic acid did not exhibit selective etching positions indicating that only zwitterionic molecules with both carboxyl and amino group affect the reaction. Thus, using the scattering spectra of nanoparticles to monitor the morphology change process in real-time offers a new way to reveal the particle synthesis mechanism and control the particle growth trends.

In addition, the resonance scattering spectra of nanoparticles are also dependent on their compositions. Gold, silver and copper nanoparticles have various resonance bands, respectively. Zhang utilized single plasmonic nanoparticle as sensitive

probe to map the distribution of NADH in living cells according to the composition change of nanostructures [25]. In the presence of NADH and copper ions, gold nanoparticles promote the reduction of copper ions into copper atoms by NADH. The produced copper atoms would adsorb on the surface of gold nanoparticles to form the Au–Cu core-shell structure, resulting in the distinct scattering spectral wavelength red shift of nanoparticles. As shown in Fig. 8.6e, gold nanospheres of 50 nm with excellent water solubility and compatibility exhibited green color after incubation in HeLa cells. With treatment of copper ions for 3 h, it was obvious that the color of nanoparticles changed into orange and red along with the spectral red shift (Fig. 8.6l) indicating the presence of NADH in cells. To confirm the function of NADH in this process, an anti-cancer drug, taxol, was added into the cells to confine the production of NADH. In Fig. 8.6i, the nanoparticles did not show clear color change owing to the suppressive effect of taxol. This cell imaging method provides an efficient means for the investigation of metabolism process, and also the screening of cancer drugs.

In the past decades, nanoparticles with core-shell structure have been widely used for their multi-functions of different compositions [26]. The scattering spectra of core-shell nanoparticles have a wide range from visible to infrared region. In addition, the water-solubility, toxicity and catalytic ability could also be optimized by modifying nanoparticles with functional shells such as silicon, magnetic materials and plasmonics. Yan He and co-workers proposed an elegant method to detect hydrogen sulphide in living cells based on the unique LSPR property of Au–Ag core-shell nanostructures [27]. It has been reported that silver atoms react with sulphide ions in the presence of oxygen, and Ag_2S is generated on the particle surface inducing the plasmon resonance peak red shift along with color change from orange to red. The authors attributed the spectral shift to the refractive index change surrounding gold cores, the refractive index of Ag_2S is 2.2 much more than Ag atoms (0.17). When the Au/Ag core-shell nanoparticles were incubated into cells, the spectral peak wavelength change of nanoparticles revealed the presence of H_2S as shown in Fig. 8.7. Due to the homogenous dispersion of nanoparticles in cells, this method enabled the mapping of H_2S in a single cell that the various spectral shift of particles indicated the concentration of H_2S at different positions. In addition, the silver-sulphide reaction showed high selectivity towards hydrogen sulphide compared with other sulfocompounds. In this work, gold core provides a plasmon resonance substrate which enhanced the observed signals, and silver shell behaved as the active reaction sites. This di-functional nanomaterial has promising potentials in biosensing and cell imaging.

Another sensor using the Au/Ag core-shell nanoparticles was fabricated for the detection of entire autophagy process at single cell level. Superoxide radicals ($O_2^{\cdot-}$) as main regulator was commonly utilized in the detection of autophagy process [28]. In the presence of $O_2^{\cdot-}$, Ag atoms were oxidized into Ag^+ ions inducing the

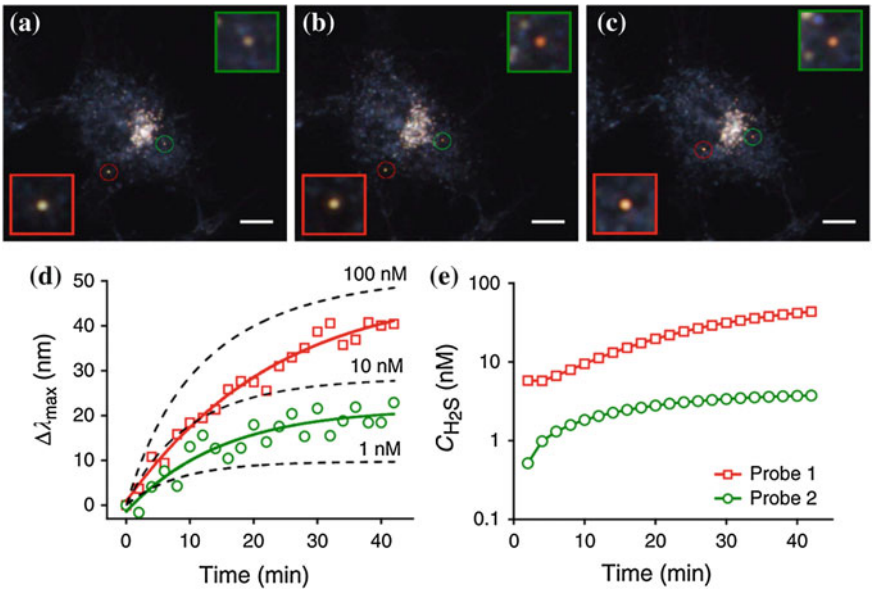

Fig. 8.7 Local variations of intracellular sulphide levels can be determined in real time. **a**–**c** Representative images showing the gradual colour changes of two individual PNPs after adding 0.1 μM Na_2S to the cell culture medium for (**a**) 2 min, (**b**) 26 min and (**c**) 42 min. *Scale bar*, 10 μm. The *red* and *green square inserts* are enlarged images of the two circled PNPs. **d** Observed (*hollow dots*) and fitted (*lines*) time-dependent λ_{max} shifts of the two particles. **e** Calculated time-dependent change in local sulphide concentrations surrounding the two particles according to the fitted results in (**d**). Reprinted by permission from Macmillan Publishers Ltd: [Nature communications] [27]. Copyright (2013)

etching of particles. This reaction also had high selectivity to $O_2^{\cdot-}$ compared with other superoxide radicals. Thus, obvious plasmon resonance scattering spectral red shift and intensity decreasing of particles were observed due to the composition and morphology change (Fig. 8.8). After modification with polyethylene glycol (PEG) and Arg-Gly-Asp-Cys (RGD) peptides, the nanoprobes were captured by cells through the specific binding interactions between RGD peptides and integrins (αvβ3 or αvβ5) on the membrane. The spectral shift was well correlated with the concentration of $O_2^{\cdot-}$ on cell membrane and made it possible to monitor the $O_2^{\cdot-}$ level in situ and in real-time. Due to the long-term autophagy process of cell, it was difficult to monitor the entire autophagy process via one single nanoparticle. Therefore, Zhu and co-workers introduced the "relay" concept in the cell imaging detection. 8 groups of nanoprobes were incubated in cells and statistic data of the time-dependent spectral shift were obtained to analyze the detailed cytometaplasia process. The "relay" concept offered an effective method to investigate continuous cell activities.

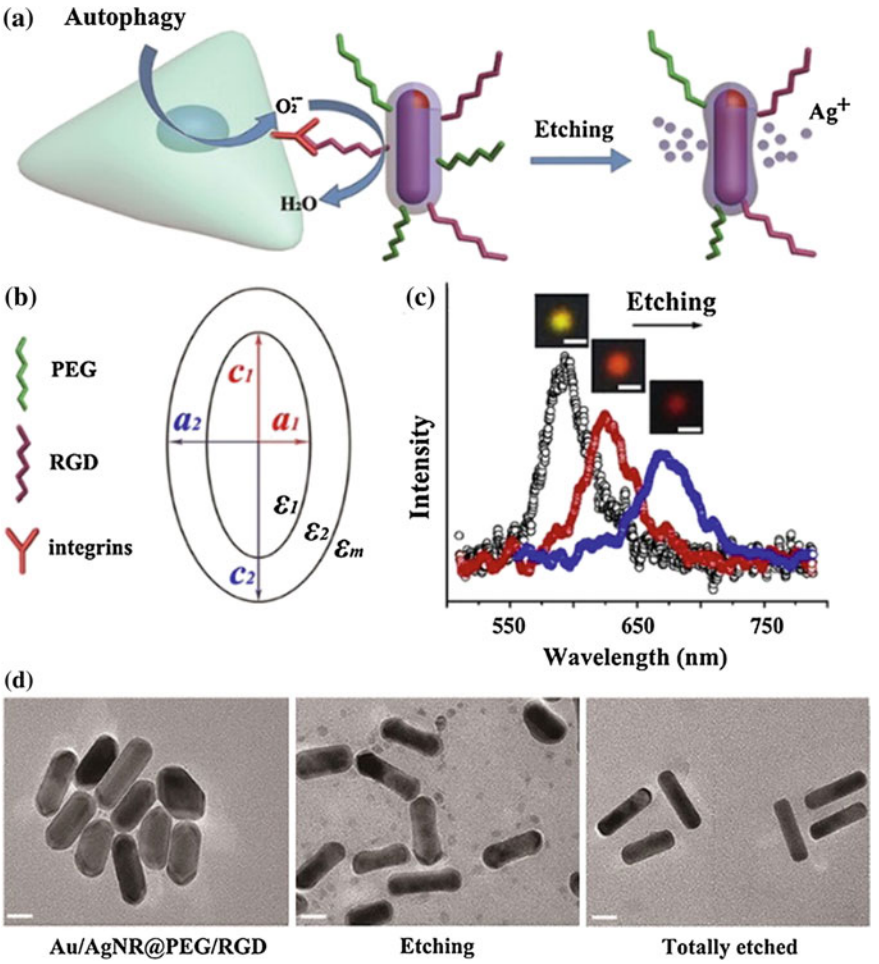

Fig. 8.8 **a** Illustration of the core-shell structure Au@AgNRs. **b** The model controlling PRS spectrum of Au@AgNRs, where the prolate spheroidal dielectric (ε_1) core, with semiaxes $a_1 < c_1$, is coated with another confocal spheroidal dielectric (ε_2) shell with semiaxes $a_2 < c_2$. ε_m is the dielectric functions of adjacent medium. **c** PRS spectra of a single probe etched by O_2^- for 0, 30 and 60 min. *Insets* showed scattering images of the probe in each status. *Scale bar* was 500 nm. **d** HRTEM micrograph illustrated the transitions of nanoprobes during the etching process. *Scale bar* was 20 nm. Reprinted with permission from [28]. Copyright (2015) American Chemical Society

8.3 Inter-particle Coupling

When two or more plasmonic nanoparticles get close to each other, their plasmon resonance band will be coupled giving rise to significant scattering spectral peak wavelength red shift and intensity increasing [29]. The coupling of nanoparticles

offers a valuable method in highly sensitive detection, even at single-molecule level [30, 31]. It is possible to monitor the coupling on an individual nanoparticle surface that per inter-particle binding event could be observed.

Li and coworkers developed a new method for imaging latent fingerprints (LFPs) based on the inter-particle coupling of plasomonic nanoparticles [32]. Cocaine as a common drug was selected as the representative analyte. In this work, 50 nm GNPs were used as both imaging and recognition probes modified with cocaine-specific aptamers. To enhance the signal to noise ratio, the cocaine-specific aptamers were divided into two flexible ssDNA pieces and were modified on the surface of different particles via Au-S bonding (Fig. 8.9). When normal sebaceous fingerprint was obtained on the glass slide surface, the added GNPs modified with DNA were monodispersed showing green color. On the contrary, if the fingerprint contained cocaine, the nanoparticles with different DNA would be conjugated leading to the inter-particle coupling. The color of aggregated GNPs displayed obvious change from green to red as illustrated in Fig. 8.9. This color-coded fingerprint detection method is fast and low-cost, and has promising application prospect in the detection of drugs, explosives and other substances.

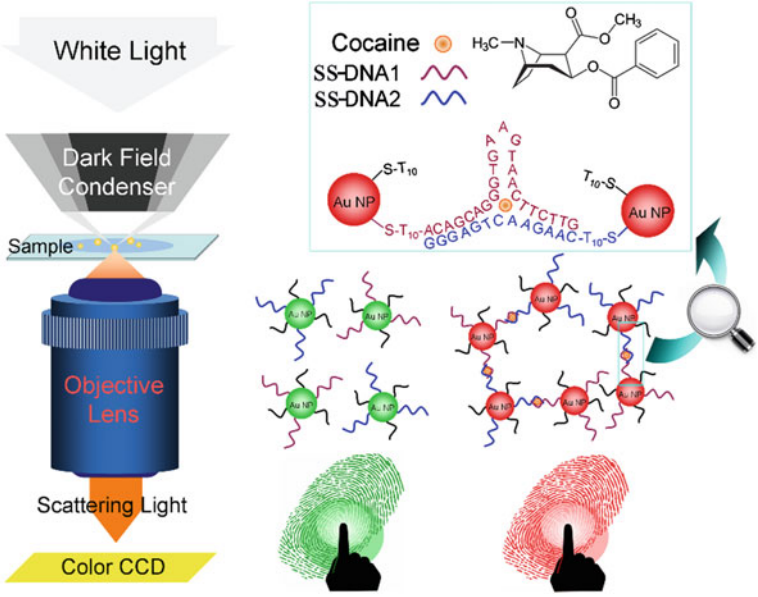

Fig. 8.9 Principle of nanoplasmonic imaging of LFPs and identification of cocaine in LFPs by dark-field microscopy. Reprinted with permission from [32]. Copyright 2013 WILEY-VCH Verlag GmbH & Co. KGaA, Weinheim

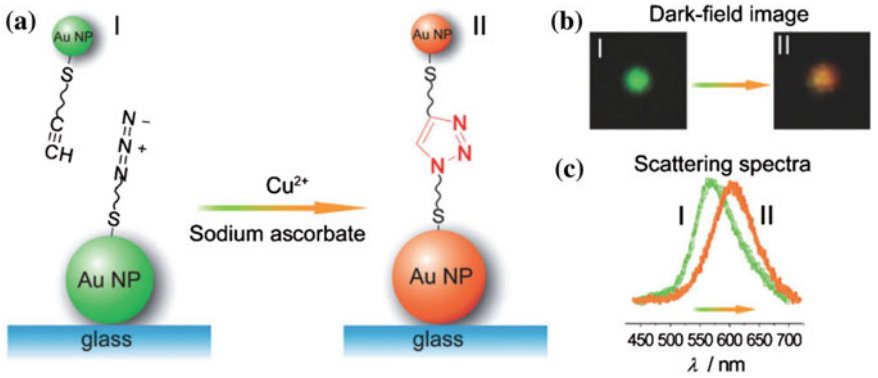

Fig. 8.10 **a** The detection of Cu^{2+} using click chemistry between two types of GNPs modified with terminal azide-functionalized and alkyne-functionalized thiols, respectively; Detailed experimental configuration; **b** Typical dark-field image of GNP modified on a microscopy slide before (*I*) and after (*II*) the addition of Cu^{2+} and sodium ascorbate; **c** Scattering spectra of single GNP before (*I*) and red-shift after (*II*) the click reaction. Reprinted with permission from [33]. Copyright 2013 WILEY-VCH Verlag GmbH & Co. KGaA, Weinheim

Owing to the ultra-sensitive response, the inter-particle coupling was applied to monitor chemical reactions at single nanoparticle level. For instance, click reaction as a powerful and widely-applied chemistry is crucial in chemical synthesis. Particularly,Cu^{+}-catalyzed azide-alkyne 1,3-dipolar cycloaddition has attracted considerable attentions. Using dark-field microscopy, the click reaction process was investigated based on plasmon resonance scattering light [33]. Azide with thiol group was modified on the surface of 60 nm gold nanoparticles which were dispersed on glass slide. Then, alkyne capped 14 nm gold nanoparticles were added in the system. From Fig. 8.10, after treatment with sodium ascorbate and copper ions, the generated Cu^{+} catalyzed the addition reaction between azide and alkyne inducing the coupling of nanoparticles. The inter-particle cross-linking obviously altered the scattering light of nanoparticles. The color in dark-field images was changed from green to red with the scattering spectral red shift. The dark-field images in Fig. 8.11 confirmed the observed reaction is universal without randomness and the reaction occurs to the major in nanoparticles showing color changes. The scattering spectral peak wavelengths were calculated via the previous home-made program based on RGB information. The statistic diagrams indicated the averaged peak wavelength of GNPs shifted from 565 to 585 nm proving the reliability and repeatability. Notably, this method makes it possible to investigate the chemical and biological reaction even at single molecule level with optimization of surface modification and reaction conditions.

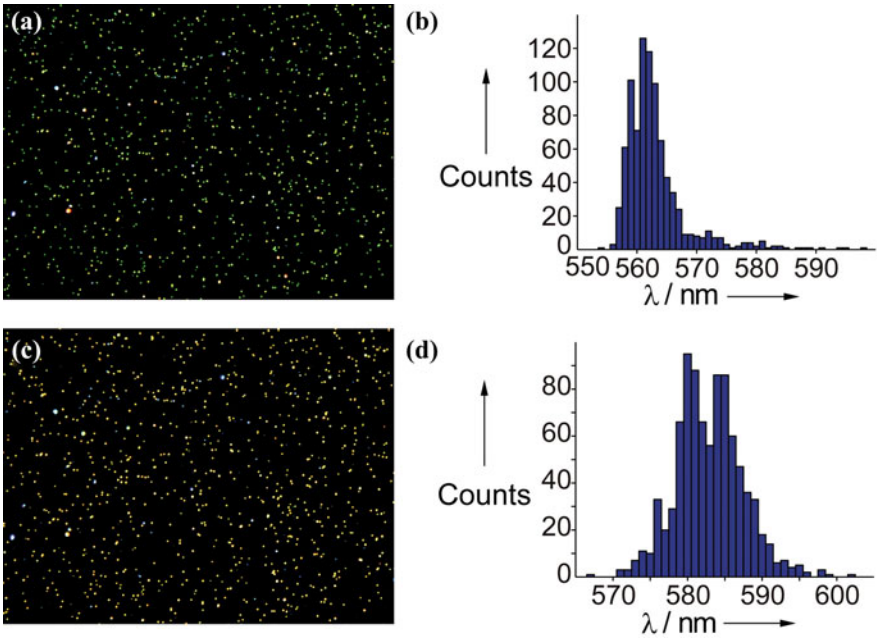

Fig. 8.11 Dark-field images and calculated wavelength of the GNPs (60 nm) before (**a** and **b**, respectively) and after (**c** and **d**, respectively) the addition of Cu^{2+} (1 μm) and excess sodium ascorbate. Reprinted with permission from [33]. Copyright 2013 WILEY-VCH Verlag GmbH & Co. KGaA, Weinheim

8.4 Plasmon Resonance Energy Transfer

In 2007, Lee and co-workers discovered the phenomenon of "plasmon resonance energy transfer" (PRET) [34]. PRET occurs on the plasmonic nanoparticle surface with modification of chromophores. When the absorption band of chromophore molecules overlaps with the scattering resonance band of nanoparticles, the energy transfers from particles to the surface molecules resulting in the quenching of scattering light. The quenching position of scattering spectra is corresponding to the absorption band of chromophores. PRET mechanism has not been fully confirmed, one hypothesis proposed that the energy transfers from nanoparticles to chromophores through dipole-dipole interactions, which is similar to the fluorescence resonance energy transfer (FRET) mechanism. This discovery enhanced the sensitivity of absorption spectroscopy with several orders of magnitude, down to hundreds of molecules adsorbed on single nanoparticle surface under dark-field microscopy as shown in Fig. 8.12.

For instance, cytochrome c (Cyt. C) molecules have absorption band between 520 and 550 nm. When Cyt. C molecules were conjugated to gold nanoparticles, distinct quenching dips were observed in the scattering spectra which were matched

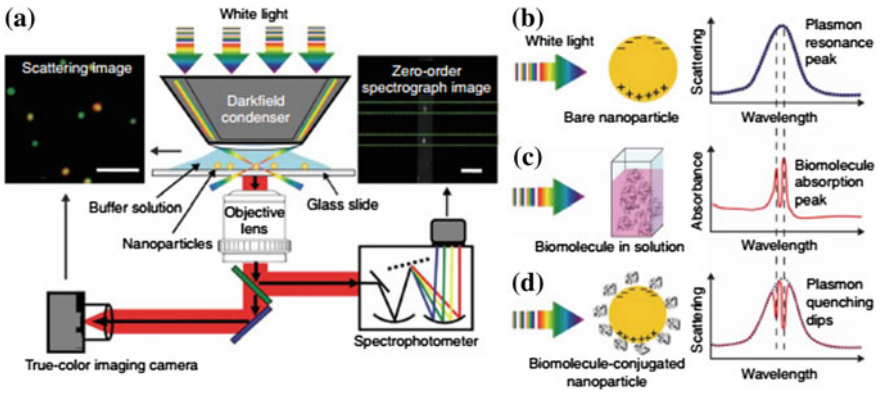

Fig. 8.12 Schematic diagrams of quantized plasmon quenching dips nanospectroscopy via PRET. **a** Experimental system configuration. **b** Typical Rayleigh scattering spectrum of bare gold nanoparticles. **c** Typical absorption spectra of biomolecule bulk solution. **d** Typical quantized plasmon quenching dips in the Rayleigh scattering spectrum of biomolecule-conjugated gold nanoparticles. Spectra were drawn based on representative data. Reprinted by permission from Macmillan Publishers Ltd: [Nature Methods] [34]. Copyright (2007)

with the absorption peaks of Cyt. C. Nevertheless, when the scattering band of GNPs was not overlapped with the absorption band of chromophores, no obvious quenching was observed. Owing to the good biocompatibility and water solubility of GNPs, PRET was applied in the real-time detection of Cyt. C in living cells [35]. After stimuli with ethanol which promoted the generation of Cyt. C, clear quenching dips were obtained in the scattering spectra of single GNPs. In addition, the real-time results of GNPs at different positions exhibited various spectral changes indicating the dynamic mapping of Cyt. C production process.

Due to the necessity of the matching between scattering band of nanoparticles and absorption band of conjugated molecules, PRET provided a new method for the highly selective detection at single nanoparticle level [36]. PRET mechanism was applied in the detection of metal ions based on the metal-ligand complex [37]. Common optical methods for the detection of heavy metal ions including fluorescence and absorption spectroscopy were generally based on organic compounds which suffered from low water solubility. However, PRET method based on single nanoparticles enabled the detection in aqueous solutions with high sensitivity.

It was reported that copper ions had high affinity with amine group to form copper-amine complex which had new absorption bands at visible range. For example, ethylenediamine could selectively bind with copper ions and the absorption band of this amine-copper complex was at ca. 550 nm. Then, 50 nm gold nanoparticles were selected as sensing probe whose scattering spectra were near 550 nm meeting the PRET conditions. The ethylenediamine molecules were firstly modified on GNPs, after binding to copper ions, the scattering spectra intensity decreased gradually indicating the PRET process. The scattering intensity decreasing showed excellent linear relationship to the concentration of copper ions

and the detection limit was as low as 1 nM. Furthermore, for other ligands which may bind with several kinds of metal ions, PRET method could enhance the selectivity by modulating the scattering band of nanoparticles to match different metal-ligands. Especially, gold nanorods have greatly potential applications in PRET detections due to their broad scattering band from 600 nm to infrared (IR) region [10]. The broad resonance bands of GNRs expanded the sensing areas significantly by constructing functional probe chromophores.

Previous PRET reports were all based on the "on to off" type that the chromophores quenched the intensity of scattering light. However, compared with "on to off" type, "off to on" detection had more sensitivity because of the low background. Therefore, Long and co-workers proposed a scattering recovered plasmon resonance energy transfer (SR-PRET) method for the "off to on" sensing [38]. In this work, the chromophore molecules were conjugated with plasmonic nanoparticle to generate the PRET process. Then, the target compound was introduced to unlock the conjugation of nanoparticles and chromophore to brighten the nanoparticles. The increasing light signals were more readily to be recognized compared with the quenching type. In Fig. 8.13, a thiol terminated compound Rhodamine B (RdBS) containing a Si–O bond with absorption band of 560 nm was modified on 60 nm GNPs whose scattering band was near 560 nm, either. The scattering intensity deceasing induced by RdBS provided a low detection background. F^- had high affinity to silicon leading to the cleavage of Si–O bond to release the rhodamine group and recovered the scattering light of GNPs. This

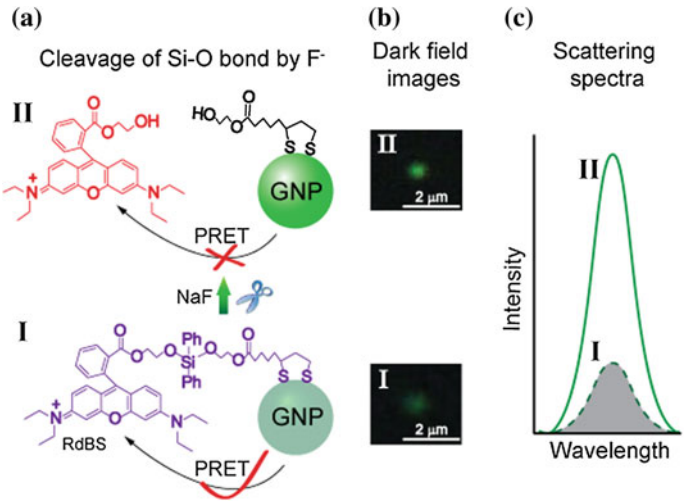

Fig. 8.13 **a** Schematic representation of the process of SR-PRET. **b** The color images of a typical GNP before (*I*) and after (*II*) adding F^- ions, demonstrating the recovery of the scattering intensity. **c** Scattering spectra intensity before (*I*) and after (*II*) the addition of F^- ions, the remarkable resonance enhancement on the Rayleigh scattering spectrum is clearly observed. Reprinted by permission from Macmillan Publishers Ltd: [Scientific Reports] [38]. Copyright (2015) (Color figure online)

SR-PRET sensor exhibited high sensitivity to F^- with detection limit of 0.1 nM and provided a new method for the living cell imaging to observe the dynamic interactions of biomolecules.

8.5 Spectroelectrochemistry

Nobel metal nanoparticles exhibit unique surface plasmon resonance property owing to their abundant free surface electrons. The oscillation of electrons and holes makes nanoparticles good electron acceptors and donors to be widely exploited in photovoltaic and catalysis [39]. Also, the excellent conductivity of nanoparticles enables their application in electrochemistry detection as conductor wires to promote the redox reaction on electrode surface [40, 41]. Nanoparticles' surface becomes the most active reaction area during the electrochemistry process. Thus, in recent years, investigating electrochemical reaction on single nanoparticles have attracted increasing attentions [42]. For instance, Tao used surface plasmon resonance imaging to determine the electrochemical reaction on single Pt nanoparticles based on the plasmonic-induced electrochemical current microscopy (P-ECM) signals [43, 44]. This method achieved the mapping of electrochemical reaction process on single nanoparticles with high time and spatial resolution.

In addition, combination of dark-field microscopy and electrochemical workstation provided a novel approach for the observation of electrochemical process on single plasmonic nanoparticle. In previous reports, the plasmon resonance bands of nanoparticles are dependent on their surface electron density as depicted in (8.1). The resonance peak wavelength is proportional to the electron density [45, 46]. Here, $\Delta\lambda_{\max}$ is the wavelength peak shift, N is the electron density of GNPs, λ is the wavelength of incident light, ε is the dielectric constant of the GNP, ε_m is the dielectric constant of the surrounding environment, and L is the shape factor. Mulvaney investigated the relationship between the electron density and scattering peak wavelength using dark-field microscopy [47, 48]. Gold nanorods modified ITO glass slide was acted as working electrode. After applying negative potentials, the electrons were injected into nanorods inducing the scattering spectra blue shift indicating the increasing of resonance energy. From (8.1), it was also found that the scattering peak shift of nanoparticles was morphology dependent. Under negative potentials, nanoparticles with lower geometric factor were more sensitive to the surface electron density change and exhibited more spectral shift. It was confirmed that nanorods had more obvious blue shift compared with nanospheres and nanotriangles.

$$\Delta\lambda_{\max} = -\frac{\Delta N}{2N}\lambda\sqrt{\varepsilon + (\frac{1-L}{L})\varepsilon_m} \tag{8.1}$$

Both the electron transfer and refractive index change resulted in the plasmonic scattering wavelength and intensity alternation. Based on this, the integrated spectroelectrochemical instrument was applied to determine the oxidation process

of single gold nanorod during cyclic voltammetry (CV) scanning [49]. The potential was applied from −1.0 to 2.3 V under double-electrode system, two ITO slides were acted as working electrode and counter electrode, respectively. From Fig. 8.14, we could see that when the potential was less than 0.3 V, the scattering spectra of nanoparticles showed slight energy loss due to the double-layer charging on the particles' surface. At the range of −0.3 to 1.0 V, the energy decreased rapidly because of the adsorption of water molecules and ions in the electrolyte which was reversible under the potential cycle. When the potential was larger than 1.0 V, the oxidation of gold atoms was the dominant reaction on the surface which induced the obvious scattering peak red shift. Studying the voltage-induced adsorbate damping on a single nanorod improved our understanding of electrochemical process and reaction mechanism.

A novel method was developed to real-time monitor the deposition of single silver nanoparticles based on dark-field microscopy [50]. Under the potential of 0.1 to −0.2 V, silver ions in solutions were reduced into silver atoms depositing on the ITO substrate. In a 100 μm × 100 μm area, the total measured scattering intensity during the potential scanning matched well with the total electrochemical current. Thus, it was possible to detect the ultra-low electrochemical current generated by a single silver nanoparticle via the scattered optical signals. Referring the SEM characterization, the size of single particles, which were corresponding to the silver atoms, were calculated on the basis of the correlation between scattering spectra intensity and size according to Mie theory. Therefore, the generated electric quantity and reduction current of a single silver nanoparticle were obtained relating to the calculated silver atoms. This work opened a new way for the observation of electrochemical curves of both entire and single nanoparticles that was extremely difficult for traditional electrochemical technique.

On the other hand, Tao used the plasmonic-induced electrochemical current microscopy to image both the electrochemical reaction process and the size of nanoparticles during the silver oxidation [51]. When the silver nanoparticles collided on electrode, the applied potential oxidized silver atoms into silver ions leading to the size and resonance light decrease. Due to the correlation between the imaging intensity and size of particles, the real-time electrochemical current of single silver nanoparticles were calculated revealing the kinetics of the reaction process. It provided a promising approach for the electrochemical activity observation of particles with different size.

The dark-field microcopy based spectroelectrochemical method was then applied in the monitoring of electrochemical catalytic reaction on a single gold nanorod [52]. Nanorods were adsorbed on ITO glass slide and two Pt wires were acted as reference and counter electrodes, respectively. During CV scanning, the scattering spectra of single GNR were recorded simultaneously. After applying scanning potential from −0.1 to 1 V in KNO_3 solution, GNRs modified ITO electrode exhibit obvious oxidation current peak at about 0.78 V in the presence of H_2O_2. As control, bare ITO electrode showed no current peaks indicating the catalytic ability of GNRs. Figure 8.15 displayed two circles of scattering spectra changes of one single GNR under the CV scanning at scan rate of 5 mV/s in the absence (a) and presence

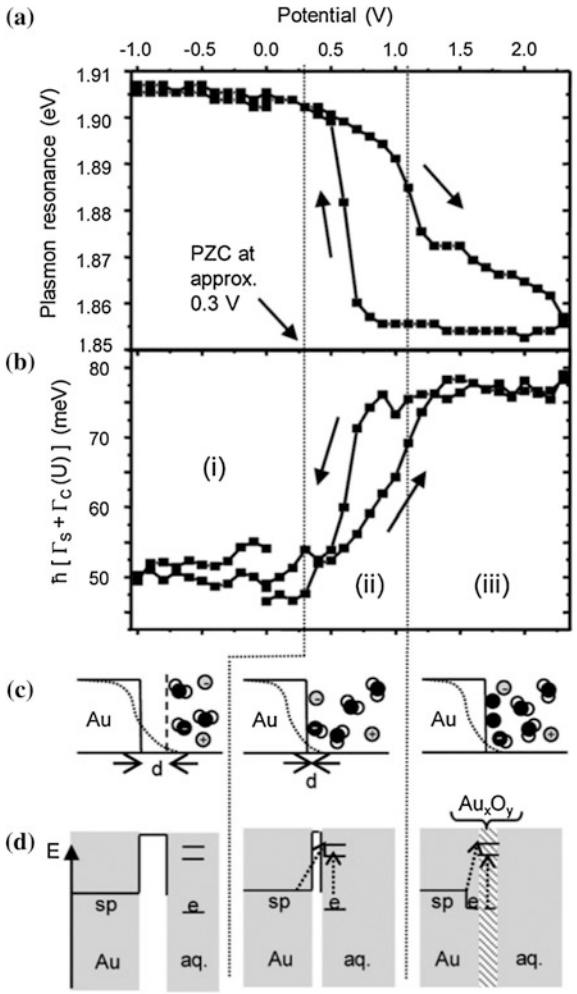

Fig. 8.14 Plasmon resonance peak energy (**a**) and damping $\hbar$ ($\Gamma_S + \Gamma_C$ (U)) (**b**) versus applied potential on the full potential range from −1 to +2.3 V. **c** Sketch of the positive jellium background in the AuNR (*solid black line*) and the sp-electron density (*dotted line*). Three different regions can be associated: (*i*) Charging of double layer capacitance leads to a spectral shift but no additional damping. An interlayer of thickness *d* is formed where the electron spill-out repels both the solvent molecules and dissolved ions (*left* sketch in **c**). No chemical damping takes place via the solvent or dissolved ions (*left* sketch in **d**). In region (*ii*), potentials positive of the point of zero charge (PZC) cause a rapid nonlinear red shift (anodic scan in (**a**)) and substantial additional damping (region (*ii*) in panel **b**). The sp-electron spill-out retracts (reducing **d**) and solvent molecules and anions adsorb (*center* sketch in **c**). Chemical surface damping of the NPPR becomes possible by the excitation of either sp-electrons or adsorbate electrons into empty adsorbate states (*dotted arrows* in the *center* sketch of **d**). (*iii*) At potentials above 1.1 V, Au oxidation leads to no additional damping (**b**) but some further spectral red shift (**a**) due to the trapping of sp-electrons at the oxide (*right* sketches in **c**, **d**). Reprinted with permission from [49]. Copyright (2012) American Chemical Society

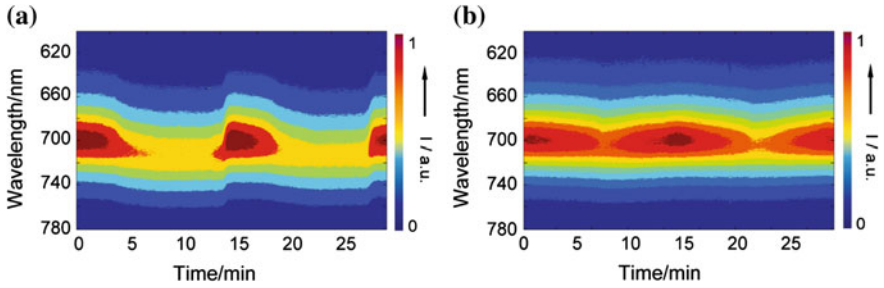

Fig. 8.15 Scattering spectra of a single gold nanorod under CV scanning from −0.1 to 1 V for two circles without (**a**) and with (**b**) H_2O_2, scan rate: 5 mV/s

(b) of H_2O_2. It was found that GNR showed distinct reversible scattering changes without H_2O_2 due to the surface oxidation as mentioned above. The scattering spectra first exhibited red shift then blue shift to the initial position. On the contrary, GNR did not show obvious spectral shift in the presence of H_2O_2. In most of the published reports, GNP's catalytic ability in electrochemical reactions was attributed to their good conductivity and active surface electrons. However, these results revealed that GNP was acted as a reactant in the catalysis process. Obviously, under high potential scanning, GNR was oxidized into hydroxide/oxide leading to the spectral red shift. After treatment with H_2O_2, the gold hydroxide/oxide was reduced into gold atoms inducing the spectral blue shift, meanwhile, H_2O_2 was oxidized into oxygen. Under positive potentials with and without H_2O_2, both the scattering peak intensity decreased due to the lower resonance energy. There may be three reasons for the energy loss: (1) the oxidation of GNR surface reduced the amount of resonant gold atoms; (2) the generated oxide and adsorbed molecules on particle surface increased the surrounding refractive index; (3) the positive potential reduced the electron density of particle surface.

Furthermore, in the presence of chloride, the catalytic reaction showed extremely different results. In 0.1 M KCl solution, after applying 1 V potential, the scattering light of GNR decreased rapidly and then disappeared in the view indicating the dissolution of GNRs. In 0.02 M KCl solution, GNR showed irreversible red shift after one circle CV scanning. After the addition of H_2O_2, the spectra showed no clear difference indicating that GNR seemed no catalytic ability. This is because of the strong interaction between gold atoms and chloride ions. After applying oxidation potential, the formed gold-chloride complex was first adsorbed on GNR surface causing spectral red shift, and then was dissolved into solution inducing the irreversible morphology change. However, H_2O_2 could not reduce the stable gold-chloride complex into gold atoms, that is, the catalytic ability of gold nanoparticles was passivated. Thus, electrochemical reaction on electrodes containing gold should avoid the influence of chloride ions. Notably, the investigation of electrochemical reaction on single gold nanorod confirmed the heterogeneity of every individual particles. Nanoparticles showed different catalysis activity and potential response under same conditions [53].

As GNPs are sensitive to the surface electron density, the spectroelectrochemical technique was applied in the detection of Faradaic reaction on single GNR [54]. The electrochemical oxidation of NADH was selected as a typical reaction in this system. As illustrated in Fig. 8.16b, GNRs were modified on ITO slide covered with graphene layer. Graphene has excellent electronic and catalytic property to catalyze the oxidation of NADH in non-biological system. When NADH was oxidized into NAD^+, one Faradaic electron was released and transferred to GNRs through graphene owing to the good electron acceptor ability of GNRs. In the absence of NADH, during the CV scanning from 0 to 0.7 V versus Ag/AgCl electrode, the scattering spectra of single GNR showed reversible red shift due to the surface electron loss induced by anodic charging. After addition of NADH, an obvious oxidation current peak was observed at about 0.55 V and the GNR exhibited a blue shift which was opposite with the condition without NADH. This indicated that a competing effect has existed for the anodic charging and Faradaic charging as depicted in Fig. 8.16a. The scattering peak shift without NADH in the CV scanning process was considered as the background. After subtracting from the spectral shift in the presence of NADH, a distinct blue shift was obtained at a positive potential. This spectral blue shift of a GNR was exclusively resulted from electron injection in Faradaic reaction.

According to the relationship between the scattering spectra shift and electron density, the electron injection amount on a single GNR was calculated as 8.43×10^4 inducing 6.5 nm peak wavelength shift. Furthermore, the rate of Faradaic reaction

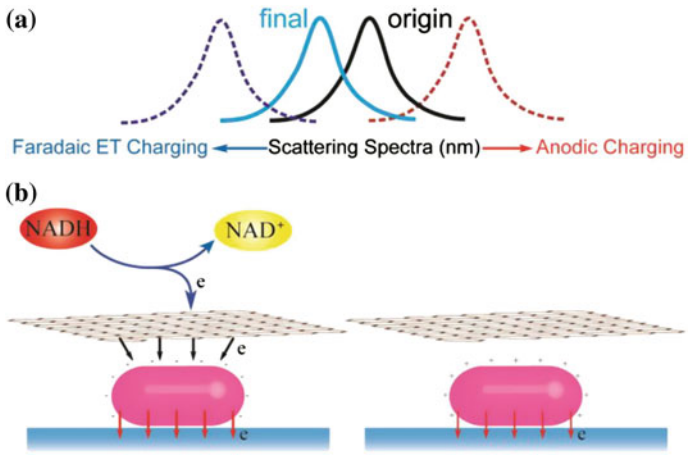

Fig. 8.16 **a** The scattering spectra for individual gold nanorods charged by synchronized Faradaic reaction and non-Faradaic double layer anodic charging current. The *black* and *blue solid lines* show the scattering spectra of gold nanorods at open circuit and an applied positive potential, while *blue* and *red dashed lines* indicate the contribution of Faradaic reaction and non-Faradaic charging, respectively. **b** The charged gold nanorods in the presence (*left*) and absence (*right*) of Faradaic reaction in the electrochemical system. Reproduced by permission from [54] of The Royal Society of Chemistry (Color figure online)

was investigated via altering the concentration of electroreactant. Interestingly, the scattering spectra showed a linear increasing blue shift along with the NADH concentration increasing. In addition, the surface property effect was observed on electrochemical reduced graphene oxide (erGO). The results indicated that the erGO showed better electron transfer ability leading to more spectral blue shift of GNRs in the presence of NADH. This work demonstrated the electron accumulation based on Faradaic reaction at different reaction conditions on a single GNR surface, which may improve the understanding of electroplasmonic effect and offer an effective approach for the observation of electrochemical reaction at single molecule level.

Except monitoring electrochemical reactions at single nanoparticle surface, this spectroelectrochemistry method was applied in the controllable fabrication of plasmonic nanoparticles including Ag, Au, and Cu NPs and real-time monitoring of the growth process [55]. Hybrid bilayer membranes (HBMs) were modified on ITO slide functioned as substrate. A ring-like stable protein 1 (SP1) was used as the template which had an inner pore of 2–3 nm and a width of 4–5 nm as shown in Fig. 8.17a. SP1 was proposed as a channel protein which could form a nanochannel on phospholipid membrane. Because of the non-conductivity of HBMs, the electrochemical reactions could only take place in the SP1 nanochannels where were

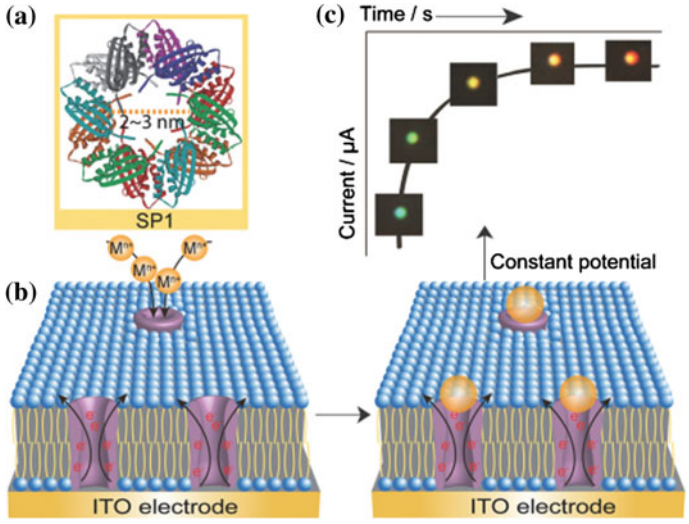

Fig. 8.17 Electrodeposition in the SP1 generated nanochannels, and Ag, Au, and Cu NPs deposited on the SP1-HBM/ITO template using a developing solution of $AgClO_4$, $HAuCl_4$, and $CuSO_4$ with the standard deposition potentials of −0.05, −0.05, and −0.6 V versus Ag/AgCl, respectively. **a** Structure of SP1. **b** SP1-HBM/ITO template. **c** The images of typical color changes of a single Ag NP changing from *blue* to *red*, as the electrodeposition time is increased, indicating the in situ and real time monitoring of the growth process of single NPs on the SP1-HBM/ITO template. Reprinted with permission from [55]. Copyright 2012 WILEY-VCH Verlag GmbH & Co. KGaA, Weinheim

conductive areas. After applying reduction potential, metal ions in the solution were reduced into metal atoms deposited in the nanochannels. Utilizing dark-field microscopy, the nanoparticles growth process in SP1 channels was monitored in situ and in real-time. Notably, it is possible to modulate the particle size and morphology through the electrochemical conditions. The visualized growth of a single plasmonic nanoparticle provided more detailed information regarding to the growth mechanism and routes. In addition, the density of nanoparticles could be modulated via the concentration of SP1 proteins. Interestingly, the growth of copper particles underwent different procedure [56]. Under reduction potentials, copper particles became larger and larger showing constantly scattering spectral red shift. However, after stopping the applied potential, the generated copper particles with various colors faded gradually with scattering intensity decrease, and the color of copper particles changed into dark red. This phenomenon was attributed to the oxidation of copper atoms for that the scattering color was recovered after adding acetic acid to dissolve the copper oxide. Thus, investigation of the synthesis process of a single plasmonic nanoparticle is important in the development of nanomaterials synthesis.

Monitoring the electrochemical reaction and electron transfer process on single plasmonic nanoparticle is significant in the development of photovoltaic conversion and opto-electro catalysis. The obtained reaction kinetics and thermodynamics at single nanoparticle/molecule level would reveal the reaction essence such as electron transfer route and temporal mediates.

8.6 Conclusions and Future Prospects

In conclusion, we have reviewed the developed sensors based on single plasmonic nanoparticles according to the morphology, composition and energy modulation. The strong and stable scattering light makes plasmonic nanoparticles excellent detection probes in the fields of biology, chemistry and catalysis [57–59]. Benefitting from their biocompatibility, water-solubility and low-toxicity, nanoplasmonics attracted considerable concerns in the fields of biosensors, cell imaging, and thermal therapy [60–62]. On the other hand, the numerous free electrons on the particle surface offer active reaction areas which promote the catalytic reactions efficiency. Also, the plasmon enhanced Raman, fluorescence and IR spectroscopy have developed rapidly in biological detection, environmental monitoring and life science [63–65].

To expand the advantages of plasmonics, one effective way is fabricating nanomaterials possessing functional morphology and compositions with multi-dimensions and multi-functions. Nanorods, stars, triangles, chains, wires and alloys, etc. exhibit absolutely different properties and have specific utilizations. The wave-guide ability of nanochains and wires, showing potential functions in the communications [66]. Additionally, plasmonics could alter the electron transfer and charge separation of semi-conductors including TiO_2, Cu_2O, etc. [67, 68]. The

metal nanoparticles are potential materials for the enhancement of photovoltaic conversion and photocatalysis, promisingly to be exploited in new type of solar cells and other optical energy resources [69, 70]. Moreover, under conjugating with other advanced technique, plasmonics exhibit more excellent and intelligent performance [71]. For instance, combination plasmonic spectroscopy with electrochemistry enables observing electrochemical process on a single plasmonic nanoparticle and provides dynamic reaction information [72]. The integration of plasmonics with electric nanopore technique promotes the detection at single-molecule level on the basis of opto-electro signals [73, 74]. Utilizing single plasmonics in Raman detection provides accurate reaction positions in cell imaging which improved spatial resolution significantly [75]. Furthermore, plasmonics play important roles in near-field spectroscopy to reveal fantastic quantum phenomena at single molecule level, even at atom scale [76, 77]. We believe that plasmonics will have great exploitations in the development of new energy resources, life science and environments in the future.

References

1. H. Chen, L. Shao, Q. Li, J. Wang, Gold nanorods and their plasmonic properties. Chem. Soc. Rev. **42**, 2679–2724 (2013)
2. Y. Li, C. Jing, L. Zhang, Y.-T. Long, Resonance scattering particles as biological nanosensors in vitro and in vivo. Chem. Soc. Rev. **41**, 632–642 (2012)
3. C. Jing, Y.-T. Long, *Localized Surface Plasmon Resonance Based Nanobiosensors* (Springer, London, 2014)
4. B. Sepúlveda, P.C. Angelomé, L.M. Lechuga, L.M. Liz-Marzán, LSPR-based nanobiosensors. Nano Today **4**, 244–251 (2009)
5. S. Eustis, M.A. El-Sayed, Why gold nanoparticles are more precious than pretty gold: Noble metal surface plasmon resonance and its enhancement of the radiative and nonradiative properties of nanocrystals of different shapes. Chem. Soc. Rev. **35**, 209–217 (2006)
6. S. Schultz, D.R. Smith, J.J. Mock, D.A. Schultz, Single-target molecule detection with nonbleaching multicolor optical immunolabels. Proc. Natl. Acad. Sci. U.S.A. **97**, 996–1001 (2000)
7. C. Sonnichsen, S. Geier, N.E. Hecker, G. von Plessen, J. Feldmann, H. Ditlbacher, B. Lamprecht, J.R. Krenn, F.R. Aussenegg, V.Z.H. Chan, J.P. Spatz, M. Moller, Spectroscopy of single metallic nanoparticles using total internal reflection microscopy. Appl. Phys. Lett. **77**, 2949–2951 (2000)
8. H.D. Song, I. Choi, Y.I. Yang, S. Hong, S. Lee, T. Kang, J. Yi, Picomolar selective detection of mercuric ion (Hg^{2+}) using a functionalized single plasmonic gold nanoparticle. Nanotechnology **21**, 145501 (2010)
9. A. Wax, K. Sokolov, Molecular imaging and darkfield microspectroscopy of live cells using gold plasmonic nanoparticles. Laser Photon. Rev. **3**, 146–158 (2009)
10. C. Jing, L. Shi, X.Y. Liu, Y.T. Long, A single gold nanorod as a plasmon resonance energy transfer based nanosensor for high-sensitivity Cu(II) detection. Analyst **139**, 6435–6439 (2014)
11. W. Haiss, N.T.K. Thanh, J. Aveyard, D.G. Fernig, Determination of size and concentration of gold nanoparticles from UV–vis spectra. Anal. Chem. **79**, 4215–4221 (2007)
12. W. Jiang, J.T. Rutka, W.C. Chan, Nanoparticle-mediated cellular response is size-dependent. Nat. Nanotechnol. **3**, 145–150 (2008)

13. C. Jing, Z. Gu, Y.L. Ying, D.W. Li, L. Zhang, Y.T. Long, Chrominance to dimension: a real-time method for measuring the size of single gold nanoparticles. Anal. Chem. **84**, 4284–4291 (2012)
14. Z. Gu, C. Jing, Y.L. Ying, P.G. He, Y.T. Long, In situ high throughput scattering light analysis of single plasmonic nanoparticles in living cells. Theranostics **5**, 188–195 (2015)
15. C.T. Campbell, PHYSICS: the active site in nanoparticle gold catalysis. Science **306**, 234–235 (2004)
16. I.L. Buurmans, B.M. Weckhuysen, Heterogeneities of individual catalyst particles in space and time as monitored by spectroscopy. Nat. Chem. **4**, 873–886 (2012)
17. Y. Wu, P. Jiang, M. Jiang, T.-W. Wang, C.-F. Guo, S.-S. Xie, Z.-L. Wang, The shape evolution of gold seeds and gold@silver core–shell nanostructures. Nanotechnology **20**, 305602 (2009)
18. X. Zheng, Q. Liu, C. Jing, Y. Li, D. Li, W. Luo, Y. Wen, Y. He, Q. Huang, Y.-T. Long, C. Fan, Catalytic gold nanoparticles for nanoplasmonic detection of DNA hybridization. Angew. Chem. Int. Ed. **50**, 11994–11998 (2011)
19. Q. Liu, C. Jing, X. Zheng, Z. Gu, D. Li, D.-W. Li, Q. Huang, Y.-T. Long, C. Fan, Nanoplasmonic detection of adenosine triphosphate by aptamer regulated self-catalytic growth of single gold nanoparticles. Chem. Commun. **48**, 9574–9576 (2012)
20. J. Becker, A. Trügler, A. Jakab, U. Hohenester, C. Sönnichsen, The optimal aspect ratio of gold nanorods for plasmonic bio-sensing. Plasmonics **5**, 161–167 (2010)
21. U. Hohenester, J. Krenn, Surface plasmon resonances of single and coupled metallic nanoparticles: a boundary integral method approach. Phys. Rev. B **72**, 195429 (2005)
22. E. Ringe, J. Zhang, M.R. Langille, C.A. Mirkin, L.D. Marks, R.P. Van Duyne, Correlating the structure and localized surface plasmon resonance of single silver right bipyramids. Nanotechnology **23**, 444005 (2012)
23. R. Jin, Photoinduced conversion of silver nanospheres to nanoprisms. Science **294**, 1901–1903 (2001)
24. T. Xie, C. Jing, W. Ma, Z. Ding, A.J. Gross, Y.T. Long, Real-time monitoring for the morphological variations of single gold nanorods. Nanoscale **7**, 511–517 (2015)
25. L. Zhang, Y. Li, D.-W. Li, C. Jing, X. Chen, M. Lv, Q. Huang, Y.-T. Long, I. Willner, Single gold nanoparticles as real-time optical probes for the detection of NADH-dependent intracellular metabolic enzymatic pathways. Angew. Chem. Int. Ed. **50**, 6789–6792 (2011)
26. M.S. Shore, J. Wang, A.C. Johnston-Peck, A.L. Oldenburg, J.B. Tracy, Synthesis of Au (Core)/Ag(Shell) nanoparticles and their conversion to AuAg alloy nanoparticles. Small **7**, 230–234 (2011)
27. B. Xiong, R. Zhou, J. Hao, Y. Jia, Y. He, E.S. Yeung, Highly sensitive sulphide mapping in live cells by kinetic spectral analysis of single Au–Ag core-shell nanoparticles. Nat. Commun. **4**, 1708 (2013)
28. Z. Chen, J. Li, X. Chen, J. Cao, J. Zhang, Q. Min, J.J. Zhu, Single gold@silver nanoprobes for real-time tracing the entire autophagy process at single-cell level. J. Am. Chem. Soc. **137**, 1903–1908 (2015)
29. C. Sönnichsen, B.M. Reinhard, J. Liphardt, A.P. Alivisatos, A molecular ruler based on plasmon coupling of single gold and silver nanoparticles. Nat. Biotechnol. **23**, 741–745 (2005)
30. D. Aili, R. Selegård, L. Baltzer, K. Enander, B. Liedberg, Colorimetric protein sensing by controlled assembly of gold nanoparticles functionalized with synthetic receptors. Small **5**, 2445–2452 (2009)
31. Y.W. Jun, S. Sheikholeslami, D.R. Hostetter, C. Tajon, C.S. Craik, A.P. Alivisatos, Continuous imaging of plasmon rulers in live cells reveals early-stage caspase-3 activation at the single-molecule level. Proc. Natl. Acad. Sci. U.S.A. **106**, 17735–17740 (2009)
32. K. Li, W. Qin, F. Li, X. Zhao, B. Jiang, K. Wang, S. Deng, C. Fan, D. Li, Nanoplasmonic imaging of latent fingerprints and identification of cocaine. Angew. Chem. Int. Ed. **52**, 11542–11545 (2013)

33. L. Shi, C. Jing, W. Ma, D.W. Li, J.E. Halls, F. Marken, Y.T. Long, Plasmon resonance scattering spectroscopy at the single-nanoparticle level: real-time monitoring of a click reaction. Angew. Chem. Int. Ed. **52**, 6011–6014 (2013)
34. G.L. Liu, Y.-T. Long, Y. Choi, T. Kang, L.P. Lee, Quantized plasmon quenching dips nanospectroscopy via plasmon resonance energy transfer. Nat. Methods **4**, 1015–1017 (2007)
35. Y. Choi, T. Kang, L.P. Lee, Plasmon resonance energy transfer (PRET)-based molecular imaging of cytochrome c in living cells. Nano Lett. **9**, 85–90 (2008)
36. W.G. Qu, B. Deng, S.L. Zhong, H.Y. Shi, S.S. Wang, A.W. Xu, Plasmonic resonance energy transfer-based nanospectroscopy for sensitive and selective detection of 2,4,6-trinitrotoluene (TNT). Chem. Commun. **47**, 1237–1239 (2011)
37. Y. Choi, Y. Park, T. Kang, L.P. Lee, Selective and sensitive detection of metal ions by plasmonic resonance energy transfer-based nanospectroscopy. Nat. Nanotechnol. **4**, 742–746 (2009)
38. L. Shi, C. Jing, Z. Gu, Y.-T. Long, Brightening gold nanoparticles: new sensing approach based on plasmon resonance energy transfer. Sci. Rep. **5**, 10142 (2015)
39. M. Turner, V.B. Golovko, O.P.H. Vaughan, P. Abdulkin, A. Berenguer-Murcia, M.S. Tikhov, B.F.G. Johnson, R.M. Lambert, Selective oxidation with dioxygen by gold nanoparticle catalysts derived from 55-atom clusters. Nature **454**, 981–983 (2008)
40. A. de la Escosura-Muñiz, A. Ambrosi, A. Merkoçi, Electrochemical analysis with nanoparticle-based biosystems. TrAC-Trend Anal. Chem. **27**, 568–584 (2008)
41. J.M. Pingarrón, P. Yáñez-Sedeño, A. González-Cortés, Gold nanoparticle-based electrochemical biosensors. Electrochim. Acta **53**, 5848–5866 (2008)
42. M. Brust, G.J. Gordillo, Electrocatalytic hydrogen redox chemistry on gold nanoparticles. J. Am. Chem. Soc. **134**, 3318–3321 (2012)
43. X. Shan, I. Díez-Pérez, L. Wang, P. Wiktor, Y. Gu, L. Zhang, W. Wang, J. Lu, S. Wang, Q. Gong, J. Li, N. Tao, Imaging the electrocatalytic activity of single nanoparticles. Nat. Nanotechnol. **7**, 668–672 (2012)
44. X. Shan, U. Patel, S. Wang, R. Iglesias, N. Tao, Imaging local electrochemical current via surface plasmon resonance. Science **327**, 1363–1366 (2010)
45. C. Novo, A.M. Funston, P. Mulvaney, Direct observation of chemical reactions on single gold nanocrystals using surface plasmon spectroscopy. Nat. Nanotechnol. **3**, 598–602 (2008)
46. C. Novo, A.M. Funston, A.K. Gooding, P. Mulvaney, Electrochemical charging of single gold nanorods. J. Am. Chem. Soc. **131**, 14664–14666 (2009)
47. P. Mulvaney, J. Pérez-Juste, M. Giersig, L.M. Liz-Marzán, C. Pecharromán, Drastic surface plasmon mode shifts in gold nanorods due to electron charging. Plasmonics **1**, 61–66 (2006)
48. C. Novo, P. Mulvaney, Charge-induced Rayleigh instabilities in small gold rods. Nano Lett. **7**, 520–524 (2007)
49. S.K. Dondapati, M. Ludemann, R. Muller, S. Schwieger, A. Schwemer, B. Handel, D. Kwiatkowski, M. Djiango, E. Runge, T.A. Klar, Voltage-induced adsorbate damping of single gold nanorod plasmons in aqueous solution. Nano Lett. **12**, 1247–1252 (2012)
50. C.M. Hill, S.L. Pan, A dark-field scattering spectroelectrochemical technique for tracking the electrodeposition of single silver nanoparticles. J. Am. Chem. Soc. **135**, 17250–17253 (2013)
51. Y. Fang, W. Wang, X. Wo, Y. Luo, S. Yin, Y. Wang, X. Shan, N. Tao, Plasmonic imaging of electrochemical oxidation of single nanoparticles. J. Am. Chem. Soc. **136**, 12584–12587 (2014)
52. C. Jing, F.J. Rawson, H. Zhou, X. Shi, W.H. Li, D.W. Li, Y.T. Long, New insights into electrocatalysis based on plasmon resonance for the real-time monitoring of catalytic events on single gold nanorods. Anal. Chem. **86**, 5513–5518 (2014)
53. C.P. Byers, B.S. Hoener, W.S. Chang, M. Yorulmaz, S. Link, C.F. Landes, Single-particle spectroscopy reveals heterogeneity in electrochemical tuning of the localized surface plasmon. J. Phys. Chem. B **118**, 14047–14055 (2014)
54. H. Zhou, Q. Liu, F.J. Rawson, W. Ma, D.W. Li, D. Li, Y.T. Long, Optical monitoring of faradaic reaction using single plasmon-resonant nanorods functionalized with graphene. Chem. Commun. **51**, 3223–3226 (2015)

55. L.-X. Qin, Y. Li, D.-W. Li, C. Jing, B.-Q. Chen, W. Ma, A. Heyman, O. Shoseyov, I. Willner, H. Tian, Y.-T. Long, Electrodeposition of single-metal nanoparticles on stable protein 1 membranes: application of plasmonic sensing by single nanoparticles. Angew. Chem. Int. Ed. **51**, 140–144 (2012)
56. L.-X. Qin, C. Jing, Y. Li, D.-W. Li, Y.-T. Long, Real-time monitoring of the aging of single plasmonic copper nanoparticles. Chem. Commun. **48**, 1511–1513 (2012)
57. Y. Ge, B. Kang, Surface plasmon resonance scattering and absorption of biofunctionalized gold nanoparticles for targeted cancer imaging and laser therapy. Sci. China Technol. SC. **54**, 2358–2362 (2011)
58. L. Cognet, C. Tardin, D. Boyer, D. Choquet, P. Tamarat, B. Lounis, Single metallic nanoparticle imaging for protein detection in cells. Proc. Natl. Acad. Sci. U.S.A. **100**, 11350–11355 (2003)
59. K.A. Willets, R.P. Van Duyne, Localized surface plasmon resonance spectroscopy and sensing. Annu. Rev. Phys. Chem. **58**, 267–297 (2007)
60. E.E. Connor, J. Mwamuka, A. Gole, C.J. Murphy, M.D. Wyatt, Gold nanoparticles are taken up by human cells but do not cause acute cytotoxicity. Small **1**, 325–327 (2005)
61. P.K. Jain, X. Huang, I.H. El-Sayed, M.A. El-Sayed, Review of some interesting surface plasmon resonance-enhanced properties of noble metal nanoparticles and their applications to biosystems. Plasmonics **2**, 107–118 (2007)
62. J.N. Anker, W.P. Hall, O. Lyandres, N.C. Shah, J. Zhao, R.P. Van Duyne, Biosensing with plasmonics nanosensors. Nat. Mater. **7**, 442–453 (2008)
63. E. Cohen-Hoshen, G.W. Bryant, I. Pinkas, J. Sperling, I. Bar-Joseph, Exciton-plasmon interactions in quantum dot-gold nanoparticle structures. Nano Lett. **12**, 4260–4264 (2012)
64. K.V. Kong, Z. Lam, W.D. Goh, W.K. Leong, M. Olivo, Metal carbonyl-gold nanoparticle conjugates for live-cell SERS imaging. Angew. Chem. Int. Ed. **51**, 9796–9799 (2012)
65. L.V. Brown, X. Yang, K. Zhao, B.Y. Zheng, P. Nordlander, N.J. Halas, Fan-shaped gold nanoantennas above reflective substrates for surface-enhanced infrared absorption (SEIRA). Nano Lett. **15**, 1272–1280 (2015)
66. M. Février, P. Gogol, A. Aassime, R. Mégy, C. Delacour, A. Chelnokov, A. Apuzzo, S. Blaize, J.-M. Lourtioz, B. Dagens, Giant coupling effect between metal nanoparticle chain and optical waveguide. Nano Lett. **12**, 1032–1037 (2012)
67. M.A. Mahmoud, W. Qian, M.A. El-Sayed, Following charge separation on the nanoscale in Cu_2O–Au nanoframe hollow nanoparticles. Nano Lett. **11**, 3285–3289 (2011)
68. W.-W. Zhao, C.-Y. Tian, J.-J. Xu, H.-Y. Chen, The coupling of localized surface plasmon resonance-based photoelectrochemistry and nanoparticle size effect: towards novel plasmonic photoelectrochemical biosensing. Chem. Commun. **48**, 895–897 (2012)
69. K.R. Catchpole, A. Polman, Plasmonic solar cells. Opt. Express **16**, 21793–21800 (2008)
70. B. Sahoo, M.N. Hopkinson, F. Glorius, Combining gold and photoredox catalysis: visible light-mediated oxy- and aminoarylation of alkenes. J. Am. Chem. Soc. **135**, 5505–5508 (2013)
71. C. Rosman, S. Pierrat, A. Henkel, M. Tarantola, D. Schneider, E. Sunnick, A. Janshoff, C. Sönnichsen, A new approach to assess gold nanoparticle uptake by mammalian cells: combining optical dark-field and transmission electron microscopy. Small **8**, 3683–3690 (2012)
72. Y. Li, J.T. Cox, B. Zhang, Electrochemical responses and electrocatalysis at single Au nanoparticles. J. Am. Chem. Soc. **132**, 3047–3054 (2010)
73. Y.L. Ying, J.J. Zhang, R. Gao, Y.T. Long, Nanopore-based sequencing and detection of nucleic acids. Angew. Chem. Int. Ed. **52**, 13154–13161 (2013)
74. M.P. Jonsson, C. Dekker, Plasmonic nanopore for electrical profiling of optical intensity landscapes. Nano Lett. **13**, 1029–1033 (2013)
75. L.A. Austin, B. Kang, M.A. El-Sayed, A new nanotechnology technique for determining drug efficacy using targeted plasmonically enhanced single cell imaging spectroscopy. J. Am. Chem. Soc. **135**, 4688–4691 (2013)

76. A.E. Klein, N. Janunts, M. Steinert, A. Tunnermann, T. Pertsch, Polarization-resolved near-field mapping of plasmonic aperture emission by a dual-SNOM system. Nano Lett. **14**, 5010–5015 (2014)
77. M. Wagner, Z. Fei, A.S. McLeod, A.S. Rodin, W.Z. Bao, E.G. Iwinski, Z. Zhao, M. Goldflam, M.K. Liu, G. Dominguez, M. Thiemens, M.M. Fogler, A.H.C. Neto, C.N. Lau, S. Amarie, F. Keilmann, D.N. Basov, Ultrafast and nanoscale plasmonic phenomena in exfoliated graphene revealed by infrared pump-probe nanoscopy. Nano Lett. **14**, 894–900 (2014)

Chapter 9
Whispering Gallery Mode Devices for Sensing and Biosensing

A. François, Y. Zhi and A. Meldrum

Abstract Optical sensors based on resonant whispering gallery mode (WGM) optical cavities are discussed in the context of recent research developments. WGM-based sensors are among the most sensitive optical sensing devices currently known, especially when combined with surface plasmon effects. The basic theory of WGM "reactive" sensing is first discussed, along with the basic parameters that are used to characterize such devices (i.e., sensitivity, signal-to-noise ratio, and detection limit). Surface chemistry methods are of critical importance for targeted sensing applications and the fundamentals of this aspect are examined. The performance of fluorescent WGM-based devices is compared to state-of-the-art "evanescently-coupled" structures. Finally, the performance of WGM-based optical sensors is compared and contrasted to a range of alternative optical microsensor technologies currently under development.

A. François
Institute for Photonics and Advanced Sensing, ARC Centre of Excellence for Nanoscale BioPhotonics, School of Physical Sciences, The University of Adelaide, Adelaide SA 5005, Australia
e-mail: alexandre.francois@adelaide.edu.au

A. Meldrum (✉)
Department of Physics, University of Alberta, Edmonton, AB T6G2E1, Canada
e-mail: ameldrum@ualberta.ca

Y. Zhi
State Key Laboratory for Mesoscopic Physics and School of Physics, Peking University, Beijing 100871, People's Republic of China
e-mail: yzhi@pku.edu.cn

M. J. Serpe et al. (eds.), *Photonic Materials for Sensing, Biosensing and Display Devices*, Springer Series in Materials Science 229,
DOI 10.1007/978-3-319-24990-2_9

9.1 Introduction

Microcavity-based optical sensors represent a promising technology for biosensing applications. They offer high sensitivity and selectivity and have recently been used to detect single specific biomolecular binding events down to masses of about 3 kDa [1]; a capacity which no other technique can currently match. Although microcavity-based sensors have not yet reached the amazing range of possibilities demonstrated for surface plasmon sensors, as demonstrated in several reviews [2–5], they offer unprecedented potential for single biomolecule detection and otherwise feature many of the same advantages as SPR devices. The combination of microcavity and plasmon resonances is now offering the highest sensitivities ever reported. In this chapter, we will describe how microcavity-based sensors work, their advantages and limitations, and conclude with an outlook for the future.

Dielectric microcavities with spherical or cylindrical geometries are among the most promising for achieving high sensitivity and low detection limits. Electromagnetic resonances in these structures—the so-called "whispering gallery modes"—can be used to sense changes in the local surroundings with high sensitivity [6–8]. Related structures with elliptical or polyhedral cross sections can show similar effects [9–19], although the resonances in non-circular structures are relatively lossy due to the presence of sharp curves or corners. Planar Fabry-Pérot microcavities [20–22] and especially photonic crystals (examples include [23–26] and Reviews [27, 28]) have also been used as interesting examples for sensing applications. Here, however, we will focus mainly on whispering-gallery-mode devices, since these have been widely studied and are relatively easy to integrate into microfluidic setups. They have also recently seen some commercial success [29, 30].

The term "whispering gallery mode" was coined over a century ago. It was used by Lord Rayleigh to refer to acoustic effects that occurred in large domed buildings like St. Paul's Cathedral in London [31]. While a historical survey is outside the scope of this chapter, it is interesting to observe that Lord Rayleigh had already at the time recognized that the solution to the circular acoustic resonances could be well described by the Bessel functions. Even before Rayleigh's work, however, others had been investigating the properties of optical resonances in liquid droplets [32]. Today, the term WGM is commonly used in the literature to describe these phenomena.

WGMs form when light is trapped by total internal reflection as it propagates around the circumference of a dielectric sphere or cylinder (Fig. 9.1). In the simplest (and very approximate) picture, the resonances can be viewed as an interference effect that occurs when the circumference of the sphere or capillary is an integer number of wavelengths. In this case, a ray propagating around the circumference will interfere constructively as it circumnavigates the equator. Accordingly, the resonance wavelengths can be approximated by

$$\lambda_m = 2\pi aN/l, \tag{9.1}$$

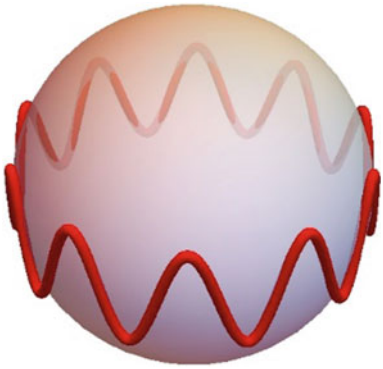

Fig. 9.1 Illustration of an equatorial WGM propagating around the circumference of a microsphere

where l is an integer (i.e., $l = 10$ in Fig. 9.1), a is the radius of the dielectric sphere or cylinder, and N is its index of refraction.

If this approximation were strictly accurate, photonic sensing based on these resonances would not work. There are several obvious problems with this simple ray picture of an optical resonance. First, of course, there is always an evanescent component of the field that extends outside the dielectric interface. While for flat surfaces this field is lossless, in microspheres or cylinders the surfaces are curved and the evanescent field becomes slightly lossy (in other words, a fraction of the circulating energy is propagated outward to infinity and the field is no longer truly "evanescent"). Additionally, the electromagnetic disturbance does not circulate exactly on the circumference but must extend slightly inward, thereby affecting the optical path length and also the resonance frequency. Thus, while (9.1) does provide a simple and approximate picture, a more complete analysis performed in Sect. 9.2 is necessary to develop the basis for optical sensing with WGMs.

WGM-based devices are among the most sensitive optical biosensors currently known. They can be parallelized and surface treatments can be used to achieve specificity comparable to that demonstrated for surface-plasmon-type sensors. Commercially relevant devices have been demonstrated (e.g., by Genalyte, Inc.) and are showing the way toward further practical applications in biomedical sensing and diagnostics. Nevertheless, some key factors must be overcome before photonic sensors based on whispering gallery modes are likely to achieve widespread success. The main motivations of this chapter are to outline the recent developments in WGM-based sensing, discuss outstanding problems and potential solutions, and look toward the developments likely to occur in the near future.

9.2 Theory of WGMs in Cylindrical and Spherical Geometries

The electromagnetic resonances of dielectric spheres and cylinders are generally characterized by a set of parameters that describes the electric field distribution. In order to summarize these key terms, we first start by defining the spherical

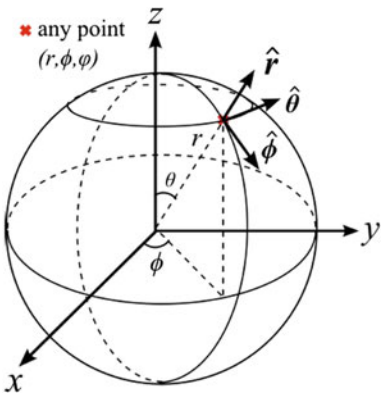

Fig. 9.2 Spherical coordinate system used in the text equations, modified after [33]

coordinates (Fig. 9.2). The important angles and directions are: ϕ: azimuthal (longitudinal) coordinate, θ: polar coordinate (i.e., latitude); and r: radius. With these directions defined, the key properties of a WGM resonance are defined as follows:

- n: radial mode number (n = 1, 2, 3…). The number of electric field intensity maxima in the radial direction
- l: angular mode number. l is related to the angular momentum of a photon circulating in the cavity, as given by $L \approx ap = a\hbar k = 2\pi a\hbar N/\lambda = \hbar l$, where p is the linear momentum.
- m: azimuthal mode number, $-l < m < l$. For a sphere, both l and m together define the number of field maxima both in the azimuthal and polar directions. All modes have m wavelengths that fit around the equator ($2m$ intensity maxima) and $l - m + 1$ intensity maxima in the polar direction. A purely equatorial mode has $l = m$ (Fig. 9.3a). The sign of m corresponds to clockwise or counterclockwise propagation. For a given l, all m are degenerate unless the spherical symmetry is broken.
- Polarization: In the transverse electric polarization, the mode E-field is perpendicular to the WGM plane of propagation (E_z). The TM polarization only has H_z and thus consists of both radial and azimuthal E-field components (E_r and E_ϕ). For a given mode number (n, l, m), the shift between the TE and TM polarized modes can be approximated by [34]:

$$\Delta f_{TE-TM} \approx \frac{\sqrt{N^2-1}}{N}\Delta f_{fsr}, \tag{9.2}$$

  where Δf_{fsr} is the free spectral range.
- Q-factor: The ability of the cavity to store optical energy, given as

$$Q = 2\pi \frac{\text{energy stored}}{\text{energy dissipated per optical cycle}} = \omega_0 \tau \approx \frac{\lambda_0}{\Delta\lambda} = \frac{\omega_0}{\Delta\omega}, \tag{9.3}$$

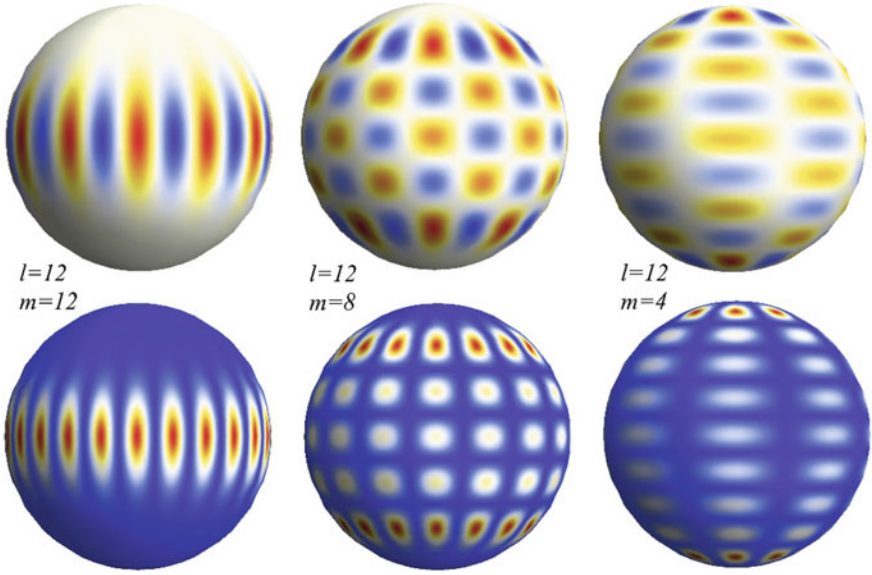

Fig. 9.3 Electric field color-maps for three first-order radial modes with the same l but differing m, plotted at the sphere surface. The *top row* shows the field amplitude and the *lower row* illustrates the intensity. In the intensity profile, the number of azimuthal maxima is $2m$, and in the polar direction it is $l - m + 1$

where ω_0 is the angular frequency of the resonant optical field, τ is the cavity ring-down time, λ_0 is the resonant wavelength, and $\Delta\lambda$ (or $\Delta\omega$) is the full-width-at-half-maximum (FWHM) of the resonance.

- Mode volume (V_m): The mode volume represents the volume occupied by the resonant mode field and is typically given by:

$$V_m = \int_V \varepsilon(r)|F^2(r)d^3r \tag{9.4}$$

where $F^2(r)$ is the normalized E-field amplitude and the volume integral is taken over all space. The field must clearly be normalized since the mode volume should not depend on the amplitude. The mode volume is a somewhat tricky concept in open resonators, since they are lossy and the integral of the mode energy therefore diverges at infinity. Generally some arbitrary limits have to be assigned to the integral. Certain approximations are often useful in estimating the mode volume; for example, for the first-order ($n = 1$) modes of a microsphere, (9.4) can be replaced with the following approximation [35]:

$$V_m \approx 3.4\pi^{3/2}\left(\frac{\lambda_0}{2\pi N}\right)^3 l^{11/6}\sqrt{l-m+1} \tag{9.5}$$

From (9.5), we can see that the mode volumes are typically on the order of hundreds of cubic micrometers and are the smallest for the equatorial modes. For cylinders, the mode volume should be roughly similar as for the sphere, and for toroids it is typically slightly smaller [36].

- Free spectral range (Δf_{fsr}): The difference in frequency between adjacent modes. In terms of wavelength the FSR is $\Delta\lambda_{FSR} = |c\Delta f_{fsr}/f_0^2|$, which will be nearly constant for high angular orders. For microspheres, the free spectral range is sometimes approximated:

$$\Delta f_{fsr} \approx \frac{c}{2\pi N a}\frac{\tan^{-1}\left(\sqrt{N_{eff}^2-1}\right)}{\sqrt{N_{eff}^2-1}} \tag{9.6}$$

  where N_{eff} is the effective index of the mode, which can be estimated by averaging relative to the fraction of the field energy in each layer, as discussed further below.
- Finesse (F): The finesse is the ratio of the free spectral range to the resonance peak width, given by

$$F = \frac{\Delta f_{fsr}}{\Delta f} = Q\frac{\Delta f_{fsr}}{f_0} = Q\frac{\Delta\lambda_{fsr}}{\lambda_0}. \tag{9.7}$$

- Visibility (V): the mode visibility is a measure of its overall intensity as compared to the background. As with the FSR and the finesse, the visibility relates mainly to spectra in which many modes are collected. The visibility is given by

$$V = \frac{I_{\max} - I_{\min}}{I_{\max} + I_{\min}}. \tag{9.8}$$

  where I_{max} and I_{min} are the maximum and minimum intensity in the mode structure, respectively.

If a microsphere is slightly elliptical, the m-degeneracy is broken (although the sign of m still remains degenerate). The corresponding frequency shifts for modes with the same l but differing m can be estimated for low ellipticity according to [37]:

$$\frac{\Delta f_{n,l,m}}{f_{n,l}} \approx \frac{e}{6}\left(1 - 3\left[\frac{|m|}{l+1/2}\right]^2\right) \tag{9.9}$$

where here $\Delta f_{n,l,m}$ is the frequency shift of a given n, l, m mode with respect to the resonance position in an ideal sphere, $f_{n,l}$, and e is the ellipticity [38]. This implies that

lower m-orders will be shifted progressively further from the "ideal" mode frequency, since these modes deviate further from the equator (Fig. 9.3). Another equation was proposed on the basis of experimental observations [39], for m close to l:

$$\frac{\Delta\lambda_{n,l,m}}{\Delta(l-|m|)} \approx \frac{e\lambda_0}{l} \tag{9.10}$$

In (9.9) and (9.10), e is given by $e = (r_p - r_e)/a$, where r_p and r_e are the polar and equatorial radii of the spheroid and a is the volume-averaged radius. The value of e is positive for a prolate spheroid and negative for an oblate one.

Finally, the sign degeneracy (i.e., between $+m$ and $-m$) can be broken by any effect that breaks the symmetry of the clockwise and counterclockwise propagating rays, such as Rayleigh scattering from particulates, roughness on the sphere surface, or interior refractive index variations [40, 41]. The scattering rate, g, is given by [42]:

$$g = \frac{\pi\alpha F^2(r)\omega_0}{2V_m} \tag{9.11}$$

where α is the polarizability of the scatterer, $F^2(r)$ is a mode function (a unitless parameter describing the normalized mode field at the scatterer location r, given by $|E(r)|^2/max[E(r)^2]$, $\omega_0 = 2\pi f_0$, and V_m is the mode volume. The mode intensity profile $E^2(r)$ can be calculated using methods described below, and the frequency splitting between $+m$ and $-m$ is given by $\Delta f_{\pm m} = \pm g/\pi$, with the sign depending on whether ΔN (of the particle relative to the medium) is positive or negative.

The values associated with $F^2(r)$ and V_m can be difficult to calculate. However, [42] showed that both of these terms can be cancelled in a way that permits one to obtain a direct estimate of the scattering particle size. The method is based on the fact that the mode widths also depend on these parameters. Accordingly, the cavity loss rate is given by

$$\Gamma = \pi|\Delta f_1 - \Delta f_2| = \frac{\alpha^2 F^2(r)\omega_0^4}{6(c/n)^3 V_m} \tag{9.12}$$

in which the terms Δf_1 and Δf_0 are, as before, the half-widths of the two split peaks. Thus, if one takes the ratio g/Γ, we obtain $3(\lambda/n)^3/(8\pi\alpha)$, leading directly to an expression for the polarizability:

$$\alpha = \left(\frac{3\lambda_0^3/N^3}{8\pi^2}\right)\left(\frac{\Gamma}{g}\right) = a^3\,\frac{\varepsilon_p - \varepsilon_m}{\varepsilon_p + 2\varepsilon_m} \tag{9.13}$$

where ε_p and ε_m are the permittivities of the particles and the microcavity, respectively, N is the refractive index of the medium, and a is the radius of the particle. The term on the right-hand-side is the Clausius-Mosotti relation for the spherical dielectric particle. One thus obtains for the size of the scattering particle:

$$\left(\frac{3\lambda_0^3/N^3}{8\pi^2}\right)\left(\frac{\varepsilon_p + 2\varepsilon_m}{\varepsilon_p - \varepsilon_m}\right)\left(\frac{\Gamma}{\pi(\Delta f_{\pm m})}\right) = a^3 \tag{9.14}$$

in which Γ, $\Delta f_{\pm m}$, and λ_0 are measured properties. The value of λ_0 can be taken as the shorter-wavelength split-peak if $\varepsilon_p > \varepsilon_m$, or vice versa otherwise. The detection limit is related to the peak splitting and peak widths such that $\Delta f_{\pm m} > (\gamma_1 + \gamma_2)/2$. The utilization of m-degeneracy breaking was demonstrated as a function of particulate size sensing for sizes down to 50 nm, with apparently good agreement between the experiment and theory [43]. While the method can distinguish particle sizes, the lower size limit of detection was on the order of a = 10 nm, which is large compared to most biomolecules of interest.

Cylinders are, obviously, closely related to spheres but can be thought of as a simpler structure with no polar coordinate. In this case, m becomes essentially irrelevant and there are only equatorial WGMs. Otherwise, the equations outlined above hold approximately true for the cylinder case also. In practice, of course, a cylinder permits the development of cylindrical WGMs, which have slightly different energy density profiles and refractive index sensitivity, as compared to the spherical ones. These aspects will be discussed further in the next section. Cylindrical structures can also have some component of the mode k-vector along the capillary axis; i.e., the spiraling WGMs [44]. Evidence for cylindrical spiraling modes is sometimes reported as a short-wavelength shoulder or skewing of an otherwise Lorentzian WGM mode shape [7, 45, 46]. The magnitude of the resonance shift as a function of spiral angle has been derived, assuming relatively small angles [44]:

$$\Delta\lambda = \frac{\pi a}{Nl}\beta^2 \tag{9.15}$$

where all of the parameters have already been defined and β is the spiraling angle in radians.

For all sensors based on the whispering gallery modes, the mode electric field profile is a key property that controls the sensitivity and detection limit. Fortunately, this profile is relatively simple to calculate. The equations are based on the solutions to the spherical or cylindrical Bessel functions under the appropriate boundary conditions, which depend on the polarization and the number of layers (generally two or three, but more are possible) in the sensor structure. Here, we briefly review the equations that define the electric field profiles, noting that the detailed derivation of these expressions can be found elsewhere [47–50].

9.2.1 Two-Layer Structures

These structures consist of microspheres, fibers, or disks with no coating. The microsphere case was dealt with explicitly in [49]. This situation is especially

simple, since there is only a single boundary between the sphere of index N_1 and the surrounding analyte medium of index N_3. The symbol N_2 will be reserved for the index of an intermediate film or coating, as described for three-layer structures below. Thus, we have:

$$N(r) = \left\{ \begin{matrix} N_1, & r < a \\ N_3, & r > a \end{matrix} \right\} \tag{9.16}$$

Inside the sphere, the energy density of the electric field is described by a Riccati-Bessel function of the first kind (ψ_l), while outside the sphere it is designated by a Riccati-Hankel function of the first kind (ξ_l), which describes an outward radiating wave. Thus, the radial field function for the two polarizations is given by

$$S(r) = \left\{ \begin{matrix} \psi_l(N_1 k_0 r), & r < a \\ D_l \xi_l^{(1)}(N_3 k_0 r), & r > a \end{matrix} \right\} \tag{9.17a}$$

for the TE case, and

$$T(r) = \left\{ \begin{matrix} \psi_l(N_1 k_0 r), & r < a \\ d_l \xi_l^{(1)}(N_3 k_0 r), & r > a \end{matrix} \right\} \tag{9.17b}$$

for the TM one. In the latter case, the E-field is proportional to $T(r)/N^2$ in each layer. The constants D_l and d_l ensure that the boundary conditions at the interface are satisfied. The order l of the functions corresponds to the angular mode number of a given WGM, as described above. The Riccati-Bessel (or Riccati-Hankel) functions are equal to the regular Bessel functions multiplied by its argument (i.e., $\psi_l(Nk_0r) = Nk_0r \cdot J_l(Nk_0r)$). These forms ensure that the radial functions are associated with the energy density of an outward expanding wave.

The boundary conditions arise directly from Maxwell's equations. They were derived by Stratton [51] and their application toward the solution for the resonant fields of a microsphere were discussed at length in [47]. Accordingly, in the TE case both $S(r)$ and its derivative are continuous across the interface. Setting this equality in (9.17a) and taking the ratio to eliminate the constants yields

$$N_1 \frac{\psi_l^{(1)'}(N_1 k_0 a)}{\psi_l^{(1)}(N_1 k_0 a)} = N_3 \frac{\mathrm{H}_l^{(1)'}(N_3 k_0 a)}{\mathrm{H}_l^{(1)}(N_3 k_0 a)} \tag{9.18}$$

where the prime notation indicates the "derivative with respect to the argument", that is $\psi_l(Nk_0r)Z' = d[\psi_l(Nk_0r)]/(Nk_0 \cdot dr)$. For the TM case, the boundary conditions dictate that $T(r)$ and $[dT(r)/dr]/N^2$ must be continuous. Accordingly, we have

$$\frac{1}{N_1} \frac{\psi_l^{(1)'}(N_1 k_0 a)}{\psi_l^{(1)}(N_1 k_0 a)} = \frac{1}{N_3} \frac{\xi_l^{(1)'}(N_3 k_0 a)}{\xi_l^{(1)}(N_3 k_0 a)} \tag{9.19}$$

For cylindrical structures, (9.16)–(9.19) hold except that the spherical Riccati-Bessel functions are replaced by the cylindrical Bessel functions $J_l(Nk_0r)$ and $H_l(Nk_0r)$. One then numerically solves whichever version of (9.18) or (9.19) is appropriate to describe the structure in order to find one or more of the roots k_0. Each solution corresponds to a particular radial mode order $n = 1, 2, 3\ldots$ Once a particular solution has been found, the constant D_l or d_l can be calculated since the radial functions are equal at a (i.e., at the interface). A plot of (9.17a) or (9.18) will then show which radial mode order the solution represents.

9.2.2 Three-Layer Structures

For three-layer structures (e.g., a coated sphere or a thin-walled capillary), we proceed exactly as before except with the addition of an extra layer. The same boundary conditions hold. Accordingly for the TE situation we have:

$$N(r) = \left\{ \begin{array}{ll} N_1, & r \leq b \\ N_2, & b < r \leq a \\ N_3, & r > a \end{array} \right\} \tag{9.20}$$

where the thickness of the layer is $t = a - b$. For a coated sphere, the radial functions for the TE and TM cases, respectively, are:

$$S(r) = \left\{ \begin{array}{cc} A_l\psi_l(m_1k_0r), & r \leq b \\ B_l\xi_l^{(2)}(m_2k_0r) + \xi_l^{(1)}(m_2k_0r), & b < r \leq a \\ D_l\xi_l^{(1)}(m_3k_0r), & r > a \end{array} \right\} \tag{9.21}$$

and

$$T(r) = \left\{ \begin{array}{cc} a_l\psi_l(m_1k_0r), & r \leq b \\ b_l\xi_l^{(2)}(m_2k_0r) + \xi_l^{(1)}(m_2k_0r), & b < r \leq a \\ d_l\xi_l^{(1)}(m_3k_0r), & r > a \end{array} \right\} \tag{9.22}$$

The boundary conditions then yield the following expression which must be numerically solved for the root k_0, as before. For the TE case one obtains

$$\frac{N_3\xi_l^{(1)'}(N_3ka)}{N_2\xi_l^{(1)}(N_3ka)} = \frac{B_l\psi_l'(N_2ka) + \xi_l^{(1)'}(N_2ka)}{B_l\psi_l(N_2ka) + \xi_l^{(1)}(N_2ka)} \tag{9.23}$$

with

$$B_l = \frac{N_2\psi_l(N_1k_0b)\xi_l^{(1)'}(N_2k_0b) - N_1\psi_l'(N_1k_0b)\xi_l^{(1)}(N_2k_0b)}{-N_2\psi_l(N_1k_0b)\xi_l^{(2)'}(N_2k_0b) + N_1\psi_l'(N_1k_0b)\xi_l^{(2)}(N_2k_0b)} \tag{9.24}$$

Similarly, for the TM case one has:

$$\frac{N_2\xi_l^{(1)'}(N_3ka)}{N_3\xi_l^{(1)}(N_3ka)} = \frac{b_l\psi_l'(N_2ka) + \xi_l^{(1)'}(N_2ka)}{b_l\psi_l(N_2ka) + \xi_l^{(1)}(N_2ka)} \tag{9.25}$$

with

$$b_l = \frac{N_1\psi_l(N_1k_0b)\xi_l^{(1)'}(N_2k_0b) - N_2\psi_l'(N_1k_0b)\xi_l^{(1)}(N_2k_0b)}{-N_1\psi_l(N_1k_0b)\xi_l^{(2)'}(N_2k_0b) + N_2\psi_l'(N_1k_0b)\xi_l^{(2)}(N_2k_0b)} \tag{9.26}$$

The complex roots k_0 can then be solved numerically for either polarization, as before, and then the coefficients determined by setting the radial functions equal at all the boundaries and solving for A_l, B_l, and D_l (or a_l, b_l, and d_l). Note that $C_l = c_l$ has been set to unity without loss of generality. The electric field profiles calculated from these equations for a mode with $n = 1$ and $l = m = 110$ is shown for both the TE and TM polarizations in Fig. 9.4.

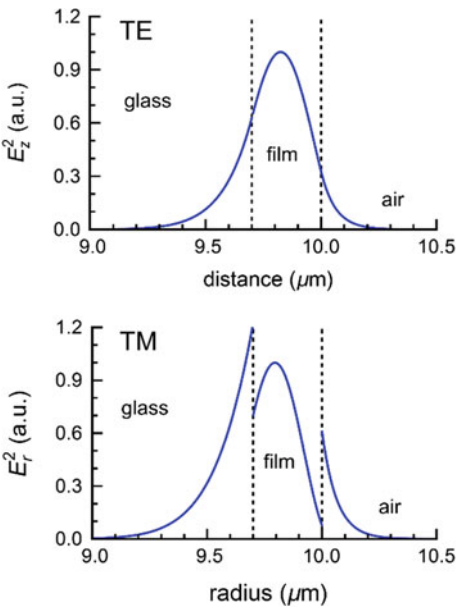

Fig. 9.4 Mode intensity profiles for an $n = 1$, $l = 110$ WGM in a 20-μm-diameter glass sphere with a high index ($N_2 = 1.67$) coating. The TE resonance is at $\lambda_0 = 842.2$ nm and the TM one is at 817.0 nm, using full dispersion. The separation between the TE and TM resonances is several times larger than predicted by (9.2), which appears more accurate for very high mode orde

For a three-layer cylindrical structure such as an optical fiber or capillary, (9.20)–(9.26) can be repeated by replacing the spherical Riccati-Bessel functions with cylindrical Bessel (or Hankel) functions, as before [50].

9.3 Sensitivity and Detection Limits

An important figure of merit for all WGM-based sensing devices is the sensitivity; that is, the mode shift per unit refractive index change in the analyte medium. Generally, a high sensitivity requires that a significant fraction of the mode energy be located in the analyte. In the case of microspheres, fibers, or disks, this implies that the mode should extend relatively far into the outside region, implying the desirability of lower Q-factors for bulk refractive index sensing. On the other hand, for biomolecular sensing a high Q-factor is more important, since it means effectively more interactions with a surface-bound biomolecule before photons are lost from the cavity. In the case of capillary-type devices, on the other hand, the tail of the mode field extending into the channel is responsible for the sensing ability. The sensitivity thus depends on the refractive index profiles and the mode order used.

For the theoretical perspective, a series of papers [52–54] showed how to calculate the sensitivity of microsphere sensors using a perturbation theory that can be applied to any type of WGM sensor structure, as long as the shifts are relatively small. Accordingly, the shift in the resonant k-vector caused by a small change in the analyte index of refraction can be written as

$$\frac{dk}{k} = -\frac{1}{2}\frac{\int_{V_p} \partial\varepsilon_r \overrightarrow{E_0^*} \cdot \overrightarrow{E_p} d^3r}{\int_V \varepsilon_r \overrightarrow{E_0^*} \cdot \overrightarrow{E_0} d^3r}, \tag{9.27}$$

This equation says that the fractional shift of the resonant wavevector, *dk/k*, depends on the energy change in the volume V_p caused by the perturbation (i.e., the shift in the permittivity) relative to the total mode energy integrated over the entire volume V.

Equation (9.27) is straightforward for the TE polarization but is complicated by the boundary conditions associated with the TM polarization. The methods used to calculate *dk/k* have, however, been shown both for spheres [52] and for cylinders [50]. The mathematical procedure is too lengthy to repeat here; instead, we simply report the results for bulk changes in the analyte medium. This yields the following cases:

sphere, *TE*:

$$S_{TE} = \lambda_0 \cdot \frac{N_3 I_3}{N_1^2 I_1 + N_2^2 I_2 + N_3^2 I_3} \tag{9.28}$$

sphere, *TM*:

$$S_{TM} = 2N_3\lambda_0 \cdot \frac{d_1^2 a}{4N_3^2(I_1+I_2+I_3)} \left[\begin{array}{l} -\left(\xi_l^{(1)'}(N_3k_0a)\right)^2 \\ +\left(\frac{l(l+1)}{(N_3k_0a)^2}-1\right)- \\ \frac{\xi_l^{(1)}(N_3k_0a)\cdot\xi_l^{(1)'}(N_3k_0a)}{N_3k_0a} \end{array} \right] \tag{9.29}$$

sphere, energy integrals:

$$I_1 = \int_0^b |A_l J_l(N_1k_0r)|^2 dr \tag{9.30a}$$

$$I_2 = \int_b^a \left|B_l\xi_l^{(2)}(N_2k_0r) + \xi_l^{(1)}(N_2k_0r)\right|^2 dr \tag{9.30b}$$

$$I_3 = \int_a^\infty \left|D_l\xi_l^{(1)}(N_3k_0r)\right|^2 dr \tag{9.30c}$$

capillary, TE:

$$S_{TE} = \frac{d\lambda_0}{dm_1} = \frac{-2\pi(dk/k_0^2)}{dm_1} = -\frac{\lambda_0}{dm_1}\cdot\frac{dk}{k_0} = \frac{\lambda_0}{m_1}\cdot\frac{I_1}{I_1+I_2+I_3} \tag{9.31}$$

capillary, TM:

$$S_{TM} = \lambda_0 \frac{(2k_1^2)}{m_1^3\left(k_0^2+\left(k_0^*\right)^2\right)} \cdot \frac{b|a_l|^2 \left(\begin{array}{l} \frac{dJ_l^*(m_1k_0r)}{dr}\Big\|_b J_l(m_1k_0b) + \\ J_l^*(m_1k_0b)\frac{dJ_l(m_1k_0r)}{dr}\Big\|_b \end{array} \right) + \frac{k_0^2+\left(k_0^*\right)^2}{k_{0,1}^2} I_1}{\left[\frac{I_1}{m_1^2}+\frac{I_2}{m_2^2}+\frac{I_3}{m_3^2}\right]} \tag{9.32}$$

capillary, energy integrals:

$$I_1 = \int_0^{m_1k_{0,1}b} x|A_l J_l(\tilde{x})|^2 dx \tag{9.33a}$$

$$I_2 = \int_{m_2 k_{0,1} b}^{m_2 k_{0,1} a} x \left| B_l H_l^{(2)}(\tilde{x}) + H_l^{(1)}(\tilde{x}) \right|^2 dx \tag{9.33b}$$

$$I_3 = \int_{m_3 k_0 a}^{\infty} x \left| D_l H_l^{(1)}(\tilde{x}) \right|^2 dx \tag{9.33c}$$

with $x_i \equiv N_i k_{0,1} r$ where $i = 1, 2, 3$ for each of the three regions, $\tilde{x} \equiv x(1 + ik_{0,2}/k_{0,1})$ and $k_0 = k_{0,1} + ik_{0,2}$. These expressions were derived to handle complex values of k_0. In contrast, the sphere sensitivity formulas (9.28)–(9.30a) do not explicitly deal with complex k_0; rather, one can approximate by taking only the real part of all the functions as was done in [53, 54], in which the Riccati-Hankel functions were replaced with Ricatti-Neuman ones.

9.3.1 Disk or Fiber

These structures are similar to a capillary except that the analyte is on the outside (N_3) rather than the inside (N_1). In order to approximate their refractometric sensitivity, one can use the capillary solutions, switching the appropriate functions and indices accordingly. For example, in (9.32) the $b|a_l|^2$ term turns into $-a|d_l|^2$ and the indices N_1 and N_3 and Bessel functions (layer 1 vs. layer 3) switch accordingly.

The refractometric sensitivity for a microsphere is shown as a function of the coating thickness in Fig. 9.5. The coating has a refractive index of 1.67, corresponding to a layer of fluorescent silicon quantum dots. The sensitivity reaches a maximum of ~28 nm/RIU for a coating thickness of ~150 nm. This behavior was reported extensively in [53, 54]; essentially there is an optimum high-index coating at which the sensitivity is maximized. For a thicker coating, the field is "pulled" into

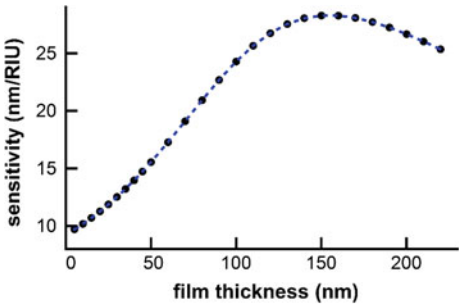

Fig. 9.5 The refractometric sensitivity as a function of the coating thickness, for a microsphere of radius of 10 μm, modified after [33]

the high index layer and does not extend as far into the outside analyte. In the case of a capillary, a thinner film leads to a higher sensitivity since the analyte is the interior medium; however, eventually the Q-factors become unacceptably low. This is because, in a capillary, the film is needed to support the WGMs; whereas in a sphere the film is not strictly needed for sensing applications and WGMs are present without it.

The detection limit can be defined as the smallest detectable change in the bulk analyte refractive index, or as the smallest detectable biomolecular concentration or mass. Regardless of whether the bulk, concentration, or mass definition is used, key aspects are how much noise is in the data and how the wavelength shift information is processed. The detection limit (*DL*), can be considered as the smallest change in the analyte that yields a shift equal to 3σ of the noise level.

This concept can be boiled down to a few simple factors. The first point is the wavelength shift resolution, *R*. If one is trying to find the central wavelength, λ_0, of a single WGM, one often uses either centroid [55] or curve-fitting [56] methods. The centroid method simply finds the center-of-mass of the resonance profile, whereas curve fitting requires an adequate model (e.g., a Lorentzian) and initial parameters. Figure 9.6 shows two simulated Lorentzian modes with Gaussian noise that provides a linear signal-to-noise ratio (SNR) of 10 and 100, respectively, having an 8-pixel width and sampled with 21 pixels. The actual sampling rate of course depends on the system used to measure the WGMs. The 3σ shift resolution

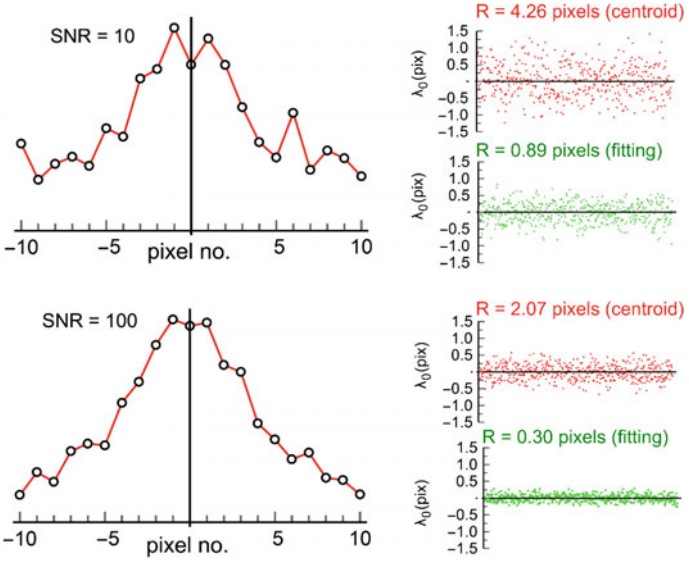

Fig. 9.6 *Left* Simulated Lorentzian curves centered at zero, with Gaussian noise added to produce SNRs of 10 and 100. On the left of each curve, the values of λ_0 for 500 repetitions are shown along with the corresponding 3s resolution (*R*) for the centroid and curve fitting methods, *unit* units of pixels

is shown for both methods as a function of the linear SNR, where $SNR = (A_{sig}/A_{noise})^2$. The curve fitting results are always better than the centroid method as long as the SNR was above ~ 1. For lower SNRs the curve fitting method becomes unstable. On the other hand, if the mode does not have a purely Lorentzian character (e.g., due to the presence of spiraling modes or instrument broadening), then unless one has a good alternative waveform model the centroid method may be better.

According to Fig. 9.6, an optical system (e.g., a spectrometer) with a pitch of 0.1 nm/pixel will yield a 3σ optimal shift resolution of $R = 89$ and 30 pm for an SNR of 10 and 100, respectively, using curve fitting for a peak width of 8 pixels. These values compare to the numerical prediction of 41 and 13 pm using the numerical equations in [57] under similar conditions. The somewhat higher values in the present case may be due to the different fitting routines employed. The centroid method is worse in both cases.

For WGMs measured by transmission, typically the scan range is only over a single peak and one of the above two methods will generally be employed. For fluorescence WGMs, on the other hand, the collected bandwidth is many FSRs wide. Such cases lend themselves well to Fourier analysis methods. To put these values into context, a fluorescence WGM spectrum typically has an SNR of 100 and a spectrometer pitch of ~ 0.1 nm/pixel, yielding a typical Fourier shift resolution of ~ 9 pm [57]; this is generally similar to or slightly better than curve fitting. In our experience the Fourier method especially shines when the SNR is low, because curve fitting then often fails to adequately converge, or when the model has more variables than a simple Lorentzian (i.e., when the WGMs appear skewed due to the presence of spiraling modes [46]).

The Fourier shift method works as follows, as summarized in [58]:

1. Convert the spectra into frequency units. This ensures a constant free spectral range.
2. Choose the reference dataset (i.e., the first WGM fluorescence spectrum) from which all shifts will be measured.
3. Interpolate the spectra to obtain uniform frequency spacing for Fourier analysis.
4. Perform a discrete Fourier transform to obtain the power and phase components associated with each spectrum.
5. Find the phase differences for all k components of a given WGM spectrum, with respect to the reference spectrum.
6. Find the phase shift for each spectrum, relative to the initial one. Use either the main Fourier component only, or employ a linear fit to several components weighted by the spectral power in each component. Convert the phase shift angle into the desired unit (e.g., that of frequency or wavelength).
7. The errors in the weighted fits correspond to the phase shift uncertainty and are also converted into the desired unit. If only the strongest Fourier component is used, then there are no error bars.

Step 1 (and therefore step 3) can be ignored if high angular orders are being used, since the FSR will then be virtually constant in wavelength units also.

Alternatively, the Fourier shift analysis can also be performed on raw spectral images and the shift measured in pixels. The result can be converted to wavelength shift, knowing the pitch of the CCD (in wavelength range per pixel).

An additional factor with respect to sensing applications is the speed of the analysis. In fluorescence systems one is usually suffering from a relatively low SNR, making it apparently difficult to increase the analysis speed. However, the Fourier shift method is fairly insensitive to noise (it depends on the square root of the SNR [57]) and can successfully find the spectral shift even for SNRs below which curve fitting fails. For transmission measurements, one has plenty of signal and the analysis speed is usually dependent on the scan rate of the laser. A time resolution of 20 ms was, for example, recently reported for a system scanning a mode at a wavelength of $\sim$780 nm [1]. This is much faster than will be possible for fluorescence system due to low light levels.

The detection limit depends on the wavelength shift resolution and inversely on the sensitivity according to $DL = R/S$. For fluorescent devices the best detection limit is on the order of 10^{-5} RIU, but for transmission devices it can easily reach 10^{-7} RIU. This is, again, a direct consequence of the lower wavelength shift resolution for tunable laser systems as compared to spectrographs. The latter is comparable to the best results for surface-plasmon sensors [59].

For biomolecular sensors, the detection of single molecules results in shifts that are generally too small to be observed, even with laser systems with 100 kHz bandwidth. However, single-molecule detection can be achieved by plasmonic enhancement of the WGM electric field [60]. This can be achieved by attaching a gold nanoparticle to the equator of a microsphere, which can enhance the local field strength by hundreds of times depending on its size, shape, and orientation [61, 62]. Gold nanoparticles with protrusions or bumps can be even more effective [63], and, perhaps counterintuitively, the enhancement is larger for smaller biomolecules (due to the small spatial extension of the field enhancement). This method was recently used to detect the binding of the smallest biomolecules so far reported [1]. It could also enhance the sensitivity of capillary-type structures (where the metal particles would be attached to the inner surface) but this has not yet been demonstrated experimentally.

9.4 Surface Chemistry for Biosensing

Every biosensor comprises three essential components: the detector or probe [64], such as an antibody, which recognizes or captures a biological molecule of interest; the transducer which converts the signal generated from the specific biological reaction occurring at the surface of the biosensor into a readable signal; and the output system which involves amplification, signal processing, and display of an intelligible results [64, 65]. Surface functionalization is a very broad term which primarily describes a wide range of techniques and processes to immobilize the detector or probe mentioned above onto the sensor's surface. Surface

functionalization is therefore crucial for achieving many applications. It involves the specific immobilization of biomolecule of interest onto the sensor surface, whether the end application aims for the detection of a virus [66, 67], bacteria [68], proteins [69, 70] or DNA strand [1].

As a consequence, surface functionalization is as important in defining the device performance as the transducing mechanisms itself [2, 64, 65]. A poor management of the surface functionalization may result in low surface density of the detector/probe molecules or loss of their biochemical functionality through a random orientation [71–73] and/or denaturation [74, 75], which results in poor binding affinity and consequently poorer detection limit. Another consideration is the impact of nonspecific binding which can be detrimental for label-free biosensing technologies [64, 76, 77]. Nonspecific binding is defined as the interaction of an unwanted biomolecule with the sensor surface, which in turns produces a false positive in the output signal [78]. This unwanted interaction could occur either through cross reactivity of the detector/probe molecules [79] immobilized onto the sensor surface or via physisorption mechanisms [77].

A less-common definition for surface functionalization refers to the modification of the physical properties of the resonator. This could involve the immobilization of fluorescent nanoparticles, such as quantum dots [46, 80–82], or dye doped polymer coatings [83, 84] in order to generate a fluorescence WGM spectrum, or rare earth nanocrystals for WGM lasing applications [80, 84], metallic nanoparticles to exploit plasmonic effects [1, 85, 86], or passive high-refractive-index polymer coating to improve the overall sensing performance [53, 87].

For biological sensing applications, the choice of the surface functionalization technique is often related to the considerations mentioned previously (binding density, probe orientation, nonspecific binding) as well as the nature of the material constituting the sensing device. It will inevitably involve some initial chemical interactions often referred to as grafting (covalent binding) or physical interactions (adsorption, physisorption, or chemisorption) associated with the sensor surface and the deposited layers [64]. The nature of the mechanisms involved is dictated by the physical and chemical properties of both the sensor surface and the material to be deposited.

9.4.1 Grafting or Covalent Binding

Grafting refers to the creation of covalent bond between the sensor surface and the molecule to be immobilized. This technique implies the utilization of intrinsic chemical groups on the sensor surface; the pathway to achieve this task is highly dependent on the intrinsic surface chemistry of the sensing platform. An often-used method is to exploit the hydroxyl (OH) groups on oxide surfaces, [88] especially in the cases of silica [89], polymers [90] and even metals [91]. A selection of different binding chemistries utilizing the hydroxyl surface groups is illustrated in Fig. 9.7; these include phosphonates, carboxylates, catechols, alkenes or alkynes, amines,

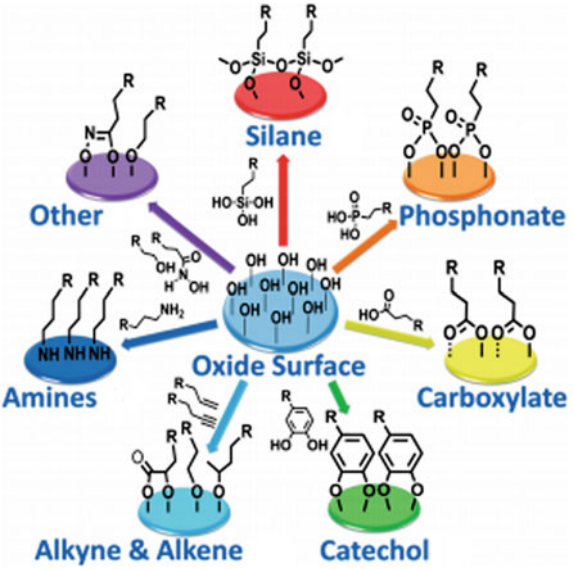

Fig. 9.7 Diagram of the various surface functionalization processes for oxide surfaces with –OH-terminated surfaces, used with permission from [88]

and silanes, the latter of which are often employed [88] due to the simplicity of the deposition process.

Silanes come with a large variety of available functional groups. However, 3-aminopropyltriethoxysilane (3-APTES) and 3-aminopropyldimethylethoxysilane (3-APDMS), and to some degree carboxylic-terminated silanes, are among the most commonly-employed for biosensing applications as they permit subsequent covalent attachment of biomolecules such as antibodies [92]. For example, silane-based surface functionalization process based on 3-APDMS has been used with silica microspheres supporting WGMs [93, 94]. The attachment silane mechanism depicted in Fig. 9.8 relies first on the hydrolysis of the silane by water molecules already adsorbed onto the sensor surface. This produces hydroxyl groups, creating the corresponding hydroxysilane. Then hydrogen bonds are formed between the hydroxysilane and the surface hydroxyl groups while lateral reordering allows the formation of a single monolayer before the Si–OH condensation occurs, to form stable Si–O–Si bonds. This is what should happen in theory; however, silanes are notoriously sensitive to moisture, which can cause extensive polymerization and strongly affect their ability to form a smooth monolayer. Depending on the deposition method and the moisture exposure during the coating process, crosslinking between silane subunits can occur during the condensation phase, resulting in the creation of a network rather than a monolayer. Another factor which can influence the quality of the silane layer is the initial surface density of OH groups on the sensor surface. A low surface density results in low reproducibility in the deposition process. OH groups can be generated on the sensor surface prior the deposition process by plasma activation [95] or extensive cleaning of the surface with acids [96].

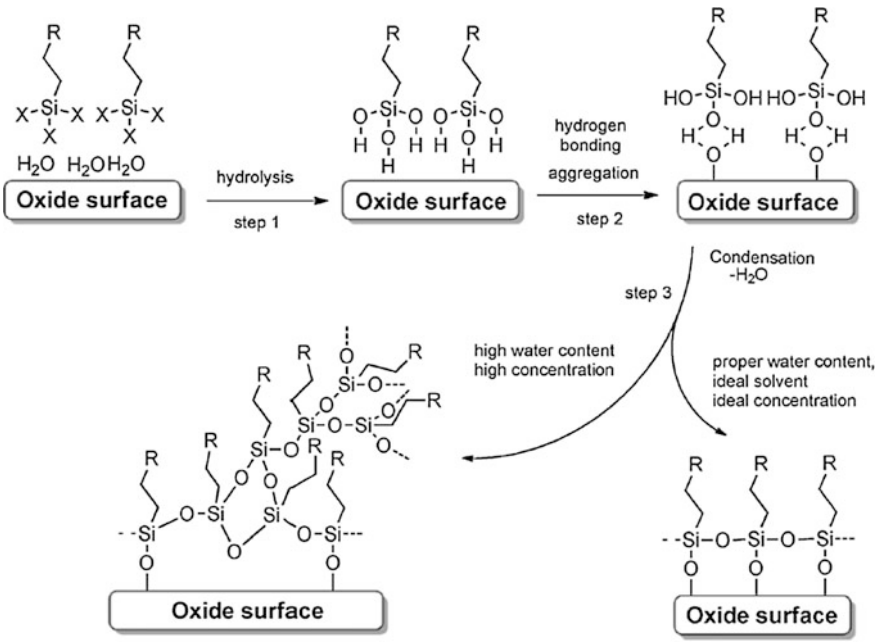

Fig. 9.8 Diagram of the silane immobilization mechanism, after [88]

Silanes can be deposited either in solution [96] or vapor phase [97, 98]. The solution deposition process involves simply exposing the freshly prepared sensor surface into silane solutions dissolved at millimolar concentrations in an anhydrous solvent such as toluene [96], yielding a full silane coating in minutes to hours. The concentration of the silane in solution is also crucial to produce an homogeneous film without cross-linking [99]. The vapor phase deposition requires more equipment as it involves placing the sensor surface in a vacuum chamber under a low pressure of silane vapor. Despite this technical limitation, vapor phase deposition has shown to be more reliable in producing consistent silane films compared with the solution phase deposition [100]. For further information, we suggest the review written by Pujari et al. [88] on oxide surfaces covalent functionalization and the review from Goddard et al. [101] on the same topic applied to polymers.

9.4.2 Physisorption

In cases when the preparation of the sensor surface, involving plasma activation or acid cleaning is not possible, another route has to be found for surface functionalization. Physisorption is an alternative which doesn't depend on the surface chemistry of the sensor surface and can be exploited on virtually every material. It

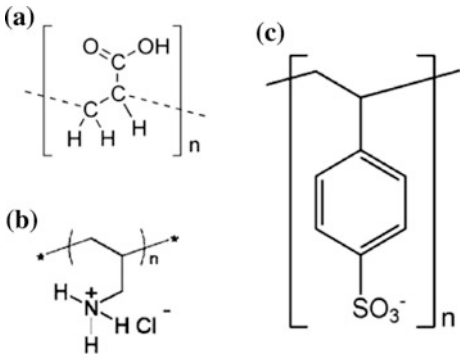

Fig. 9.9 Chemical diagrams of some of the more commonly-used polyelectrolytes for functionalization. **a** Polyacrylic acid (PAA), **b** polyallylamine hydrochloride (PAH), **c** polystyrene sulfonate (PSS)

is also a simple process although unlikely to result in a single self-assembled monolayer due to the attachment mechanisms involved.

Physisorption has been widely used in many disciplines and is commonly employed for the preparation of glass slides or plastic well plates coated with proteins such as gelatin, which promotes tissue adhesion [102], or for immunofluorescence. One particular approach is to use charged polymers in solution, often called polyelectrolytes (PEs). Like silanes, there is a large variety of PEs available; among the most commonly used are polyacrylic acid (carboxylic group), polyallylamine hydrochloride (amino group) and polystyrene sulfonate (Fig. 9.9).

Polyelectrolytes can be either positively or negatively charged. The deposition of PE layers is done in a layer-by-layer process according to the charge. The initial PE layer should have a charge opposite to the intrinsic surface charge of the substrate. Deposition of the first layer is followed by a rinsing step and then a second PE layer with opposite charge to the first one [103] (Fig. 9.10). The process can be repeated multiple times to stack PE layers onto any substrate, resulting in an increase of the functional group density on the sensor surface. The amount of functional groups available on the surface can be tailored for specific application by optimizing the surface coverage, which depends on the number of PE layers deposited. This is unique among all surface chemistry approaches, enabling a high versatility of applications beyond surface functionalization. Branched PEs can further enhance the number of functional groups available for immobilization [104].

The deposition process relies exclusively on electrostatic forces rather than on the chemical nature of the PE layers. This is unlike other surface functionalization process such as those based on thiols or silanes, which only work on silver or gold, or require substantial preparation of the substrate in order to create the required hydroxyl groups. Therefore, PE coatings can be deposited on metallic [105, 106], polymer [107, 108], and glass surfaces [109, 110], and even on living organisms [111] which highlights their biocompatibility. PE coatings are also highly reproducible with the thickness of individual layers being only dictated by both the ionic

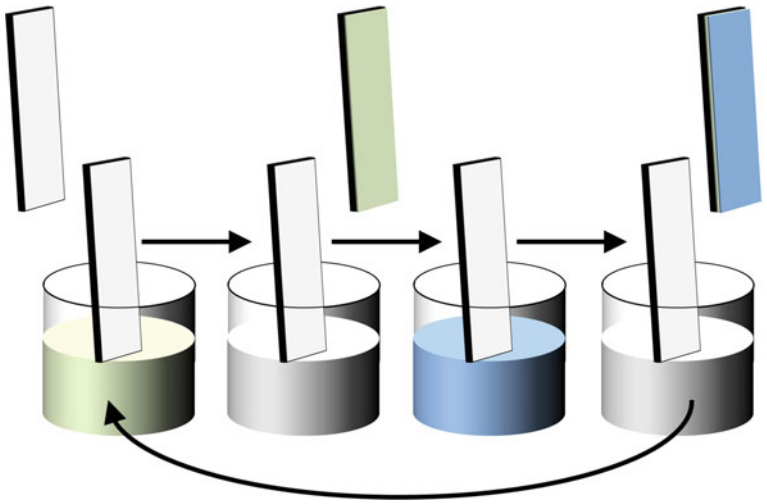

Fig. 9.10 Depiction of the layer-by-layer deposition process used for polyelectrolyte coating. Here, the substrate is dipped into alternating PE layers with opposite surface charges (*blue* and *red*). The rinsing steps are not shown (Color figure online)

strength of the buffer in which the PE are dissolved (usually NaCl solutions) as well as the concentration of the PE in solution [112].

Despite the advantages provided by the physisorption of PE layers, some intrinsic limitations still exist. PE layers are sensitive to variation of pH and ionic strength [113, 114], which induces swelling of the deposited layers. This swelling of charged PE layers in charged buffer, either due to pH or ionic strength, is induced by a displacement of the charge uncompensated equilibrium within the PE multilayer stack and is dictated by the charge of the last deposited layer [115]. While this property has been exploited for pH sensing [116], it can be detrimental for a refractive-index-based sensing mechanisms. This behavior can be prevented by carefully choosing the PEs constituting the multilayer coating and cross-linking the polymeric chains to prevent their relative mobility [116]. PE layers are thought to be fairly stable in a wide range of pH; however, exposure to strong basic solution (e.g., 1 M NaOH) will denature and eventually remove the PE multilayer assembly from the sensor surface [117]. Despite these limitations, one can argue that for biosensing applications, where the pH is close to 7.4 and deviates only slightly from this value, the PE multilayers are effectively stable.

A physisorption-based surface functionalization process, using bovine serum albumin (BSA) directly deposited onto the sensor surface and subsequently cross-linked with antibodies [107], has been used with fluorescent polystyrene microspheres, while a PE-based surface functionalization process has also been used with both fluorescent polystyrene microspheres [108] and glass capillaries [118, 119], demonstrating the applicability of such approach for biosensing applications involving whispering gallery modes.

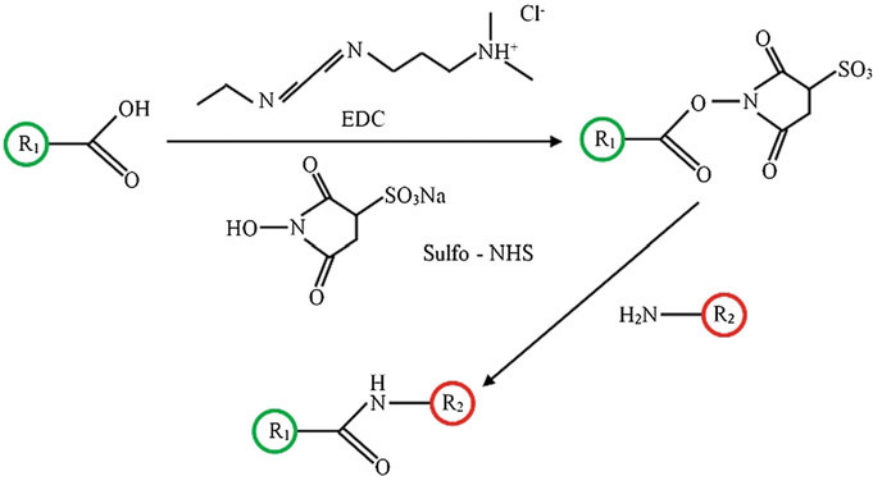

Fig. 9.11 Example reaction pathway between carboxyl and primary amine groups using EDC as cross linker, from [121]

Biomolecule immobilization, non-specific binding, and specific orientation

The deposition of either silanes or PE multilayers is merely the first step of a complex process. The first deposited layers are simply aiming to provide the adequate functional groups for further chemical reactions to occur for the immobilization of a detector probe such as an antibody. Similarly to the first deposited layer there is a vast choice of chemical processes which can be exploited [120]. However, carbodiimides such as 1-ethyl-3-(3-dimethylaminoropyl) carbodiimide (EDC) have been among the most successful. Carbodiimides operate by activating a carboxylic group (–COOH) towards amide or ester formation, enabling the chemical reaction between carboxylic (–COOH) and the primary surface amine ($–NH_2$) groups via amide bonds (Fig. 9.11). Additives such N-hydroxysuccinimide (NHS) or sulfo-NHS can be added to the reaction to increase the reaction yield. Proteins naturally present carboxylic functionality which implies that, in order to use a carbodiimide cross linker, the surface has to present primary amine groups.

For immunoassays involving antibodies as molecular probes, the orientation of the antibodies with respect to the surface can drastically change the performance of the sensor [106, 122, 123], with binding "efficiency" $\sim$2.5 times better for oriented antibodies compared to a random orientation [123]. Several strategies have been used to promote the specific orientation of antibodies onto primary amine functionalized surfaces. Among the most successful approach is the use of protein A or G which present specific binding sites against the antibody Fc fragments (blue rectangles) shown in Fig. 9.12. Immobilizing either protein A [122, 123] or G onto the sensor surface allows the subsequent attachment of the antibodies onto the surface using the Fc fragments (blue rectangles) as an anchor and leaving the variable regions or epitopes (red rectangles) in Fig. 9.12, which are meant to interact specifically with the counterpart antigen, facing outward the sensor surface.

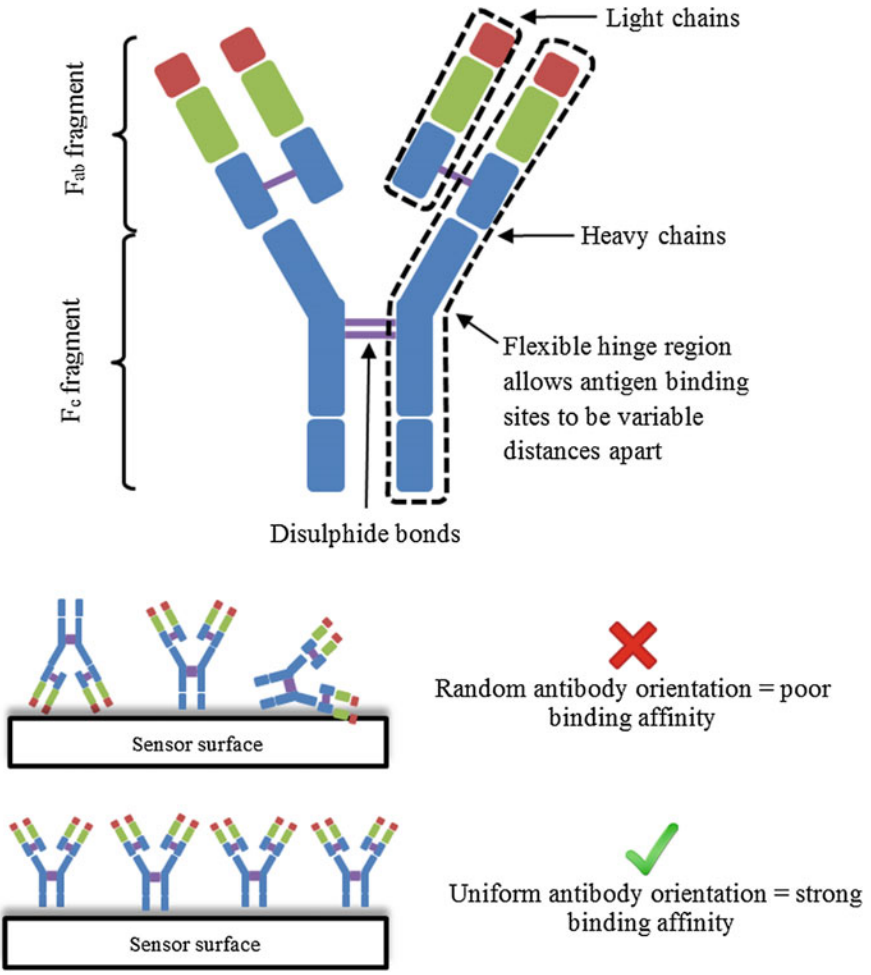

Fig. 9.12 Depiction of an IgG antibody structure. The blue regions of the antibody are fixed regions while the grey and red portions are variable regions. The ref fragments are the recognition elements responsible for the specific interaction with the antigen

The choice between using either protein A or protein G as an intermediate layer for promoting antibody orientation is primarily dictated by their relative affinity against the antibodies to be used [124].

The second approach takes advantages of the recent commercial development of biotinylated antibodies. Most antibody providers are now able to manufacture a biotinylated version of most of their antibodies, although the exact position where the biotinylation takes place is subjected to debate. Similarly to the previously-described approach, this process relies on using streptavidin, avidin or neutravidin, all of which present specific binding sites for biotin, only differing in

their isoelectric point. First, the primary amine-coated surface is biotinylated using EDC/NHS to promote the creation of amide bonds between the surface and the biotin carboxylic group. Then, the biotinylated surface is exposed to avidin until a full monolayer is formed and then to the biotinylated antibodies [105]. These two approaches have been shown to significantly increase the capture efficiency of the immobilized antibodies, enabling better sensing performance regardless of the transducing mechanism involved. Other less straightforward approaches have been developed using either covalent or non-covalent interactions. For more details we suggest the recent review by Trilling et al. [123].

Nonspecific binding is another crucial element in all immunoassays. This is particularly true for label-free transducing mechanisms where nonspecific interactions can be misinterpreted as a binding event. Once the probe has been attached to the sensor surface is it important to passivate all nonspecific binding sites. Protein-protein interactions are widely used to achieve this task, for example, by exposing the sensor surface to BSA, casein, or gelatin, which will "fill the gaps" between antibodies and prevent physical or chemical interaction with other proteins present in the sample. However, for a real clinical sample like blood, this protein-protein interaction strategy is often not sufficient to prevent nonspecific binding due to the large variety of proteins present in the sample. Interestingly, comb-like assemblies of peptides have been developed on metallic surfaces for plasmonic applications; these can successfully suppress nonspecific binding even in full blood [125]. Similar approaches have been developed using polyethylene glycol (PEG) chains of different lengths, covalently attached to a primary amine-coated silica microsphere [126].

9.5 Fluorescent Microspheres, Fibers, and Capillaries

Fluorescent microsphere resonators were historically the first optical resonator enabling the study of WGMs in the optical domain. Benner et al. [127] was the first to report the observation of modulated fluorescence spectra in dye-impregnated polystyrene microspheres although the theoretical formalism describing these experiments was known since the initial work of Chew et al. [128]. Ten years later Chew perfected his model predicting the WGM modulated fluorescence emission of fluorescent microspheres [129, 130]. Since then a large effort has been dedicated to research on fluorescent microspheres for studying fundamental aspects as well as for applications in biosensing.

Multiple approaches have been used to incorporate a gain medium within a microsphere. In many cases, the material can be a laser medium, and the transition between fluorescent versus lasing WGM sensors has been established. A common method employed since at least the 1990s is to introduce various fluorescent dyes via diffusion into polymer based microspheres [131]. Attaching quantum dots or promoting their diffusion through the resonator [82, 132, 133] has also proven successful without significantly worsening the Q factor, despite the increased

probability for scattering. Fluorescent microspheres have also been fabricated by melting the tip of an optical fiber containing rare earth ions such as erbium [39, 134, 135]. Alternatively, bulk fluorescent coatings can be deposited onto the microsphere, such as a thin film of silicon nanocrystals [136]. Finally the intrinsic microsphere fluorescence can be exploited to achieve similar results. For example, zinc oxide [137] and titanium oxide [138] microspheres have been used for such purpose with a photoluminescence emission ranging from 550 to 750 nm.

There are several advantages in using fluorescent microspheres for WGM-based sensing. First, the WGMs can be excited and analyzed without the need for optical fiber tapers or prisms to couple light inside the resonator. This particular feature of fluorescent microspheres allows different architectures for sensing applications. It also permits the use of smaller microspheres ranging from few microns to tens of microns in diameters which could be used as localized probes in the vicinity of a single cell or within a living cell itself [139, 140]. Furthermore, reducing the size of the resonator increases the sensitivity to the surrounding refractive index [93], because of the larger fraction of the field propogating outside the resonator (see Sect. 9.2 of this chapter). However using smaller microspheres, especially in aqueous environments, for biosensing applications implies that the resonator's refractive index has to be large enough to achieve sufficient optical confinement. This typically requires the use of polymers such as polystyrene (PS) [132, 141] or melamine formaldehyde [140], high refractive index glass such as Er^{2+} or Tm^{3+} doped tellurite [134, 142], or other oxides [137, 138].

Fluorescent microspheres can also be used to decrease the lifetime of the fluorescent medium at the resonance wavelengths, via the Purcell effect [143]. The Purcell enhancement factor F_P is related to both the mode volume and the Q factor (Sect. 9.2) as described in the (9.34), where λ_C and N are the resonance wavelength and the resonator's refractive index, respectively. Under ideal conditions, the Purcell factor can be as large as:

$$F_p = \frac{3}{4\pi^2}\left(\frac{\lambda_0}{N}\right)^3 \frac{Q}{V} \tag{9.34}$$

This enhancement factor is observable experimentally by the sharp peaks corresponding to the WGM resonances, which modulate the fluorescence emission from microspheres as shown in Fig. 9.13 for a 10 μm dye doped polystyrene in water, both below (a) and above (b) the lasing threshold.

Beyond the fluorescence regime, stimulated emission can be achieved with a suitable fluorescent dye or gain medium [131, 144]. Stimulated emission not only results in a higher intensity, as demonstrated in Fig. 9.13b for the same 10 μm diameter polystyrene microsphere operated above the lasing threshold, but also in sharper resonances. Figure 9.14 shows both the Q factor and the resonance amplitude for the same 10 μm polystyrene sphere as function of the pump power. Upon initiation of lasing, the Q factor is increased by a factor 3–4 [144, 145]. This effect resulted in an increase by the same factor in the sensing resolution and may

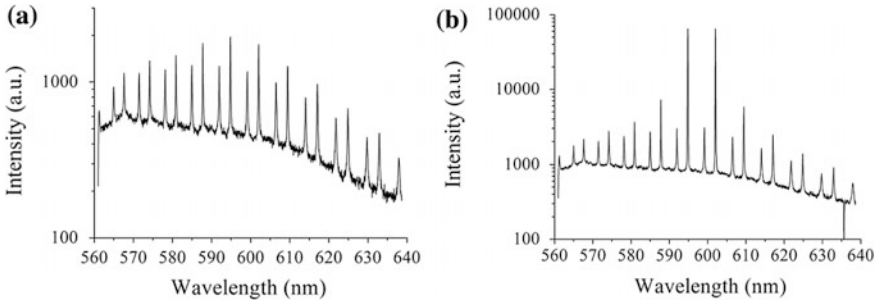

Fig. 9.13 **a** and **b** WGM spectra of a 10 μm diameter dye doped polystyrene microsphere in water below and above the lasing threshold respectively

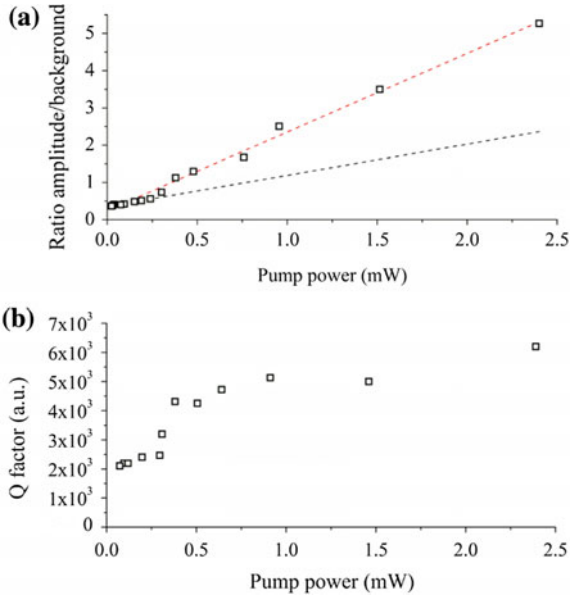

Fig. 9.14 **a** Lasing characteristic of a 10 μm in diameter polystyrene microsphere. The *black* and *red dash lines* show the fluorescence and stimulated emission characteristics respectively. Their intersection defines the lasing threshold. **b** Q factor measured as function of the pump power for the same microsphere (Color figure online)

permit lower detection limits to be achieved for refractive index applications [146]. This has been demonstrated experimentally by comparing the detection limit of biotinylated microspheres for the capture of neutravidin, below and above the lasing threshold [108]. Furthermore, the strong electromagnetic field circulating around lasing microsphere is thought to be responsible for faster binding kinetics [144] because of the optical "carousel force" [147].

Despite these advantages, fluorescent microspheres used for sensing applications often exhibit lower Q factors, typically below 10^4 in aqueous environment, compared the "pure" non-fluorescent counterparts which typically have Q factors of 10^6–10^8. Certain strategies have been developed in order to increase the Q factor. In one example, breaking the symmetry of the resonator by encasing it into a microstructured optical fiber (Fig. 9.15) results in an increase of the Q factor. This

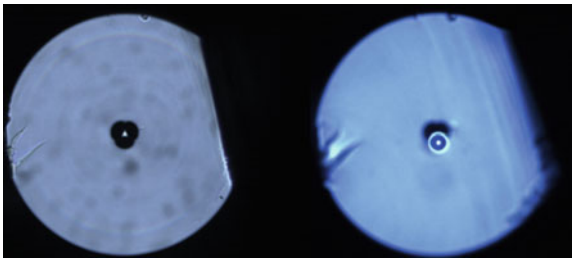

Fig. 9.15 Tip of a suspended core microstructured optical fiber before (*left*) and after (*right*) positioning a 10 μm diameter polystyrene microsphere into one of the fiber holes

appears to be caused by the directional emission from selected equatorial planes and mode polarization [148, 149]. Beyond the improvement of the Q factor, positioning the microsphere onto the tip of a microstructured optical fiber permits the microsphere to be physically manipulated while both the excitation and collection of the WGM modulated fluorescence signal can be achieved through the fiber.

Free-floating fluorescent microspheres can also be used in a slightly different context. Taking the high throughput Luminex Bead Assay technology [150] as an example, fluorescent microspheres doped with different fluorophores and therefore emitting at different wavelengths can be used for multiplexed sensing [151]. While a similar approach has been pursued with passive microspheres coupled to a tapered optical fiber [152], it is difficult to imagine extending multiplexing beyond the simultaneous detection of two different analytes considering the challenge related to positioning the microspheres at the optimum coupling distance from the tapered fiber. Furthermore, one has the difficulty of detecting and tracking multiple resonances from different microspheres simultaneously in an evanescent coupling scheme. On the other hand, fluorescent microspheres doped with different gain media and therefore emitting in different wavelength regions would be easier to implement for multiplexed sensing. In a similar spirit, multiple fluorescent microspheres have been used for flow cytometry, in which a simple algorithm based on the Chew model may permit the concurrent determination of individual microsphere radius and refractive index [81, 153]. While the full demonstration of this approach remains open, it presents a promising application of fluorescent microspheres.

Normal mode coupling between adjacent microspheres has also been investigated. Initially this work aimed toward designing low loss waveguides [154]; however finding two identical microspheres with overlapping resonances is very difficult. Nevertheless, coupling effects have been exploited based on the assumption that a cluster of closely-spaced microspheres has a random and unique emission pattern resulting from overlapping resonances as well as the coupled resonances which may arise [155]. This property of microsphere clusters permits them to be independently identified, which is particularly useful for the integration of a large number of detection sites within a single biosensor chip, ensuring that

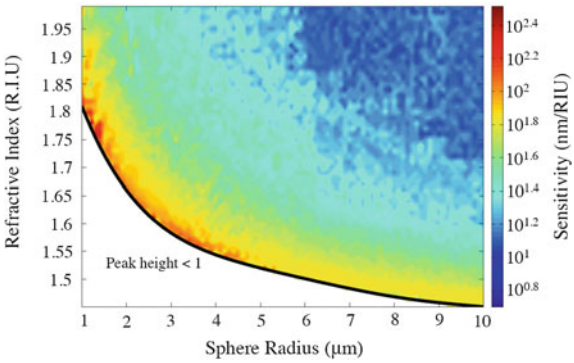

Fig. 9.16 Contour plot of the sensitivity in nm/RIU derived using the analytical Chew model for spherical resonators over the parameter space ranging from R = 1–10 μm and refractive index range from n_1 = 1.45–2.0 within the wavelength range of 600–615 nm. The *black line* demarcates the parameters below which no resonance can exist when the microsphere is immersed in water

each cluster can be read out properly, even without the knowledge of its precise position on the chip surface.

The refractive index sensitivity is a parameter that ultimately controls the detection limits both for index sensing and for biosensing applications. As discussed in Sect. 9.3, the refractive index sensitivity depends on both the index contrast between the resonator and its surrounding environment and on the resonator dimension. Both control the fraction of the energy associated with the field that probes the surrounding environment. Figure 9.16 shows refractive index sensitivity as function of both the microsphere radius and it's refractive index, calculated using Chew's model [129, 130] for fluorescent microspheres. As discussed in Sects. 9.2 and 9.3, further enhancements of the sensitivity can be obtained by coating the sphere with a high-index layer [53], as has been demonstrated experimentally [132, 136].

Instead of relying on fluorescence, the WGMs can also be measured via evanescent coupling through a fiber taper or waveguide. This method is based on the overlapping of the evanescent field of the microcavity and a fiber taper or a waveguide. The distance between the sphere and the taper should be less than $\sim$1 μm to obtain effective coupling [156]. In this setup the WGMs appear dips in the transmission spectrum from a tunable light source coupled into the taper or waveguide (Fig. 9.17).

This method has several advantages over fluorescence WGM measurements. First, as mentioned above, the Q factors are often higher (e.g., $\sim 10^8$ [157] for a microsphere and 10^5 for a microcapillary [158]). This also means that the sensor can be operated in WGM "intensity mode" as well as in "shift mode". The intensity mode requires scanning a tunable laser over a narrow range of wavelengths centered on one side of a sharp WGM and observing intensity changes caused by the WGM mode shifts. This method can be extremely sensitive but has a small dynamic

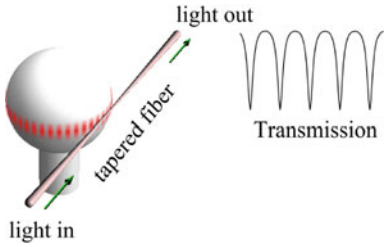

Fig. 9.17 Diagram of an evanescent coupling setup for a microsphere, using a fiber as an example. The fiber taper can be replaced by a waveguide. The spectrum illustrates that the WGMs will be dips in the transmitted light intensity

range [159]. In the shift mode too, the excellent sampling rate of a narrow bandwidth tunable laser means that the detection limits can be very low in comparison to fluorescence-based devices. In addition, this method has high light intensity, meaning that the measurement system can be quite fast.

The lightest single molecules so far detected (8-mer oligonucleotides) has been shown via evanescent coupling to the plasmon-enhanced WGMs of a microsphere, with plasmonic field enhancement [1]. Other biomolecules such as BSA-streptavidin [93, 160], viruses [161], and proteins [60, 69] have been detected with increasing efforts towards single-molecules detection [162]. Single dielectic nanoparticles can also be detected via plasmonic enhancement [61] of the microsphere WGM field.

However, there are negatives to the evanescent coupling method as well. First, it is expensive, often requiring a narrow bandwidth tunable light source and micro-positioning equipment (e.g., to get a taper sufficiently close to the microcavity). This often has to be done in a fluid chamber of some sort, further complicating the experiment. The fragility of a tapered fiber (or a thin-walled capillary) is another problem. These difficulties are especially acute for microspheres and capillaries; for disks, however, many of these issues can be solved by building the disks on the same chip as the bus waveguides, obviating the need for positioning equipment and retaining good mechanical strength.

Other than microspheres, a further WGM sensing option is to use a capillary structure. Here the modes must sample the medium in the channel; i.e., on the *inside* of the resonator. The liquid-core optical ring resonator (LCORR) is a well-studied example that consists of a thin-walled glass capillary supporting cylindrical WGMs. The capillary walls must be typically less than ~ 2 μm thick, so that the tail of the mode field can extend sufficiently far into the channel to obtain a good sensitivity. By chemically treating the silica channel walls, LCORRs have been demonstrated for a variety of sensing applications including but not limited to bovine serum albumin (BSA) [163], DNA [164], viruses [165], cancer biomarkers [166], pesticides [167], and streptavidin [168], as well as for basic refractometry [7]. The sensitivity of these structures is typically on the order of a few tens of

nm/RIU but can reach 500 nm/RIU for higher-order radial modes [6]. The concentration detection limit has been demonstrated as low as 15 fM for BSA detection [169]. LCORRs can also be used as temperature sensors or can be designed to have minimal thermal sensitivity [170], and can potentially be parallelized for multiple detection [171]. Evanescent coupling to LCORR devices shows similar advantages (excellent detection limits) and problems (fragility, difficulty of experimental design, and equipment expense) as compared to their fluorescent capillary counterparts.

Fluorescent tubes or capillaries are an alternative class of WGM-based sensor structure. These "fluorescent core microcavities" consist of a fluorescent layer coated onto the channel wall of a thick capillary [46, 172], although some realizations also use rolled-up tubes formed from highly stressed thin films [173, 174]. The latter devices are difficult to couple into a fluidic system, but the former ones are mechanically robust and easy to interface to a syringe pump [58]. Like for microspheres [175], fluorescent capillaries can be stabilized against thermal fluctuations via control over the various layer thicknesses [176]. The highest sensitivity is reported over 400 nm/RIU for thin disks [173] and up to 250 nm/RIU for the second-order radial mode of thick capillaries with a high-index fluorescent coating [8], although values of around 10 nm/RIU are more common. The concentration detection limit for neutravidin was in the nM range [118]; considerably higher than the best results for evanescent measurements (again, illustrating the trade-offs in sensitivity vs. durability and experimental simplicity between the two techniques).

9.6 Microdisks and Toroids

The microdisk is another type of cylindrical microcavity that supports whispering gallery modes. The mode Q-factors for microdisks are typically on the order of 10^4 [177] (i.e., lower than that of a typical microsphere) mainly due to scattering loss from surface roughness [177] unless reflow methods are used. However, as discussed in Sect. 9.3, a high Q-factor is not always strictly necessary to achieve good sensing performance. A significant advantage of microdisk-based WGM sensing is that the devices can be easily parallelized for multiple analyses on a single chip. The only commercial WGM sensor systems currently on the market are based on microdisk arrays (i.e., from Genalyte Inc.).

Among the large diversity of optical resonators that have been used for biosensing applications, microdisks, toroids and ring resonators represent by themselves a specific class of resonators. Due to the additional degree of confinement provided by the particular resonator's architecture, with the thickness being much smaller than the diameter, these resonators support fewer azimuthal modes in contrast with microspheres [178]. Furthermore, the mode volume is also strongly reduced in microdisks, microtoroids and alike while still exhibiting very high Q-factors [36], which makes them ideal for QED applications.

Typically, this class of resonator is fabricated using the state-of-the-art microfabrication technologies commonly used in the microelectronic industry involving wet thermal oxidation, lithography, or dry etching to define the resonator disk [179] to define the resonator disk. This template is then annealed by a CO_2 laser, inducing a reflow of the material on the edge of the resonator and resulting in a toroidal shape due to surface tension. This annealing process generates smoother edges and results in a higher Q factor by minimizing scattering losses [179]. A wedge edge version of this architecture with a surface finished using wet etching allows for tuning of the zero dispersion wavelength which is highly desired for frequency comb generation and stimulated Brillouin lasing [180]. Further developments have permitted the disk to be detached from its post, allowing for an extra degree of freedom in the design of WGM-based photonic devices [181]. Surface functionalization can be applied to these resonators for various applications, as discussed in Sect. 9.4.

Beyond their biosensing capabilities [182], microtoroids have been used as laser sources, for example by applying an erbium doped film [178, 183] or quantum-dot coating [184] onto the resonator surface. Toroids are particularly suited for such applications, as the lasing operation is favored by the Purcell effect [36] as a result of the high Q/V ratio associated with microdisk resonators. Other gain mechanisms have been exploited in the same context, such as Brillouin lasing in CaF_2 toroids [185] or as mentioned earlier wedge edge toroids [180] and Raman lasing [186].

In-coupling light into microdisks is often achieved via the evanescent field coupling with a phase-matched tapered fiber. The distance between the taper and the resonator has to be maintained constant in order to optimize the coupling conditions, which is important for exploiting non-linear processes [186]. However in a biological sensing context where the resonator is embedded into a microfluidic flow cell and subjected to constant liquid flow, it becomes difficult to keep the distance between the resonator and the taper constant unless the resonator is in contact with the tapered fiber. Any fluctuation of this coupling distance will be "seen" by the resonator as a change of local effective refractive index within its evanescent field [187], resulting in a spectral noise that limits the performance of the sensor [146]. Recently, packaging approaches have been attempted to solve this problem, which would enable this technology not only to be used in a lab but also in an industrial setting for both microsphere [188] and toroid [189] resonators. However the processes developed so far involve embedding both resonator and taper into a polymer matrix, rendering them insensitive to their surrounding environment beyond the measurement of temperature change. On-chip ring resonators were also developed with the idea to provide a robust coupling scheme where the resonator and the taper coupler are both patterned onto the same substrate [190].

The WGMs of a microdisk are measured by in-coupling light from a tunable laser via a lithographically-defined waveguide as well. Waveguides are more useful for applications than tapered fibers, since the coupling distance can be precisely controlled and a single waveguide can easily sample multiple disks in parallel [191]. Sampling multiple disks does require simultaneous monitoring of at least one

mode from each disk, at a slightly different resonance frequency. For biosensing applications, one must know which mode in the transmission spectrum corresponds to which disk.

Similar to the case for spheres and capillaries, the WGM resonance wavelengths of a microdisk depends on the refractive index of the surroundings. Like for a fiber or microsphere, the field extends outward into the surrounding medium; one therefore needs an external fluid "chamber" into which the microdisk can be immersed. Several methods have been used to achieve this. For example, in [192], a microfluidic channel was built by sealing a microdisk and a waveguide inside a PDMS cover, under which the fluid could be exposed to the microdisk. Inlet and outlet ports were used to injected fluid into the channel via tubing and a syringe pump.

Microdisks have been employed in many different kinds of sensing experiments. Of course, one can detect the change of the surrounding refractive index by immersing the microdisk in different analyte fluids [192–199]. Microdisks have also been tested as displacement sensors [200], gamma ray sensors [201], gas sensors [202], surface curvature sensors, [203] and of course as biosensors [194, 197, 204–210]. Each of these applications will be briefly discussed.

9.6.1 Refractive Index Sensing

Refractive index sensing is one of the easiest experiments to perform, so there are numerous investigations that have reported on the refractometric sensitivity and detection limit of various microdisk resonators. The reported refractometric sensitivity is often higher than for other types of WGM-based sensors, with values of several hundred nm per refractive-index-unit not uncommon. For example, a sensitivity of 460 nm/RIU was reported for various NaCl solutions [193] with a hydrogenated amorphous silicon microdisk operated at a wavelength near 1550 nm. This corresponded to a surprisingly modest detection limit of $\sim 10^{-4}$ RIU [194], which is comparable to typical microsphere refractometric sensors [211]. However, better data processing methods like those discussed in Sect. 9.3 of this chapter would likely produce a *DL* of $\sim 10^{-5}$ RIU for such a high sensitivity. Glucose solutions have also been frequently used for sensitivity measurements [195–197], with values of ~ 300 nm/RIU [196] being reported for a TiO_2-coated polymer disk at a wavelength near 1550 nm. In the latter example, a high-index TiO_2 coating was used to enhance the WGM sensitivity (e.g., see Fig. 9.5). One of the lowest *DL* values so far reported is 10^{-6} RIU, measured using calibrated refractive index oils with indices ranging from 1.305 to 1.395 [192, 198]. A higher index generally helps "pull" the field into the analyte and increases sensitivity.

9.6.2 Displacement Sensors

Microdisks have also been used as sensitive displacement sensors. In one representation of this idea, two microdisks can be spaced close enough that their evanescent fields interact [200]. The basic idea is to achieve coupled resonances, which leads to normal mode splitting (NMS) [212] and potentially also electromagnetically-induced transparency in coherently coupled resonators [213]. NMS occurs when two resonators have a resonance at the same frequency; this degeneracy is then broken via mode coupling when the resonators are close enough [214]. The mode splitting has an exponential dependence on the gap between the two cavities [215], making it ideal for displacement sensing. Although experimental results weren't obtained for the two-microdisk structure, simulations concluded that the ultimate displacement measurement of this system is comparable to that of a Fabry-Perot cavity system [200], which can have 20 pm displacement measurement resolution [216].

9.6.3 Gas Sensors

Microdisks have also been used frequently for gas sensing. The basic idea behind gas sensors is usually to coat the disk with a compound that can absorb a gaseous analyte, resulting in swelling [217] or a change of the refractive index [218]. In one example, a thin layer of ZnO nanocrystals was grown on an SiO_2 microdisk and used to sense volatile organic compounds such as toluene and nitrobenzene [202]. This particular WGM sensor was operated in the lasing mode, which can increase sensitivity and performance as discussed for microspheres in Sect. 9.5. Adsorption of the vapor resulted in an increase of the refractive index of the coating, and the WGM lasing wavelengths shifted to longer wavelengths. This particular device could be "rejuvenated" by flushing it with pure N_2 for a few minutes to reverse the adsorption of the gas molecules. Surprisingly, even without coating the surface with different vapor-sensitive polymer layers, the results show a considerable sensitivity difference for toluene *vs.* nitrobenzene. The response time is about half a minute, which was not as fast as a microcapillary-based gas sensor [219]. However, the ZnO-coated microdisk does not require a tunable laser and a waveguide to explore the resonance wavelength shift [219, 220].

9.6.4 Gamma-Ray Sensors

Gamma ray sensors are useful for detecting nuclear radiation. WGM-based sensing using a microdisk has been demonstrated for γ-ray sensing in a compact-size device. This is of potential interest for applications requiring small or lightweight

detectors, since the standard Geiger-Muller counters usually have a long tube. The basic idea is that when a microdisk is irradiated by γ-radiation, the refractive index changes due to defect creation caused by ionizing radiation [221]. By measuring the WGM wavelength shift, the radiation dose can be determined [201]. Since the refractive index of pure silica does not change much upon exposure to ionizing radiation, in one example a silica microdisk was doped with germanium in order to render the material more radiation-sensitive [201, 221]. The resonance frequency as a function of γ-ray radiation dose was given by a Cauchy-like polynomial [201]:

$$f = 275.2010 - 0.2189\gamma + 0.1963\gamma^2 - 0.7620\gamma^3 \tag{9.35}$$

This formula was obtained by fitting the experimental data for radiation doses ranging from 0 to 1 MGy. Although the radiation detection limit was not specified, the device appears to be able to detect a dose of 0.1 MGy. This cannot currently compete with a Geiger-Muller counter which can detect μGy radiation (for example, the ED150 model from PCE instruments [222]); however, the sensitivity and detection limit could potentially be enhanced by doping the disk with a more radiation-sensitive material.

9.6.5 Surface Curvature Sensors

Optical fibers can be used for sensing curvature in the material components of large-scale structures, such as bridges and buildings, as a diagnostic method against stress or failure [223, 224]. However, this kind of sensor cannot easily monitor curvature or two-dimensional in-plane bending on the microchip-scale, due to its size and geometry. A microdisk has one advantage over a fiber sensor, insofar as it can be readily applied at the micro-scale [203]. The WGM lasing wavelength of a microdisk is a function of the disk curvature along its diameter. To test the curvature sensing ability, an InGaAsP microdisk on a PDMS substrate was mounted flat in direct contact with metal surfaces whose bending radii could be varied. This caused the PDMS disk itself to be bent accordingly along its diameter, and the WGM lasing wavelength then decreased with decreasing bending radius. The sensitivity, defined as the ratio of lasing wavelength shift to the curvature bending radius, was measured to be -23.7 nm/mm^{-1}. The sensitivity is not higher than that measured using large-scale fiber sensors [225, 226], but is sufficient for a μm size sensor to detect few micrometers of local curvature variation [203, 227].

9.6.6 Biosensors

Microdisks can also be used for bio-sensing applications [194, 197, 204–210], much like the case for microspheres discussed earlier. The surface of the microdisks

can be functionalized by methods listed in Sect. 9.4 for specific biomolecular recognition. WGM shifts in microdisks were used to detect specific binding of streptavidin with a sensitivity of 0.26 nm/nm, defined as the ratio of the WGM shift to the protein layer thickness [205], and a concentration detection limit of 74 ng/mL [207]. A mass detection limit in the fg range was reported for BSA [194]. Although single bio-molecule detection experiments haven't been conducted yet, simulations imply the capability to detect as few as several tens [204] or possibly a single biomolecule [210] even without plasmon enhancement, assuming ideal coupling and a high sensitivity.

9.7 WGM Sensors: Comparison with Competing Technologies

There is a wide range of microfluidic sensing technologies, each with different strengths and limitations. We follow [228] and divide them according to electrochemical methods, mass spectroscopy, optical techniques, and "other methods" (including nuclear magnetic resonance, magnetoresistive, and acoustic detection techniques). Here, we focus on optical methods, but can briefly mention the first two main microfluidic techniques as well.

9.7.1 Mass Spectroscopy

The basic idea behind mass spectroscopy in microfluidics is to perform sample preparation and separation on a microfluidic chip, followed by analysis with a small, relatively low-energy "soft ionizing" mass spectrometer that is capable of ionizing but not destroying complex biomolecules [229, 230]. Essentially, most or all of the pre-chemical treatments are done on a highly parallelized microfluidic chip, with the output sent from the chip via a coupling system (e.g., "spray"-type emitters [231]) directly for analysis via mass spectroscopy. There are many advantages to these methods, including a detection limit in the sub-attomolar range [232]. Mass spectroscopy is also versatile and spectrometers are becoming less expensive and bulky than they were in the past. However, despite technological advances in size and capacity, in comparison to some optical methods the total system cost remains high and requires the use of trained personnel.

9.7.2 Electrochemical Methods

Electrochemical methods measure the current, voltage, or conductivity between electrodes exposed to the analyte. Capillary electrophoresis (CE) is one of the most

common and well-known microfluidic analysis methods [233]. When a potential difference is applied across the ends of a capillary, charged species in the analyte separate and travel toward one of the electrodes. Since different species travel along the potential gradient at a different rate, the analyte becomes separated according to the ion mobility. CE is now widely used in a range of applications, for example in environment [234], water safety [235], pharmaceuticals [236], and food quality [237]. For laser-induced fluorescence (LIF), of a high-quantum-efficiency dye, the mass detection limit for capillary electrophoresis is a few molecules and the concentration DL is on the order of fM [238], although LIF usually requires fluorescent tagging. More common methods have a concentration DL in the picomolar range. However, CE has been limited by the requirement to produce large electric fields, which usually requires large, heavy, or expensive equipment. Current research efforts aim toward miniaturization and portability of CE systems [239].

9.7.3 Optical Methods

Numerous optical methods exist for biosensing in microfluidic geometries, of which WGM-type structures are just one example. A good review of optical biosensor systems can be found in [240].

Opto-mechanics. Opto-mechanical systems measure either the deflection or resonance frequency of a microscale cantilever, when biomolecules bind to the surface. They can be label free, since the cantilever surface (e.g., silicon, or gold-coated SiN) can be functionalized for a specific analyte. For micromechanical transduction (i.e., non-optical) the mass detection limit is incredibly low, on the order or the atomic mass [241], with similar zeptogram limits for opto-mechanics more recently demonstrated as well [242]. Of course, such extreme mass sensitivity requires ultra-high vacuum and often low temperatures that are incompatible with biosensing applications. For biosensing, the mass detection limit for opto-mechanical systems is more generally on the order of pg [243]. An important limitation of opto-mechanical sensors is that they are difficult to operate in a liquid due to damping forces, so most applications are limited to an air ambient (for example, explosives sensing) [244].

Interferometers. These structures can be classified into Mach-Zender (MZ) interferometers, double beam "Young's" interferometers, Fabry-Perot interferometers, and Hartman interferometers. Each is based on the same basic principles: interference between multiple beams (or multiply-reflected beams) is monitored as a function of changes in the analyte medium. In the Mach-Zender case, a reference arm is typically functionalized for a target biomolecule. In order to achieve detection limits similar to those for much smaller multi-pass structures like WGM cavities, these single-pass devices must be fairly long (e.g., centimeters) in order to ensure sufficient interaction lengths.

A refractometric detection limit of 10^{-8} RIU can be achieved [245, 246] with interferometers, which is lower than so far possible experimentally for WGM-type devices. The concentration detection limits on the order of ng/mL or less [247]. Disadvantages of MZ sensors include the relatively large size and the requirement to be on the "steep" part of the interference response needed to have good sensitivity. Essentially, the two arms go in and out of phase according to a cosine function; somewhat like an intensity-type WGM sensing methods one needs to be on the high-slope part of the response in order to get good sensitivity, and one is limited to a narrow dynamic range. Fabry-Perot interferometers, in which the analyte is pumped between two high-reflectivity distributed Bragg reflectors, have recently reached a refractometric detection limit as low as 2.0×10^{-9} RIU [248], which may be a record. Biomolecular concentration detection limits as low as a few pM were demonstrated in a porous silicon Fabry-Perot almost 20 years ago [249].

Hartman-type sensors are based on planar waveguides that are functionalized into parallel grating patterns along the length of the waveguide. Light is coupled into the differently-functionalized strips by optical elements and the resulting interference pattern is read out by combining signals that have passed through parallel lengths of the waveguide. Protein concentration detection limits are on the order of a few ng/mL [250]. Similar values (bulk sensitivity of 10^{-5} [251] to 10^{-8} RIU [252], concentration limits around the fM range [252]) can also be obtained for Young's interferometers.

Interferometers generally feature excellent detection limits and can be functionalized using many of the methods described in Sect. 9.4. The low detection limit especially is one of the strongest points of interferometric sensors. However, as single-pass methods they cannot currently be used for single molecule detection. Whispering-galley-mode devices are better in this regard, because light can interact with analyte biomolecules millions of times before escaping the structure. Finally, interferometer structures often have cm length scales and can thus be too large to be easily integrated into a microfluidic geometry.

Waveguides and fibers. Several interferometric designs utilize waveguides, as discussed above, but other forms are also possible. One especially interesting example is the spiral waveguide resonator [253]. This device has been multiplexed up to a 128-sensor array. The basic idea is that light is coupled into a silicon photonic waveguide resonator with a closed spiral configuration (hence bearing a strong resemblance to a racetrack WGM resonator, but featuring a longer interaction length per unit chip area). The surface coverage detection limit for proteins was ~ 1 pg/mm^2, corresponding to a tiny fraction of a monolayer.

Fiber-optic sensors have found applications for many years for sensing strain, pressure, temperature, displacement, and acceleration [254], and there is a huge literature on this topic. The basic method is to measure modulations or changes in the fiber transmission properties due to changes in the above parameters. Computer algorithms are then used to locate the region of the disturbance in the fiber and determine whether the signal is real. Fiber-optic biosensors [255] or chemical sensors [256] can instead be based on absorbance, reflectance, or fluorescence measurements, rather than laser transmission. The transducer can be a Bragg

grating, a long-period grating, a fiber Fabry-Perot cavity, a fluorescent substance coated onto the fiber, or simply a bare piece of exposed single-mode core. Concentration detection limits as low as pM to fM have been reported for gold-nanoparticle-labeled proteins [257]. Label free DLs have been reported at least in the nM range [258]. Bulk detection limits are in the range of 10^{-7} RIU [259, 260]. Fiber-loop ringdown spectroscopy is another method in which losses can be measured in an analyte chamber interfaced to a long fiber loop [260].

Photonic crystals. Sensors based on photonic crystal cavities (PCCs) share many features in common with WGM sensors. Like for WGMs, the basic sensing mechanism is associated with the shift of a resonant cavity mode. One advantage of PCCs is that the mode volumes are small and the analyte can be injected directly into the cavity region. For these reasons, the bulk sensitivity is higher than for WGM cavities, with values of 400-600 nm/RIU fairly typical [261, 262], and the detection region can have a volume as small attoLitres [261]. The high sensitivity of PCC structures also enables gas sensing [263, 264], in which the refractive index changes are small. Additionally, parallelization and on-chip integration has been demonstrated [265]. The concentration detection limit was reported to be $\sim$20 nM for single-strand DNA [266] or within the low-pM for anti-biotin binding to biotinylated BSA, with fg mass detection limits [267].

In addition to PCC sensors, photonic crystals may be employed in a variety of other sensor geometries [268], such as enhanced absorption-based sensors (in which low concentrations of the analyte can be detected due to the strong overlap between the resonant field and the analyte molecules). Photonic crystals can be combined with opto-mechanical or surface-plasmon sensors as well [268]. Perhaps most notable, however, is photonic crystal fiber sensors, in which monumental sensitivities upwards of 30,000 nm/RIU can be achieved by filling one of the air channels with the analyte medium [269]. However, coupling such structures into a microfluidic system is extremely difficult and they work only within a narrow range of refractive indices.

Surface plasmon resonances. The literature on biosensing with localized (nanoparticles) and extended (continuous films) surface plasmons (LSPR and SPR, respectively) is enormous, and has been summarized in some recent reviews [5, 270–272]. The technique has already seen commercial success [273]. Surface plasmons polaritons (SPP) [2] are electromagnetic waves caused by oscillations in electron plasma at an interface between a metal and dielectric. For SPPs to exist one must have light incident at a certain angle, wavelength, and polarization. Unlike for cavity-based sensors, the plasmon resonance is an intrinsically lossy, low-Q phenomenon that demonstrates resonances from tens to hundreds of nanometers wide. Thus, peak-finding algorithms [274] are crucial in achieving low detection limits. The bulk sensitivity of SPR-based sensors is usually quite good, from several hundred nm/RIU for LSPR to few μm/RIU for SPR [275]. The ultimate bulk detection limits are on the order of 10^{-7} RIU [59], with surface binding concentrations of ng/cm^2 readily achievable [276]. New technologies, such as the

cell-phone-based surface plasmon biosensor [277] are continually being advanced, indicating the relative ease of incorporating SPR sensors into "real world" devices.

In 2008, Anker et al. [278] accurately predicted the three key areas for advancing SPR technologies: (i) single-molecule detection, (ii) combining localized SPR with other sensor techniques to enhance the sensitivity and detection limits, and (iii) the development of practical sensors. The development of devices that work with a common cell-phone represent excellent examples of point (iii) [277, 279]. With respect to point (i), detection of as few as 20–100 streptavidin molecules was recently demonstrated on an LSPR array [280]. In accordance with Anker et al.'s second prediction, remarkable success has recently been achieved via the combination of LSPR and WGM phenomena [1, 63, 281] has led to the specific detection of single biomolecules as a few thousand Daltons, with millisecond time resolution.

Surface-enhanced Raman scattering. SERS essentially utilizes localized surface plasmon effects to strongly increase the amplitude of Raman vibrational signals [282]. The incident laser must be tuned at or near the SPR peak and a detector (i.e., a spectrometer) measures the scattered radiation. The vibrational signals associated with analytes bound to a roughened metal surface or plasmonic "hotspots" can be enhanced by an incredible 10–15 [283] orders of magnitude. This leads to the ability to detect single molecules [284]; in fact, along with WGM sensors, SERS is one of the few techniques currently possessing this capability. Biosensing specificity is obtained via metal surface functionalization chemistries as for SPR sensors. Concentration detection limits extend down to the nM to fM range [285] typical of many optical biosensor techniques. Explosives sensing down to the parts-per-billion level represents one current and especially interesting applications of SERS optical methods [286, 287].

Optofluidics. Unlike the previous categories, optofluidics is not a measurement technique. The word has two main definitions: it can refer to the use of light to control the flow of fluids, or, conversely, the applications of fluids to control the flow of light. The transition from a microfluidic WGM-type sensor to an optofluidic one was recently shown as a function of increasing analyte refractive index in the channel of a fluorescent capillary [8]. Once the fluid index exceeds that of the capillary walls, the confinement leading to the formation of WGMs is effectively within the fluid itself. Thus, the fluid controls the development of the optical resonances. The latter definition has important ramifications with respect to photonic biosensors based on any of the above-described methods.

Four years ago, a set of review papers described the field of optofluidics as it was at the time [288–291], and its potential for future development. Some of the most exciting recent examples of optofluidic devices are within the new area of biolasers [292]. Biolasers are devices in which the laser gain medium is biologically compatible; such devices could offer considerable enhanced sensitivity as compared with standard biosensors [293, 294]. A fully optofluidic biolaser was recently demonstrated using vitamins and biopolymers [295]; this device did not use dielectric reflectors and was non-immunogenic. These recent illustrations may

represent the "tip of the iceberg" for novel, fully biocompatible, highly sensitive biosensors.

9.7.4 Biosensing Technologies for Medical Diagnostics

Immunoassays represent a specific type of biosensing aiming to detect proteins or other biomolecules (i.e., antigens) through their specific interaction with the corresponding antibody that is immobilized onto the sensing device. Immunoassays represent the cornerstone of medical diagnostic through the detection and quantification, whenever possible, of biomarkers that indicate specific pathologies. The current "gold standard" for such applications revolves around two technologies listed below, which are currently dominating the medical diagnostic market.

Enzyme-linked immunosorbent assay (*ELISA*): One of the most sensitive techniques so far developed is the ELISA method for biosensing [296, 297]. This technique involves the attachment of a known amount of antibody to a surface. The unknown sample is then washed over the surface and any target molecules in the solution will bind to the specifically-chosen antibody. Finally a detection antibody links to target molecule. This detection antibody converts a surrounding buffer to allow detection via fluorescence or change in color. This technique is sensitive; even a small amount of the target molecule present in the solution bonds to the antibody on the surface and causes measurable fluorescence or absorption due to the enzyme linked amplification [297]. This ultimately allows even a single molecule to be detected (10^{-23} M) [6]. One of the main problems with this method is a long time period of approximately 3–4 h required to produce the necessary signal.

Electrophoretic transfer of proteins also referred as Western Blot: Electrophoresis is a technique by which an electromotive force is applied to a gel matrix. By placing the sample in the wells of the gel matrix, the different molecules will move at speeds determined by the mass and the charge of the molecule. This technique is usually applied for the separation of proteins based on mass and can take from 1 to 20 h. Once separation has occurred, the target proteins need to be transferred from the gel and bound to a membrane in preparation for detection. This transfer can be performed either by electro-blotting or capillary action. As the antibody used for detection is also a protein, all the binding sites on the membrane must be blocked using a blocking reagent such as Bovine Serum Albumin (BSA) after the transfer of the target protein, in order to prevent the detection antibody binding directly to the membrane. Finally the detection antibody is applied to the membrane and is able to bond to the target protein. This detection antibody allows detection through the change of color of a buffer or through chemiluminesence. These signals will be dependent on the number of the target proteins bonded to the surface of the membrane. Similar sensitivities to those of ELISA methods, can be realized, however this technique also requires time periods on the order of hours.

9.8 Outlook

Despite the wealth of research developed on optical based biosensing technologies for biomedical applications, only a small fraction have ever made it into the market. SPR-based sensors are the main example with the success of the GE Healthcare's Biacore systems. Currently, optical methods in medical diagnostics is dominated by ELISA and Western Blot for protein detection and to some extent quantification, or PCR for DNA sensing. Genalyte Corp. is producing probably the most advanced WGM-based sensors using methods for multiplexed microdisk sensing [191, 298]. The same situation applies for Point of Care (POC) diagnostics, which are often perceived by researchers working on optical biosensing technologies as an emerging market and often a justification for funding their work, while in reality this market is dominated by more compact version of the immunofluorescence assays such as lateral flow assays, with pregnancy tests being an obvious example for this technology, or electrochemical sensors for glucose. This somewhat grim report doesn't mean that applying WGM-based sensing for biological applications is hopeless but instead that several improvements would be required for success, or as an alternative, WGM technologies have to be tailored for more specific applications as research instruments. NanoBioAnalytics is an example of a company which is developing WGM sensing systems based on fluorescents polystyrene microspheres for research purposes [30].

While single-molecule and/or particle detection has been demonstrated with passive resonators [1, 182, 299], the same has never been shown with fluorescent resonators. This is likely to be due to the lower Q factor often related to the free space detection approach which eventually constrains the detection limit to the nanomolar range [108, 118, 151]. Improvement of the performance is therefore necessary for fluorescent microresonators beyond the technical advantages enabled by the free space excitation and collection of the WGM signal. Improvement of the performance could be achieved through two distinct approaches: improving the sensitivity or improving the WGM shift resolution via instrumentation, analysis, and the stabilization of mechanical noise and thermal drifts.

Essentially, one hopes to combine the detection parallelizability of disk-based sensors with the high sensitivity of plasmon-enhanced microspheres and LCORRs, and the durability and low-cost of fluorescent capillaries. Part of this is a packaging problem—for example, how does one physically construct a "real world" device that is cheap, durable, reliable, and sensitive? Another part of the problem is related to the signal-to-noise ratio, optimized data analysis, and sensor speed. A third key factor remains to overcome the analytical challenges implied by the requirement to perform sensing experiments in incredibly complex environments such as plasma and blood [191].

As mentioned earlier, different approaches have been implemented in order to increase the stored energy within the resonator without compromising the sensitivity, by either inducing lasing [144, 145] or using a microstructured environment to break the resonator's symmetry [148, 149], or both [108]. Further development of

this concept, especially exploiting coupled resonators, seems worth exploring. For example one may consider using Vernier effect between two resonators with overlapping resonances to amplify the refractive index sensitivity [300]. While this approach has been investigated in passive ring resonators [301–303] this has never been done with active resonators. The amplification factor on the sensitivity is proportional to the FSR of the first resonator divided by the FSR difference for the two resonators involved [303]. Another possibility for improving the measurement accuracy is through better data processing. While for passive resonators, measurements of binding events is performed through the wavelength tracking of a single resonance, active resonators enable access to a larger number of resonance features. This allows, for example, autocorrelation functions for tracking a specific resonator through its unique emission pattern [155], or the use of higher accuracy algorithms based on Fourier transformation of a train of evenly-spaced resonances [57].

Beyond the performance improvement, coupled resonators could be used for high throughput multiplexing and even self-referencing. In every biosensing experiment, a reference has to be set at the beginning of the experiment. Every subsequent wavelength shift of the resonance indicates a binding event. However, other effects such as a temperature drift can influence the position of the reference baseline, resulting in a misinterpretation of the results. Multiplexed sensing architecture with either coupled or uncoupled resonators, where at least one of the resonators is not perturbed by any biochemical interaction and can therefore act as a floating reference, can be valuable in improving the sensing performance and reliability of the measurement process. Similarly, mode splitting has been explored to produce the same behavior (i.e. dynamic self-referencing) with a single resonator [304], however the application of this strategy for fluorescent resonators and especially fluorescent microspheres is somewhat questionable as it will inevitably result in lower resolution for small wavelength shifts.

Other effects are worth considering which fall beyond the improvement of sensing performance. Nonlinear effects such as Raman spectroscopy are worth investigating for a new range of chemical sensing applications. While Raman is inherently a weak-signal process, taking advantage of the nature of the propagating high-Q WGM would increase the propagation length and consequently the interaction length of any pump Raman wavelength. This could result in a higher SNR while limiting the geometrical fingerprint of the sensing device. In this context, WGM lasers, while being currently limited in terms of power delivery, might yet be an interesting alternative. Combining WGM with plasmonic resonances is also highly relevant to improved sensitivity. Arnold et al. introduced the concept of the localized surface plasmon resonance produced by metallic nanoparticles positioned at specific position on the resonator surface to enhanced the sensitivity of the WGM detection modality [86], and experimentally demonstrated the detection of single molecules few year later following the same approach [305]. While this is truly remarkable, LSPR can also be used in different aspect and especially for SERS [306] (Sect. 9.7), enabling further amplification of the Raman signal in combination with WGMs. Furthermore, metallic nanoparticles can be exploited by taking advantage of the “Metal Enhanced Fluorescence” phenomenon [307], enabling a

higher emission rate from the gain medium. This effect could be used to reduce the lasing threshold of fluorescence microresonators.

Remote excitation/collection scheme for small, free floating microresonators may also open a pathway for in vivo sensing applications. Probing a single cell is no longer something of the future and has been done to some degree with fluorescent microspheres [139]. Yet the detection of specific biomolecules within a single cell has not been achieved despite being highly relevant in numerous biological fields.

Optofluidic biolasers and "living lasers" appear poised to become a fundamental research areas in the next few years [292–295, 308, 309]. Whether truly alive or "simply" biocompatible, biolasers appear to offer tremendous performance benefits that include enhanced light-matter interactions, a large signal-to-noise enhancement, and high sensitivity. Biocompatibility of the lasing gain medium is a bonus because there is no toxicity (e.g., enabling in vitro sensing) and one avoids deleterious or unwanted immunogenic events in the sensor. Finally using living organisms as optical resonators instead of man-made ones has not yet been realized. While this concept seems unlikely to producing positive outcomes due to the irregular shape and small size of most cells, making them unlikely to support high Q resonances if any at all, it may present a way to realize the first "natural" WGM resonator. Given further developments in genetic manipulation to this apparently farfetched idea, one might even realize a way to "cultivate" a biosensor. It could be genetically modified to produce its own gain medium for lasing applications [295, 308] and/or the required recognition element on the cellular membrane to capture a relevant biomolecule.

Acknowledgments A. Francois thanks for Prof Tanya M. Monro for her continuous support through an ARC Georgina Sweet Laureate Fellowship, and the ARC Centre of Excellence for Nanoscale BioPhotonics. A. Meldrum and Y. Zhi thank AITF IciNano and NSERC for support.

References

1. M.D. Baaske, M.R. Foreman, F. Vollmer, Nat. Nanotechnol. **9**, 933 (2014)
2. J. Homola, S.S. Yee, G. Gauglitz, Sensor. Actuat. B-Chem. **54**, 3 (1999)
3. A.K. Sharma, R. Jha, B.D. Gupta, IEEE Sens. J. **7**, 1118 (2007)
4. L.M. Tong, H. Wei, S.P. Zhang, H.X. Xu, Sensors **14**, 7959 (2014)
5. M.C. Estevez, M.A. Otte, B. Sepulveda, L.M. Lechuga, Anal. Chim. Acta **806**, 55 (2014)
6. H. Li, X.D. Fan, App. Phys. Lett. **97** (2010)
7. V. Zamora, M. Diez, M.V. Andres, B. Gimeno, Opt. Express **15**, 12011 (2007)
8. V. Zamora, Z. Zhang, A. Meldrum, Oil and Gas Science and Technology. Revue d'IFP Energies nouvelles (2013)
9. A. Mekis, J.U. Nockel, G. Chen, A.D. Stone, R.K. Chang, Phys. Rev. Lett. **75**, 2682 (1995)
10. J.U. Nockel, A.D. Stone, Nature **385**, 45 (1997)
11. I. Braun, G. Ihlein, F. Laeri, J.U. Nockel, G. Schulz-Ekloff, F. Schuth, U. Vietze, O. Weiss, D. Wohrle, Appl. Phys. B-Lasers O **70**, 335 (2000)
12. W.H. Guo, Y.Z. Huang, Q.Y. Lu, L.J. Vu, IEEE J. Quantum Elect. **39**, 1106 (2003)
13. Y.L. Pan, R.K. Chang, Appl. Phys. Lett. **82**, 487 (2003)

14. M. Mohageg, A. Savchenkov, L. Maleki, Opt. Express **15**, 4869 (2007)
15. Y.F. Xiao, C.H. Dong, Z.F. Han, G.C. Guo, Y.S. Park, Opt. Lett. **32**, 644 (2007)
16. Y.Y. Lin, C.Y. Chen, W. Chien, J.S. Pan, T.D. Lee, R.K. Lee, Appl. Phys. Lett. **94** (2009)
17. C.P. Dietrich, M. Lange, T. Bontgen, M. Grundmann, Appl. Phys. Lett. **101** (2012)
18. C. Tessarek, G. Sarau, M. Kiometzis, S. Christiansen, Opt. Express **21**, 2733 (2013)
19. T. Kouno, M. Sakai, K. Kishino, K. Hara, Jpn. J. Appl. Phys. **53**, 068001 (2014)
20. G. Gervinskas, D.J. Day, S. Juodkazis, Opt. Mater. Express **2**, 279 (2012)
21. R. St-Gelais, J. Masson, Y.A. Peter, Appl. Phys. Lett. **94** (2009)
22. J.J. Tian, Y.J. Lu, Q. Zhang, M. Han, Opt. Express **21**, 6633 (2013)
23. T. Xu, N. Zhu, M.Y.C. Xu, L. Wosinski, J.S. Aitchison, H.E. Ruda, Opt. Express **18**, 5420 (2010)
24. J. Wu, D. Day, M. Gu, Appl. Phys. Lett. **92** (2008)
25. P.S. Nunes, N.A. Mortensen, J.P. Kutter, K.B. Mogensen, Sensors **10**, 2348 (2010)
26. P.S. Nunes, N.A. Mortensen, J.P. Kutter, K.B. Mogensen, Opt. Lett. **33**, 1623 (2008)
27. D. Threm, Y. Nazirizadeh, M. Gerken, J. Biophotonics **5**, 601 (2012)
28. D. Erickson, S. Mandal, A.H. Yang, B. Cordovez, Microfluid. Nanofluid. **4**, 33 (2008)
29. http://www.genalyte.com
30. http://www.nanobioanalytics.com/englisch/index.php
31. L. Rayleigh, Phil. Mag. **20**, 1001 (1910)
32. L.V. Lorenz, H. Valentiner, Carlsbergfondet, *Œuvres scientifiques de L. Lorenz,* vol. 1 (Johnson Reprint Corp., 1898)
33. Y. Zhi, University of Alberta PhD thesis (2014)
34. S. Schiller, Appl. Opt. **32**, 2181 (1993)
35. V.B. Braginsky, M.L. Gorodetsky, V.S. Ilchenko, Phys. Lett. A **137**, 393 (1989)
36. T.J. Kippenberg, S.M. Spillane, K.J. Vahala, Appl. Phys. Lett. **85**, 6113 (2004)
37. C.G. Righini, Y. Dumeige, P. Féron, M. Ferrari, G. Nunzi Conti, D. Ristic, S. Soria, Revista del Nuovo Cimento **34**, 435 (2011)
38. V. Lefevre-Seguin, Opt. Mater. **11**, 153 (1999)
39. F. Treussart, N. Dubreuil, J.C. Knight, V. Sandoghdar, J. Hare, V. Lefevre-Seguin, J.-M. Raimond, S. Haroche, Ann. Telecommun. **52**, 557 (1997)
40. V.S.C.M. Rao, S.D. Gupta, J. Opt. A-Pure Appl. Opt. **7**, 279 (2005)
41. S. Blaize et al., Opt. Lett. **35**, 3168 (2010)
42. A. Mazzei, S. Goetzinger, L.D. Menezes, G. Zumofen, O. Benson, V. Sandoghdar, Phys. Rev. Lett. **99** (2007)
43. J.G. Zhu, S.K. Ozdemir, Y.F. Xiao, L. Li, L.N. He, D.R. Chen, L. Yang, Nat. Photonics **4**, 46 (2010)
44. A.W. Poon, R.K. Chang, J.A. Lock, Opt. Lett. **23**, 1105 (1998)
45. V. Zamora, A. Díez, M.V. Andrés, B. Gimeno, Photonics Nanostruct. Fundam. Appl. **9**, 149 (2011)
46. C.P.K. Manchee, V. Zamora, J.W. Silverstone, J.G.C. Veinot, A. Meldrum, Opt. Express **19**, 21540 (2011)
47. B.R. Johnson, J. Opt. Soc. Am. B **10**, 343 (1993)
48. R. Yang, A. Yun, Y. Zhang, X. Pu, Optik Int. J. Light Electron Opt. **122**, 900 (2011)
49. I. Teraoka, S. Arnold, F. Vollmer, J. Opt. Soc. Am. B **20**, 1937 (2003)
50. A. Meldrum, F. Marsiglio, Rev. Nanosci. Nanotechnol. **3**, 193 (2014)
51. S.J. Adams, *Electromagnetic Theory* (Read Books, 2008)
52. I. Teraoka, S. Arnold, J. Opt. Soc. Am. B **23**, 1381 (2006)
53. I. Teraoka, S. Arnold, J. Opt. Soc. Am. B **23**, 1434 (2006)
54. I. Teraoka, S. Arnold, J. Opt. Soc. Am. B **24**, 653 (2007)
55. L.L. Martin, S.F. Leon-Luis, C. Perez-Rodriguez, I.R. Martin, U.R. Rodriguez-Mendoza, V. Lavin, J. Opt. Soc. Am. B **30**, 3254 (2013)
56. I.S. Grudinin, V.S. Ilchenko, L. Maleki, Phys. Rev. A **74** (2006)
57. J.W. Silverstone, S. McFarlane, C.P.K. Manchee, A. Meldrum, Opt. Express **20**, 8284 (2012)

58. S. McFarlane, C.P. Manchee, J.W. Silverstone, J. Veinot, A. Meldrum, J. Vis. Exp. JoVE e50256 (2013)
59. M. Piliarik, J. Homola, Opt. Express **17**, 16505 (2009)
60. M.A. Santiago-Cordoba, S.V. Boriskina, F. Vollmer, M.C. Demirel, Appl. Phys. Lett. **99** (2011)
61. S.I. Shopova, R. Rajmangal, S. Holler, S. Arnold, Appl. Phys. Lett. **98**, 243104 (2011)
62. J.D. Swaim, J. Knittel, W.P. Bowen, Appl. Phys. Lett. **99** (2011)
63. V.R. Dantham, S. Holler, C. Barbre, D. Keng, V. Kolchenko, S. Arnold, Nano Lett. **13**, 3347 (2013)
64. V. Dugas, A. Elaissari, Y. Chevalier, in *Recognition Receptors in Biosensors*, edited by M. Zourob (Springer, New York, 2010), pp. 47
65. L. Nicu and T. Leïchlé, J. Appl. Phys. **104** (2008)
66. F. Vollmer, S. Arnold, D. Keng, Proc. Natl. Acad. Sci. U.S.A. **105**, 20701 (2008)
67. L. He, S.K. Ozdemir, J. Zhu, W. Kim, L. Yang, Nat. Nano **6**, 428 (2011)
68. H.-C. Ren, F. Vollmer, S. Arnold, A. Libchaber, Opt. Express **15**, 17410 (2007)
69. S. Arnold, M. Khoshsima, I. Teraoka, S. Holler, F. Vollmer, Opt. Lett. **28**, 272 (2003)
70. A.L. Washburn, M.S. Luchansky, A.L. Bowman, R.C. Bailey, Anal. Chem. **82**, 69 (2009)
71. S. Chen, L. Liu, J. Zhou, S. Jiang, Langmuir **19**, 2859 (2003)
72. M.M.L.M. Vareiro, J. Liu, W. Knoll, K. Zak, D. Williams, A.T.A. Jenkins, Anal. Chem. **77**, 2426 (2005)
73. N. Tajima, M. Takai, K. Ishihara, Anal. Chem. **83**, 1969 (2011)
74. A. Wörn, A. Plückthun, FEBS Lett. **427**, 357 (1998)
75. H.E. Indyk, J.W. Williams, H.A. Patel, Int. Dairy J. **18**, 359 (2008)
76. P.S. Waggoner, H.G. Craighead, Lab Chip **7**, 1238 (2007)
77. D. Kim, D. Kang, Sensors **8**, 6605 (2008)
78. C.M. Mendel, D.B. Mendel, Biochem. J. **228**, 269 (1985)
79. S.A. Frank, *Immunology and Evolution of Infectious Disease* (Princeton University Press, Princeton, 2002)
80. S.I. Shopova, G. Farca, A.T. Rosenberger, W.M.S. Wickramanayake, N.A. Kotov, Appl. Phys. Lett. **85**, 6101 (2004)
81. M. Charlebois, A. Paquet, L.S. Verret, K. Boissinot, M. Boissinot, M.G. Bergeron, C.N. Allen, Nanoscale Res. Lett. **5**, 524 (2010)
82. K.E. Meissner, A. Allen, in *Sensors, 2005* (IEEE, 2005), 4 pp
83. K.J. Rowland, A. François, P. Hoffmann, T.M. Monro, Opt. Express **21**, 11492 (2013)
84. Y. Kawabe et al., Appl. Phys. Lett. **72**, 141 (1998)
85. M.R. Foreman, W.L. Jin, F. Vollmer, Opt. Express **22**, 5491 (2014)
86. S. Arnold, V.R. Dantham, C. Barbre, B.A. Garetz, X. Fan, Opt. Express **20**, 26147 (2012)
87. I. Teraoka, S. Arnold, J. Opt. Soc. Am. B **24**, 653 (2007)
88. S.P. Pujari, L. Scheres, A.T.M. Marcelis, H. Zuilhof, Angew. Chem. Int. Ed. **53**, 6322 (2014)
89. M. Qin et al., Colloids Surf. B **60**, 243 (2007)
90. K.S. Lee, R.J. Ram, Lab Chip **9**, 1618 (2009)
91. R. Müller et al., Biomaterials **26**, 6962 (2005)
92. E. Asenath Smith, W. Chen, Langmuir **24**, 12405 (2008)
93. F. Vollmer, D. Braun, A. Libchaber, M. Khoshsima, I. Teraoka, S. Arnold, Appl. Phys. Lett. **80**, 4057 (2002)
94. C.E. Soteropulos, H.K. Hunt, A.M. Armani, Appl. Phys. Lett. **99** (2011)
95. S. Fiorilli et al., J. Colloid Interface Sci. **321**, 235 (2008)
96. J.J. Cras, C.A. Rowe-Taitt, D.A. Nivens, F.S. Ligler, Biosens. Bioelectron. **14**, 683 (1999)
97. U. Jönsson, G. Olofsson, M. Malmqvist, I. Rönnberg, Thin Solid Films **124**, 117 (1985)
98. K.C. Popat, R.W. Johnson, T.A. Desai, Surf. Coat. Technol. **154**, 253 (2002)
99. J. Zhang, J. Hoogboom, P.H.J. Kouwer, A.E. Rowan, T. Rasing, J. Phys. Chem. C **112**, 20105 (2008)
100. R.D. Lowe, M.A. Pellow, T.D.P. Stack, C.E.D. Chidsey, Langmuir **27**, 9928 (2011)
101. J.M. Goddard, J.H. Hotchkiss, Prog. Polym. Sci. **32**, 698 (2007)

102. R. Louise Meyer, X. Zhou, L. Tang, A. Arpanaei, P. Kingshott, F. Besenbacher, Ultramicroscopy **110**, 1349 (2010)
103. D. Decher, Science **277**, 1232 (1997)
104. S. Peleshanko, V.V. Tsukruk, Prog. Polym. Sci. **33**, 523 (2008)
105. B. Sciacca, A. François, P. Hoffmann, T.M. Monro, Sens. Actuators B: Chem. **183**, 454 (2013)
106. B. Sciacca, A. François, M. Klingler-Hoffmann, J. Brazzatti, M. Penno, P. Hoffmann, T.M. Monro, Nanomedicine: nanotechnology. Biol. Med. **9**, 550 (2013)
107. M. Himmelhaus, S. Krishnamoorthy, A. Francois, Sensors **10**, 6257 (2010)
108. A. François, T. Reynolds, T. Monro, Sensors **15**, 1168 (2015)
109. L.V. Nguyen, S.C. Warren-Smith, A. Cooper, T.M. Monro, Opt. Express **20**, 29378 (2012)
110. S.C. Warren-Smith, S. Heng, H. Ebendorff-Heidepriem, A.D. Abell, T.M. Monro, Langmuir **27**, 5680 (2011)
111. A.J. Swiston, C. Cheng, S.H. Um, D.J. Irvine, R.E. Cohen, M.F. Rubner, Nano Lett. **8**, 4446 (2008)
112. S.T. Dubas, J.B. Schlenoff, Macromolecules **32**, 8153 (1999)
113. S.T. Dubas, J.B. Schlenoff, Langmuir **17**, 7725 (2001)
114. J. E. Wong, F. Rehfeldt, P. Hänni, M. Tanaka, and R. v. Klitzing, Macromolecules **37**, 7285 (2004)
115. B. Schwarz, M. Schönhoff, Langmuir **18**, 2964 (2002)
116. T. Mauser, C. Déjugnat, G.B. Sukhorukov, Macromol. Rapid Commun. **25**, 1781 (2004)
117. C.P. Kapnissi-Christodoulou, M. Lowry, R.A. Agbaria, L. Geng, I.M. Warner, Electrophoresis **26**, 783 (2005)
118. S. Lane, P. West, A. François, A. Meldrum, Opt. Express **23**, 2577 (2015)
119. J. Chan, T. Thiessen, S. Lane, A. Meldrum, P. West, A. Francois, K. Gardner, Sens. J. 1 (2015)
120. V.M. Mirsky, M. Riepl, O.S. Wolfbeis, Biosens. Bioelectron. **12**, 977 (1997)
121. https://www.lifetechnologies.com/au/en/home/life-science/protein-biology/protein-biology-learning-center/protein-biology-resource-library/pierce-protein-methods/carbodiimide-crosslinker-chemistry.html#/legacy=www.piercenet.com
122. S.K. Vashist, C.K. Dixit, B.D. MacCraith, R. O'Kennedy, Analyst **136**, 4431 (2011)
123. A.K. Trilling, J. Beekwilder, H. Zuilhof, Analyst **138**, 1619 (2013)
124. A. Grodzki, E. Berenstein, in *Immunocytochemical Methods and Protocols*, edited by C. Oliver, and M.C. Jamur (Humana Press, 2010), p. 33
125. O.R. Bolduc, J.N. Pelletier, J.-F.O. Masson, Anal. Chem. **82**, 3699 (2010)
126. C.E. Soteropulos, K.M. Zurick, M.T. Bernards, H.K. Hunt, Langmuir **28**, 15743 (2012)
127. R.E. Benner, P.W. Barber, J.F. Owen, R.K. Chang, Phys. Rev. Lett. **44**, 475 (1980)
128. H. Chew, P.J. McNulty, M. Kerker, Phys. Rev. A **13**, 396 (1976)
129. H. Chew, Phys. Rev. A **38**, 3410 (1988)
130. H. Chew, J. Chem. Phys. **87**, 1355 (1987)
131. M. Kuwata-Gonokami, K. Takeda, Opt. Mater. **9**, 12 (1998)
132. H.T. Beier, G.L. Cote, K.E. Meissner, Ann. Biomed. Eng. **37**, 1974 (2009)
133. D.E. Gomez, I. Pastoriza-Santos, P. Mulvaney, Small **1**, 238 (2005)
134. Y. Ruan, K. Boyd, H. Ji, A. Francois, H. Ebendorff-Heidepriem, J. Munch, T.M. Monro, Opt. Express **22**, 11995 (2014)
135. V. Sandoghdar, F. Treussart, J. Hare, V. Lefèvre-Seguin, J.M. Raimond, S. Haroche, Phys. Rev. A **54**, R1777 (1996)
136. Y. Zhi, T. Thiessen, A. Meldrum, J. Opt. Soc. Am. B **30**, 51 (2013)
137. R.S. Moirangthem, A. Erbe, Appl. Phys. Lett. **103**, 051108 (2013)
138. A. Paunoiu, R.S. Moirangthem, A. Erbe, Phys. Status Solidi (RRL) Rapid Res. Lett. **9999** (2015)
139. M. Himmelhaus, A. Francois, Biosens. Bioelectron. **25**, 418 (2009)
140. R. Bischler, M. Olszyna, M. Himmelhaus, L. Dähne, Eur. Phys. J. Spec. Top. **223**, 2041 (2014)

141. A. Weller, F.C. Liu, R. Dahint, M. Himmelhaus, Appl. Phys. B **90**, 561 (2008)
142. K. Sasagawa, Z.-O. Yonezawa, R. Iwai, J. Ohta, M. Nunoshita, Appl. Phys. Lett. **85**, 4325 (2004)
143. E.M. Purcell, Phys. Rev. **69**, 674 (1946)
144. A. Francois, M. Himmelhaus, Appl. Phys. Lett. **94**, 031101 (2009)
145. A. François, N. Riesen, H. Ji, S. Afshar V., T.M. Monro, Appl. Phys. Lett. **106**, 031104 (2015)
146. I.M. White, X.D. Fan, Opt. Express **16**, 1020 (2008)
147. S. Arnold, D. Keng, S.I. Shopova, S. Holler, W. Zurawsky, F. Vollmer, Opt. Express **17**, 6230 (2009)
148. A. François, K.J. Rowland, S. Afshar, V, M. R. Henderson, and T. M. Monro. Opt. Express **21**, 22566 (2013)
149. A. François, K.J. Rowland, T.M. Monro, Appl. Phys. Lett. **99**, 141111 (2011)
150. http://www.lifetechnologies.com/au/en/home/life-science/protein-biology/protein-assays-analysis/luminex-assays.html
151. H.A. Huckabay, R.C. Dunn, Sens. Actuators B Chem. **160**, 1262 (2011)
152. F. Vollmer, S. Arnold, D. Braun, I. Teraoka, L.A., Biophys. J. **85**, 1974 (2003)
153. R. Lessard, O. Rousseau-Cyr, M. Charlebois, C. Riviere, O. Mermut, C.N. Allen, *SPIE Photonics West LASE, Laser Resonators, Microresonators, and Beam Control XV* (SPIE, San Francisco, 2013), p. 86001Q
154. Z. Chen, A. Taflove, V. Backman, Opt. Lett. **31**, 389 (2006)
155. A. Francois, M. Himmelhaus, Appl. Phys. Lett. **92**, 141107 (2008)
156. B.E. Little, J.P. Laine, H.A. Haus, J. Lightwave Technol. **17**, 704 (1999)
157. P. Bianucci, Y.Y. Zhi, F. Marsiglio, J. Silverstone, A. Meldrum, Phys. Status Solidi A-Appl. Mat. **208**, 639 (2011)
158. I. M. White, H. Oveys, and X. Fan, **- 31** (2006)
159. C. Chung-Yen, L. Jay Guo, J. Lightwave Technol. **24**, 1395 (2006)
160. J.L. Nadeau, V.S. Iltchenko, D. Kossakovski, G.H. Bearman, L. Maleki, in *Laser Resonators and Beam Control V*, ed. by A.V. Kudryashov (Spie-Int Soc Optical Engineering, Bellingham, 2002), p. 172
161. F. Vollmer, S. Arnold, D. Keng, Proc. Natl. Acad. Sci. U.S.A. **105**, 20701 (2008)
162. F. Vollmer, S. Arnold, Nat. Methods **5**, 591 (2008)
163. H.Y. Zhu, I.M. White, J.D. Suter, P.S. Dale, X.D. Fan, Opt. Express **15**, 9139 (2007)
164. J.D. Suter, I.M. White, H.Y. Zhu, H.D. Shi, C.W. Caldwell, X.D. Fan, Biosens. Bioelectron. **23**, 1003 (2008)
165. H.Y. Zhu, I.M. White, J.D. Suter, M. Zourob, X.D. Fan, Analyst **133**, 356 (2008)
166. J.T. Gohring, P.S. Dale, X. Fan, Sens. Actuators B Chem. **146**, 226 (2010)
167. G.M. Yang, I.M. White, X.D. Fan, Sens. Actuator B-Chem. **133**, 105 (2008)
168. H.Y. Zhu, I.M. White, J.D. Suter, X.D. Fan, Biosens. Bioelectron. **24**, 461 (2008)
169. M. Li, X. Wu, L.Y. Liu, X.D. Fan, L. Xu, Anal. Chem. **85**, 9328 (2013)
170. J.D. Suter, I.M. White, H.Y. Zhu, X.D. Fan, Appl. Optics **46**, 389 (2007)
171. I.M. White, H. Oveys, X. Fan, T.L. Smith, J. Zhang, Appl. Phys. Lett. **89**, 191106 (2006)
172. K.J. Rowland, A. Francois, P. Hoffmann, T.M. Monro, Opt. Express **21**, 11492 (2013)
173. G.S. Huang, V.A.B. Quinones, F. Ding, S. Kiravittaya, Y.F. Mei, O.G. Schmidt, ACS Nano **4**, 3123 (2010)
174. V.A.B. Quinones, G.S. Huang, J.D. Plumhof, S. Kiravittaya, A. Rastelli, Y.F. Mei, O.G. Schmidt, Opt. Lett. **34**, 2345 (2009)
175. Y. Zhi, A. Meldrum, Appl. Phys. Lett. **105**, 031902 (2014)
176. S. Lane, F. Marsiglio, Y. Zhi, A. Meldrum, Appl Optics **54**, 1331 (2015)
177. R. Kekatpure, M. Brongersma, Phys. Rev. A **78** (2008)
178. L. Yang, D.K. Armani, K.J. Vahala, Appl. Phys. Lett. **83**, 825 (2003)
179. D.K. Armani, T.J. Kippenberg, S.M. Spillane, K.J. Vahala, Nature **421**, 925 (2003)
180. H. Lee, T. Chen, J. Li, K.Y. Yang, S. Jeon, O. Painter, K.J. Vahala, Nat. Photon. **6**, 369 (2012)

181. M. Hossein-Zadeh, K.J. Vahala, Opt. Express **15**, 166 (2007)
182. A.M. Armani, R.P. Kulkarni, S.E. Fraser, R.C. Flagan, K.J. Vahala, Science **317**, 783 (2007)
183. B. Min, T.J. Kippenberg, L. Yang, K.J. Vahala, J. Kalkman, A. Polman, Phys. Rev. A **70**, 033803 (2004)
184. B. Min, S. Kim, K. Okamoto, L. Yang, A. Scherer, H. Atwater, K. Vahala, Appl. Phys. Lett. **89**, 191124 (2006)
185. I.S. Grudinin, A.B. Matsko, L. Maleki, Phys. Rev. Lett. **102**, 043902 (2009)
186. T.J. Kippenberg, S.M. Spillane, M. Bumki, K.J. Vahala, IEEE J. Sel. Top. Quantum Electron. **10**, 1219 (2004)
187. G. Zhixiong, Q. Haiyong, P. Stanley, J. Phys. D Appl. Phys. **39**, 5133 (2006)
188. Y.-Z. Yan et al., Opt. Express **19**, 5753 (2011)
189. F. Monifi, S.K. Ozdemir, J. Friedlein, L. Yang, IEEE Photon. Technol. Lett. **25**, 2458 (2013)
190. S. Lin, E. Schonbrun, K. Crozier, Nano Lett. **10**, 2408 (2010)
191. M.S. Luchansky, R.C. Bailey, Anal. Chem. **84**, 793 (2012)
192. S. Yegnanarayanan, W. Roman, M. Soltani, G. Cremona, H. Lu, A. Adibi, IEEE, in *2007 Ieee Leos Annual Meeting Conference Proceedings*, vols. 1 and 2 (IEEE, New York, 2007), p. 50
193. T. Lipka, J. Amthor, J. Muller, Nano-Bio Sens. Imaging Spectro. **8879**, 7, 88790a (2013)
194. T. Lipka, L. Wahn, H.K. Trieu, L. Hilterhaus, J. Muller, J. Nanophotonics **7**(10), 073793 (2013)
195. L. Luan, M.W. Royal, R. Evans, R.B. Fair, N.M. Jokerst, IEEE Sens. J. **12**, 7 (2012)
196. G.D. Kim, G.S. Son, H.S. Lee, K.D. Kim, S.S. Lee, Opt. Lett. **34**, 1048 (2009)
197. N. Jokerst, M. Royal, S. Palit, L. Luan, S. Dhar, T. Tyler, J. Biophotonics **2**, 212 (2009)
198. B. Momeni, S. Yegnanarayanan, M. Soltani, A.A. Eftekhar, E.S. Hosseini, A. Adibi, J. Nanophotonics **3**(23), 031001 (2009)
199. Y.W. Hu, B.B. Li, Y.X. Liu, Y.F. Xiao, Q.H. Gong, Opt. Commun. **291**, 380 (2013)
200. I.S. Grudinin, N. Yu, J. Opt. Soc. Am. B-Opt. Phys. **29**, 3010 (2012)
201. M. Sabaeian, H. Nadgaran, Z. Kargar, S. Sheikhi, M. Afkhami-Garaei, Proc. SPIE **8073** (2011)
202. W. Fang, D.B. Buchholz, R.C. Bailey, J.T. Hupp, R.P.H. Chang, H. Cao, Appl. Phys. Lett. **85**, 3666 (2004)
203. M.H. Shih, K.S. Hsu, W. Kunag, Y.C. Yang, Y.C. Wang, S.K. Tsai, Y.C. Liu, Z.C. Chang, M.C. Wu, Opt. Lett. **34**, 2733 (2009)
204. R.W. Boyd, J.E. Heebner, Appl. Optics **40**, 5742 (2001)
205. H. Jeong, S. Lee, G.Y. Sung, J.H. Shin, IEEE Photonics Technol. Lett. **23**, 88 (2011)
206. V.M.N. Passaro, B. Casamassima, F. De Lconardis, F. Dell'Olio, F. Magno, and IEEE, *Modeling and Design of a Microdisk Photonic Sensor for Biological Applications* (IEEE, New York, 2007), 2007 2nd International Workshop on Advances in Sensors and Interface
207. S. Lee, S.C. Eom, J.S. Chang, J.H. Shin, G. Y. Sung, C. Huh, IEEE, 2010 7th IEEE International Conference on Group IV Photonics (GFP), (2010), p. 258
208. S.C. Eom, J.H. Shin, IEEE Photonics Technol. Lett. **25**, 1859 (2013)
209. T. Yoshie, L.L. Tang, S.Y. Su, Sensors **11**, 1972 (2011)
210. H.Y. Quan, Z.X. Guo, Nanotechnology **18**(5), 375702 (2007)
211. Y. Zhi, C.P.K. Manchee, J.W. Silverstone, Z. Zhang, A. Meldrum, Plasmonics **8**, 71 (2013)
212. V.S. Ilchenko, M.L. Gorodetsky, S.P. Vyatchanin, Opt. Commun. **107**, 41 (1994)
213. A. Naweed, G. Farca, S. Shopova, A. Rosenberger, Phys. Rev. A **71** (2005)
214. H. Lin, J.H. Chen, S.S. Chao, M.C. Lo, S.D. Lin, W.H. Chang, Opt. Express **18**, 23948 (2010)
215. I.S. Grudinin, H. Lee, O. Painter, K.J. Vahala, Phys. Rev. Lett. **104**(4), 083901 (2010)
216. L. Howard, J. Stone, J. Fu, Precis. Eng.-J. Int. Soc. Precis. Eng. Nanotechnol. **25**, 321 (2001)
217. M.C. Lonergan, E.J. Severin, B.J. Doleman, S.A. Beaber, R.H. Grubb, N.S. Lewis, Chem. Mat. **8**, 2298 (1996)
218. R. P. Podgorsek, H. Franke, Appl. Phys. **41**, 601 (2002)
219. Y. Sun, S.I. Shopova, G. Frye-Mason, X. Fan **33** (2008)

220. S.I. Shopova, I.M. White, Y. Sun, H.Y. Zhu, X.D. Fan, G. Frye-Mason, A. Thompson, S. J. Ja, Anal. Chem. **80**, 2232 (2008)
221. B. Brichard, O.V. Butov, K.M. Golant, A.F. Fernandez, J. Appl. Phys. **103**(4), 054905 (2008)
222. Y. Louyer, D. Meschede, A. Rauschenbeutel, Phys. Rev. A **72** (2005)
223. H.J. Patrick, C.C. Chang, S.T. Vohra, Electron. Lett. **34**, 1773 (1998)
224. R. Yun-Jiang, W. Yi-Ping, R. Zeng-Ling, Z. Tao, J. Lightwave Technol. **21**, 1320 (2003)
225. Y. Liu, L. Zhang, J.A.R. Williams, I. Bennion, IEEE Photonics Technol. Lett. **12**, 531 (2000)
226. F.F. Pang, W.B. Liang, W.C. Xiang, N. Chen, X.L. Zeng, Z.Y. Chen, T.Y. Wang, IEEE Photonics Technol. Lett. **21**, 76 (2009)
227. M.H. Shih, K.S. Hsu, in *Current Trends of Optics and Photonics*, ed. by C.C. Lee (Springer, Berlin, 2015), p. 387
228. J. Wu, M. Gu, BIOMEDO **16**, 080901 (2011)
229. X. Feng, B.-F. Liu, J. Li, X. Liu, Mass Spectrom. Rev. (2014)
230. D. Gao, H. Liu, Y. Jiang, J.-M. Lin, Lab Chip **13**, 3309 (2013)
231. G.T.T. Gibson, S.M. Mugo, R.D. Oleschuk, Mass Spectrom. Rev. **28**, 918 (2009)
232. P. Vinuselvi, S. Park, M. Kim, J.M. Park, T. Kim, S.K. Lee, Int. J. Mol. Sci. **12**, 3576 (2011)
233. A.P. Lewis, A. Cranny, N.R. Harris, N.G. Green, J.A. Wharton, R.J.K. Wood, K.R. Stokes, Meas. Sci. Technol. **24** (2013)
234. J. Muse, V. Tripodi, S. Lucangioli, Curr. Anal. Chem. **10**, 225 (2014)
235. T. Buchberger, M. Himmelsbach, W. Buchberger, J. Chromatogr. A **1318**, 22 (2013)
236. C. Borst, F. Belal, U. Holzgrabe, Pharmazie **68**, 526 (2013)
237. B. Vallejo-Cordoba, A.F. Gonzalez-Cordova, Electrophoresis **31**, 2154 (2010)
238. C.M. Boone, J.C.M. Waterval, H. Lingeman, K. Ensing, W.J.M. Underberg, J. Pharmaceut. Biomed. **20**, 831 (1999)
239. A.P. Lewis, A. Cranny, N.R. Harris, N.G. Green, J.A. Wharton, R.J.K. Wood, K.R. Stokes, Meas. Sci. Technol. **24**, 042001 (2013)
240. X. Fan, I.M. White, S.I. Shopova, H. Zhu, J.D. Suter, Y. Sun, Anal. Chim. Acta **620**, 8 (2008)
241. K. JensenK, Kim, and ZettlA. Nat. Nano **3**, 533 (2008)
242. D. Ramos, E. Gil-Santos, V. Pini, J. M. Llorens, M. Fernández-Regúlez, Á. San Paulo, M. Calleja, J. Tamayo, Nano Lett. **12**, 932 (2012)
243. K.H. Kim, X.D. Fan, Appl. Phys. Lett. **105** (2014)
244. L. Senesac, T.G. Thundat, Mater. Today **11**, 28 (2008)
245. R.G. Heideman, P.V. Lambeck, Sens. Actuators B Chem. **61**, 100 (1999)
246. S. Dante, D. Duval, B. Sepúlveda, A.B. González-Guerrero, J.R. Sendra, L.M. Lechuga, Opt. Express **20**, 7195 (2012)
247. J. Hong, D. Yoon, T.S. Kim, Biochip J. **3**, 1 (2009)
248. H. Wu, H. Huang, M. Bai, P. Liu, M. Chao, J. Hu, J. Hao, T. Cao, Opt. Express **22**, 31977 (2014)
249. V.S.-Y. Lin, K. Motesharei, K.-P.S. Dancil, M.J. Sailor, M.R. Ghadiri, Science **278**, 840 (1997)
250. B.H. Schneider, J.G. Edwards, N.E. Hartman, Clin. Chem. **43**, 1757 (1997)
251. M. Wang, J. Hiltunen, C. Liedert, L. Hakalahti, R. Myllylä, J. Eur. Opt. Soc. **7** (2012)
252. K. Schmitt, B. Schirmer, C. Hoffmann, A. Brandenburg, P. Meyrueis, Biosens. Bioelectron. **22**, 2591 (2007)
253. S. Janz et al., Opt. Express **21**, 4623 (2013)
254. H. Qazi, A. Mohammad, M. Akram, Sensors **12**, 16522 (2012)
255. M. Bosch, A. Sánchez, F. Rojas, C. Ojeda, Sensors **7**, 797 (2007)
256. W.R. Seitz, Anal. Chem. **56**, 16A (1984)
257. K. Misiakos, S.E. Kakabakos, P.S. Petrou, H.H. Ruf, Anal. Chem. **76**, 1366 (2004)
258. A.N. Chryssis, S.S. Saini, S.M. Lee, Y. Hyunmin, W.E. Bentley, M. Dagenais, IEEE J. Sel. Top. Quantum Electron. **11**, 864 (2005)
259. W. Yuan, G.E. Town, O. Bang, IEEE Sens. J. **10**, 1192 (2010)

260. R.S. Brown, I. Kozin, Z. Tong, R.D. Oleschuk, H.-P. Loock, J. Chem. Phys. **117**, 10444 (2002)
261. J. Jágerská, H. Zhang, Z. Diao, N.L. Thomas, R. Houdré, Opt. Lett. **35**, 2523 (2010)
262. H.S. Dutta, A.K. Goyal, S. Pal, J. Nanophotonics **8**, 083088 (2014)
263. S. Olyaee, A. Naraghi, V. Ahmadi, Optik **125**, 596 (2014)
264. H. Clevenson, P. Desjardins, X. T. Gan, D. Englund, Appl. Phys. Lett. **104** (2014)
265. Y. Zou, S. Chakravarty, W.C. Lai, C.Y. Lin, R.T. Chen, Lab Chip **12**, 2309 (2012)
266. V. Toccafondo, J. García-Rupérez, M.J. Bañuls, A. Griol, J.G. Castelló, S. Peransi-Llopis, A. Maquieira, Opt. Lett. **35**, 3673 (2010)
267. S. Zlatanovic, L.W. Mirkarimi, M.M. Sigalas, M.A. Bynum, E. Chow, K.M. Robotti, G.W. Burr, S. Esener, A. Grot, Sens. Actuators B Chem. **141**, 13 (2009)
268. B. Troia, A. Paolicelli, F.D. Leonardis, V. M.N. Passaro, *Photonic Crystals for Optical Sensing: A Review*. Advances in Photonic Crystals 2013
269. D.K.C. Wu, B.T. Kuhlmey, B.J. Eggleton, Opt. Lett. **34**, 322 (2009)
270. X.W. Guo, J. Biophotonics **5**, 483 (2012)
271. M. Bauch, K. Toma, M. Toma, Q. Zhang, J. Dostalek, Plasmonics **9**, 781 (2014)
272. M. Li, S.K. Cushing, N.Q. Wu, Analyst **140**, 386 (2015)
273. J.D. Newman, A.P.F. Turner, in *Handbook of Biosensors and Biochips* (Wiley, New York, 2008)
274. J. Knut, S. Ralph, L. Ingemar, L. Bo, Meas. Sci. Technol. **11**, 1630 (2000)
275. E.M. Hicks, X. Zhang, S. Zou, O. Lyandres, K.G. Spears, G.C. Schatz, R.P. Van Duyne, J. Phys. Chem. B **109**, 22351 (2005)
276. A.B. Dahlin, J.O. Tegenfeldt, F. Höök, Anal. Chem. **78**, 4416 (2006)
277. P. Preechaburana, M.C. Gonzalez, A. Suska, D. Filippini, Angew. Chem. **51**, 11585 (2012)
278. J.N. Anker, W.P. Hall, O. Lyandres, N.C. Shah, J. Zhao, R.P. Van Duyne, Nat. Mater. **7**, 442 (2008)
279. Y. Lu, W. Shi, J. Qin, B. Lin, Electrophoresis **30**, 579 (2009)
280. V.G. Kravets et al., Nat. Mater. **12**, 304 (2013)
281. S. Arnold, S.I. Shopova, S. Holler, Opt. Express **18**, 281 (2010)
282. B. Sharma, R.R. Frontiera, A.-I. Henry, E. Ringe, R.P. Van Duyne, Mater. Today **15**, 16 (2012)
283. S. Nie, S.R. Emory, Science **275**, 1102 (1997)
284. S.L. Kleinman, E. Ringe, N. Valley, K.L. Wustholz, E. Phillips, K.A. Scheidt, G.C. Schatz, R.P. Van Duyne, J. Am. Chem. Soc. **133**, 4115 (2011)
285. B. Esteban Fernandez de Avila, H.M. Watkins, J.M. Pingarron, K.W. Plaxco, G. Palleschi, F. Ricci, Anal. Chem. **85**, 6593 (2013)
286. S. Tamane, C.O. Topal, A.K. Kalkan, in *Nanotechnology* (*IEEE-NANO*)*, 2011 11th IEEE Conference on* 2011, pp. 301
287. Z. Gong, H. Du, F. Cheng, C. Wang, C. Wang, M. Fan, ACS Appl. Mater. Interfaces **6**, 21931 (2014)
288. X.D. Fan, I.M. White, Nat. Photonics **5**, 591 (2011)
289. D. Erickson, D. Sinton, D. Psaltis, Nat. Photon **5**, 583 (2011)
290. H. Schmidt, A.R. Hawkins, Nat. Photon **5**, 598 (2011)
291. D. Psaltis, S.R. Quake, C. Yang, Nature **442**, 381 (2006)
292. X. Fan, S.H. Yun, Nat. Methods **11**, 141 (2014)
293. Q. Chen, X. Zhang, Y. Sun, M. Ritt, S. Sivaramakrishnan, X. Fan, Lab Chip **13**, 2679 (2013)
294. A. Jonas, M. Aas, Y. Karadag, S. Manioglu, S. Anand, D. McGloin, H. Bayraktar, A. Kiraz, Lab Chip **14**, 3093 (2014)
295. S. Nizamoglu, M.C. Gather, S.H. Yun, Adv. Mater. **25**, 5943 (2013)
296. R.M. Lequin, Clin. Chem. **51**, 2415 (2005)
297. S. Avrameas, J. Immunol. Methods **150**, 23 (1992)
298. S.M. Grist et al., Opt. Express **21**, 7994 (2013)
299. J. Zhu, S.K. Ozdemir, Y.-F. Xiao, L. Li, L. He, D.-R. Chen, L. Yang, Nat. Photon **4**, 46 (2010)

300. S.V. Boriskina, Opt. Lett. **31**, 338 (2006)
301. G. Griffel, IEEE Photonics Technol. Lett. **12**, 1642 (2000)
302. L. Jin, M. Li, J.-J. He, Optics Commun. **284**, 156 (2011)
303. Z. Xu, Q. Sun, B. Li, Y. Luo, W. Lu, D. Liu, P.P. Shum, L. Zhang, Opt. Express **23**, 6662 (2015)
304. L. Yang, J. Zhu, S.K. Ozdemir, L. He, W. Kim, D.-R. Chen, Proc. SPIE 7913, Laser Resonators and Beam Control XIII, p. 791312 (February 21, 2011)
305. V.R. Dantham, S. Holler, C. Barbre, D. Keng, V. Kolchenko, S. Arnold, Nano Lett. **13**, 3347 (2013)
306. S. Schlücker, Angew. Chem. Int. Ed. **53**, 4756 (2014)
307. E. Fort, S. Grésillon, J. Phys. D Appl. Phys. **41**, 013001 (2008)
308. M.C. Gather, S.H. Yun, Nat. Photonics **5**, 406 (2011)
309. X. Wu, Q. Chen, Y. Sun, X. Fan, Appl. Phys. Lett. **102**, 203706 (2013)

Chapter 10
High Sensitivity Polymer Fibre Bragg Grating Sensors and Devices

Kishore Bhowmik, Gang-Ding Peng, Eliathamby Ambikairajah and Ginu Rajan

Abstract Research on single-mode polymer optical fibres, Bragg gratings based on polymer optical fibre and their applications has been considerably progressed in the recent years. This chapter provides an overview on recent research developments on solid core polymer fibre Bragg grating sensors, devices and their applications.

10.1 Introduction

It is well known that the majority of optical fibre sensors are based on silica optical fibres due to their wide use in telecommunication applications and the wide availability of components, instrumentation, and optical fibre specifications. However more recently, interest in grating based sensors fabricated in polymer optical fibre (POF) increased mainly due to the different material properties of polymers compared to silica. Since the first demonstration of polymer optical fibre Bragg gratings (POFBG) in 1999, significant research efforts have been devoted to its sensing applications. In recent times, the advancement in the fabrication of single-mode polymer fibre enhanced the research and development of Bragg grating sensors for different applications. Their unique advantages compared to the silica counterparts are their high flexibility, large strain and temperature measurement range, low Young's modulus and bio-compatibility [1]. This has led to further research in device development and application of polymer FBGs. Some application-oriented research works are reported [2, 3] and further efforts are ongoing in exploring further potential of polymer FBGs.

K. Bhowmik · G.-D. Peng · E. Ambikairajah · G. Rajan (✉)
School of Electrical Engineering and Telecommunications, UNSW, Kensington, Australia
e-mail: ginu@uow.edu.au

G. Rajan
School of Electrical, Computer and Telecommunications Engineering,
University of Wollongong, Wollongong, Australia

M. J. Serpe et al. (eds.), *Photonic Materials for Sensing, Biosensing and Display Devices*, Springer Series in Materials Science 229,
DOI 10.1007/978-3-319-24990-2_10

Other developments occurred with single-mode polymer fibres are the emergence of micro-structured polymer fibre, improved photosensitive single-mode polymer fibres and polymer micro fibres. The aim of this chapter is to present an overview on the recent progress in the development of POFBG sensors, polymer micro-fibre Bragg grating and POFBG array. The sensing applications of polymer FBGs are also an emerging area with some promising research ongoing in a number of fields. In this chapter we discuss about the properties of solid core single-mode POFs that are critical to their sensing performance including their pressure, temperature and strain sensitivity. Some of the recent developments in this area such as POFBG based fast response humidity sensors, force and pressure measurements etc. are also reviewed. Moreover the potential of etched single-mode polymer fibres to develop intrinsic high sensitivity sensors are also discussed in this chapter. Finally, comments are made on the outlook of POF sensors and suggestions for future research directions to enable new sensing capabilities.

10.2 Polymer Optical Fibres

Poly methyl methacrylate (PMMA) is the most common used polymer for POFs and the first POF was fabricated by Du Pont in the 1960s [4]. The several critical advantages of polymer over silica optical fibres include their large elasticity capabilities, negative thermal sensitivities, high numerical aperture and lower stiffness. Light weight and low cost further add to the advantages of POF. Due to the difficulties in fabricating single-mode POFs, commercially available POFs are typically multimode at their operating wavelengths. Both step index and graded index configurations of multimode POFs are commercially available. Advantages owing to the large core size are the reason why single-mode POF are given less attention. Also during that time POF have experienced a surge in applications for short haul telecommunication systems due to its ease of implementation where multimode POFs were used. However more interestingly many researchers have realized their unique properties for sensing of strain, temperature, humidity etc. and looked into the sensing potential of polymer fibres [5]. Simultaneously, researchers are also focussed into the development of POFs with new properties including single-mode fibres, micro-structured fibres and polymer micro fibres. Also the unique material properties of polymer fibre have been used to expand the envelope of sensing applications beyond those previously realized with silica optical fibre sensors.

When coming to single-mode fibres, silica fibre technology is abundant while POF technology has focused exclusively on large core step and graded index multimode fibres. The first reported single-mode polymer was in early 1990s and was demonstrated by Kuzyk et al. [6]. These fibres had dye doped cores and the core size was approximately 8 μm and the cladding diameter was 125 μm. Single-mode fibres with copolymer for both core and cladding were later reported by Bosc and Toinen [7] where compositions of the copolymer in the core and cladding were adjusted to get a refractive index profile that yielded single-mode guidance.

One of the most photosensitive polymer fibre so far reported was fabricated at UNSW by Peng et al. [8–10], where the fibre manufacture followed a multiple step process thereby a hollow polymer preform was filled with core monomer mixture of methyl methacrylate, ethyl methacrylate and benzyl methacrylate, while the cladding is PMMA without dopants. The fibre had a core refractive index of 1.4793 and cladding index was 1.4707 and the difference in the refractive index of core and cladding was 0.0086. Single-mode photosensitive POF with different diameters are reported those ranging from 100 to 240 μm for the cladding and the core diameter ranging from 6 to 12 μm [8, 11]. These fibres are typically single mode only in the infrared region and suffer high transmission loss in the C-L band and are approximately 0.6 dB/cm, which is considerably higher compared to the silica fibre standards. Doped photosensitive single-mode POFs are still experimental, with only one commercial manufacturer, Paradigm Optics supply single mode POFs.

10.3 Polymer Fibre Bragg Gratings

FBG sensors are one of the most widely applied fibre sensors as they can provide sensing information's and also can be multiplexed in large numbers along in a single optical fibre. The first studies of photosensitivity in PMMA were carried out in the early 1970s at Bell labs in the United States [12]. They used 325 nm light from a He-Cd laser, which is the most common source today for POFBG fabrication. Despite this early start, more than 25 years were to pass before the first demonstration of a Bragg gratings in a multimode POF [1] that lead to the development of several photosensitive PMMA based POFs made from un-doped, dye-doped and oxidated preforms. Initial work with the polymer optical fibre Bragg gratings was undertaken by Peng and Chu et al. at UNSW Australia. They were able to demonstrate gratings in single-mode polymer fibre with very high reflectivity (28 dB) [9] and a large (70 nm) tuning range [8]. By applying tensile strain to the FBG, the authors shifted the Bragg wavelength by a total of 52 nm [13], which is an order of magnitude larger than that previously achieved with FBGs in silica optical fibres. Another reported work is by Yu et al. [14] where POFBG is demonstrated in a fibre with a MMA-EMA-BZMA core doped with trans-4-stilbenemethanol. The fibre was irradiated with 325 nm laser light using a phase mask technique. Xu et al. [15] realized birefringent gratings in azobenzene doped PMMA fibres written with 532 nm laser light. Researchers from Aston University also demonstrated Bragg gratings inscribed in polymer fibres using photo sensitive single-mode polymer fibres and also its use for humidity sensing applications [16]. They have also investigated the time response of polymer FBGs with change in humidity. An electrically tunable Bragg grating filter in polymer optical fibre is also reported by this group [17]. Other reported works on POFBG includes the ones with peak reflected wavelength 962 nm; a study on the intrinsic temperature sensitivity of polymer FBG and also thermo-optic effects in polymer fibre gratings [18].

10.3.1 POF Grating Fabrication

PMMA shows high intrinsic absorption loss from visible to near infrared region due to C–H bond in its molecular structure. The attenuation of PMMA based POF can be as high as 10^4 dB/km and sometimes it can be as high as 10^5 dB/km at 1550 nm region. That's whys, the POF used for Bragg grating inscription is very short.

The Bragg gratings are normally fabricated in the polymer fibre by standard phase mask technique using He–Cd laser emitting light at 325 nm [17, 19]. A schematic of the polymer FBG fabrication setup is shown in Fig. 10.1. The laser beam is irradiated onto the side of the polymer fibre through the phase mask placed parallel to the fibre. Two plano-convex cylindrical lenses are also used in the setup, one to expand the beam to cover approximately 10 mm of the fibre and the other to focus the expanded beam to the core region of the POF. An XYZ translation stage is used to adjust the position of the fibre, so that UV light is uniformly focused onto the core of the polymer fibre.

Due to high transmission loss of the polymer fibre in the wavelength of operation (1530 nm), a short length POF of approximately 10–12 cm is normally used to inscribe the FBG and either glued or butt coupled to a silica fibre pigtail to obtain the measurements. To observe the Bragg wavelength reflection spectrum as shown in Fig. 10.2, a high power broadband source is used as the input light source and the reflected signal from the grating is directed via a fibre circulator to the optical spectrum analyser (OSA) and is then monitored. A transmission and reflection spectrum of a typical POF grating is shown in Fig. 10.2. The observed multiple peaks in the spectrum arise from the short-comings of the side illumination inscription technique and also due to coupling mismatch between the polymer and

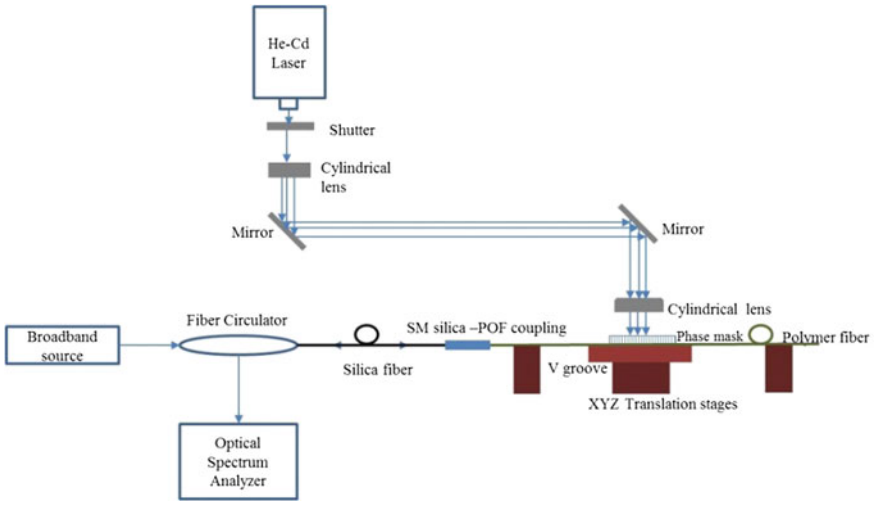

Fig. 10.1 Schematic of a standard polymer FBG fabrication setup

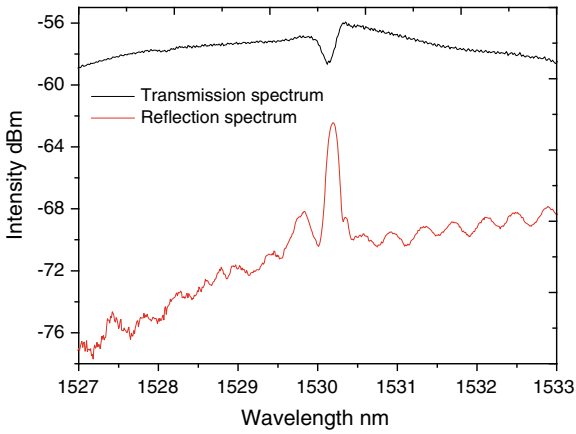

Fig. 10.2 Measured reflection and transmission spectra of the POF grating

silica fibre which can be controlled by improving the coupling accuracy and by optimizing the inscription technique. The reflectivity of the grating shown in Fig. 10.2 is approximately 50 % which largely depends on the inscription setup as UV laser power, inscription time, stability and alignment, POF type etc.

To use this fabricated POFBGs for a particular application, POFBG pigtails are fabricated by gluing the polymer fibre to a silica fibre pigtail. A stable POFBG pigtail is highly important to reduce the error and the uncertainty due to fibre coupling issues while characterizing the grating. A schematic diagram of the gluing procedure and a photograph of the glued region of the POF grating pigtail are shown in Fig. 10.3a, b respectively. A 3 cm long transparent plastic capillary tube (approximately 2–3 mm diameter) with a small hole in the middle of the tube is first inserted to the silica fibre pigtails. Then the POF and single mode silica fibre are aligned properly and after that a small quantity of UV epoxy is applied at the junction to connect the fibres. The output spectrum is continuously monitored and the fibres are slightly realigned to maintain the alignment and the UV epoxy is cured for 10 min. After curing, more epoxy is added to enhance the strength of the connection and cured further. After this process the glued fibre is slightly lifted upwards and the capillary tube is brought to the glued section. More epoxy is added through the side hole in the middle of the tube until the tube is filled with epoxy. The epoxy is cured for approximately 60 min. In that way a very stable and permanent POF grating pigtail can be made.

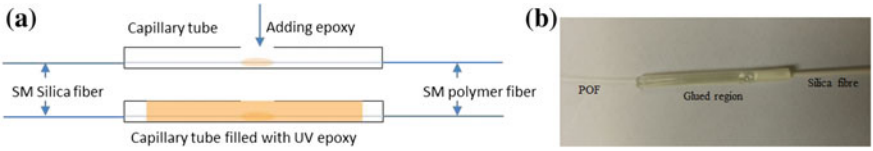

Fig. 10.3 **a** Schematic diagram showing the polymer-silica fibre connection procedure and **b** photograph of a POFBG pigtail

10.3.2 Polymer Micro-fibre Bragg Gratings

Polymer micro-fibre Bragg grating is another recent addition to the polymer FBG family, which can improve the measurement capabilities of the polymer gratings [20]. To fabricate the polymer micro-fibre, a two stage process is introduced, where the fibre is etched to a certain diameter and then tapered down to a final diameter. This method ensures that a sufficient amount of photosensitive core is retained within the fibre which allow inscription of a grating with a usable reflectivity. After etching, the fibre is placed in between the heating plates (temperature is around 160 °C) for approximately 5 min to ensure that the fibre is heated uniformly and soft enough for effective tapering. Then the fibre is pulled from both sides using a pair of high precision translation stages to form the tapered polymer micro-fibre. Figure 10.4 shows the micrographs of the un-etched fibre (253 μm), etched fibre (27 μm) and the final tapered fibre (16 μm).

The Bragg grating structure can be fabricated in the polymer micro-fibre in the same way as described in previous section. The growth behaviour of the grating is shown in Fig. 10.5a. The Bragg peak started appearing just after the fibre is illuminated with the UV laser and grew thereafter, reaching saturation and then decreasing with maximum reflected power obtained in 3 min. This grating growth behaviour is similar to that of the original photosensitive polymer fibres, but the

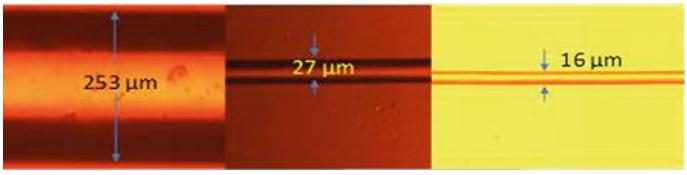

Fig. 10.4 Micrographs of original polymer fibre, etched polymer fibre and polymer micro-fibre

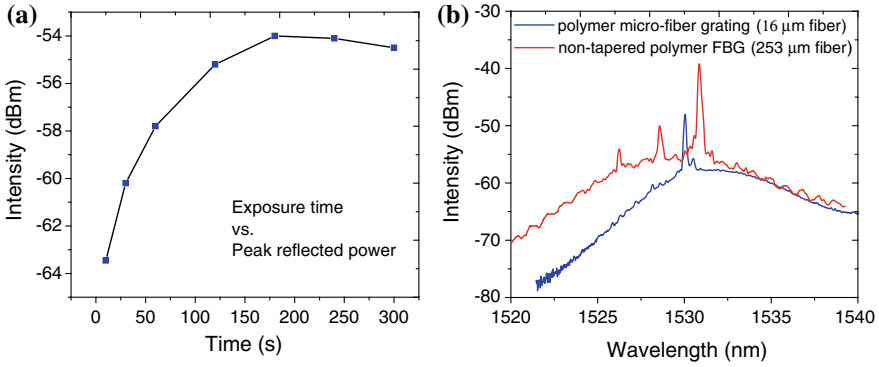

Fig. 10.5 **a** Variation in peak intensity with UV exposure time. **b** Comparison of reflection spectra of the original POFBG and the polymer micro-fibre grating

exposure time to obtain the maximum peak is lower than that of non-tapered POFBG, which is normally 7–10 min with the same experimental setup. This phenomenon is attributed to the relation between the thickness of the polymer fibre and the UV laser power, where the effective power in the core of the fibre is dependent on the penetration depth. Figure 10.5b shows a comparison of reflection spectrum in the micro-fibre Bragg grating and polymer fibre Bragg grating. A small blue shift in the reflection peak is due to the decrease in the effective refractive index (n_{eff}) of the polymer fibre at smaller radii. In the case of micro-fibres, the reflectivity depends on the amount of photosensitive core region left in the fibre after the tapering process and the estimated reflectivity obtained is approximately 5 % for a 16 μm diameter polymer micro-fibre grating.

10.3.3 Polymer FBG Arrays

FBGs are ideal wavelength selective components for detecting multiple sensing parameters. Here a method is described to inscribe multiple FBGs on a single-mode polymer fibre using a single phase mask and by applying strain to the fibre [21]. In this technique, initially a grating is inscribed at the far at zero strain condition and then at each step, an elongation of 0.2 % is applied to the fibre using the translation stage and the position of the UV exposed region is changed by moving the fibre using the motorized translation stage. In the case of gratings inscribed in a strained condition, after releasing the strain, the grating period of the fibre will change by a factor of $\frac{\wedge E_l}{100}$, where E_l is the percentage of elongation applied to the fibre. As a result of this grating period change the FBG exhibits a different peak wavelength. The zero strain state peak reflected wavelength of an FBG inscribed in the elongated fibre condition can be expressed as:

$$\lambda_G = 2n_{eff} \wedge \left(1 - \frac{E_l}{100}\right)$$

Upon releasing the tension, the spectrum will shift to the blue side and given the capability of polymer fibre to apply larger elongation, grating with a different centre wavelength can be inscribed. A schematic of the location of the FBGs in the FBG array is shown in Fig. 10.6 where the gratings are fabricated at a 1 cm interval. The reflection spectra (normalized) of the polymer FBG array is shown in Fig. 10.7. The dotted spectrum is the one measured at the maximum strain state (0.8 % elongation)

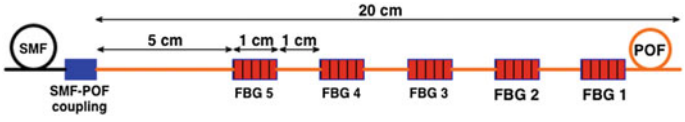

Fig. 10.6 Schematic of the location of different FBGs on the grating array

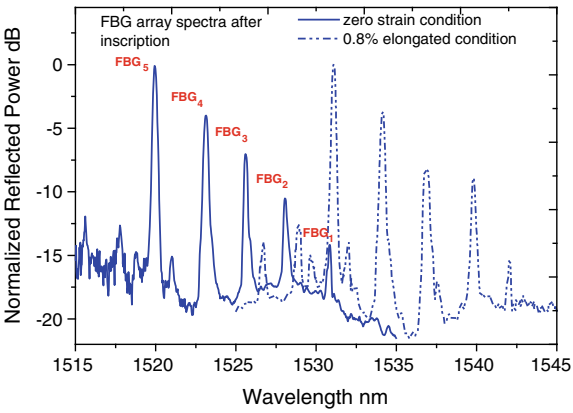

Fig. 10.7 Reflected spectrum of the Bragg grating array at zero strain condition and at 0.8 % elongated condition

and the bold spectrum shows the reflected peaks of the FBGs at the zero strain condition. The peak wavelength of FBG_1 is 1530.90 nm and FBG_5 shows a peak wavelength of 1519.90 nm, which gives an 11 nm separation between the peak wavelengths of FBG_1 and FBG_5.

The percentage of fibre elongation, Bragg wavelength, 3 dB bandwidth and the reflectivity of the gratings are summarized in Table 10.1. From the table it can be seen that all the parameters are approximately same for all the gratings in the array. This indicates that, without any degradation in the quality, multiple gratings with large peak wavelength separation can be inscribed single-mode polymer optical fibre by using the method of inscribing gratings at varying elongated conditions. The small variation in the reflectivity could be due to the slight change in writing condition such as change in temperature, fibre non-uniformity etc. This FBG array can be used in applications where multipoint sensors are required.

In order to see any effects of applied elongation during the grating inscription on the reflected spectra, the 3 dB bandwidth of the polymer FBGs are also needs to checked. The 3 dB bandwidth of the grating with elongation 1.25 % is 0.86 nm, and for the grating inscribed at 0.9 % elongation condition is 0.33 nm, a slight increase from other gratings (Fig. 10.8). The measured reflectivity of the grating inscribed with 1.25 % elongation is also lower than that of the other FBGs, which is only 6 % compared to ~20 % reflectivity of other FBGs. From these results, it is clear that the prolonged elongation for 5 min during UV exposure and the resulted creep and hysteresis during the inscription can affect the quality of the inscribed grating at

Table 10.1 Parameters of the FBG array

	FBG_1	FBG_2	FBG_3	FBG_4	FBG_5
Percentage of elongation	0.0	~0.2	~0.4	~0.6	~0.8
Bragg wavelength (nm)	1530.85	1528.07	1525.61	1523.14	1519.92
3 dB bandwidth (nm)	0.29	0.29	0.31	0.31	0.3
Reflectivity (%)	19.7	19.7	20.9	20.8	22.3

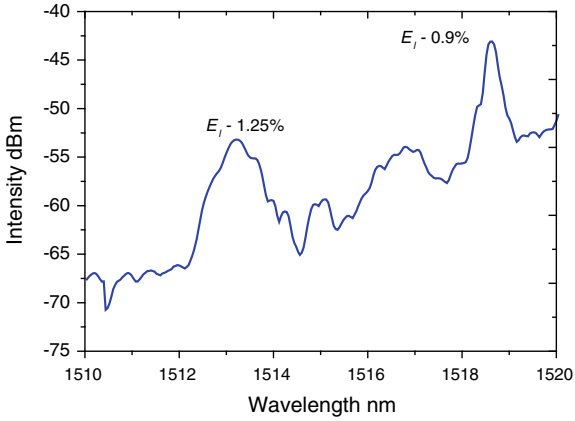

Fig. 10.8 Reflection spectra of FBGs inscribed at 0.9 % and 1.25 % fibre elongation

higher strain states. The UV laser induced temperature change in the polymer fibre can also enhance this effect. Therefore to have a good quality FBG array inscribed into the fibre using this technique, the elongation should be restricted to below 0.9 % otherwise the reflectivity of the grating is affected due to creep and hysteresis of the fibre during the inscription of the grating.

10.4 Characteristic Properties of Polymers Fibre Bragg Grating

It is well demonstrated that sensors based on polymer fibre has a number of advantages compared to its silica counterparts such as the inherent fracture resistance, large strain measurement range, high thermal sensitivity, sensitive to humidity and bio compatibility [5]. These unique material properties of polymer fibre have been used to expand the envelope of sensing applications beyond those previously realized with silica optical fibre sensors. However for certain applications such as in biomedical/biomechanical sensors, higher sensitivity is required. Though there may be many techniques available to enhance the sensitivity of different types of fibre sensors extrinsically [22–25], they increase size and involve further physical complexities. Therefore any technique to improve the sensitivity intrinsically will be valued higher compared to extrinsic techniques.

10.4.1 Etching the POF Gratings

The polymer fibre can be etched by using solvent etching technique [26] and the etching time depends on the required cladding thickness. A laboratory grade acetone with 99.5 % concentration is mixed with methanol by 1:1 ratio can be used

and then one end of the fibre is inserted into the mixture solution and then removed and cleaned using a soft dry tissue. To obtain a fibre diameter of 43 μm, the fibre was immersed in the solution for approximately 10 min and the etching rate is approximately 14 μm/min. A microscopic image of the fibres before (180 μm) and after etching (80 and 43 μm) is shown in Fig. 10.9.

Hu et al. [27] reported that a cladding diameter decrease of 12 % via etching is an ideal trade-off to produce highly reflective gratings by using Trans-4-stilbenemethanol-doped photosensitive step index poly(methyl methacrylate) (PMMA) POFs. However to investigate the effect of etching on the material properties of the polymer fibre, Young's modulus and absorption spectrum of the etched polymer fibres are experimentally obtained by Kishore et al. [28]. In order to measure the Young's modulus, a standard procedure is adopted that is valid for fibres of dimension in the range of optical fibres [29]. In this case, each fibre sample is mounted in the testing machine and then stressed to failure at a constant cross-head displacement rate. The estimated Young's modulus from the stress-strain data obtained from the experiment for fibres with different diameters is shown in Table 10.2. From the table it is clear that Young's modulus of the polymer fibre has significantly reduced with reduction in the fibre diameter [28]. The observed reduction in Young's modulus could be due to two reasons; the irreversible relaxation of the polymer chain of the material due to the solvent absorption and also due to the stress relaxation of fibre due to cladding diameter reduction. When the fibre is immersed in the etching solution, the internal stress distribution of the fibre varies with fibre diameter reduction [30] which changes the fibre material properties. So the combined effect of polymer chain relaxation and fibre stress relaxation can soften the fibre material that reduces the Young's modulus.

Also it is well understood that Young's modulus is inversely proportional to thermal expansion coefficient of a material. This means that a decrease in Young's modulus for the etched fibre increases their thermal expansion coefficient, which will have a considerable influence on the thermal sensitivity of sensors based on

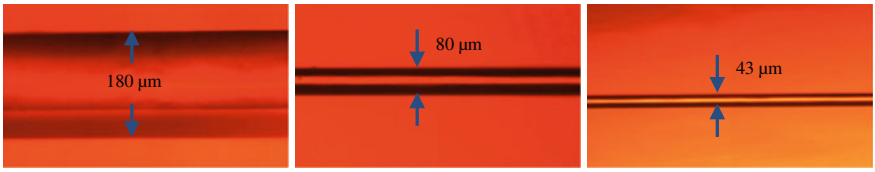

Fig. 10.9 Microscopic images of the polymer fibre before etching (180 μm) and after etching (80 and 43 μm)

Table 10.2 Measured young's modulus of the polymer fibre

Fibre diameter (μm)	Young's modulus (GPa)
180 (un-etched)	2.56
100	2.07
70	1.71

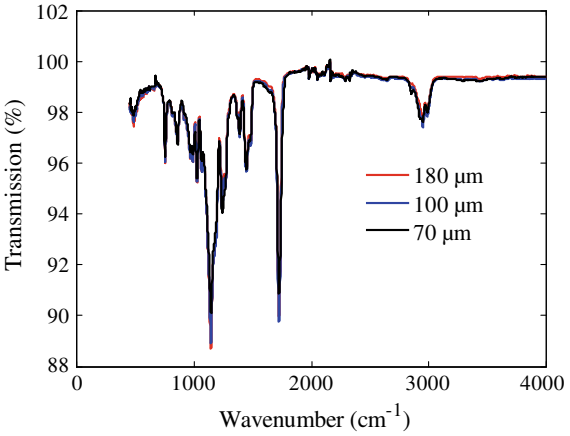

Fig. 10.10 Absorption spectrum of the etched and un-etched polymer optical fibres

etched polymer fibres. Moreover it may be assumed that the etching can change the Poisson's ratio of the fibre as well. In order to see the effect of etching on the chemical properties of the polymer fibre, Fourier transform infrared spectroscopy (FTIR) technique is used to obtain the absorption spectrum of the polymer fibre before and after etching as shown in Fig. 10.10. From the figure it can be seen that spectrum before and after etching are identical and thus it can be assumed that no major chemical structural alteration has happened. This significant information indicates that solvent etching technique did not alter the photosensitivity properties of polymer fibre. Thus it is evident that the cladding diameter reduction via solvent etching process alters the two most important material parameters, the Young's modulus and thermal expansion coefficient. This observed phenomenon is vital for any sensor designs based on etched polymer fibres as it can improve the sensitivity to various measurands.

10.4.2 Temperature Sensitivity

The first reported temperature sensitivity for a grating in a PMMA based step-index fibre was −360 pm/°C resulted due to a 50 °C temperature rise [31], and the response was nonlinear with a greater thermal sensitivity at higher temperatures. After that, the authors reported a temperature sensitivity of −149 pm/°C [32]; this time a linear response and a working temperature up-to 65 °C. Again this is significantly larger than that of silica and is in the negative direction due to the dominance of the negative thermo-optic co-efficient of polymers.

In the work reported by Kishore et al. [28] studied the effect of change in diameter obtained by etching on their temperature characteristics. In this case also due to negative thermo-optic coefficient of the polymer fibre, a negative Bragg wavelength shift is observed for an increase in temperature and the wavelength shift

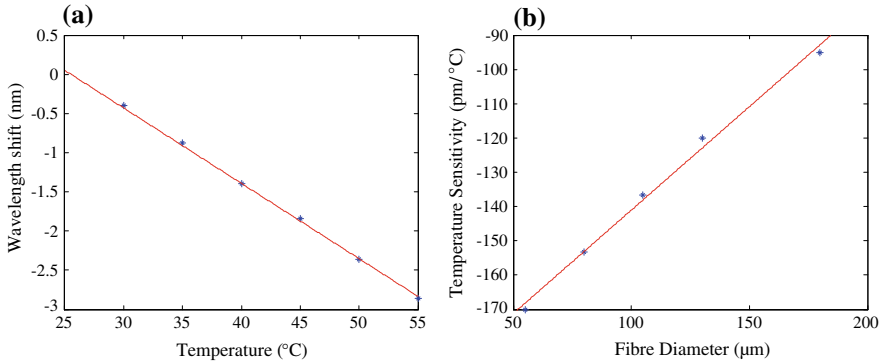

Fig. 10.11 **a** Measured wavelength shift of un-etched POFBG with applied temperature. **b** Measured temperature sensitivity of POFBG with different fibre diameters

is shown in Fig. 10.11a for an unetched fibre. In this case, to measure the temperature sensitivity of polymer FBGs, a Peltier cooler based system is used, which has an accuracy of ±0.1 °C, and the temperature of gratings are varied from 25 to 55 °C at 5 °C intervals [28]. For an un-etched fibre with diameter of 180 μm, the temperature sensitivity of the polymer FBG is −95 pm/°C. It should also be noted that etched POFBG can exhibit higher temperature sensitivity compared to an un-etched POFBG due to the material property change after etching which leads to an increase in thermal expansion co-efficient of the fibre. Figure 10.11b shows the result of the temperature sensitivity of all the etched POFBGs by using the same setup and from the figure it can be seen that the temperature sensitivity of etched POFBG has increased considerably and the values are −120, −136.7, −153.3 and −170 pm/°C for 130, 105, 80 and 55 μm diameters respectively. Thus it is evident from the figure that Bragg gratings in etched fibre exhibits considerable increase in temperature sensitivity and the sensitivity increases with decrease in fibre diameter.

10.4.3 Pressure Sensitivity

Pressure sensors based on FBGs are considered as a very good alternative compared to traditional sensors due to its size, weight, sensitivity, electro-magnetic interference, safety etc. However high sensitivity pressure measurements are challenging for silica FBGs because of the inherent limitations of the material properties of the silica optical fibre [33]. The hydrostatic pressure induced wavelength shift for a silica FBG is −0.22 nm for a 0–70 MPa range which gives a pressure sensitivity of −0.003 pm/kPa. Due to the relatively low intrinsic pressure sensitivity of silica FBG, further sensitivity enhancement is introduced and several techniques are reported for this [22, 23, 34]. On the other hand, the Young's modulus of POF is 30 times lower than that of silica fibre, so it can provide high pressure sensitivity

compared to silica fibre. This makes polymer fibre a potentially good candidate for pressure sensing applications.

Kishore et al. [35, 36] has recently reported the inherent pressure sensitivity of single-mode polymer FBG and also investigated the effect of change in diameter through etching on the pressure sensitivity experimentally. The schematic of the experimental setup to measure the hydrostatic pressure of POFBG is shown in Fig. 10.12. In the set-up, compressed air from a cylinder is used to increase the hydrostatic pressure within the chamber. The top of the chamber needs to be sealed perfectly after inserting the polymer fibre pigtail. When hydrostatic pressure is applied to an FBG, both the effective refractive index and grating period of the fibre will change and leads to the Bragg wavelength shift of:

$$\Delta\lambda_B = \lambda_B^{/} - \lambda_B = \lambda_B\left(\frac{\Delta n_{eff}}{n_{eff}} + \frac{\Delta\Lambda}{\Lambda}\right)$$

where $\Delta n_{eff} = n_{eff}^{/} - n_{eff}$ is change in effective index, $\Delta\Lambda = \Lambda^{/} - \Lambda$ is change in grating period.

Johnson et al. [37] reported that for single-mode silica FBG, the pressure sensitivity was negative and is −0.00388 pm/kPa and also for a multimode micro-structured POF grating the sensitivity was 0.10 pm/kPa. As the Young's modulus of the polymer fibre is much less than that of silica fibre, one would expect high pressure sensitivity compared to silica fibre. Figure 10.13 shows the result of Bragg wavelength shift of un-etched POFBG with a diameter of 180 μm for a pressure change from 0 kPa to 1 MPa, resulting in a sensitivity of 0.24 pm/kPa inclusive of the temperature effect. For POFBG, a positive sensitivity is observed when the hydrostatic pressure is increased, whereas it was negative for silica FBG. In the case of silica FBG, the hydrostatic pressure induced grating period change (strain effect) dominates the change in refractive index and as a result a negative sensitivity is observed. While for a POFBG, the dominant effect is the refractive index change than the grating period change and as a result the sensitivity becomes positive.

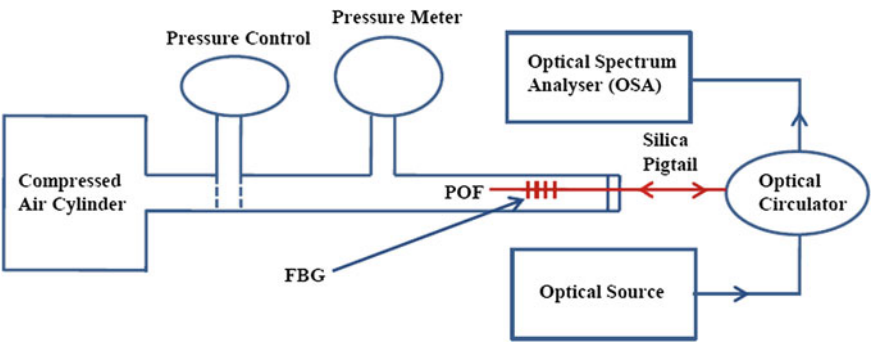

Fig. 10.12 Experimental setup for hydrostatic pressure sensitivity measurement

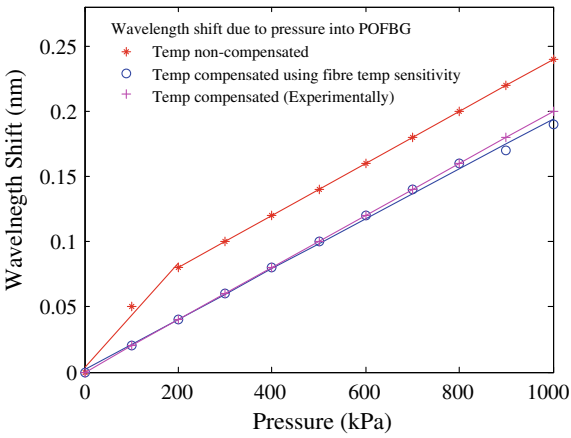

Fig. 10.13 Measured wavelength shift of POFBG with applied hydrostatic pressure

As the pressure inside the chamber increases the temperature as well and therefore the results are influenced by the change in temperature inside the chamber. This is clearly evident from the graph, as the slope of the wavelength versus pressure response is large for the 0–200 kPa range compared to the 200 kPa–1 MPa range. Moreover POFBG is sensitive to temperature change; therefore prior to the pressure sensitivity experiment, the temperature change due to increase in pressure inside the chamber need to be measured by using a temperature sensor kept inside the chamber. The temperature profile of the chamber while applying pressure is shown in Fig. 10.14 and it can be seen that a −0.58 °C nonlinear temperature change is observed for a pressure change from 0 kPa to 1 MPa within the duration of the experiment.

To experimentally eliminate the temperature and humidity effect, the chamber is filled with high viscous fluid and one end of the fibre is immersed to the viscous

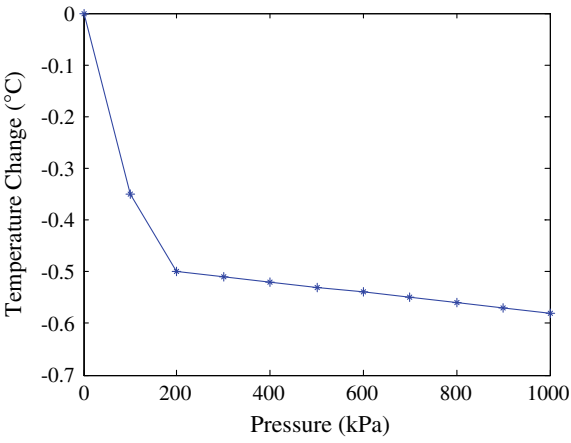

Fig. 10.14 Temperature profile of the chamber

fluid in the same way as in previous experiment and the end was sealed properly after inserting the fibre. The result obtained using this approach is also shown in Fig. 10.13 and the measured sensitivity of a POFBG with 180 μm diameter is 0.20 pm/kPa and the change in wavelength exhibits a linear relation with change in hydrostatic pressure. Therefore it can be considered that the temperature effect is eliminated and the obtained sensitivity of 0.20 pm/kPa is the true pressure sensitivity of 180 μm diameter POFBG.

In order to verify this result, the temperature sensitivity of the POFBG is used to extract the true inherent pressure sensitivity of the fibre. By using this sensitivity value and based on the temperature profile of the pressure chamber, the effect of temperature on the POFBG can be compensated to some extent. Using this approach, the estimated pressure sensitivity of the 180 μm diameter POFBG is 0.19 pm/kPa which is close to the value obtained using the first approach (viscous fluid method). The temperature compensated wavelength shift of the FBG versus applied pressure is also shown in Fig. 10.13. Similar measurements are reported for another un-etched fibre of a different diameter of 243 μm and the temperature compensated pressure sensitivity was measured the same as is 0.20 pm/kPa. Therefore from the results it can be confirmed that the actual intrinsic pressure sensitivity of an un-etched POFBG is approximately 0.20 pm/kPa. This result also reveals that, the intrinsic pressure sensitivity of POFBG is 52 times higher than that of silica FBG.

Also to investigate the etching effect into sensitivity, the fibres containing the FBG are etched to different diameters (130, 105, 80 and 55 μm) to measure its intrinsic pressure sensitivity. The pressure sensitivity of each of the etched POFBG is measured under the same hydrostatic pressure conditions as of the un-etched POFBG and the same experimental setup is used. Even with the high temperature sensitivity of the etched POFBG, using the temperature compensation techniques, the effect of temperature is completely eliminated and the measured temperature compensated wavelength shift due to hydrostatic pressure for POFBGs with different diameters is shown in Fig. 10.15a and the corresponding calculated pressure sensitivity is shown in Fig. 10.15b. The calculated pressure sensitivity for 180, 130, 105, 80 and 55 μm diameters POFBGs are 0.20, 0.32, 0.45, 0.60 and 0.75 pm/kPa respectively. It can be seen from the figure that the pressure sensitivity for un-etched POFBG (180 and 243 μm) is unchanged while for etched POFBG, it increases with a decrease in fibre diameter through etching.

10.4.4 Strain Sensitivity

POF Bragg gratings are advantageous with much higher tunability and stress sensitivity in comparison with silica FBGs because of the small Young's modulus. A simple strain tuning range of 73 nm has been achieved in PMMA based POF Bragg gratings [8]. On the other hand for silica FBGs, a tuning range of 32 nm Bragg wavelength shift has been reported by uniform compression [38]. However

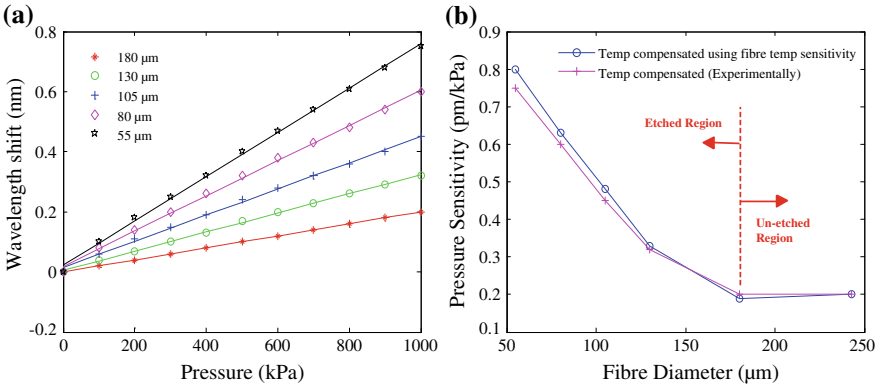

Fig. 10.15 **a** Measured wavelength shift of POFBG of different diameters. **b** Hydrostatic pressure sensitivity of POFBG with different fibre diameters

given the large elastic range and failure strain for polymer Bragg gratings, it can have unique advantage for strain sensing applications.

The strain sensitivity of etched polymer FBGs of different diameters are reported [28] and is shown in Fig. 10.16. From the figure it can be seen that the Bragg gratings inscribed in un-etched fibre exhibits a strain sensitivity of 1.26 pm/με, while a Bragg grating inscribed in an etched fibre of diameter 43 μm shows an enhanced sensitivity of 2.07 pm/με. Moreover for gratings in the 1550 nm region, strain sensitivity is 1.15 pm/με have been reported [39]. Stefani et al. [40] characterized the dynamic behaviour of different polymer fibres (TOPAS fibre) at frequencies up-to 100 Hz. They found that viscoelastic relaxation introduced nonlinearities that increased with increasing strain and frequency. However, performance sufficient for accelerometer applications could be obtained for strains up-to 0.28 %.

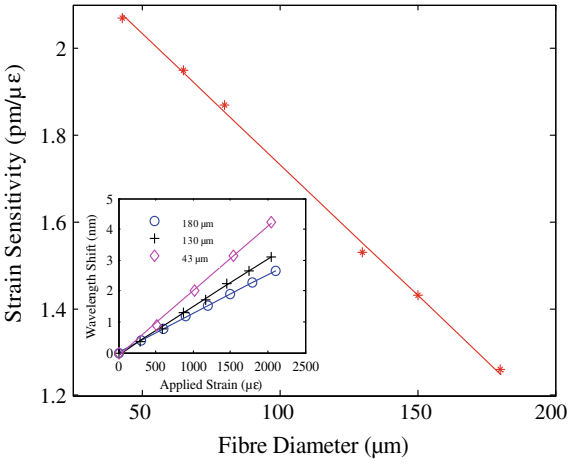

Fig. 10.16 Strain sensitivity of polymer FBG with different fibre diameters (*inset* wavelength shift for strain sensitivity)

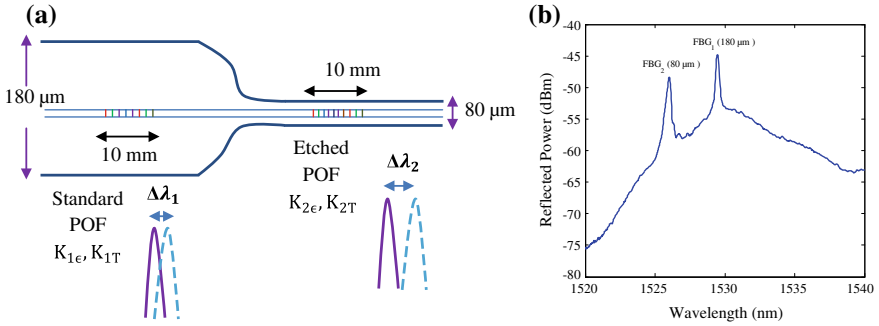

Fig. 10.17 **a** Schematic diagram of the fabricated grating pair for simultaneous measurement. **b** Reflection spectrum of the fabricated FBG array

The observed intrinsic change in strain and temperature sensitivity of etched and un-etched polymer FBG leads to the possibility of developing a sensing configuration for simultaneous strain and temperature measurement. The schematic of the concept is shown in Fig. 10.17a, where an FBG array with one grating is in the etched section and another in the un-etched section (3 cm apart), both having two distinct peak reflected wavelengths as shown in Fig. 10.17b. The difference in peak reflected power (3.62 dB) is due to the transmission loss as the gratings are inscribed 3 cm apart (loss ~0.60 dB/cm). To demonstrate simultaneous strain and temperature measurement, we considered the case of an FBG array with gratings inscribed in the un-etched (180 µm—FBG_1) and etched (80 µm—FBG_2) region. By knowing the strain and temperature sensitivities of this configuration ($K_1\varepsilon$ = 1.26 pm/µε, K_{1T} = –95 pm/°C, $K_2\varepsilon$ = 1.87 pm/µε, K_{2T} = –153.3 pm/°C), strain and temperature change can be measured simultaneously by utilizing the well-known characterization matrix [41] as shown below:

$$\begin{bmatrix} \Delta\varepsilon \\ \Delta T \end{bmatrix} = \frac{1}{K_{1\varepsilon}K_{2T} - K_{2\varepsilon}K_{1T}} \begin{bmatrix} K_{2T} & -K_{1T} \\ -K_{2\varepsilon} & K_{1\varepsilon} \end{bmatrix} \begin{bmatrix} \Delta\lambda_1 \\ \Delta\lambda_2 \end{bmatrix}$$

where $\Delta\lambda_1$ and $\Delta\lambda_2$ are the net wavelength shift exhibited by the 180 µm and 80 µm FBGs. Thus, exploiting the different strain and temperature sensitivities exhibited by the etched and un-etched polymer FBGs and by using this simple configuration, strain and temperature can be measured simultaneously and also with very high sensitivity.

10.5 Applications of Polymer Fibre Bragg Grating

The potential of fabricated POFBGs are demonstrated in a number of applications where the use of the polymer FBG can be of a distinct advantage. Given the low Young's modulus, high failure strain and intrinsic humidity sensitivity, FBGs based on polymer fibres are generally used in application in these sensing areas. In this

section we give an update of some of recently reported research work on applications of polymer FBGs.

10.5.1 Force and Pressure Sensors

Fibre optic methods for high sensitivity and low pressure measurements are considered as a challenging area due to the inherent limitations of the material properties of the silica optical fibre [33]. Force and pressure sensors based on silica FBGs are reported by many research groups over the years [22, 23, 25, 33, 34]. Due to low intrinsic sensitivity of silica FBGs, various methods are investigated to improve the sensitivity of FBGs to force and pressure, but are complicated in nature [22, 25, 34]. The unique material properties of the polymer optical fibre such as Young's modulus 30 times lower than that of silica fibre, sensors based on polymer FBGs have shown higher sensitivity compared to silica fibre gratings [42, 43].

Typically the force and pressure sensitivity of an FBG depends on the cross sectional area of the fibre, which can be increased by reducing the diameter of the fibre. Rajan et al. [19] reported a sensitivity of 680 nm/N for a polymer FBG with a diameter of 30 μm. The focus of the measurement range was at the lower end of the spectrum ranging from 0.005 to 0.05 N. Force sensitivity of polymer FBG with different diameters are shown in Fig. 10.18. It is observed that sensitivity increases considerably with decrease in fibre diameter.

Rajan et al. [19] also demonstrated high sensitivity pressure using a POF grating based sensor, where a thin vinyl diaphragm which has low Young's modulus is used to transfer the applied pressure to the POF grating. A pre-strained POF grating is attached to the diaphragm vertically as shown in the Fig. 10.19a. Due to very low Young's modulus (2–2.5 GPa) of the vinyl material, higher strain can be produced for very low pressure. The maximum deformation (δ) that can occur at the middle

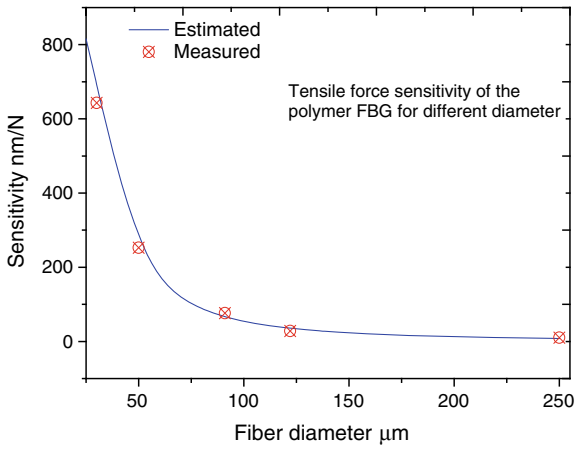

Fig. 10.18 Force sensitivity of the polymer fibre Bragg grating with different fibre diameter

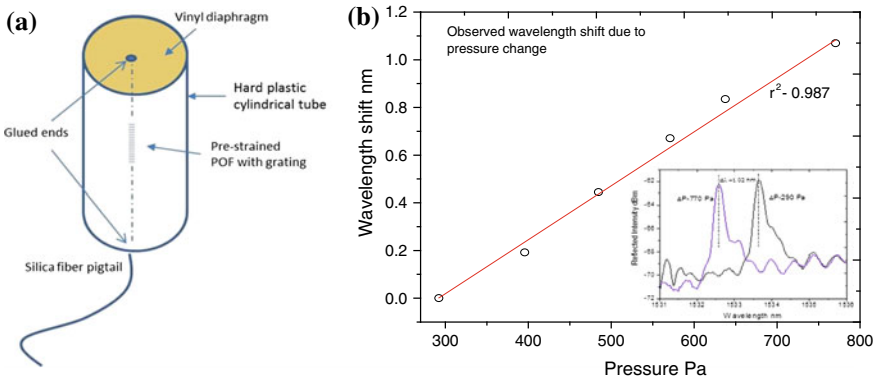

Fig. 10.19 **a** Schematic of the pressure transducer. **b** Pressure induced wavelength shift (*inset* pressure induced spectral shift)

of the diaphragm for an applied pressure also depends on the diaphragm radius (r) and thickness (t) and can be expressed as:

$$\delta = \frac{3P}{16t^3E}(1-\mu^2)r^4$$

where P is the applied pressure, E is the Young's modulus and μ is the Poisson ration of the vinyl diaphragm.

In this configuration a 91 μm diameter POF grating is attached perpendicular at the middle of an 8 mm diameter vinyl diaphragm. The total length of the fibre containing the grating was 7.5 cm and the thickness of the diaphragm was approximately 60 μm. The diaphragm was attached to one end of a hard plastic cylindrical tube of length 8 cm with an inner diameter of 8 mm. Pre-strain is applied to the fibre and the glued POF-silica junction is securely connected at the other end of the plastic cylindrical tube using an epoxy. The cylinder was sealed properly to have accurate pressure measurements. Low value pressure changes ranging from 290 to 770 Pa were applied to the diaphragm and the corresponding change in wavelength shift is shown in Fig. 10.19b and the estimated sensitivity approximately 1.32 pm/Pa. This sensitivity can be further improved by changing the diameter of the fibre. Such high sensitivity force/pressure sensors can find applications in bio-medical field such as in artificial heart pumps, minimally invasive surgical devices etc. That means for high sensitivity tensile force and pressure measurements, an etched polymer FBG will be a good alternative.

10.5.2 Humidity Sensors

A variety of optical fibre relative humidity sensors has been reported in the last decade and most of them are based on externally coated moisture sensitive reagents

[44]. Some of the recent studies on photonic crystal fibre interferometer based humidity sensors infiltrated with a hygroscopic material show a fast response time less than a second [45]. However in such sensors, the PCF holes are open to atmosphere, it can be contaminated and can affect the performance of the sensor for long term monitoring of relative humidity. FBGs coated with a thermoplastic/polyimide material also show sensitivity to humidity and exhibits a response time in seconds [46, 47]. However a very thin layer of coating is required to achieve this response time which reduces the sensitivity of the sensor. Due to water absorption properties of PMMA, the intrinsic humidity sensitivity of polymer FBG can make it superior compared to others. The humidity sensitivity of POFBGs was first demonstrated by Harbach [48] and showed a linear response in the range 40–90 % RH, though this breaks down at lower humidity's. The sensitivity displayed by this device is 38 pm/% RH. The response times tend to be typically a few tens of minutes, being 30 min. Some applications would benefit from response times much faster than 30 min. To address this issue, Zhang et al. [16] reported that the diffusion time of water content into the polymer fibre can be improved from around 30 min down to 10 min by reducing the cladding thickness of the polymer fibre.

Rajan et al. [49] reported a simple, low cost and fast response time intrinsic relative humidity sensor system based on an etched polymer FBG. The time response of the polymer FBG humidity sensor with a thickness of 25 μm is shown in Fig. 10.20a, when the RH is changed from 90 to 60 %, a voltage variation 9.8 mV is observed in 4.5 s, while for a RH change of 60–90 % a voltage variation of 8.2 mV is observed 5.5 s. The small kink observed in the response is due to the sudden temperature change in the chamber during the transition from wet air to dry air. The response time of POFBG with diameter varying from 25 to 125 μm is shown in Fig. 10.20b. From the figure it can be seen that the response time decreases exponentially as the diameter decreases in the measured range. The exponential nature of the change in response time is mainly attributed to the

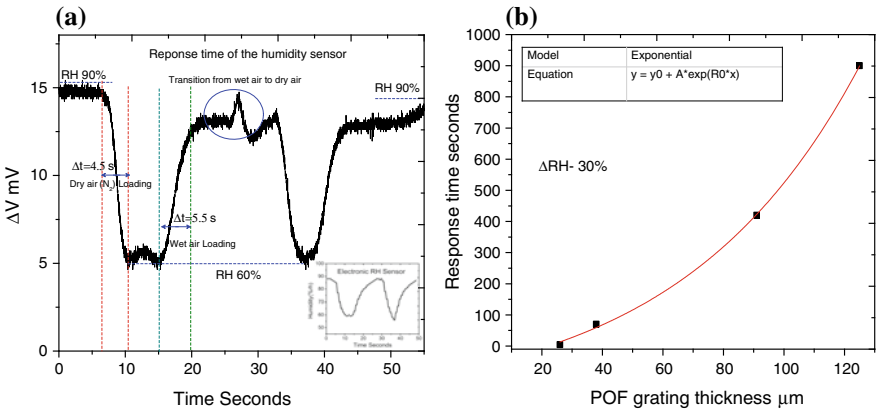

Fig. 10.20 **a** Plot showing response time of the humidity sensor. **b** Response time of humidity sensor with different thickness

absorption mechanism of PMMA. The results demonstrates that polymer FBGs can respond to a change in humidity within seconds if etched to micron level diameter and could be ideal for many industrial applications where real time humidity measurements are required.

10.5.3 Biochemical Concentration Sensor

Another reported application of polymer FBG is a biochemical concentration sensor. Significant Bragg wavelength shifts can be obtained for different concentration of water-soluble substances. Zhang et al. [50] reported a sensor using a saline concentration as shown in Fig. 10.21 where it seen that significant changes in Bragg wavelength occur with varying concentration and the process is reversible as well. The POFBG was first inserted into a test tube of distilled water for around 2 h, so that the POFBG was fully swelled by the water, and then pulled out and inserted into a test tube of saline solution. Four samples of saline solution (8.5, 13, 17.5, and 22 %) were tested in order of ascending concentration and then in order of descending concentration. The POFBG device was left for 60 min in each sample to allow equilibrium to be reached. The POFBG wavelength was monitored with an interval of 60 s. If solute exits in the water, then the water content absorbed in the polymer fibre will change because of the osmotic effect. It is also reported that the sensor is reversible and thus can be used for in situ repeatable measurement and monitoring of concentration.

10.5.4 Composite Materials with Embedded Polymer FBGs

Composite material structures are widely used in the aerospace, aviation, marine and civil industries because of their advantages of high strength and stiffness with

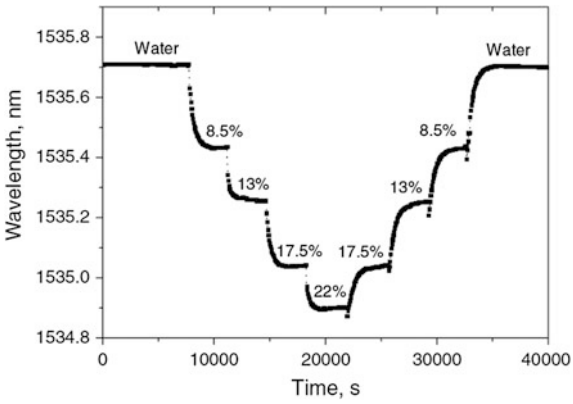

Fig. 10.21 Polymer FBG sensor response against step change of saline concentration [50]

less weight [51, 52]. Traditional evaluation techniques are effective in detecting damage in materials and structures, but are difficult to use under operational conditions due to the size and weight of the devices [53]. For these reasons fibre optic sensors have been considered as an alternative for in situ monitoring of composite materials for both the manufacturing process and during service life [54, 55]. For composite materials, the attractive characteristics of polymer FBGs include their high temperature sensitivity, large strain range and the absence of buffer coating. In a recent work reported by Rajan et al. [56], for a polymer FBG embedded in a glass reinforced composite material, a spectral broadening was observed due to the thermal expansion of the composite, but the sensitivity of the embedded polymer FBG to temperature remains the same as that of the free space polymer FBG.

The composite material sample can be fabricated by using a hand lay-up method with glass fibre fabrics (E-glass) as the reinforcement and a general purpose unsaturated polyester resin as the matrix material [57, 58]. The matrix material is prepared from the polyester resin with a catalyst added to the resin at a rate of 1 % by volume. The fabricated composite sample has 8 piles with the fibre gratings placed in the 2nd layer. A schematic of the cross section of the composite material with embedded fibre sensors is shown in Fig. 10.22a. FBG sensors are placed adjacently 1 mm apart from each other in the middle region of glass fabric, approximately 5 cm from both ends. Before embedding within the composite, pre-strain was applied to the fibre by fixing both ends of the fibres on a translation stage. The sample is cured as per the manufacturer's specifications at room temperature for three days. The thickness of the cured composite sample was 2.1 mm. A photograph of the fabricated sample is shown in Fig. 10.22b.

For an FBG sensor embedded inside a composite material, the magnitude of the wavelength shift due to thermal expansion may vary based on the type of reinforcement used, orientation of the reinforcement ply and matrix materials. The values of strain components acting upon the optical fibre in different directions also depend on the orientation of the reinforcement fibre ply. The wavelength shifts observed for the polymer FBG and silica FBG are shown in Fig. 10.23a. From the figure it can be seen that a blue shift is observed for the polymer FBG due to the

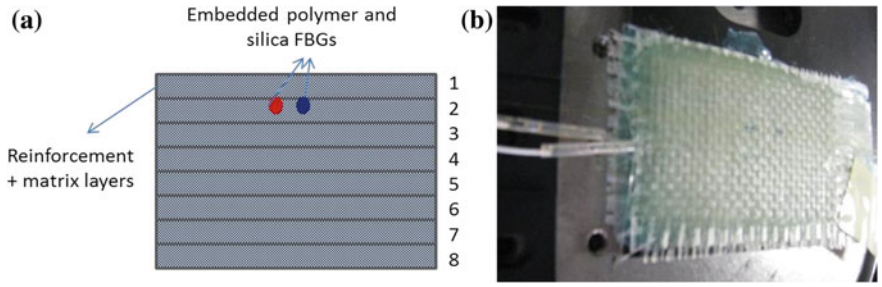

Fig. 10.22 **a** Schematic of the cross section of the composite material with embedded sensors. **b** Photograph of the cured composite material with embedded FBGs

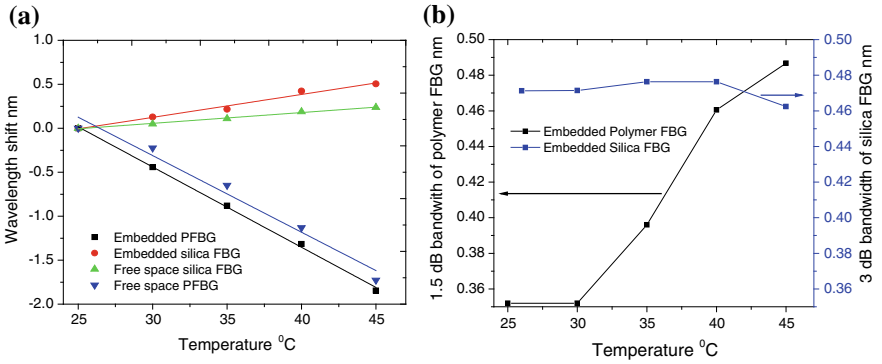

Fig. 10.23 **a** Temperature induced wavelength shift of the embedded polymer and silica FBGs and its comparison with free space FBGs. **b** Measured 1.5 dB bandwidth of polymer FBG and 3 dB bandwidth of silica FBG at different temperatures

negative thermo optic coefficient, while a red shift is observed for the silica FBG. The observed temperature sensitivity of the embedded polymer FBG is 92.28 pm/°C which is close to the free space temperature sensitivity 95 pm/°C. On the other hand, a spectral broadening is also observed due to the thermal stress/transverse strain on the embedded polymer FBG. In order to quantify the effect of broadening, the change in bandwidth of the reflection spectra of the polymer FBG can be measured at different temperatures. The measured 1.5 dB bandwidth of the polymer FBG is shown in Fig. 10.23b and it can be seen that the bandwidth increases as the temperature increases. The measured bandwidth change for the embedded polymer FBG within the temperature range of 30–45 °C was 8.5 pm/°C. This indicates that with appropriate calibration, the temperature and thermal expansion of the composite can be measured using the embedded polymer FBG.

10.6 Conclusions

In this chapter a review on the recent updates of research on solid core polymer fibre Bragg grating sensors and its applications were presented and it is noted that it is an emerging area with potential engineering applications. The development of these sensors could be vital in a number of application areas and some examples of the devices based on polymer FBGs are presented. Some valuable and important inventions on POF Bragg grating are presented in this chapter but the research on POF Bragg grating is still in a primitive phase compared to silica FBGs. The mechanism of photosensitivity of polymer fibre Bragg gratings are not fully known. The optimization of fabrication procedure and the growth dynamics of polymer FBG is another research subject that needs attention. The need for single mode polymer fibre compatible components, splicers etc. are other areas of research that

can provide acceleration to polymer FBG sensing. With the ongoing research activities on single-mode polymer FBGs, the research has a bright future outlook and potential applications in niche areas such as in biomedical.

References

1. G.D. Peng, X. Xiong, P.L. Chu, Photosensitivity and gratings in dye-doped polymer optical fibers. Opt. Fiber Technol. **5**, 242–251 (1999)
2. D.J. Webb, K. Kalli, C. Zhang, I.P. Johnson, X.F. Chen, D.S. Rodriguez et al., Applications of polymer fibre grating sensors, in *18th International Conference* on *Plastic* Optical *Fibers* (2009)
3. K.S.C. Kuang, S.T. Quek, C.G. Koh, W.J. Cantwell, P.J. Scully, Plastic optical fibre sensors for structural health monitoring: a review of recent progress. J. Sens. **2009**, 1–13 (2009)
4. W. Daum, J. Krauser, P.E. Zamzow, O. Ziemann (ed.), *POF—Polymer Optical Fibers for Data Communication*. Springer, Berlin (2002)
5. K. Peters, Polymer optical fiber sensors—a review. Smart Mater. Struct. **20**, 013002_1–013002_17 (2011)
6. M.G. Kuzyk, U.C. Paek, C.W. Dirk, Guest-host polymer fibers for nonlinear optics. Appl. Phys. Lett. **59**, 902–904 (1991)
7. D. Bosc, C. Toinen, Full polymer single-mode optical fiber. Photonics Technol. Lett. IEEE **4**, 749–750 (1992)
8. Z. Xiong, G.D. Peng, B. Wu, P.L. Chu, Highly tunable Bragg gratings in single-mode polymer optical fibers. IEEE Photonics Technol. Lett. **11**, 352–354 (1999)
9. H.Y. Liu, G.D. Peng, P.L. Chu, Polymer fiber Bragg gratings with 28-dB transmission rejection. Photonics Technol. Lett. IEEE **14**, 935–937 (2002)
10. G.D. Peng, P.L. Chu, X. Lou, R.A. Chaplin, Fabrication and characterization of polymer optical fibers. J. Electr. Electron. Eng. **15**, 289–296 (1995)
11. H.B. Liu, H.Y. Liu, G.D. Peng, P.L. Chu, Novel growth behaviors of fiber Bragg gratings in polymer optical fiber under UV irradiation with low power. Photonics Technol. Lett. IEEE **16**, 159–161 (2004)
12. I.P. Kaminow, H.P. Weber, E.A. Chandross, Poly (Methyl Methacrylate) dye laser with internal diffraction grating resonator. Appl. Phys. Lett. **18**, 497–499 (1971)
13. H.Y. Liu, H.B. Liu, G.D. Peng, Tensile strain characterization of polymer optical fibre Bragg gratings. Optics Commun. **251**, 37–43 (2005)
14. J. Yu, X. Tao, H. Tam, Trans-4-stilbenemethanol-doped photosensitive polymer fibers and gratings. Optics Lett. **29**, 156–158 (2004)
15. X. Xu, M. Hai, Z. Qijin, Properties of polarized laser-induced birefringent gratings in azobenzene-doped poly(methyl methecrylate) optical fibers. Optics Commun. **204**, 137–143 (2002)
16. W. Zhang, D.J. Webb, G.D. Peng, Investigation into time response of polymer fiber Bragg grating based humidity sensors. J. Lightwave Technol. **30**, 1090–1096 (2012)
17. K. Kalli, H.L. Dobb, D.J. Webb, K. Carroll, C. Themistos, M. Komodromos et al., Development of an electrically tuneable Bragg grating filter in polymer optical fibre operating at 1.55 μm. Meas. Sci. Technol. **18**, 3155–3164 (2007)
18. Z. Zhi Feng, Z. Chi, T. Xiao-Ming, W. Guang Feng, P. Gang-Ding, Inscription of polymer optical fiber Bragg grating at 962 nm and its potential in strain sensing. Photonics Technol. Lett. IEEE **22**, 1562–1564 (2010)
19. G. Rajan, B. Liu, Y.H. Luo, E. Ambikairajah, G.D. Peng, High sensitivity force and pressure measurements using etched singlemode polymer fiber Bragg gratings. IEEE Sens. J. **13**, 1794–1800 (2013)

20. G. Rajan, M.Y. Mohd Noor, N.H. Lovell, E. Ambikaizrajah, G. Farrell, G.-D. Peng, Polymer micro-fiber Bragg grating. Opt. Lett. **38**, 3359–3362 (2013)
21. G. Rajan, M.Y.M. Noor, E. Ambikairajah, P. Gang-Ding, Inscription of multiple Bragg gratings in a single-mode polymer optical fiber using a single phase mask and its analysis. Sens. J. IEEE **14**, 2384–2388 (2014)
22. D.C. Song, J.L. Zou, Z.X. Wei, S.M. Yang, H.L. Cui, High-sensitivity fiber Bragg grating pressure sensor using metal bellows. Opt. Eng. **48**, 034403–034403-3 (2009)
23. M.G. Xu, L. Reekie, Y.T. Chow, J.P. Dakin, Optical in-fiber grating high-pressure sensor. Electron. Lett. **29**, 398–399 (1993)
24. W. Yuan, A. Stefani, M. Bache, T. Jacobsen, B. Rose, N. Herholdt-Rasmussen et al., Improved thermal and strain performance of annealed polymer optical fiber Bragg gratings. Opt. Commun. **284**, 176–182 (2011)
25. W. Zhang, F. Li, Y. Liu, Fiber Bragg grating pressure sensor with ultrahigh sensitivity and reduced temperature sensitivity. Opt. Eng. **48**, 024402–024402-4 (2009)
26. D.F. Merchant, P.J. Scully, N.F. Schmitt, Chemical tapering of polymer optical fibre. Sens. Actuators a-Physical **76**, 365–371 (1999)
27. X. Hu, C.-F.J. Pun, H.-Y. Tam, P. Mégret, C. Caucheteur, Highly reflective Bragg gratings in slightly etched step-index polymer optical fiber. Opt. Express **22**, 18807–18817 (2014)
28. B. Kishore, G-D. Peng, E. Ambikairajah, V. Lovric, W.R. Walsh, B.G. Prusty, G. Rajan., Intrinsic high-sensitivity sensors based on etched single-mode polymer optical fibers. Photonics Technol. Lett. IEEE **27**, 604–607 (2015)
29. Active Standard ASTM C1557 (ed), *Standard Test Method for Tensile Strength and Young's Modulus of Fibers* (2003)
30. K.S. Lim, H.Z. Yang, W.Y. Chong, Y.K. Cheong, C.H. Lim, N.M. Ali et al., Axial contraction in etched optical fiber due to internal stress reduction. Opt. Express **21**, 2551–2562 (2013)
31. H.Y. Liu, G.D. Peng, P.L. Chu, Thermal tuning of polymer optical fiber Bragg gratings. Photonics Technol. Lett. IEEE **13**, 824–826 (2001)
32. H.B. Liu, H.Y. Liu, G.D. Peng, P.L. Chu, Strain and temperature sensor using a combination of polymer and silica fibre Bragg gratings. Opt. Commun. **219**, 139–142 (2003)
33. L. Yunqi, C. Kin Seng, C. Pak Lim, Fiber-Bragg-grating force sensor based on a wavelength-switched self-seeded fabry-perot laser diode. IEEE Photonics Technol. Lett. **17**, 450–452 (2005)
34. D.J. Hill, G.A. Cranch, Gain in hydrostatic pressure sensitivity of coated fibre Bragg grating. Electron. Lett. **35**, 1268–1269 (1999)
35. B. Kishore, G. Rajan, E. Ambikairajah, G.-D. Peng, Hydrostatic pressure sensitivity of standard polymer fibre Bragg gratings and etched polymer fibre Bragg gratings, in *OFS-23 Conference* (2014), pp. 91573G–91573G-4
36. Bhowmik K., Peng G-D., Ambikiarajah E., Lovric V., Walsh B., and Rajan G., "Experimental Study and Analysis of Hydrostatic Pressure Sensitivity of Polymer Fibre Bragg Gratings", J Lightwave Technol, **33**(12) (2015)
37. I.P. Johnson, D.J. Webb, K. Kalli, Hydrostatic pressure sensing using a polymer fibre Bragg gratings. in *SPIE* 2012, pp. 1–7
38. G.A. Ball, W.W. Morey, Compression-tuned single-frequency Bragg grating fiber laser. Opt. Lett. **19**, 1979–1981 (1994)
39. X. Chen, C. Zhang, D.J. Webb, G.-D. Peng, K. Kalli, Bragg grating in a polymer optical fibre for strain, bend and temperature sensing. Meas. Sci. Technol. **21**, 094005 (2010)
40. A. Stefani, S. Andresen, Y. Wu, O. Bang, Dynamic characterization of polymer optical fibers. Sens. J. IEEE **12**, 3047–3053 (2012)
41. M.G. Xu, J.L. Archambault, L. Reekie, J.P. Dakin, Discrimination between strain and temperature effects using dual-wavelength fibre grating sensors. Electron. Lett. **30**, 1085–1087 (1994)
42. Y. Luo, B. Yan, M. Li, X. Zhang, W. Wu, Q. Zhang et al., Analysis of multimode POF gratings in stress and strain sensing applications. Opt. Fiber Technol. **17**, 201–209 (2011)

43. T. Wang, Y. Luo, G.-D. Peng, Q. Zhang, *High-sensitivity stress sensor based on Bragg grating in BDK-doped photosensitive polymer optical fiber* (2012), pp. 83510M–83510M-8
44. T.L. Yeo, T. Sun, K.T.V. Grattan, Fibre-optic sensor technologies for humidity and moisture measurement. Sens. Actuators A **144**, 280–295 (2008)
45. J. Mathew, Y. Semenova, G. Farrell, Relative humidity sensor based on an agarose-infiltrated photonic crystal fiber interferometer. Sel. Top. Quantum Electron. IEEE J. **18**, 1553–1559 (2012)
46. X.F. Huang, D.R. Sheng, K.F. Cen, H. Zhou, Low-cost relative humidity sensor based on thermoplastic polyimide-coated fiber Bragg grating. Sens. Actuators B Chem. **127**, 518–524 (2007)
47. T.L. Yeo, S. Tong, K.T.V. Grattan, D. Parry, R. Lade, B.D. Powell, Polymer-coated fiber Bragg grating for relative humidity sensing. Sens. J. IEEE **5**, 1082–1089 (2005)
48. N.G. Harbach (ed.), Fiber Bragg gratings in polymer optical fibers. Switzerland: EPFL (2008)
49. G. Rajan, Y.M. Noor, B. Liu, E. Ambikairaja, D.J. Webb, G.-D. Peng, A fast response intrinsic humidity sensor based on an etched singlemode polymer fiber Bragg grating. Sens. Actuators, A **203**, 107–111 (2013)
50. W. Zhang, D. Webb, G. Peng, Polymer optical fiber Bragg grating acting as an intrinsic biochemical concentration sensor. Opt. Lett. **37**, 1370–1372 (2012)
51. D.L. Chung Deborah, Composite Materials: Science and Applications, in *Engineering Materials and Processes*. (Springer Publications, London, 2010)
52. J.K. Kim, D.Z. Wo, L.M. Zhou, H.T. Huang, K.T. Lau, M.Wang, Advances in composite materials and structures, 334–335, ed: Key Engineering Materials (2007)
53. S.R. Reid, G. Zhou, *Impact Behaviour of Fibre-Reinforced Composite Materials and Structures*. (CRC Press, 2000)
54. D.P. Garg, M.A. Zikry, G.L. Anderson, Current and potential future research activities in adaptive structures: an ARO perspective. Smart Mater. Struct. **10**, 610–623 (2001)
55. X.E. Gros, Current and future trends in non-destructive testing of composite materials. Annales de Chimie Science des Matériaux **25**, 539–544 (2000)
56. G. Rajan, M. Ramakrishnan, Y. Semenova, E. Ambikairajah, G. Farrell, P. Gang-Ding, Experimental Study and Analysis of a Polymer Fiber Bragg Grating Embedded in a Composite Material. Lightwave Technol. J. **32**, 1726–1733 (2014)
57. M. Ramakrishnan, G. Rajan, Y. Semenova, A. Boczkowska, A. Domański, T. Wolinski et al., Measurement of thermal elongation induced strain of a composite material using a polarization maintaining photonic crystal fiber sensor. Sens. Actuators A **190**, 44–51 (2013)
58. G. Rajan, M. Ramakrishnan, P. Lesiak, Y. Semenova, T. Wolinski, A. Boczkowska et al., Composite materials with embedded photonic crystal fiber interferometric sensors. Sens. Actuators A **182**, 57–67 (2012)

Chapter 11
Photonic Materials for Holographic Sensing

Monika Zawadzka, Tatsiana Mikulchyk, Dervil Cody, Suzanne Martin, Ali Kemal Yetisen, Juan Leonardo Martinez-Hurtado, Haider Butt, Emilia Mihaylova, Hussein Awala, Svetlana Mintova, Seok Hyun Yun and Izabela Naydenova

Abstract Holography is a practical approach to fabricating optical sensors for applications in the detection of chemical analytes and physical changes. Holographic sensors incorporate diffraction gratings within functionalized polymers or natural organic polymer matrices, that allow indirect optical measurements of physical and chemical stimuli. The advantages of holographic sensors over other optical sensors are the ability to produce three-dimensional (3D) images and amenability to mass manufacturing at low-cost. The aim of this chapter is to (1) describe the principle of operation of holographic sensors (2) describe the

M. Zawadzka · T. Mikulchyk · D. Cody · S. Martin · E. Mihaylova · I. Naydenova (✉)
Centre for Industrial and Engineering Optics, School of Physics, College of Sciences and Health, Dublin Institute of Technology, Dublin 8, Ireland
e-mail: izabela.naydenova@dit.ie

A. K. Yetisen (✉) · S. H. Yun
Harvard Medical School and Wellman Center for Photomedicine, Massachusetts General Hospital, 50 Blossom Street, Boston, MA 02114, USA
e-mail: ayetisen@mgh.harvard.edu

J. L. Martinez-Hurtado
Department of Chemical Engineering and Biotechnology, University of Cambridge, Tennis Court Road, Cambridge CB2 1QT, UK

H. Butt
School of Mechanical Engineering, University of Birmingham, Edgbaston, Birmingham B15 2TT, UK

E. Mihaylova
Department of Mathematics, Informatics and Physics, Agricultural University, Plovdiv, 12 Mendeleev Street, Plovdiv 4000, Bulgaria

H. Awala · S. Mintova
LCS, 7CRISMAT, University of Caen, 6, Boulevard Du Maréchal Juin, 14050 Caen Cedex, France

M. J. Serpe et al. (eds.), *Photonic Materials for Sensing, Biosensing and Display Devices*, Springer Series in Materials Science 229,
DOI 10.1007/978-3-319-24990-2_11

holographic recording techniques used for their fabrication (3) discuss approaches to preparing recording media and overview strategies of their functionalization in order to obtain stimuli responsive devices, and (4) highlight emerging applications in environmental sensing and point-of-care diagnostics. Particular emphasis is put on the photonic materials used for holographic sensors recording and the different approaches used for their functionalization with the view of how this can be used to improve sensors sensitivity, selectivity and response time. The main challenges in holographic sensors research and possible solutions to these challenges are outlined.

11.1 Introduction

11.1.1 The Need for Rapid Tests for Environmental Sensing and Medical Diagnostics

The development of rapid and reliable sensors that can be used at point-of-care settings is needed more than ever. However, the applicability of commercial sensors is still limited and further progress is needed to provide low-cost, miniature, user-friendly and reliable sensors for use in sectors such as environmental, food and beverage, healthcare, sports and recreation, advertisement, and security [1]. The sensor market is driven by a raising awareness of the environmental impact and healthcare, which results in new legislations. These legislations concern (1) communal and industrial waste management, (2) working environment conditions (3) carrying out environmental friendly agriculture (4) delivery of products to the market from various industries ranging from food, beverage to technologically advanced products (e.g., electronics) that are safe to human and environment [2]. Another area of sensor applications is medical diagnostics, which becomes more and more important with regard to the problem of ageing of societies [3]. The market for portable sensors which can be integrated with mobile devices for health but also in sport and reaction applications is rapidly increasing in size [4], and it can be predicted that it will accelerate upon further development in sensors sector.

With regard to simplicity of sensor use, which enables sensor's application for public use, sensors that change color in the presence of an analyte are very appealing. Holographic sensors can offer not only colorimetric response but also visual effects like appearance or disappearance of a text/image triggered by an analyte, and thus convey a message to the end user [5–7].

11.1.2 Advantages of Holographic Sensors

The capability of a holographic sensor to display visual information in the presence of a chemical or physical stimulus makes them appealing for applications where

quick analytical information is needed. Such characteristics of the sensors are of interest for applications ranging from environmental sensing to medical diagnostics, but are not limited to those fields. Holographic sensors can also be used indirectly, for example in security devices to identify forgery, or smart windows that change color or transparency when subject to a specific wavelength or electric field [8].

Holographic sensors offer many other advantages such as low-cost production, which make them suitable for disposable devices; they are lightweight devices; additionally for a reflection type of holographic sensors, no additional readout panel or power supply is required for their functioning. All these characteristics make them candidates for wearable/portable applications. Sensors in the form of labels that can be attached to packaging or clothing informing about storage condition of the product such as temperature or humidity, displays providing information about contamination in the industrial work space, or contact lenses measuring the concentration of glucose in tear fluid are examples of potential applications. Further applications of holographic sensors are yet to come with the advances in holographic materials, as well as with their integration with other enabling technologies such as microfluidics, which is possible due to another advantage of the holographic devices—their capability for miniaturization.

Evidently, there is a market need for holographic sensors, which are promising for many applications. Yet, to understand the challenges in holographic sensors fabrication, the principle of their operation and the properties of the materials used for their fabrication should be understood. Holographic sensors are 3D structures created in functionalized polymers with the ability to change their optical properties upon interaction with a chemical or physical stimulus. There are two main requirements that the photonic material must fulfill to be used in holographic sensing: (1) it must be suitable for holographic recording and (2) the presence of stimuli must cause a change in the optical properties of the sensing material.

The aim of this chapter is to illustrate how to balance these two requirements in optimizing the recording materials to obtain efficient and reliable holographic sensors. The book chapter introduces the principle of recording of holographic structures, the types of holographic sensors and their operation. It describes photonic materials used in holographic sensing, strategies for their functionalization and design by theoretical modeling. Applications in sensing of gas phase analytes, humidity, temperature, pressure, metal ions and glucose are demonstrated. The main challenges in the development of photonic materials for holographic sensors are discussed.

11.2 Fundamentals of Holographic Sensors

11.2.1 Principle of Recording of the Holographic Structures

Holographic sensors are photonic structures created by optical image recording [5, 6]. This involves interferometric patterning of a photosensitive material that as a

result of the recording process undergoes change of its optical properties. The structure created by this optical recording process is called a hologram. Typically as a result of the recording process, the refractive index of the material and/or the absorption coefficient is spatially varied, thus copying the spatially varied recording light field. This variation is normally observed in the volume of the material in volume holograms [9]. In some cases, the recording field pattern can also be copied in the form of thickness variation of the recording material to form surface holograms [9]. The variations in its refractive index, absorption coefficient, and thickness of the hologram affect the diffraction of light propagating through. When illuminated by one of the beams used to create the interference pattern, due to diffraction, the hologram reconstructs the other one (Fig. 11.1). There are two main types of holograms depending on the type of material optical property is altered: phase and amplitude holograms [9]. Phase holograms are recorded in the form of refractive index and/or thickness variation of the photonic material, and they change the phase of the propagating light. Amplitude holograms are recorded in the form of absorption coefficient variation, and they lead to alteration of the amplitude of the propagating light. Depending on the wavelength of the interrogating light, a hologram can be considered being phase or amplitude only or combination of both types.

There are different photochemical and physical processes involved in holographic recording [6]. In photopolymers, for example, the response to light causes photopolymerization and accompanying diffusion of photopolymer components, and this leads to spatially varied density of the recording material, causing modulation of the refractive index [10]. In silver halide based materials, the variation of the refractive index is caused by the formation of silver nanoparticles with a concentration that is proportional to the laser light intensity [11, 12]. This causes spatial variation of the refractive index of the material at visible wavelengths. Photobleaching is involved in recording amplitude holograms as it leads to spatial variation of the absorption coefficient of the material [13]. The variety of the photosensitive materials used in holographic sensing, the photochemical processes involved in holographic recording, and the type of the recorded holograms in these materials are summarized in Table 11.1. A hologram recorded in such material has

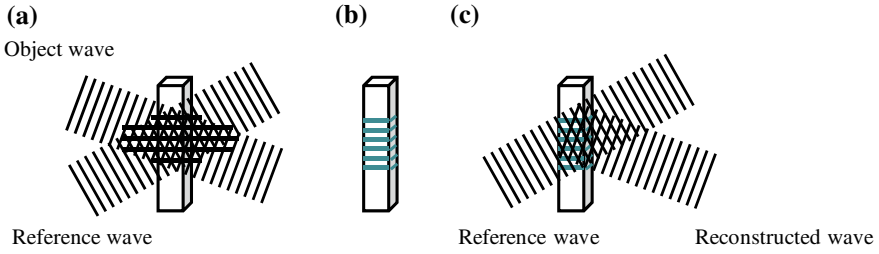

Fig. 11.1 Recording and reconstruction of a hologram. **a** Illumination of the photosensitive material by interference pattern. **b** The copy of the interference pattern into the recording material. **c** Reconstruction of the recorded beam through diffraction

Table 11.1 Type of photosensitive materials used for holographic sensor recording, photochemical and physical processes involved in the recording, and type of holograms recorded in these materials

Photosensitive materials		Photochemical and physical processes	Hologram type
Nanoparticle free materials	Photopolymers	Photopolymerization and diffusion of photopolymer components leads to spatially varying density of the material	Phase
Nanoparticle containing materials (uniformly distributed, or patterned by the recording process)	Silver halide impregnated functionalized polymers (gelatin, poly (2-hydroxyethyl methacrylate) (pHEMA), poly (acrylamide) (pAAm), and poly(vinyl alcohol) (PVA))	Silver halide photochemistry leading to formation of spatially patterned silver grains	Phase
	Zeolite nanoparticles doped polymers	Optical patterning of the nanoparticles within the polymer matrix	Phase

all necessary components to act as a sensor. Therefore, the analyte sensitive film acts as a recognition component, changes in the physical dimensions of the holographic structure and/or the refractive index variation of the sensitive film as sensing mechanisms, the periodic structure as a transducer, and diffracted light as a signal. Changes in the physical dimensions of the structure originate from swelling or shrinkage of the sensitive film caused by the interaction with the analyte. Refractive index variation change can be caused by the physicochemical modification of the holographic material during exposure to the analyte. The principle of operation of the sensors, depending on their type is provided in the following section.

Volume phase holograms are typically used in the development of holographic sensors [1], and for this reason the following description concerns this type of holograms.

11.2.2 Types of Holographic Sensors

Holograms can be distinguished as (1) surface or volume holograms depending on their physical characteristics and (2) phase or amplitude holograms depending on the optical property of the material, which is altered during the recording. Further

classification is carried out depending on the holographic recording geometry; in this regard two types of photonic structures that can be inscribed in the photonic materials are transmission and reflection holograms [9]. Herein, the focus will be put on volume phase transmission and reflection holograms, as the devices of these two types are of most scientific relevance to holographic sensors. The recording beam geometries and principles of operation of sensors based on transmission and reflection volume phase holograms are described in the following sections.

11.2.2.1 Sensors Based on Reflection Holograms

Reflection holograms offer the ability to provide visual information in the presence of a stimulus and are therefore suitable for applications where an additional readout device is not needed.

There are two main approaches in recording reflection holograms: split beam and Denisyuk modes of recording (Fig. 11.2).

In split beam mode of recording, the laser beam is split in two or more beams either by dividing its amplitude or wavefront. An example of the split beam mode used for recording of reflection hologram sensors is shown in Fig. 11.2a. A laser beam is expanded, split in two, and then recombined at the recording material film.

In Denisyuk mode of recording [14], there is only one beam incident on the recording material. The second beam is either scattered by an object or reflected by a mirror positioned behind the recording medium (Fig. 11.2b). The most important feature of the holograms recorded in reflection mode is that they replay under white light illumination. The structure created in reflection mode is effectively a Bragg

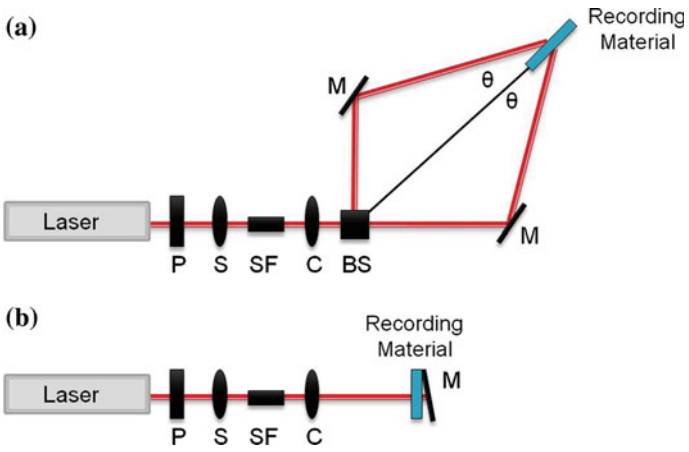

Fig. 11.2 Experimental setups for recording reflection gratings (**a**) split beam mode (**b**) Denisyuk reflection geometry. *P* polarizer, *S* shutter, *BS* beam splitter, *SF* spatial filter, *C* collimator, *M* mirror

mirror. Upon shining incident white light, constructive interference of the light reflected from the planes of varying refractive index occurs. As a result a diffraction maximum in a given direction is observed for light of a specific wavelength. The relation between the spacing Λ between the planes of varying refractive index, the diffracted light wavelength λ, the effective refractive index of the recording medium n and the angle θ between the incident beam of light and the planes of varying refractive index (Bragg angle) can be expressed by a simple formula that assumes uniformly distributed layer gratings.

$$\lambda = 2n\Lambda\sin(\theta) \tag{11.1}$$

In reflection holograms, the planes of varying refractive index are nearly parallel to the substrate surface if the hologram is recorded at low tilt angles from the surface of the mirror (Fig. 11.3).

The holograms recorded in reflection mode are useful when easy-to-interpret information is sought. Such information is provided by the color change in the reconstructed holographic image under exposure to the target analyte. The change in the spectral response of the sensors $\Delta\lambda$ is determined by the change in the effective refractive index of the material Δn, change in fringe spacing $\Delta\Lambda$ and in Bragg angle $\Delta\theta$.

$$\frac{\Delta\lambda}{\lambda} = \frac{\Delta n}{n} + \frac{\Delta\Lambda}{\Lambda} + \cot\theta \cdot \Delta\theta \tag{11.2}$$

The typical Bragg angles in this geometry of recording are close to 90° thus the contribution of the last term in (11.2) is negligible unless there is a significant deviation from this angle.

Changes in both lattice spacing $\Delta\Lambda$ and the refractive index Δn can contribute simultaneously to sensor's response but change in one of them usually dominates. This behavior can be modeled by incorporating electromagnetic wave equations and parameters describing the media, or material governing equations such as free energy of mixing [15]. The changes in lattice spacing $\Delta\Lambda$ arise due to swelling or shrinking of the material in the presence of an analyte. To make use of the second

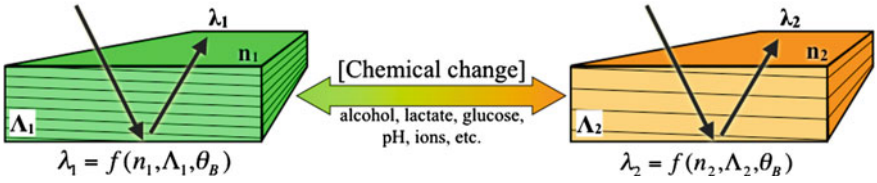

Fig. 11.3 The principle of holographic sensing. The reflectivity of the incident wavelength depends on the refractive index of the materials and their geometry. A chemical change triggers the sensor response from one state to the other resulting in a change in the wavelength of the diffracted light

mechanism to obtain observable change in the wavelength of the diffracted light, a significant change of the effective refractive index n must occur upon absorption of an analyte. One way of increasing the change in the average refractive index is to lower the refractive index of the holographic material, which can be achieved by increasing its porosity. Increasing the porosity has also another advantage; it increases the surface area for the interaction with the analyte, and facilitates diffusion of the analyte within the holographic matrix.

In addition to the spectral characteristics of the reconstructed holographic image, its brightness which is related to the diffraction efficiency of the hologram can also change. The diffraction efficiency of a volume phase reflection hologram is determined by [9]:

$$\eta = \tanh^2\left(\frac{\pi n' d}{\lambda \cos\theta}\right) \tag{11.3}$$

Differentiation of (11.3) shows that the change in the diffraction efficiency is determined by the change in the refractive index modulation n', change in the Bragg angle $\Delta\theta$, change in the probe wavelength $\Delta\lambda$ and change in the thickness of the grating Δd (11.4).

$$\frac{\Delta\eta}{\eta} = \frac{4}{\sinh\left(\frac{2\pi n' d}{\lambda\cos\theta}\right)}\left(\frac{\pi n' d}{\lambda\cos\theta}\right)\left(\frac{\Delta n'}{n'} + \frac{\Delta d}{d} - \frac{\Delta\lambda}{\lambda} + \tan\theta\Delta\theta\right). \tag{11.4}$$

11.2.2.2 Sensors Based on Transmission Holograms

This type of sensors requires an additional readout device such as a spectrometer or an optical power meter to detect changes in the optical properties arising upon interaction with a stimulus.

A split beam geometry used for recording a transmission hologram is shown in Fig. 11.4. The two recording beams are incident from the same side of the

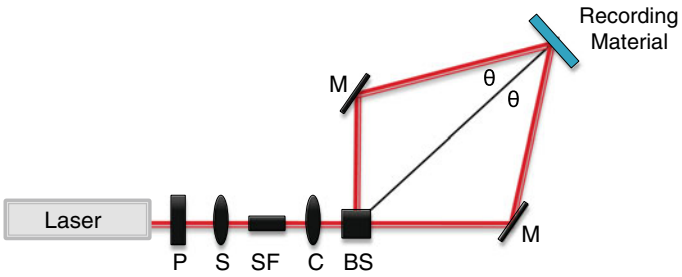

Fig. 11.4 Experimental setup for recording transmission gratings. *P* polarizer, *S* shutter, *SF* spatial filter, *C* collimator, *BS* beam splitter, *M* mirror

recording layer. When the two incident beams have the same incident angles to the recording layer's surface, the recorded structure (unslanted hologram) consists of planes of varying refractive indexes, that are perpendicular to the surface of the recording layer. Gratings recorded with two beams at different incidence angles to the surface of the recording layer are called slanted gratings, and for such structures, the resulting planes of varying refractive indexes are at an angle to the layer's surface.

The principle of operation of transmission holograms relies on the changes in the diffraction efficiency and the peak wavelength of the diffracted light upon interaction with a stimulus. The transmission hologram is probed with light of a specific wavelength and the readout of the transmitted light is carried out at a given angle. The diffraction efficiency of a volume phase transmission hologram is determined by [9]:

$$\eta = \sin^2\left(\frac{\pi n' d}{\lambda \cos\theta}\right). \tag{11.5}$$

where η is the diffraction efficiency, being the ratio of the diffracted and the incident beam intensities, n' is the refractive index modulation, d is the thickness of the holographic grating, and λ is the wavelength of the probe beam, and θ is the Bragg angle. When probed at the Bragg angle and at a particular wavelength the change in η arises due to variation in refractive index modulation or material thickness d. The latter can arise due to shrinkage or swelling and can result in a change in the Bragg angle and the wavelength of the maximal diffraction efficiency.

Figure 11.5 illustrates the sensing principle of a holographic transmission grating. Consider the case of a volume transmission grating with the following parameters: d_1, n'_1, Λ_1 and θ_1. Upon illumination, the grating diffracts the light and the diffraction efficiency of the grating is a function of d_1, n'_1, Λ_1 and θ_1. The interaction with the analyte causes dimensional changes of the sensitive film, producing changes in the optical properties of the film and in the geometry of the holographic grating. These changes cause alterations in the direction of the diffracted light and the diffraction efficiency, which is now a function of d_2, n'_2, Λ_2 and θ_2.

The exact contribution of each of the parameters can be estimated by modeling the diffraction efficiency change:

$$\frac{\Delta\eta}{\eta} = \frac{2}{\tan\left(\frac{\pi n' d}{\lambda \cos\theta}\right)}\left(\frac{\pi n' d}{\lambda \cos\theta}\right)\left(\frac{\Delta n'}{n'} + \frac{\Delta d}{d} - \frac{\Delta\lambda}{\lambda} + \tan\theta\Delta\theta\right) \tag{11.6}$$

Sensors based on transmission holographic gratings require both a light source for its illumination and a photodetector to monitor a diffraction efficiency alteration or a variation of the diffracted light direction. The main advantage of this type of sensors is that small changes in order of 10^{-5} in diffraction efficiency can be detected.

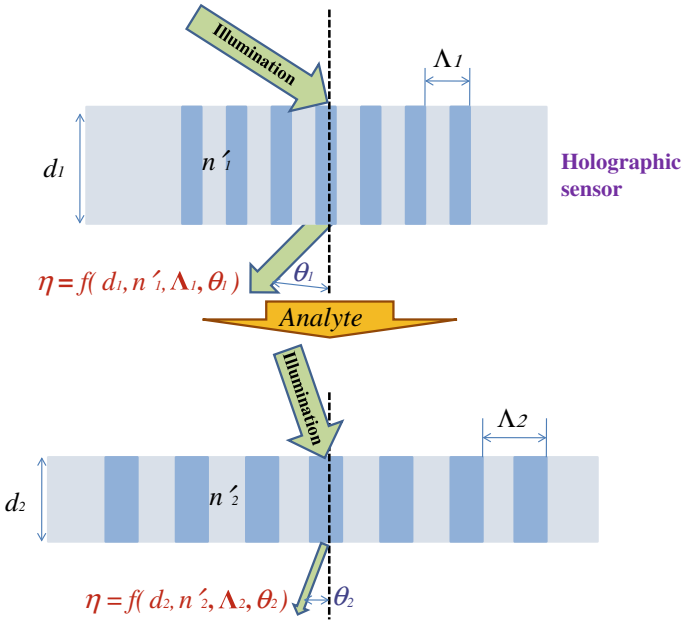

Fig. 11.5 The principle of operation of a holographic transmission grating sensor

11.2.3 Holographic Recording by Ultra-Short Laser Pulses

Contrary to typical holographic recording protocols, particles can be organized within a polymer matrix to produce a holographic grating using a high-energy frequency doubled Nd:YAG (Neodynium doped-Yttrium-Aluminum-Garnet) nanosecond pulsed lasers or other high energy nanosecond lasers. The typical output for laser ablation is 300 mJ with a 532 nm wavelength and a 258 s Q-switch delay. High energy laser radiation can reduce the size of metallic particles to nanometric scales by ablation to smaller particles [16], thus affecting their optical properties [17–20]. In Denisyuk reflection mode for holographic recording by high-energy laser writing, the nodes of the standing waves provide concentrated energy to reorganize the preformed silver nanoparticles, which are incorporated and formed in situ by perfusing silver salts [21]. In this setup, the laser beam is diverted using dichroic mirrors and lenses to strike the recording material at desired angles [22]. An important parameter during patterning is the total laser energy that reaches the recording material. This energy is typically affected by the optics and can be modulated by changing the spot area of incidence; larger patterning areas will have less energy striking the particles. For a high-energy laser, areas up to 2.5 cm in diameter can be used for effective recording [22]. Any material sensitive to absorption of the high laser energy can be used for holographic recording, typically silver nanoparticles (Ø = 50–100 nm) are used due to the coincidence of their absorption spectrum due to their surface plasmon resonance (SPR) with that of

green lasers [15, 21, 22]. The interaction between the laser light and the matter in situ may influence matter diffusion, ejection, oxidation, structure and distribution. These effects can contribute to the reorganization of the matter in the polymer matrix to form a grating. Since this fabrication approach is based on passing an absorption threshold to pattern the material, it may allow forming gratings for other low-cost and novel materials such as ink [23] to construct optical devices. Furthermore, this approach also opens the possibilities for patterning other materials such as graphene [24, 25], carbon nanotubes [26], and other nanostructures [27].

11.3 Holographic Sensing Materials

A holographic material suitable for sensing application must meet two main requirements: (1) it must enable holographic recording and (2) must be sensitive to a specific chemical or physical stimulus. This imposes specific requirements on the materials that can be employed in holographic sensors, and different strategies have been adopted to functionalize the materials, and thus make them sensitive to a specific stimulus. The simplest and the earliest explored approach to design of holographic sensing materials exploits the intrinsic properties of materials used for holographic recording i.e. hygroscopic nature of gelatin was utilized to fabricate reflection-type holographic sensors for detecting water content in hydrocarbons [28]. Yet, to broaden the applications of the sensors and to improve their sensitivity and selectivity, further modifications of holographic materials were carried out.

11.3.1 Photonic Materials in Sensing Applications

Holographic sensing materials can be divided into three groups based on their fabrication: (1) silver halides-based materials, (2) photopolymers, and (3) hybrid materials. In the first group of materials, the holographic grating consists of periodic planes of silver nanoparticles formed in a functionalized polymer matrix; sensitivity of the hologram to a specific stimulus arises from changes in the properties of the polymer matrix functionalized with stimuli responsive moieties. In photopolymers, refractive index grating is formed as a result of localized photopolymerization during holographic recording; the polymer formed bears receptor units sensitive to a specific stimulus. The third group of sensing materials i.e. hybrid materials are photopolymers modified with analyte sensitive nanoparticles such as zeolities, which can be redistributed in the photopolymer matrix during holographic recoding. The strategies used for the preparation of these three groups of materials are discussed in the following sections.

11.3.1.1 Silver Halide Chemistry

Silver halide chemistry is the earliest technique developed to fabricate holographic sensors. This approach is largely based on photography dating back to late 19th century, and the development of holography in the 1970s [29]. Traditional hologram emulsion contained a mixture of solidified gelatin doped with silver bromide nanocrystals (AgBr NCs) coupled with laser light-absorbing dye. In contrast to the traditional emulsion, the fundamental fabrication difference in holographic sensors is the development of a diffusion technique that allows impregnation of the recording media with silver halides after the formation of a polymer film [30].

The fabrication of a silver halide based holographic sensor consists of three main steps: (1) preparation of a functionalized polymer matrix that can consistently respond to an analyte or physical parameter, (2) photosensitization of the polymer matrix, and (3) formation of diffraction gratings in the polymer matrix through multibeam interference of laser light and photographic processing [1]. Figure 11.6 shows each step in fabricating holographic sensors through silver halide chemistry. The first step in the silver halide system is to prepare a functionalized polymer

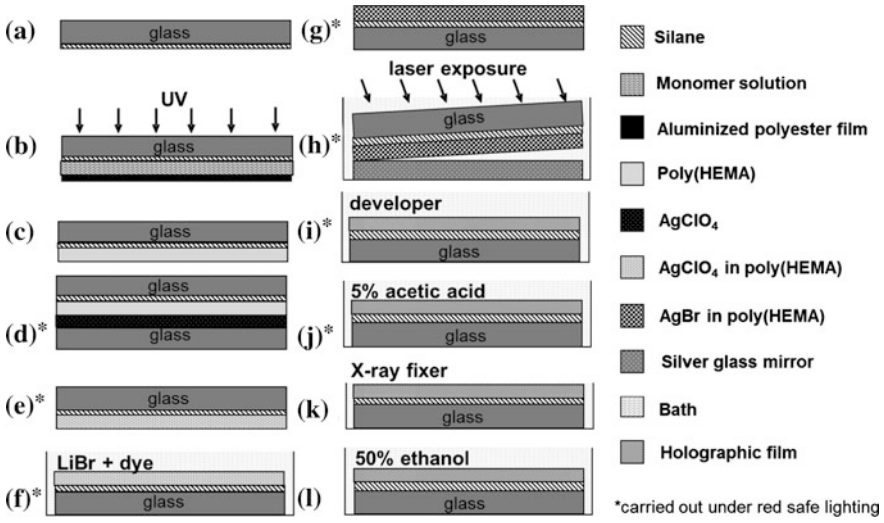

Fig. 11.6 Formation of holographic sensors through silver halide chemistry. **a** Formation of a layer of silane on the glass slide. **b** UV-light initiated free radical polymerization of the monomers on the slide. **c** Rinsing the system with ethanol to remove the unreacted residues, and drying it under tepid air current. **d** Silver nitrate diffusion into the polymer matrix. **e** Drying the polymer under tepid air current to fix the silver ions into the polymer matrix. **f** Immersing the polymer in a LiBr bath to obtain AgBr NCs in the polymer matrix. **g** Rinsing the system with deionized water and treatment with ascorbic acid to increase the sensitivity to laser light. **h** Laser light exposure in Denisyuk reflection mode to form a multilayer diffraction grating in the polymer matrix. **i** Formation of silver nanoparticles in the recording medium using a photographic developer. **j** Stopping the developer's action using acetic acid. **k** Hypoing the hologram using sodium thiosulfate. **l** Rinsing the system with ethanol solution to remove the residual dye in the hologram matrix

matrix, and impregnate the polymer matrix with silver ions [31, 32]. This step is needed because forming an emulsion consisting of the functional monomers in solvents and aqueous silver halides is hindered due to their immiscibility. Hence, silver halides are introduced into the polymer matrix using so-called diffusion technique. Silver salts such as aqueous silver nitrate or silver perchlorate in organic solvents (0.1–0.5 M) are diffused into a polymer matrix, which may be poly (2-hydroxyethyl methacrylate) pHEMA or poly(acrylamide) pAAm with a thickness of ∼10 to 20 μm. After the polymer matrix is dried under tepid air, the polymer matrix is submerged into an aqueous solution consisting of LiBr (0.3 mM) and a photosensitizing dye (e.g., 1,1′-diethyl-2,2′-cyanine iodide) under safe lighting. The reaction of LiBr with silver ions (Ag^+) produces AgBr NCs with diameters ranging from 10 to 30 nm [31]. The photosensitizing dye permanently attaches to surface of the AgBr NCs. After this step, the polymer matrix is rinsed with deionized water. The polymer matrix maybe immersed in ascorbic acid to improve the sensitivity to laser light. At this stage, the polymer matrix and AgBr NCs system is called recording medium.

Formation of a grating in the recording medium consists of laser writing of a latent image and photographic development of this image. The latent image is a collection of labeled AgBr NCs, which are subject to photographic development. The latent images are recorded in Denisyuk reflection mode, in which the recording medium is placed over a mirror with a tilt angle from the surface. Tilting the sample allows offsetting the diffraction angle [33]. Under safe lighting, an expanded laser beam is exposed onto the sample, where the incoming beam and the beam reflected from the mirror forms a standing wave in the recording medium (Fig. 11.7). The standing wave forms a multilayer pattern running parallel to the surface of the recording medium. This pattern has a lattice spacing of approximately half of the wavelength of the laser light.

Under safe lighting, the recording medium with latent image is submerged in an aqueous photographic developer. This solution consists of a number of chemicals

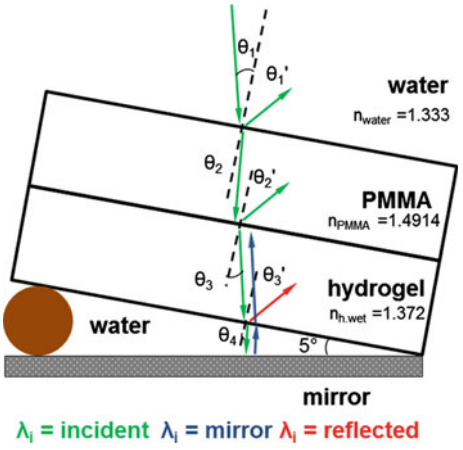

Fig. 11.7 Formation of holographic sensors in Denisyuk reflection mode

that attack labeled AgBr NCs and reduce them to silver metal (Ag^0) nanoparticles (NPs). A typical developer consists of 4-methylaminophenol sulfate (0.3 %, w/v), ascorbic acid (2 %, w/v), sodium carbonate (5 %, w/v), and sodium hydroxide (1.5 %, w/v) dissolved in deionized water [34]. Following the development of Ag^0 NPs, the recording medium is submerged in acetic acid solution (5 %, v/v), which allows stopping the action of the developer to prevent overdevelopment and distortion in the recorded image. The diameter of resulting Ag^0 NPs ranges from $\sim$10 to 50 nm [35]. This process yields a diffraction grating consisting of periodic Ag^0 NPs in the polymer matrix.

The efficiency of the diffraction can be further improved by removing excess AgBr. The post-development process consists of hypoing and bleaching the hologram. Sodium thiosulfate is the standard hypo solution that dissolves undeveloped AgBr NCs and improves the diffraction efficiency, which is otherwise reduced by the interference of light with undeveloped AgBr NCs. The second step in the post-development step is bleaching the hologram. Ag^0 NPs are converted back to AgBr NCs, which yields improved diffraction efficiency due to the change in its refractive index that can transfer the incoming light to the next lattice spacing more efficiently than Ag^0 NPs.

The ability to produce holographic gratings with silver halide chemistry allows a range of diffraction gratings utilizing the traditional approaches. However, the number of fabrication steps is lengthy and tedious, and this process is incompatible with biological assays inhibiting enzymes [36]. Nevertheless, this image recording technique remains a robust approach to fabricate holograms in hydrophilic polymers for aqueous applications.

11.3.1.2 Photopolymer Chemistry

Photopolymers are materials that change their optical properties in response to illumination with light. However, to be suitable for holographic recording, the photopolymer must be capable of a localized response to the light, ideally capable of recording interference patterns of thousands of lines per millimeter, or features of sub-micron dimensions. This allows the creation of a photonic structure within the polymer that is capable of diffracting light, via the recording of the hologram in the material.

To be used in sensing applications, however, the photonic structure formed by the above methods must also respond to the analyte so that characteristics of the hologram are altered. For volume holograms, layer permeability is also a key issue, because the analyte needs to diffuse through the polymer layer to cause a detectable change in the hologram's characteristics [1]. The polymer must also be sufficiently robust to maintain the photonic structure under exposure to the analyte's environment and, in most applications, it must maintain this for multiple cycles of use.

This need to balance permeability with stability of the photonic structure narrows down the suitable sensing materials. Photopolymerizable systems using

acrylamide monomers and poly(vinyl alcohol) PVA have been shown to produce holograms that shift their reconstruction wavelength with complete reversibility through many cycles of low and high humidity [37].

Such photopolymer layers are prepared by coating and drying a solution, which is a mixture of monomers, sensitizers, and dissolved polymer on a suitable substrate. Because of the ease of preparation of the polymer films and the fact that the holograms are self-developing, fabrication of holographic sensors in such materials is a straightforward two or three step process. First, the components of the photopolymer are mixed and coated on a substrate. The mixture usually consists of at least two monomers, a photoinitiator, co-initiator and a polymeric binder such as PVA [38–45]. Heat is usually needed to dissolve the binder, but otherwise it is a simple mixing process. The photopolymer solution is then coated onto the glass or plastic substrate and allowed to dry for several hours on a level surface to form the photosensitive layer as shown in Fig. 11.8a. The next step is to expose the photosensitive layer to the appropriate interference pattern, at the appropriate laser wavelength to create the photonic structure. This is shown in Fig. 11.8b. Where light is absorbed by the layer (via the photoinitiator), a polymerization process is initiated which converts the monomers into polymer and triggers local diffusion processes. The local refractive index is thereby altered through changes in the local density and polarizability of the molecules, and the spatial variation in intensity in the interference pattern is recorded as a spatial variation of refractive index. The hologram can be viewed immediately, but with some formulations a short

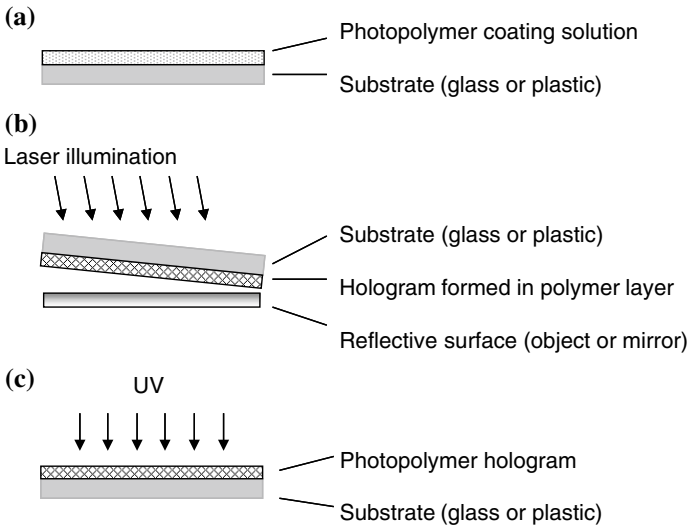

Fig. 11.8 Formation of holographic sensors through photopolymer chemistry. **a** Drying the photopolymer coating solution on the glass slide. **b** Laser light exposure in Denisyuk reflection mode to form a volume diffraction grating/hologram in the polymer matrix. **c** UV-light fixing of the hologram

additional step is advisable, exposure to white or UV light [46] to remove remaining sensitizer and stabilize the hologram (Fig. 11.8c).

The self-developing nature of the photopolymer materials means that the photonic structure is fully formed during the exposure step and the hologram is visible at that point. Denisyuk reflection hologram recording is one of many formats that can be used to form the hologram. The final appearance depends on whether a reflective object or mirror was used to create the hologram, what wavelengths and angles were used in this step, and whether multiple recording beams were used. For most holograms, a small tilt angle is introduced between the photosensitive layer and the mirror/object beam, typically between 5° and 10°. This prevents the beam diffracted by the photonic structure from being obscured by the beam that is specularly reflected from the layer surface.

The flexibility of this preparation process has allowed for a wide range of characteristics in the final hologram. For example, by altering components of the basic formulation, hard impermeable layers have been formed [47], new sensing properties have been introduced [48] and new sensing strategies have been developed in which the ability to form a hologram is the sensing action [49]. Because of the role of diffusion in the recording process, it has also been possible to pattern the dopant materials within the layer. This gives further scope for a tailored sensing response. There is also significant flexibility around the wavelength used as long as the appropriate initiator is chosen. Initiators sensitive to red, green and blue are available [50] which is useful in sensing applications where a particular initial color is desirable in the hologram. For example, if shrinkage rather than swelling is expected, a hologram diffracting the longer, red wavelengths is likely to be a desirable starting point, but a blue diffraction might be a more suitable starting point for an analyte that swells the layer.

Photopolymer materials have a key role to play in holographic sensing because of the ease of preparation of the sensors, which facilitates their mass production. Further development is needed in ensuring specificity for certain analytes, and to further improve robustness in some environments, however the variety of formulations possible and the wide flexibility in the photonic structures that can be formed indicate the potential for these materials. One approach to the functionalization of photopolymer materials is the incorporation of zeolite nanoparticles in them. The following section describes the features of nanozeolites and their use in holographic sensing.

11.3.1.3 Sensors Containing Zeolite Nanoparticles

The synthetic zeolites, historically referred to as ‘molecular sieves’, are low-density crystalline aluminosilicates possessing regular micropores of dimensions commensurate with molecules (0.3–2.0 nm). These micropores (one-, two- and three-dimensional) create a vast network of channels and cages with well-defined sizes and shapes. Other molecular sieves, the so-called zeotype materials, containing different tetrahedral (T = Si, Al, Ti, P, Ga, Ge, B) framework cations have

also been synthesized. Their corner-sharing tetrahedral building units (TO_4) further extend the diversity of zeolite structures. This remarkable flexibility in structure type (220 different structures known to date) and chemical composition allows tunable chemical and physical properties [51].

Over the past decade, much effort was devoted to prepare zeolites with enhanced accessibility to their micropores. Many new routes to hierarchical zeolites have been revived and discovered, such as: (1) post synthesis modification by de-silication, de-alumination or steaming, (2) one-step hydrothermal crystallization in the presence of specific organosilane surfactants acting as mesopore modifiers, and (3) synthesis of nanosized zeolite crystals with or without organic templates. The post-synthesis methods, such as steaming and chemical treatments are well documented and in commercial use, but they unavoidably lead to, inter alia, a decrease in zeolite crystallinity, the loss of a portion of the starting material, the creation of many defects, inhomogeneous chemical compositions and a hitherto uncontrolled broad distribution of mesopores, not always properly connected to the microporosity.

The nanometer scale (<500 nm) zeolite crystals develop large external surface where up to 30 % of their T atoms can be located and are intrinsically of better quality than the crystals produced by an intrinsically destructive top-down approach. A decrease in the size of zeolite crystals results in a considerable increase of their external surface and the properties associated with the latter (adjustable surface charge, hydrophilicity/hydrophobicity, ion-exchange) play an ever-increasing role (Fig. 11.9). The surface properties provide new possibilities to explore adsorption and reaction of bulky molecules that do not normally interact with the micropore volume of the zeolites.

The zeolite nanoparticle research faces new challenges in their shaping in the form of membranes, films, self-supported bodies, since the interactions between the zeolite and its binder or support will involve the external surface of the zeolite.

Besides, the kinetics of adsorption and desorption are related to the particle size and therefore nanosized zeolites have the potential to increase substantially the productivity of existing processes or to drastically reduce the size of new devices.

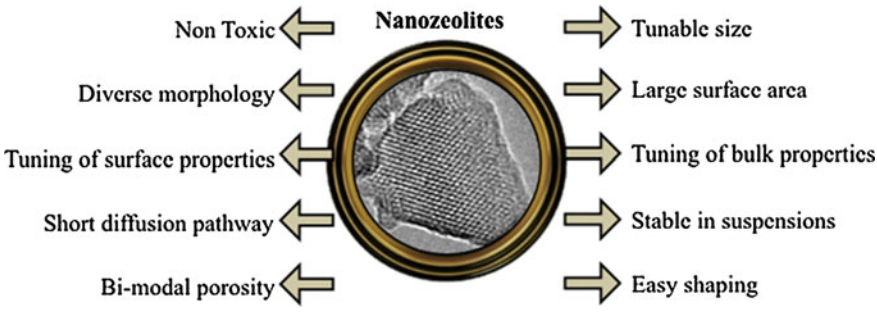

Fig. 11.9 Properties of nanosized zeolites

Nanosized zeolites are usually synthesized at low temperature under hydrothermal conditions. The initial system is usually an aluminosilicate suspension that evolves under the combined action of mineralizing (OH^-, F^-) and structure-directing agents (SDAs). The SDAs could be alkali metal cations or positively charged organic molecules. The generally accepted scheme includes the arrangement of SiO_4- and AlO_4-tetrahedra around charged templating species, i.e. hydrated alkali metal cations or organic molecules. The synthesis of nanosized zeolites is strongly influenced by the: (1) organic additives or structure-directing agents, (2) type of precursor synthesis gel/suspension, (3) initial silicon and aluminium source, (4) synthesis conditions as temperature, pressure and time, and (5) heating method like conventional, microwave and sonication. A dedicated effort to understand the fundamentals of the above-mentioned parameters generated valuable knowledge to direct the synthesis and harvest zeolite nanocrystals with pre-determined properties [52–54].

The nanosized zeolites have high quality crystals with diverse sizes and morphology that are important for fundamental studies and advanced applications (Fig. 11.10). In addition the crystals can be modified via post-synthesis treatment that changes the surface and bulk properties and lead to high selectivity and also allows fast diffusion (Fig. 11.11).

New fields will also open up to due to their exceptional properties and because they can be supplied in various forms, such as colloidal suspensions, optical quality thin films, membranes and self-supported morphologies (Fig. 11.12).

A large research effort is dedicated to the use of zeolite nanocrystals to prepare thin-to-thick zeolite layers for optical devices and gas/liquid sensors. The common preparation techniques of such devices include: (1) screen-printing, (2) sol-gel techniques, (3) dip- and spin-coatings, (4) direct growth with or without pre-seeding of the substrates, and (5) ink-jet printing. Factors to consider when selecting the production technique include the required film characteristics, purity, porosity, reliability, reproducibility and costs. Zeolite films are used for preparation of optical quality films with a thickness in the range 50–170 nm through spin-on or sol-gel deposition methods [55, 56].

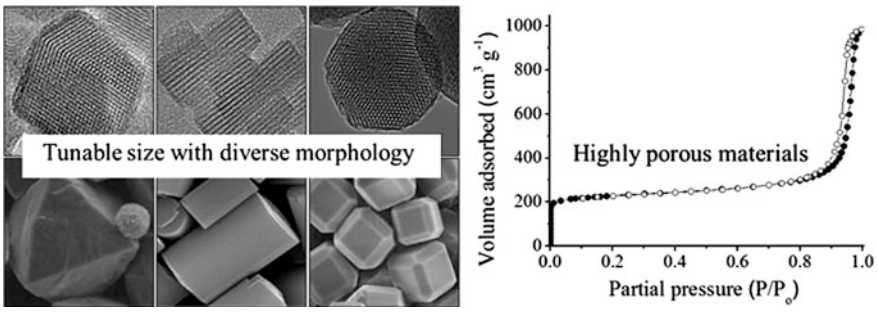

Fig. 11.10 Highly porous zeolite nanoparticles exhibiting different shape and size

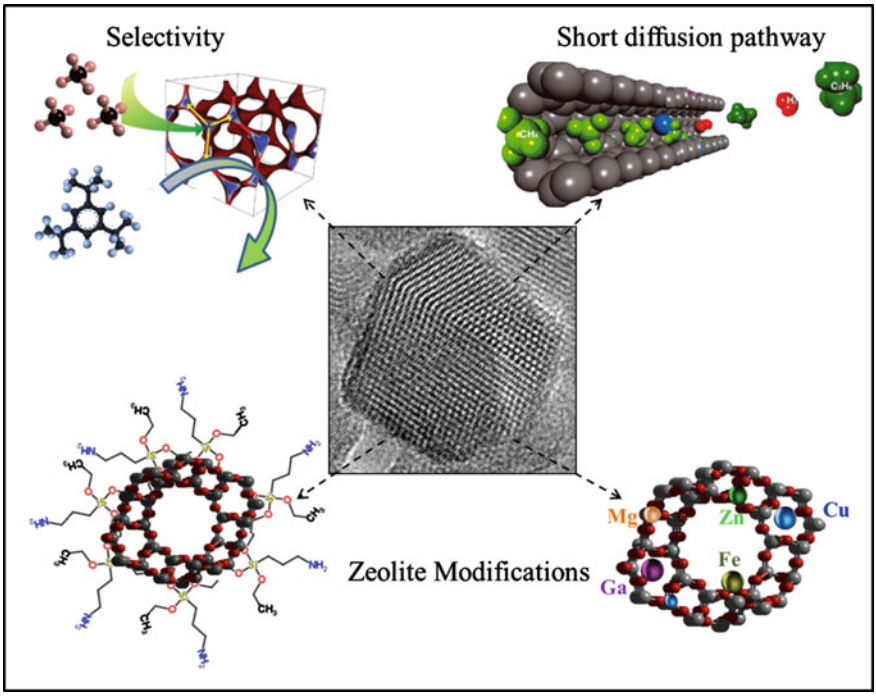

Fig. 11.11 Nanosized zeolite crystals: high selectivity, short diffusion path, surface and bulk modification

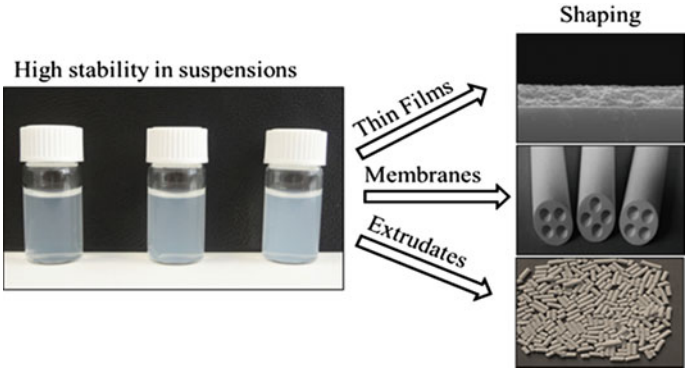

Fig. 11.12 Nanosized zeolites in colloidal suspensions and shaped in films, membranes and self-supported bodies

The large and reactive external surface of the zeolite nanocrystals is critical to design different morphological constructions, where the consequence processing does not affect the intrinsic properties of nanocrystals. The supported zeolite films

are used for separation, membrane, optical devices, chemical sensors and medical applications.

The versatility of zeolites properties like their pore structure, surface area, catalytic activity, particle size and morphology is of particular interest for different types of sensors. Their adsorption capacity, high-surface area and porosity, presence of mobile ions, and catalytic activity make them attractive candidates for chemical sensing/detection. In general the sensors are categorized in four groups based primarily on their mode of action: (1) chromatography and spectrometry, (2) electrochemical sensors, (3) mass sensors, and (4) optical sensors. Zeolite-based chemical sensors are divided in two groups depending on the respective role of the molecular sieves. The zeolite can act as the main functional element, in the case of sensors based on conductive, adsorptive, or catalytic properties of one specific type molecular sieve and its interaction with the analytes. The second group includes devices where the zeolites are supplementary or secondary elements, e.g. host-guest materials with active sites encapsulated within the zeolite pores.

The application of nanosized zeolites in chemical sensing, biomedical and biological analyses has shown their great potential [57–62]. Zeolite nanocrystals offer promises in the above applications due to their highly tuneable size- and shape-dependent chemical and physical properties. Their unique surface chemistry, high thermal stability, high surface area and large micropore volume are important for designing of optical devices. Useful strategies for functionalization of zeolite nanoparticles open up the possibility of using the materials in areas such as environmental drug delivery, medical imaging and other biomedical applications.

An example of the potential of zeolite nanoparticles in sensing is their use in functionalizing photopolymer materials for holographic sensors. The incorporation of these nanoparticles into a holographic photopolymer medium can improve its dynamic range, and thus its ability to record high diffraction efficiency holograms [63]. This improvement is ascribed to the redistribution of the nanoparticles during holographic recording. The nanoparticles are redistributed within the photopolymer material into either the bright or dark fringe regions [64, 65]. For example zeolite nanoparticles incorporated in an acrylamide-based photopolymer are redistributed into the dark fringe regions during holographic recording (Fig. 11.13a) [66]. The total refractive index modulation n' created during recording (Fig. 11.13b) has two components: (1) photopolymerization and diffusion driven density variation of the polymer material and (2) the zeolite nanoparticle redistribution. The contribution of the zeolite nanoparticles to the refractive index modulation n'_n can be expressed as:

$$n'_n = \frac{2f_{nanoparticle}}{\pi}\left(n_{nanoparticle} - n_{host}\right)\sin(\alpha\pi), \tag{11.7}$$

where $n_{nanoparticle}$ and n_{host} are the refractive indexes of the nanoparticles and the host polymer matrix and $f_{nanoparticles}$ is the volume fraction of the redistributed nanoparticles, α a is the fraction of the period spacing with a high-concentration of nanoparticles.

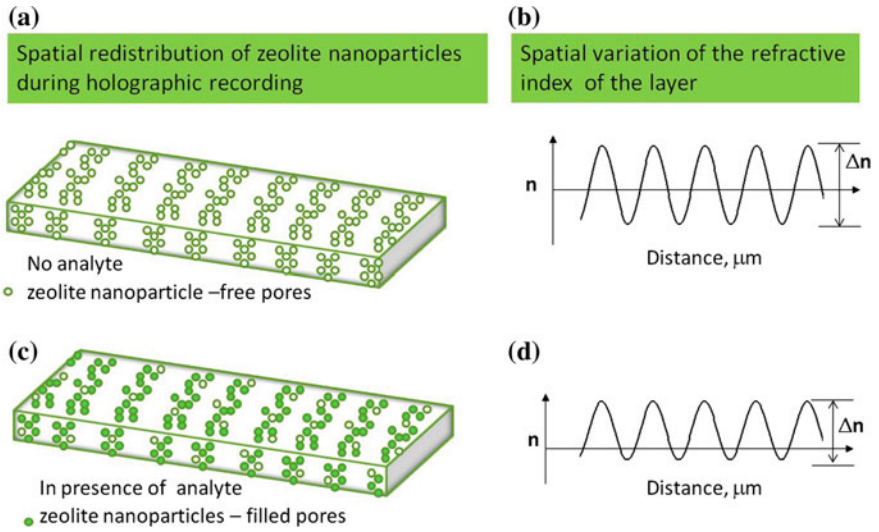

Fig. 11.13 Schematic showing the redistribution of nanoparticles within the holographic grating and the effect of analyte molecules on Δn of the grating before (**a**, **b**) and after exposure to the analyte (**c**, **d**)

Upon exposure to an analyte, the target molecules are adsorbed to the nanoparticles, causing $n_{nanoparticle}$ to increase, and change n_n'. This therefore changes the overall refractive index modulation n'. If the nanoparticles are preferentially distributed in the dark fringes, the exposure to the target analyte Fig. 11.13c decreases the overall refractive index modulation Fig. 11.13d. As shown in (11.5), the intensity of the light diffracted by the grating is directly related to the refractive index modulation n'. Therefore, by monitoring changes in the diffracted beam intensity during exposure to an analyte, holographic gratings recorded in the nanoparticle-doped photopolymer can be used as a sensing device. By selecting nanoparticles with a porous structure e.g. zeolite nanoparticles, adsorption of the target molecules to the nanoparticles can be maximized, thus maximizing the sensor's sensitivity. By controlling zeolite pore size or by incorporating functionalized nanoparticles (e.g. having metal ions/nanoparticles in the zeolite pores) [60], an improved selectivity of the holographic sensing device to the target analyte can be achieved.

11.3.2 Strategies for Materials Functionalization

Holographic sensors can be classified with regard to their fabrication process as silver halide based materials, photopolymers or nanoparticle doped materials, which were discussed in the previous sections. Depending on the mechanism of operation,

another classification of holographic sensors can be adopted: (1) structures with patterned analyte sensitive species; in such structures, interaction of the analyte with the patterned holographic structure changes the refractive index modulation; such structures can operate both in transmission or reflection holographic sensors (2) in the second type of structures, no spatial redistribution of stimuli responsive functionalities is needed; such structures work best in reflection mode; the interaction of such sensors with the stimuli results in changes in Bragg peak and thus color of the reconstructed holographic image.

11.3.2.1 Structures with Redistributed Analyte-Sensitive Species

To produce such structures, the analyte-sensitive species must be able to diffuse within the material during holographic recording to produce analyte receptor-reach and receptor-depleted regions. This approach was applied to nanozeolite doped photopolymers [60, 67, 68]. Extensive research into acrylamide-based photopolymer nanocomposites containing three different zeolite nanoparticles with varying microporosity, namely Silicalite-1 (MFI-structure, Ø = 30 nm), AlPO-18 (AEI-structure, Ø = 180 nm) and Beta (BEA-structure, Ø = 40 nm) has been reported [63, 68–70]. Preliminary studies into the sensing ability of transmission gratings recorded in BEA- and MFI-type zeolite-doped acrylamide photopolymer layers have been reported for the analytes such as toluene [67] and isopropanol [60].

11.3.2.2 Structures with No Redistribution of the Analyte Sensitive Species

The simplest examples of such structures exploit intrinsic properties of holographic recording media, and the earliest research in the holographic sensors area relies upon such structures. Hygroscopic properties of gelatin were employed in the earliest holographic sensors that were capable of detecting water content in hydrocarbon solvents [28]. The recorded grating acts as a readout system and is not involved in sensing. More advanced sensors within this category comprise various hydrogels containing appropriate receptor groups. Polymer matrices can be functionalized with a range of monomers that allow in sensing analytes specifically. The functionalization can be achieved before or after polymer formation. A criterion in selecting these functional groups is that they should have acrylate or methacrylate groups that allow covalent crosslinking in the polymer matrix. This strategy was used for pAAm and pHEMA hydrogels to obtain sensors sensitive to pH [31, 32, 71–73], ions [73–77], glucose [73, 78–80], temperature [37, 81] and other stimuli [1]. For example, copolymerization of a hydrogel with the monomers bearing acidic or basic groups, along with the suitable crosslinkers, enabled the fabrication of sensors with tunable pH response [32]. Ionization of the functional groups in pH sensors swells the grating due to electrostatic and osmotic forces which draws or expels counterions and water into or out of the hydrogel matrix.

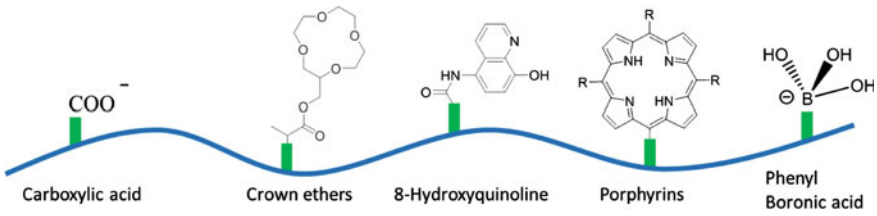

Fig. 11.14 Functionalization of holographic sensors with various monomer groups

Over the last two decades, a range of functional groups has been utilized in sensing chemical species (Fig. 11.14). These include carboxylic acid, crown ethers, 8-hydroxyquinoline, porphyrin and phenyl boronic acid derivatives. The sensing properties of these functionalities are well known in other types of sensors. Structures with no redistributed sensing species were also applied for zeolite nanoparticles based sensors to obtain structures sensitive to toluene [67]. Further description of holographic materials bearing these functionalities can be found in Sect. 11.4 in regard to their applications.

11.3.2.3 Functionalization Strategies Based on the Hydrophobicity and Hydrophilicity of the Recording Material

Holographic sensors can also be classified by the type of fabrication materials and their properties, for example, there are holographic sensors fabricated in hydrophilic materials for sensing in aqueous solutions, and there are holographic sensors fabricated in hydrophobic materials for non-aqueous applications. The polymers used in holographic sensor fabrication determine not only the nature and type of analyte, but also the recording technique of the holographic layers. Hybrid materials can be conceived for the integration of multianalyte holographic sensing by having hydrophobic and hydrophilic domains. These domains can include nanoparticles as in traditional holography and enhance the holographic sensitivity and refractive index contrast, also useful for high laser energy patterning. These materials can be selected from block copolymers or hybrids with nanoparticles with enhanced optical contrast [82]. In sensing mechanisms, changes in Λ for example can be originated by expansion or contraction of the polymer matrix material. This expansion and contraction is caused by the chemical interactions with the analytes. The fringes are made of refractive index varying material and could also be made of metallic particles that do not swell or contract. However, changes in refractive index can be triggered by physicochemical modifications of the fringes or the polymer matrix. For instance, metallic nanoparticles can undergo chemical transformations that modulate their refractive index upon reduction or oxidation with chemical analytes [83].

11.3.3 Design of Sensors by Dynamic Simulations of the Properties of a Multilayer Structure

Rational design of holographic sensing materials can be facilitated by computer simulations. It has been demonstrated that the principle of sensing of a multilayer structure can be modeled by finite element analysis. For example [31], finite-element simulations of the multilayer structured allowed analyzing the wave propagation and optical response in holographic sensors [71, 78]. There are other analytical methods that predict the reflectivity of light in periodic structures that work for arbitrary periodic dielectric structures and can be applied to the particular case of one dimensional photonic devices such as holograms. These methods can be exact solutions to the Maxwell equations or approximations by matrix formalisms. The simulated model comprised a cross-section of several stacks of silver nanoparticles with a mean radius of 13 ± 10 nm (Fig. 11.15a). Within each stack the particles were uniformly distributed in the vertical direction, while in horizontal direction, normal random distribution was used. The spacing (vertical lattice constant) between stacks was initially set to 188 nm. The model was used to simulate the wave propagation through the lattice for the wavelength range of 400–1000 nm. Simulations were performed to analyze the effect of expanding the holographic sensor on the reflection band gaps. Figure 11.15d shows that the multilayer structure displayed a reflection band gap centered at a wavelength of ~500 nm (the least transmitted). This is equivalent to the optical response displayed by the holographic sensors at a pH of 4.00 [71]. To simulate the dynamic tunability, the multilayer structure was expanded while keeping the number and dimensions of the nanoparticles the same. As shown in Fig. 11.15a–c, the expansion increased the effective-stack spacing, and stack size, however reduced the concentration of nanoparticles per stack. The reflection spectra showed a red shift in the reflection bands as the stack spacing was increased (Fig. 11.15d). The expanding multilayer structure displayed a color change varying across the visible spectrum from ~500 to 815 nm. With an increase in stack spacing, the efficiency of the multilayer structure decreased, shown by the decrease in the intensity of the reflection dip. This was due to the decrease in the concentration of nanoparticles present in each stack, which reduced the effective index contrast between the nanoparticle stacks and medium.

To further test this hypothesis, additional simulations were performed with varying number of particles per stack. Figure 11.15e illustrates the simulated reflection spectra for the two geometries with same lattice spacing but different number of nanoparticles per layer. Decreasing the number of nanoparticles from 60 to 30 decreased the effective refractive index of the stacks, and therefore this trend reduced the index contrast between stacks and the hydrogel. This led to a weaker reflection dip, which could be observed from the simulated reflection spectra (Fig. 11.15e). The multilayer structure with 30 particles per stack displayed about 55 % weaker band gap and reflected less light. The position of the reflection band did not change as the effective lattice constant remained unchanged.

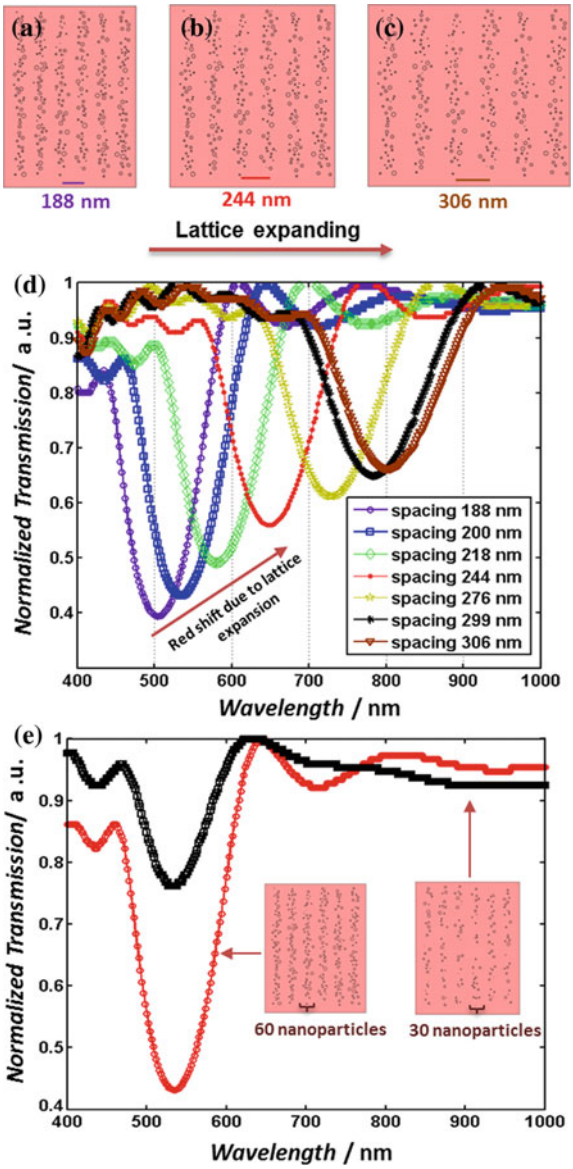

Fig. 11.15 Simulated optical transmission spectra for the nanoparticle stack based holographic sensors [31]. **a**–**c** Modeled geometries of a horizontally expanding multilayer structure consisting of silver nanoparticles dispersed within a hydrogel matrix. **d** The simulated transmission spectra for multilayer structure with fringe spacing expanding from 188 to 306 nm. **e** Simulated spectra and modeled geometries of a holographic sensor with a lattice constant of 200 nm containing 60 and 30 nanoparticles per fringe

Even though the efforts to simulate the photonic properties given the appropriate material result in full understanding on the light propagation, the selection of the materials remains empirical and work on the incorporation of physicochemical models and photonic models is still required. Furthermore, on the coupling such models with those of inter-molecular interactions between the sensor materials and analytes, models for practical application can be created.

11.4 Applications

The applications of holographic sensors range from gases, pH, and temperature to drugs and enzymes. In the following section, some examples of holographic sensors are described.

11.4.1 Sensors for Gas Phase Analyte

The gas sensors have expanded into a sizeable field, both in terms of financial investment and the number of published articles [84–90]. Effective monitoring of levels of potentially hazardous or toxic gases in the workplace is a necessity and requirement. The level of toxic fumes from waste products must also be monitored to minimize contamination to the environment. The global market for gas sensors is expected to reach $2.5B by 2020, driven largely by new regulatory initiatives [90]. The range of fields that require gas sensing technologies is diverse involving areas such as the chemical processing, petrochemicals, atmospheric monitoring, and breath analyses. A breakdown of the different gases for which sensors are most in demand is reported by Grand View Research Inc. [90]. The market report indicates that sensors for carbon dioxide, carbon monoxide, oxygen and nitrogen monoxide are the most in demand, making up 63.6 % of the total market segment. Other required sensors primarily comprise methane (CH_4), ammonia (NH_3), hydrogen, and hydrocarbon sensors.

There are many different technologies under development for optical gas sensors, most of which are based on the principles of optical absorption, fluorescence, or chemiluminescence [91]. Refractometric sensors, for which the resonant wavelength depends on changes in the refractive index of the surrounding medium, are another option with potential for gas sensing purposes. This principle has been used to develop SPR and optical fiber based gas sensors [92, 93].

Holographic gratings recorded in photopolymer media can operate as refractometric gas sensors due to changes in the refractive index or thickness of the grating medium on exposure to a gaseous analyte. The variety of fabrication techniques and materials for optical gratings recording enabled fabrication of structures sensitive to several analytes so far. Photonic structures have been suggested for gas sensing but are limited to operation based on light absorption properties of gas molecules in near infrared [94, 95]. Holographic gratings have been used as sensors for analytes in solution, but in limited cases for gaseous analytes. The use of hydrogel holographic sensors is limited to aqueous environments. Fabrication of holograms in hydrophobic materials enables their use in non-aqueous environments or without interference from water. This is paramount for gas sensing since water moisture is present in the atmosphere and would affect the holographic sensor performance.

Additionally, electronics accompanying the sensor devices are a hurdle when remote access or monitoring is required; holograms on the contrary can use diffraction gratings as a transducer of the signal [96].

11.4.1.1 O_2, N_2, Alkanes, Alkenes, Alkynes, and NH_3

Oxygen is traditionally measured by redox reactions on electrode surfaces that consume it in the process, and other methods use fluorescence quenching. These processes are limited by the availability of materials or the oxygen consumption. The irreversibility of the sensing process imposes a limitation, and the reversibility can yield weak interactions and a complex readout signal. This is similar for hydrocarbon gases alkanes, alkenes and alkynes, and volatile organic compounds (VOCs). Current technologies for real time sensing of hydrocarbon gases and VOCs [97] are not able to distinguish molecular differences or get high signals. Ammonia, as oxygen, is measured with potentiometric techniques that consume or solubilize the analyte; others include absorbent semiconductors, which also consume the analyte or themselves [98]. Ammonia sensors are easily exhausted, requiring sensor's replacement after measuring large quantities of ammonia; furthermore, typical ammonia sensors cannot measure high concentrations of ammonia and exhibit a detection limit of 100 ppm [99]. Therefore, these sensors are not suitable for high analytes concentration environments, where special protection and rapid continuous monitoring is required. Holographic gas sensors provide a solution to these hurdles since they are able to measure such gases reversibly.

Hydrocarbons and VOCs have aliphatic chains that can hydrophobically interact via Van der Waals' forces. Hydrophobic interactions are sufficient to trigger sensing action in holographic sensors, and are reversible. The design of holographic sensors for VOCs and hydrocarbons is based on these mechanisms. The recognition component of the sensor should have reversible hydrophobic interactions with gaseous analytes. This material not only must be compatible with the analyte but also comply with holographic recording. In other words, the material should be hydrophobic, optically transparent and light sensitive for recording the laser light wavefronts. Ultrashort laser pulse patterning by ablation has been used in polystyrene and polypropylene, and also more successfully with poly(dimethylsiloxane) (PDMS) [15, 21]. VOCs are inert to silver particles, and there is no evidence of chemical reactions between the silver particles and hydrocarbons, that change their refractive index. Therefore, hydrocarbons and VOCs swell the holographic sensor matrix. A plethora of VOCs can be distinguished: branched and unbranched alcohols, polyols, molecules with carbonyl groups. High molecular weight ketones, alcohols and hydrocarbons in the liquid state such as *n*-pentane, 1-pentene, 1-pentyne, hexane, heptane, octane, decane, 4-methyl-2-pentanone, heptanone, hexanol, heptanol, iso-amyl alcohol and *tert*-amyl alcohol can be detected by holographic gas sensors. Since hydrophobic interactions swell PDMS chains, surface electrostatic potentials are the cause of the holographic response.

Oxygen and ammonia can form weak dipoles upon interaction with other molecules or species and are able to form reversible covalent bonds due to partial charges in their molecular structure [98, 100]. Thus, a holographic sensor aiming to detect these gases should exploit the nature of their molecular interactions. A drawback is the high reactivity of these gases. The holographic sensor response can also be affected by refractive index in combination to swelling, hence, a sensor material for oxygen and ammonia should selectively accept charged or partially charged molecules and generate molecular changes that affect either refractive index or swelling. For example, ion-exchange membranes are transparent, and selectively interact with charged or partially charged molecules and are therefore ideal candidates for the construction of holographic oxygen and ammonia sensors. Polar hydrophilic interactions with sulphonate groups in Nafion cause changes in the position of the Bragg peak and intensity in reflection-type holographic sensors. Physical phenomena such as absorption, diffusion, swelling, and ionic dissociation may affect the sensing process [101].

11.4.1.2 Zeolite Nanoparticle Doped Sensors for the Detection of Alcohols

As described in Sect. 11.3.1.3, zeolite nanoparticles are an attractive option for the functionalization of photopolymer-based sensors. They are particularly promising for developing gas sensors due to their porosity, which allows for increased adsorption of gas molecules and selectivity.

The diacetone-acrylamide-based photopolymer doped with BEA type zeolite nanoparticles shows improvement in refractive index modulation as a result of holographic recording in this material [102]. This behavior has been ascribed to the redistribution of the zeolite nanoparticles. The zeolite pores remain empty due to the larger size of the monomer molecules than the nanoparticle pore sizes [102]. Therefore, gas molecules can be adsorbed inside the BEA zeolite pores (depending on the gas molecule size) as well as to the zeolite surface, potentially maximizing the gas molecules' effect on the refractive index modulation change. The synthesis of the BEA zeolites is described in literature [63]. The BEA zeolites are hydrophilic, which ensures they are compatible with the water-soluble diacetone acrylamide (DA) photopolymer. In addition, the DA monomer demonstrates reduced toxicity in comparison to the acrylamide (AA) monomer, which is advantageous to reduce occupational and environmental hazards of any sensor.

For this study, alcohol gases were selected as the main test analyte. The detection of alcohol in its gaseous form allows for in situ, real-time measurements to be carried out. The sensing ability of gratings recorded in the photopolymer doped with zeolites (0–2 %, w/w) was investigated for three different alcohols: methanol, isopropanol, and 2-methylpropan-2-ol. These three alcohol molecules were selected due to their differing molecular structures and physical properties (Table 11.2). The adsorption of the gas molecules within the holographic grating depends on the molecular size and structure of the adsorbing molecule (Table 11.2).

Table 11.2 Physical properties of methanol, isopropanol, and 2-methylpropan-2-ol [103]

	Molecular weight (g/mol)	Refractive index [103]	Relative polarity (RP)
Methanol (CH_4O)	32.0	1.329	0.762
Isopropanol (C_3H_8O)	60.1	1.377	0.546
2-Methylpropan-2-ol ($C_4H_{10}O$)	74.1	1.387	0.389

The diffracted intensity was monitored in real time as a function of gas exposure duration at 16 torr to allow for comparison of the different gases tested. Gratings were recorded in 38 ± 3 μm thick photopolymer layers at a spatial frequency of 1000 ± 30 l/mm with a recording wavelength of 532 nm.

For undoped gratings, there was a limited effect on the diffraction efficiency of the hologram at low gas pressure (16 torr) for all three alcohol gases (Fig. 11.16a). For 2-methylpropan-2-ol, the largest change was observed with the normalized intensity decreasing by 5 %.

For the 2 wt% doped gratings, there was a more significant change in normalized diffraction intensity on exposure to the three gases (Fig. 11.16b). For isopropanol and 2-methylpropan-2-ol, normalized intensity decreased by 5 and 8 %, respectively. For methanol, the intensity initially decreased by 5 % after 3 min of exposure; however, the intensity then began to increase, eventually exceeding the initially intensity by 2 %.

The same trend of decreasing diffracted beam intensity with increasing exposure time was observed for both the isopropanol and 2-methylpropan-2-ol gases in the zeolite-doped gratings. For both gases, only a limited effect on diffraction efficiency of the undoped grating was observed. The data matches the predicted effect of the gas on the zeolite-doped grating; gas molecules are adsorbed to the porous zeolite nanoparticles causing the refractive index of the regions containing the redistributed nanoparticles to increase, therefore decreasing the overall refractive index modulation. In the case of methanol, the smallest gas molecule tested, the normalized intensity began to increase after 3 min of gas exposure for the 2 wt% zeolite-doped samples.

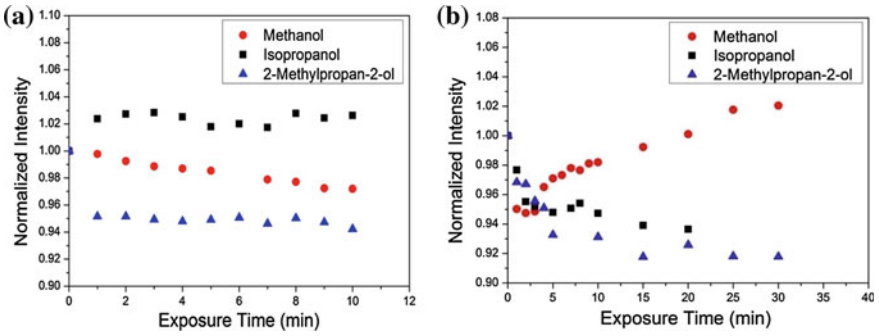

Fig. 11.16 Normalized intensity versus exposure time (s) for a (**a**) 0 and (**b**) 2 wt% zeolite-doped grating exposed to methanol, isopropanol and 2-methlypropan-2-ol at a gas pressure of 16 torr [104]

This is the opposite of the trend observed for isopropanol and 2-methylpropan-2-ol. Adsorption of the gas molecules to the zeolites redistributed within the grating increases their refractive index, and have the opposite effect on n_1, therefore another process may occur simultaneously independent of the zeolite nanoparticles. One possible explanation is that the small size combined with the high polarity of the methanol molecule allows it to freely enter the pores of the permeable polymer and swells the photopolymer layer doped with zeolite crystals. A more polar molecule such as methanol (RP = 0.762) is more reactive in comparison to isopropanol (RP = 0.546) and 2-methylpropan-2-ol (RP = 0.389), and thus higher swelling of the layer is expected in the presence of methanol.

For all three gases, the effect of the gas molecules on the holographic gratings was fully reversible. This implies that the gas molecules can readily enter and exit the polymer matrix as well as the zeolites.

11.4.1.3 Humidity Sensors

Humidity can be detected by a number of techniques varying from the simplest method exploited the contraction/expansion of human hair to the advanced techniques used electronic chips. Crucial parameters of a humidity sensor are its accuracy, operating relative humidity (RH) range, response time, reversibility, compactness and weight, cost, ease of operation, and maintenance. Holographic sensors are capable of providing fast, real-time, reversible or irreversible, visual colorimetric or optical readouts. Moreover, remote monitoring and multiplexing of different sensors are possible. Additionally, they are lightweight, small, and relatively low cost. Thus, holographic sensors can be used for the fabrication of disposable devices.

Holograms with the capacity to respond to humidity with easily identifiable change in their optical properties, accompanied by resistance to damage by the environment, are of particular interest in humidity sensor development. The application of photopolymers for the development of humidity holographic sensors is under active study [47, 48, 105, 106]. Humidity response of reflection holograms recorded in a self-processing acrylamide-based photopolymer [39] has been demonstrated in the range of 5–80 % RH [81, 105]. Reversible changes in fringe spacing due to water vapor absorption causes fully reversible changes in the color of the light diffracted by the reflection grating. The mechanical capacity of the photopolymer layer to swell or shrink at different levels of relative humidity was used for the development of holographic humidity indicator.

Photopolymers are suitable for the development of sensors as its sensitivity to humidity can be altered by varying the photopolymer composition. The first approach is to use different photoinitiators. Photopolymer layers containing triethanolamine are permeable to water vapor, and as a result the properties of photopolymer-based holographic gratings are humidity-dependent. However, photopolymer layers containing *N*-phenylglycine are robust and non-sensitive to humidity up to RH = 70 %.

Recently, it has been shown that humidity response of transmission gratings recorded in an acrylamide-based photopolymer containing triethanolamine could be utilized for the development of irreversible holographic humidity sensors [106]. Both diffraction efficiency change and shift in the Bragg peak were observed after exposure to RH = 90 %. Reversibility of the observed changes in properties of gratings was dependent on ambient temperature (T); specifically changes were irreversible at T > 16 °C, and fully reversible at lower temperatures.

The substitution of triethanolamine by *N*-phenylglycine allowed the development of a humidity-resistant acrylamide-based photopolymer [43]. No response to humidity changes was observed at RH = 20–70 % [47]. Moreover, fully reversible decrease in normalized diffraction efficiency defined as the ratio of diffraction efficiency at given humidity level and the diffraction efficiency measured at the start of the experiment at RH = 20 % was detected at RH = 80–90 %. This photopolymer can be applied where non-sensitive humidity material is needed. For example, humidity-resistant material is beneficial for the development of holographic sensors when the response to environmental changes should be minimized. Thereby, humidity-resistant acrylamide-based photopolymer can be utilized as a basic composition for the development of novel sensors with introduced response to other analytes, accompanied by resistance to humidity.

The second approach to the design of humidity sensitive photopolymers is to use different monomers. A non-toxic and environmentally-compatible photopolymer material [107, 108] is an alternative to acrylamide-based photopolymers for many holographic applications including holographic humidity sensors. In this photopolymer formulation, low-toxic DA is used as the main monomer.

Humidity response of slanted transmission gratings recorded in DA-based photopolymer layers with the thickness of 60 μm was investigated in the range of 20–90 % RH [48]. In this study, a two-beam holographic optical setup was utilized to record slanted transmission gratings with a slant angle of 13° and a spatial frequency of 1250 l/mm using a Nd:YVO_4 laser (532 nm). Figure 11.17 shows the relative change in the diffraction efficiency of gratings recorded in DA-based and AA-based photopolymers as compared to relative humidity. Relative change in the diffraction efficiency was calculated as follow. The difference of the diffraction efficiency measured at certain relative humidity and the diffraction efficiency measured at RH = 20 % was normalized to the diffraction efficiency at RH = 20 %. The humidity response of DA-sample was significant (Fig. 11.17). Thus, even at low relative humidity of 20–40 % (Fig. 11.17), there was a 50 % increase in the diffraction efficiency of DA-sample, whereas the diffraction efficiency of AA-sample was increased by few percent. Reversibility of the observed changes was confirmed at RH < 80 %. Thus, due to substantial humidity sensitivity of DA-based photopolymer, this photopolymer can be utilized for the development of a reversible sensor for continuous humidity monitoring in the relative humidity range from 20 to 70 %.

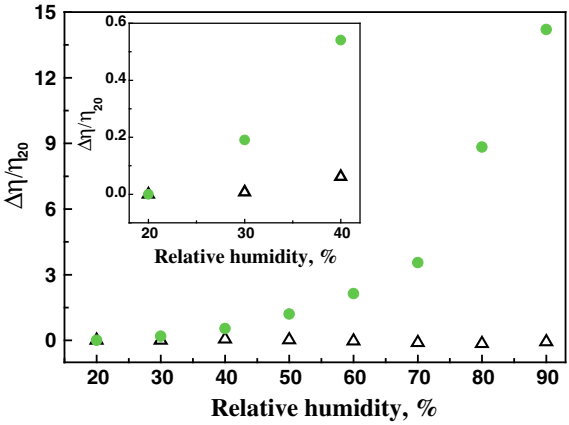

Fig. 11.17 Relative changes of the diffraction efficiency of slanted transmission gratings recorded in DA-based (*bullet*) and AA-based (*triangle*) photopolymers at different levels of relative humidity [48]

11.4.2 Temperature Sensors

Among the large variety of non-electrical temperature sensors, holographic temperature sensors can be classified as the sub-category of thermal indicators and thermometers based on thermal expansion. Firstly, the operation of holographic temperature sensors is based on thermal expansion/contraction of the polymer matrix. Secondly, temperature changes the reflectivity/transmittance of the holographic grating or the wavelength of the refracted light. When a holographic sensor is based on a reflection holographic grating, it works as a thermal visual indicator.

Most of the photopolymers including acrylamide-based photopolymers have low glass transition temperatures. In these materials, temperature exposure is known to induce grating detuning effects originating from changes in the refractive index and the dimensions of the photopolymer layers [109]. Thus, the ability of photopolymers to expand under temperature can be implemented for the development of holographic temperature sensors.

The temperature response of reflection holograms recorded in an acrylamide-based photopolymer was investigated in the range of 15–50 °C [37, 81]. The shift of the spectral peak wavelength highly depended on the relative humidity level so that it is negligible below 30 % of relative humidity, and is 25 nm at 45 % of relative humidity. Recently, investigation of the temperature response of slanted transmission gratings with a slant angle of 13° recorded in photopolymers was carried out by the characterization of Bragg angle shift at different temperatures [48]. Three types of photopolymers containing different monomers and photoinitiating systems were used as recording media. The first type, photopolymer A, was an acrylamide-based photopolymer containing triethanolamine as the electron donor [39]. The second type, photopolymer B, was a derivative of the acrylamide-based photopolymer that uses *N*-phenylglycine as the electron donor [43]. The third type, photopolymer C, was a diacetone acrylamide-based photopolymer containing triethanolamine [108].

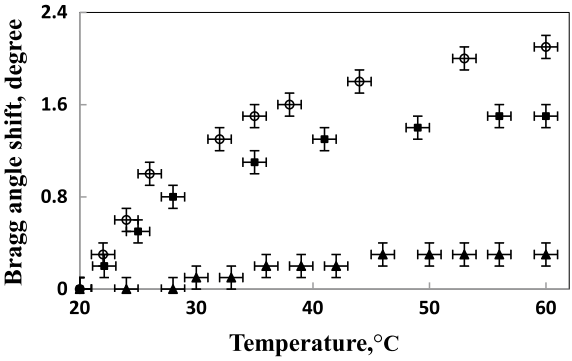

Fig. 11.18 Temperature dependence of the Bragg angle shift in photopolymer A (*filled square*), photopolymer B (*filled triangle*) and photopolymer C (*open circle*) [48]

Figure 11.18 presents the Bragg angle shift of slanted transmission gratings recorded in photopolymers with different composition in the range of 20–60 °C. According to the recording geometry, if Bragg angle shifts to a bigger value the shrinkage of the layer is expected.

In the case of photopolymers containing triethanolamine (photopolymer A and C) exposure to temperature shrinks the layers leading to a significant Bragg angle shift, whereas photopolymer B containing *N*-phenylglycine exhibits a low response to temperature changes (Fig. 11.18). Analysis of the three materials by differential scanning calorimetry showed that the behavior of the Bragg angle shift for different photopolymers can be explained by different ability of photopolymers to release water due to temperature increase [48].

Photopolymer C is a humidity-sensitive material suitable for sensor development [48]. To analyze the thermal effect on properties of holographic gratings recorded in photopolymer C, the temperature response of sealed layers was investigated. Figure 11.19 shows that the behaviors of the Bragg angle shift of sealed and unsealed samples are fully opposite, i.e. exposure to temperature swells the sealed

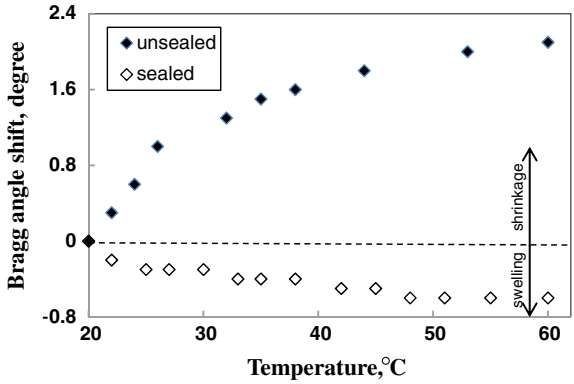

Fig. 11.19 Temperature dependence of the Bragg angle shift in photopolymer C [48]

layer and shrinks the unsealed layer. Swelling of the sealed layer can be explained by relatively large thermal expansion of photopolymer C inherent to polymer materials with low glass transition temperature.

The results demonstrate an effective approach to obtain photopolymer-based gratings with tunable temperature sensitivity. Thus, photopolymers containing triethanolamine can be exploited as a thermo-responsive materials for the development of holographic temperature sensors.

11.4.3 Pressure Sensors

Sensors are widely used for controlling and monitoring of pressure. The sectors requiring pressure sensing devices include the petrochemicals, automotive, dental and medical industries. The market size of pressure sensors in 2011 was $5.11 B and is expected to reach $7.34 B by 2017 [110].

Photopolymers are an attractive option for pressure-sensing applications due to their elasticity and compressibility. Reflection gratings recorded in photopolymer formulations have been shown to work as effective relative humidity sensors due to their ability to swell and shrink as the humidity of the surrounding environment is changed [111]. The same principle of operation can be applied to a photopolymer-based holographic pressure or stencil stretch sensor [111–115] (Fig. 11.20). A reflection hologram was recorded in an elastic photopolymer material which compressed under pressure, reducing the hologram thickness and therefore the fringe spacing [5]. This reduction in fringe spacing corresponds to a decrease in the diffraction wavelength at which the hologram reconstructs. Assuming the hologram has high enough diffraction efficiency, this change may be visible to an observer, as well as quantifiable with a spectrometer.

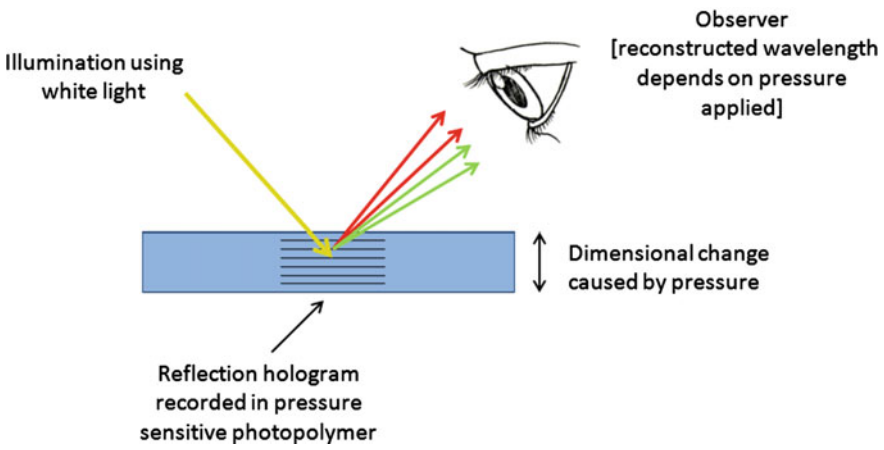

Fig. 11.20 Principle of operation of a holographic pressure sensor

A photopolymer-based holographic sensor that responds to pressure has been described [5]. In this work, an emulsion consisting of acrylamide:methacrylamide (2:1, v/v) and a crosslinker methylenebisacrylamide (5 mol%) was deposited on a substrate to create a film, which was then polymerized via free radical polymerization. A hologram was recorded using a frequency doubled Nd:YAG laser. The resulting hologram was sandwiched using another transparent substrate and pressure was applied onto the holograms using a pair of G-clamps. The pressure of the clamps on the hologram contracted the volume of the hologram, thus causing the λ to blue-shift by 3 nm. While this work demonstrated the principle of operation of a pressure-sensitive hologram, further improvement of the sensitivity of the photonic structure to pressure is needed because the wavelength change is not large enough to produce a visible change in the color of the reconstructed hologram. An elastic reflection hologram recorded in a silicon-based polymeric film that changes colour when compressed or stretched has also been reported [116]. A shift in λ of the reconstructed hologram of up to 30 nm is reported for an applied stretching force of 6 N, whereas the application of a pressure of 671 kPa produces a λ shift of approximately 10 nm.

The ability of reflection gratings recorded in the DA-based photopolymer composition to act as a pressure sensing device has been reported [104, 117]. Gratings were recorded in 80 $\pm$ 5 μm thick photopolymer layers at a spatial frequency of 3050 $\pm$ 30 l/mm using a recording wavelength of 633 nm, producing gratings with a diffraction efficiency of 30 %. Pressure was applied to the reflection gratings using a Tensile Tester (Instron, Series 5569). The DA composition was selected due to its ability to record high diffraction efficiency reflection holograms.

The effect of increasing pressure on fringe spacing of the DA-based reflection gratings was investigated for pressures ranging from 0.4 to 10 GPa. The change in fringe spacing was monitored using a spectrometer. Figure 11.21 shows the values for the change in fringe spacing, $\Delta\Lambda$, as a percentage of the original fringe spacing (0.3448 μm). As pressure is increased, $\Delta\Lambda$ increases from 1 to 12 %. Up to 97 % of

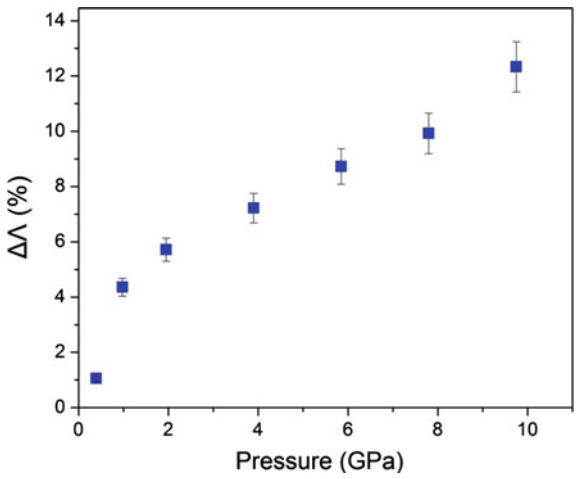

Fig. 11.21 $\Delta\Lambda$ (%) versus pressure (GPa) for reflection gratings recorded in the DA-based photopolymer [104]

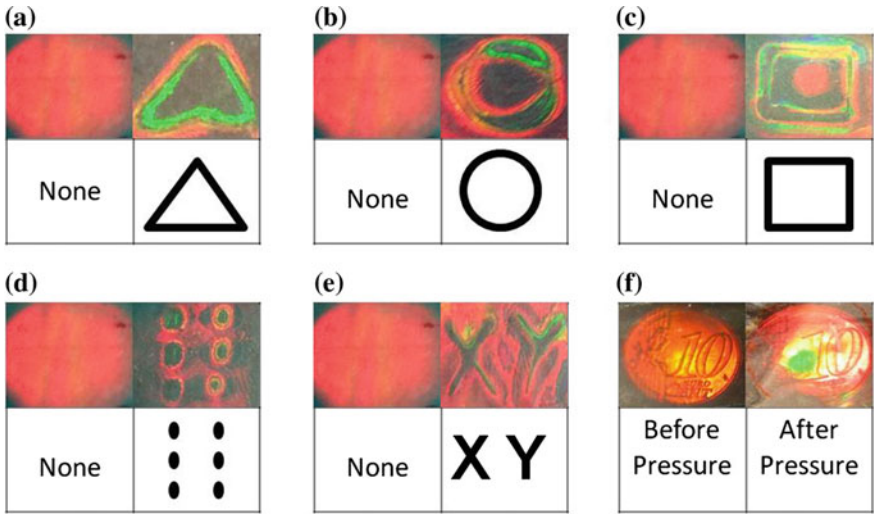

Fig. 11.22 Reflection grating before and after application of pressure using (**a**) a triangular-shaped stamp, (**b**) a circular-shaped stamp, (**c**) a square-shaped stamp, (**d**) a six-pronged stamp and (**e**) a stylus to write the letters X and Y (**f**) Reflection hologram of a 10 cent euro coin before and after application of pressure [104]

the original fringe spacing was recovered after 48 h. The pressure sensitivity of Denisyuk reflection gratings recorded in the DA-based photopolymer is shown in Fig. 11.22. In the regions where pressure has been applied, a change in color of the reconstructed grating is visible from the red color of the original recorded grating to orange, yellow, green and blue, with increasing pressure (Fig. 11.22). The ability of the reflection gratings recorded in the DA photopolymer layer to respond to pressure in a visible and quantifiable way is promising for the development of holographic pressure sensors.

11.4.4 Ions Sensors

11.4.4.1 H^+

Holographic pH sensors consist of pendant carboxyl groups that are introduced to the polymer matrix by adding methacrylic acid in the monomer solution before free radical polymerization [32, 49, 84–90]. Upon illumination with a light source, the device diffracts, reflects and refracts the incoming light (Fig. 11.23a). Figure 11.23 illustrates the principle of operation of a reflection-type holographic pH sensor, which allows measurements from pH 4–7 producing Bragg peak shifts up to 350 nm with response time within 30 s. Figure 11.24 shows photographs of a holographic sensor at different pH values.

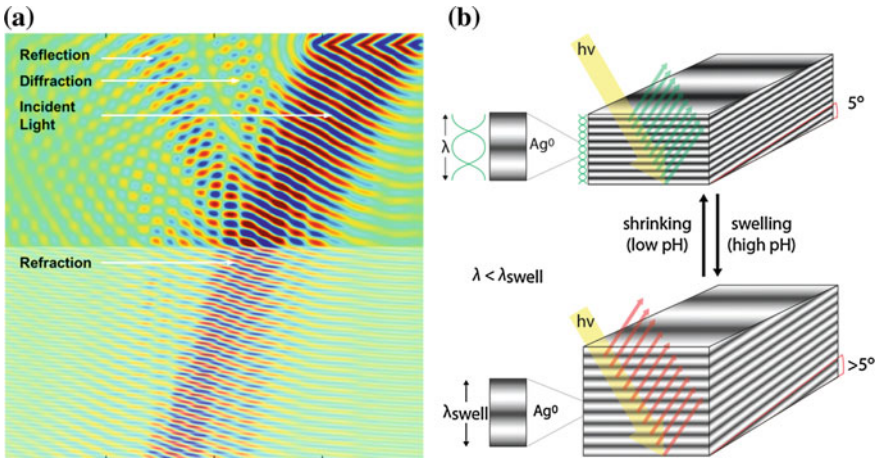

Fig. 11.23 Principle of operation of holographic pH sensors. **a** The diffraction of light from a multilayer structure in the sensor. **b** Tuning the multilayer grating by changing the pH, and its color change

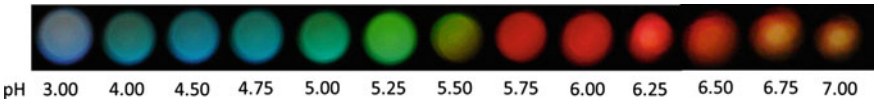

Fig. 11.24 Photographs of a holographic sensor at different pH values

Microfluidic devices comprising of holographic pH sensors were also described. For instance, these sensors were integrated into a PDMS-based microbioreactor for continuously monitoring pH caused by *Lactobacillus casei* [72]. Holographic devices have the potential to be integrated in paper-based microfluidic devices that allow construction of low-cost diagnostics for applications in resource-limited settings [118–121]. Additionally, holographic sensors can be integrated in contact lens sensors that may provide monitoring tear fluid in a minimally invasive manner [122].

11.4.4.2 Monovalent Metal Ions

For sensing metal ions, holographic sensors were functionalized with crown ethers. To incorporate crown ethers in polymer matrixes, methacrylated derivatives were synthesized [74]. These derivatives consisted of methacrylated 12/15/18-crown-4/5/6, which were copolymerized with hydroxyethyl methacrylate (HEMA) to form a pHEMA matrix with pendant crown ethers. After the diffraction gratings were formed by silver halide chemistry, the holograms were tested with a range of metal ions. The 18-crown-6 (50 mol%) holograms with a cavity diameter of 2.6–3.2 Å were found to be sensitive to K^+ ions. The Bragg peak of the hologram

shifted ~200 nm in the presence of 30 mM K^+ ions and the selectivity was not interfered by the background Na^+ ion concentrations [74].

11.4.4.3 Divalent Metal Ions

Holographic sensors were also utilized to sense divalent metal ions. Holographic sensors were functionalized with a porphyrin derivate, which also served as the crosslinker. In the presence of Cu^{2+} and Fe^{2+} ions (0.05–1.00 M), the Bragg peak shifted ~5 nm [77]. While such small wavelength shifts can be quantified by a spectrophotomer, it is not possible to see colorimetric changes by eye. Hence, pendant porphyrin derivatives are need for improving the sensitivity [123]. Recently, holographic sensors were functionalized with 8-hydroxyquinoline for divalent metal ion sensing. After the hologram was recorded, *N*,*N*′-dicyclohexylcarbodiimide-initiated condensation reaction was used to link the 8-hydroxyquinoline to the polymer matrix. The sensor was used to quantitatively measure Pb^{2+} and Cu^{2+} ions (0.1–10.0 mM) with limits of detection of 11.4 and 18.6 μM [124]. The same sensor was reused for repeat analyses by using an ethylenediaminetetraacetic acid solution.

11.4.5 Glucose Sensors

Holographic sensors were also utilized for quantifying glucose concentrations. An acrylamide matrix was functionalized with 3-(acrylamido)-phenylboronic acid to form pendant *cis*-diol moieties [79]. Holographic glucose sensor can operate at 510–1100 nm. The response of the sensor to glucose was tested at different pH values and glucose concentrations. The initial Bragg peak was at ~565 nm, and as the concentration of the glucose was increased to 10.0 mM, the peak shifted by 21, 81, 365, 379 and 420 nm at pH values of 7.00, 7.25, 7.40, 7.75 and 8.00, respectively [78, 79]. Figure 11.25 shows photographs of a holographic sensor as the concentration of glucose was changed. The holographic sensor was also tested in urine samples of diabetic patients (n = 33). In these experiments, the Bragg peak was measured from 1 to 5 min. Using an algorithm on the basis of slope estimation, the corresponding concentration values were assigned to each trend of Bragg peak shift. As compared to the fully automated gold standard analyzers the holographic sensors showed a coefficient of correlation (R^2) of 0.79. However, commercial dipsticks showed an R^2 value of 0.28 [78]. The holographic sensors were reusable, where the position of the Bragg peak was reset using acetic acid (1 %, v/v). While the results showed promising results, several aspects of holographic glucose sensors need improvement. The first significant limitation is the requirement of adjusting the pH to a fixed value (7.40) to standardize the measurements, indicating that small fluctuations in the pH can affect the readouts. Another limitation of holographic glucose sensors is that the polymer matrix is also responsive to other carbohydrates

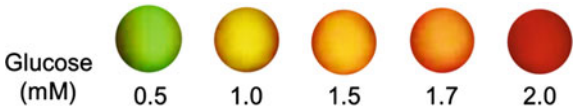

Fig. 11.25 Photographs of a holographic glucose sensor

such as fructose and lactate. While this is not a significant concern in urine samples, low-selectivity is a limitation in other biological samples such as blood. The third aspect that requires improvement is the sensor response. It takes from 30 min to 1 h for the sensor to saturate, however the readout time can be decreased by complex algorithms. Hence, the ligand and polymer chemistries require improvement for point-of-care diagnostics that require high sensitivities and fast response time [125].

11.5 Future Directions

There are a number of challenges that need to be addressed to achieve the full potential of holographic sensors. The demonstration of sufficient selectivity of holographic sensors is a significant challenge that needs to be addressed. To achieve this, the research in holographic sensors must focus on the development of novel functionalized photonic materials for holographic recording. Further research into new materials and their properties such as size, porosity of nanoparticles, chemical structure of the copolymerizing monomers, crosslinkers will enable broadening the knowledge on the sensing mechanisms and to further tailor the sensors' properties for specific applications as well as to expand the range of their applications. To improve selectivity of the holographic sensors, highly-selective sensing materials must be used. One possible approach to achieve this goal is to take the advantage of the advances made in material science for other types of sensors such as dye-based sensors. For example, tailored pocket porphyrins used for selective detection of various vapors in colorimetric sensors could be effectively used in holographic sensors [126]. A further approach is to explore the functionalization of the sensing moieties to obtain a unit capable of copolymerizing with the monomer solution in holographic recording. Yet, such approach will be justified if the produced sensors provide additional advantages in terms of cost, ease in use or compatibility with other technologies, in comparison to the commercial sensors.

In the case of visual colorimetric sensors, the visibility of the hologram is of key importance. The inherently narrow view angle of holographic sensors which is determined by the recording geometry is another important challenge that needs to be addressed. This requires the development of innovative methods for sensor fabrication. For example, digital printing facilitating localized functionalization of the holographic recording material can be utilized for the fabrication of more complex photonic structures that can improve the optical properties of the structure and render it easily observable. Research into increasing the dynamic range of the

recording material and thus the brightness of the recorded holograms is needed in order to address this challenge. The relatively slow response time, especially in the case of biomolecular sensing applications requires further research into polymer chemistry involving the design of the host polymer matrix characteristics such as porosity and hydrophobicity/hydrophilicity. Another challenge is to demonstrate advantage over the large number of sensing technologies that are currently being developed. This requires flexible production on a mass scale and easy integration of the sensors with new and emerging technologies. Ability for integration with wearable/portable devices and technologies such as microfluidics would be particularly beneficial. Due to their amenability to miniaturization holographic sensors hold great potential for integration into microfluidic devices. The field of microfluidics has seen many advances over the last two decades and these technologies have practical and commercial applications [127–129]. Now new platforms such as liver-on-a-chip [130], lung-on-a-chip [131], and plant-on-chip [132] are available. Holographic sensors have the potential to be miniaturized in array formats for multiplexing and sensing in these lab-on-a-chip devices. For example, they can be constructed in array spot gratings using contact printing [133].

Mobile phones and growing telecommunication technologies are an opportunity for the quantification of holographic sensors and other colorimetric tests [134]. The strong growth is evident from global mobile-cellular subscriptions, which increased 70 % over the last 5 years, reaching 6.9 billion as of 2015 [135]. The development of smartphone readers that allow reading colorimetric data can enable rapid and quantitative measurement in real time [136]. This technology can be applied to holographic sensors. One of the most important characteristic of holographic sensors is the ability to diffract monochromatic colors, and this hold a great potential to quantify the target analyte concentrations using mobile devices such as smartphones, tablets, smart watches, or other wearable devices [137].

11.6 Conclusions

The properties of holographic sensors, the principle of their operation, and their fabrication were described. The key properties of photonic materials suitable for fabrication of holographic sensors and different strategies for their realization were presented. Photonic materials currently used in holographic sensing such as materials based on silver halide chemistry, photopolymer chemistry and nanoparticle doped polymer materials were described. It was demonstrated that theoretical dynamic simulation of multilayer structures could be utilized in the design of the holographic sensors. Also efforts towards the theoretical understanding of the inter-molecular interactions to predict the sensor response were discussed. Sensors for detection of chemical analytes such as O_2, N_2, alkanes, alkenes, alkynes and ammonia, alcohols, metal ions, pH and glucose were presented. In addition sensors for the detection of changes in their environment such as humidity, temperature and pressure were also described.

The improvement of the selectivity, response time, brightness and viewing angle (for colorimetric type sensors) and sensitivity were identified as the main challenges in holographic sensor research. In order to successfully address these challenges a deeper theoretical understanding of the analyte-sensor interactions in holographic sensing materials, and their relationship with the material optical properties affecting the holographic response is required. The niche technologies for holographic sensors include reusable, wearable, implantable, wireless, powerless devices, contact lenses, and disposable devices. Bringing new capabilities to holographic sensors will help the society to maintain the environment clean, to improve human health, and to contribute to other sectors such as security.

Author contributions A.K. Yetisen and I. Naydenova designed the book chapter. M. Zawadzka contributed to Sects. 11.1, 11.2.2, 11.3.2, 11.5. T. Mikulchyk contributed to Sect. 11.2.2.2 and wrote Sects. 11.4.1.3, 11.4.2; D. Cody contributed to Sects. 11.4.1.2 and wrote 11.4.3; S. Martin wrote Sect. 11.3.1.2; E. Mihaylova contributed to Sect. 11.4.3; A.K. Yetisen contributed to Sect. 11.2.2.3, 11.3.2 and wrote 11.3.1.1, 11.4.4, 11.4.5 and 11.5; J.L. Martinez-Hurtado contributed to Sects. 11.2.2, 11.3.2 and wrote 11.4.1.1; H. Butt wrote 11.3.3; H. Awala and S. Mintova contributed to 11.3.1.3; I. Naydenova contributed to 11.2.2, 11.3.1.3, 11.4.1.2 and 11.5. A.K. Yetisen, S.H. Yun, J.L. Martinez-Hurtado and I. Naydenova edited the manuscript.

References

1. A.K. Yetisen, I. Naydenova, F. da Cruz Vasconcellos, J. Blyth, C.R. Lowe, Chem. Rev. **114**, 10654 (2014)
2. Environment policies, http://ec.europa.eu/environment/index_en.htm. 17 Mar 2015
3. World Population Agening: 1950–2050; United Nations: New York, 2001
4. Wireless Portable Medical Device Market by Technology (BT/BLE, Wi-Fi, ZigBee, ANT+), Component (Sensors, ICs, Processors), Application (Monitoring, Medical Therapeutics, Diagnosis, Fitness & Wellness), and Geography—Global Forecast to 2020; marketsandmarkets.com, 2014
5. C.R. Lowe, R.B. Millington, J. Blyth, A.G. Mayes, *Hologram used as a sensor.* WO Patent Application 1995026499 A1, October 5, 1995
6. V. Toal, *Introduction to Holography* (CRC Press, Boca Raton, FL, 2011)
7. V.A. Postnikov, A.V. Kraiskii, V.I. Sergienko, in *Holography—Basic Principles and Contemporary Applications*, ed. by Mihaylova, E. InTech: Rijeka (2013)
8. A. Llordes, G. Garcia, J. Gazquez, D.J. Milliron, Nature **500**, 323 (2013)
9. R.J. Collier, C.B. Burckhardt, L.H. Lin, *Optical Holography* (Academic Press, New York, 1971)
10. J.A. Jenney, J. Opt. Soc. Am. **60**, 1155 (1970)
11. M. Iwasaki, T. Kubota, T. Tanaka, In *Selected Papers on Holographic Recording Materials*, ed. by Bjelkhagen, H.I., Vol. MS 130 (1996)
12. H.I. Bjelkhagen, *Silver-Halide Recording Materials* (Springer, Berlin, 1993)

13. Y.D. Lantukh, G.A. Ketsle, S.N. Pashkevich, S.N. Letuta, D.A. Razdobreev, J. Opt. Technol. **73**, 484 (2006)
14. Y.N. Denisyuk, Dokl. Akad. Nauk SSSR **144**, 1275 (1962)
15. J.L. Martinez Hurtado, *Gas-Sensitive Holographic Sensors*, PhD dissertation, University of Cambridge (2013)
16. J.L. Martinez Hurtado, Nanotech. **3**, 549 (2011)
17. F. Hajiesmaeilbaigi, A. Mohammadalipour, J. Sabbaghzadeh, S. Hoseinkhani, H.R. Fallah, Laser Phys. Lett. **3**, 252 (2006)
18. F. Mafuné, J.-Y. Kohno, Y. Takeda, T. Kondow, H. Sawabe, J. Phys. Chem. B **104**, 8333 (2000)
19. F. Mafuné, J.-Y. Kohno, Y. Takeda, T. Kondow, H. Sawabe, J. Phys. Chem. B **104**, 9111 (2000)
20. T. Tsuji, N. Watanabe, M. Tsuji, Appl. Surf. Sci. **211**, 189 (2003)
21. J.L. Martínez-Hurtado, C.A.B. Davidson, J. Blyth, C.R. Lowe, Langmuir **26**, 15694 (2010)
22. J.L. Martinez Hurtado, C.R. Lowe, ACS. Appl. Mater. Interfaces **6**, 8903 (2014)
23. F. da Cruz Vasconcellos, A.K. Yetisen, Y. Montelongo, H. Butt, A. Grigore, C.A.B. Davidson, J. Blyth, M.J. Monteiro, T.D. Wilkinson, C.R. Lowe, ACS Photonics **1**, 489 (2014)
24. X.T. Kong, A.A. Khan, P.R. Kidambi, S. Deng, A.K. Yetisen, B. Dlubak, P. Hiralal, Y. Montelongo, J. Bowen, S. Xavier, K. Jiang, G.A.J. Amaratunga, S. Hofmann, T.D. Wilkinson, Q. Dai, H. Butt, ACS Photonics **2**, 200 (2015)
25. S. Deng, A.K. Yetisen, K. Jiang, H. Butt, RSC Adv. **4**, 30050 (2014)
26. H. Butt, A.K. Yetisen, R. Ahmed, S.H. Yun, Q. Dai, Appl. Phys. Lett. **106**, 121108 (2015)
27. X.T. Kong, H. Butt, A.K. Yetisen, C. Kangwanwatana, Y. Montelongo, S. Deng, F. da Cruz Vasconcellos, M.M. Qasim, T.D. Wilkinson, Q. Dai, Appl. Phys. Lett. **105**, 053108 (2014)
28. J. Blyth, R.B. Millington, A.G. Mayes, E.R. Frears, C.R. Lowe, Anal. Chem. **1996**, 68 (1089)
29. H.I. Bjelkhagen, *Silver-Halide Recording Materials for Holography and Their Processing*, vol. 2 (Springer, Heidelberg, 1995), pp. 13–33
30. J. Blyth, R.B. Millington, A.G. Mayes, C.R. Lowe, Imaging Sci. J. **47**, 87 (1999)
31. C.P. Tsangarides, A.K. Yetisen, F. da Cruz Vasconcellos, Y. Montelongo, M.M. Qasim, T. D. Wilkinson, C.R. Lowe, H. Butt, RSC Adv. **4**, 10454 (2014)
32. A.J. Marshall, J. Blyth, C.A.B. Davidson, C.R. Lowe, Anal. Chem. **75**, 4423 (2003)
33. A.K. Yetisen, Y. Montelongo, N.M. Farandos, I. Naydenova, C.R. Lowe, S.H. Yun, Appl. Phys. Lett. **105**, 261106 (2014)
34. T.H. Jeong, R.W. Aumiller, R.J. Ro, J. Blyth, In practical holography XVI and holographic materials VIII. Proc. SPIE **4659**, 103 (2002)
35. A. K. Yetisen, Fundamentals of Holographic Sensing. *Holographic Sensors*. Springer International Publishing, pp. 27–51 (2015)
36. E.V. Tan, C.R. Lowe, Anal. Chem. **81**, 7579 (2009)
37. I. Naydenova, R. Jallapuram, S. Martin, V. Toal, in *Humidity Sensors: Types, Nanomaterials and Environmental Monitoring*, ed. by C.T. Okada (Nova Science Publishers, Hauppauge, 2011)
38. Y.B. Boiko, V.S. Solovjev, S. Calixto, D.J. Lougnot, Appl. Opt. **33**, 787 (1994)
39. S. Martin, P.E. Leclere, Y.L.M. Renotte, V. Toal, Y.F. Lion, Opt. Eng. **33**, 3942 (1994)
40. S. Blaya, L. Carretero, R.F. Madrigal, A. Fimia, Opt. Mater. **23**, 529 (2003)
41. I. Naydenova, R. Jallapuram, R. Howard, S. Martin, V. Toal, Appl. Opt. **43**, 2900 (2004)
42. L. Hai, L. Ruo-Ping, S. Cai-Xia, X. Yong, T. Dao-Guang, H. Ming-Ju, Chin. Phys. B **19**, 024212 (2010)
43. Q. Gong, S. Wang, M. Huang, F. Gan, Mater. Lett. **59**, 2969 (2005)
44. S. Gallego, A. Márquez, D. Méndez, M. Ortuño, C. Neipp, E. Fernández, I. Pascual, A. Beléndez, Appl. Opt. **47**, 2557 (2008)
45. J.T. Sheridan, M.R. Gleeson, C.E. Close, J.V. Kelly, J. Nanosci. Nanotechnol. **7**, 232 (2007)
46. E. Fernández, R. Fuentes, M. Ortuño, A. Beléndez, I. Pascual, Appl. Opt. **52**, 6322 (2013)

47. T. Mikulchyk, S. Martin, I. Naydenova, Opt. Mater. **37**, 810 (2014)
48. T. Mikulchyk, J. Walshe, D. Cody, S. Martin, I. Naydenova, *Proc. SPIE* **2015**, Humidity and temperature response of photopolymer-based holographic gratings, Proc. SPIE 9508, Holography: Advances and Modern Trends IV, 950809 (May 8, 2015); doi:10.1117/12.2183782
49. I.G. Naydenova, S. Martin, V. Toal, J. Eur. Opt. Soc.-Rapid **4**, 09042 (2009)
50. C. Meka, R. Jallapuram, I. Naydenova, S. Martin, V. Toal, Appl. Opt. **49**, 1400 (2010)
51. Baerlocher, Ch., McCusker, L.B., *Database of Zeolite Structures*. The Structure Commission of the International Zeolite Association. http://www.iza-structure.org/databases/. (2015)
52. L. Tosheva, V.P. Valtchev, Chem. Mater. **17**, 2494 (2005)
53. S. Mintova, N.H. Olson, V. Valtchev, T. Bein, Science **283**, 958 (1999)
54. S. Mintova, N.H. Olson, T. Bein, Angew. Chem. Int. Ed. **38**, 3201 (1999)
55. Z. Wang, H. Wang, A. Mitra, L. Huang, Y. Yan, Adv. Mater. **13**, 746 (2001)
56. Z.B. Wang, A. Mitra, H.T. Wang, L.M. Huang, Y. Yan, Adv. Mater. **13**, 1463 (2001)
57. S. Mintova, J.-P. Gilson, V. Valtchev, Nanoscale **5**, 6693 (2013)
58. X. Xu, J. Wang, Y. Long, *Sensors 6*, 1751 (2006)
59. D. Banerjee, Z. Hu, J. Li, Dalton Trans. **43**, 10668 (2014)
60. M. Zaarour, B. Dong, I. Naydenova, R. Retoux, S. Mintova, Micropor. Mesopor. Mater. **189**, 11 (2014)
61. A. Dubbe, Solid State Ionics **179**, 1645 (2008)
62. D. Jadsadapattarakul, C. Thanachayanont, J. Nukeaw, T. Sooknoi, Sens. Actuators B **144**, 73 (2010)
63. I. Naydenova, E. Leite, T. Babeva, N. Pandey, T. Baron, T. Yovcheva, S. Sainov, S. Martin, S. Mintova, V. Toal, J. Opt. **13**, 044019 (2011)
64. Y. Tomita, N. Suzuki, K. Chikama, Opt. Lett. **30**, 839 (2005)
65. K. Chikama, K. Mastubara, S. Oyama, Y. Tomita, J. Appl. Phys. **103**, 113108 (2008)
66. A.M. Ostrowski, I. Naydenova, V. Toal, J. Opt. A: Pure Appl. Opt. **11**, 034004 (2009)
67. E. Leite, I. Naydenova, S. Mintova, L. Leclercq, V. Toal, Appl. Opt. **49**, 3652 (2010)
68. E. Leite, T. Babeva, E.P. Ng, V. Toal, S. Mintova, I. Naydenova, J. Phys. Chem. C **114**, 16767 (2010)
69. T. Babeva, R. Todorov, S. Mintova, T. Yovcheva, I. Naydenova, V. Toal, J. Opt. A: Pure Appl. Opt. **11**, 024015 (2009)
70. E. Leite, I. Naydenova, N. Pandey, T. Babeva, G. Majano, S. Mintova, V. Toal, J. Opt. A: Pure Appl. Opt. **11**, 024016 (2009)
71. A.K. Yetisen, H. Butt, F. da Cruz Vasconcellos, Y. Montelongo, C.A.B. Davidson, J. Blyth, L. Chan, J.B. Carmody, S. Vignolini, U. Steiner, J.J. Baumberg, T.D. Wilkinson, C.R. Lowe, Adv. Opt. Mater. **2**, 250 (2014)
72. L.L. Bell, A.A. Seshia, C.A.B. Davidson, C.R. Lowe, Procedia Eng. **5**, 1352 (2010)
73. A.V. Kraiskii, V.A. Postnikov, T.T. Suitanov, A.V. Khamidulin, Quantum Electron. **40**, 178 (2010)
74. A.G. Mayes, J. Blyth, R.B. Millington, C.R. Lowe, Anal. Chem. **74**, 3649 (2002)
75. B. Madrigal González, G. Christie, C.A.B. Davidson, J. Blyth, C.R. Lowe, Anal. Chim. Acta **528**, 219 (2005)
76. D. Bhatta, G. Christie, B. Madrigal-González, J. Blyth, C.R. Lowe, Biosens. Bioelectron. **23**, 520 (2007)
77. A.K. Yetisen, M.M. Qasim, S. Nosheen, T.D. Wilkinson, C.R.J. Lowe, Mater. Chem. C **2**, 3569 (2014)
78. A.K. Yetisen, Y. Montelongo, F. da Cruz Vasconcellos, J.L. Martinez-Hurtado, S. Neupane, H. Butt, M.M. Qasim, J. Blyth, K. Burling, J.B. Carmody, M. Evans, T.D. Wilkinson, L.T. Kubota, M.J. Monteiro, C.R. Lowe, Nano Lett. **14**, 3587 (2014)
79. S. Kabilan, A.J. Marshall, F.K. Sartain, M.-C. Lee, A. Hussain, X. Yang, J. Blyth, N. Karangu, K. James, J. Zeng, D. Smith, A. Domschke, C.R. Lowe, Biosens. Bioelectron. **20**, 1602 (2005)

80. G.J. Worsley, G.A. Tourniaire, K.E.S. Medlock, F.K. Sartain, H.E. Harmer, M. Thatcher, A. M. Horgan, J. Pritchard, Clin. Chem. **2007**, 53 (1820)
81. I. Naydenova, R. Jallapuram, V. Toal, S. Martin, Sens. Actuators, B **139**, 35 (2009)
82. J.L. Martinez-Hurtado, Nanomater. **1**, 20 (2011)
83. R.K. Kostuk, J.W. Goodman, Appl. Opt. **30**, 369 (1991)
84. J. Hodgkinson, R.P. Tatam, Meas. Sci. Technol. **24**, 012004 (2013)
85. H. Bai, G. Shi, Sensors **7**, 267 (2007)
86. A.M. Azad, S.A. Akbar, S.G. Mhaisalkar, L.D. Birkefeld, K.S. Goto, J. Electrochem. Soc. **139**, 3690 (1992)
87. G. Eranna, B.C. Joshi, D.P. Runthala, R.P. Gupta, Cr. Rev. Sol. State **29**, 111 (2004)
88. Y. Wang, J.T.W. Yeow, J. Sens. **2009**, 24 (2009)
89. Transparency Market Research, Gas Sensors Market—Global Industry Size, Share, Trends, Analysis and Forecast, 2012–2018, July 2013. Available online at: http://www.transparencymarketresearch.com/s-market.html. Accessed 19, 2014
90. Grand View Research, Gas Sensors Market Analysis And Segment Forecasts To 2020, March 2014. Available online at: http://www.grandviewresearch.com/industryanalysis/sensors-market. Accessed 03 June 2014
91. G. Korotcenkov, *Handbook of Gas Sensor Materials: Properties, Advantages and Shortcomings for Applications Vol. 1: Conventional Approaches*. Springer Science & Business Media (2013)
92. B. Liedberg, C. Nylander, I. Lunström, Sensor Actuator **4**, 299 (1983)
93. K. Cherif, S. Hleli, A. Abdelghani, N. Jaffrezic-Renault, V. Matejec, *Sensors* **2**, 195 (2002)
94. N. Gayraud, W. Kornaszewski, J.M. Stone, J.C. Knight, D.T. Reid, D.P. Hand, W.N. MacPherson, Appl. Opt. **47**, 1269 (2008)
95. T.M. Geppert, S.L. Schweizer, J. Schilling, C. Jamois, A.V. Rhein, D. Pergande, R. Glatthaar, P. Hahn, A. Feisst, A. Lambrecht, R.B. Wehrspohn, Photonic crystal gas sensors. Proc. SPIE **5511**(61) (2004)
96. J.L. Martínez-Hurtado, C.A.B. Davidson, C.R. Lowe, Monitoring organic volatiles and flammable gases with holographic sensor. Proc. SPIE **8024**, 80240Y1 (2011)
97. N. Yamazoe, K. Shimanoe, Overview of gas sensor technology. *Science and Technology of Chemiresistor Gas Sensors*. eds. by D. Aswal, S. Gupta, Nova Publishers (2007)
98. B. Timmer, W. Olthuis, Berg, A. v. d., *Sensor. Actuat. B-Chem.* **107**, 666 (2005)
99. RAE Systems, *Measuring ammonia (NH3) with photoionization detectors, application note ap-201, RAE Systems Inc.*: San Jose, CA, USA (2011)
100. P.C. Lee, M.A.J. Rodgers, J. Phys. Chem. **88**, 4385 (1984)
101. P. Choi, *Investigation of Thermodynamic and Transport Properties of Proton-Exchange Membranes in Fuel Cell Applications,* PhD thesis, Worcester Polytechnic Institute (2004)
102. D. Cody, E. Mihaylova, L. O'Neill, T. Babeva, H. Awala, R. Retoux, S. Mintova, I. Naydenova, Opt. Mater. **37**, 181 (2014)
103. *Chemicals—Technical Data, Properties of solvents*. http://www.sigmaaldrich.com/chemistry/stockroom-reagents/learning-center/technical-library/solvent-properties.html
104. D. Cody, Low-toxicity diacetone acrylamide-based photopolymer for applications in holography, PhD thesis, Dublin Institure of Technology, 2015
105. I. Naydenova, R. Jallapuram, V. Toal, S. Martin, Appl. Phys. Lett. **92**, 031109 (2008)
106. T. Mikulchyk, S. Martin, I. Naydenova, J. Opt. **15**, 105301 (2013)
107. D. Cody, I. Naydenova, E. Mihaylova, J. Opt. **14**, 015601 (2012)
108. D. Cody, I. Naydenova, E. Mihaylova, Appl. Opt. **52**, 489 (2013)
109. L. Dhar, M.G. Schnoes, T.L. Wysocki, H. Bair, M. Schilling, C. Boyd, Appl. Phys. Lett. **73**, 1337 (1998)
110. MarketsandMarkets, *Pressure Sensor Market (2012–2017)—Global Forecast, Trend & Analysis—Segmentation by technology [Piezoresistive, Capacitive, Electromagnetic (Reluctance), Resonant Solid State, Optical], Applications [process and non process] and Geography*; Market Research Report 2012

111. C.R. Lowe, J. Blyth, A.P. James, *Interrogation of a sensor*. WO Patent Application 2006008531 A1, January 26, 2006
112. K.L. Johnson, *Contact Mechanics* (Cambridge University Press, Cambridge, 1985)
113. Contact Stresses and Deformation; http://www.mech.utah.edu/~me7960/lectures/Topic7-ContactStressesAndDeformations.pdf. 10 July 2014
114. N. Giordano, *College Physics: Reasoning and Relationships*; Cengage Learning, 2009
115. L.R.G. Treloar, *The Physics of Rubber Elasticity* (Oxford University Press, Oxford, 1975)
116. J. L. Martinez Hurtado, *Elastic holograms. Diverse Engangement: Drawing in the Margins Conference* 2010
117. E. Mihaylova, D. Cody, I. Naydenova, S. Martin, V. Toal, *Diacetone Acrylamide based pressure sensitive photopolymer* No. GB1411640.4, June 31, 2014
118. A.K. Yetisen, The Prospects for Holographic Sensors. *Holographic* Sensors (Springer International Publishing, 2015), pp. 149–162
119. A.K. Yetisen, M.S. Akram, C.R. Lowe, Lab Chip **13**, 2210 (2013)
120. A.K. Yetisen, Point-of-Care Diagnostics. *Holographic Sensors*. (Springer International Publishing, 2015) pp. 1–25
121. M. Akram, R. Daly, F. Vasconcellos, A. Yetisen, I. Hutchings, E.H. Hall, Lab-on-a-chip devices and micro-total analysis systems, in *Applications of Paper-Based Diagnostics*, ed. by J. Castillo-León, W.E. Svendsen (Springer, Berlin, 2015), pp. 161–195
122. N.M. Farandos, A.K. Yetisen, M.J. Monteiro, C.R. Lowe, S.H. Yun, Contact lens sensors in ocular diagnostics. Adv. Healthcare Mater. **4**, 792 (2015)
123. A.K. Yetisen, Holographic metal ion sensors. *Holographic Sensors*. (Springer, Berlin, 2015), pp. 85–99
124. A.K. Yetisen, Y. Montelongo, M.M. Qasim, H. Butt, T.D. Wilkinson, M.J. Monteiro, S.H. Yun, Anal. Chem. **87**, 5101 (2015)
125. A.K. Yetisen, Holographic glucose Sensors. *Holographic Sensors*. (Springer, Berlin, 2015), pp. 101–134
126. N.A. Rakow, A. Sen, M.C. Janzen, J.B. Ponder, K.S. Suslick, Angew. Chem. Int. Ed. **44**, 4528 (2005)
127. S.N. Bhatia, D.E. Ingber, Nat. Biotech. **32**, 760 (2014)
128. L.R. Volpatti, A.K. Yetisen, Trends Biotechnol. **32**, 347 (2014)
129. A.K. Yetisen, L.R. Volpatti, Lab Chip **14**, 2217 (2014)
130. S.-A. Lee, D.Y. No, E. Kang, J. Ju, D.-S. Kim, S.-H. Lee, Lab Chip **13**, 3529 (2013)
131. D. Huh, B.D. Matthews, A. Mammoto, M. Montoya-Zavala, H.Y. Hsin, D.E. Ingber, Science **328**, 1662 (2010)
132. A.K. Yetisen, L. Jiang, J.R. Cooper, Y. Qin, R. Palanivelu, Y. Zohar, J. Micromech. Microeng. **21**, 054018 (2011)
133. C.R. Lowe, C.A.B. Davidson, J. Blyth, A.J. Marshall, A.P. James, *Holographic Sensors and their production*, WO Patent Application 2004081546 A1, September 23, 2004. Lowe, C.R., Davidson, C.A.B., Blyth, J. Marshall, A.J. James, A.P. *Holographic Sensors and their production*, September 23, 2004
134. A.K. Yetisen, J.L. Martinez-Hurtado, F. da Cruz Vasconcellos, M.C.E. Simsekler, M.S. Akram, C.R. Lowe, Lab Chip **14**, 833 (2014)
135. Mobile-Cellular Subscriptions (2014) International Telecommunication Union. Place des Nations: http://www.itu.int
136. A.K. Yetisen, J.L. Martinez-Hurtado, A. Garcia-Melendrez, F. da Cruz Vasconcellos, C.R. Lowe, Sens. Actuators B **196**, 156 (2014)
137. A. Yetisen, Mobile medical applications. *Holographic Sensors*. (Springer, Berlin, 2015), pp. 135–148

Index

M. J. Serpe et al. (eds.), *Photonic Materials for Sensing, Biosensing and Display Devices*, Springer Series in Materials Science 229,
DOI 10.1007/978-3-319-24990-2